

AD-A175 224

Bulletin 56
(Part 1 of 3 Parts)

①

THE SHOCK AND VIBRATION BULLETIN

Part 1
Welcome,
Invited Papers, Shipboard Shock,
Blast and Ground Shock
Shock Testing and Analysis

AUGUST 1986

A Publication of
THE SHOCK AND VIBRATION
INFORMATION CENTER
Naval Research Laboratory, Washington, D.C.



DTIC
ELECTE
DEC 18 1986
S D
E

Office of
The Under Secretary of Defense
for Research and Engineering

Bulletin 56
(Part 1 of 3 Parts)

THE SHOCK AND VIBRATION BULLETIN

AUGUST 1986

A Publication of
THE SHOCK AND VIBRATION
INFORMATION CENTER
Naval Research Laboratory, Washington, D.C.

Accession For	
NTIS GRA&I	<input checked="" type="checkbox"/>
DTIC TAB	<input type="checkbox"/>
Unannounced	<input type="checkbox"/>
Justification	
By _____	
Distribution/	
Availability Codes	
Dist	Avail and/or Special
A-1	

The 56th Symposium on Shock and Vibration was held in Monterey, California, October 22-24 1985. The Naval Postgraduate School and the Defense Language Institute were the hosts.



Office of
The Under Secretary of Defense
for Research and Engineering

PAGES _____
ARE
MISSING
IN
ORIGINAL
DOCUMENT

YIELD EFFECTS ON THE RESPONSE OF A BURIED BLAST SHELTER	161
T.R. Slawson, S.C. Woodson, and S. A. Kiger U.S. Army Engineer Waterways Experiment Station, Vicksburg, MS	
SHELTER RESPONSE IN A SIMULATED 1-MT NUCLEAR EVENT	167
S. C. Woodson, S. A. Kiger, and T. R. Slawson U.S. Army Engineer Waterways Experiment Station, Vicksburg, MS	
VIBRATION CHARACTERISTICS OF A LARGE-SCALE BURIED STRUCTURE	173
F. D. Dallryva and S. A. Kiger U.S. Army Engineer Waterways Experiment Station, Vicksburg, MS	
A "NUMERICAL GAUGE" FOR STRUCTURAL ASSESSMENT	179
T. Krauthammer, Department of Civil and Mineral Engineering University of Minnesota, Minneapolis, MN	
ACTIVE ONE-DIMENSIONAL PROTECTIVE LAYERS	195
S. Ginsburg, Kansas University Transportation Center, Lawrence, KS	
DEPENDENCE OF FREE-FIELD IMPULSE ON THE DECAY TIME OF ENERGY EFFLUX FOR A JET FLOW	203
K.S. Fansler, Ballistic Research Laboratory, Aberdeen Proving Ground, MD	
COMPUTER IMPLEMENTATION OF A MUZZLE BLAST PREDICTION TECHNIQUE; and	213
C.W. Heaps, K. S. Fansler, and E. M. Schmidt Ballistic Research Laboratory, Aberdeen Proving Ground, MD	
INTERIM DESIGN CRITERIA AND ACCEPTANCE TEST SPECIFICATIONS FOR BLAST-RESISTANT WINDOWS	231
G. E. Meyers, Naval Civil Engineering Laboratory, Port Hueneme, CA	

Shock Testing and Analysis

SHOCK RECONSTRUCTION FROM THE SHOCK SPECTRUM	273
C. T. Morrow, Consultant, Encinitas, CA	
THE SHOCK RESPONSE SPECTRUM AT LOW FREQUENCIES	279
D. O. Smallwood, Sandia National Laboratories, Albuquerque, NM	
RELATIVE CONSERVATISM OF DROP TABLE AND SHAKER SHOCK TESTS	289
T. J. Baca and T. D. Blacker, Sandia National Laboratories, Albuquerque, NM	

PAPER APPEARING IN PART 2

Modal Test and Analysis

MULTIPLE TESTS CONCEPT FOR IMPROVED VALIDATION OF LARGE SPACE STRUCTURE MATHEMATICAL MODELS
B.K. Wada, C-P Kuo, and R.J. Glaser, Jet Propulsion Laboratory California Institute of Technology, Pasadena, CA
THE ALGORITHM AND APPLICATION OF A NEW MULTI-INPUT-MULTI-OUTPUT MODAL PARAMETER IDENTIFICATION METHOD
L. Zhang, Nanjing Aeronautical Institute, Nanjing, China and H. Kanda Yanmar Diesel Engine Co., Osaka, Japan
MODAL PARAMETER IDENTIFICATION USING ADAPTIVE DIGITAL FILTERS
B.H. Wendler, TRW Space and Technology Group, Redondo Beach, CA
SAFE/DAE: MODAL TEST IN SPACE
T.E. Nesman and D.K. Reed, Marshall Flight Center, Huntsville, AL

CONTENTS

PAPERS APPEARING IN PART I

Welcome

WELCOME	1
Dr. Paul J. Marto, Distinguished Professor and Chairman Department of Mechanical Engineering, Naval Postgraduate School, Monterey, CA	

Partial contents:

Invited Papers

SOLID MECHANICS PROGRAM AT ONR:	3
Alan S. Kushner, Solids and Structures Group, Office of Naval Research, Arlington, VA and Benjamin Whang, David Taylor Naval Ship Research and Development Center, Bethesda, MD	
ARMY RESEARCH IN SHOCK MECHANICS:	21
John F. Mescall and Richard Shea, U.S. Army Materials, Technology Laboratory, Watertown, MA	
AIR FORCE BASIC RESEARCH IN DYNAMICS AND CONTROL OF LARGE SPACE STRUCTURES:	39
Anthony K. Amos, Bolling Air Force Base, Washington, DC	
STATE-OF-THE-ART ASSESSMENT OF STRUCTURAL DYNAMIC RESPONSE ANALYSIS METHODS (DYNAS):	59
David J. Ewins and M. Imregun, Imperial College of Science and Technology London, UK	
THE DYNAS SURVEY - PART 2/A PARTICIPANT'S VIEW:	91
R.W. Windell, Admiralty Research Establishment, Portland, Dorset, UK	

Shipboard Shock

COMPUTATION OF EXCITATION FORCES USING STRUCTURAL RESPONSE DATA	101
D. G. Dubowski and B. J. Dobson, Royal Naval Engineering College Manadon, Plymouth, Devon, UK	
UNDERWATER SHOCK TRIALS ON A PLAIN, UNREINFORCED CYLINDER:	107
R. J. Randall, Admiralty Research Establishment, Portland, Dorset, UK	
INVESTIGATION INTO THE EFFECTS OF USING DETONATING CORD TO REMOVE A CONVENTIONAL PROPELLER FROM A WATER BORNE SURFACE SHIP:	121
J. H. Strandquist III and Y. S. Shin, Department of Mechanical Engineering Naval Postgraduate School, Monterey, CA	

Blast and Ground Shock

DYNAMIC RESPONSE OF ARMOR PLATE TO NON-PENETRATING PROJECTILE IMPACT:	135
W.S. Walton, U.S. Army Combat Systems Test Activity, Aberdeen Proving Ground, MD	
EVALUATION OF SHOCK RESPONSE IN COMBAT VEHICLES: - - SCALE MODEL RESULTS:	151
J.F. Unruh, D. J. Pomering, and D.C. Scheidt, Southwest Research Institute, San Antonio, TX	

Testing Techniques

RANDOM VARIATION OF MODAL FREQUENCIES—EXPERIMENTS AND ANALYSIS

T.L. Paez, L.J. Branstetter, and D.L. Gregory, Sandia National Laboratories
Albuquerque, NM

STRUCTURAL DEGRADATION OF IMPACTED GRAPHITE/EXPOXY LAMINATES

D. Liu, Michigan State University, East Lansing, MI and C.T. Sun and
L.E. Malvern, University of Florida, Gainesville, FL

UPDATING RAIL IMPACT TEST METHODS

R.A. McKinnon, U.S. Army Combat Systems Test Activity, Aberdeen Proving Ground, MD

Machinery Dynamics

PREDICTION OF NATURAL FREQUENCIES OF FLEXIBLE SHAFT-DISC SYSTEM

P. Bremond, G. Ferraris, and M. Lalanne, Institut National Des Sciences
Appliquees, Villeurbanne, France

IMPLEMENTATION OF ACTION FORCE CONTROL FOR ROBOTS SUBJECT TO DYNAMIC LOADING

R. Hollowell, R. Guile, P. FitzPatrick, and S. Foley, United Technologies
Research Center, East Hartford, CT

FORCE MAGNITUDE AND ANGULAR VELOCITY FLUCTUATION REDUCTION IN A SPRING-RESTRAINED, FLEXIBLY-SUPPORTED FOUR-BAR MECHANICAL LINKAGE

R.A. McLaughlan, Texas A&I University, Kingsville and S.H. Hong
Texas Tech University, Lubbock, TX

BLADE DAMPING MEASUREMENTS IN A SPIN RIG WITH NOZZLE PASSING EXCITATION SIMULATED BY ELECTROMAGNETS

J.S. Rao, Embassy of India, Washington, DC, and K. Gupta and N. Vyas
Indian Institute of Technology, New Delhi, India

A NEW APPROACH FOR GEARBOX MODELLING IN FINITE ELEMENT ANALYSES OF TORSIONAL VIBRATION OF GEAR BRANCHED PROPULSION SYSTEMS

H.F. Tavares, Cepstrum Engenharia Ltda., Rio de Janeiro, Brazil and V. Prodonoff,
PETROBRAS Research Center, Rio de Janeiro, Brazil

Isolation and Damping

A GRAPHICAL METHOD OF DETERMINING THE RESPONSE OF THE CASCADED TWO DEGREE OF FREEDOM SYSTEM

G.M. Hieber, Hieber Engineering, Watchung, NJ

TEMPERATURE SHIFT CONSIDERATIONS FOR DAMPING MATERIALS

L. Rogers, Air Force Wright Aeronautical Laboratories, Wright-Patterson AFB, OH

EFFECTIVENESS OF ON-OFF DAMPER IN ISOLATING DYNAMICAL SYSTEMS

S. Rakheja and S. Sankar, Concordia University, Montreal, Canada

Structural Dynamics

BUCKLING OF RING-STIFFENED CYLINDRICAL SHELLS WITH DYNAMIC LOADS

T.A. Butler and W.E. Baker, Los Alamos National Laboratory, Los Alamos, NM
and C.D. Babcock, California Institute of Technology, Pasadena, CA

FORCED VIBRATIONS OF STRINGER STIFFENED DAMPED SANDWICH PANEL

N. Kavi and N.T. Asnani, Indian Institute of Technology, Delhi, India

STRUCTURAL DYNAMIC REANALYSIS USING RITZ VECTORS

L. Kitis, University of Central Florida, Orlando, FL and W.D. Pilkey, University of Virginia, Charlottesville, VA

Fatigue and Acoustics

PREDICTION OF METAL FATIGUE USING MINER'S RULE

H.H.E. Leipholz, University of Waterloo, Waterloo, Ontario, Canada

OPTIMIZATION OF AEROSPACE STRUCTURES SUBJECTED TO RANDOM VIBRATION AND FATIGUE CONSTRAINTS

V.K. Jha, Spar Aerospace Limited, Ste. Anne de Bellevue, Quebec, Canada
and T.S. Sankar and R.B. Bhat, Concordia University, Montreal, Quebec, Canada

EVALUATION OF VIBRATION SPECIFICATIONS FOR STATIC AND DYNAMIC MATERIAL ALLOWABLES

S.P. Bhatia and J.H. Schmidt, Northrop Corporation, Hawthorne, CA

SUPERSONIC FLOW INDUCED CAVITY ACOUSTICS

L.L. Shaw, Air Force Wright Aeronautical Laboratories, Wright-Patterson AFB, OH

PAPERS APPEARING IN PART 3

Invited Papers — Plenary A

PYROTECHNIC SHOCK

Dr. Sheldon Rubin, The Aerospace Corporation, Los Angeles, CA

VIEWS OF THE WORLD OF PYROTECHNIC SHOCK

Mr. Charles Moening, The Aerospace Corporation, Los Angeles, CA

Pyrotechnic Shock

THE PRE-PULSE IN PYROSHOCK MEASUREMENT AND ANALYSIS

A. E. Galef, TRW Electronics and Defense, Redondo Beach, CA

SUPER*ZIP (LINEAR SEPARATION) SHOCK CHARACTERISTICS

K. Y. Chang and D. L. Kern, Jet Propulsion Laboratory,
California Institute of Technology, Pasadena, CA

NUMERICAL SIMULATION OF ATLAS-CENTAUR STAGE-SEPARATION SHAPED CHARGE FIRING AND STRUCTURAL RESPONSE

S. Hancock, D. Davison, J. Gordon, and P. Chao, Physics International Company, San Leandro, CA and N. Viste and J. Weber, General Dynamics Convair Division, San Diego, CA

Pyrotechnic Shock Workshop

CHAIRMAN'S REMARKS — SESSION I

D. L. Van Ert, The Aerospace Corporation, El Segundo, CA

CHAIRMAN'S REMARKS — SESSION II

G. Wasz, TRW, San Bernardino, CA

A VIBROACOUSTIC DATABASE MANAGEMENT SYSTEM AND ITS APPLICATION FOR A PYROSHOCK DATABASE

W. Henricks and Y. A. Lee, Lockheed Missiles and Space Co., Inc., Sunnyvale, CA

STATE-OF-THE-ART ACCELEROMETER CHARACTERISTICS FOR PYROTECHNIC SHOCK MEASUREMENT

J. Wilson, Consultant, San Juan Capistrano, CA

ZERO-SHIFTED ACCELEROMETER OUTPUTS

A. E. Galef, TRW Electronics and Defense, Redondo Beach, CA

QUESTIONABLE EFFECTS OF SHOCK DATA FILTERING

P. Strauss, Rocketdyne, Canoga Park, CA

COMPARISON OF RESPONSE FROM DIFFERENT RESONANT PLATE SIMULATION TECHNIQUES

R. E. Morse, TRW Electronics and Defense, Redondo Beach, CA

THE CONTROLLED RESPONSE OF RESONATING FIXTURES USED TO SIMULATE PYROSHOCK ENVIRONMENTS

N. Davie, Sandia National Laboratories, Albuquerque, NM

MULTI-AXIS TRANSIENT SHOCK SIMULATION USING MECHANICAL PULSE GENERATORS

F. B. Safford, Agbabian Associates, El Segundo, CA

SUMMARY OF TESTING TECHNIQUES

D. Powers, McDonnell Douglas Astronautics, Huntington Beach, CA

SESSION CHAIRMEN AND COCHAIRMEN

56th Shock and Vibration Symposium
October 22-24, 1985, Monterey, CA

<u>Date</u>	<u>Session Title</u>	<u>Chairmen</u>	<u>CoChairmen</u>
Tuesday 22 October, A.M.	Opening Session	Dr. Young S. Shin, Naval Postgraduate School, Monterey, CA	Dr. J. Gordan Showalter Shock and Vibration Information Center, Naval Research Laboratory, Washington, DC
Tuesday 22 October, P.M.	Pyrotechnic Shock/ Shipboard Shock	Mr. Henry N. Luhrs, TRW Electronics Systems, Redondo Beach, CA	Dr. John DeRuntz, Lockheed Palo Alto Research Laboratory, Palo Alto, CA
Tuesday 22 October, P.M.	Blast and Ground Shock	Mr. James D. Cooper, Defense Nuclear Agency, Washington, DC	Dr. Anatole Longinow, Wiss, Janney, Elstner Associates, Inc. Northbrook, IL
Wednesday 23 October, A.M.	Plenary A	Dr. J. Gordan Showalter, Shock and Vibration Information Center, Naval Research Laboratory Washington, DC	
Wednesday 23 October, A.M.	Pyroshock Workshop, Session I, Data Interpretation, Design and Test Requirements	Mr. Daniel Van Ert, The Aerospace Corporation, El Segundo, CA	Mr. Henry N. Luhrs, TRW Electronics Systems, Redondo Beach, CA
Wednesday 23 October, A.M.	Modal Test and Analysis	Dr. Robert Coppolino, MacNeal Schvender Corporation, Los Angeles, CA	Mr. Strether Smith, Lockheed Palo Alto Research Laboratory, Palo Alto, CA
Wednesday 23 October, A.M.	Testing Techniques	Mr. Steven Tanner, Naval Weapons Center, China Lake, CA	Mr. Peter Bouclin, Naval Weapons Center, China Lake, CA

Wednesday 23 October, P.M.	Pyroshock Workshop, Session II, Instrumentation, Data Acquisition, and Data Bank	Mr. Glen Wasz, TRW, San Bernardino, CA	Mr. Paul Strauss, Rocketdyne, Canoga Park, CA
Wednesday 23 October, P.M.	Pyroshock Workshop, Session III, Simulation and Testing	Mr. Dan Powers, McDonnell Douglas Aeronautics, Huntington Beach, CA	Mr. Robert E. Morse, TRW, Redondo Beach, CA
Wednesday 23 October, P.M.	Machinery Dynamics	Mrs. Milda Z. Tamulionis, Vibration Institute, Clarendon Hills, IL	Mr. Robert L. Leon, Liberty Technology Center, Inc., Conshohocken, PA
Wednesday 23 October, P.M.	Isolation and Damping	Dr. Bhakta B. Rath, Naval Research Laboratory, Washington, DC	Mr. Ahid Nashif, Anatrol Corporation, Cincinnati, OH
Thursday 24 October, A.M.	Plenary B	Mr. Rudolph H. Volin, P.E., Shock and Vibration Information Center, Naval Research Laboratory, Washington, DC	
Thursday 24 October, A.M.	Structural Dynamics	Dr. John L. Gubser, McDonnell Douglas Aeronautics Company, St. Louis, MO	Mr. David W. Gross, RCA Astroelectronics, Princeton, NJ
Thursday 24 October, A.M.	Fatigue, Acoustics and Fluid Flow	Mr. Leonard L. Shaw, Air Force Wright Aeronautical Laboratories, Wright-Patterson Air Force Base, OH	
Thursday 24 October, P.M.	Shock Testing and Analysis	Mr. John D. Favour, Boeing Aerospace Company, Seattle, WA	Mr. William J. Kacena, Martin Marietta Denver Aerospace, Denver, CO
Thursday 24 October, P.M.	Short Discussion Topics	Mr. Howard Camp, U.S. Army Electronics Research and Development Command, Ft. Monmouth, NJ	Mr. Tommy Dobson, 6585 Test Group, Holloman Air Force Base, NM

WELCOME

Dr. Paul J. Marto
Distinguished Professor and Chairman
Department of Mechanical Engineering
Naval Postgraduate School
Monterey, CA

On behalf of Rear Admiral Robert H. Shumaker, the Superintendent of the Naval Postgraduate School, I welcome all of you to our beautiful Monterey Peninsula. I am very honored to have the opportunity to be present at this opening session, and to represent the Naval Postgraduate School which is serving as co-host for this 56th Shock and Vibration Symposium.

For over 75 years, the Postgraduate School has been serving the U.S. Navy by providing graduate education for commissioned officers. From its modest beginning in 1909 on the Naval Academy campus in Annapolis, with 10 officer students and three faculty, the School's programs have expanded dramatically in response to the growing needs of the Navy and the Department of Defense. Today, with an enrollment of over 1,600 students, including representatives from all the U.S. Armed Services and from more than 25 allied countries, the School has established a strong academic reputation. Admiral James D. Watkins, Chief of Naval Operations and a mechanical engineering graduate from this institution, has said: "I consider the investment in graduate education of

selected officers to be a strategic requirement for the Navy. With today's technological, managerial and political/economic complexities, the need for graduate-level expertise has never been greater."

We, therefore, appreciate the significant importance of research in achieving and maintaining technological superiority, and encourage our faculty to participate in conferences such as this one, where the latest ideas and research results may be shared with colleagues from other universities, from industry, other branches of the government and, I'm happy to say, with our friends from other countries. Of course, the subject of shock and vibration plays a fundamental role in the welfare of the Department of Defense, and I commend the organizers of this conference, and all of you present, for your continued dedication to uphold the high standards established for this Symposium over the years. In closing, I wish all of you a professionally rewarding experience and an enjoyable visit with us. Thank you.

INVITED PAPERS

SOLID MECHANICS PROGRAM AT ONR

Alan S. Kushner
Solids and Structures Group
Office of Naval Research
Arlington, VA

(Presented by Ben Whang, Head
Submarine Survivability Group
David Taylor Naval Ship R&D Center)

This morning, my task is to tell you the ONR's philosophy on basic research, and the contents of the current Solid Mechanics Program, and, by doing so, I hope to give you a flavor for the type of research ONR is interested in supporting, and to stimulate you to come up with new directions in Solid Mechanics, related to Shock and Vibration.

Within ONR, the Solid Mechanics Program is in the Engineering Sciences Directorate. The Program has close ties, through jointly funded interdisciplinary programs, with two other Programs in the Mechanics Division, namely, the Fluid Mechanics and Propulsion & Energetics, in addition to the materials Division (Fig. 1). At ONR, the basic philosophy is to support fundamental research which provides an expanded scientific basis for an enhanced understanding of a field (Fig. 2). Specifically, within the Solid Mechanics Program, the emphasis is in understanding the behavior of solids and structures over a wide range of length and time scales. Such an understanding and a unification of the interplay between the physical processes taking place at various scales is essential, if a sound physically rather than empirically based prediction of mechanical behavior is to be established.

The Solid Mechanics Program is divided into four subareas as shown below:

Fundamental Solid Mechanics
Failure Mechanics
Fluid-Structure Interaction
Structural Mechanics.

I will briefly discuss each of these subareas.

In the Fundamental Solid Mechanics area, the objective is to understand the thermo-mechanical behavior of all current and future classes of materials (Fig. 3). The importance of the scale of response is clearly seen in this area. A growing part of the program is in

Micro-mechanics. The emphasis here is in the mechanistic description of damage in the materials, for example, grain boundary cracking and shear band formation. In addition, research is supported to establish theoretical framework to incorporate these micro-mechanical mechanisms into effective or average macro-scale descriptions of damage, eventually leading to improved constitutive equations. Research in this area is critically important in the Shock & Vibration area, since it provides a framework for the description of material damage under shock conditions. As an example, there is a study to see whether the Gurson-Rice model for ductile void initiation and growth, coupled to a J_2 Corner Theory of Plasticity, can predict the dynamic tearing in a Charpy Impact Test.

The Failure Mechanics area encompasses fracture mechanics and NDE (Fig. 4). This area is to understand and predict the failure processes, which occur on the macroscopic and/or the structural level. A major thrust is in the concept of material toughness under both static and dynamic conditions. Crack propagation under shock loading, as well as structural fatigue under vibration are the areas of interest here. The theoretical foundations for wave transmission and scattering in composites as a basis for NDE is an expanding part of the program.

The Fluid-Structure Interaction area continues to undergo major changes in direction (Fig. 5). A major new thrust is aimed at establishing an in-depth understanding of the interfacial mechanics of deforming structure-fluid systems through refining interface representation, including full-coupled computational capability, and controlling structural response to acoustic/fluid-dynamic loading, which includes active and passive coatings.

To address these issues the classical structural acoustics and structural shell theories cannot

be used. Pressure, shear stress, and velocity must be primitive variables in the basic theories. This area will be discussed in more detail, later.

The final area is Structural Mechanics (Fig. 6). A major goal is to establish a capability to control the response modes of structures. The emphasis is in establishing computational techniques and in understanding structural response transitions such as deformation localization and buckling or collapse transitions. The question is what are the conditions which cause static buckling processes to transition to dynamically unstable processes and the ultimate transition to collapse? An exciting new class of structural materials is the piezo-electric composites which may play a critical role in future active systems for controlling fluid-structure interaction. Two examples of the type of research supported by ONR are Fluid Structure Interaction and Micro-mechanics of Composites.

A new interdisciplinary thrust in Fluid-Structure Interaction is jointly supported by Solid Mechanics and Fluid Mechanics Programs and the Materials Division at ONR. The issue is an in-depth understanding for the generation of stress and velocity fields at the interface of layered solids and turbulent flow fields (Fig. 7). All three components of both surface stress and surface velocity at the interface must be predictable. The Fluid-Structure Interaction capability just described is essential in advancing the state-of-the-art in many critical areas for the Navy (Fig. 8). Currently, sonar search speeds for ships and submarines are speed-limited because of increasing flow noise with speed. A way around this would be to separate sound inputs by their source, acoustic radiation, or turbulent flow. Current sensors cannot do this because they respond to surface pressures in a quasi-statically deforming mode. Because the velocity fields associated with acoustic and turbulent pulses are quite different, a dynamically deforming sensor can serve as a source discriminator for pressure pulse sources.

The specific objectives of the program are listed in Figure 9. The first three involve interface responses, and the last three combine the Mechanics and Materials thrusts to tailor structural coating systems to obtain optimum responses. The response optimization can address acoustic isolation and identification issues, and possibly at the same time, address flow drag reduction issues. The technical issues listed in Figure 10 point out a significant aspect of this program. It is not a standard interdisciplinary research program, which attempts to merge the state-of-the-art technologies in disparate fields. Rather, each aspect of the program, that is, Solid Mechanics, Fluid Mechanics, and Materials Science, involves critical forefront research in its own field. For example, the third item listed in Figure 10, the deterministic descriptions of turbulent

flows are just now emerging for non-interacting fields with clean geometries. In attempting to isolate acoustic pulses from turbulent flow noise, an important research question is whether a critical small eddy structure can be identified and its evolution predicted (Fig. 11). This critical eddy state would correspond to the development of a turbulent event, with noise sufficient to mask the desired acoustic sound level. If such a critical state could be identified, active surface materials such as flexible piezo-electric composites could be used to control the turbulence!

The use of new materials such as the piezo-electric composites in stress wave applications poses many new challenges to the solid mechanics community. In addition to their electro-mechanical coupling, these materials are composites made of composites. Figure 12 shows a multi-level concept in which a matrix of piezo-electric composites is embedded in a composite.

The next example deals with Micro-mechanics of Composites. It was mentioned earlier that the key element in the program is the linking together of response mechanisms at different scales. To show how this issue is addressed, a new thrust in theoretical and experimental research in composites will be considered - specifically, the nonlinear, multivariable theory, and an ultra high-resolution optical technique (Fig. 13). The computational effort has just begun, and it is not yet ready for presentation.

For the Nonlinear Multivariable Field Representation in Composites, consider a uniaxially reinforced composite as shown on the left in Figure 14. Classically, the properties are based on the uniform deformation in a representative unit cell. The multivariable cell displacement field shown at the right in Figure 14, not only allows for more accurate description of material nonlinearities such as matrix plasticity, but also allows description of local damage states such as fiber matrix separation in a consistent manner. Experimentally, an ultra high-resolution optical technique using the Subwavelength Moire' Interferometry has shown great promise. An argon laser beam, with a wavelength of 20 micro-inches, can give a fringe sensitivity for displacement contours of 16 micro-inches. At the right in Figure 15, a fringe pattern for the U-displacement in a three-point laminated beam is shown. The bottom of Figure 15 clearly shows the delineation of shear strain concentrations in the resin-rich zones between each layer. The current research is to extend the fringe sensitivity down to 0.3 micro-inches per fringe, and a time resolution of one micro-inch per frame! This will produce experimental data necessary for the higher-order continuum theories for composites.

In summary, a brief description has been attempted on the ONR's philosophy of basic

research and the current Program in Solid Mechanics, along with a few examples. Much of it is relevant to the Shock and Vibration Community, and ample opportunities exist for this community to define exciting, new, basic research directions. The Program is continually evolving and expanding. ONR solicits your ideas!



ONR TECHNICAL ORGANIZATION RELATIONSHIP TO MECHANICS DIVISION (CODE 432)

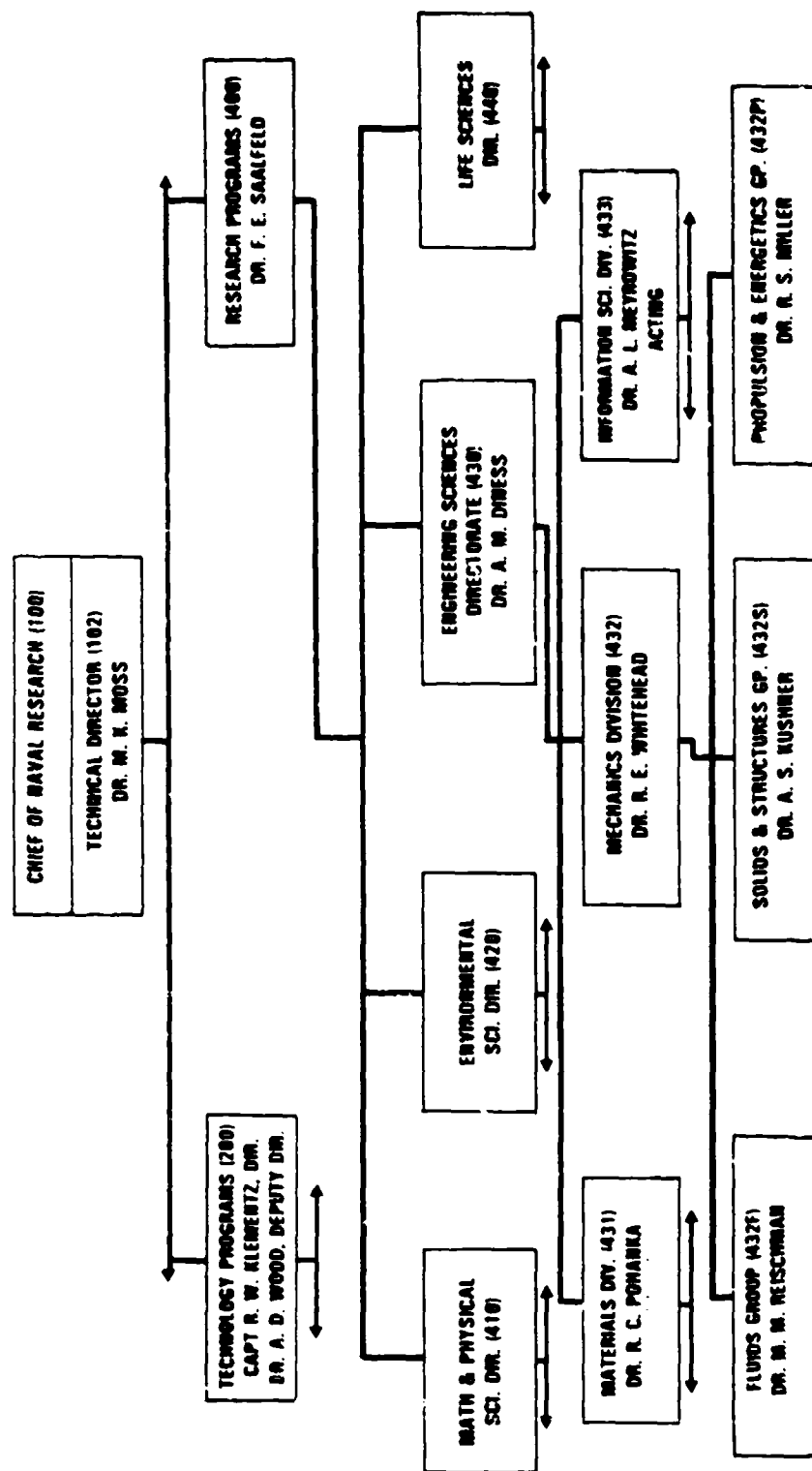


Fig. 1 - ONR technical organization

PROGRAM PHILOSOPHY:

**EXPAND THE BASIS FOR UNDERSTANDING
THE MECHANICAL BEHAVIOR OF ALL
CLASSES OF SOLID MATERIALS AND
STRUCTURES AT THE SCALES APPROPRIATE
TO THE PHENOMENA OF INTEREST.**

Fig. 2 — Solid mechanics program philosophy



MECHANICS DIVISION FUNDAMENTAL SOLID MECHANICS PROGRAM

OBJECTIVE

- **FUNDAMENTAL UNDERSTANDING OF NONLINEAR THERMOMECHANICAL DEFORMATION AND FAILURE MECHANISMS**
 - MECHANISTIC RESPONSE OF ADVANCED MATERIALS
 - RELATIONSHIPS ACROSS VARIOUS RESPONSE SCALES

AREAS OF INTEREST

- **MICROMECHANICS (E.G., GRAIN/VOID SCALE) REPRESENTATION**
 - HOMOGENIZATION, LOCALIZATION AND DAMAGE INITIATION/PROGRESSION
- **CONSTITUTIVE EQUATION (MACROSCALE) REPRESENTATION**
 - THREE-DIMENSIONAL, NON-PROPORTIONAL, NON-ISOTHERMAL AND HIGH RATE PHENOMENA
- **EFFECTIVE PROPERTY REPRESENTATION FOR STRUCTURED MATERIALS**
 - LOCAL MATRIX, FIBER, INTERFACE PHENOMENA FOR COMPOSITES
 - RELATION BETWEEN LOCAL PHENOMENA AND OVERALL STRESS LEVEL / DEFORMATION RESPONSE

Fig. 3 — Fundamental solid mechanics program



MECHANICS DIVISION FAILURE MECHANICS PROGRAM

OBJECTIVE

- UNDERSTAND THE MECHANICAL PROCESSES OF CRACK INITIATION AND GROWTH, AND THEIR DETECTION, IN STRUCTURAL MATERIALS
- PROVIDE BASIS TO UNDERSTAND AND CONTROL STRUCTURAL LIFE CYCLE BEHAVIOR (FATIGUE)

AREAS OF INTEREST

- STABLE CRACK GROWTH
 - MICROSCALE PHENOMENA IN PROCESS ZONE
 - FINITE DEFORMATIONS, NONLINEARITIES AND CREEP EFFECTS
- DYNAMIC FRACTURE
 - INFLUENCE OF DUCTILITY
 - DEFINITION OF TOUGHNESS
- THEORETICAL BASIS FOR NDE TECHNIQUES
 - ULTRASONICS, ACOUSTOELASTICITY AND ACOUSTIC EMISSION

Fig. 4 — Failure mechanics program



MECHANICS DIVISION FLUID/STRUCTURE INTERACTIONS PROGRAM

OBJECTIVE

- UNDERSTAND AND CONTROL COUPLED HYDRODYNAMIC, HYDROACOUSTIC AND MATERIAL/STRUCTURAL DYNAMIC PHENOMENA IN THE FLUID—SOLID INTERFACE REGION

AREAS OF INTEREST

- REFINED INTERFACE REGION REPRESENTATION
 - FLUID/SOLID INTERFACIAL COMPATIBILITY
 - HIGH RESOLUTION INTERFACE DIAGNOSTICS
 - FULLY COUPLED COMPUTATIONAL CAPABILITY
- NON-INTERFACE FLUID RESPONSE TO INTERFACE GEOMETRY FLUCTUATIONS
- CONTROLLED MATERIAL/STRUCTURE RESPONSE TO ACOUSTIC/FLUID DYNAMIC LOADING
 - LAYERED ELASTIC/VISCOELASTIC STRUCTURES
 - MATERIAL PROPERTY SPECIFICATION AND SYNTHESIS FOR DESIRED RESPONSE
 - ACTIVE AND PASSIVE COATINGS

Fig. 5 — Fluid-Structure interaction program



MECHANICS DIVISION STRUCTURAL MECHANICS PROGRAM

OBJECTIVE

- **UNDERSTAND AND CONTROL COMPLEX VIBRATION, DEFORMATION AND FAILURE MODES AS APPROPRIATE FOR STRUCTURAL AND MECHANICAL SYSTEMS SUBJECT TO TIME-DEPENDENT THERMOMECHANICAL LOADS**

AREAS OF INTEREST

- **IMPROVED SOLUTION TECHNIQUES AND COMPUTATIONAL SCHEMES**

- NON-CLASSICAL CONSTITUTIVE EQUATIONS AND HIGHLY NONLINEAR RESPONSE
- PROPER ERROR MEASURES
- SHELL THEORY COMPATIBLE WITH COMPUTATIONAL METHODS

- **DAMAGE MECHANISMS AND TRANSITION TO FAILURE**

- LOCAL STRUCTURAL DEFORMATION CONCENTRATION
- BUCKLING TRANSIENT AND TRANSITION TO COLLAPSE

- **STRUCTURAL ACOUSTICS IN A HYDRODYNAMIC ENVIRONMENT**

- WAVE MECHANICS OF SOUND GENERATION, PROPAGATION AND ISOLATION
- FLEXIBLE PIEZOELECTRIC COMPOSITES

Fig. 6 — Structural mechanics program

CRITICAL ISSUE:

**ADVANCES IN UNDERSTANDING THE
ACOUSTICAL BEHAVIOR OF FUTURE NAVAL
SYSTEMS WILL REQUIRE AN IN-DEPTH
UNDERSTANDING AND PREDICTIVE THEORY
FOR THE GENERATION OF STRESS AND
VELOCITY FIELDS AT THE INTERFACE OF
LAYERED SOLIDS IN COMPLEX STRUCTURAL
CONFIGURATIONS AND TURBULENT ,
HYDRODYNAMIC FLOW FIELDS**

Fig 7 - Critical issue in understanding the acoustical
behavior of future naval systems

NAVY NEED:

- **SEPARATION OF TURBULENT NOISE & ACOUSTIC SIGNALS**
- **UNIFIED SOUND/VIBRATION ABSORPTION & ISOLATION**
- **ACOUSTICALLY ACTIVE STRUCTURES**
- **ACTIVE HYDRODYNAMIC CONTROL**

Fig. 8 — Research needs to understand the acoustical behavior of future naval systems

OBJECTIVES:

- **THEORETICAL/NUMERICAL THEORY FOR STRESS & VELOCITY AT INTERFACE**
- **COUPLING OF INTERFACE ZONE WITH BULK SOLID & FLUID FIELDS**
- **REFINED EXPERIMENTAL TECHNIQUES FOR MEASURING INTERFACIAL FRICTIONAL RESPONSE**
- **MICROMECHANICALLY BASED CONSTITUTIVE LAWS CAPABLE OF DESIGNING COMPOSITES FOR DESIRED RESPONSE**
- **MATERIAL PROCESSING SCIENCE FOR COMPOSITES**
- **MATERIALS SYSTEMS TAILORING FOR COATINGS**

Fig. 9 — Objectives of interdisciplinary fluid-structure interaction research program

ISSUES:

- **CAN BOTH THE LOCAL AND GLOBAL RESPONSE BE SOLVED FOR SIMULTANEOUSLY?**
- **DO INTERFACIAL STRESSES & VELOCITIES DUE TO SOLID-FLUID INTERACTION RESOLVE THE SOURCE (TURBULENCE OR ACOUSTIC) OF PRESSURE PULSES?**
- **ARE DETERMINISTIC DESCRIPTIONS OF INTERACTIVE TURBULENT FIELDS ACHIEVABLE VIA ASYMPTOTIC THEORIES?**
- **CAN OPTIMAL COATINGS BE SYNTHESIZED UTILIZING ANISOTROPY, NONLINEAR VISCOELASTICITY, AND PIEZO-ELECTRICITY?**
- **CAN MATERIAL SYSTEMS BE SYNTHESIZED FOR PRESCRIBED FLUID-SOLID INTERACTION?**

Fig. 10 — Technical issues surrounding interdisciplinary fluid-structure interaction research program

MECHANICS OF THE SOLID—FLUID INTERFACE

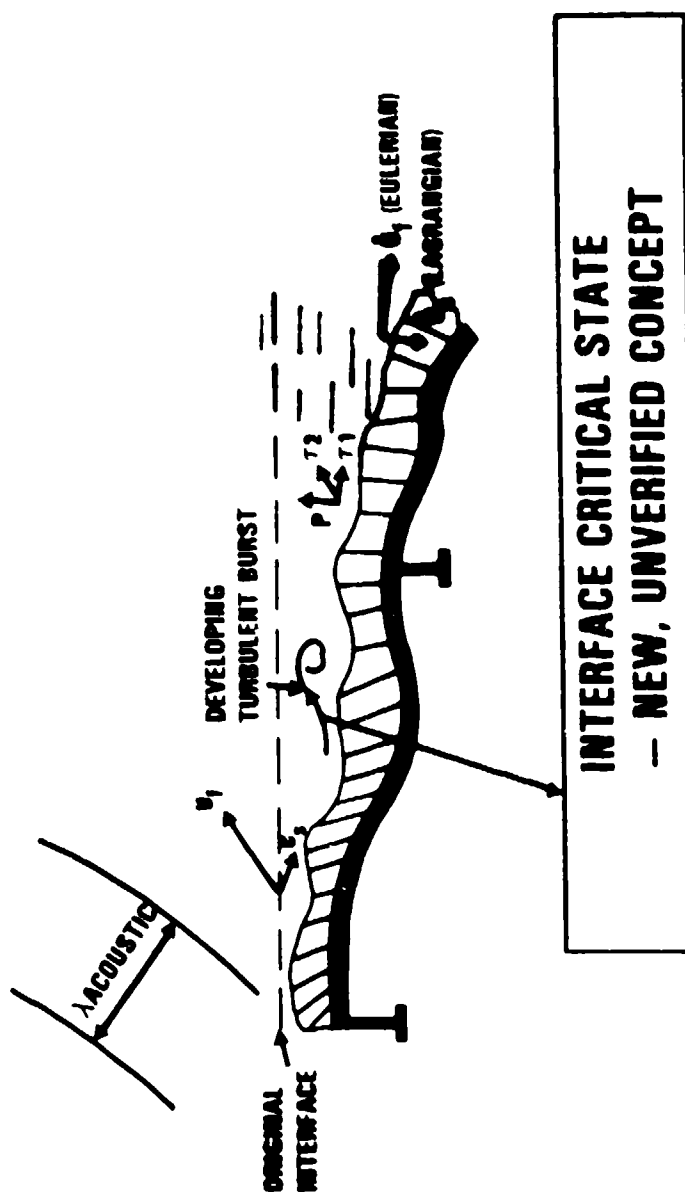


Fig. 11 — Identification of critical small eddy structures

NEW MATERIALS MAY REQUIRE MULTILEVEL COMPOSITES THEORY WITH LOCAL AND GLOBAL FLUID INTERACTION UNDERSTANDING

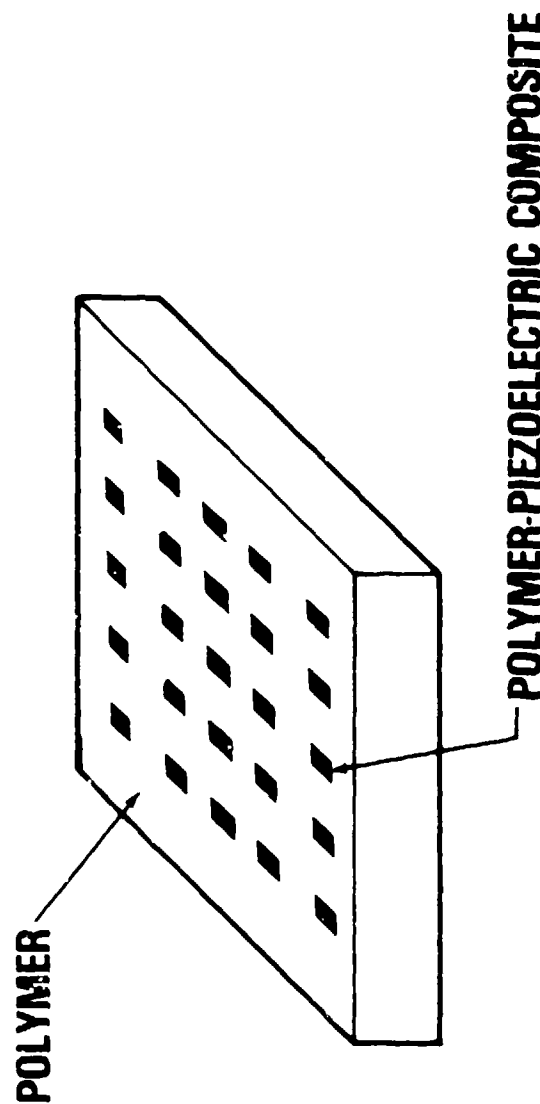


Fig. 12 — Matrix of piezo-electric composites embedded in a composite material

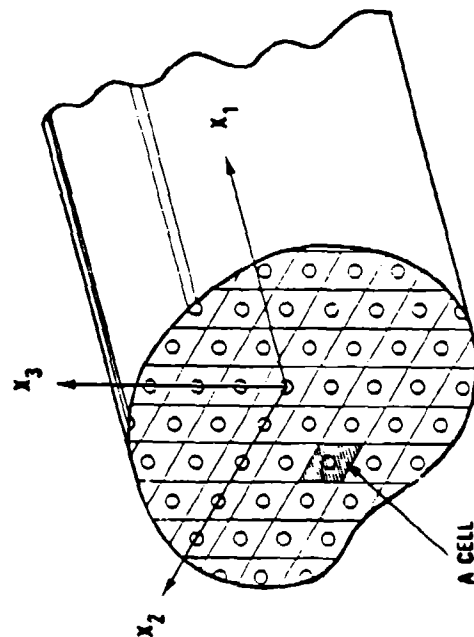
LOCAL DEFORMATION FIELDS EXHIBITING HIGHER ORDER VARIATIONS

- **THEORETICAL — HOMOGENIZATION THEORY AND
MICROMECHANICS**
- **EXPERIMENTAL — ULTRA HIGH RESOLUTION
OPTICAL TECHNIQUES SUCH
AS SUBWAVELENGTH MOIRE
INTERFEROMETRY**
- **COMPUTATIONAL — ERROR MEASURES FOR
NONLINEAR PROBLEMS
AND ADAPTIVE MESH
STRATEGIES**

Fig. 13 — Research in micromechanics of composite materials

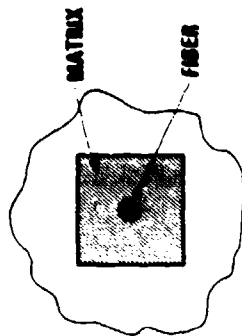
MULTIVARIABLE FIELD REPRESENTATION IN COMPOSITES

UNIAXIALLY REINFORCED COMPOSITE

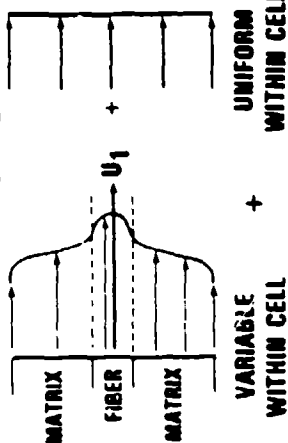


CLASSICAL CONTINUUM PROPERTIES
OF COMPOSITES ARE BASED ON
ASSUMPTION OF UNIFORM DEFORMATION
IN REPRESENTATIVE UNIT CELL

TYPICAL UNIT CELL



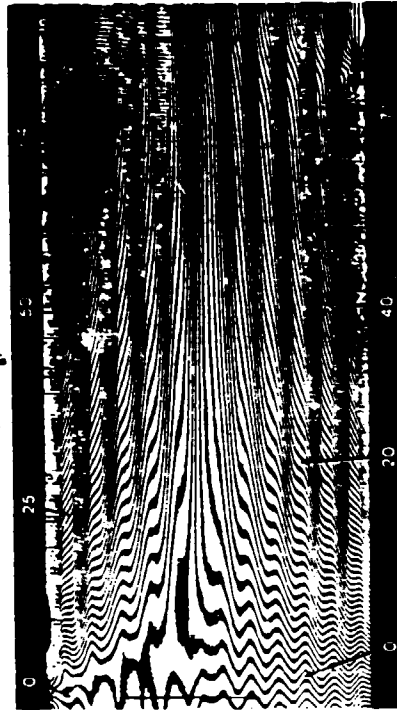
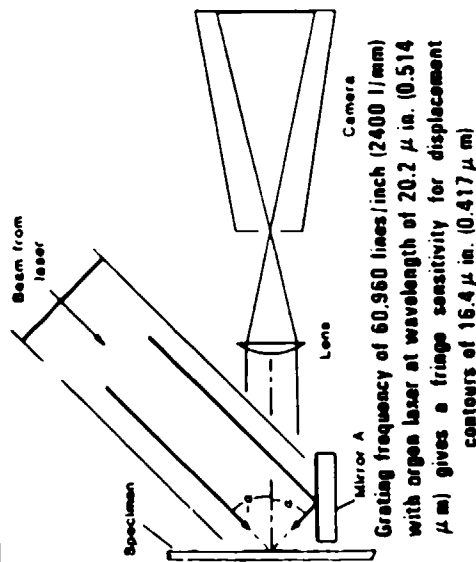
MULTIVARIABLE CELL DISPLACEMENT FIELD
NORMAL TO $x_3 - x_2$ PLANE



THE INCLUSION OF LOCALLY VARIABLE CELL
DISPLACEMENT FIELDS FACILITATES
THE CONSISTENT INCLUSION OF
MICROSTRUCTURAL DAMAGE AND
INELASTIC EFFECTS

Fig. 14 — Nonlinear multivariable field representation in composite materials

SUBWAVELENGTH MOIRE INTERFEROMETRY PROVIDES WHOLE FIELD DEFORMATION PATTERNS WITH EXTREME SENSITIVITY



U-displacement field; quasi-isotropic composite; 3-point beam with overhang; $P/P_f = 38\%$. The numbers are fringe orders N_x which specify U-displacements when multiplied by 16.4 μ in. (0.417 μ m)

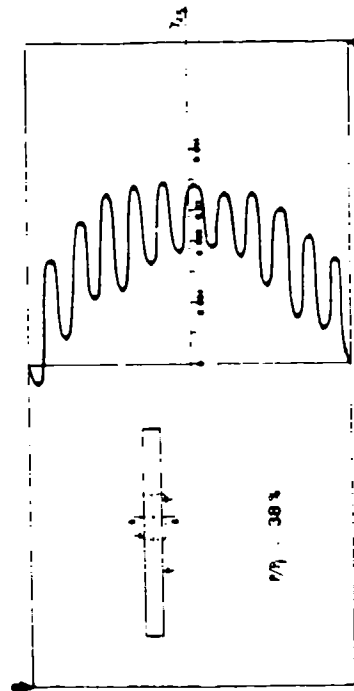


Fig. 15 — Ultra high-resolution optical technique for measuring deformations in composite materials

ARMY RESEARCH IN SHOCK MECHANICS

John F. Mescall* and Richard Shea**
U.S. Army Materials Technology Laboratory
Watertown, MA 02172

ABSTRACT

The U.S. Army Materials Technology Laboratory (MTL) has mission responsibility for managing the Army's technology base programs in structural materials, solid mechanics and materials testing. One of MTL's major programs is in Armor/Anti-Armor Materials. A key ingredient of this program is shock mechanics research. The research seeks to understand the mechanisms associated with the complex processes of projectile impact of targets and explosive-metal interactions.

The analytical basis for research in shock mechanics is presented. Several of the mechanisms, test procedures and applications of the research are discussed.

INTRODUCTION

The Shock and Impact Mechanics Team at MTL is conducting a combined theoretical/experimental program aimed at understanding the mechanisms involved in such complex processes as projectile impact of targets and explosive-metal interactions. Of particular interest is the role that material properties such as dynamic strength and fracture resistance play in such encounters.

The analytic procedures employed primarily involve the use of the HEMP code to simulate ballistic events. HEMP is a finite difference procedure which begins with the fundamental conservation laws in two or three spatial dimensions, couples to these a constitutive model which is appropriate for the high pressure fields involved, and integrates the equations of motion step-by-step in time. Output from the code consists of all the physical parameters of interest: position, velocity, stress, strain, and temperature as functions of time.

DYNAMIC STRESS-STRAIN CURVES

The response of materials to high compression fields associated with impact or explosive loadings is described in terms of the so-called Hugoniot curve. The Hugoniot Equation-of-State (Figure 1) is the locus of pressure-volume states a material follows when dynamically loaded and is obtained via a series of plate-slap tests. In these tests a flyer plate of known characteristics impacts in a planar fashion a specimen whose Hugoniot is being determined. The specimen's rear surface is monitored by a laser velocity interferometer. This signal is then interpretable in terms of the peak pressure and associated volume change induced by the impact conditions. A series of such experiments then maps out the entire P-V curve and determines the coefficients listed. The role of material strength of solids (vis-a-vis the hydrodynamic regime) is superimposed on the Hugoniot by the employment of a Von-Mises yield criterion which regulates permissible amplitudes of the stress deviators S_1 , S_2 , and S_3 .

These resultant dynamic stress-strain curves are then employable in computer simulations of general impact or explosive events. They are of particular significance to our work at MTL since our interests focus primarily upon the materials oriented issues as opposed to the kinematic issues associated with this problem class.

EROSION MECHANISM

As an example of how the theoretical and experimental approaches to ballistic complement each other and of why both are needed, consider the following:

Figure 2 shows some results from a HEMP simulation of a long-rod ($L/D = 10$) uranium

*Leader, Shock and Impact Mechanics Team

**Director, Mechanics and Structural Integrity Laboratory

penetrator impacting a massive steel target at a velocity of 4,000 ft/sec. It is evident from the distorted grid that as penetration proceeds, the region of intense plastic deformation is quite localized and is confined to a "process zone" whose radius is less than two projectile diameters. Material outside this process zone is hardly affected by the impact. In particular, projectile material is decelerated only as it enters the zone following material closer to the projectile tip which is in the process of being eroded; i.e., compressed and washed backward toward the cavity opening.

Figure 2 also provides the physical basis for this erosion mechanism in terms of ambient stress levels. We plot isobars of those pressure fields which are sufficiently intense to induce significant deformation and/or deceleration. For example, 10 kilobars is the approximate yield strength of both target and projectile. Although the initial pressure levels are an order of magnitude higher than this, they decline rapidly and never extend very far spatially. During the steady-state phase of the penetration process (most of the problem duration), we are dealing with a spatially limited pressure field of moderate intensity.

Figure 3 shows a set of flash x-ray observations of essentially the same problem. They reveal that the rear end of the penetrator is not decelerating even in the third exposure (when it is nearly embedded in the target), thus confirming the HEMP results. It is also clear that today's x-ray equipment cannot reveal details of what is occurring at the projectile/target interface, thus stressing the utility of the HEMP simulation. A considerable amount can be learned about the penetration process by varying the projectile and target material properties in a succession of simulations.

BUFFETING MECHANISM

A more realistic penetration problem representative of armor systems on modern vehicles concerns the process of long-rod projectiles perforating spaced arrays such as that shown in Figure 4. Flash x-rays of such an encounter are shown in Figures 5 and 6, where the projectile is seen to bend significantly between plates 2 and 3. Such bending is of course deleterious to penetrator performance and needs to be corrected since this behavior tends to worsen for modern designs with increased L/D ratios.

There is considerable controversy over the cause of such bending. We take the position that it is not due to a "buckling" nor to a wave propagation process associated with target obliquity. Instead, the HEMP simulation shown in Figure 7 lends support to the mechanism of a mechanical contact with the sides of the hole in the target by the side of the penetrator.

Figure 7 also considers a plausible set of conditions for the projectile interaction with the second plate of a spaced armor system. We stipulate that the problem begins after the projectile tip has bored a hole in the second plate. It has an L/D of 20, is moving with a velocity of 3,000 ft/sec in the x direction, but as a result of its interaction with the first plate element, it has an induced yield of 10 degrees and a y velocity of 100 ft/sec. The initial diameter of the hole in the target element is twice the projectile diameter.

Initial contact with the side of the target hole is a grazing incidence; by 15 microseconds the projectile has been pushed down to the lower edge of the hole and by the time of exit (180 usec), has been badly bent while the hole has been greatly enlarged. Post-mortem examinations of second plate elements reveal a hole with a strongly elliptic rather than a circular hole.

We would stress that the point of this simulation is to provide guidance for improved penetrator design by more clearly identifying the mechanical cause of the bending action which works against projectile efficiency. More work would be needed in stipulating precise impact conditions if complete agreement with x-ray observations is sought.

ADIABATIC SHEAR

Adiabatic shear is the name attached to a process of extreme localization of a deformation which has been proceeding in a relatively uniform manner until an instability suddenly intervenes. It appears that higher strength materials are more vulnerable to this phenomenon.

Figure 8 gives an example associated with ballistics. All these targets were impacted with identical projectiles at the velocities shown. The upper target is a soft (annealed) 4340 steel. It has nearly been perforated by a process involving massive plastic deformation. The middle and lower targets are both very hard 4340 steel. Clearly, the perforation process is quite different and involved very local deformation along the white shear bands visible in the lower target. Ballistic consequences of this process are shown in Figure 9, where improved ballistic performance is observed as target hardness is increased up to a point, when suddenly continued increases in hardness results in poorer ballistic protection.

Details of this mechanism are being studied in the laboratory again by a combined theoretical/experimental program involving a stepped projectile (Figure 10). Figure 11 shows examples of how this procedure provides close control over the nucleation and growth of shear bands. The stepped projectile is the dark area at the top of the photographs; the shear band is readily visible as the white line in the lower photograph.

Analytically, this experimental procedure is modeled by incorporating in the HEMP code a constitutive law which accounts for strain hardening of a material as plastic deformation proceeds, followed by a thermal softening as the work of plastic deformation is converted into heat, and the material responds to the temperature rise. The net result is a stress-strain curve exhibiting a local maximum. This is not typical of static testing results simply because at static testing rates there is sufficient time for the temperature rise to diffuse through the specimen, and not produce a localization of deformation. Dynamic tests exhibit a different behavior.

Figures 12 and 13 show the nucleation and growth of shear bands emanating from the corners of the indenting projectile tip. (The body of the stepped projectile is not shown here for convenience.) We note in passing that even though the impact velocity is low (200 ft/sec) the bands grow quickly and are developed by 24 usec. This procedure will prove useful for both mechanistic studies and as a quantitative measure of a specific materials resistance to adiabatic shear.

TAYLOR TESTS

One example of a procedure for measuring the dynamic (vs. static) strength of material is that of the split Hopkinson bar. This is limited to "medium" strain rates, somewhat low for ballistic applications. Another procedure is the Taylor Test in which one impacts a cylindrical specimen against a rigid target and from post-mortem measurements of deformation infers estimates of dynamic material flow strength. Figure 14 shows experimental results, including progressive failure with increased impact velocity; Figure 15 shows a HEMP simulation of the deformation. The latter is useful in making more precise estimates of dynamic material behavior.

EXPLOSIVE HARDENING

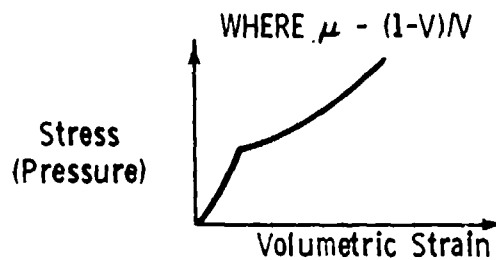
One interesting experimental technique frequently used to harden pre-fabricated items of complex shape, such as railroad frogs, is that of explosive hardening. One places a thin layer of explosive on the surface of a specimen, detonates it, and the result is an increase in hardness for a certain depth into the material. One advantage of the procedure is that one can achieve desirable levels of hardness without extensive deformation of the specimen as would be necessary for more conventional work-hardening procedures. This is attributable to the intense pressure fields associated with the explosive process. Figure 16 shows some HEMP results which prove useful in assessing such issues as how thick a layer of explosive, or what type of explosive is necessary to achieve a prescribed hardening depth.

EQUATIONS-OF-STATE

a) PRESSURE-VOLUME-ENERGY (P-V-E) RELATIONSHIP

- DOMINATES FOR VERY HIGH PRESSURE FIELDS
- HUGONIOT CURVE OBTAINED FROM PLATE-SLAP TEST CHARACTERIZES SPECIFIC MATERIAL

$$P = A\mu + B\mu^2 + C\mu^3 + T(1+\mu) E$$



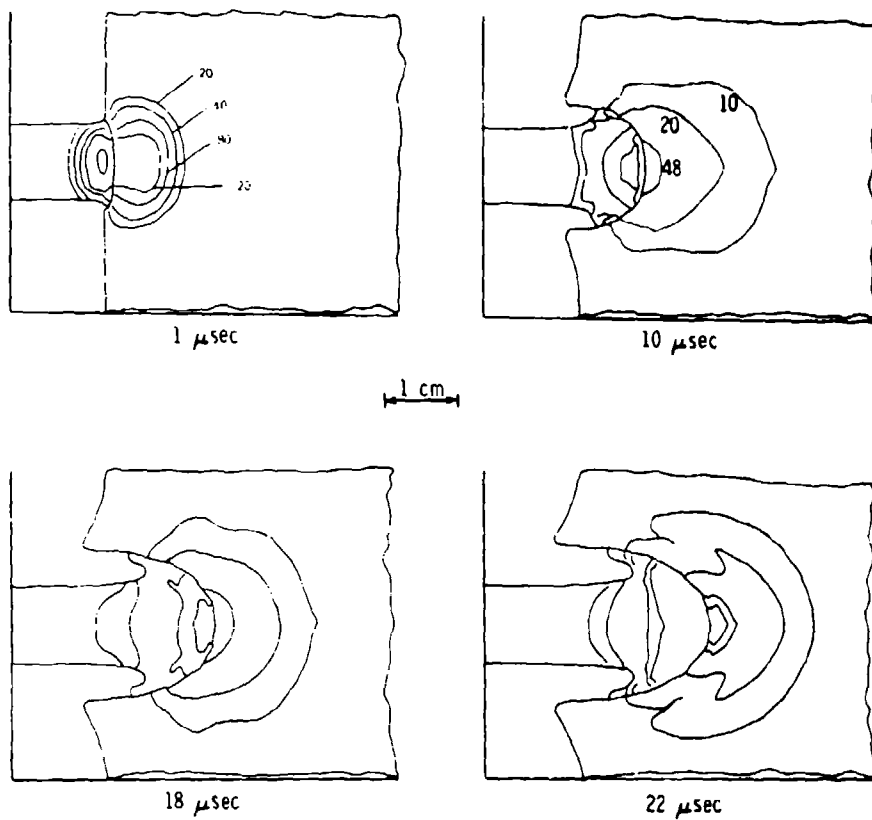
b) MATERIAL STRENGTH EFFECTS DOMINATE FOR MODERATE PRESSURE FIELDS

- INCORPORATED VIA VON MISES YIELD CONDITION

$$s_1^2 + s_2^2 + s_3^2 \leq (2/3) Y_0^2$$

(TAYLOR TESTS OR HOPKINSON-BAR TESTS)

Fig. 1 — Hugoniot equation of state



Pressures in kilobars

Fig. 2 — HEMP simulation of long rod penetrator into steel target

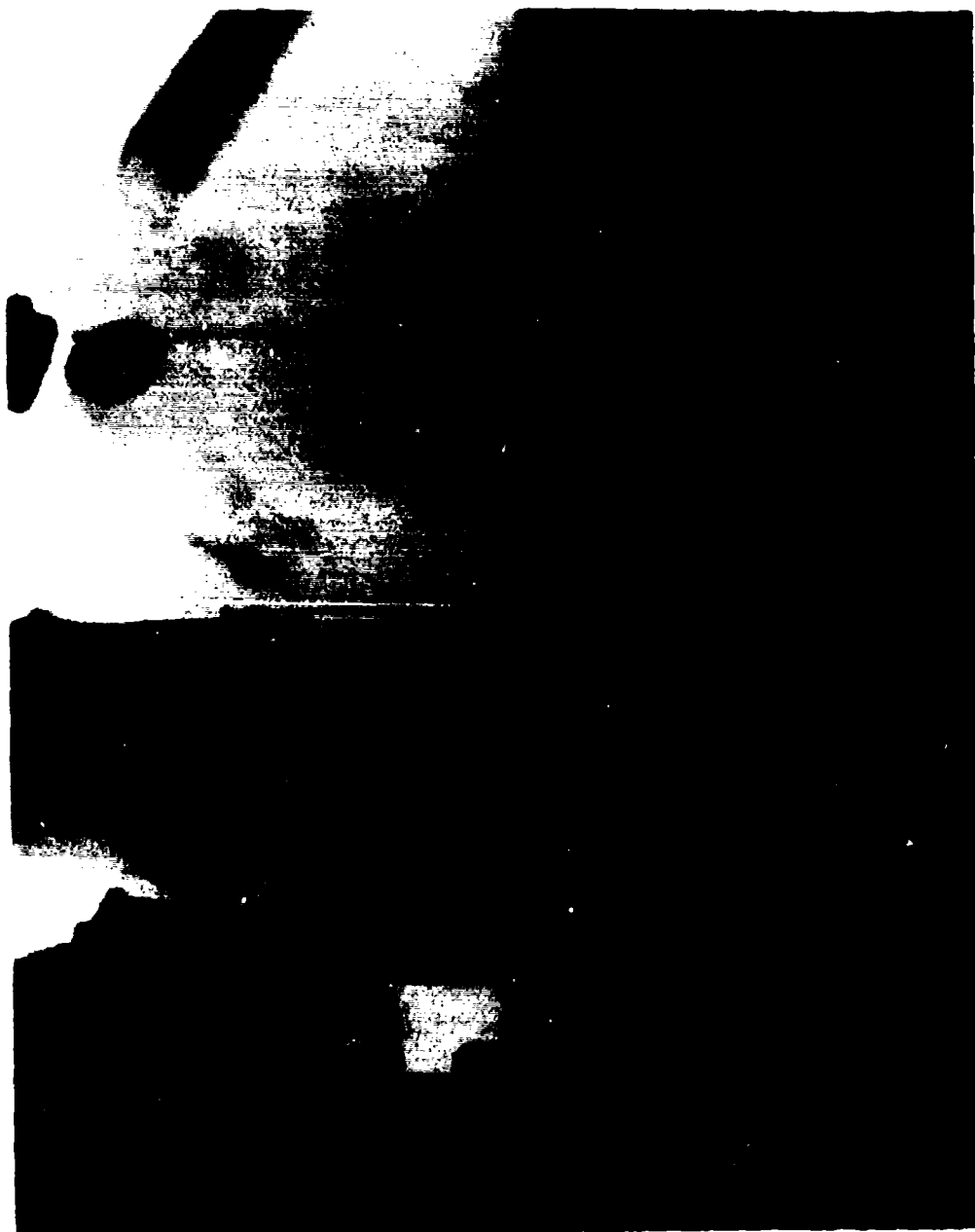
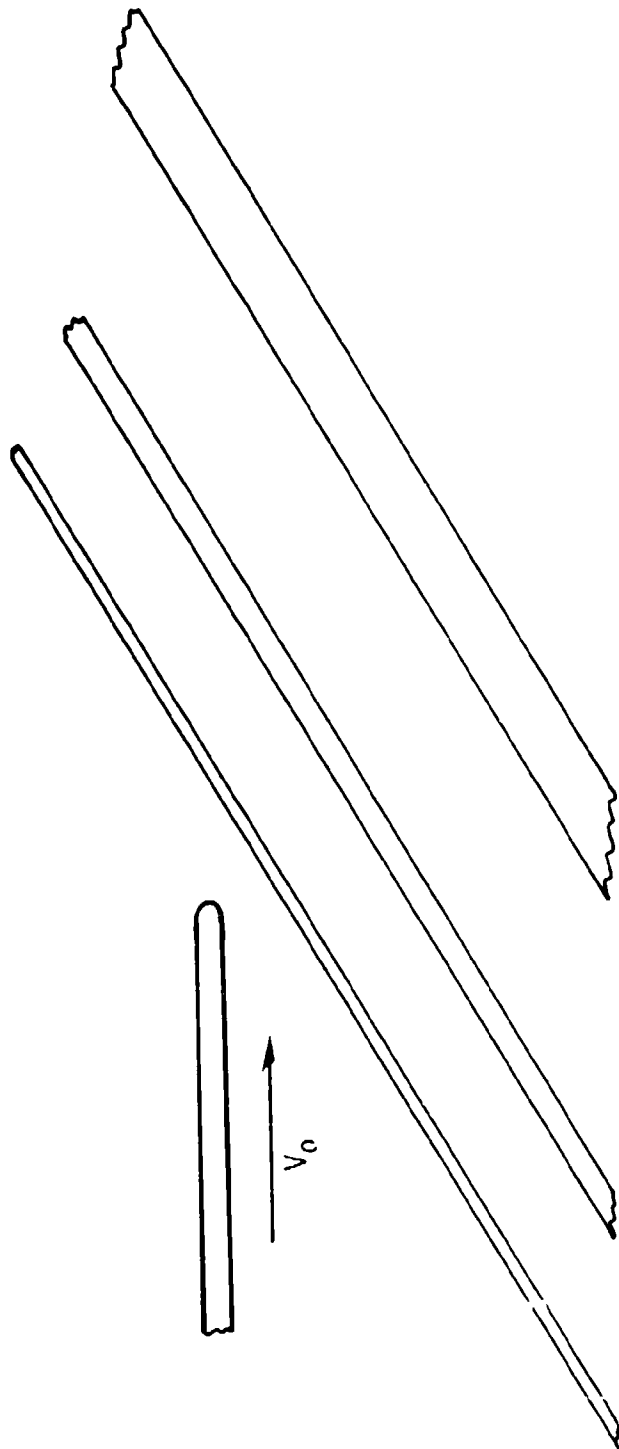


Fig. 3 — Flash X-ray of long rod penetrator into steel target



SPACED ARMOR ARRAY

Fig 4 — Spaced armor array



Fig. 5 — Flash X-ray of penetrator between first and second plates of array



Fig. 6 — Flash X-ray of penetrator between second and third plates of array

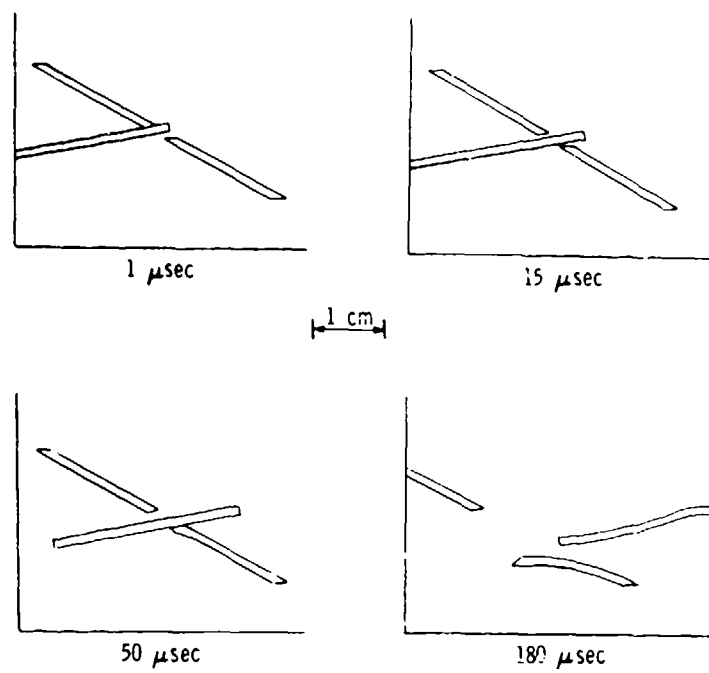
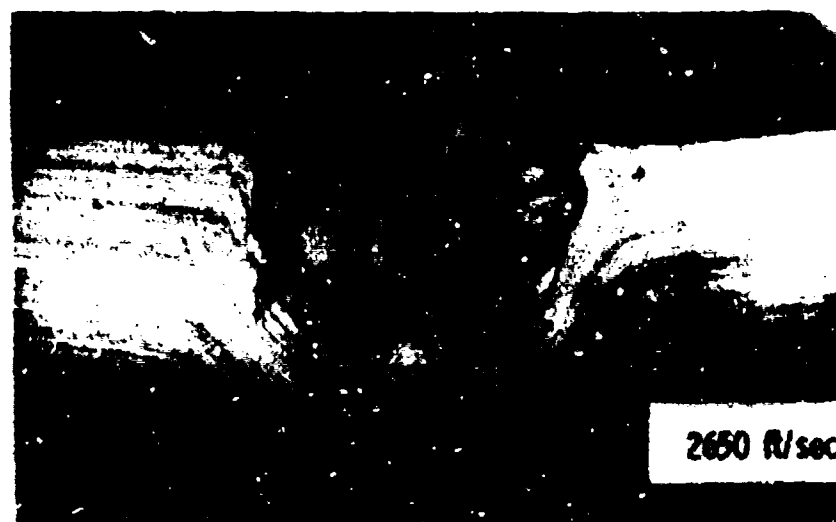


Fig. 7 — HEMP simulation of penetrator interaction with second plate of array



(a)



(b)

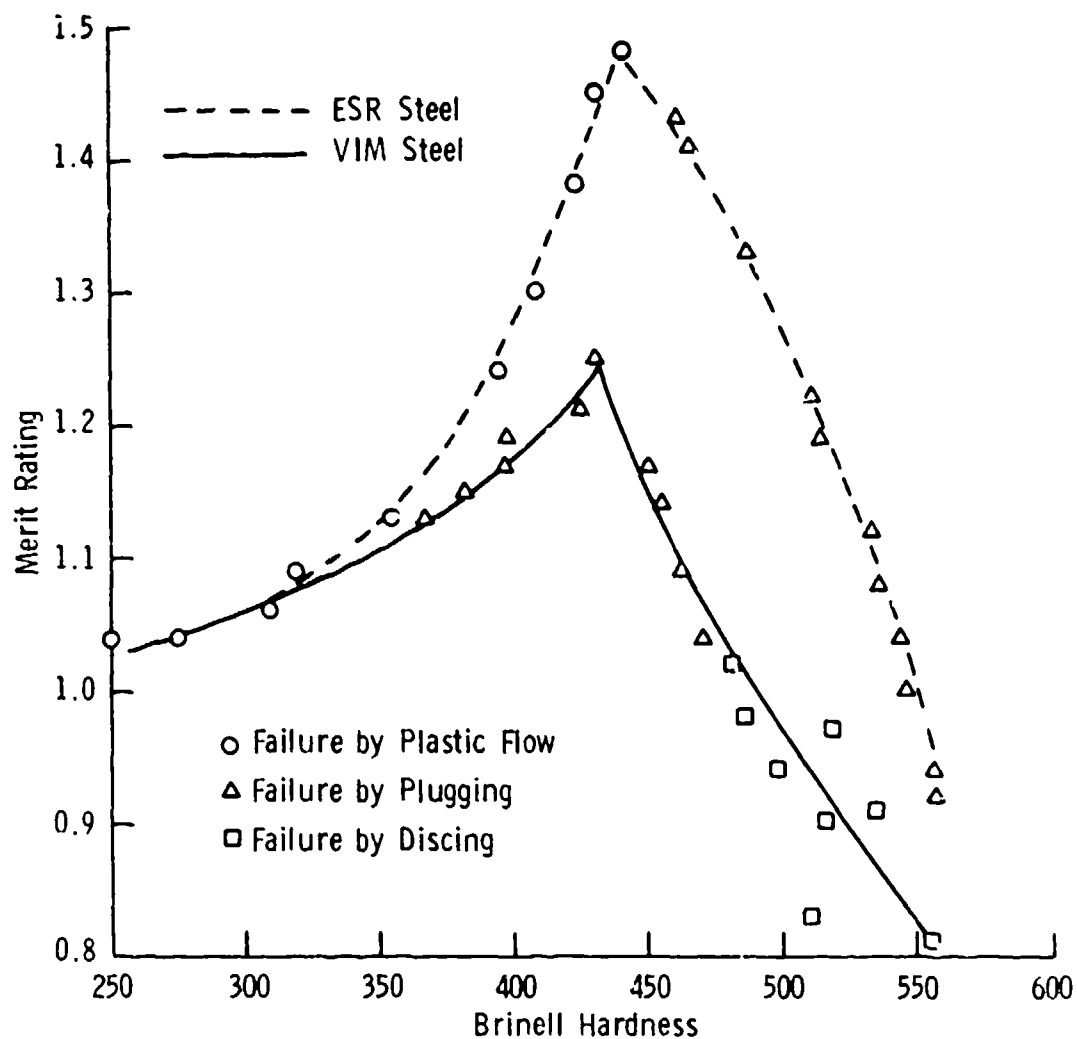
1900 ft/sec



(c)

2400 ft/sec

Fig. 8 — Post-mortem showing dependence of failure mode on target strength



MERIT RATING-HARDNESS RELATIONSHIPS FOR VACUUM INDUCTION
MELTED AND ELECTROSLAG REFINED STEELS

Fig 9 — Merit rating-hardness relationship for vacuum induction melted and electroslag refined steels

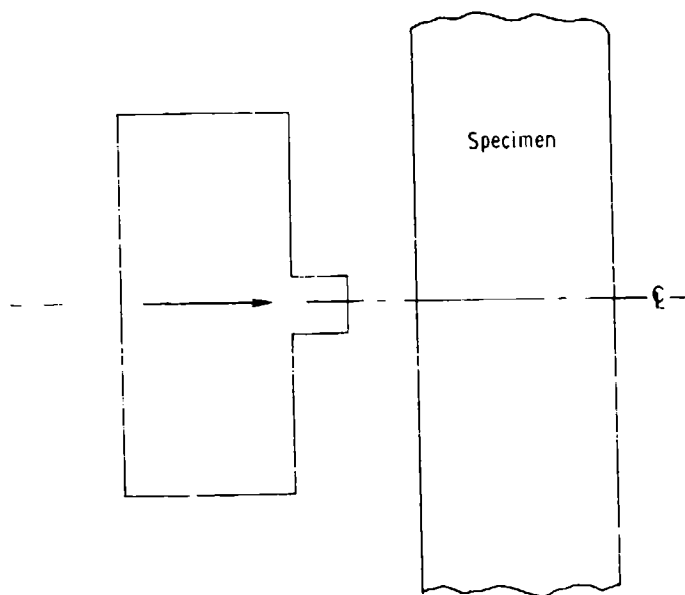


Fig 10 — Stepped projectile

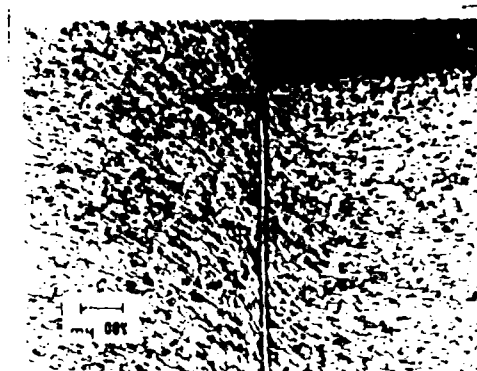
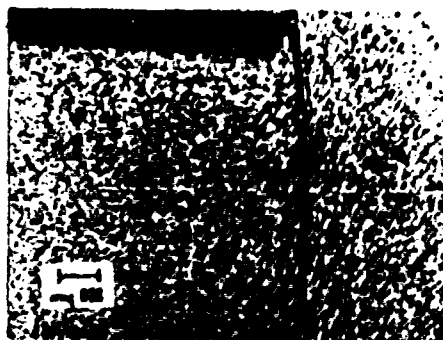
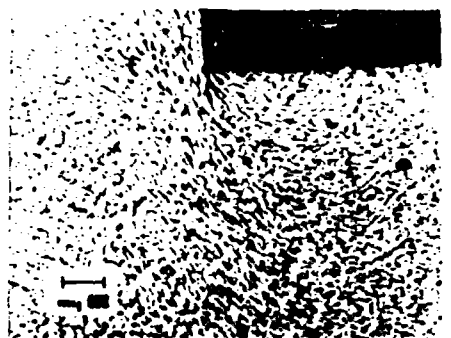


Fig. 11 - Post mortem of stepped projectile experiment

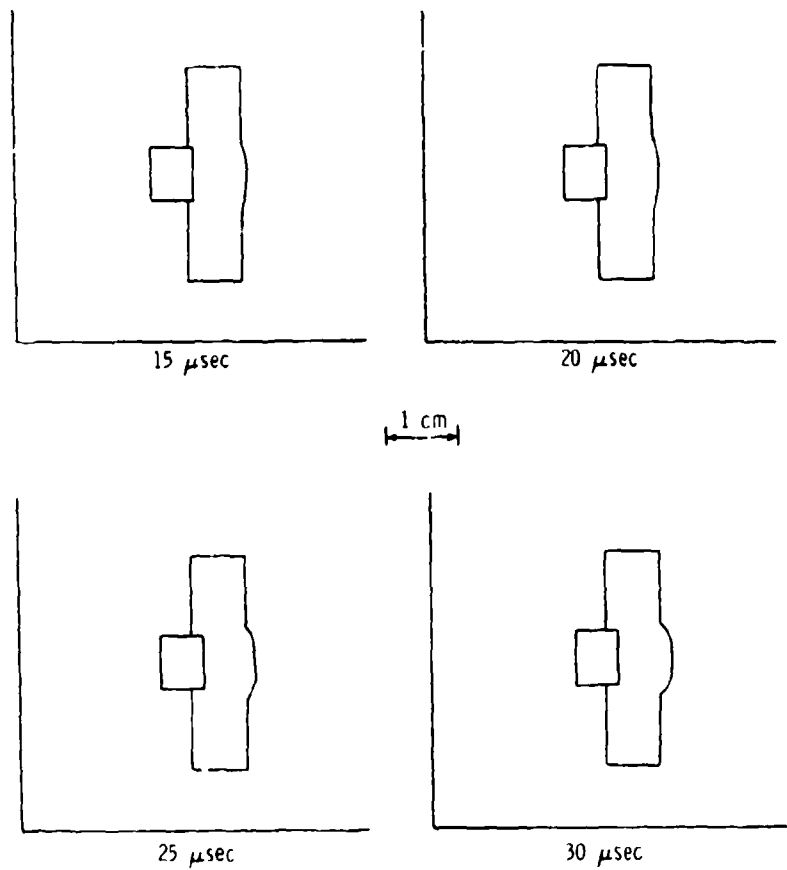


Fig 12 — HEMP simulation of stepped projectile experiment

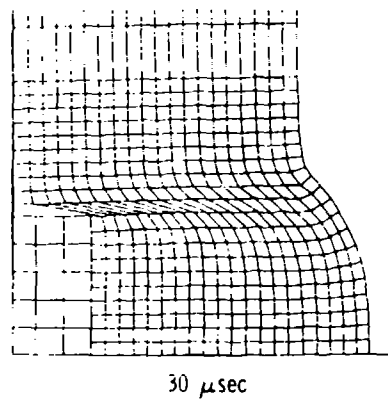
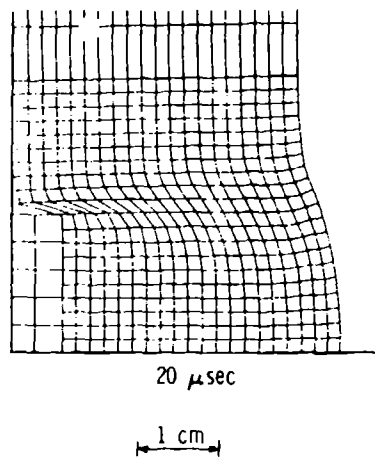


Fig. 13 — Close-up view of stepped projectile simulation

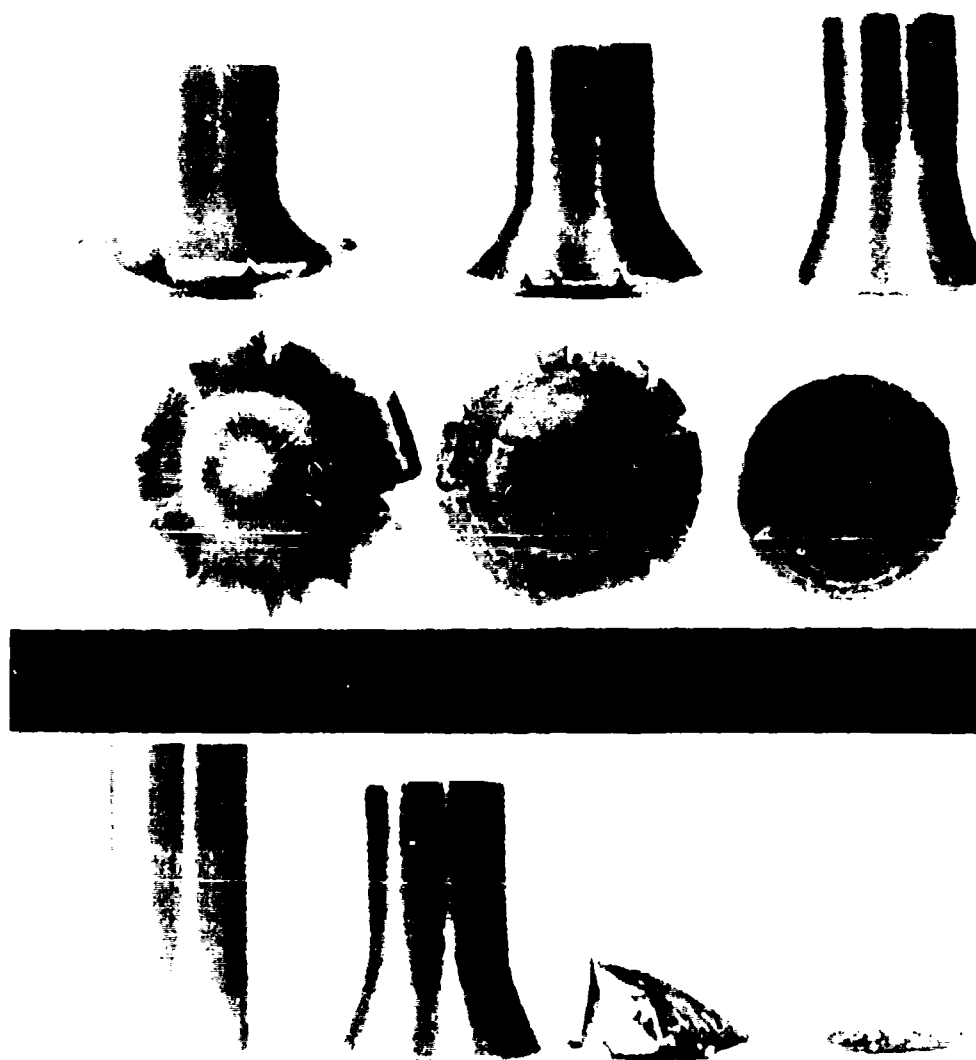


Fig. 14 — Taylor test experiments

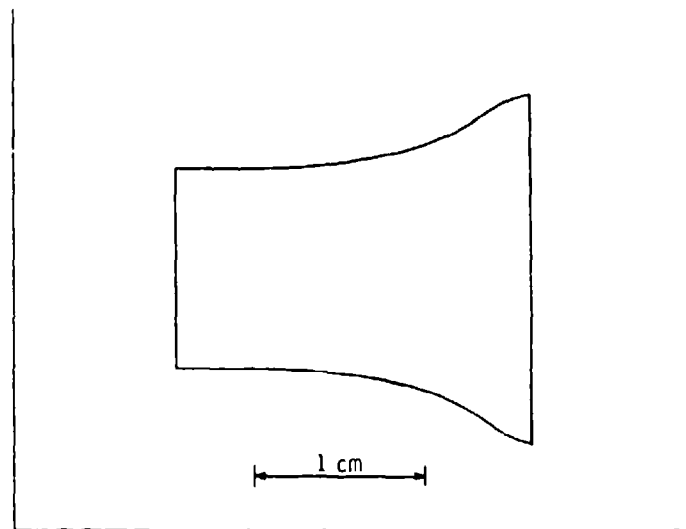


Fig. 15 — HEMP simulation of taylor test

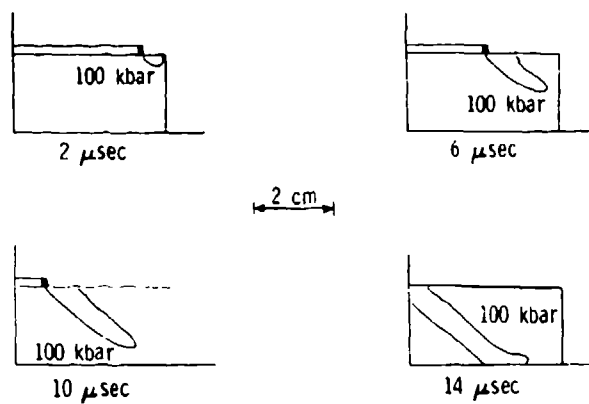


Fig. 16 — HEMP simulation of explosive hardening

AIR FORCE BASIC RESEARCH IN DYNAMICS AND CONTROL OF LARGE SPACE STRUCTURES

Anthony K. Amos
Program Manager
Aerospace Sciences
Bolling Air Force Base, DC 20332-6448

INTRODUCTION

The future of the U.S. national security lies in space! Space provides unparalleled opportunities for global surveillance, communication, and directed energy weapons basing. These activities are necessary to implement national policies of denying the enemy ready access to space with offensive weapons, of creating a defensive shield against strategic weapons, and of assuring compliance by all parties of international arms limitation agreements. The physical assets needed to support such activities must meet much higher performance and precision requirements than can be assured by current technology. Hence the last five to ten years have seen intensive research by many organizations (NASA, DARPA, and DoD) to assess and develop the needed technologies in many topics including space power and propulsion, space communication, directed energy weaponry, and large space structures. The U.S. Air Force has and continues to play a major role in this effort with system studies to define possible future missions, preliminary and advanced developments to validate concepts and define specific technology requirements, and basic research to assure future availability of the requirements.

As manager of all Air Force basic research the Air Force Office of Scientific Research is the focus of ongoing space related basic research covering many topics such as Space Power and Propulsion, Spacecraft Survivability, Imaging, Laser Communication and Weaponry, Spacecraft Materials and Structures. Participants include in-house researchers at the Air Force Laboratories as well as extramural researchers from industry and academia. This paper provides an overview of an element of the Spacecraft Materials and Structures program dealing with the dynamics and control of evolving spacecraft structural systems. The relevant active projects are listed in Figure 1. The detailed material presented here is based primarily on the AFOSR Structural Mechanics activity since time and space precludes a broader scoped presentation covering all the projects.

The projected structural systems are typically large in comparison with current spacecraft designs due primarily to the nature of the missions involved. For example, military communication would require RF Antennas of effective diameters in the range of 100 meters or more depending on the wavelengths of the RF carriers involved. Economic considerations would require that they be lightweight and either deployed or assembled in orbit from components transported from earth. In addition, operational requirements demand effective attitude control to maintain prescribed line-of-sight within very close tolerances, and the ability to rapidly change line-of-sight by slewing with minimal distortion due to structural vibrations. For reflective surfaces of antennas and optical mirrors additional distortion arising from deformations of the surface from a desired geometric shape must also be reduced to a minimum.

For the above reasons positive control of the system dynamics (including structural flexibility contribution) must be exercised at all times during the operational lives of these future high performance systems. Both active and passive means of control are viable options; they may both be necessary under certain conditions.

PASSIVE CONTROL

Passive control relies on mechanisms for dissipation of mechanical energy from a dynamic system to minimize vibrations and dynamic loads, and to reduce the likelihood of mechanical instabilities. The commonest of these mechanisms is structural damping which originates from a variety of sources including internal hysteresis, joint friction, aerodynamic loading and external devices.

Damping technology is, from the applications standpoint, fairly well developed. The turbomachinery, rotorcraft and aircraft engine communities routinely rely on damping for controlling the dynamics of rotating components. Nonetheless, there is a perceived

lack of adequate understanding of the basic phenomenology of damping which is reflected in a high degree of quantitative unpredictability of its effect in specific designs. The state-of-the-art in damping design is one of virtual "trial and error".

Air Force Basic Research in passive control consists of efforts to (a) identify and model friction: a major contributor to damping in built-up structures, (b) develop constitutive models of material viscoplasticity and internal damage responsible for hysteretic behavior, and (c) explore the use of viscoelastic and piezoelectric materials for damping enhancement.

A non-local friction theory has been under development over the last three years by J. Tinsley Oden of the University of Texas, Austin. It is based on the premise that Coulomb's Law applies not on a pointwise basis but rather to a summation of interactions over actual areas of material contact which depend on the nature and distribution of asperities over the interface surfaces. It further accounts for the deformations of the asperities which are generally non-elastic even for metals. For newly formed surfaces under moderate normal loads, interface constitutive models have been developed involving power law relationships. Variational principles have been established for integrating these relations into the system dynamic equations and finite element computational schemes have been developed for numerical approximation of the resulting nonlinear equations. Figure 2 shows the results of a sample application of the theory. The friction stress results clearly depict stick-slip motion which has long been observed experimentally. The normal stress results are new revelations requiring further verification.

The Bodner-Partom thermoviscoplastic constitutive model is the product of about ten years of Air Force sponsorship of research by Sol Bodner and co-investigators at the Technion, Israel Institute of Technology. This is a phenomenological model of the unified theory variety, i.e. it describes simultaneous occurrence of both elastic and plastic deformations under all loading conditions, and requires no yield surface specification. It uses internal variables to model damage, hardening and temperature dependence. It has demonstrated good correlation with experimental data generated for a wide range loading situations. Figure 3 depicts some results of one such correlation study based on cyclic loading tests involving out-of-phase axial-torsion combination. This study was performed by the Southwest Research Institute under a NASA contract.

A cooperative industry-academia research effort just completed has been focused on the development of analytical and experimental methods of characterizing the localized dynamic properties of structural joints which incorporate viscoelastic treatments for damping

enhancement, and for representing the effects of the local dynamics in the analytical models of the parent structures. Richard Trudell of McDonnell Douglas Astronautics Company and Lawrence Rehfield of the Georgia Institute of Technology as co-investigators developed a lap joint concept with viscoelastic layers that is optimized for damping subject to stiffness constraints. They developed finite element modeling techniques for the nonlinear hysteretic behavior of the joint and evolved a unique experimental technique for determining the effective damping of such joints. This involves the transmission of a pulse wave through the joint and use of the amplitude and phase modulation of the exit signal to calculate the effective joint stiffness and damping. Plans to extend these results from the axial loading conditions studied to combined axial and bending situations, and to examine other joint concepts have been temporarily suspended due to budgetary constraints. Similarly, the subject of piezoelectric damping enhancement is a planned future focus of research investment.

ACTIVE CONTROL

Active control of the dynamics of flexible structures is the result of judicious application of forces (and/or torques) additional to the normal inertial, stiffness and damping effects by means of actuators permanently incorporated into the structure, and activated according to some control logic implemented in onboard electronic subsystems that may or may not require dynamic response inputs from sensors attached to the structure. These additional forces provide the means for modifying the dynamic behavior of the unaided structure to improve system performance. Their proper selection is the essence of active dynamic control. As indicated in Figure 4, the selection process (control synthesis) must meet two fundamental and potentially disparate goals: maximum performance improvement over the unaided structure, and stability of the resulting controlled structure (robustness).

The basis of current control synthesis practice is Linear Quadratic Gaussian (LQG) theory. It requires a linear model of the structural dynamics, a linear relationship between the forces and input signals of the actuators, a linear transfer matrix relationship between estimates of the dynamic state (or sensor outputs) and the actuator input signals, and the minimization of a quadratic "cost" functional of the dynamic state in the presence of Gaussian white noise as the criterion for the selection of the various coefficients in the transfer functions. This is briefly outlined in Figure 5. As indicated, the optimization procedure leads to a set of Riccati Equations whose solution establishes the control gain matrix. These are nonlinear matrix differential (algebraic under special conditions) equations with no known analytic solutions. Numerical integration, the only practical solution

approach, is so computationally intensive as to be feasible only for problems with "few" state variables (in the teens on current generation mainframe computers). On the other hand the dynamic variables of the structure can number several orders of magnitude in excess of these limits. Consequently it is necessary to base the control synthesis on a low order model derived from the dynamic equations of the structure. Development of criteria to govern this model order reduction process is one of the major research thrusts.

Another thrust is the establishment of robustness criteria and procedures. Implementation of a control design on the structure can be expected to result in suboptimal performance realizations because of inevitable differences between the real system and that represented by the control synthesis model, arising from a variety of sources. Among them are system parameter uncertainty and randomness - the properties characterizing the dynamics of the system are represented by idealized parameters that ignore possible random variability and measured within limited precision, unmodelled dynamics - the consequence of order reduction, and unpredictable noise inputs from the real operational environments. Without proper accommodation these differences can lead to serious degradation in performance and possible loss of dynamic stability.

Other research thrusts include extensions to active control methodologies to directly address system nonlinearities, and experimental validation of novel active control concepts and procedures. Figure 6 lists currently active research efforts in active controls. A few of these are described below as a demonstration of the scope and approaches being used to address the issues above.

David Hyland and Nick Bernstein of the Harris Corporation are addressing the issues of model reduction and robustness through the application of stochastic modeling and subspace projection concepts. The stochastic modeling approach entails the explicit representation of system uncertainty and model error in the system dynamic equations using "maximum entropy" ideas from stochastic theories. The subspace projection approach using optimality criteria results in model order reduction which is optimal with respect to dynamic fidelity to the full order model. Figure 7 illustrates how the maximum entropy approach modifies the system dynamic equations and the performance criterion for optimal control. The optimal projection approach is illustrated in Figure 8, and Figure 9 shows how the combination of the two features with optimal control results in both the modification of the Ricatti equations and their augmentation with Lyapunov type conditions. Figure 10 illustrates robustness improvement over standard LQG that results from application of the Maximum Entropy/Optimal Projection (ME/OP) to a sample problem involving control of the line-of-sight (LOS) of a hypothetical

shuttle-borne antenna experiment. The specific application was supported by NASA Langley under the "Spacecraft Control Laboratory Experiment" (SCOLE) program.

An adaptive strategy for accommodating parameter uncertainty is the premise of the research effort by Michael Lyons and Robert Kosut of the Integrated Systems, Inc. (ISI). In adaptive control, the control synthesis model is based on online estimation of the system parameters. The schematics of Figure 11 illustrate both the adaptive control and the parameter estimator structures. As indicated therein, the parameter estimation procedure involves the use of a mathematical model whose input-output relations can be adjusted to approximate those of the plant (controlled system) within acceptable error. The model then forms the basis of the control synthesis procedure. As with fixed gain control of large scale systems, a reduced order model is necessary for practicality of implementation. Consequently the model error will always be finite in contradiction of classical adaptation theory which presumes a perfect model: i.e. the model error can be made arbitrarily small for all bounded disturbances.

Stability criteria of the classical theory - conditions for global stability - are therefore not applicable to the large scale systems control problem. A new theory which admits of finite model errors and guarantees stability only for specified disturbances - local theory - must be established. This is the thrust of the ISI effort. The local theory development has been aimed at extending adaptive theory from finite dimensional discrete systems to distributed large order systems, and at accounting explicitly for non-vanishing model error. Analytical formulation of model error has been developed based on parametric models for identification and control synthesis. The model error serves as the basis of a procedure developed for implementing both the model reduction and parameter identification steps of adaptive control. Minimization of the model error serves as criterion for the parameter identification step, and defines the allowable error for the control synthesis step. The adaptation process therefore becomes one of iteratively driving the estimated error for the closed loop system below the computed allowable error. The procedure is illustrated in Figure 12 for a simulation application involving the CSDL No. 2 model (a hypothetical optical system developed at the Charles C. Draper Laboratory for use in the development and validation of active control methodology under the DARPA ACROSS program). Figure 13 presents some simulation results from the application of active controls technology to the problem of vibration reduction in a helicopter cockpit. Fixed gain and adaptive control schemes are shown to be both effective in an order of magnitude reduction in vibration levels. However it is evident that the adaptive control scheme required much less control inputs than the fixed gain approach in

achieving identical performance levels; a consequence of the ability of adaptive control to tailor the reduced order model for control synthesis to the specific parameters (by identification) associated with desired performance.

Experimental verification of active control laws for flexible dynamic systems is being pursued by Bill Hallauer, Jr. of VPI. The research consists of the development of laboratory test articles with dynamic characteristics representative of large space structures, analytical modeling for control synthesis, testing of the models interfaced to the controllers as implemented in the laboratory, and examination and interpretation of the results. Configurations tested to date include a pendulous beam and an oblique grillage system.

STRUCTURAL MODELING

A number of ongoing research projects are concerned with various aspects of structural dynamic modeling. The development of accurate models representing both the structural dynamics and the controls elements of the coupled system is the general goal of the efforts of Ed Haug of Iowa University, Ed Crawley of MIT, Satya Atluri of the Georgia Institute of Technology, and Ahmed Noor of the George Washington University. Ed Haug's interest is in the simulation of multi-body dynamics with due consideration of flexibility effects and the resulting nonlinearities of large scale motions. Ed Crawley is pursuing the concept of "intelligent" structures composed of constituent elements made up of passive structure and associated control system components, interacting with each other in a hierarchical format. Satya Atluri's research is developing computational algorithms for the nonlinear transient analysis of actively controlled structures. Ahmed Noor is developing equivalent continuum modeling concepts for large flexible systems.

Another aspect of the modeling activity is that of optimization of the integrated structure-controls system. From the design standpoint it is reasonable to expect that significant benefits of performance and economy are achievable if the structure and control were synthesized from the outset to meet desired performance objectives, in contrast to the traditional approach of first designing the structure and then augmenting its performance through controls. To explore the possibility of this new methodology Bob Skelton and Henry Yang of Purdue University in a joint effort have been developing a finite element-based approach in which the modal cost criterion for model order reduction has been reformulated to include finite element characteristics (grid profile, polynomial shape function order, etc.) and the control objective function incorporates direct structural model parameters. A similar approach

being investigated by Mohan Aswani and G. T. Tseng of the Aerospace Corporation uses equivalent continuum modeling concept as a basis. Sam McIntosh of McIntosh Structural Analysis is investigating approaches for the incorporation of controller gains in design optimization constraints and grammians. In a similar vein, John Junkins of the Texas A&M University (formerly VPI) is extending control synthesis methodology to account for structural and flight mechanics parameters - with particular emphasis on the nonlinearities they generate. Results to date include methodologies for optimal maneuvering control and eigenvalue placement for optimum performance and robustness.

Transient dynamic phenomena in the form of propagating disturbances are expected to play a major role in the on-orbit dynamic response of large space structures due to their greater flexibility and physical size. Conventional methods of dynamic analysis using vibration modes are not well suited to the propagating wave event because the highly localized nature of the disturbance requires the superposition of large numbers of modes. Research to understand and model travelling waves in structures and to exploit them for more effective active controls is being pursued at Stanford University by Holt Ashley, at MIT by Jim Williams, and by K. C. Park of Lockheed Palo Alto Research Laboratory. Figure 14 is an illustration of an early result of the Stanford effort. It depicts a unique property of periodic structures in filtering waves in discrete frequency bands centered around the fundamental and higher harmonic frequencies of a unit repeating cell.

At Cornell University Francis Moon, in collaboration with Phillip Holmes and Richard Rand, is engaged in the investigation of nonlinear dynamics from a topological perspective. The goal is to identify conditions under which dynamic systems become chaotic. Using simple models (e.g. buckled beam) the basic attributes of chaos have and continue to be explored. The results of this fundamental study are enabling research into chaotic tendencies of more practical systems such as the two segment manipulator arm shown in Figure 15. As dynamic systems, robotic devices with flexible linkages are known to exhibit chaotic behavior under certain conditions. It is the goal of the Cornell effort to identify these conditions.

CONCLUSION

The Air Force Basic Research in Dynamics and Control of Large Space Structures is, as has been demonstrated here, a comprehensive program that addresses several of the many scientific and technological issues relating to the development and operation of very large and sophisticated high performance systems in the relatively unfamiliar space environment. The design challenge has motivated most of the

ongoing research to date. It is perceived that these have evolved modeling concepts, computational algorithms and performance/stability criteria capable of supporting the design process. However, analytical and experimental methods and the experience data base needed to support the validation of designs prior to commitment to launch are still sparse or nonexistent. The AFOSR program is therefore in the process of shifting emphasis from the synthesis to the simulation objectives of the technologies. It is intended to embark on the development of modeling and computational capabilities needed to perform high fidelity simulation of orbital dynamics including operational maneuvers and developmental functions of deployment and assembly.

Since it is perceived that transient phenomena of the travelling wave variety will be dominant in the orbital dynamics of the systems, it is intended to aggressively pursue this topic in the near future. It is further intended to continue research of nonlinear dynamics effects with particular emphasis on chaos.

Air Force Basic Research Aerospace Sciences

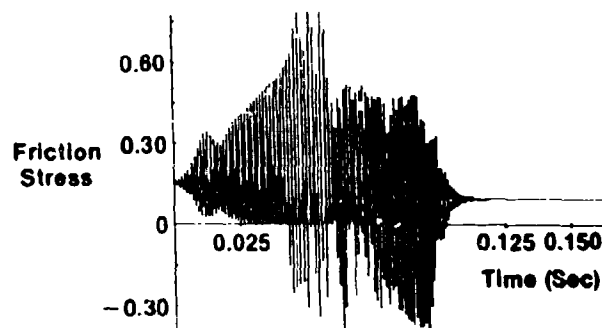
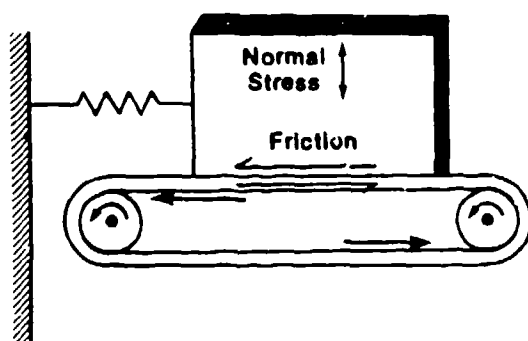
SPECIFIC PROGRAMS

AFOSR - STRUCTURAL MECHANICS	DR ANTHONY AMOS
- DISTRIBUTED CONTROLS	DR MARC JACOBS
AFWAL - STRUCTURES & DYNAMICS	DR VIPPERLA VAIKAYYA
- FLIGHT CONTROLS	DR SIVA BANIDA
FJSRL - AEROSPACE MECHANICS	CAPT STEVE LAMBERSON

Fig. 1 — Active programs in spacecraft materials and structures

Air Force Basic Research Aerospace Sciences

New Friction Model Reveals Parasitic Normal Vibrations During Sliding



MODEL FEATURES

- Interface Medium of Microscopic Dimensions
- Interface Constitutive Relations
 - Power Law Elastic Component
 - Nonlinear Dissipative Component
- Variational Principle

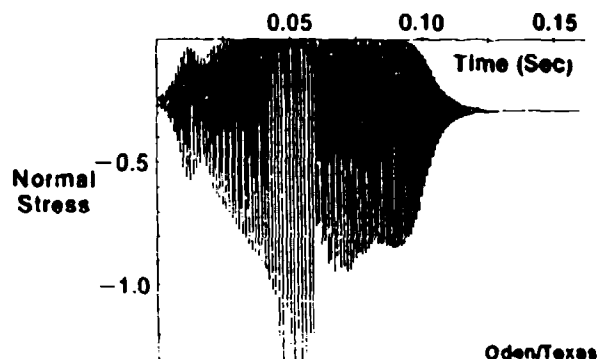
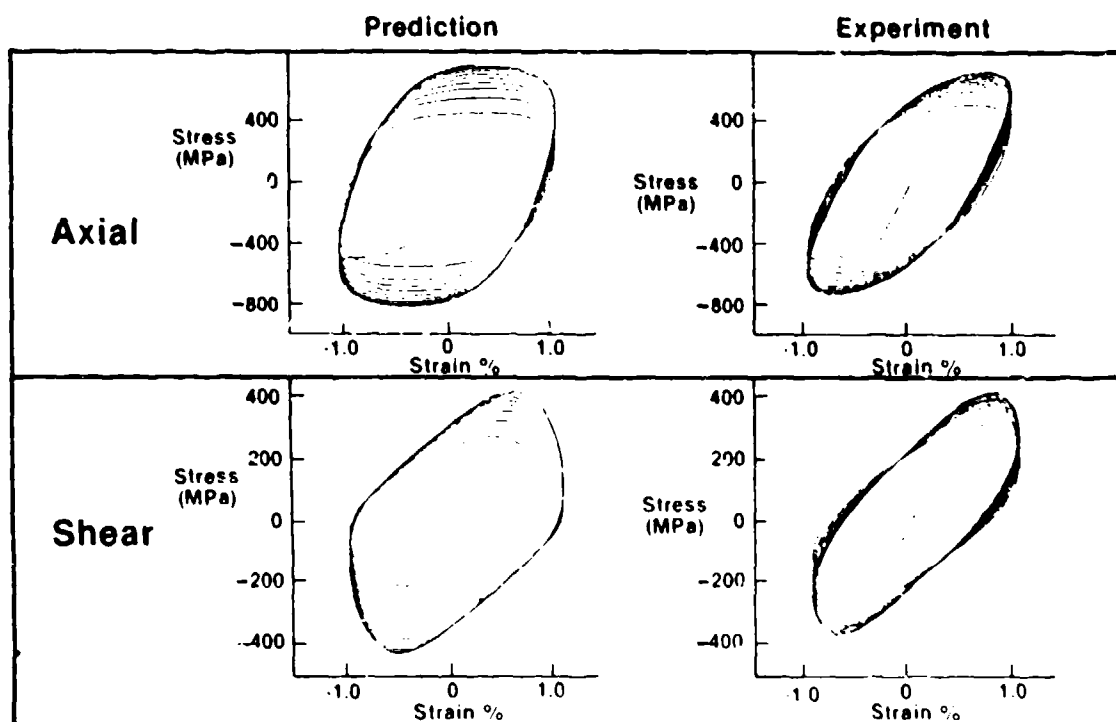


Fig. 2 — New friction model reveals parasitic vibrations during sliding

Air Force Basic Research Aerospace Sciences

Constitutive Modeling

Bodner-Partom Theory Accurately Simulates Tension-Torsion Cyclic Behavior of Hastelloy-X.



U.S. Lindholm/SWR1

Fig. 3 — Bodner-Partom thermoviscoplastic constitutive model

Air Force Basic Research Aerospace Sciences

ACTIVE DYNAMIC CONTROL

$$M\ddot{x} + C\dot{x} + Kx = f^E(t) + f^A(x)$$

STATE SPACE FORMULATION:

$$z = \begin{Bmatrix} x \\ \dot{x} \end{Bmatrix}$$

$$\dot{z} = Az + F^E(t) + F^A(z)$$

- SELECTION OF F^A TO GIVE "BEST" z (CONTROL SYNTHESIS)
- ASSURE STABILITY OF "BEST" z IN PRESENCE OF
UNCERTAINTIES IN PARAMETERS - M, C, K
- F^E, F^A (ROBUSTNESS)

Fig. 4 - Active dynamic control of flexible structures

Air Force Basic Research Aerospace Sciences

CONTROL SYNTHESIS

LINEAR THEORY (LQG)

$$\dot{Z} = AZ + BU$$

$$Y = CZ$$

$$\text{MIN } J = \int [Z^T Q Z + U^T R U] dt$$



RICATTI EQUATIONS



$$U = GZ$$

Z = STATE VARIABLE

U = ACTUATOR INPUTS

Y = SENSOR OUTPUTS

J = COST FUNCTION

Q, R = WEIGHTING MATRICES

G = FEEDBACK GAIN MATRIX

- PROCEDURE PRACTICABLE FOR LOW ORDER SYSTEMS ONLY
- ORDER OF STRUCTURAL MODELS MUST BE REDUCED FOR CONTROL SYNTHESIS

Fig 5 — Equations for control synthesis

Air Force Basic Research Aerospace Sciences

ON-GOING EFFORTS IN ACTIVE CONTROLS

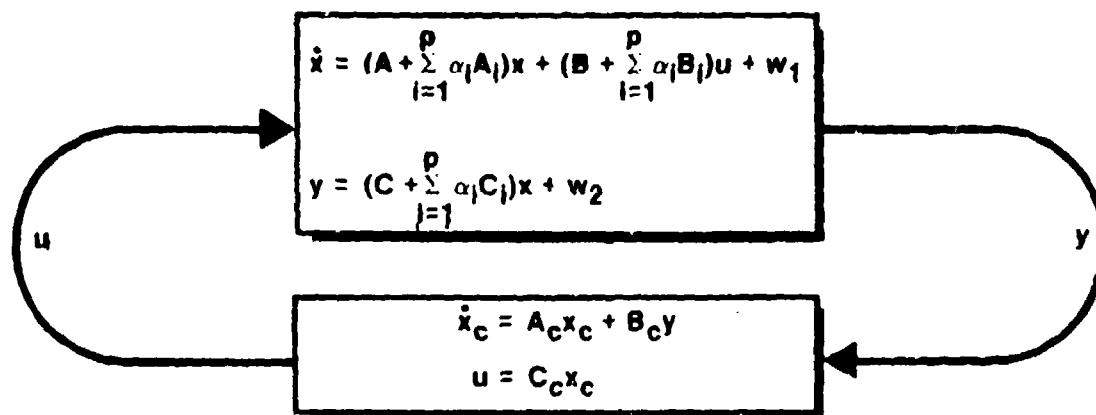
- | | |
|--|-----------------------------|
| • OPTIMAL PROJECTION/MAX ENTROPY CONTROL SYNTHESIS | HYLAND, BERNSTEIN/HARRIS CO |
| • ADAPTIVE CONTROL THEORY FOR LSS | LYONS, KOSUT/ISI |
| • EFFECTS OF IMPLEMENTATION? OPERATIONAL CONSTRAINTS | MEIROVITCH/VPI |
| • EXPERIMENTAL VALIDATION OF CONTROL LAWS | HALLAUER/VPI |
| • HIERARCHICAL CONTROL CONCEPTS FOR LSS | CRAWLEY/MIT |
| • NONLINEAR OPTIMIZATION OF STRUCTURE AND CONTROLS | JUNKINS/VPI, TAMU |

Fig. 6 - On-going research efforts in active controls

Air Force Basic Research Aerospace Sciences

ROBUST CONTROL

HIGH-ORDER, UNCERTAIN PLANT



LOW-ORDER CONTROLLER

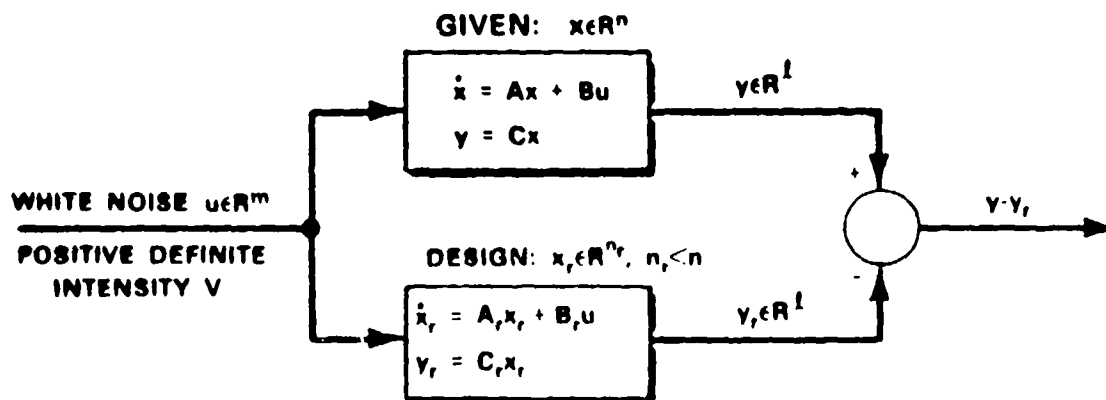
PERFORMANCE CRITERION

$$J(A_c, B_c, C_c) = \lim_{t \rightarrow \infty} E[x^T R_1 x + 2x^T R_{12} u + u^T R_2 u]$$

Fig. 2 - Maximum entropy approach for modifying system dynamic equations

Air Force Basic Research Aerospace Sciences

OPTIMAL MODEL REDUCTION PROBLEM



STEADY STATE TRACKING CRITERION

$$J(A_r, B_r, C_r) \equiv \lim_{t \rightarrow \infty} E[(y - y_r)^T R (y - y_r)] \quad (R \text{ positive definite})$$

Fig. 8 — Optimal model reduction problem

Air Force Basic Research Aerospace Sciences

OPTIMAL PROJECTION/MAXIMUM ENTROPY DESIGN SYNTHESIS

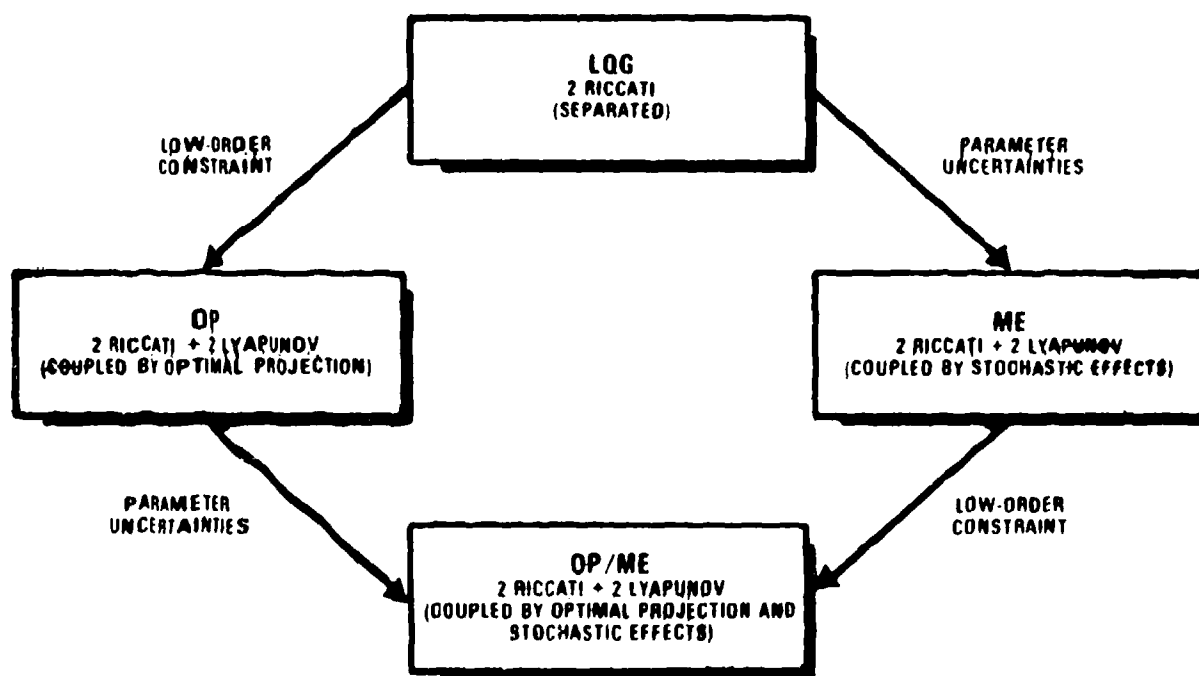
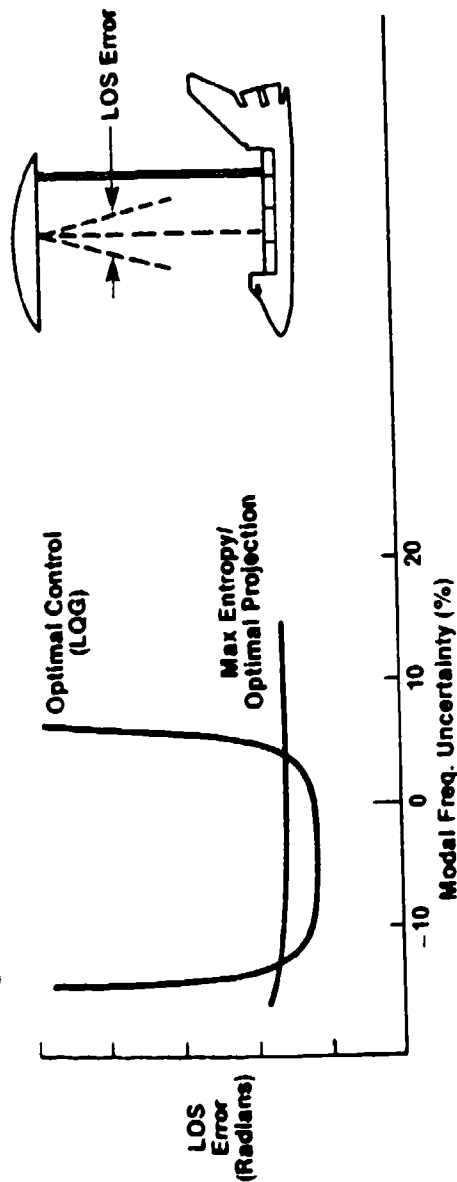


Fig. 9 — Optimal projection/maximum entropy design synthesis

Air Force Basic Research Aerospace Sciences

Improved Robustness of New Control Synthesis Procedure Over Optimal Control Demonstrated in Simulation



FEATURES OF NEW METHOD

- Combines Linear Quadratic Optimization with Stochastic Modeling
- Leads to Four Coupled Synthesis (2 Riccati, 2 Lyapunov) Equations
- Provides Systematic Procedure for Optimal Order Reduction

$$X = (A_0 + \Delta A)X + BU + W$$

Hyland/Harris Corp.

Fig 10 - Application of maximum entropy/optimal projection to the control of line-of-sight of a hypothetical shuttle-borne antenna experiment

Air Force Basic Research Aerospace Sciences

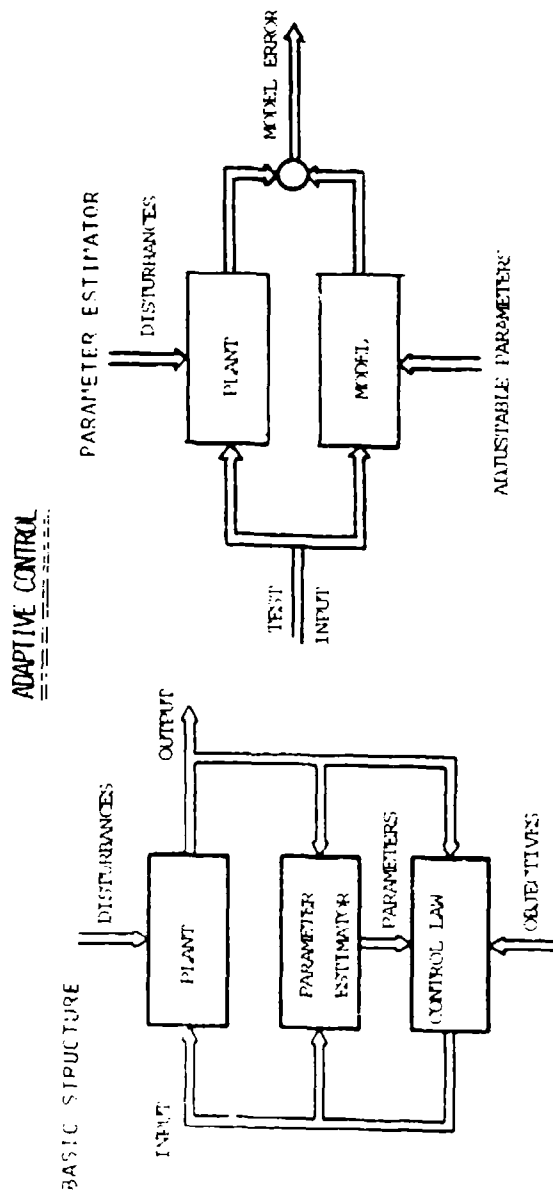


Fig. 11 — Adaptive control and parameter estimator structures

GLOBAL THEORY PRESUMES PERFECT MODEL
LOCAL THEORY DEVELOPMENT TO ESTABLISH STABILITY CRITERIA
IN PRESENCE OF MODEL ERROR
SYSTEM IDENTIFICATION BASED ON MODEL ERROR MANAGEMENT

Air Force Basic Research Aerospace Sciences

RESULTS OF ADAPTIVE CALIBRATION FOR PERFORMANCE ENHANCEMENT (ONE ITERATION)

STIMULATION SYSTEM (SUSL 140.2)

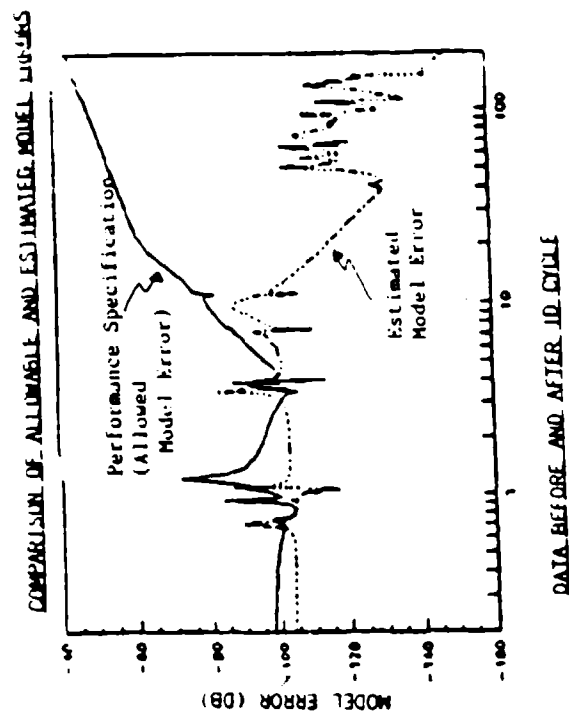
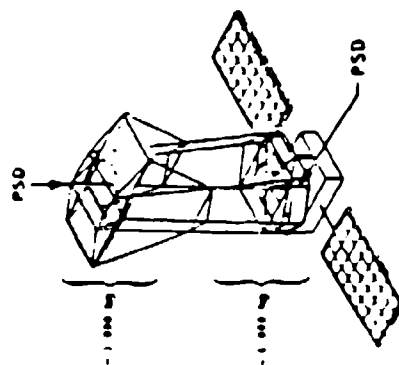
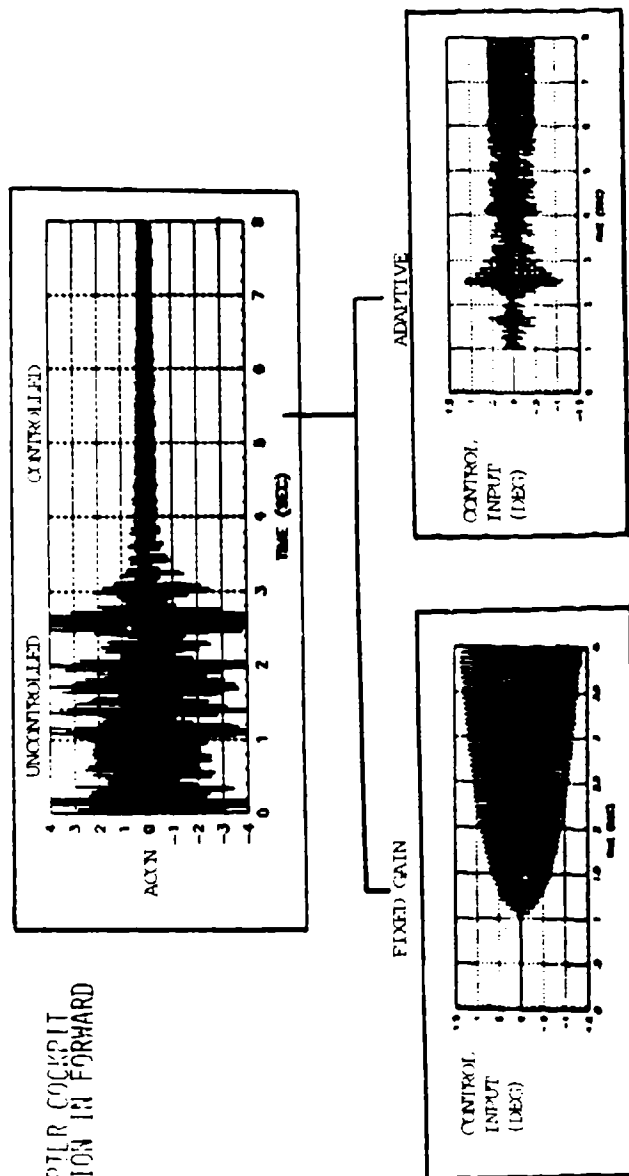


Fig. 12 — Results of adaptive calibration for performance enhancement (one iteration)

Air Force Basic Research Aerospace Sciences

ADAPTIVE CONTROL APPLICATION

HELICOPTER COCKPIT
VIBRATION IN FORWARD
FLIGHT



REDUCED CONTROL INPUT IMPLIES EXTENDED FATIGUE
LIFE FOR ROTOR COMPONENTS

Fig. 13 — Results from the simulation of the application of adaptive controls technology to the reduction of helicopter cockpit vibrations

Air Force Basic Research

Structural Periodicity Filters Bands of Travelling Wave Frequencies

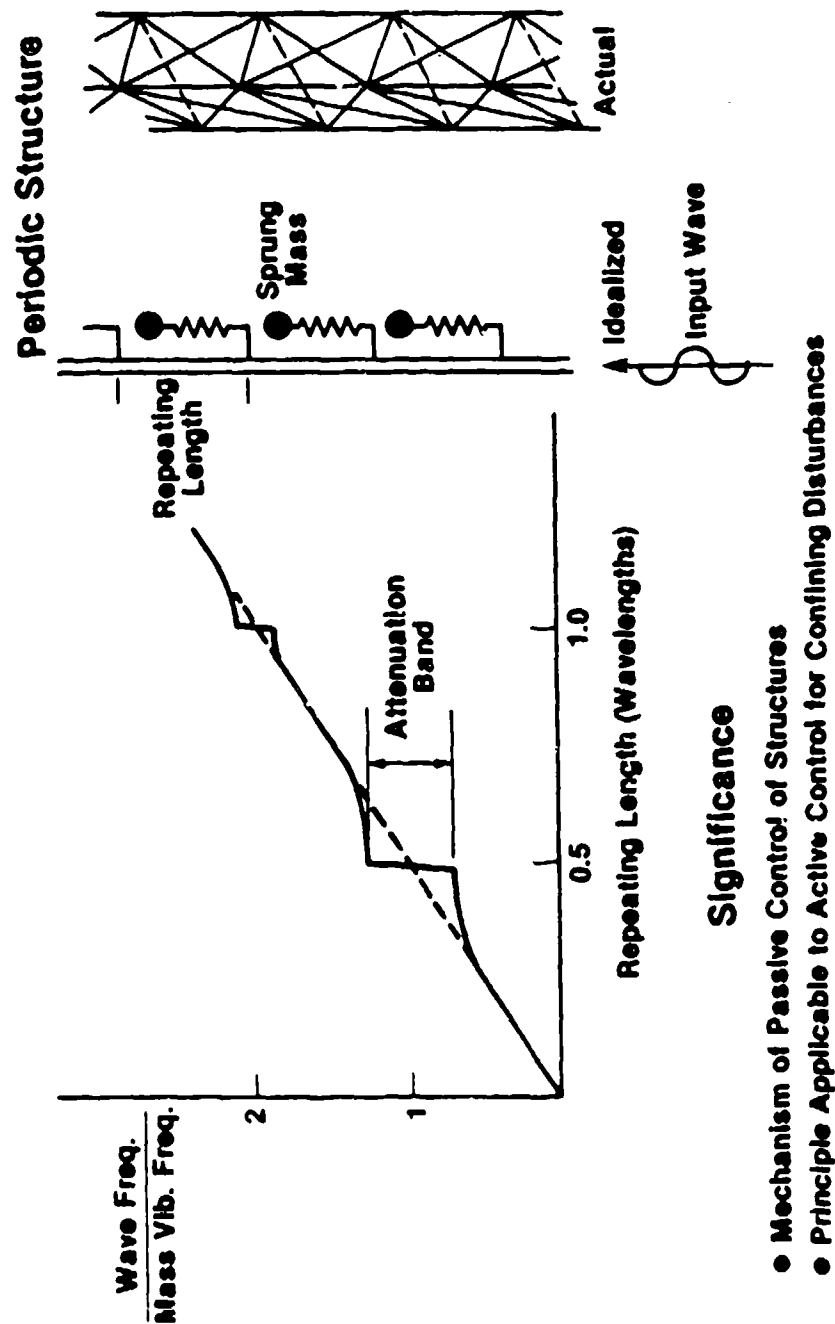


Fig 14 — The use of structural periodicity to filter bands of travelling wave frequencies

Air Force Basic Research Aerospace Sciences

Chaotic Dynamic Systems

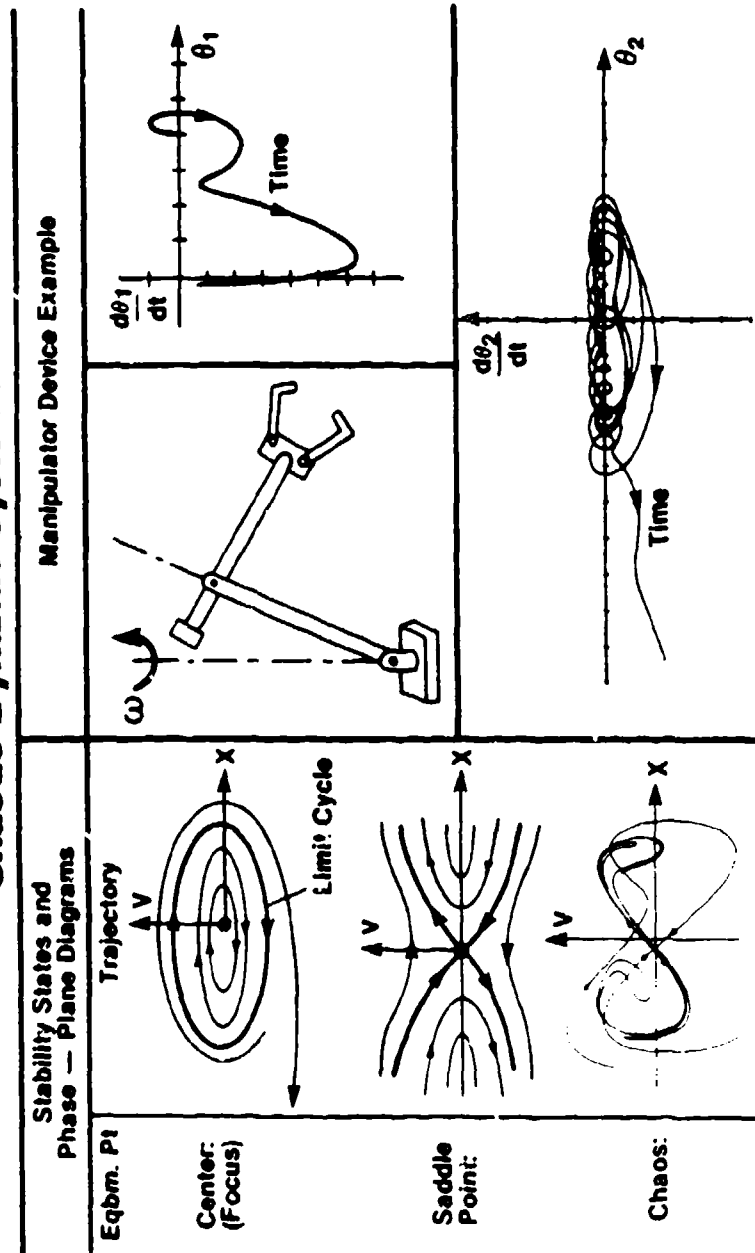


Fig. 15 — Choxotic dynamic systems

STATE-OF-THE-ART ASSESSMENT OF
STRUCTURAL DYNAMIC RESPONSE ANALYSIS METHODS
(DYNAS)

D. J. Ewins and M. Imregun
Dynamics Group
Mechanical Engineering
Imperial College of Science & Technology
London, UK

ABSTRACT

Following interest in surveys to assess current capabilities in the field of measuring structural dynamic data, a new study (codename DYNAS) has been undertaken to make a corresponding assessment of dynamic analysis prediction methods. A test structure has been designed and its specification distributed to a number of organisations who have undertaken a structural dynamic analysis of it. The first phase of results from the DYNAS survey have been collected and compared and are presented in this paper, including modal properties and various response characteristics (both frequency responses and transient response histories). The results from 12 submissions are found to exhibit a wide range of levels of agreement. It is concluded that although accurate analyses are possible, a number of techniques used by participants in the survey did not produce reliable results. Some form of self-assessment is considered desirable for such complex dynamic analysis tasks.

1. INTRODUCTION

The origins of the survey described in this paper go back over 20 years to the 'Round Robin' exercise conducted by the Naval Research Laboratory (USA) in order to assess the reliability of the mobility (then impedance) measurement methods which were becoming of increasing importance in the experimental study of structural vibration [1]. At that time, a set of simple test structures were circulated amongst some 20 laboratories in the USA actively engaged in measuring mobility data. Their respective estimates of specified mobilities were collated and compared, resulting in the realisation that a relatively high degree of unreliability existed in this process. Some years later, in the late 1970's, a similar exercise was conducted in Europe under the codename "SAMM" (State-of-the-art Assessment of Mobility Measurements) [2], followed by a restricted version in the USA. One of the structures used in this later exercise is shown

in Fig. 1(a) and a typical result from the 15 individual measurements of one of the specified mobility parameters is shown alongside in Fig. 1(b). Clearly, the situation at that time indicated there existed considerable scope for improvement in some of the testing techniques used. The essential conclusion drawn from the SAMM survey was that although accurate and reliable measurements of mobility (or other forms of FRF) are possible, not all methods used are capable of achieving the generally-required standard, and considerable care is usually required. Subsequent to the publication of the SAMM survey results, there have been proposals for a standard or reference testpiece which could be easily made and calibrated by individual laboratories [3], and it is probable that some such reference will become more widely used in the future.

The somewhat sobering experiences from the assessment of structural dynamic measurement methods eventually raised similar questions in respect of the corresponding prediction capabilities. Indeed, the SAMM IIB structure illustrated in Fig. 1(a) was occasionally used as a 'testpiece' for predictions of natural frequencies and even FRF properties. However, this is not an ideal design for such applications, and its use in this role was sporadic and varied. Thus it was decided that a specific survey should be conducted along similar lines to the predecessors but this time focussing on the capabilities of prediction (rather than measurement) methods. The survey, codenamed DYNAS (Dynamic Analysis of Structures) has now completed its first phase, the results from which are of some interest and relevance to the dynamic analysis methods in use today.

2. PLAN OF THE SURVEY

The general plan for the DYNAS survey was as follows:

PHASE I

- Design a suitable test structure
- Build and test the structure

- Make reference drawings of structure
- Distribute details of the design (but not test results) to participants
- Specify requirements for dynamic analysis
- Collect and collate the various results
- Review Phase I results

PHASE II

- Provide experimental results (together with collected Phase I predictions) and specify (reduced) analysis requirements for Phase II
- Collect and collate Phase II analyses
- Review Phase II results

Various parameters were to be specified for analysis - all of these being of significance in the dynamic analysis of structures - including inertia properties, modal properties and response characteristics.

At each stage, it was intended to make a detailed comparison of the various predictions for each of the specified parameters of interest, but primarily amongst themselves. Although comparisons were to be made with the experimental measurements, these were considered to be secondary to the comparisons between one prediction and the others.

This report considers the collected results from Phase I of the survey.

3. TEST STRUCTURE

3.1 Specifications The structure to be used for the survey was required to possess a number of features intended to ensure an efficient and effective evaluation of the prediction methods used. First, the structure needed to be complicated to some degree but without being unduly extensive. Thus, any complex features should appear only once or twice and not be repeated many times around the structure. (For example, a complex joint should be included, but it need not be repeated 8 or 12 times as this latter aspect merely adds to the extent of the modelling requirements, and not to the difficulty.)

Next, it was decided that the model should possess one plane of symmetry so that a two-dimensional analysis would be possible. Again, this specification was imposed in the interests of minimising the scale of the modelling and computation tasks. Third, the structure was to be 'buildable' so that an actual testpiece could be constructed and tested for comparison with the various predictions.

3.2 Design The design eventually chosen consisted of a cylinder and an I-section beam connected together through two relatively soft spring units, as illustrated in Fig. 2. Fig. 2(a) gives a general view of the proportions of the structure while Fig. 2(b) provides more details of the spring connectors. It was anticipated that this design would possess vibration modes which were effectively (i) rigid

bodies bouncing on the springs; (ii) beam bending modes; (iii) cylinder bending modes or (iv) complete system modes.

3.3 Data Provided The information provided to participants in the survey consisted of the following data:

- Detailed drawings of the structure (see Fig. 3, for example)
- Specification of master coordinate grid points
- Measured data on the spring stiffness
- Force-time histories (for transient response analysis)

All these data, together with details of the analysis requirements were provided in a booklet [4].

3.4 Preliminary Tests As mentioned earlier, a set of preliminary tests were made on the structure, partly to ensure that the dynamic characteristics to be predicted were relevant and partly to provide an experimental reference against which to compare these predictions. These measurements included estimates of the structure mass, primary modes of vibration, FRF curves and transient responses.

4. ANALYSIS REQUIREMENTS

4.1 General All the requirements for participation in the survey, and the details necessary to define the test structure, were provided in a booklet (Ref. [4]). Although the detailed modelling stage was left entirely to the individuals taking part, there was a number of reference coordinates prescribed at which data concerning mode shapes were to be specified: while each individual model would use its own grid to describe the structure, these 16 reference points were required to be included in each, see Figure 4.

4.2 Required Results Data were required in four groups, pertaining to various aspects of structural dynamic analysis:

The first group of data concerned the basic inertia properties of the structure and included:

- the total mass (M_G)
- the position of the mass centre (x_G, y_G)
- the moment of inertia about the z-axis (I_{zz})

These data were required in Tabular form.

The second group of data consisted of the basic modal properties of natural frequency (ω) and mode shape ($\{ \phi \}_r$) for each of the modes in the specified frequency range or $0 - 2500$ Hz. These data were required in tabular and sketch form and also included the number of modes (N).

The third group of data consisted of selected frequency response functions (FRF's), computed in a standard format (Inertance, or

acceleration/force) over a specified frequency range (0-2500 Hz) and with a standard frequency spacing. A uniform level of modal damping was prescribed and four FRF plots were required:

- $H_{7,7}$, $H_{7,10}$, $H_{10,7}$ and $H_{10,10}$ (referred to the grid numbering system shown in Figure 4.)

These data were required in digital form.

The fourth group of data were transient response predictions. Two separate single-point impulsive excitation time histories were provided as input information (see section 3.3) and a small number of corresponding response time histories to each of these in turn were required from the analyses. The two pulses were essentially a short duration one (identified as F_1) and a longer duration one, F_2 , both applied at grid point number 7. Participants were requested to compute the displacement and acceleration responses to each of these forces separately, for the four key grid points 7, 8, 9, and 10. Once again, a value of modal damping was specified to be applied to all modes.

The individual responses are identified as follows:

- R7F1, R8F1, R9F1 and R10F1 for the first pulse, and
- R7F2, R8F2, R9F2 and R10F2 for the second pulse.

These data were also required in digital data form.

This complete set of data requirements was formulated in order to exercise the participants' capabilities to perform the various stages of a structural dynamic analysis: starting from the simplest level (of inertia properties), through the 'standard' eigenanalysis for mode shapes and frequencies, to the more demanding response predictions which require the combination of the modal properties both in the frequency domain (FRF's) and in the time domain (transient responses).

5. RESPONSE TO SURVEY

5.1 Initial Response The initial announcement of the survey attracted some 25 organisations to attend the preliminary planning meeting. Of these, 20 agreed to participate although not all succeeded in submitting results - there being just 12 sets of data at the closure of Phase I. Subsequently, publicity about the survey has drawn interest from a wider area, and there are several independent studies under way (not part of the formal survey) in Canada, India, Australia and the USA.

5.2 Data Submission All digital data was to be submitted on magnetic tape (or disc) in an agreed format, but in spite of detailed specification of the requirements and options, there were still many difficulties encountered

by the standard data submissions. In addition to the (inevitable?) corruption of occasional data files, there were numerous errors in labelling and formats as well as duplicated files.

Perhaps more serious were the several cases where the data indicated on the submission were in fact different from those actually provided, either by being the wrong units (often different by a factor of 1000) or being a different type of function (i.e. displacement instead of acceleration). On some occasions, there errors seemed to indicate less than ideal familiarity with the analysis packages used to generate the data being submitted: on others, simply poor housekeeping practices.

5.3 Basic Statistics Although only peripheral to the main results of the survey, some overall statistics on the methods and resources used by the participants are included here. Table 1 summarises the hardware and software systems employed by the 12 participants whose results are included, together with an indication of the type of mathematical model used to analyse the structure. Also presented, in Table 2, is a record of the approximate effort which was expended on the whole analysis.

6. RESULTS

6.1 Introduction It must be stressed at the outset of the presentation of the results that the primary comparisons to be made are between the various predictions themselves, and not against the measured data. Although comparison with measurement is undoubtedly of interest and relevance, it is secondary to a review of the scatter or variation amongst the different analysis methods. For this reason, the experimental data are presented later, in the Appendix, although in the same format as the submitted results so that comparisons can be made.

6.2 Inertia Properties The simplest set of data required were the basic inertia properties and the results submitted are presented in Table 3.

6.3 Modal Properties The results presented in Table 4 constitute a summary of the major modal properties submitted. The far right hand column indicates the number of modes predicted by each participant for the specified frequency range of 0 to 2500 Hz, but for simplicity, only the nine major modes identified as the first three 'spring', 'beam', and 'cylinder' modes have been included in the Table. Figure 6 shows examples of the mode shapes submitted by three participants for the first mode in each group. It had been intended that some form of direct comparison would be made of the mode shapes themselves, but in the event, relatively few sets were mass-normalised (a requirement) and so only simple graphical sketches of the type shown in Figure 6 were made.

6.4 Frequency Response Plots The next set of results consist of a group of four displacement/force FRF plots and examples of these are presented in Figures 7, 8, and 9. Fig. 7 shows the complete set of predicted curves for the point FRF $H_{10,10}$ while Fig. 8 shows the corresponding plot for the transfer FRF, $H_{7,10}$. It will be noticed that an extremely wide dynamic range is necessary on the FRF modulus axis and partly as a result of this, all the curves appear to be in relatively close agreement. Fig. 9 presents the data from Fig. 7 in somewhat greater detail by displaying in three smaller frequency ranges - (a) 0 to 150 Hz, (b) 300 to 1300 Hz, and (c) 1300 to 2500 Hz. From these plots it is easier to gauge the level of agreement between the 12 different predictions. It can be seen that although there is generally a wide envelope encompassing the different curves - and this would tend to indicate a large degree of variation between the results - there are a number of results (perhaps 5 or 6) which are in quite close agreement amongst themselves. Attempts to relate these by a particular FE code produced no correlation at all, suggesting that the way the modelling was done was more significant than the system used.

6.5 Transient Response The final set of data to be submitted were the transient response time histories for the two specified input pulses, F_1 and F_2 . Samples of the results from this section are shown in Figures 10 and 11, both relating the acceleration response at point 7 (to the excitations applied at point 10). The first of these is for the so-called 'hard' impact, and it is seen that a very wide range of response levels were predicted by the different analyses. Of course, in displaying time histories it is not possible to use logarithmic scales and, as a result, it has been necessary to use three plots for this first case, each having a response scale an order of magnitude (or two) different from the others. Fig. 11 shows a less severe result for the 'soft' impact case.

7. DISCUSSION

We hesitate to draw sweeping conclusions from the results presented in this paper. Our experience from previous surveys is that the correct conclusions are not always immediately clear even though the results might seem to suggest the contrary. Some care and considerable thought need to be devoted to the interpretation of the findings.

It is clear that there is a wide variation in the various predictions of the dynamic properties of modal parameters and responses and that several of the predicted data must be seriously in error. Others are almost certainly good estimates of the parameters of interest, and so it must not be concluded (from the scatter) that accurate predictions cannot be made. What is seen is that inaccurate predictions can be made by poor analysis

methods, and this is probably the essence of the variations throughout. That being the case, there is clearly some need for procedures which could indicate the quality or reliability of a given prediction so that a good analysis can be identified (as, indeed, can a poor one).

The analyses which have been reported here were undertaken in the most arduous of conditions in that no one had any prior experience on structures of similar design, nor were any experimental data provided to guide the analyses. Either one of other of these aids would generally be available in a more 'practical' application of the same prediction techniques. Thus, the next stage, or Phase 2, will seek to assess the methods of model refinement or adjustment which are used in order to develop the mathematical model which can be used with confidence in dynamic analysis design.

It will be noted that direct comparisons between the predicted results and the experimental data have not been made, although some relevant measurements are included in the Appendix. This procedure was adopted for a number of reasons: the predicted responses used a uniform modal damping factor which was certainly different from that exhibited by the structure, the experimental data were themselves subject to error as the structure turned out to be difficult to test and, as mentioned before, the main objective was to compare one prediction with another. One of the complications with the testpiece was that the two-dimensional nature of the properties produced by the analyses (i.e. absence of out-of-plane modes) could not be so readily matched by the measurements and several of the lightly damped transverse modes are clearly visible in FRF measurements.

However, the results submitted for Phase 1 of the survey have shown the existence of potential hazards when making dynamic analyses for structures. The need for some systematic self-checking procedures in these analysis methods is clearly identified.

ACKNOWLEDGEMENTS

The survey reported in this paper was funded by the Ministry of Defence (Admiralty Research Establishment), and the authors wish to record their gratitude for the support thus provided. The authors would also like to record their thanks to the many individuals and organisations who, through their participation in the survey, have provided most of the information described above.

REFERENCES

1. Remmers, G. & Belsheim, R. O., 1964 "Effects of Technique on Reliability of Mechanical Impedance Measurement," Shock and Vibration Bulletin 34

2. Ewins, D. J., 1981 "State-of-the-Art Assessment of Mobility Measurement Techniques: A Summary of European Results," Shock and Vibration Bulletin 51
3. Smallwood, D. O. & Gregory, D. L., "A Rectangular Plate is Proposed as an IES Modal Test Structure," Proceedings, 4th IMAC, Los Angeles, CA, February, 1986, pp 1246 - 1255 (February 1986)
4. Imregun, M. & Ewins, D. J., "DYNAS Participants' Booklet," Imperial College Dynamics Group Report No. 8405, 1984

APPENDIX

Some of the measured data from tests on the structure are included in Figures A1 to A3.

In Fig. A1 a plot is presented which compares the various predictions for the natural frequencies of the nine major modes with the values deduced from tests. Ideally, all points should lie on a line of 45° slope.

Figures A2(a) and (b) show the measured FRF curves $H_{10,10}$ and $H_{7,10}$ respectively and relate to the predicted results shown in Figures 7 and 8.

Figures A3(a) and (b) show measurements of the response at point 7 to the transient excitations F_1 and F_2 respectively and which compare with the predictions shown in Figures 10 and 11.

Discussion

Mr. Hanna (Synergistic Technology): Can you make any comment about the case where you had several users of the same finite element code? Can you make any comment about the consistency that you observed in the results that you got with that tool, as opposed to the consistency across the users of several different codes?

Mr. Ewins: We looked at the results for just that correlation, and we could not find any. I think one of the conclusions we are lead to is, it is the user, and not the code that is critical. There are discussions about approving or validating or licensing finite element codes. It is quickly coming around to the suggestion of approving or validating or licensing the users, and not the codes. But there was no obvious correlation in that sense.

Mr. Goff (General Electric): You had a set of participants that seemed to get reasonably good results for the low frequency end of the frequency response function. Did you have a similar subset that seemed to be able to give you reasonable results for the transient response, at least to the soft impact? Was there any consistency there at all?

Mr. Ewins: There is an element, but it is less clear cut in the transient response; a number of participants did get consistent results for the transient response to the soft impact. But, they were not the same people. We have not shown you the hard impact results because they are not digestable this early in the morning. We had to plot them in three stages, the standard range, which is more or less the same scale as the experimental results, 1/10 of the standard scale, and 10 times the standard scale. The second and third of those groups are not in the right ball park; but the others are. For each of the cases with the frequency response and the transient response, there is a group which came out with something that looked consistent among themselves, and perhaps the most important, also in line with the measured data.

Voice: Was the omission of constraints and going to a free free case due to the fact that the constraints would have complicated the case, or were there other considerations?

Mr. Ewins: It was really because, in spite of the comments from my learned friend here, the experimental data would be more reliably produced for a quasi free-free case than for a quasi clamped case. It was also slightly deliberate, malicious you might say, because the analysis packages sometimes have more difficulty coping with the zero frequency modes. In trying to exercise the analysis procedures, that was felt to be a little bit more demanding.

Mr. Tustin (Tustin Institute of Technology): What sort of estimated man hours would go into

an analysis such as this, assuming that one had the tools with which to do it?

Mr. Ewins: I have a plot which shows that, and it also shows the number of modes that the participants found. We asked the participants that question, and there are the results. It is a ratio of 10 to 1 in the effort put into it.

Mr. Tustin: How many hours would it take to build the physical model, the actual hardware? Did anybody fake what they turned in?

Mr. Ewins: I do not know whether anybody built one, I hope they didn't. We had a slight problem with the threaded two-section cylinder because, when they put the two parts together, they found they had made the two threads of different pitches. We had to make a second one.

Mr. Paladino (Naval Sea Systems Command): Several years ago we kicked off the "Uncle Sam" project at San Diego. I think what is missed by the audience is, when the U.S. participated, we selected the real experts. You did not give the results of the U.S. program, but they were poor! We had one expert who missed the first fundamental mode. Here we are going into analytics, and we haven't solved the measurements problem. How can we get to the end if we don't know how to measure? How can you analyze it? It is very difficult. You people are the experts of the United Kingdom. What would you do if you turned the project over to senior engineers who are not the experts you are? How can we get there? We should go back to the basic measurement and find out why we failed there with known structures, and then proceed to the analytics.

Mr. Ewins: I said earlier you have to be careful about the conclusions you draw; it is tempting to draw the conclusion that we cannot collectively measure or analyze. That is not what the results say. The results say that it is possible, and a large number of the participants were able to make measurements which correlated well with other people's measurements and with their predictions. What you see here is a mixture of successful results and unsuccessful ones. The eye is drawn to the scatter produced by the numbers, 20%, 30%, or 50% of the poorer results. One of the conclusions which is buried in there, and is not immediately obvious, is, it is possible if you do the right things. If you use the right measurement techniques you can get consistent results, and ones which agree reasonably from one lab to the next. If you use the appropriate analysis techniques you can get sensible results. But what shows up more dramatically is, if you don't use the right techniques, then you can get nonsense. I do not think it is a question of different nationalities.

Mr. Paladino: No, I want to go back to our experiments. We told the people where to put the force, where to put their pick ups, and to give a dynamic calibration of their total

instrumentation. These were experts. These were mobility measurement experts. They failed. These people knew what they were doing. There is something basically wrong as to why we cannot make measurements and come out to what we should. We heard a paper yesterday, where someone spent \$20,000 to analyze a simple four legged foundation, and could not come up with the answer.

Mr. Ewins: I repeat, the difficulty lies in getting the right conclusions to this. I am sure, on the measurement exercise, if you looked at the way the measurements were made, as we did, blow by blow, participant by participant, you can identify some areas of bad practice. You can certainly say with hindsight; "Well that is the reason why that particular result missed the fundamental, or whatever." I do not think it is a situation that we cannot make the measurements, it is just that we are often not careful enough in both the measurement and the analysis techniques. If one is careful enough, and Rich's last slide is quite valuable, because I think the secret to all this is to be very skeptical about everything that one does and all results one gets. Question everything and check everything. There were obviously cases where simple checks were not made. Results came in where the mass was off by a factor of 10. When you get on the telephone, and you ask; "are you sure you got three kilograms, everybody else thinks it is 30 kilograms." That shows a lack of checks. It is not the fault of the analysis procedures, it is the way they are used. That is the difficulty, we do not always use the techniques properly.

Mr. Windell: Let me I add something from a participant's eyeview. Do not forget we asked the participants to bear their own costs, both computing and man power costs on this; this tends to get you to rush things, and not do the checks properly. So in doing that, we have actually encouraged the scatter that there really was. I think from the participant's point of view, it ought to be said, it was do it in your lunch time and that sort of thing. For me it was all right, because we do not have explicit costings like that, so I can lose it. But, for a commercial organization, it might be quite a constraint.

Mr. Ewins: I should add that the details of the structure are available to anybody that is interested. We have sent them all over the world. Unlike the measurement survey, there is no overhead involved. You do not have to ship a structure around so all you need is a little booklet with the details in it. Our experience with the measurement survey is, that having seen the results is no help. So, if anybody is interested, we can send copies of the booklet to anybody who wants them.

Mr. Smallwood (Sandia National Laboratories): It seems to me you are building a case for the necessity of always doing experimental, analytical, model verification. If you have

both the experimental results and the analytical results, and they don't compare, then obviously you have to spend some time trying to figure out which one is wrong. But if they do compare, it seems like you would at least get some kind of a warm feeling that perhaps they are both correct.

Mr. Ewins: I guess we have an ulterior motive which you have put your finger on; we believe that a lot of predictions should be backed up with tests, not necessarily the whole way, but components at various stages. Some of these results support the contention that you can't rely on predictions. As you said, if you get correspondence between your measurements and your analysis, and if you feel comfortable about it, you obviously have both sides almost certainly working correctly. However, behind this is the suggestion that testing has a major role to play in validating models before they are used in the ultimate design process.

Table 1 — Hardware, software and model types used in the survey
The figures in brackets refer to the number of participants

<u>Hardware</u>		<u>Software</u>		<u>Model type</u>
IBM	(5)	PAFEC	(5)	Beam elts only (5)
DEC	(3)	NASTRAN	(2)	Shell elts only (5)
Prime	(2)	BERDYNE	(2)	Beam & plate elts (1)
Sperry Univac	(1)	GSS	(1)	Beam & shell elts (1)
Amdahl	(1)	VOSTAN	(1)	
		COUPLE	(1)	

Table 2 — Time spent on analysis

<u>Participant</u>	I	II	III	IV	V	VI	VII	VIII	IX	X	XI	XII
<u>Man hours</u>	50	80	75	300	200	100	25	200	80	110	NS	38

Table 3 - Inertia Properties

Participant	Mass (Kg)	Mass Moment (Kg.m ²)	X _G (m)	Y _G (m)
I	31.5	2.88	0.494	-0.103
II	35.9	3.37	0.494	-0.116
III	32.2	2.99	0.493	-0.103
IV	32.0	2.94	0.493	-0.102
V	32.3	2.96	0.493	-0.102
VI	32.2	2.84	0.490	-0.102
VII	32.2	2.91	0.493	-0.103
VIII	31.3	0.20	0.493	-0.105
IX	33.0	3.00	0.450	-0.090
X	31.9	2.90	0.493	-0.097
XI	NS	NS	NS	NS
XII	34.6	3.36	0.493	-0.100

X_G = Abscissa of the gravity centre

Y_G = Ordinate of the gravity centre

NS = Not submitted

Table 4 - Major modes of the DYNAS Structure
Natural Frequencies (Hz)

Participant	S1	S2	S3	B1	B2	B3	C1	C2	C3	NOM
I	54	74	-	503	1464	2552	630	1670	-	12
II	45	61	-	448	1130	2110	518	1380	-	42
III	54	73	67	512	1380	2385	561	1553	2503	12
IV	57	35	80	434	1080	1645	544	1436	-	22
V	59	-	188	644	1608	2313	566	1565	2464	14
VI	54	74	84	440	1125	1920	530	1355	2384	15
VII	54	73	-	370	908	1580	553	1126	-	11
VIII	55	75	-	570	1574	2573	617	1588	-	8
IX	55	75	96	424	1052	1571	534	1435	-	24
X	55	75	110	428	1048	1559	545	1478	-	23
XI	55	75	123	445	1137	1935	537	1365	2379	18
XII	38	51	74	461	1140	1708	499	1358	2389	27
Min	38	35	67	370	908	1571	499	1126	2379	8
Max	59	75	188	644	1608	2573	630	1670	2503	42
Mean	54	68	103	473	1220	1998	553	1442	2420	19
Measured	59	80	118	426	1072	2002	532	1470		

S1 = Vertical extension/compression on U-springs (Y direction)
 S2 = Horizontal extension/compression on U-springs (X direction)
 S3 = Rotation on U-springs (θ_z direction)
 B1 = First I-Beam bending
 B2 = Second I-Beam bending
 B3 = Third I-Beam bending
 C1 = First Cylinder bending
 C2 = Second Cylinder bending
 C3 = Third Cylinder bending
 NOM = Number of modes (including rigid body modes) predicted

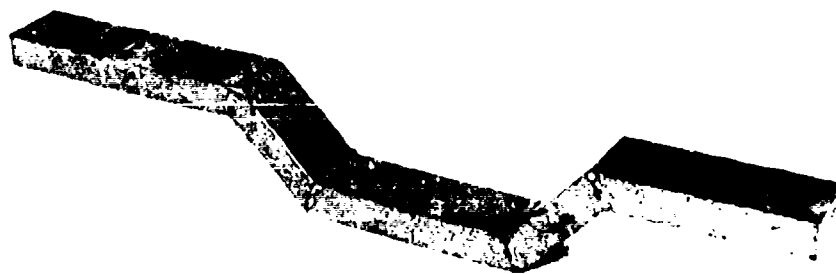


Fig. 1(a) — SAMM Structure (IIB)

BACKGROUND DATA 205

2151L

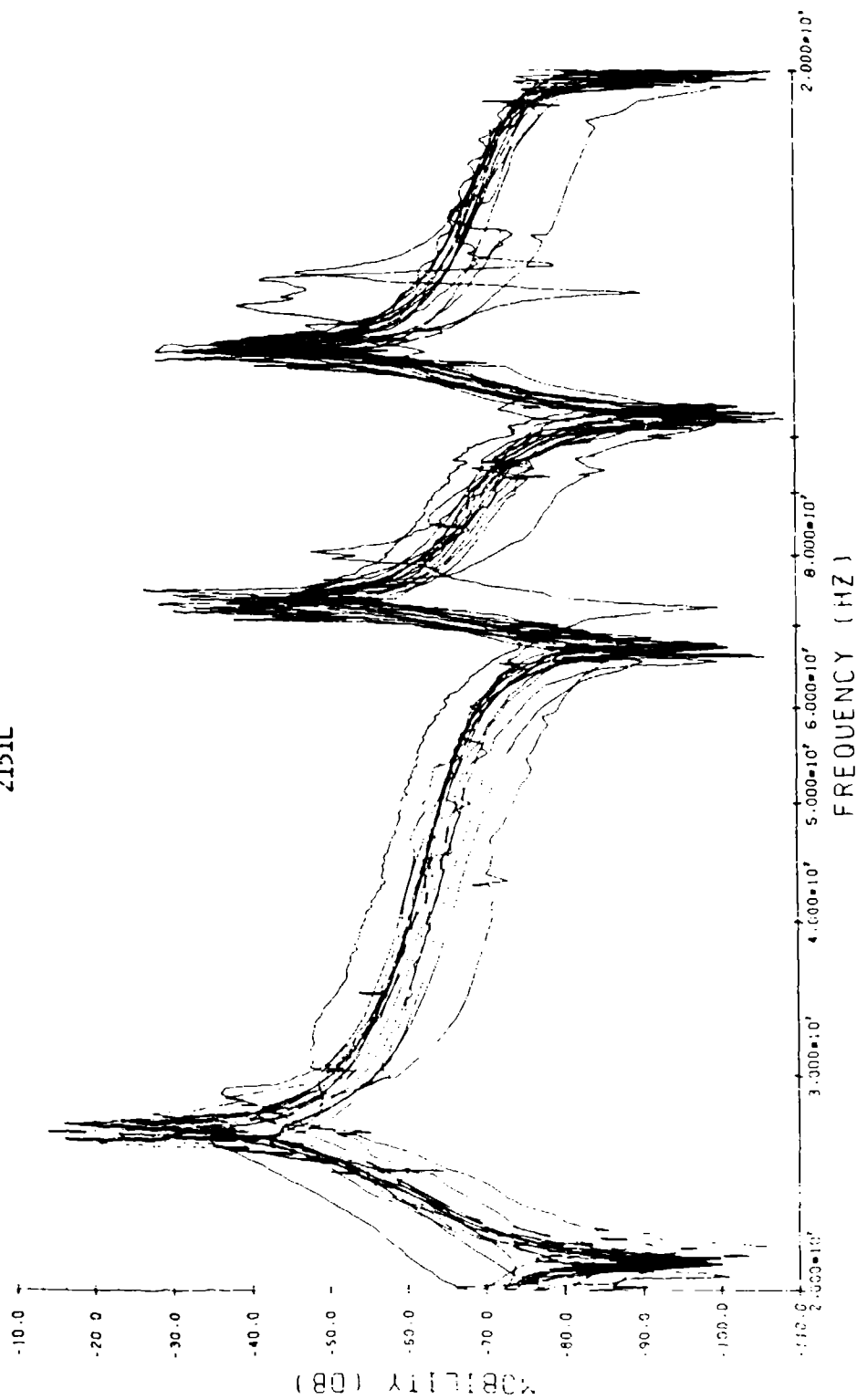


Fig 1(b) — Measurements on SAMM (IB



Fig. 2(a) — DYNAS Structure

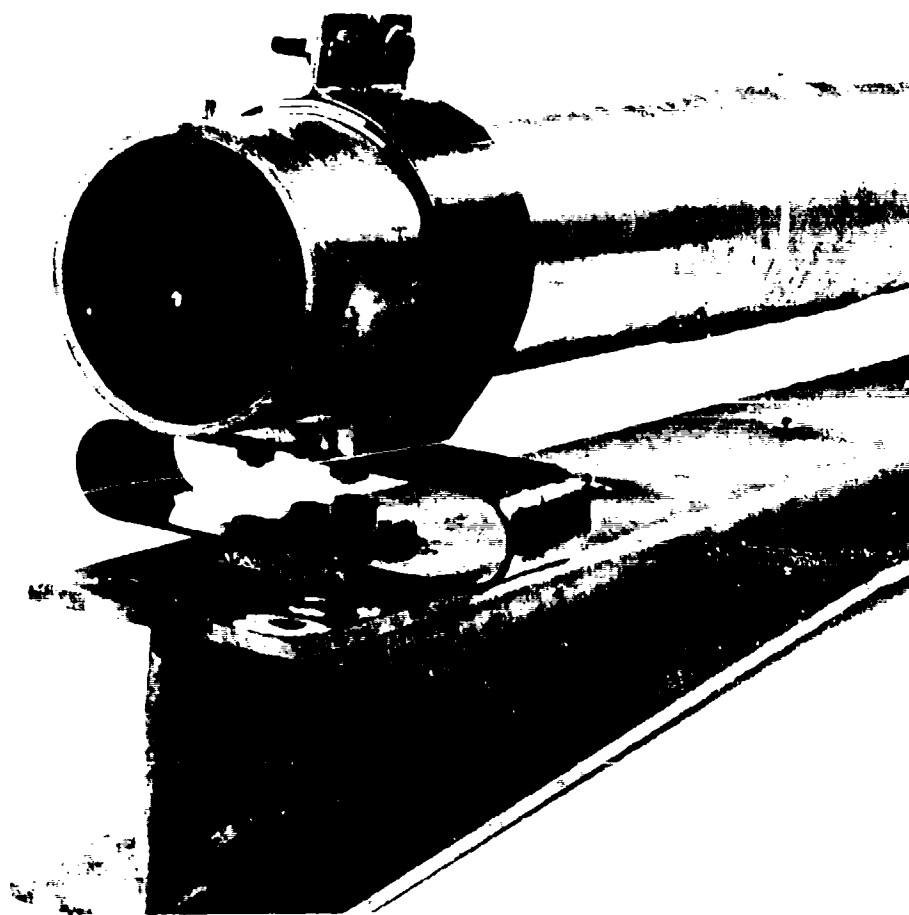


Fig. 2(b) — DYNAS Structure (details)

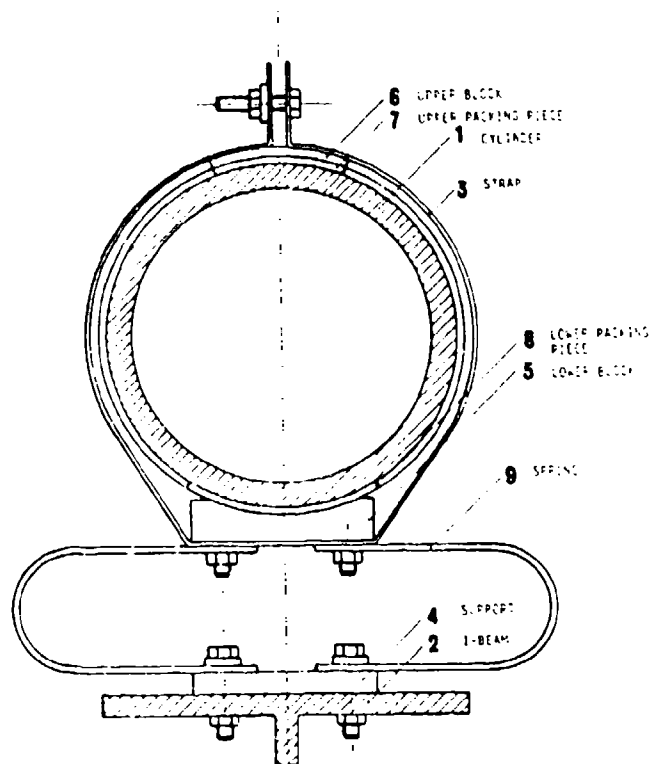


Fig 3a - Structure detail (i)

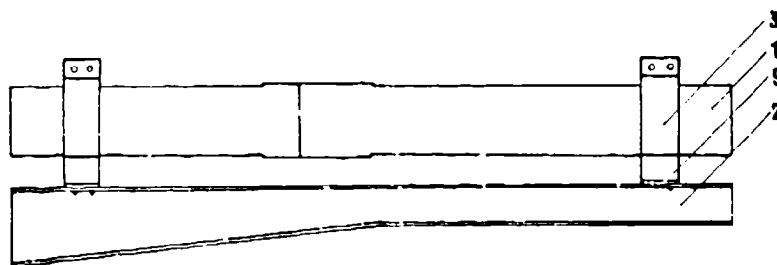


Fig 3b - Structure details (ii)

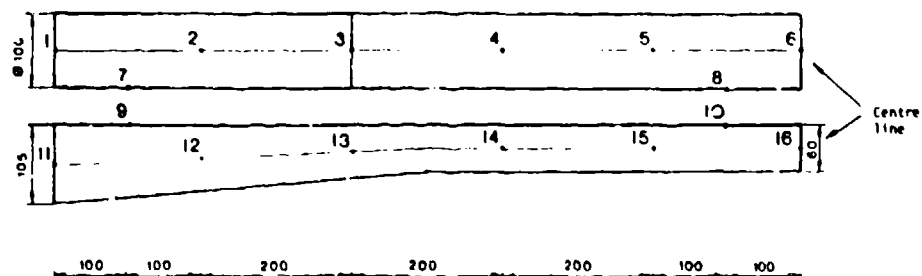


Fig. 4 — Primary locations on DYNAS structure

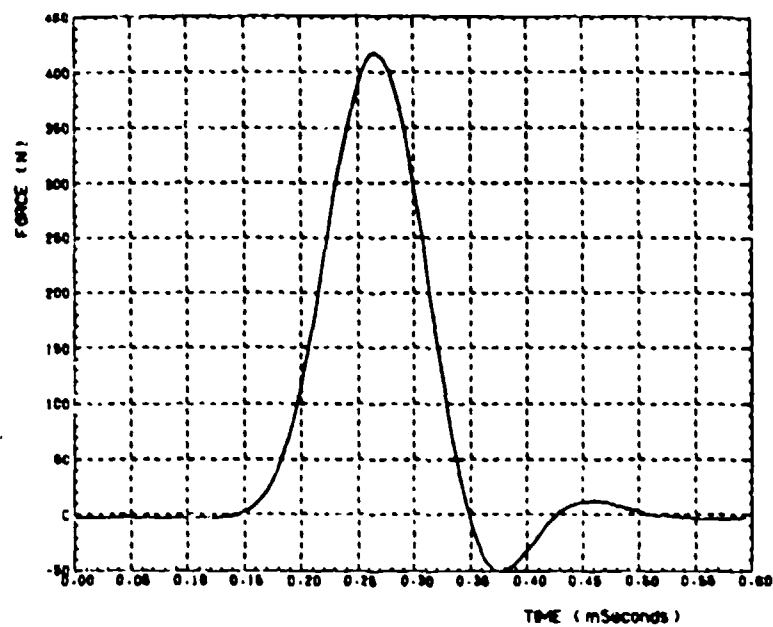


Fig. 5(a) — Impulse for hard impact

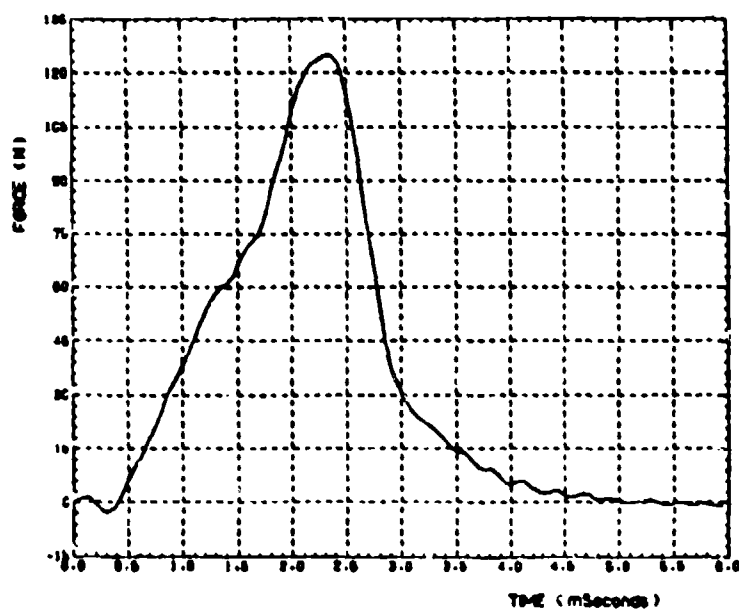
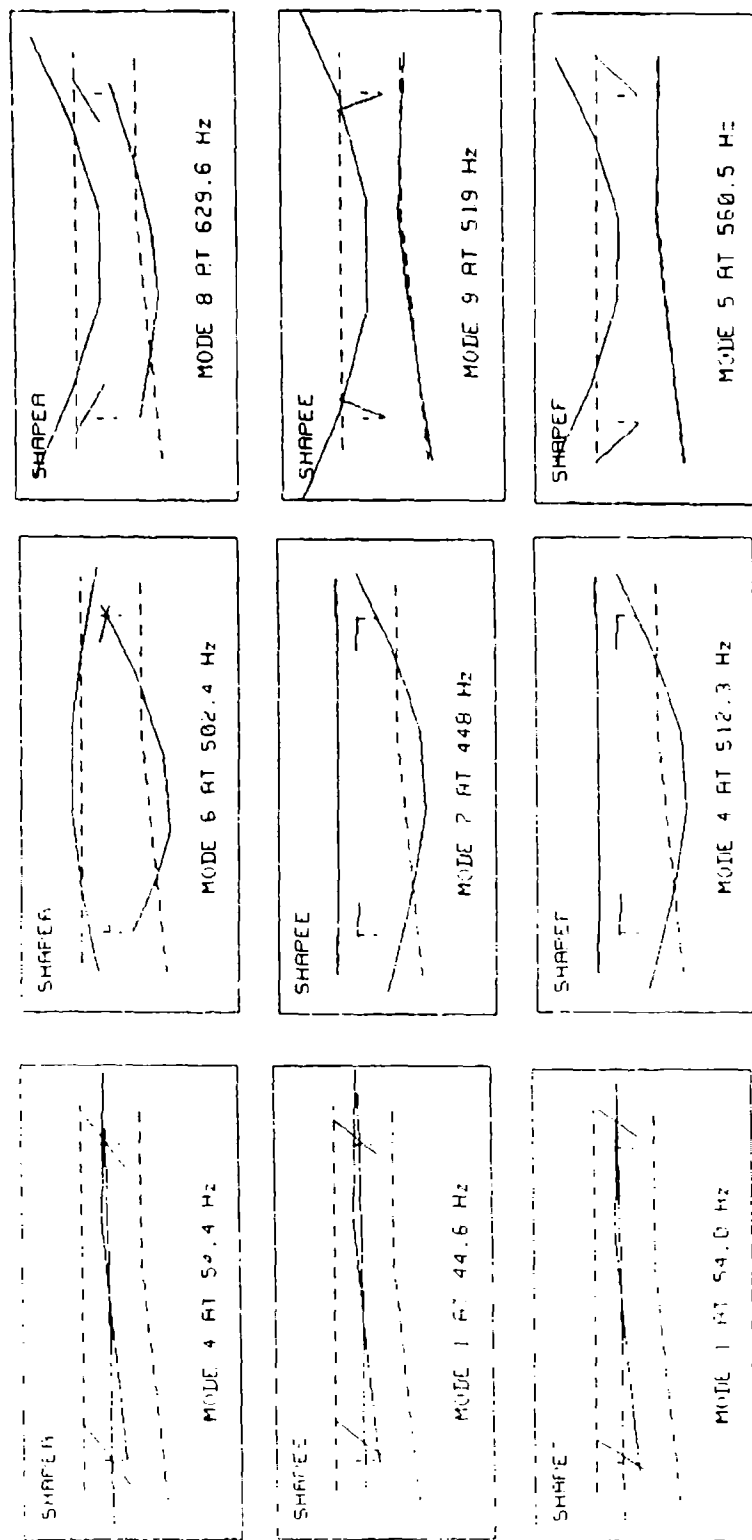


Fig. 5(b) — Impulse for soft impact



(c) - 1st cylinder bending

(b) - 1st beam bending

(a) - Extension on springs

Fig 6 - Examples of predicted mode shapes

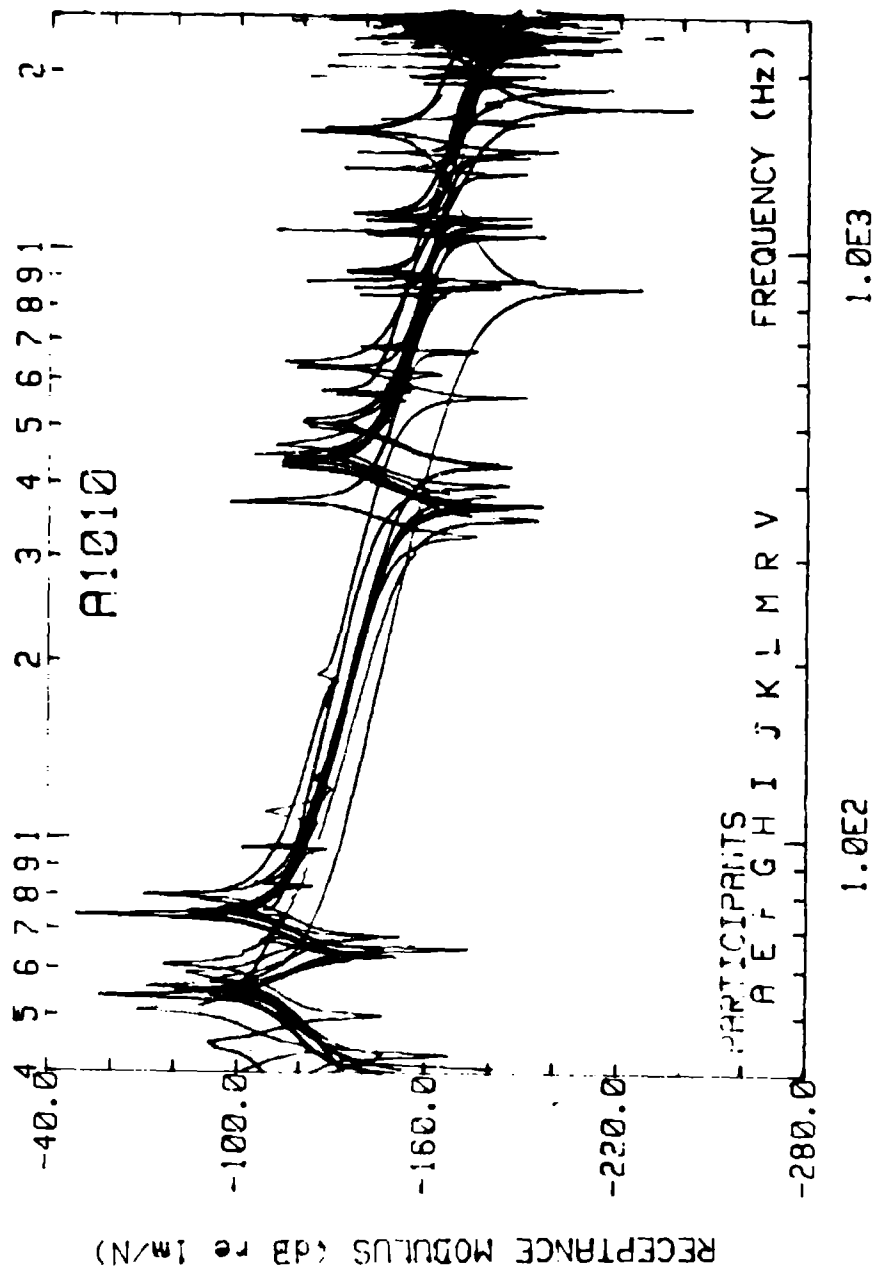


Fig. 7 — Predicted FRF H_{1010}

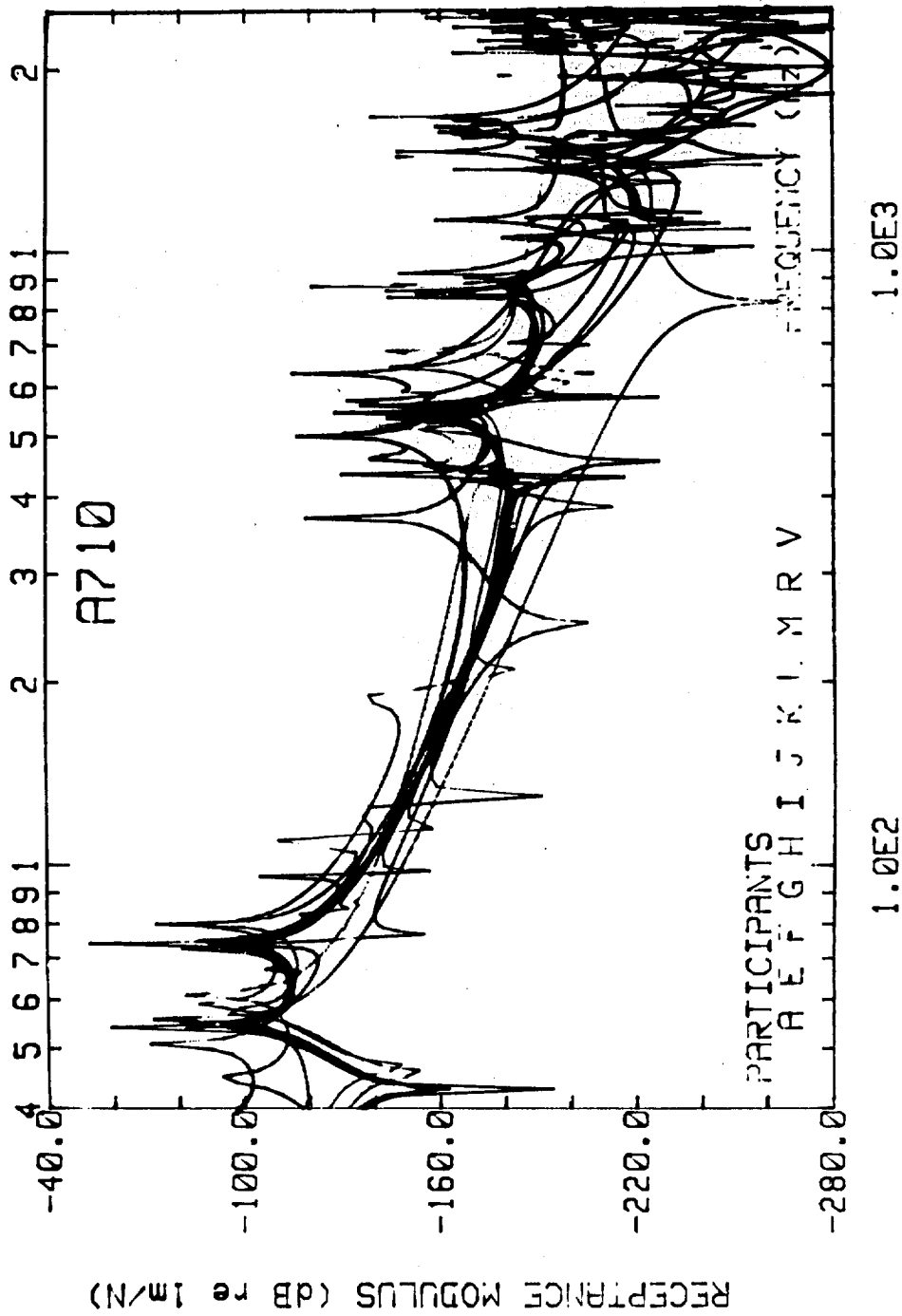
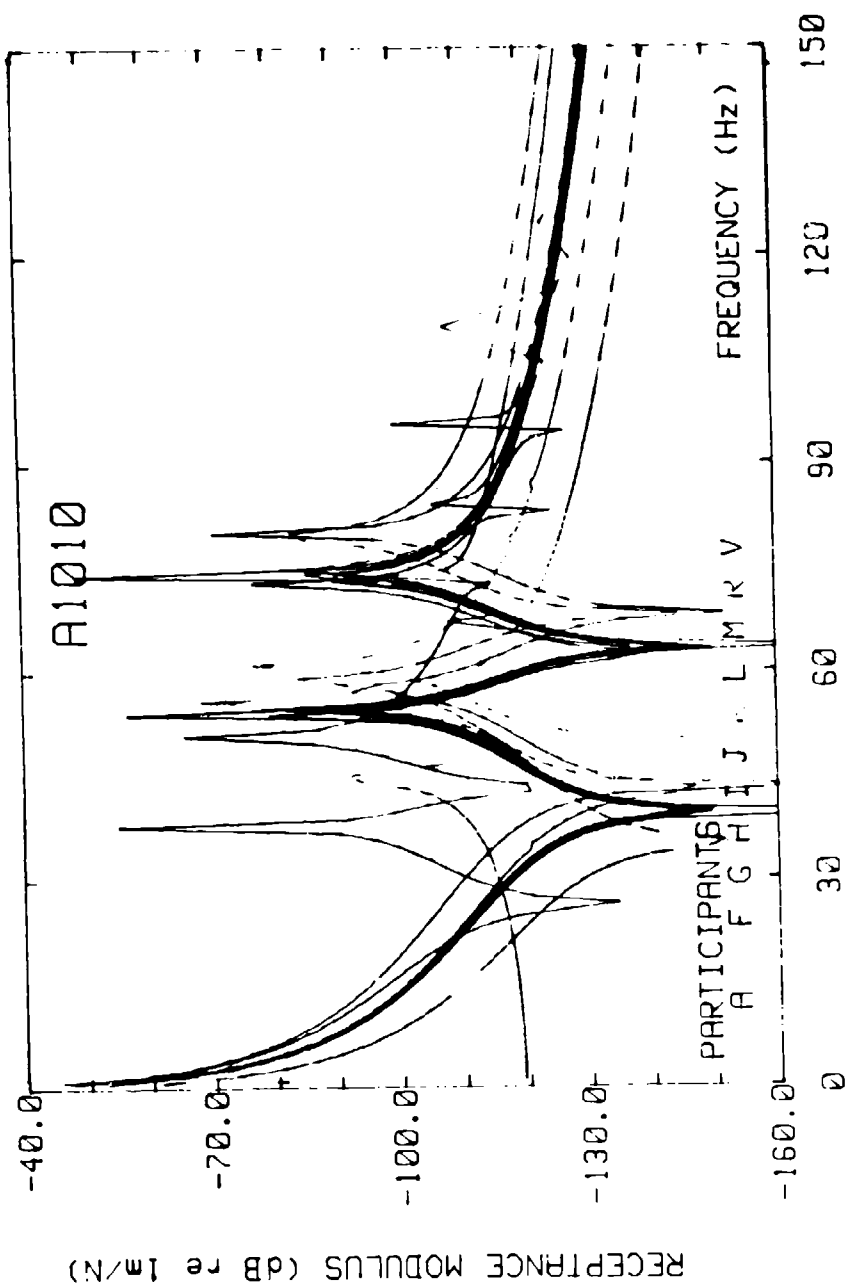
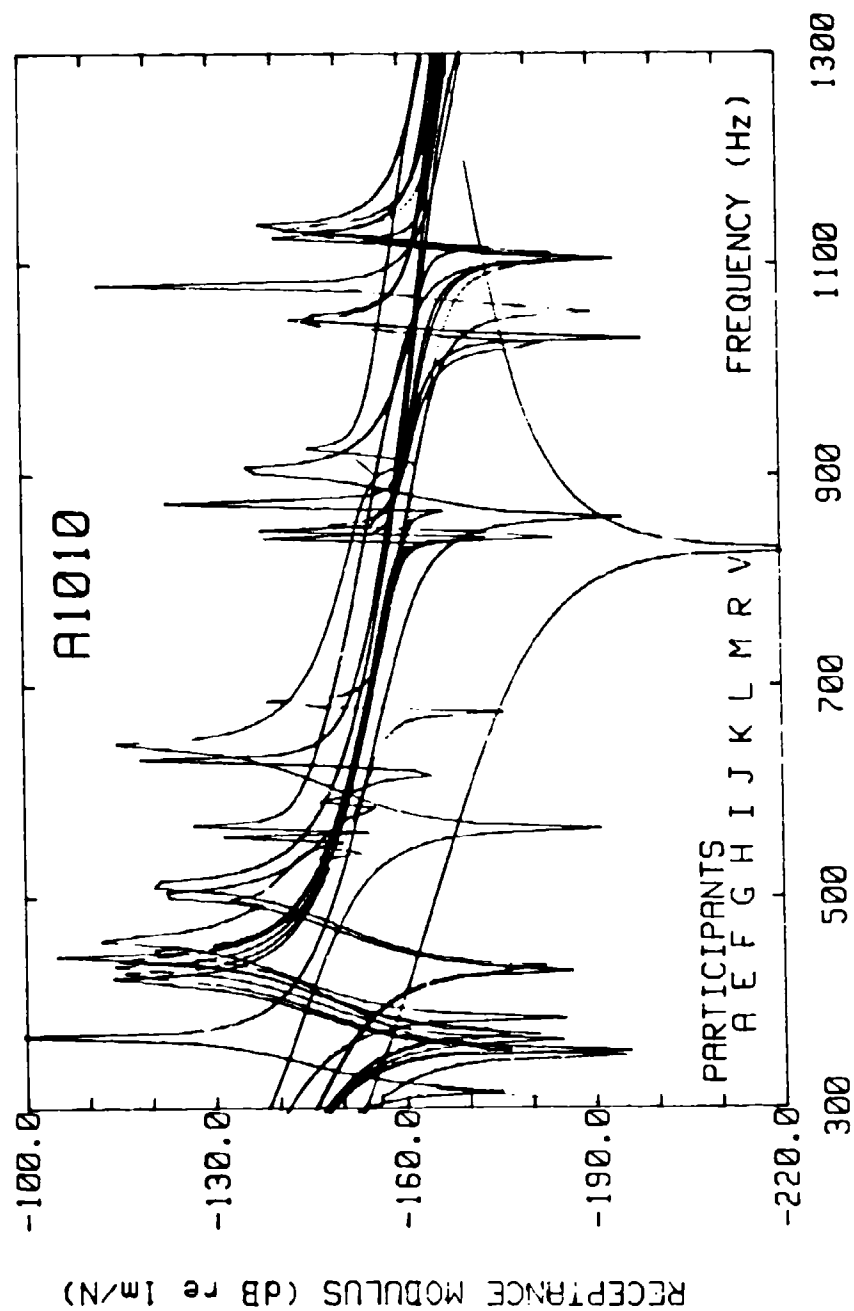


Fig. 8 — Predicted FRF H₇₁₀



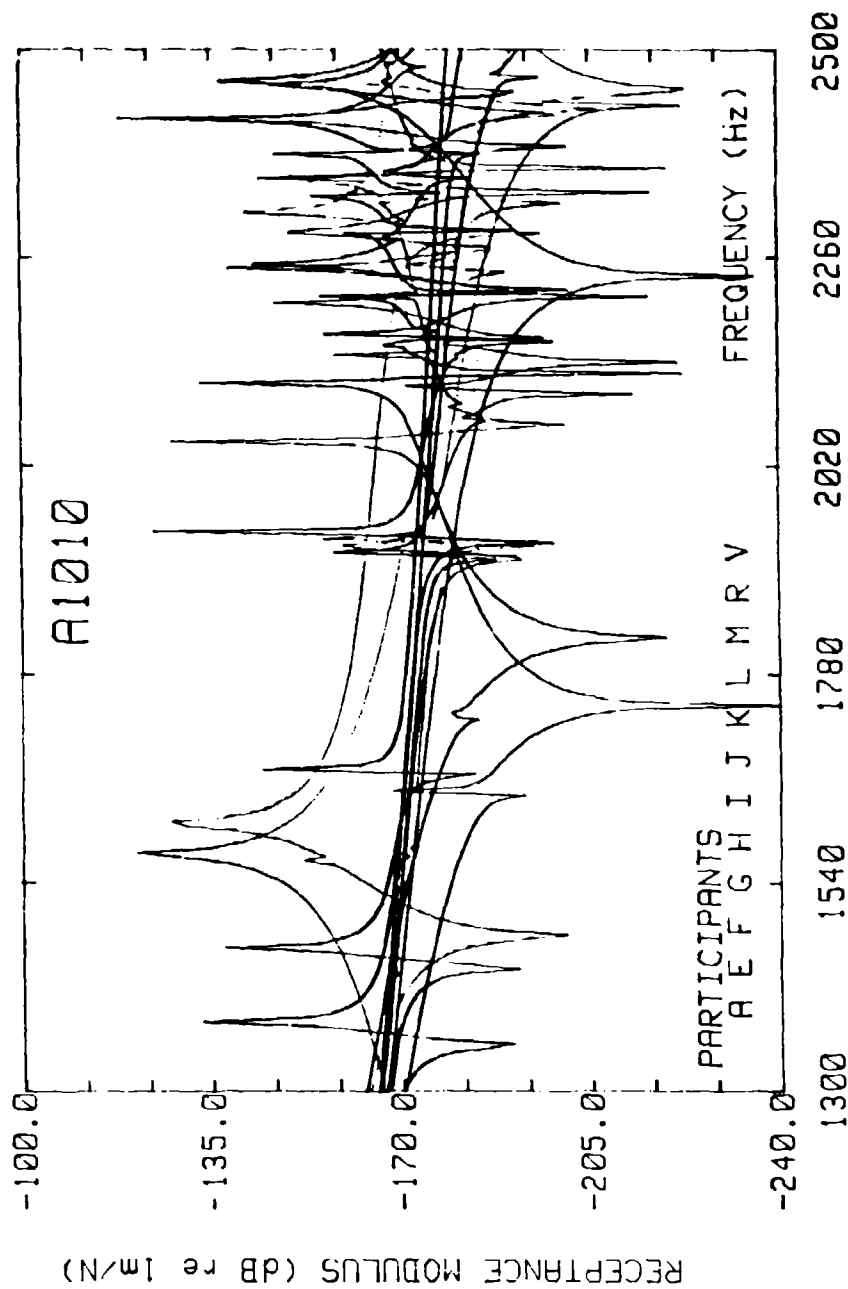
(a) — 0.150 Hz frequency range

Fig. 9 — Further details of FRF H_{100}



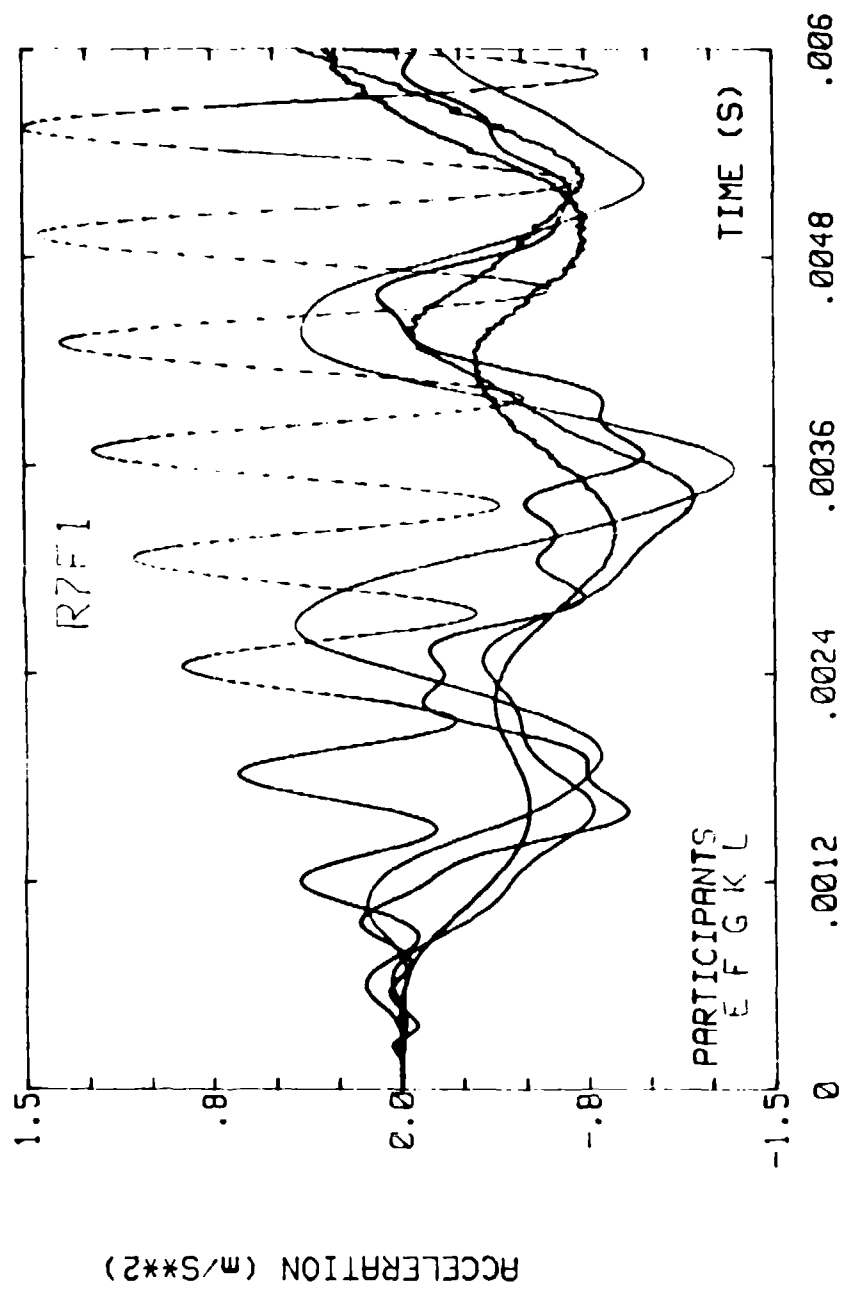
(b) — 300-1300 Hz frequency range

Fig. 9 (Cont'd) — Further details of FRF H_{1010}

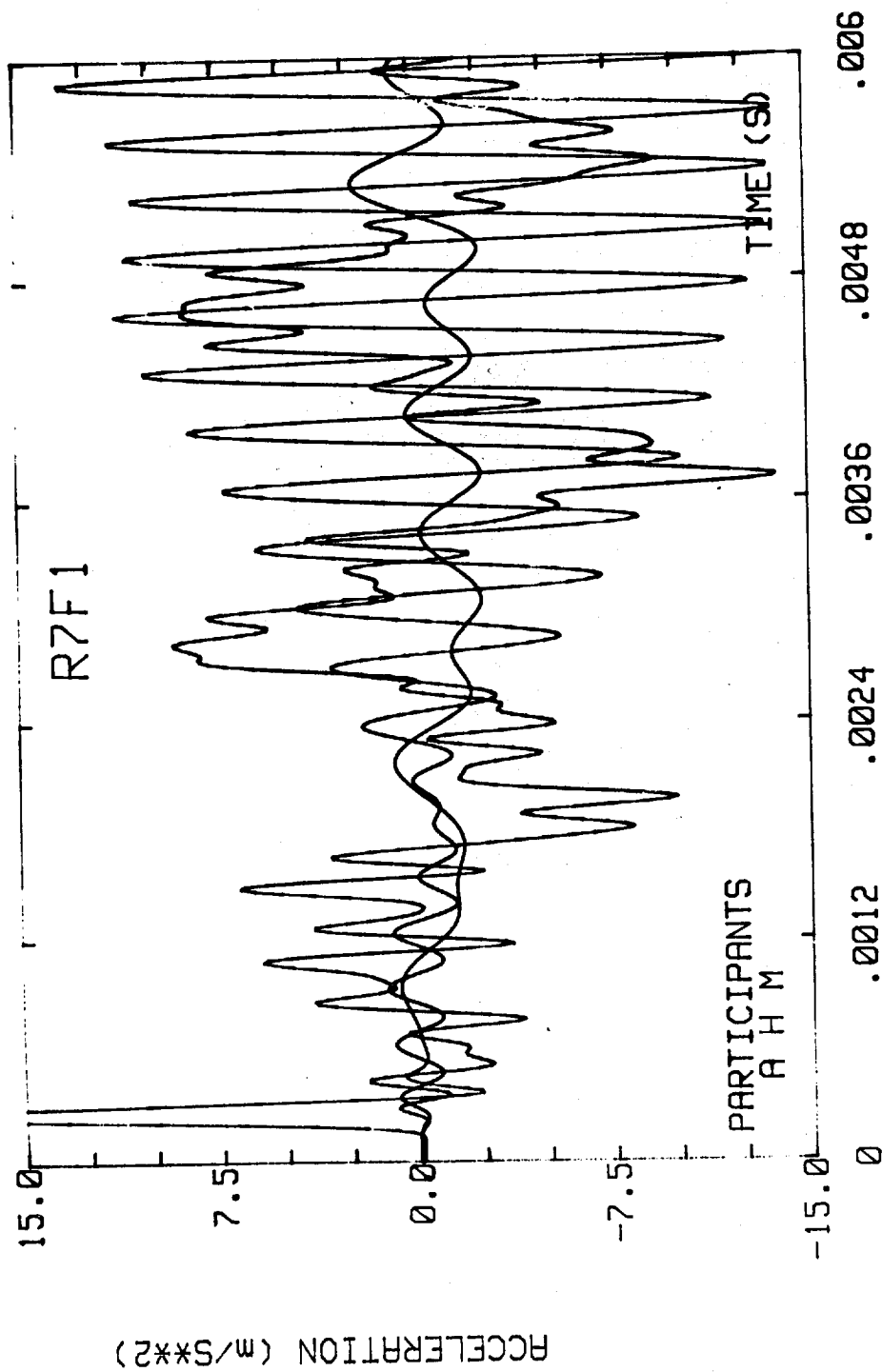


(c) — 1300-2500 Hz frequency range

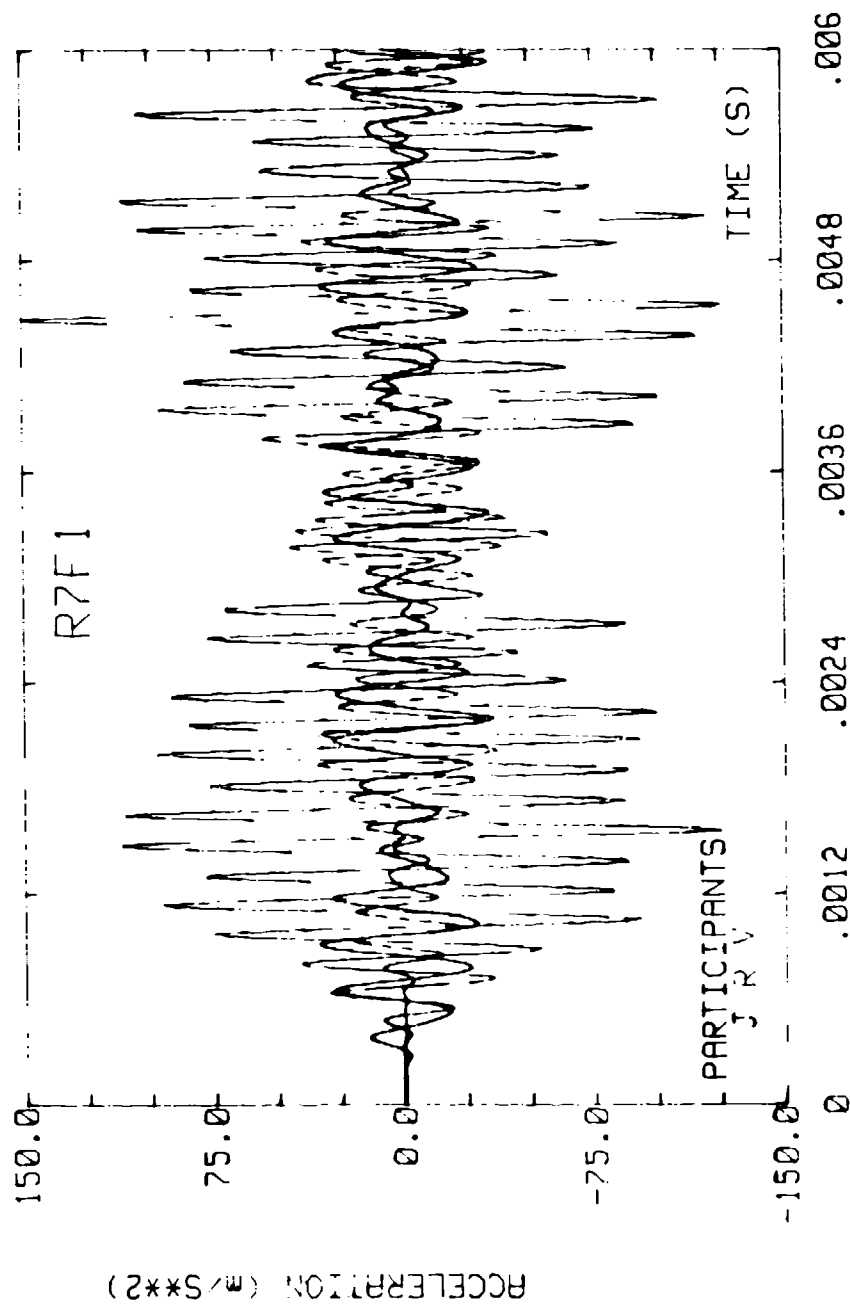
Fig. 9 (Cont'd) — Further details of FRF H₁₀₁₀



(a) — $\pm 1.5 \text{ m/s}^2$ range
 Fig. 10 — Transient response at point 7 to hard impact (R7F1)



(b) — $\pm 15 \text{ m/s}^2$ range
 Fig. 10 (Cont'd) — Transient response at point 7 to hard impact (R7F1)



(c) — $\pm 150 \text{ m/s}^2$ range
Fig 10 (Cont'd) — Transient response at point 7 to hard impact (R7F1)

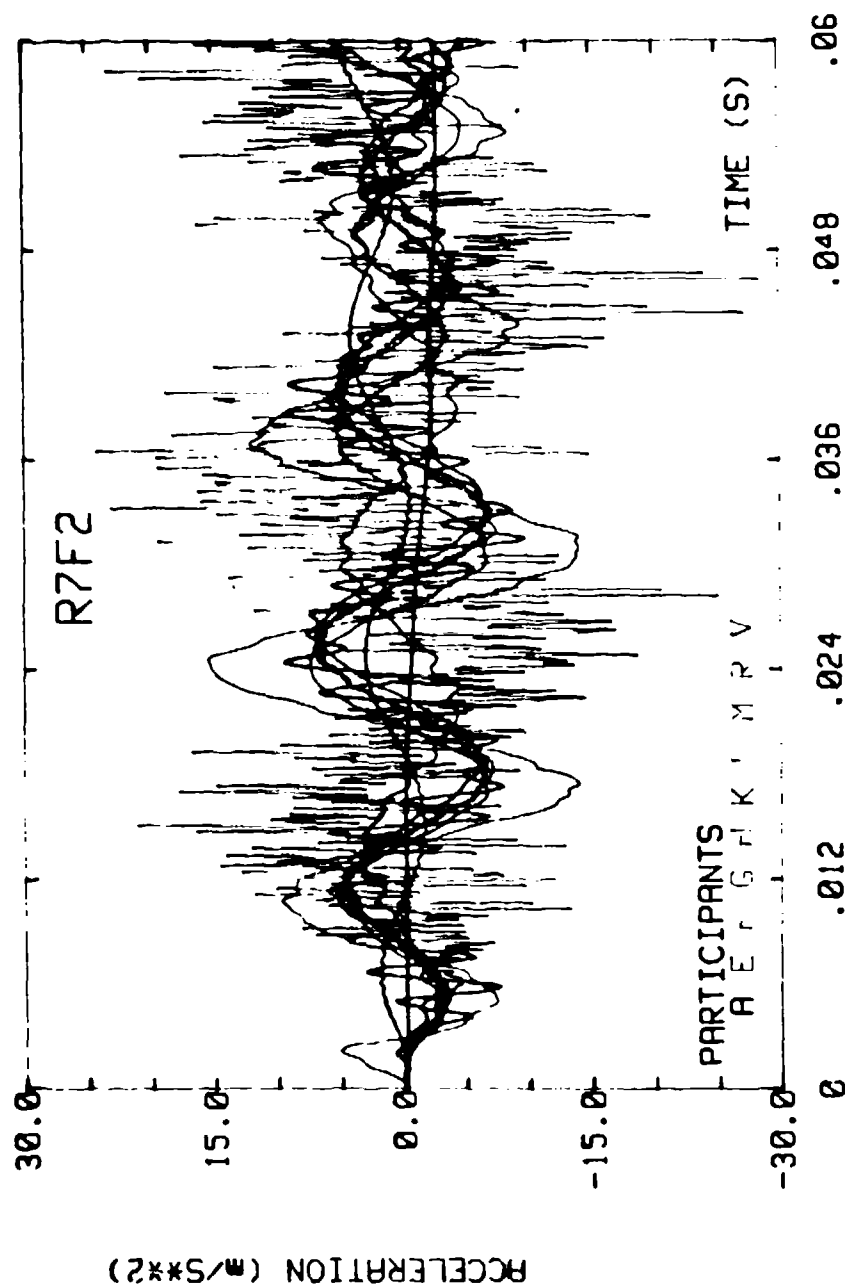
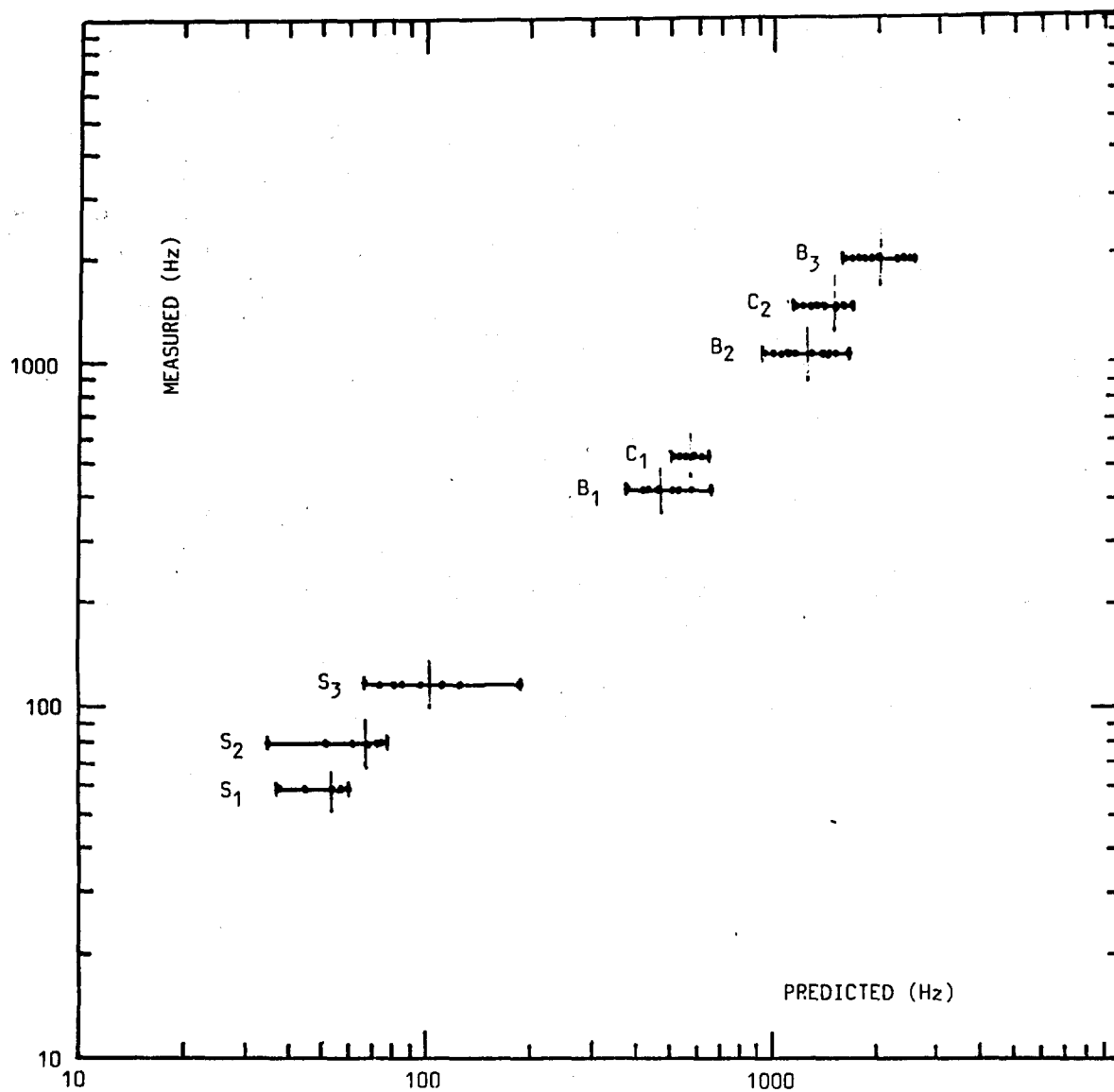


Fig. 11 - Transient response at point 7 to soft impact (R7F2)



(a) — [The vertical bar indicates the mean of the predicted values
(see Table 3 for notation)]

Fig. A1 — Correlation between predicted and measured natural frequencies
for spring, beam and cylinder modes.

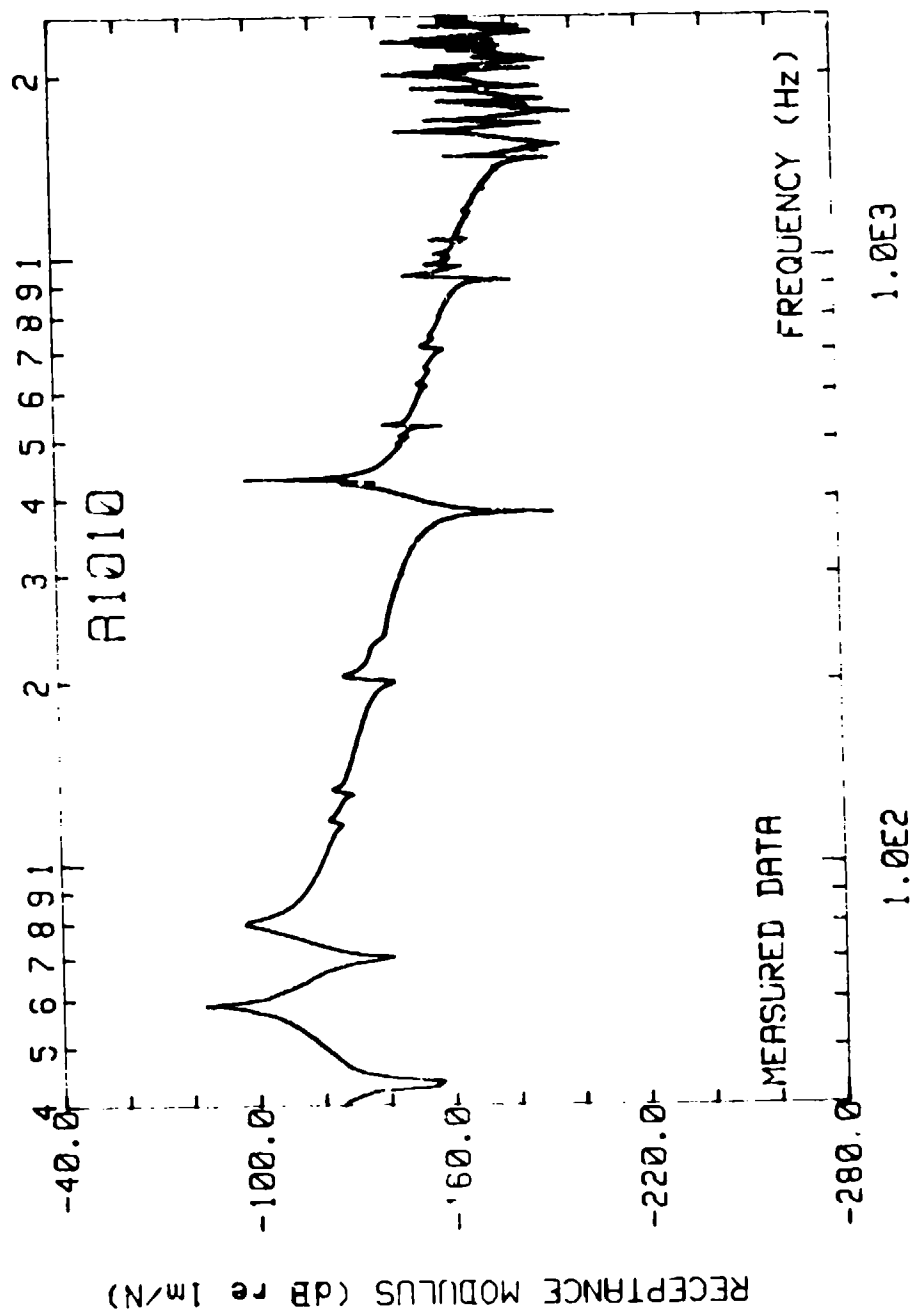
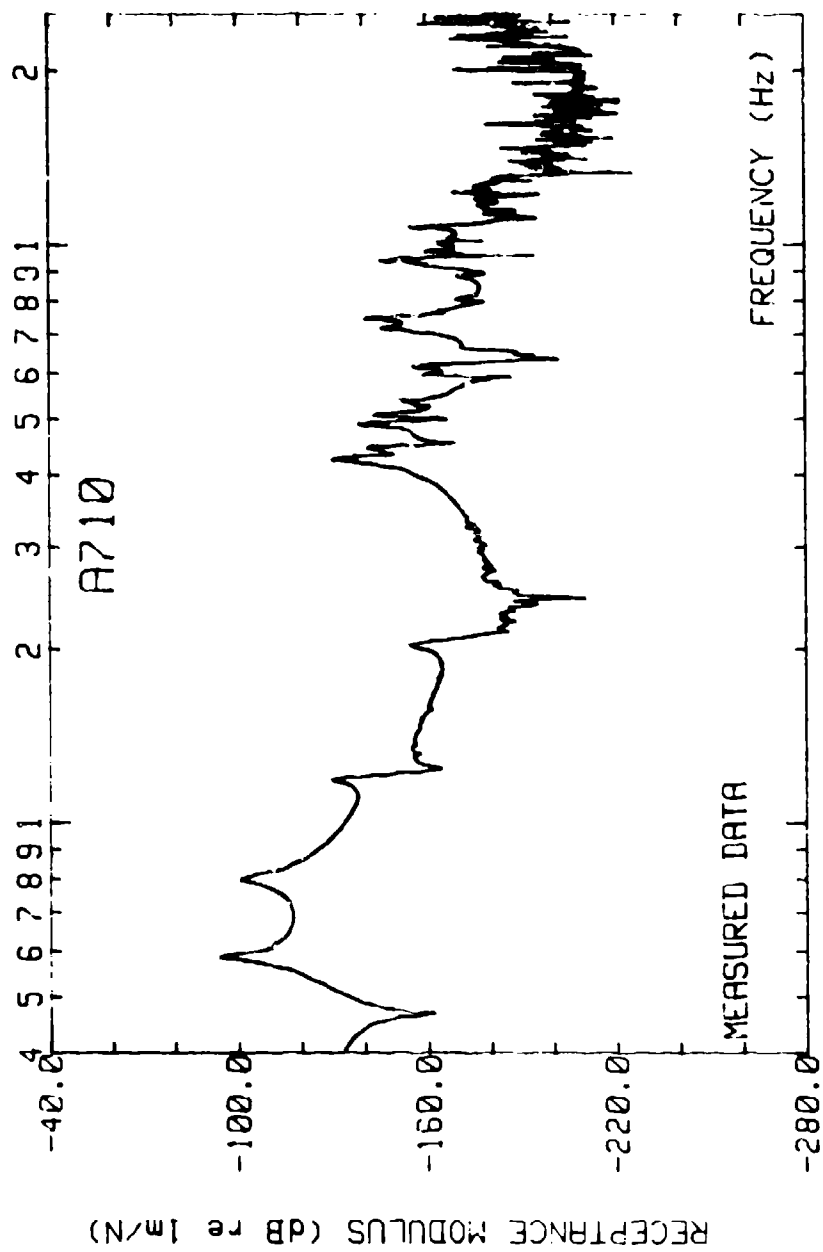


Fig. A2(a) — Measured FRF H_{1010}



1.0E2

1.0E3

Fig A2(b) - Measured FRF H_{710}

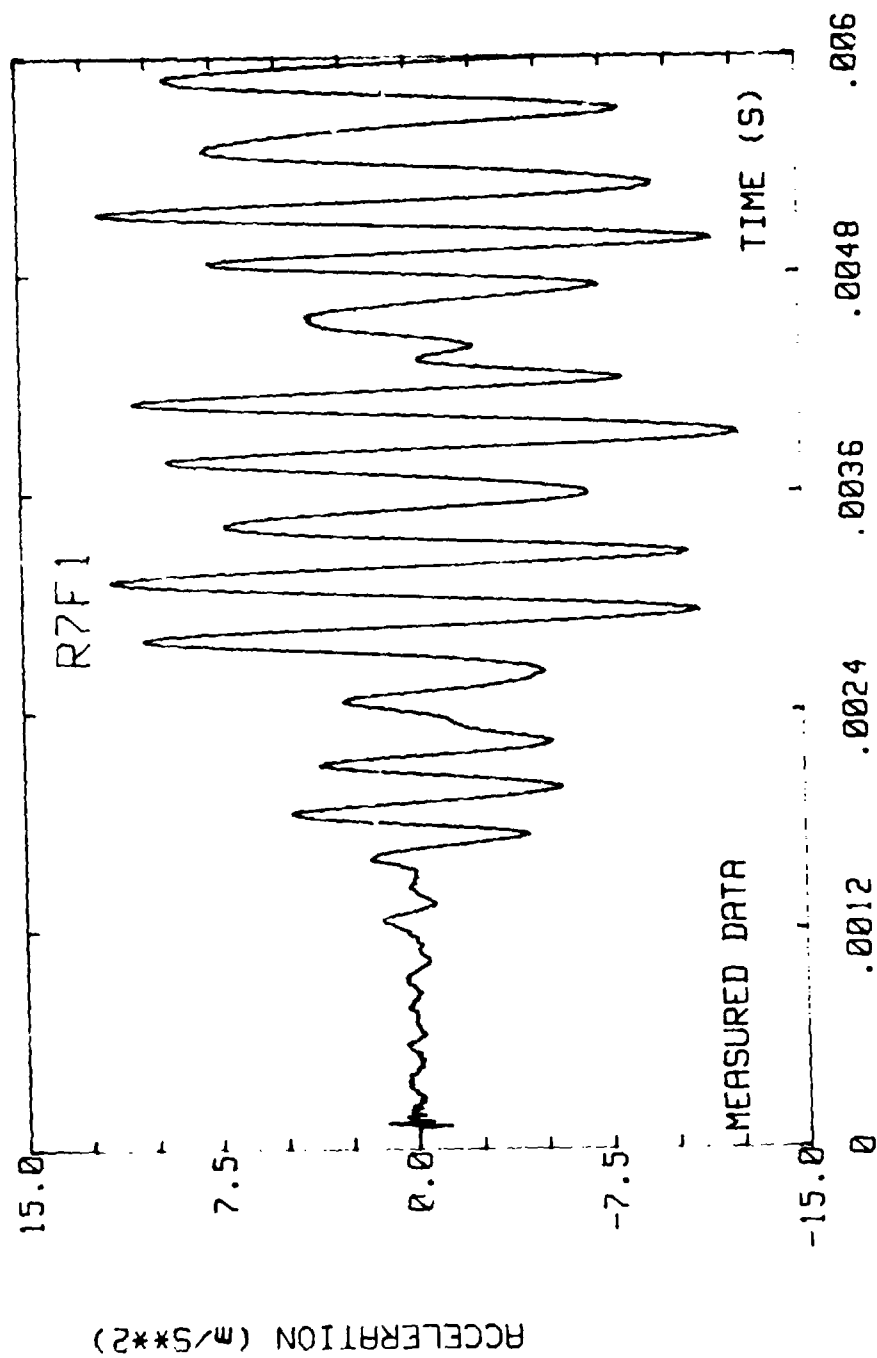


Fig. A3(a) — Measured transient response R7F1

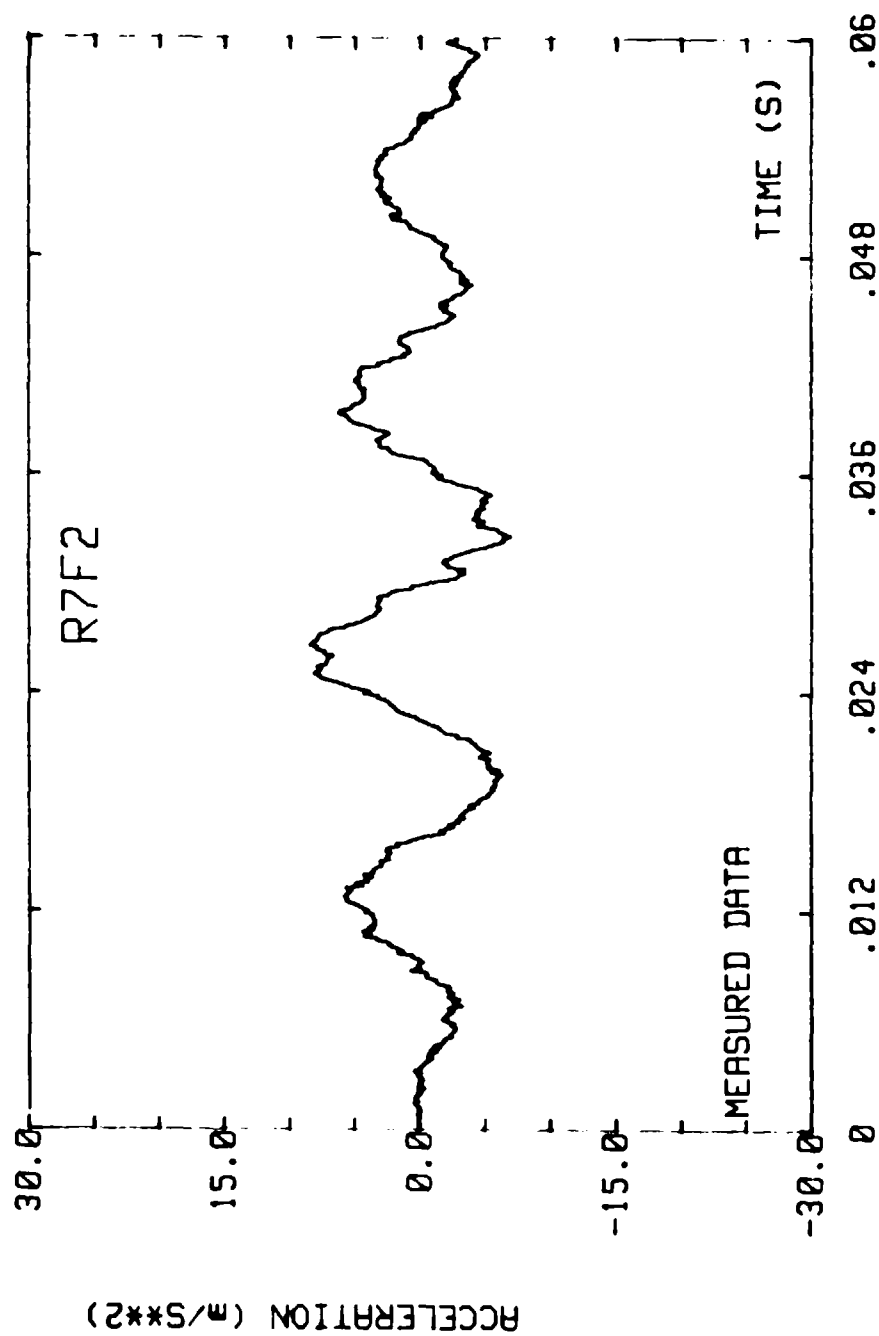


Fig. A3(b) — Measured transient response R7F2

THE DYNAS SURVEY - PART 2: A PARTICIPANT'S VIEW

R. W. Windell

Admiralty Research Establishment
Portland, Dorset, United Kingdom.

Various possible Finite Element modelling solutions for the DYNAS structure are explored. The author's solution and modelling assumptions are presented and final predictions compared with measured data. Good agreement is demonstrated for the "soft" impact with poor agreement for the "hard" impact due to modelling limitations.

INTRODUCTION:

The DYNAS survey invited a number of organisations to take part in mathematically modelling a defined structure to predict the response to both harmonic and transient forcing functions [1]. The object of the survey was to compare the results presented by each participant to examine the variability of the modelling techniques used and thereby assess the "state-of-the-art" for dynamic modelling. The collation and analysis of the data submitted were carried out by the Mechanical Engineering Department of Imperial College of Science and Technology, London. The general findings of the survey have been presented in part 1 by Professor D. J. Ewins; this part attempts to provide a "participant's view" of the activity.

Approaching twenty participants within the U.K. took part in the survey all with different modelling experience, analysis methods and modelling philosophies. Furthermore, since the costs of the individual analyses had to be borne by the participant organisations, very different amounts of time and effort were devoted to the problem.

This part of the paper attempts to explore the problems and considerations involved in modelling the structure seen through the eyes of one participant - the author. Although any mathematical or computational technique could be used, the majority employed Finite Element (F.E.) modelling including the author. Consequently, this paper restricts comment to F.E. modelling of the structure and examines possible alternative strategies. The model developed by

the author is presented with specific reference to the modelling assumptions used and some results from this model are discussed and compared with measured data.

It must be stressed that the modelling approach presented here is not intended to be regarded as definitive, but merely one for the purposes of discussion.

THE STRUCTURE:

The complete structure has been described in part 1 and a sectional view showing the most important features is shown in fig. 1. A non-uniform circular cylinder is connected to the flanges of a tapered I-beam by means of four springs and two thin straps. The springs themselves take the form of U-straps and various packing pieces and bolts are used in the complete assembly. In exploring modelling the structure as a whole, the problems associated with each component are discussed in turn.

THE CYLINDER:

The cylinder is made in two parts with an off centre screw joint. The wall of the cylinder is locally thickened at the joint and a rebate is cut at the shoulder of the thread. A sketch of the cylinder is presented in fig. 2. Note that all dimensions are expressed in millimetres.

When contemplating the modelling of the cylinder, the following points might be considered:

Is the screw joint significant?

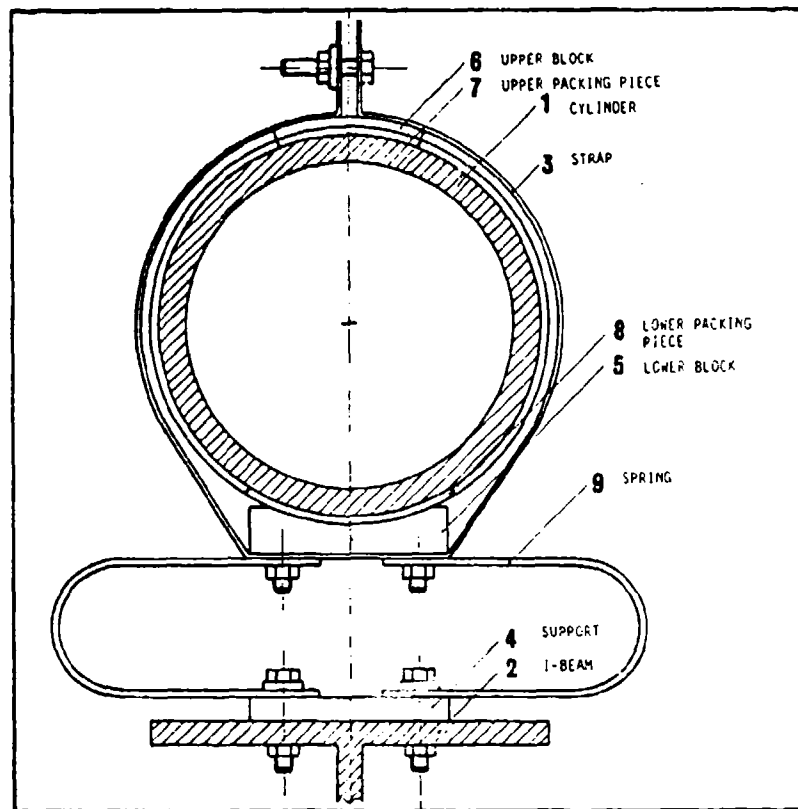


FIG.1. SECTION THROUGH THE COMPLETE STRUCTURE

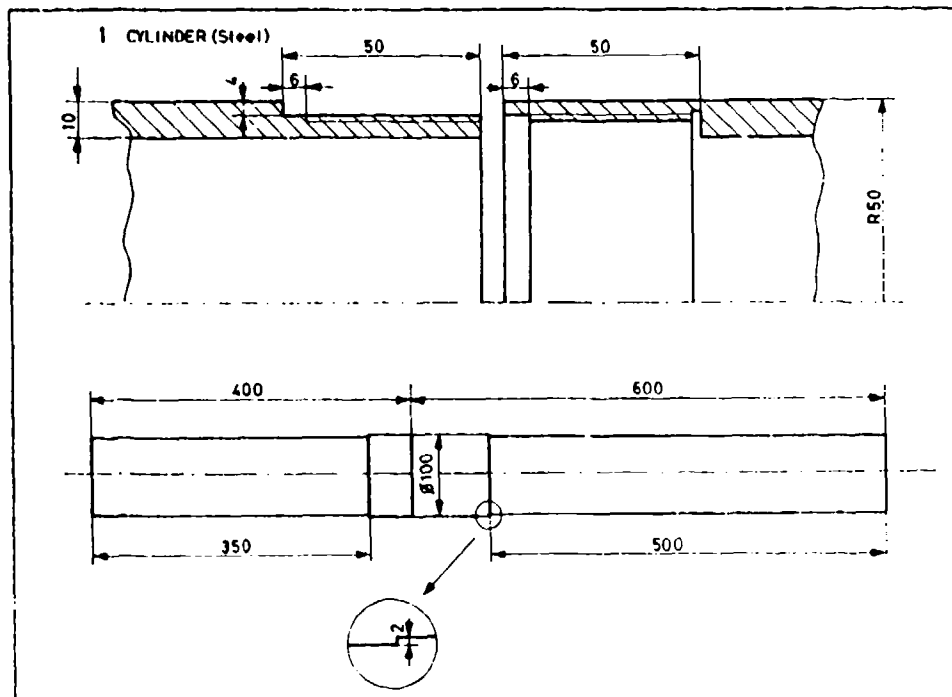


FIG.2. DETAILS OF THE CYLINDER

Is the rebate significant?
 Are circumferential harmonics important?
 The cylinder is not of constant thickness.
 Is the cylinder "thick" or "thin"?

Modelling a screw joint using F.E. is not simple, and in general, is likely to be unreliable. If the joint is loose fitting then opening and closing gaps may be significant and the stiffness of the joint effectively undeterminable without measurement. Such a joint is also likely to exhibit non-linear behaviour. In this case the screw joint is quite long, positively butting against the shoulder when assembled. It may therefore be reasonable to assume that the joint may be ignored except for the local thickening of the cylinder wall. This is also the most convenient and inexpensive approach.

In general, the modes of such a cylinder are combinations of beam bending, circumferential and torsional harmonics. Any torsional behaviour is not required in this survey and the ordering of the remaining modes depends on the geometry of the cylinder. Since this cylinder is not especially long nor especially thick it is difficult to judge if either of the types of modes may be ignored. Modelling the cylinder as a beam using beam elements of the appropriate sectional properties is easy and inexpensive but cannot predict circumferential harmonics. To model the cylinder fully is considerably more difficult and expensive, requiring either flat shell elements, semi-loof elements or thin shells of revolution. Furthermore, the choice of element will also depend on whether the cylinder is thick or thin. In this case the average thickness to diameter ratio is about 0.1 and therefore may be considered as thin. Consequently, in this case, any of the above shell elements may be used and full modelling at some stage seems advisable.

THE I-BEAM:

A sketch of the I-beam is presented in fig.3. It is of constant section for half its length, the remaining half having a uniform straight taper. The top and bottom flanges are wide in relation to their thickness, but the thickness of both flanges and web are the same.

There are three possible approaches to modelling the beam. Flat plate elements is the most obvious but beam elements might be considered or a combination of both. To use beam elements requires different averaged properties per element for the tapered portion. Furthermore, beam elements cannot model the behaviour of the flanges, which since they are wide, may be significant. It perhaps would be better to model the web of the beam with flat plates and the flanges with beams. This would overcome the problem of the taper but the flange width problem would remain. Consequently, the most satisfactory approach is to use flat plate elements for the entire beam.

THE SPRINGS:

The springs are made in the form of deep U-straps from sheet spring steel with two holes in each "leg" for fixings. A sketch of the springs is presented in fig.4. The spring stiffness in the vertical direction when mounted within the structure is given by implication from the resonant frequency given in fig.4. However, there further considerations for modelling, namely:

What are the twisting and sideways stiffnesses of the springs?
 What is the effective stiffness of the bolted mounting?
 There are different contacts under compression and tension.
 During the transient response do the springs "bottom"?

If the spring stiffnesses in all directions had been given, then modelling of the springs would have been trivial and could be most easily achieved using spring elements. However, in this case some stiffnesses are unknown and can only be obtained by modelling. The springs themselves are thin and therefore may be modelled using either flat plate or semi-loof elements. Furthermore, each spring has four holes which are likely to influence the stiffness and therefore should at least be considered in the modelling. Finally, if flat plate elements are used around the curve of the springs then they are likely to give a slightly over-stiff prediction.

THE FIXINGS:

The complete structure is assembled using various fixings shown in fig.1 including:

Twenty bolts.
 Two straps.
 Ten packing pieces.

Such fixings are in general difficult and expensive to model and some decision must be taken as to their significance.

The simplest approach is to ignore any effects except that of their mass, and incorporate this effect using correctly placed mass elements. However, this is clearly not actually correct failing specifically to model the stiffness of the bolted joints and assuming "single point" contacts. Alternatively the bolts could be modelled as stiff springs, but their actual stiffness would depend on the torque to which they are tightened which is not defined. The packing pieces could be modelled using 3D brick elements and the straps with thin semi-loof or shell elements. Again the pre-tension in the straps is not defined.

THE ASSEMBLY:

Finally, in modelling the assembly the following additional information should be considered:

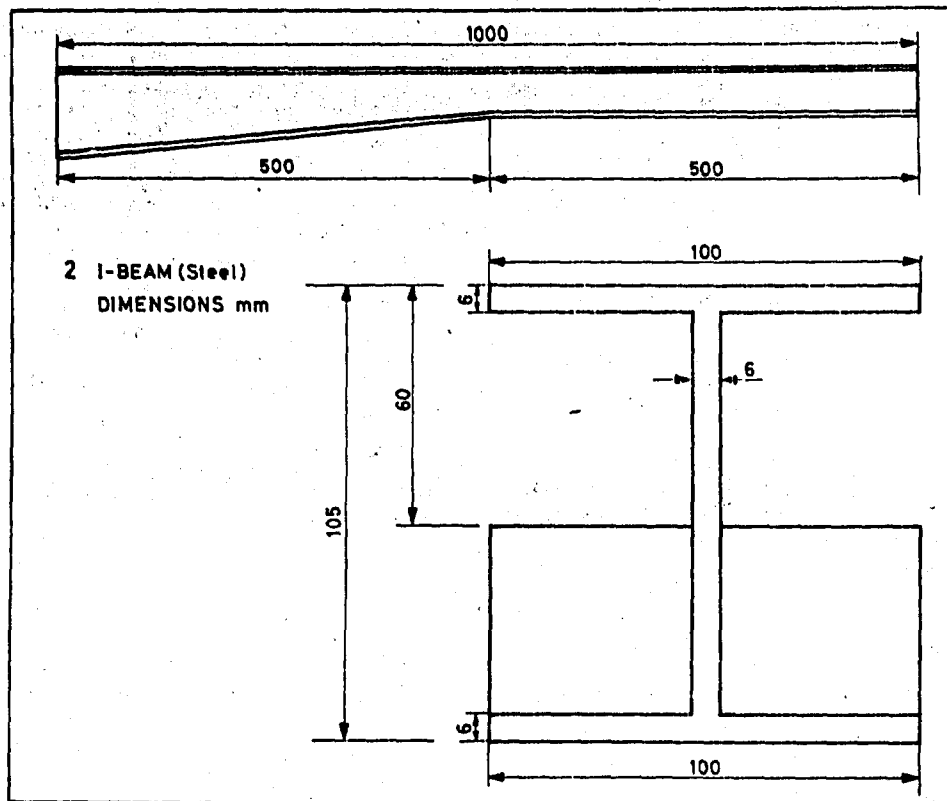


FIG.3. DETAILS OF THE I-BEAM

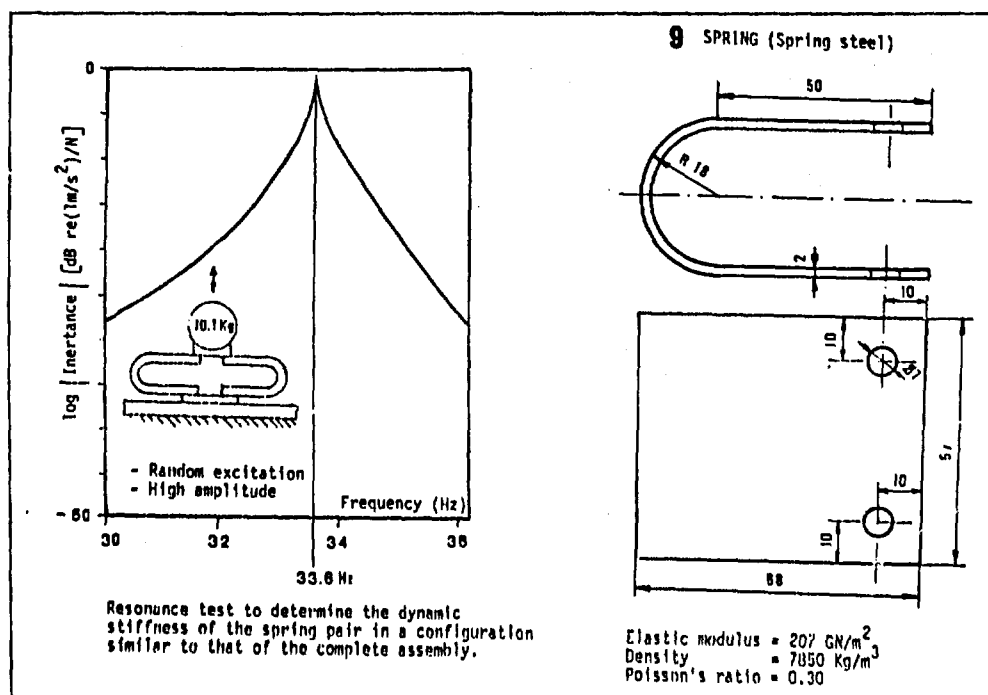


FIG.4. DETAILS OF THE SPRINGS

The structure has a free-free support.
 Measured transient forcing functions
 are given.
 Transient time-step defined.
 Damping value defined.
 F.R.F. range up to 2500 Hz.

THE AUTHOR'S MODEL:

As has been indicated previously in this text, the model representation depends almost entirely on the assumptions made by the modeller. Consequently, the author's main assumptions, on which his model is based, are as follows:

1. The cylinder may be modelled as a beam.
2. The bending stiffness of the cylinder is not affected by the screw joint.
3. The straps do not affect the stiffness of the cylinder.
4. The springs are linear in all three directions with identical stiffness in tension and compression.
5. The four springs may be represented by two spring elements between the beam web and cylinder.
6. The fixings only contribute to the

local mass and therefore may be represented by local mass elements.

7. The system is linear.

A diagram of the author's model is presented in fig.5. The cylinder is represented by eleven straight uniform beam elements type 34100 [2] with two of the eleven representing the thicker portion around the joint. The neutral axes of the beam elements are set along the central axis of the cylinder and a material module written to exactly model the material properties defined. The decision to model the cylinder simply as a beam was checked first by modelling the cylinder alone to prove that circumferential harmonics were not significant up to 2500 Hz. This was done using thin shells of revolution which are efficient, accurate and inexpensive and which can be used quickly. An alternative approach could be to estimate these harmonics using empirical design codes or data sheets.

The I-beam is represented by 120 eight noded thin quadrilateral flat shell elements of type 44210 [2]. Both the web and flanges are divided into two along their centre-lines to preserve good proportions for the element geometries. Another material module was defined and the density was factored to allow for overlapping material at the joints between the web and the flanges. This overlapping comes about because the beam geometry is defined along the mid-thickness lines with elements of the appropriate thickness. Consequently, some of the intersecting volume is used twice in the

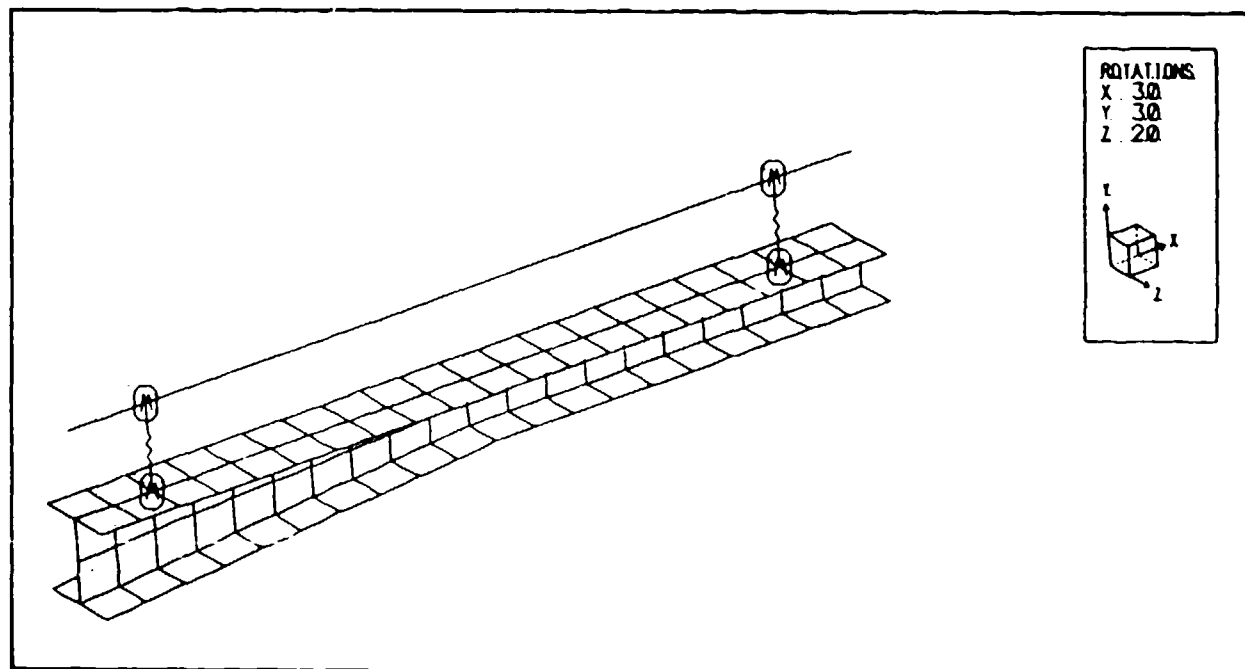


FIG.5. GENERAL VIEW OF THE OVERALL F.E. MODEL USED

mass estimate. The element mesh is so arranged that there are nodes in the correct position to join to the spring elements.

The four springs are represented by two spring elements type 30100 [2] which have three translational and three rotational stiffnesses. The appropriate values for these stiffnesses were calculated by again modelling a spring alone, including fixing holes, as shown in fig.6. The spring model uses 124 thin flat plate elements again with an appropriate material module. The accuracy of this model was verified by modelling the situation depicted in the inset of fig.4 and the frequency of the vertical mode checked to be 33.6 Hz. With this confidence in the model, static analyses were performed to give the required stiffnesses.

Finally, the mass of the bolts, fixings and packing pieces are added to the model by introducing four mass elements type 30200 [2]. Two mass elements are positioned on the axis of the cylinder each representing the upper and lower blocks, upper and lower packing pieces, six bolts and the strap. Another two masses are positioned on the top flange of the I-beam each representing the support and four bolts.

The resulting complete model comprises the following:

425 nodes.
137 elements.
2223 D.O.F.

The model was run on a DEC VAX 11/780 computer

4 megabytes of core and used a total of 1.8 CPU hours for all analyses and check runs. The modelling activity required a total of 300 hours man-time, but this includes the use of the activity as a training exercise for two students.

RESULTS:

The predicted mass properties for the structure are as follows:

1. Total mass - 32.0 kg predicted.
32.0 kg measured.
2. C.G. position - (0.493m, -0.102m).
Measured values not available.
3. Mass moment of inertia - 2.94 kgm².
Measured value not available.

These results display a noteworthy point. Although it is easy to weigh such a structure, the physical measurement of C.G. position and inertia are difficult. This illustrates an immediate advantage of an F.E. model providing it is accurate.

The next results to be obtained in the usual sequence of analysis are the modes and frequencies from an eigensolution. These are not presented here but the reader is referred to part 1 by Professor Ewins. It should be noted that strictly, pictorial comparison of mode shape is insufficient. The values of the

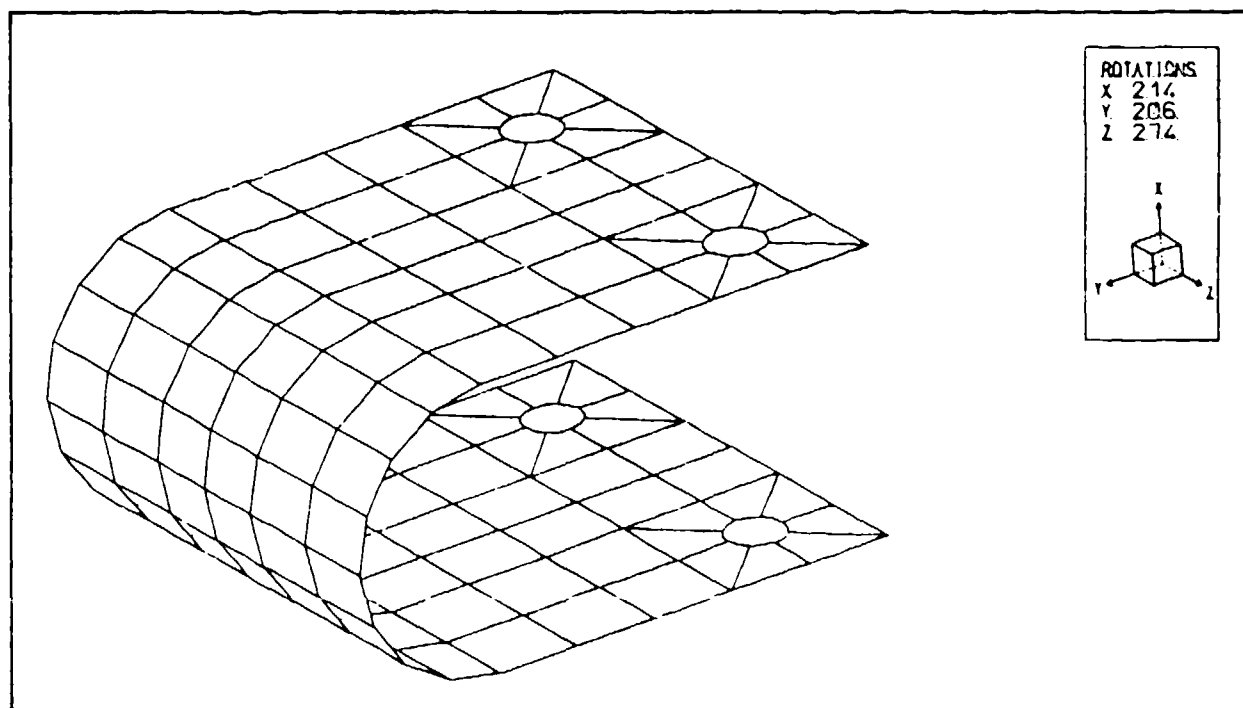


FIG.6. DETAILED SPRING MODEL USED TO DETERMINE THE STIFFNESS

eigenvector for the particular mode should be correlated with the equivalent measured data where available.

An indication of the accuracy of the prediction of a Frequency Response Function - F.R.F. is presented in figs. 7, 8 and 9. This represents a point prediction and is one of

four that were requested.

Consider fig.7. Generally very good agreement is demonstrated between the predicted and measured results [3] with, perhaps, the exception of the damping. However, the damping was defined prior to measurement for use by all participants. This illustrates the real problem

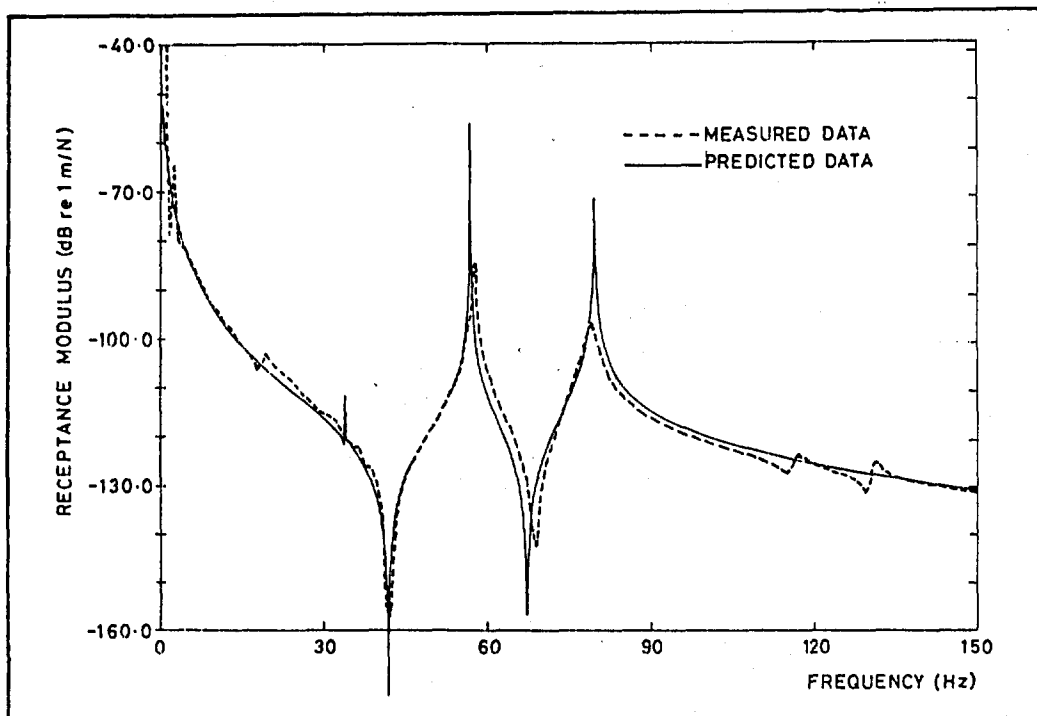


FIG.7. COMPARISON BETWEEN MEASURED AND PREDICTED RECEPTANCE UP TO 150Hz

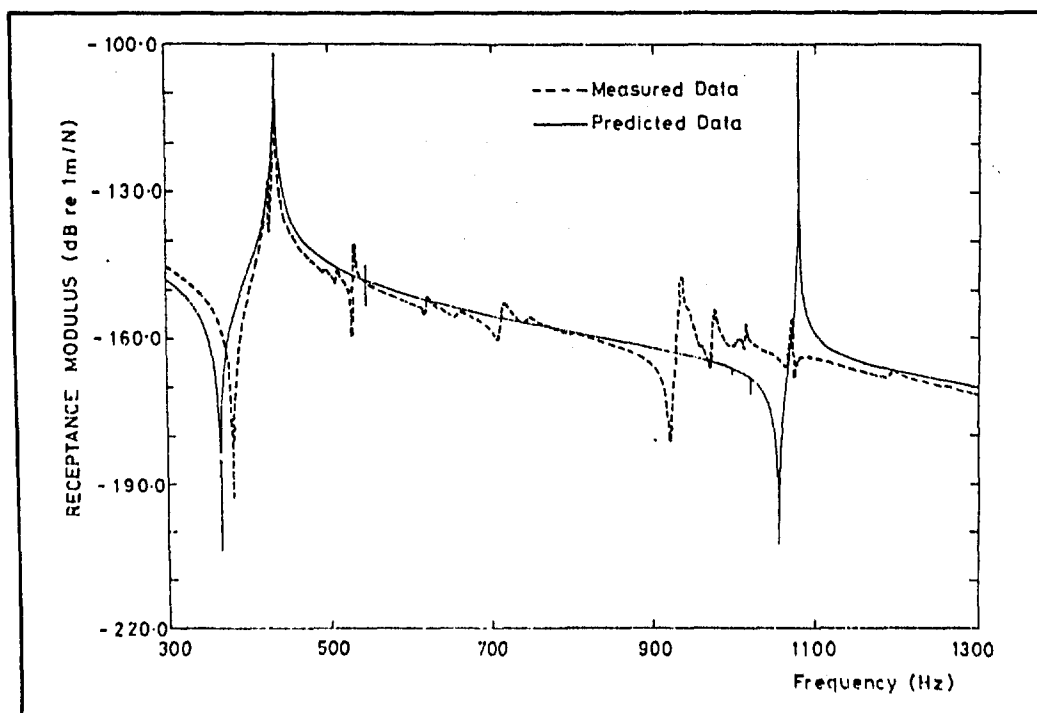


FIG.8. COMPARISON BETWEEN MEASURED AND PREDICTED RECEPTANCE BETWEEN 300 AND 1300Hz

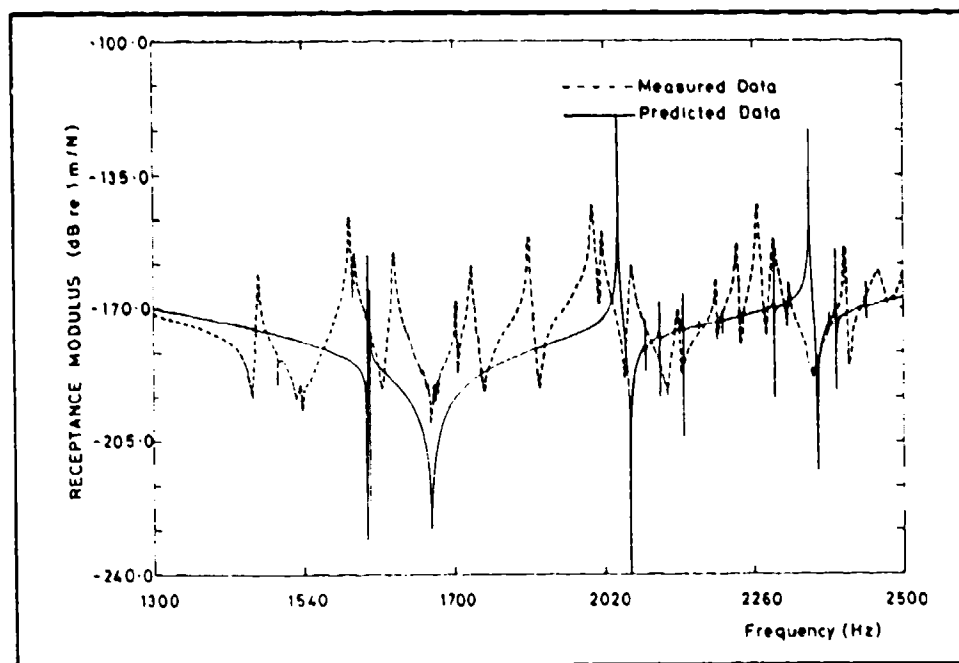


FIG.9. COMPARISON BETWEEN MEASURED AND PREDICTED RECEPTANCE BETWEEN 1300 AND 2500Hz

of estimating damping in any structure which must be put into any F.E. model as data. At very low frequencies (5Hz) there appears to be an anomaly in the measured data; this is possibly a suspension resonance. Furthermore, there is a false prediction at about 35Hz.

Fig.8 shows the same function but this time between the frequencies 300 and 1300Hz. Although the general level of the prediction agrees with the measurement, the comparison is worse than in fig.7. Fig.9 shows the data between 1300 and 2500Hz. Again the general level is fair but the agreement is poor.

The above observations clearly reinforce the well known fact that the accuracy of any dynamic F.E. model decreases with frequency or mode number. Only the lowest third to half of the modes can be expected to be acceptably accurate.

Fig.10 presents one of eight transient response comparisons for the "soft" hammer impact. Excellent agreement has been achieved here, the major discrepancy being a slight mismatch in frequencies leading to an apparently poor agreement above 25msec. The response is dominated by two modes, a spring "bounce" mode at 57Hz and the first bending mode of the I-beam at 433Hz. It should be noted that the presented data is acceleration and therefore represents an effective post-processing of the F.E. data since the problem is actually solved in terms of displacement. This point again illustrates an interesting comparison between modelling and experimental techniques. The survey required that transient accelerations and displacements be produced. However, the measurements only yielded acceleration since the accuracy of results

obtained by double integration of accelerometer signals are believed to be unreliable. Yet the predictions are effectively differentiated to give acceleration and still give acceptable results. Furthermore, close examination of fig.10 reveals that the measured data is "trended" towards the negative direction. This is possibly due to the low frequency suspension resonance since the true free-free condition is of course impossible to set experimentally.

It would be wrong to suggest that all the transient predictions are as good as fig.10. Results for the "hard" hammer impact are poor by comparison and examination of the frequency bandwidth of the model may reveal why. Fig.11 and 12 presents the spectral moduli of the input forcing functions for the "soft" and "hard" impacts respectively. The author's model was developed to predict behaviour up to 2500Hz as prescribed by the requirements of the harmonic analysis, and the frequency content of the transient forcing functions were unfortunately overlooked. The consequence is that although the model bandwidth satisfactorily encompasses the "soft" case, it is clearly inadequate for the "hard" impact. However, an attempt to widen the bandwidth of the model might itself prove difficult. From fig.12 it may be seen that such a widening should extend the upper frequency limit up to about 10kHz. In doing this an alarming number of new modes are likely to become significant and since two or three times this number will be needed for the required accuracy an F.E. solution seems unlikely.

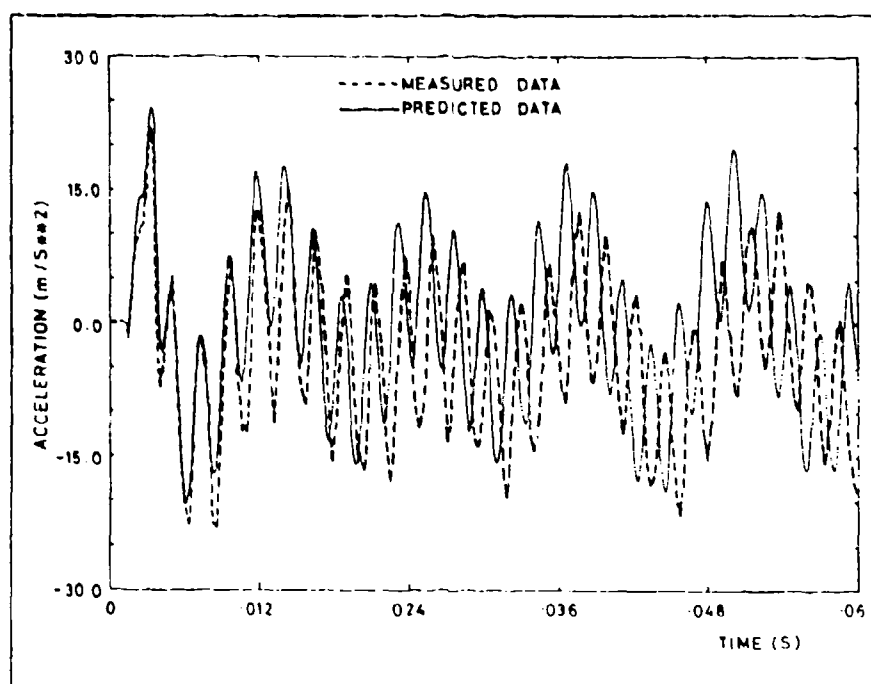


FIG.10. TYPICAL COMPARISON OF ACCELERATION RESPONSE FOR THE SOFT IMPACT

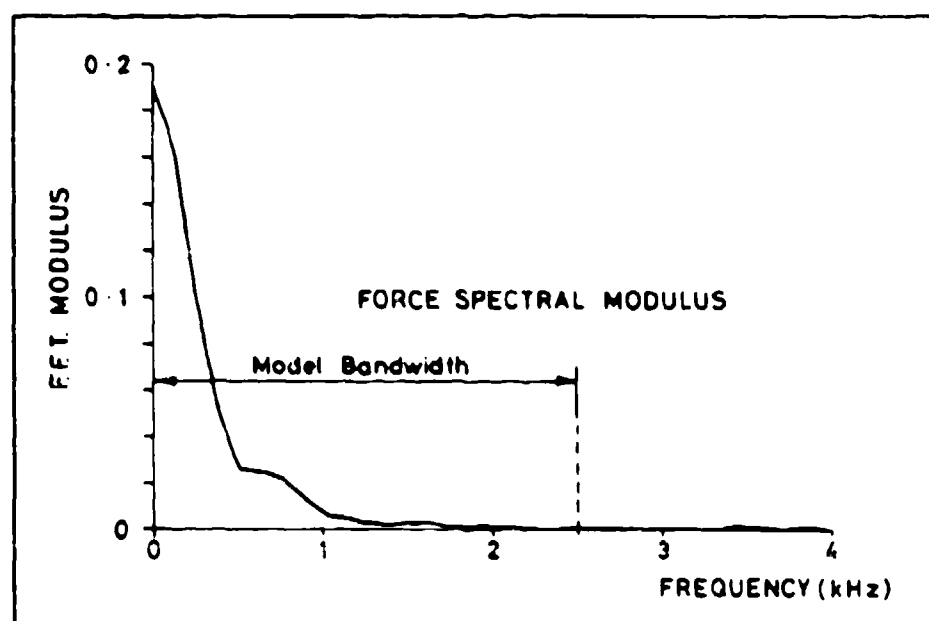


FIG.11. SPECTRUM OF THE SOFT IMPACT

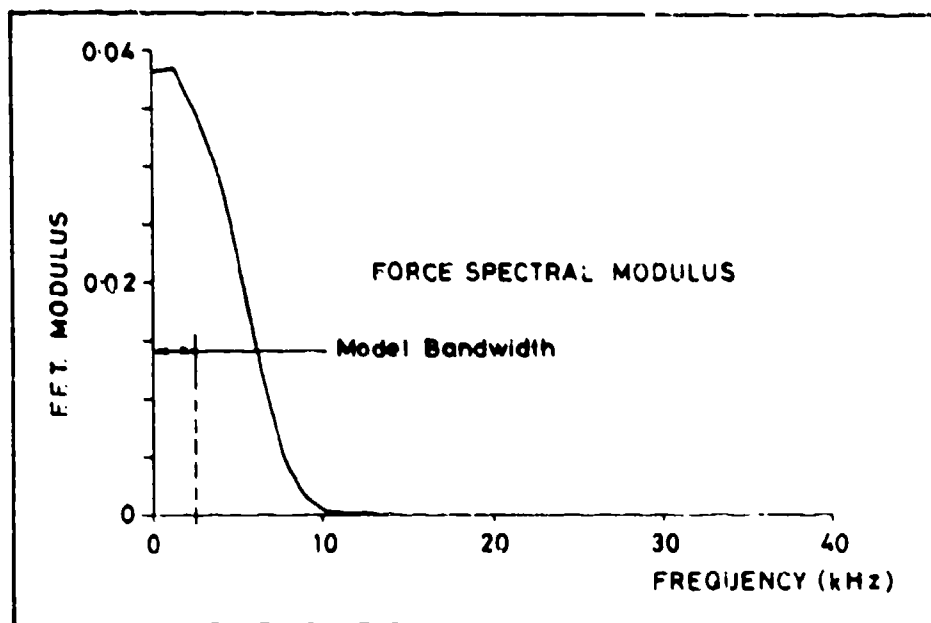


FIG.12. SPECTRUM OF THE HARD IMPACT

CHECKING OF PREDICTIONS:

In this paper the predictions of one specific model are presented for comparison with measured results. It must be stressed however that this was not the prime interest of the survey nor the way in which the author's model was developed. All truly predictive analyses, especially for complicated structures, need independent checks to indicate the accuracy of the results. These may be simple "hand calculations" or involve more sophisticated techniques. The checks carried out by the author in this case are presented below. The list is by no means exhaustive.

1. Calculate mass and C.G. position by hand.
2. Check the beam assumption for the cylinder with a shell analysis of the cylinder alone.
3. Calculation of additional spring stiffnesses required by modelling the spring alone. Verification of this model by reference to the single given value.
4. Examination of the mode shapes for "oddities".
5. Examination of the F.R.F.s for "oddities".
6. Checking of "rigid body" displacements by rigid body mechanics.

7. Examination of the transient responses for "oddities".

CONCLUSION:

The most useful conclusion is that an F.E. model can be constructed for such a problem and can give valuable results but great care is needed in its preparation. Consequently, the F.E. modelling technique for structural dynamic problems is not one which can necessarily be carried out by the inexperienced or novice modeller. Beware all models give some results.

REFERENCES:

1. M. Imregun and D. J. Ewins, "Dynamic Analysis Survey - DYNAS. Participant's booklet (information sheet no.2.)", Imperial College Dynamics Section report 8405, May 84.
2. "Pafec 75 data preparation handbook", PAFEC Ltd., Nottingham, England, 1978.
3. M. Imregun and D. J. Ewins, "DYNAS survey - phase 1. Preliminary results", Imperial College Dynamics Section report 8507, Jun 85.

SHIPBOARD SHOCK

COMPUTATION OF EXCITATION FORCES USING STRUCTURAL RESPONSE DATA

by

Lieutenant Commander D G DUBOWSKI MSc BEng Canadian Forces
Lieutenant Commander B J DOBSON PhD BSc(Eng) Royal Navy

Royal Naval Engineering College, Manadon
Plymouth, Devon, UK

A finite difference technique is described that permits the computation of excitation forces from measured response data in conjunction with a spatial model of a structure. The method is illustrated using a beam structure in which a model was developed from an experimental modal analysis. Single and multi-point impact excitations were investigated. It is shown that accurate prediction of the excitation forces are possible if responses can be monitored at the locations of the applied impacts.

INTRODUCTION

Modern computed based techniques enable designers to predict the dynamic response of structures to anticipated loading conditions. Reliable models may be developed using finite element techniques or experimental methods. Provided that the excitation forces are known, accurate responses may be calculated using either a time domain approach (such as Newmark's [1] finite difference equations) or a frequency domain approach based upon frequency response functions.

In many instances such as explosive loading or loading within a hostile environment it is not possible to obtain accurate information about excitation forces. In these cases excitations can be approximated using empirical relationships or extrapolated using functions developed from experimental trials. However, these functions often represent gross simplifications of the real loading conditions and are usually restricted to low frequency information.

A number of attempts has been made [2], [3] to invert the response from excitation. Frequency domain models have been applied in order to calculate the excitation forces from measured response data. However, it has been shown [4] that this approach is highly sensitive to errors in the frequency response function and the Fourier transforms necessary to perform the analysis.

The aim of this paper is to describe a time domain technique based upon finite difference equations and a model based upon experimental modal analysis.

THEORY

Development of Model

Using experimental modal analysis, it is possible to extract the natural frequencies, damping and mass normalized mode shapes of a structure. Provided the number of measurement locations is equal to the number of resonances considered, assuming "light" and proportional damping, the equivalent mass, damping and stiffness matrices may be computed as:

$$[M] = [\phi]^T^{-1} [\phi]^{-1} \quad (1)$$

$$[K] = [\phi]^T \left[\omega_r^2 \right] [\phi]^{-1} \quad (2)$$

$$[C] = [\phi]^T^{-1} [C_r] [\phi]^{-1} \quad (3)$$

where

$$[C_r] = \left[-2\zeta_r \omega_r \right]$$

$[\phi]$ = mass normalized mode shapes:

$[M]$ = mass matrix

$[K]$ = stiffness matrix

$[C]$ = damping matrix

$\left[\omega_r^2 \right]$ = diagonal matrix of eigenvalues

ζ_r = modal damping coefficient

Calculation of Responses from Known Excitations

The equations of motion for a linear system may be represented by the matrix equation

$$[M]\{\ddot{x}\} + [C]\{\dot{x}\} + [K]\{x\} = \{f\} \quad (4)$$

Where $[M]$, $[C]$ and $[K]$ are $N \times N$ mass, damping and stiffness matrices respectively (N is the number of degrees of freedom in the model) and $\{f\}$ is the vector of applied forces.

Using the finite difference equation [1]

$$\{\dot{x}\}_{n+1} = \{\dot{x}\}_n + \frac{h}{2} \left(\{\ddot{x}\}_n + \{\ddot{x}\}_{n+1} \right) \quad (5)$$

$$\{x\}_{n+1} = \{x\}_n + h\{\dot{x}\}_n + \left(\frac{1}{2} - \beta \right) h^2 \{\ddot{x}\}_n + \beta h^2 \{\ddot{x}\}_{n+1} \quad (6)$$

it can be shown that the displacement, velocity and acceleration responses are defined by: [5] and [6].

$$[D]\{x\}_{n+1} = [B]\{x\}_n - [F]\{x\}_{n-1} + \beta h^2 \left(\{f\}_{n+1} + \left(\frac{1}{\beta} - 2 \right) \{f\}_n + \{f\}_{n-1} \right) \quad (7)$$

$$[D]\{\dot{x}\}_{n+1} = [B]\{\dot{x}\}_{n-1} - [F]\{\dot{x}\}_{n-1} + \frac{h}{2} \left(\{f\}_{n+1} - \{f\}_{n-1} \right) \quad (8)$$

$$[D]\{\ddot{x}\}_{n+1} = [B]\{\ddot{x}\}_{n-1} - [F]\{\ddot{x}\}_{n-1} + \left(\{f\}_{n+1} - 2\{f\}_n + \{f\}_{n-1} \right) \quad (9)$$

where

$$[D] = [M] + \frac{h}{2} [C] + \beta h^2 [K]$$

$$[B] = 2[M] - (1-2\beta) h^2 [K]$$

$$[F] = [M] - \frac{h}{2} [C] + \beta h^2$$

and

h = time step size

β = parameter defining the "form" of the acceleration during the time step [1]

$n+1$, n , $n-1$ = subscripts denoting force and response at times $(n+1)h$, nh and $(n-1)h$.

These are "three-point" finite difference equations that permit calculation of the responses at time $(n+1)h$ from a knowledge of the responses at times nh and $(n-1)h$ and the forcing

functions at times $(n+1)h$, nh and $(n-1)h$.

Calculation of Excitation Forces from known Responses

It has been shown that equations (7), (8) and (9) cannot be re-arranged to yield the excitations forces from measured responses [5]. Thus an alternative formulation is necessary to obtain the forces. Using the central difference equations:

$$\{\dot{x}\}_n = \frac{1}{2h} \left(\{x\}_{n+1} - \{x\}_{n-1} \right) \quad (10)$$

$$\{\ddot{x}\}_n = \frac{1}{h^2} \left(\{x\}_{n+1} - 2\{x\}_n + \{x\}_{n-1} \right) \quad (11)$$

and substituting these into equation (1) yields:

$$h^2 \{f\}_n = ([M] + (h/2)[C])\{x\}_{n+1} + (h^2[K] - 2[M])\{x\}_n + ([M] - (h/2)[C])\{x\}_{n-1} \quad (12)$$

Equations (7), (8), (9) and (12) may be partitioned to permit the solution of mixed boundary value problems in which forces and responses are known at specific (but different) locations. To this end, "Selector" matrices $[E]$ and $[H]$ are introduced [5] defined as follows:

$[E]$ diagonal elements of 1 for known forces and 0 for known responses.

$[H]$ diagonal elements of 1 for known responses and 0 for known forces.

(NOTE: $[E] + [H] = \text{Identity Matrix}$).

To facilitate computation, equations (7) and (12) may be re-written in the forms ie

$$([E][D] + (h^2/4)[H])\{x\}_{n+1} = [E]\{\phi\}_n + (h^2/4)\{\Omega\}_{n+1} \quad (13)$$

$$h^2 \{f\}_n = [H]\{\theta\}_{n+1} + h^2 [E]\{\Omega\}_n + [H](h^2[K] - 2[M])\{x\}_n \quad (14)$$

where

$$\{\phi\}_n = [B]\{x\}_n - [F]\{x\}_{n-1} + (h^2/4)(2\{f\}_n + \{f\}_{n-1})$$

$$\{\theta\}_{n+1} = ([M] + (h/2)[C])\{x\}_{n+1} + ([M] - (h/2)[C])\{x\}_{n-1}$$

and $\{n\}_{n+1} = N \times 1$ vector of input data at time $(n+1)h$ that represents the known excitations and displacements.

These equations differ from the backward difference equations quoted in reference [5].

The solution of the equations may be achieved directly for a quiescent structure without the need for separate two-point formulations at the initial time step [6].

EXPERIMENTAL STUDY

A double cantilever structure, figure 1, fixed at the centre, was used as the test structure. Ten measurement locations were selected as shown, although only one arm of the model was investigated in detail. An experimental modal analysis was performed over a frequency band encompassing the first six natural frequencies of the structure (160 Hz to 1600 Hz). Using the results obtained from locations 1 to 6, equivalent mass, damping and stiffness matrices were formed using equations (1), (2) and (3).



Figure 1 The Test Structure

In order to test the validity of the model, the structure was excited with a measured impact load at location 1 and responses were computed at locations 1 to 6 using equation (9). The computed results were compared with those measured using accelerometers mounted at the six locations on the structure. Figure 2 shows a typical comparison between measured and predicted acceleration responses resulting from a versed-sine type of force input.

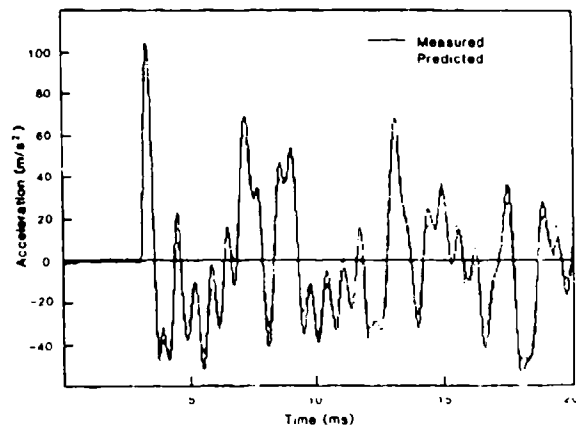


Figure 2 Comparison of Predicted and Measured Acceleration Response at Location 2 for versed sine Impact at Location 1.

Different time step sizes were employed in these studies and it was concluded that a step size of 20 μs (ie approximately 30 points in the highest mode) yielded very good agreement between the predicted and actual acceleration response. In all of these trials a value of 0.25 was assumed for the β parameter (ie constant acceleration during each time step).

Additionally, responses at different locations were computed using the measured response at the point of impact as the excitation in equation (13). A typical result is shown in Figure 3.

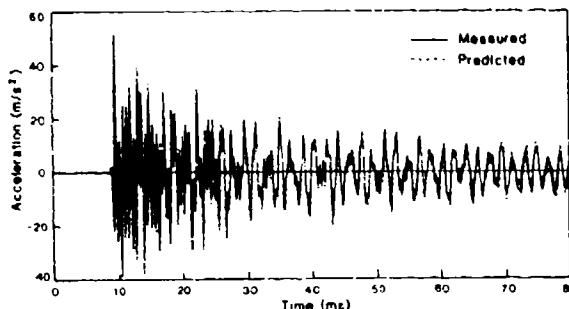


Figure 3 Comparison of Predicted and Measured Acceleration Response at Location 5 using Measured Response at Impact Site 1.

The agreement achieved in these experiments indicated that the spatial model derived from the modal analysis was an accurate representation of the structure under study. Further, the finite difference equations were shown to be stable and to produce minimal frequency and amplitude distortion.

In order to investigate the prediction of applied force, the structure was impacted at site 1 and the force and response monitored at this point. Using equations (13) and (14) the force was predicted from the measured response and compared with the measured history as shown in figure 4. This involved a numerical integration routine to convert the accelerometer data into displacement data for substitution in equation (13). It was noted that the analysis was capable of predicting the force history during the impact to within 5% but that in the post-shock period the predicted force continued to oscillate and showed divergence as shown in figure 5. A similar behaviour has also been reported in reference [2] in which the analysis was based upon a frequency domain approach.

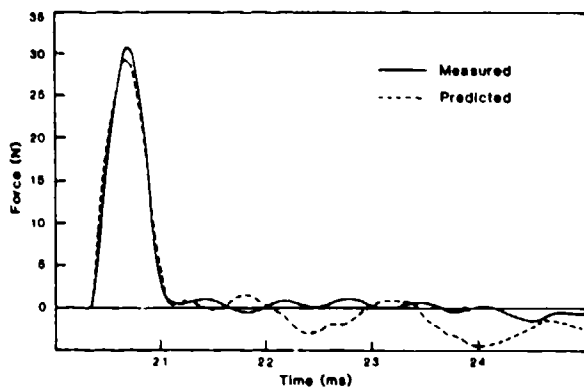


Figure 4 Comparison of Measured and Predicted Force at Site 1 using Response Measured at Site 1.

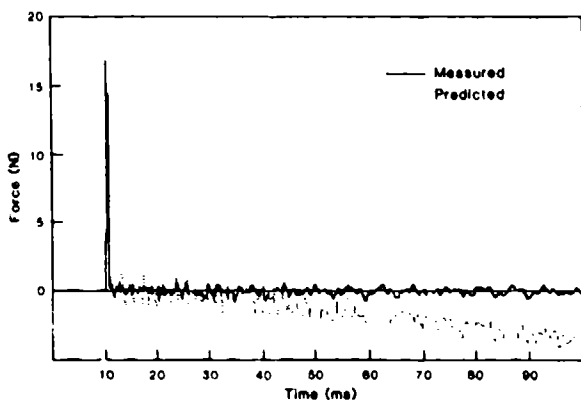


Figure 5 Post-Impact Ripple and Divergence

The case of multiple impact was also investigated in which two forces were applied and the responses measured at the two impact locations. Figure 6 shows a comparison between the measured and predicted forces. Again it was shown that the analysis was capable of accurate results during impact but that the solution became unreliable in the post-impact phase.

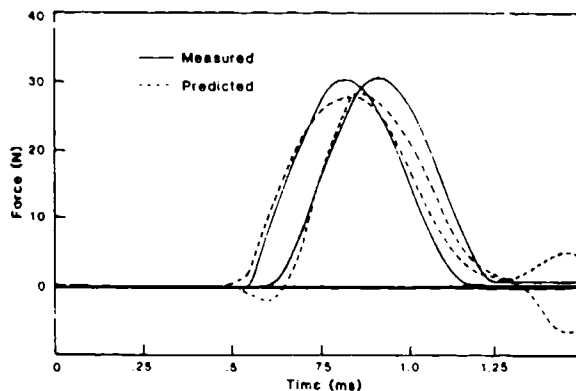


Figure 6 Comparison of Measured and Predicted Forces for Multiple Impact.

DISCUSSION

The results of this study have shown that experimental modal analysis and time domain finite difference techniques can be used with considerable confidence to predict the behaviour of a structure to a prescribed impact load. With a suitable choice of time step it was possible to obtain results that predicted the acceleration response of the structure to better than 5%.

The prediction of excitation forces from measured response was encouraging for the duration of the impact with errors again in the region of 5% for both single and multi-force excitations. However, a number of problems remain and are currently under investigation. The post-impact behaviour appears to contain two phenomena; a residual "ripple" and possible instability. The residual has been attributed to the behaviour of the accelerometers [3] in which residual "ringing" in the transducers may appear as a "phantom" structural response. The divergent behaviour is probably associated with the finite difference algorithms. In particular it was shown that the form of the post-impact results could be altered by using different numerical integration routines to convert the measured accelerations into displacement data. It was noted during multi-impact tests that the two predicted forces tended to diverge in opposite senses such that the additive effects cancelled.

Despite these problems it appears that the time domain approach yields acceptable predictions of the excitation forces during impact and that it is immediately apparent when these predictions become unreliable. At present the study has been restricted to the case where it is possible to locate transducers to measure the response at the point of impact. Whilst this may be possible in some situations, such as around a hull subjected to shock loading, it is somewhat restrictive.

Further research is being conducted to permit remote monitoring of responses from which the location and magnitude of the excitation forces may be computed.

REFERENCES

- [1] Newmark M N "A Method of Computation for Structural Dynamics". Journal of the Engineering Mechanics Division, Proceedings of the American Society of Civil Engineers, July 1959, pp67-93.
- [2] Jordan R W, Whiston G S "Remote Impact Analysis by Use of Propagated Acceleration Signals, I: Theoretical Methods". Journal of Sound and Vibration, Volume 97 January 1984, pp35-51.
- [3] Jordan R W, Whiston G S "Remote Impact Analysis by Use of Propagated Acceleration Signals, II: Comparison Between Theory and Experiment". Journal of Sound and Vibration, Volume 97 January 1984, pp53-63.
- [4] Hillary B "Indirect Measurement of Vibration Excitation Forces". PhD Thesis Imperial College, London, April 1983.
- [5] Chan S P, Cox H L, Benfield W A "Transient Analysis of Forced Vibrations of Complex Structural-Mechanical Systems". Journal of the Royal Aeronautical Society. Volume 66, July 1962, pp457-460.
- [6] Dobson B J "The Newmark Beta Method of Transient Analysis". RNEC-TR-82003, Manadon, Plymouth, February 1982.

UNDERWATER SHOCK TRIALS ON A PLAIN, UNREINFORCED CYLINDER

Lt-R J RANDALL, RN
Admiralty Research Establishment
Portland Dorset

Strain was recorded at 14 locations on a submerged plain unreinforced cylinder when subjected to the blast from a small explosive charge. This work was carried out as part of a larger study into the topic of fluid-structure intersection. The cylinder was selected as a simple geometric shape which could be analysed theoretically so that the experimental results could validate the applicability of approximations in current use. Only the preliminary findings together with details of the testing environment and procedure are presented in this report. The results show how the hoop and meridional strain levels vary with the angle of the incident shock wave, and how the shock is transferred from the fluid through the structure. Changes in the frequency response spectrum are also presented for the envelopment and post envelopment periods.

INTRODUCTION

In the latest reviews [1-4] assessing the developments in analytical techniques for dealing with the fluid-structure interaction problem, little or no evidence is given of experimental data than can be used to evaluate the analytical predictions. The reason for this, is probably that a good general formal method for dealing with the transient response of complex structures has not yet appeared. The most widely used approach is to adopt a decoupling scheme such as the 'doubly asymptotic approximation' [5]. This and later more refined schemes have been evaluated against the response of idealised structures for which an exact solution can be obtained. However all these schemes stem from an approximation which its author notes [6] is not satisfactory for situations involving prominent intermediate frequency components as it overestimates the radiation damping, and although they may prove adequate in certain circumstances they must be used with caution. Nevertheless computer codes are now being used and developed [7] which embody these approximations and therefore a more thorough validation should be performed.

As instrumentation and other practical considerations will introduce additional uncertainties into the problem it will assist the interpretation of results if the test structure retains a simplistic shape. There follows detailed information about a series of shock tests carried out on a simple test structure in collaboration with the staff of the Admiralty Research Establishment (ARE) Dunfermline in HM Naval Base, Rosyth.

The test structure was a plain unreinforced mild steel cylinder, whose geometry and dynamic characteristics were known from previous tests [8]. The cylinder was held in position underwater and subjected to a spherical shock wave caused by firing small explosive charges at a pre-determined stand-off. The only limitations on the size of the charge and the distance of the stand-off were that no permanent structure damage was to occur.

The charge size and stand-off were determined first and then remained unaltered for the remainder of the trial. The angle of incidence of the shock wave was varied, though, to investigate what effect this had on the maximum levels of stress recorded. The cylinder was maintained in position and for successive shots the location of the charge was altered in the same horizontal plane.

TESTING ENVIRONMENT

It is inevitable that there will be a compromise between the idealised system that is conceived for the sake of theoretical analysis and what can be physically set up to represent that system. The requirements, in this instance, are for a prescribed pressure to apply a force to a simple structure in a fluid environment.

The practical problems of representing this in the laboratory are evident from the photograph (Fig 1) of the structure suspended above the tank before testing.

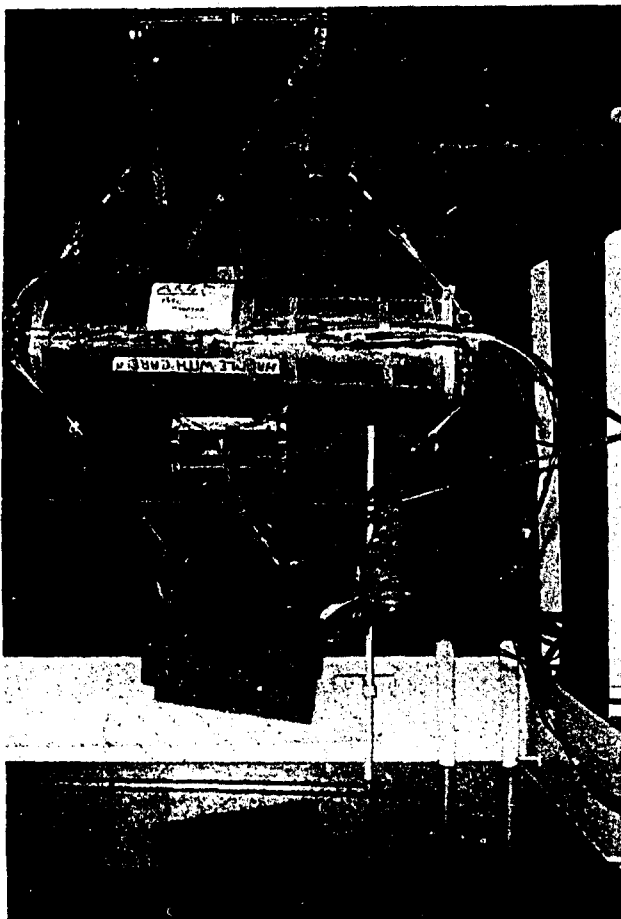


Fig 1 - General Arrangement

This arrangement is obviously divorced from the original concept of an idealised system. Hard reflective tank walls are clearly in close proximity to the structure. The cylinder itself is thin walled (3mm MS tube) with an aspect ratio of 120:1, but it is only 1.284m long and has flat ends. In addition ballast weights are needed to maintain the structure at the required depth (300mm below the free surface) and support arms have been

welded to the ends to hold the explosive charge and pressure transducers.

The charges used in this trial were electric detonators, type N79, each containing 1 gm of plastic explosive. This small charge fixed relatively near to the structure produced a spherical shock wave but satisfied the requirements of the enclosed testing area and the limitation that no permanent damage was to be sustained by the structure. Each pressure time history has a unique signature but are characterised by a very brief duration.

A typical pressure time history is shown in Fig 2; the duration of the pulse is about 50 μ s and the rise and decay of pressure is very rapid. Subsequently the pressure returns to zero.

A consequence of this characteristic pressure signature is that a very rapid sampling rate (1×10^6 sps) has to be employed on the ADC to prevent maxima being clipped. With this high sampling rate and the limitations of 32K of computer memory only the immediate response of the structure could be studied closely.

However five separate shocks and responses were measured and analysed. Fig 3 indicates the position of the charge relative to the structure for each individual firing (Shots 1 and 2 were calibration shots and are not included).

INSTRUMENTATION

Pressure Transducers

Two types of tourmaline underwater blast pressure transducer were used to record the pressure time history, one was manufactured by PCB Piezotronics Inc and the other was an ARE design. Both types have a volumetric sensitive tourmaline crystal element suspended in insulating oil and contain a built-in micro-electronic line driver amplifier which outputs a high voltage low impedance signal.

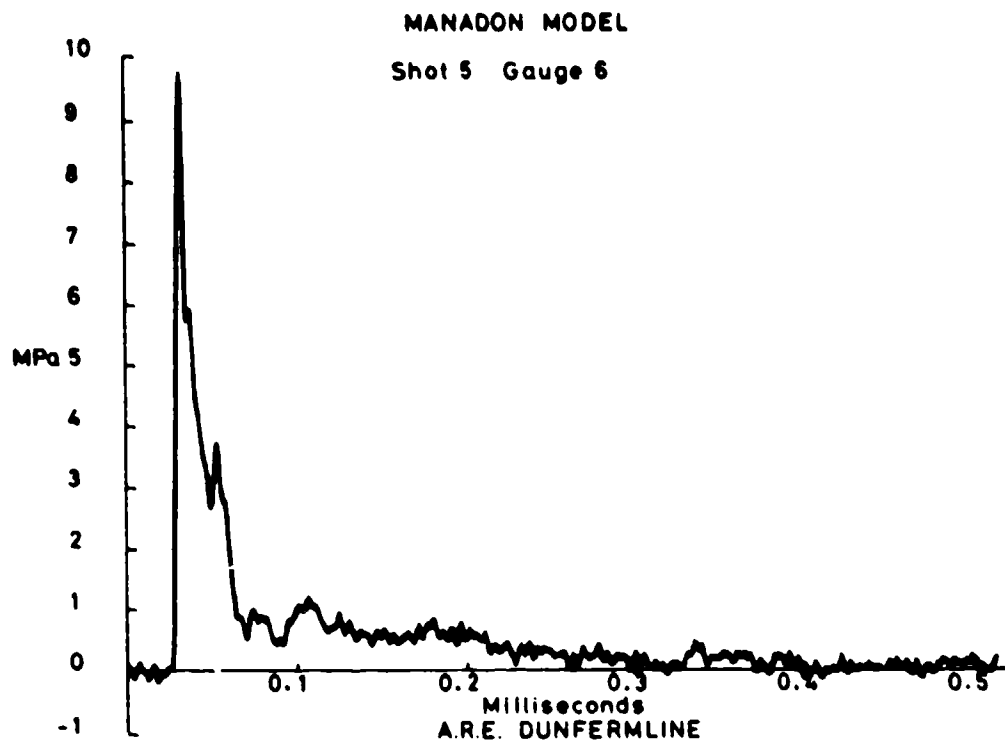


Fig 2 - Typical Pressure Time History

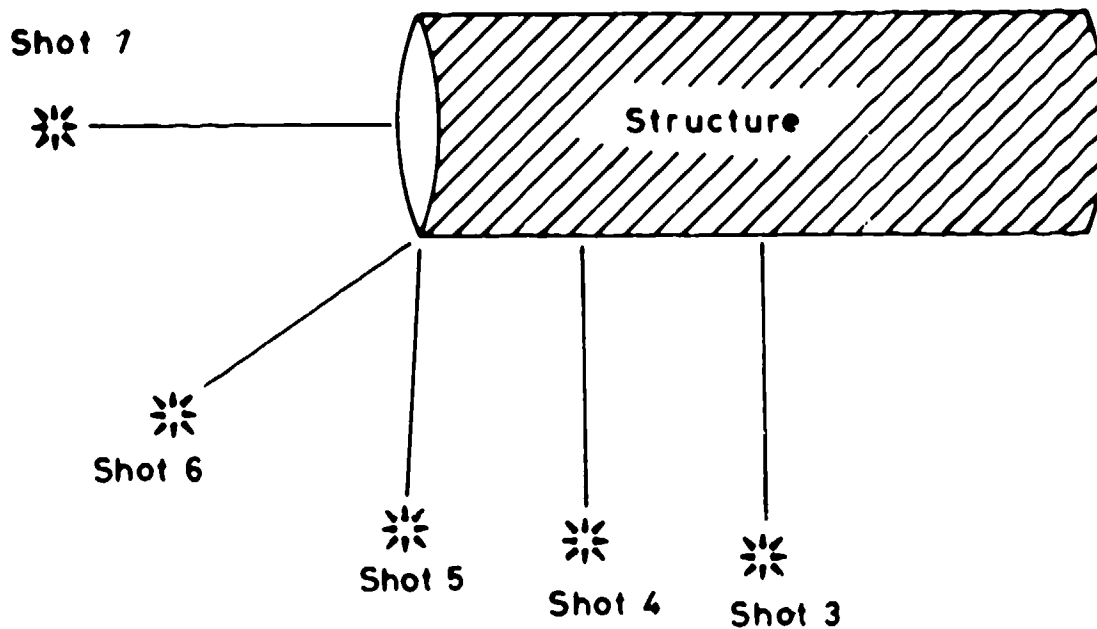


Fig 3 - Firing Sequence

Tourmaline gauges are not generally consistent or reliable and for this reason it would have been desirable to have a large number of transducers to measure the combined pressure field consisting of incident, reflected and radiated components. However, the presence of any pressure gauge and its associated cabling must interfere with the pressure field through shadowing and diffraction effects, therefore only 2 gauges were used to monitor 'free' field and 'near' field pressures.

The mounting arrangement for the 'free' field pressure sensor (Gauge No 6) is as shown (Fig 4). The 'near' field pressure sensor (Gauge No 5) was taped to the cylinder.

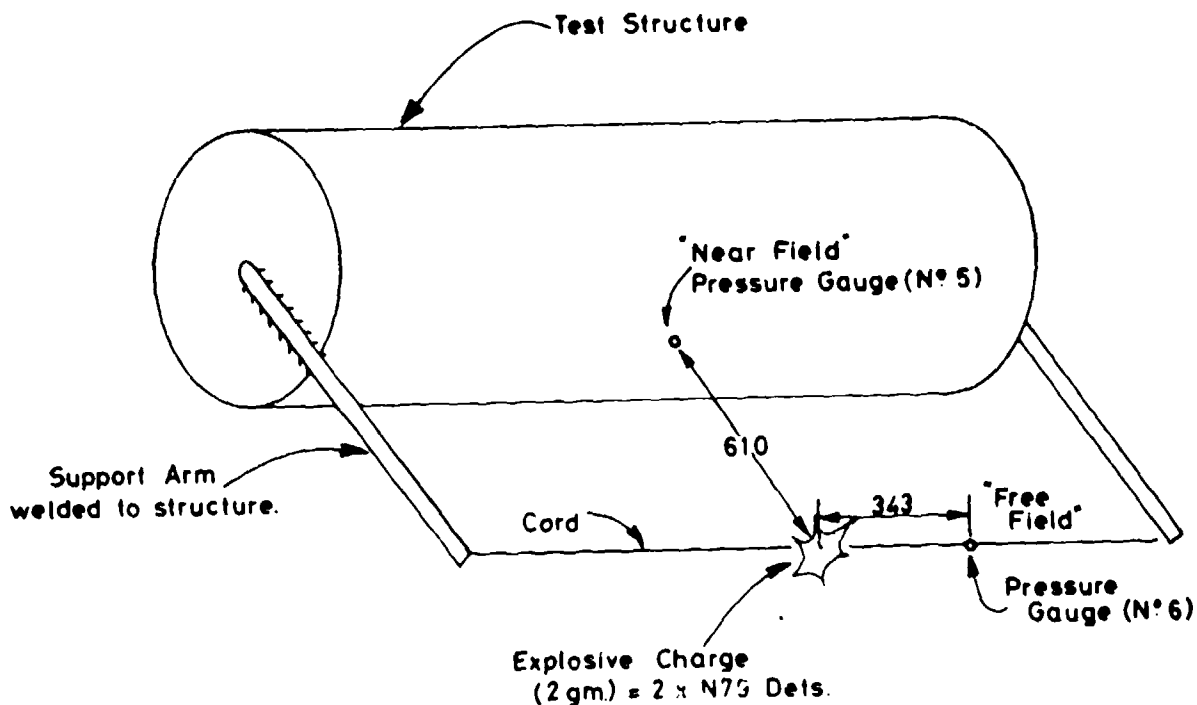


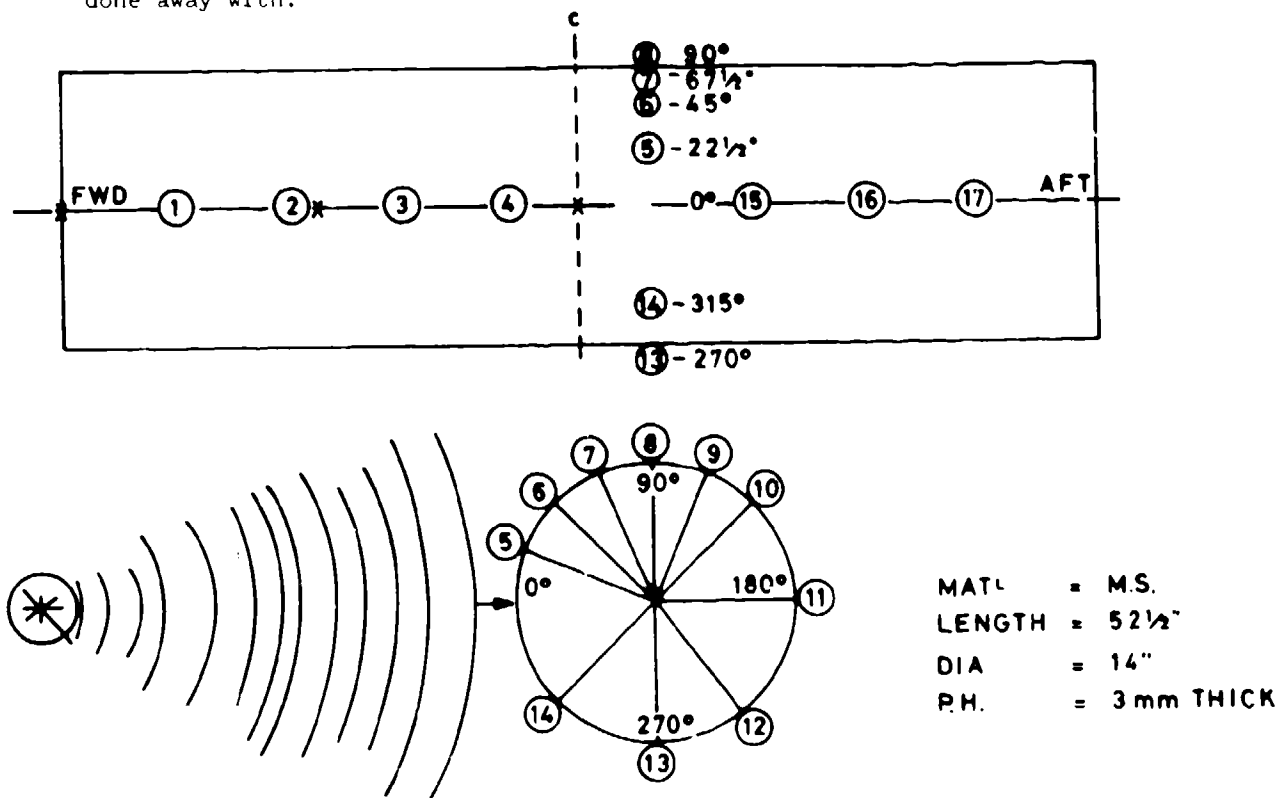
Figure 4 Charge handling Arrangement

Strain Gauges

The structural response was measured at 17 locations to obtain axial and circumferential (hoop) deformations (Fig 5). It was decided in this instance to use strain gauges rather than accelerometers. Each site was equipped with a right-angled pair of gauges set up to measure hoop and axial strain.

The advantages of obtaining strain as a structural response rather than accelerations were that:

- (1) Strain is a direct measure of structural damage which is of prime importance.
- (2) Less processing of data will be required as rigid body motions will not be recorded and zero shift, base strain and cross axis sensitivity problems encountered with accelerometers are largely done away with.



DEC 1984

R.N.E.C. MANADON S/M MODEL

Fig 5 - Strain Gauge Positions
(17 No right angled pair)

RESULTS AND ANALYSIS

A representative selection of the results is included to demonstrate the major conclusions.

Shot 3 Channel 4C Time 0-8.191 ms

Fig 6 shows a typical pattern for the response at the centre of the structure subjected to a broadside shock wave. The peak response corresponds to the occurrence of the peak pressure and is followed by rapid, lightly damped, oscillations.

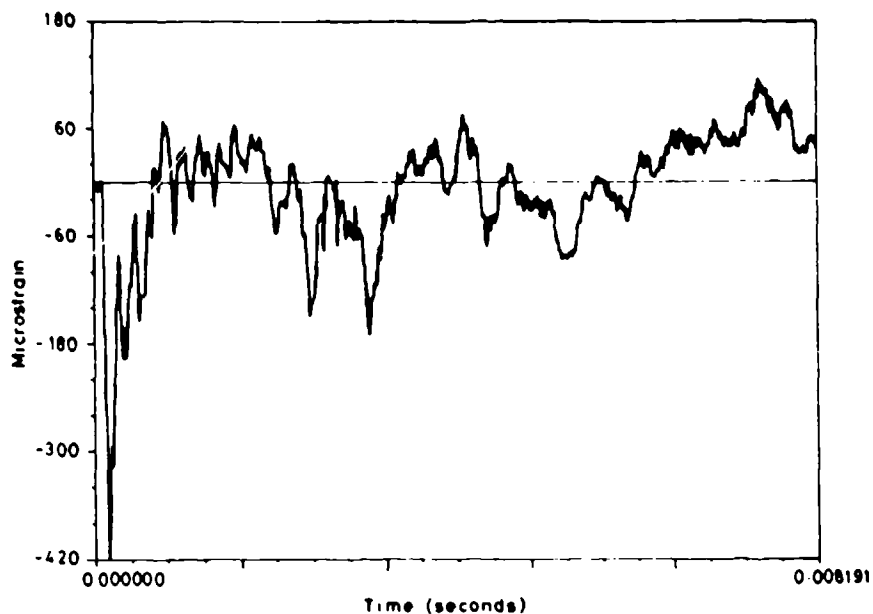


Fig 6 - Hoop Strain Time History
(Shot 3 Channel 4)

All recorded channels were measured simultaneously and then synchronised to a single event, namely the peak of the near field pressure pulse.

As stated previously the length of the signal was curtailed by the size of the processing unit but within this time window the maximum strain always occurs soon after the pressure pulse. Effects due to reflections and bubble collapse happen comparatively much later (circa 28 ms), therefore the period 0-1 millisecond is studied in greater detail.

Each record was examined to assess the relationship between the onset of movement (as recorded by strain) and the arrival times of the pressure pulse. The shock wave can arrive at a point on the structure via two routes.

- (1) directly through the field.
- (2) by the most direct route between the charge and the structure and then through the structure to the point in question as a compression wave.

The second route is longer but as the speed of sound is $3\frac{1}{2}$ times faster in steel than it is in water this is more often the quicker route.

Shot 7 Channel 1C Time 0-1 ms (Fig 7)

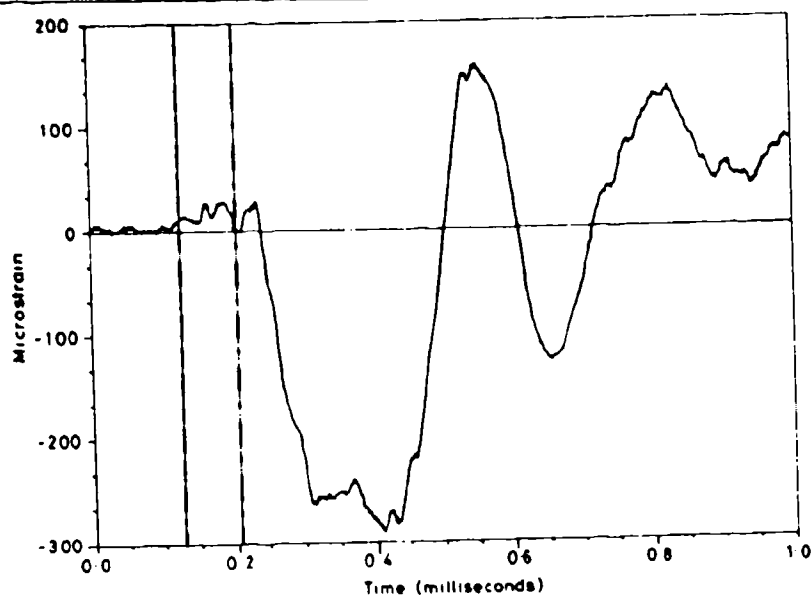


Fig 7 - Hoop Strain Time History
(Shot 7 Channel 1)

The two vertical lines signify the first arrival times of the shock wave travelling through the structure (shown dashed) and, secondly, directly through the water (shown chain-dotted). In this instance where variations in hoop strain are shown for the location nearest the charge causing an end-on attack, there is no correlation between these event times and the onset of strain.

Shot 7 Channel 1L Time 0-1ms (Fig 8)

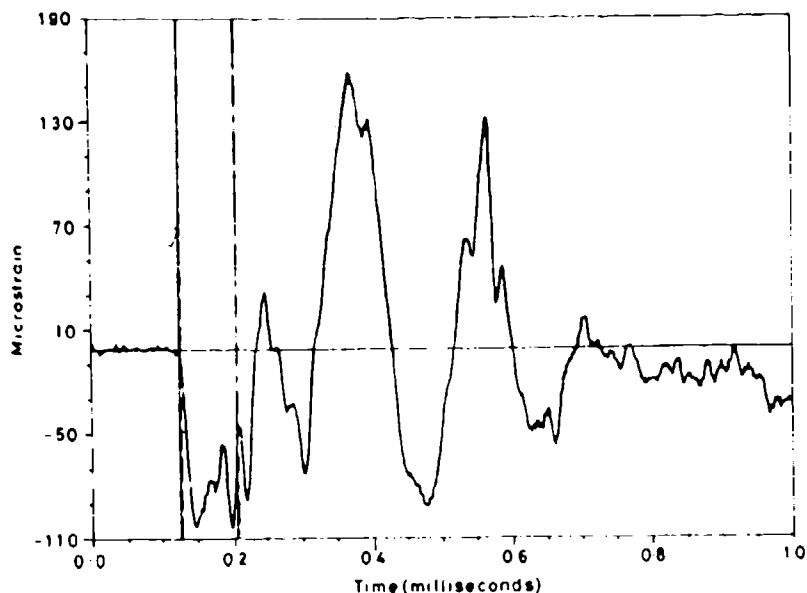


Fig 8 - Axial Strain Time History
(Shot 7 Channel 1)

However Fig 8 shows the variation of axial strain at the same location and it can be seen that the onset of axial strain coincides very closely with the arrival of the shock wave which travels through the structure.

Shot 7 Channel 17L Time 0-1ms (Fig 9)

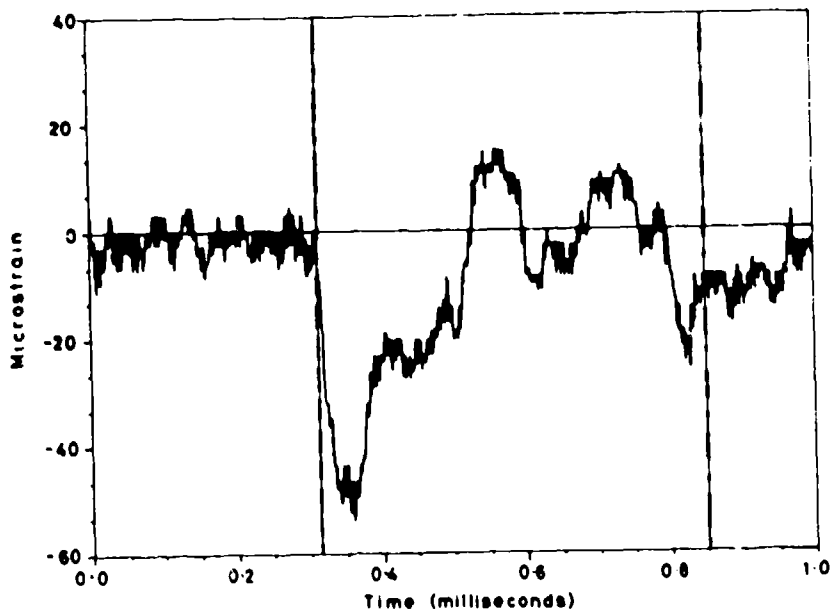


Fig 9 - Axial Strain Time History
(Shot 7 Channel 17)

Fig 9 shows the axial response at another point to the same shock. Location 17 is further away from the source and by the time the shock wave has travelled to the opposite end of the structure the gap between the two arrival times as shown by the vertical lines has widened due to the $3\frac{1}{2}$ times difference in their rates. The intensity of the response has decreased as shown by the signal to noise ratio but the onset of axial strain clearly coincides with the shock wave travelling in steel.

Shot 4 Channel 12C Time 0-1ms (Fig 10)

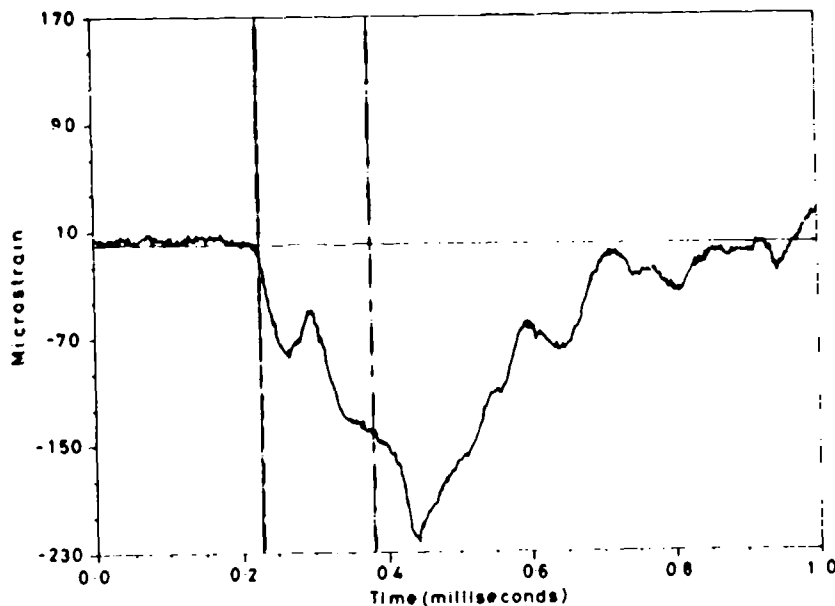


Fig 10 - Hoop Strain Time History
(Shot 4 Channel 12)

The variations in axial strain that were observed when the cylinder was acted upon by an end-on incident wave were also observed for hoop strain at locations under side-on attack. Fig 10 shows the response of a point on the opposite side of the structure from the source of a side-on attack.

Shot 4 Channel 6C Time 0-1ms (Fig 11)

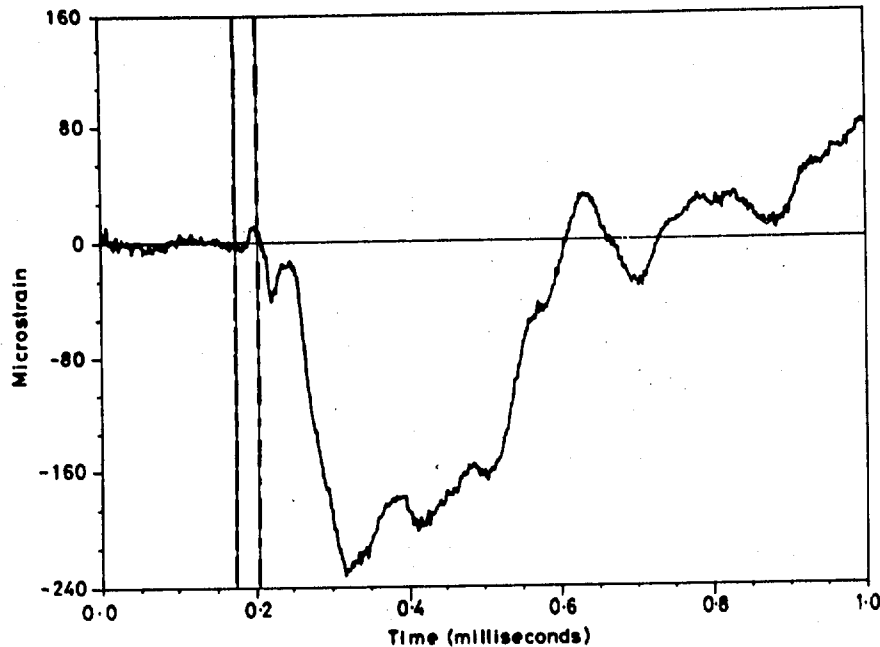


Fig 11 - Hoop Strain Time History
(Shot 4 Channel 6)

The response to Shot 4 at a different site on the same side of the cylinder as the source (directly opposite Channel 12), does not show what triggers movement; both arrival times are within 30 μ s of each other. It does show however that the maximum strain recorded at two sites 180° apart varies by less than 10%.

None of the results of these trials support the view that the zone 'behind' the structure is sheltered from the shock wave. However having demonstrated that the compression wave that travels through the structure is an important event as far as the initiation of strain is concerned then it is not surprising that there is no sheltering as the forcing function is carried through the steel and all points on the structure are visible to the shock.

Further examination of Figs 10 and 11 does offer a possible explanation, as some of the evidence in support of a shadow zone is from large scale tests involving velocity meters and the rate of change of strain is always less for those points in the lee of the shock.

The importance of the shock wave travelling through the structure may also explain why the angle of incidence was not critical. The maximum response was always either nearest to the source of the shock or at the midpoint of the cylinder where the structure is most flexible. In retrospect it was not easy to determine what the effective angle of incidence was, as for many locations of the charge the extreme end of the structure will be disturbed first and initiate a shock wave which always travels to internal points by the same (most direct) route.

Shot 5 Channel 1C Time 0-1ms (Fig 12)
Shot 5 Channel 17C Time 0-1ms (Fig 13)

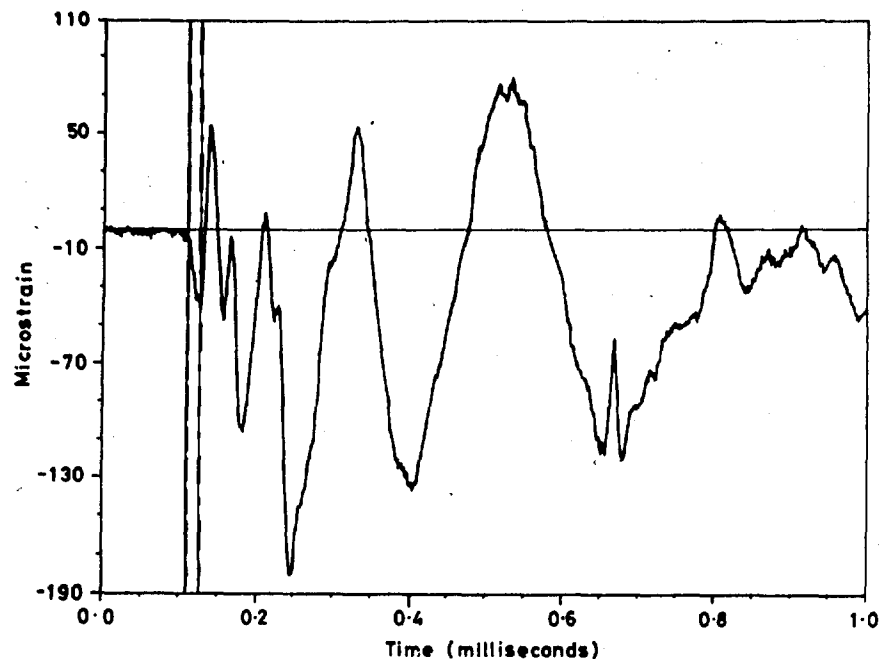


Fig 12 - Hoop Strain Time History
 (Shot 5 Channel 1)

Figs 12 and 13 show hoop strain response at two points to a shot fired opposite the end of the cylinder. Fig 12 shows the response near the shock source where there are rapid oscillations in the level of strain and a high rate of change of strain. Whereas Fig 13 shows the time history at the other end of the structure and has less frequent oscillations and a lower rate of change of strain. The most significant difference however between the two locations is that there is considerable movement and the maximum strain level is achieved at the one site before the other side records anything.

Therefore one is lead to the conclusion that for a flexible structure such as this, initial movement is not in recognised modes but rather as local deformations.

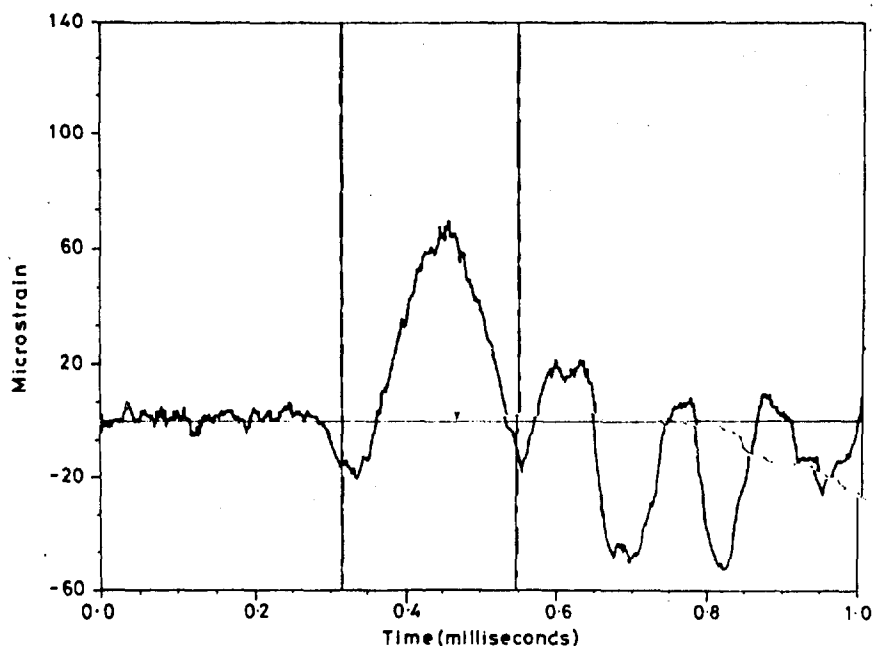


Fig 13 - Hoop Strain Time History
 (Shot 5 Channel 17)

Shot 3 Channel 6C Time 0-1.024 secs
(Fig 14)

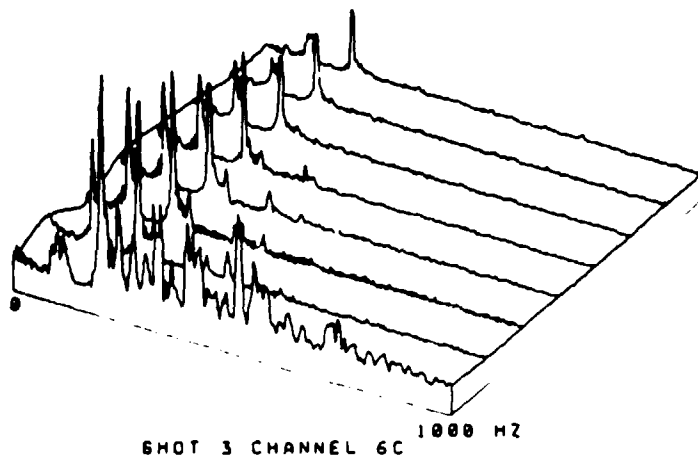
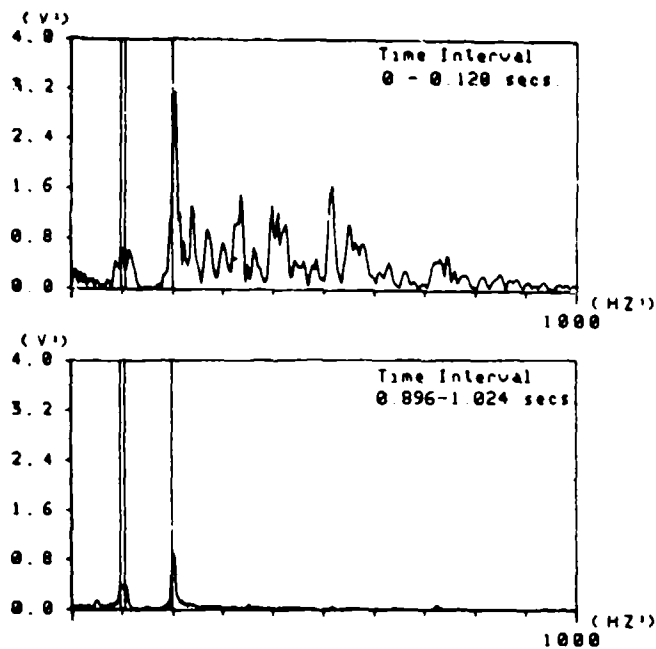


Fig 14 - Frequency Domain Analysis

The data from this series of tests was also analysed over a longer time period with an approach that considers the frequencies of vibration.

The response of each channel from 0-1.024 seconds was split into 8 equal increments and the frequency content of each increment compared. The resonant frequencies that were obtained from the shock data were readily identified with those obtained by steady-state testing and apart from the fact that certain modes increased in magnitude before eventually subsiding nothing extraordinary was observed.

SUMMARY

Although these are only preliminary findings and the results have yet to be compared with calculated values of strain several interesting points have been discovered or reaffirmed.

a. Strain gauges can be used to monitor the behaviour of a structure in the shock environment. Whether to assess damage, or to record deformations and stresses within the structure; strain is a good parameter to measure. However, most theoretical analyses are formulated in terms of displacements and although it is possible to establish strain from displacement there is no easy way of working back again.

b. The initial deformation of the cylinder when acted upon by the shock wave started a membrane or stretching wave which travelled through the structure at the speed of sound in steel. This is $3\frac{1}{2}$ times faster than the speed of sound in water. Therefore the membrane or stretching wave arrives at points that are further away from the source of the explosion before the acoustic pulse. In these tests some strain gauges achieved their maximum values before the pressure pulse arrived. So although some points may be sheltered as far as the pressure pulse is concerned this is unimportant if the stress wave is causing maximum strain (or displacement) as all points of the structure will be visible to the stress wave.

c. On the other hand those locations on the opposite side of the structure from the source of the explosion were sheltered as far as the rate of change of strain was concerned.

d. It is unlikely that a theoretical analysis can produce accurate answers unless the effect of membrane forces is considered in derivations of the equations of motion.

e. From the tests as performed there was no evidence to support the view [9] that broadside loading is not the most severe condition for this type of structure.

f. Deformations of sections of the cylinder occurred at appreciable, sometimes maximum levels whilst other sections were undeformed. A structure that is undergoing local deformation is not particularly suited to modal analysis in the normal sense.

g. Modes corresponding to frequencies measured by steady-state testing [8] were readily identified from the shock data.

h. The structure is very lightly damped with very few dominant frequencies which persist for longer than 1 second after the shock event. As the structure rings down after all external loading has ceased, some modes were observed to increase in magnitude before subsiding again.

REFERENCES

1. "Underwater Fluid-Structure Interaction", LH Chen M Prerucci Shock and Vibration Digest, April 1977.
2. "Response of shells to acoustic shocks", J M Klosner, Shock Vib Digest 0 (5) pp 3-13, 1976.
3. "Interaction of Acoustic Pulses with Fluid Loaded Shell Structures", R T Menton, 2nd E B Magrab Shock Vib Digest, 5 (12), pp 1-12, 1973.
4. "Fluid-Structure Interaction", Ed P Bettess, Int J Num Meth Engng 13 (1) 1-201, 1978.
5. "Residual Potential and Approximate Methods for Three Dimensional Fluid-Structure Interaction Problems", Geers JASA Vol 49, Number 5 (part 2), 1970.
6. "Transient Response Analysis of Submerged Structures", T L Geers, ASME, AMD-Vol 14, 1975.
7. "Fluid-Structure Interaction". Shock and Vibration Computer Programs, Washington DC, Naval Research Laboratory, Shock and Vibration Information Centre, 1975.
8. "Modal Analysis of a Cylindrical Structure Immersed in Water", R J Randall. Proceedings of the 3rd Int modal Analysis Conf, Orlando, Florida, Jan 1985.
9. "Angle of Incidence Effects for Underwater Shock Using Generic Computational Models", C E Rosenkilde and V H Ginsberg, 55th Shock and Vibration Symposium Dayton, Ohio 1984.
10. "DATS 11 Help Manual" Data Analysis Centre, ISVR, University of Southampton. September 1978.

Discussion

Voice: If you are oriented this way, and the charge is over here, then the stress or strain should be lower on the top than it would be on either the front or the back.

Mr. Randall: I didn't notice that. It seems the levels of stress or strain were constant around the circumference.

Voice: Did you have gages around the circumference of the cylinder?

Mr. Randall: Yes. There were ten locations around the circumference.

Voice: Do you have any plans to add some ring stiffeners?

Mr. Randall: I don't have any plans to add ring stiffeners. We are trying to understand what is happening to a simple structure. The idea is to be able to predict the response of the simple structure before we make the structure more complicated.

INVESTIGATION INTO THE EFFECTS OF USING DETONATING CORD
TO REMOVE A CONVENTIONAL PROPELLER FROM A WATER BORNE SURFACE SHIP

by

J. H. Strandquist III, LCDR, USN* and Y. S. Shin**
Department of Mechanical Engineering
Naval Postgraduate School
Monterey, California 93943

The relation between the shock wave pressure on the propeller hub and the size of the detcord charge was determined experimentally by a series of shots conducted on a full-scale test platform. The shock-induced response of the shaft was measured directly with strain gages and accelerometers. Additionally, the experimental shock wave pressure data provided the basis for numerical prediction of the response profile of the shaft.

INTRODUCTION

The use of detonating cord (detcord) in waterborne propeller maintenance has been practiced for many years by U.S. Navy diving and repair activities, with little knowledge of the potential effects on the shaft and related ship components. In order to quantify both the displacement and acceleration of the shaft caused by a detcord detonation on the propeller, a decommissioned Cost Guard cutter, ex-USCGC CAMPBELL (WHEC-32), was identified and chosen as a platform for the conduct of a series of test shots. The response of the shaft to these tests was measured, and the results are presented herein.

As provided for in the Naval Ships Technical Manual [Ref. 1], detonating cord may be used to remove a damaged conventional propeller from a waterborne surface ship where drydocking or the use of alternative waterborne methods have been ruled out due to constraints in time, logistics, funding, or the tactical situation. The procedure is described in detail in [Ref. 2]. After clearing all interference (rope guard, fairwaters, and dunce cap removed: gland retaining ring moved forward as far as possible), the propeller hub boss nut is backed off several turns, as shown in Figure 1. Detcord is wound around the shaft against the forward face of the propeller hub a predetermined number of turns, or wraps. To predict the shaft sleeve, the detcord is placed on top of an underlying layer of manila line. Several turns of line are also wound around the shaft between the propeller hub and the boss nut to cushion the impact there. When the charge is detonated, the impulse created by the

pressure wave in the water overcomes the tremendous static friction between the propeller hub and the shaft taper, and the propeller is pushed back along the shaft toward the boss nut. At this point the propeller replacement operation proceeds independent of the method used to loosen the damaged propeller. Details can be found in [Ref. 2].

The following is quoted from [Ref. 3]:

Detonating cord is round flexible cord containing a center cord of high explosive. The explosive cord, usually pentaerythritol tetranitrate (PENTN), is covered with various combinations of materials --these include textiles, waterproofing materials, and plastics which protect it from damage caused by physical abuses or exposure to extreme temperatures, water, oil, or other elements, and provide such essential features as tensile strength, flexibility, and other desirable handling characteristics... Detonating cord is relatively insensitive and requires a proper detonator...for initiation... As such, detonating cords are safe and reliable nonelectric detonating devices.

The detcord used in this investigation conforms with Military Specification Mil-C-17124C (Type I, Class c) [Ref. 4]. This reinforced detcord has a nominal explosive weight of 50 grains-per-foot, or seven pounds of explosive core per 1000 feet of detcord. According to several references, including [Ref. 3], the detonation velocity of 50 grain-per-foot detcord is on the order of 22,000 feet per second.

* Former graduate student

** Associate Professor

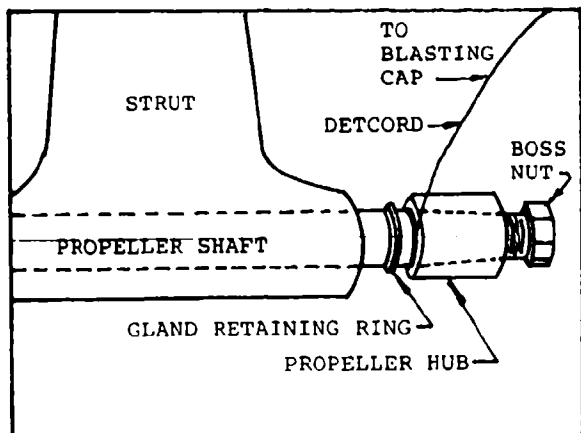


Figure 1 Underwater Propeller Removal Using Detcord

THEORETICAL PREDICTIONS

A. SHOCK WAVE FROM AN UNDERWATER EXPLOSION

The nature of the shock wave near the surface of an explosive charge detonated underwater is not well understood, owing to the uncertainties in the equations of state in this region. It becomes very difficult, therefore, to predict the response of an assumed rigid body, in this case the propeller, from a contact or near contact underwater explosion. Empirical formulae for the shock wave pressure profile which have been derived to date are based primarily on tests conducted with spherical charges where the minimum target standoff distance was approximately five charge radii [Ref. 5].

An approximation of the pressure profile, $p(t)$ from an underwater explosion as a function of time after detonation is,

$$p(t) = P_m \exp\left(-\frac{T_r}{\lambda}\right) \quad (1)$$

where P_m is the initial peak pressure, and λ is the time constant defined as the time in milliseconds required for the shock to decay to P_m/e , or about one-third of its maximum value. Both P_m and λ are functions of standoff distance. It was discovered during the testing that for short distance (i.e., inches), λ is relatively insensitive to variations in standoff distance, and an average value of time constant (λ) was used. Equation (1) is generally considered to be a close approximation of the actual shock profile for about one time constant: beyond this point, it usually can be relied upon to provide only a rough estimate, although in

the present case it appears to have been a very good one.

The retarded time T_r in equation (1) is defined by the charge geometry for the test platform illustrated in Figure 2, and must account for a finite detonation velocity. For example, if the detonation process commences at $\beta = 0^\circ$, it will take approximately 0.15 milliseconds to complete the process at $\beta = 360^\circ$. Thus,

$$T_r = t - \frac{|R|}{c} - \frac{R_0 \beta}{D_v} \quad (2)$$

where

- t = real time from initial detonation (msec)
- R = radial standoff distance between detcord and point of interest
- c = speed of sound in water (nominally five feet per msec)
- R_0 = radius of detcord charge
- β = angular distance from the point of initial detonation to point of interest
- D_v = detonation velocity of 50 grain-per-foot detonating cord

Note that if $T_r < 0$, physical reasoning tells us that the pressure at such times is equal to zero (or more precisely, hydrostatic pressure, although this is negligible at propeller depth).

When the shock wave from an underwater explosion contacts a rigid structure, the pressure at the surface is primarily the sum of the incident free-field pressure wave and the reflected pressure wave caused by interaction of the incident wave with the rigid structure. Although the relative magnitude of the reflected pressure can vary slightly depending on the magnitude and angle of incidence of the free-field wave, the total pressure on the incident surface is generally about twice the free-field value. Thus, the final expression for the axial force on the propeller as a function of time is:

$$F(t) = 2 \int_{-1}^1 \int_0^{2\pi} P_m \exp\left(-\frac{T_r}{\lambda}\right) R d\beta dR \quad (3)$$

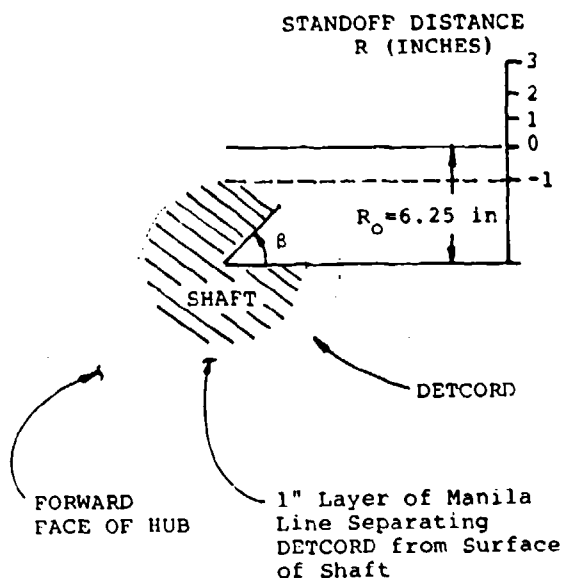


Figure 2 Propeller Hub Geometry (USCGC CAMPBELL)

Numerical integration of equation (3) can be readily accomplished once a relationship between peak pressure and standoff distance is established to provide values of P_m .

B. RESPONSE OF THE SHAFT

As shown in Figure 3, the shaft is to be modeled as a fixed-free bar, with motion restricted to one dimension. The connection between the shaft and the main engine is considered rigid in the horizontal direction, where the shaft collar has been jacked back against the aft thrust bearing shoes in accordance with [Ref. 2]. The effects of system damping are negligible with shock loading: hence, these are not considered. The shaft is assumed to be continuous of a constant cross-section, although a slight approximation is made here in the case of CAMPBELL.

The equation of motion for axial vibration of a bar with constant cross section is:

$$\frac{\partial^2 u}{\partial t^2} - a^2 \frac{\partial^2 u}{\partial x^2} = 0 \quad (4)$$

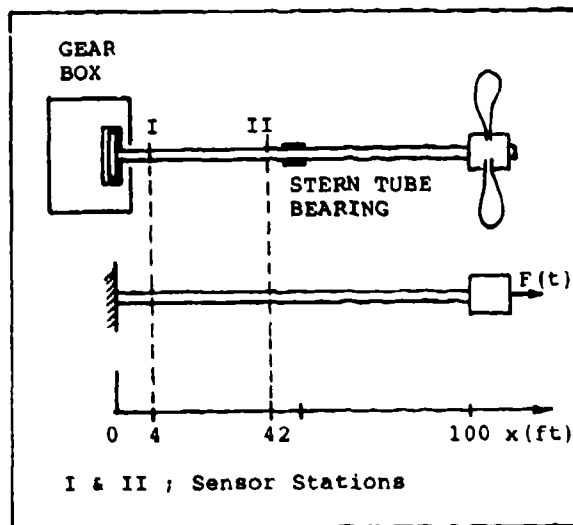


Figure 3 Propulsion Shaft Model (USCGC CAMPBELL)

where $u(x,t)$ is shaft particle displacement, and is a function of both time and position along the shaft. The wave propagation velocity (a) in the steel is about 200 inch per msec. The general solution to equation (4) is:

$$u(x,t) = f(x-at) + g(x+at) \quad (5)$$

For the case of a wave traveling in the $-x$ direction in Figure 3, this reduces to,

$$u(x,t) = g(x+at) \quad (6)$$

The longitudinal strain (ϵ) in the shaft can be defined as,

$$\epsilon(x,t) = g'(x+at) \quad (7)$$

where ($'$) is the derivative with respect to x .

The shaft particle velocity, $v(x,t)$ is similarly defined as,

$$v(x,t) = \dot{u} = \dot{g}(x+at) \quad (8)$$

where ($\dot{}$) is the derivative with respect to time. Using equations (6) through (8), the shaft particle velocity can be expressed as,

$$v(x,t) = a g'(x+at) = a \epsilon(x,t) \quad (9)$$

Integrating both sides of equation (9) with respect to time provides a relationship between shaft displacement and longitudinal strain:

$$u(x,t) = a \int_0^t \epsilon(x,t) dt \quad (10)$$

This relation is valid at any point along the shaft except very close to the fixed end, where the displacement is always theoretically zero.

The strain $\epsilon(x,t)$ is a relatively simple quantity to measure experimentally. Alternatively, however, it can be evaluated by observing the following from static analysis:

$$\epsilon_{\max} = D F_{\max} / [EA] \quad (11)$$

where F_{\max} is the maximum value of the axial force expressed by equation (3). The (D) is a dynamic magnification factor to be determined from the response spectrum for the particular impulse type experienced [Ref. 6]. (E) is modulus of elasticity and (A) is sectional area of shaft.

Thus, an approximation for the maximum shaft displacement can be arrived at in two ways. The strain wave can be measured directly, or the forcing function defined by equation (3) based on experimental shock wave pressure data, can be used to solve equation (11). Both should give similar results, which can then be used to solve equation (10) for the displacement of the shaft.

FIELD EXPERIMENT

A. TEST PLATFORM

The test platform, ex-USCGC CAMPBELL (WHEC-32), was inspected both underwater and within at its berth at Naval Station, San Diego, California, and was found to represent an excellent model for the planned experiment. Original ship drawings were obtained to determine as precisely as possible such parameters as shaft length, propeller weight, etc.

The CAMPBELL-class high endurance cutters are equipped with two shafts of about 103 feet in length. The ship's dimensions are 327 feet LOA, mean draft of 15 feet, and a standard displacement in excess of 2200 tons. CAMPBELL was chosen as a test platform because its dimensions and layout are roughly proportional to a small combatant's.

B. OBJECTIVES OF THE EXPERIMENT

The objectives of the experiment were to obtain the following information:

- (1) Free-field pressure measurements for 50 grain-per-foot detonating cord to be used in later numerical modeling.
- (2) Strain wave data for two points on the shaft. These are labeled Stations I and II in Figure 3, and correspond to the locations of the reduction gears and stern tube seal.
- (3) Shaft acceleration data near gear box.

The free-field pressure data would provide values of P_m in equation (3) to be used as input for numerical modeling. The strain gages would provide direct measurement of the strain wave as defined by equation (7). Finally, the accelerometers would provide a direct measurement of the maximum acceleration of the shaft near the main engine.

C. EXPERIMENTAL APPARATUS

All data was captured with a Honeywell M101 Wideband II (direct record) tape recorder using a recording speed of 120 inches-per-second, providing a frequency band-width capability of 500 kHz. Additionally, onsite verification of test results was provided by a Honeywell 1508B Visicorder. Two types of piezoelectric pressure transducers were utilized for this experiment. Both transducer types feature a volumetric-sensitive tourmaline crystal element suspended in an insulating oil. As discussed in [Ref. 5], tourmaline crystals are ideally suited for underwater explosion pressure measurements. The strain gages used at Stations I and II were 350 ohm, constantan foil strain gages. Finally, two accelerometers, including one with a 500g range, were positioned at Station I near the gear box. The accelerometers were glued to the shaft with Devcon Plastic Steel, No. 10240.

D. EXPERIMENTAL PROCEDURE

A total of 14 shots were conducted during the five day period of the experiment: they will be referred to by the order in which they were performed. Eight of these were so-called free-field pressure shots in which the propeller and shaft were not subjected to a shock loading. The remaining six shots comprised the actual shock tests.

(a) Preliminary Testing (Shots 1-4)

The first four shots were free-field tests conducted for the purpose of checking out the electronics and for determining a proper standoff for the pressure transducers. Three wraps, or turns of detcord were placed spirally directly on the shaft at a location remote from the propeller and bearings. The pressure transducers were placed in the free field, at the same depth as an outboard of the shaft. The first shot at nine feet registered no pressure rise on any of the transducers. The second shots at two feet registered a peak value of approximately 2,000 psi. The third and fourth shots brought the range to within inches, registering peak pressures on the order of 20,000 and 40,000 psi, respectively.

These first four shots demonstrated several important facts. First, the transducers would have to be very close to the charge to record any significant pressures. Second, there was excellent correlation between both types of pressure transducers. Finally, these first four shots demonstrated excellent performance from the Honeywell M101 tape recorder, verified in the field with a strip chart recorder.

(b) Shock Testing (Shots 5-10)

Upon completion of the four preliminary free-field shots, enough information had been obtained to commence the actual shock testing. The shaft was carefully inspected both underwater and inside the ship to ensure that it was, in fact, in a fixed-free condition as shown in Figure 3. Weld restraints installed to prevent the propeller from windmilling during towing were removed, so that the only fixed point in the one-dimensional removed, so that the only fixed point in the one-dimensional analysis undertaken was the gear box end of the shaft. The propeller dunc cap and rope guards had been removed previously. All sensors were placed in position. In all respects, the port propeller was ready for removal using the detcord method discussed in [Ref. 2], with one exception: the

prepeller hub boss nut was not backed off at all. The reason for this was two-fold. First, once the propeller had broken free of the static friction generated by its original installation around the shaft, this initial condition would have been lost for subsequent shots. Second, by restraining the propeller on the shaft and thus making them integral unit, none of the energy from the detcord detonation imparted to the propeller hub would be lost either through heat generated by dynamic friction between hub and shaft, or thorough momentum transfer between the propeller blades and the water. Thus, a worst-case situation with respect to the total impulse imparted to the shaft made available for each shock test.

According to [Ref. 2], the size of the detcord charge in actual practice is to be limited to four wraps. This rule of thumb is true regardless of the shaft diameters. It was decided, therefore, to subject CAMPBELL's shaft to shock loading from one, three and five-wrap charges.

The first two shock tests, shots 5 and 6, were essentially the same test conducted twice. One wrap of detonating cord was used for each of these two shots. As in all the shock tests, the detcord was wound on top of a one inch layer of manila line, thus separating it from direct contact with the shaft sleeve.

Three wraps of detcord were used for shots 7 and 8. For shot 7, the detcord was wrapped spirally, as is probably done in practice in most cases. For shot 8, however, it was wrapped concentrically against the propeller hub in accordance with [Ref. 2], and held in place with underwater epoxy.

Shots 9 and 10 were similar to the previous two. This time five wraps of detcord were used. For shot 9, the detcord was wrapped spirally; for shot 10, concentrically against the hub.

(c) Free-Field Testing (Shots 11-14)

When the first set of free field shots described above were conducted, there was no data or experience base available to assist in determining an appropriate transducer standoff distance. After ten shots had been completed, this was no longer a problem, and a more precise method was devised for obtaining pressure-time histories within the range of interest for the last series of free-field tests. Three pressure transducers were arranged so that the standoff from the detcord was sequentially one, two, and three inches, respectively. The detcord was wrapped around the shaft at

a location where the ship's hull or appendages would not affect the early time pressure readings. This time, however, the detcord was wound on top of a layer of manila line to more accurately simulate conditions near the propeller hub. Shots 11 and 1 were with one wrap of detcord, shot 13 was with three wraps, and shot 14 was with five wraps. The last series of free-field pressure measurements completed the experimental testing.

EXPERIMENTAL RESULTS

From the standpoint of quality data collection in the field, the experiment was considered a success. These tests were performed shortly after the first two in a series of experiments being conducted at Naval Postgraduate School under the sponsorship by the Defense Nuclear Agency to investigate the response of stiffened flat plates to underwater explosions of much greater magnitude. The hard lessons learned during these earlier experiments were quite valuable to the present investigation [Ref. 7].

Figure 4 illustrates the data acquisition and reduction scheme used in the experiment. All data was reviewed on-site using the Honeywell 1508B Visicorder. These records, such as the one shown in Figure 5 provided a means of partially verifying the results in the field. Note that the relative distance between each pressure transducer can be determined by comparing the real time delay between pulses to the theoretical values of approximately 16.7 μsec . The measured shock pressure profiles for shots 2, 12 through 14 are shown in Figures 6 through 9. The pressure-time histories showed a near-constant rise time of about four μsec , which is approximately the limit of the instrumentation. The measured strain time histories for shots 6, 7, 9 and 10 are shown in Figures 10 through 13. The measured strain data shows that the strains at both Stations I and II are close to each other.

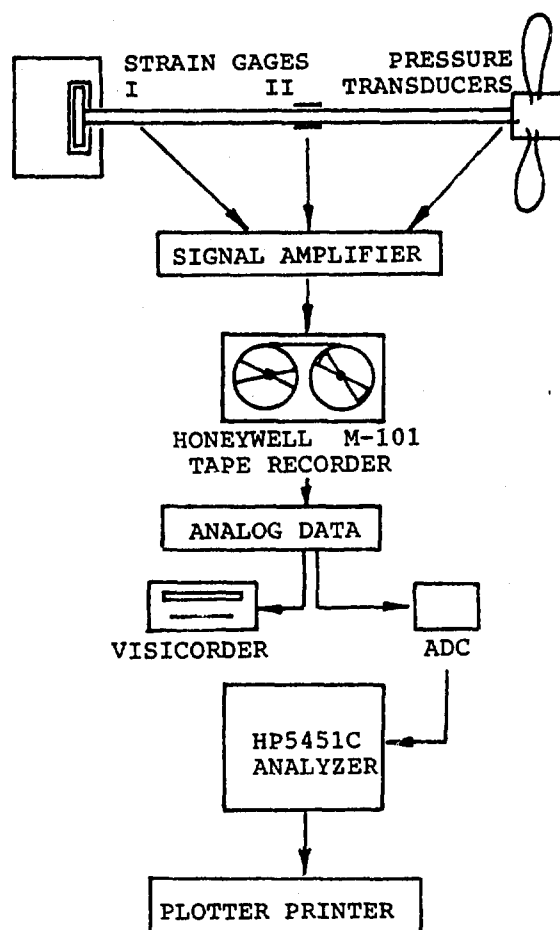


Figure 4 Data Acquisition and Reduction Scheme

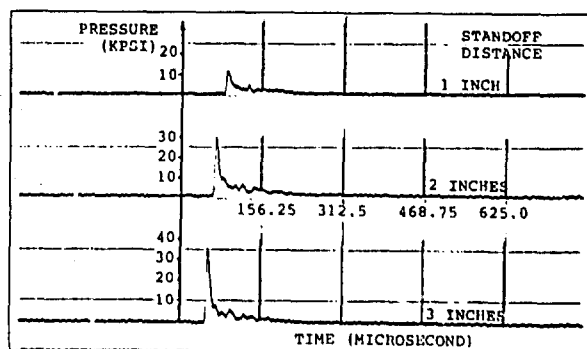


Figure 5 Pressure Profiles for a 5-Wrap

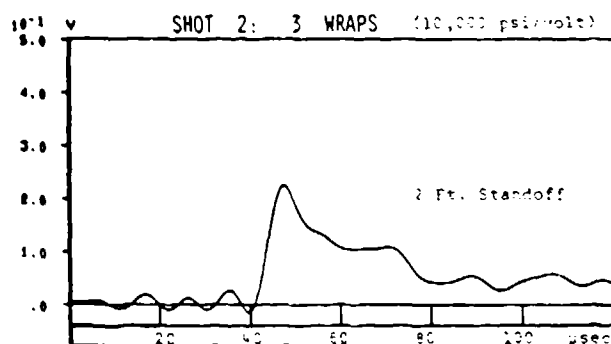


Figure 6 Measured Shock Pressure Time History for Shot 2

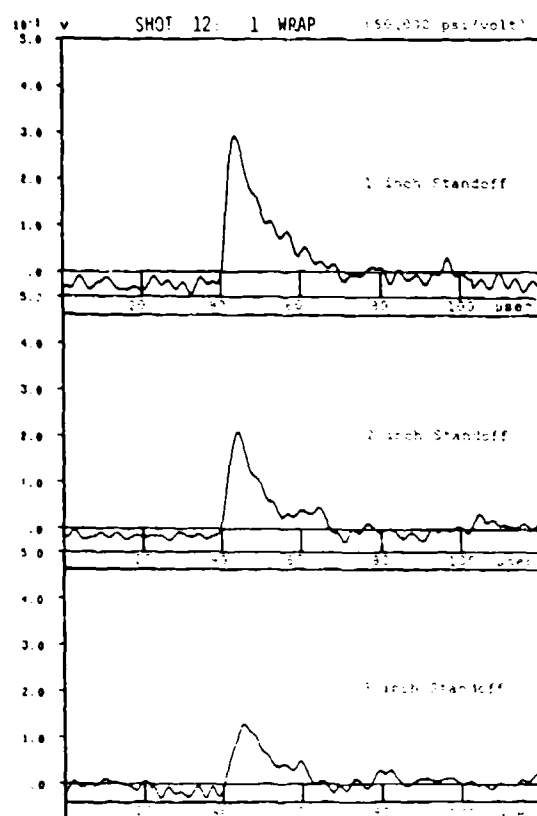


Figure 7 Measured Shock Pressure Time History for Shot 12

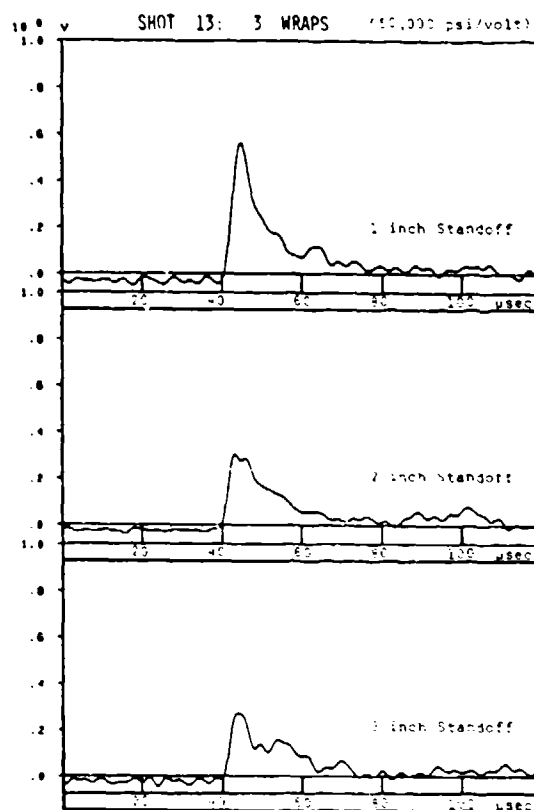


Figure 8 Measured Shock Pressure Time History for Shot 13

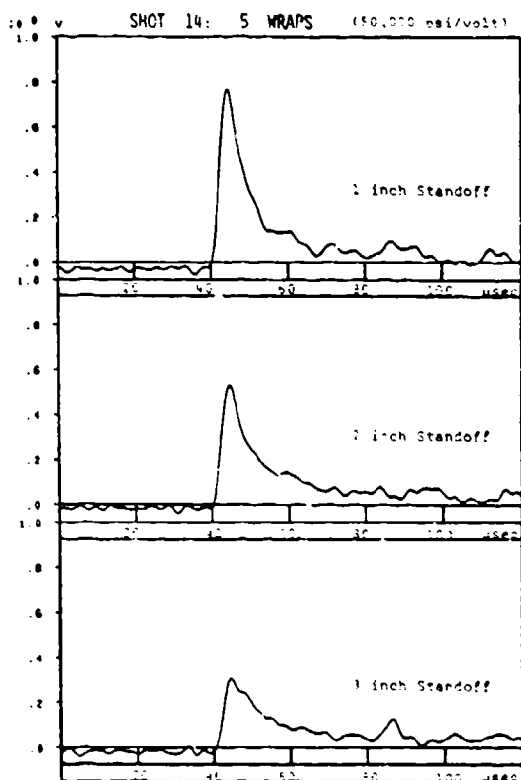


Figure 9 Measured Shock Pressure Time History for Shot 14

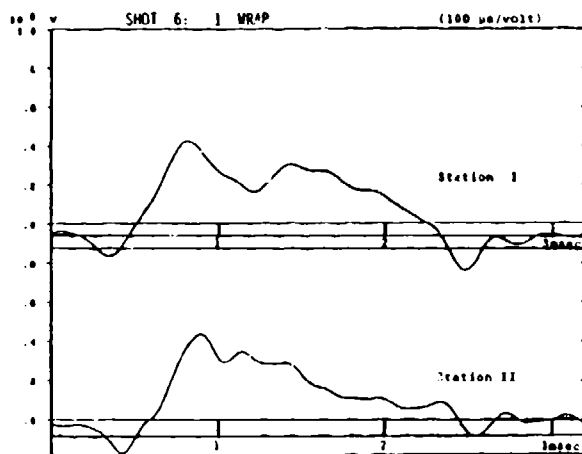


Figure 10 Measured Strain Data for Shot 6

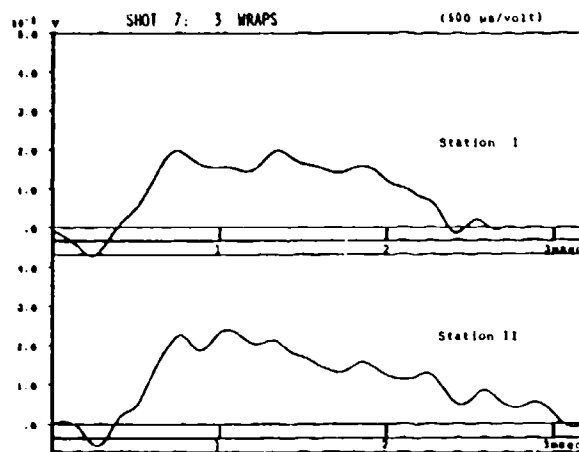


Figure 11 Measured Strain Data for Shot 7

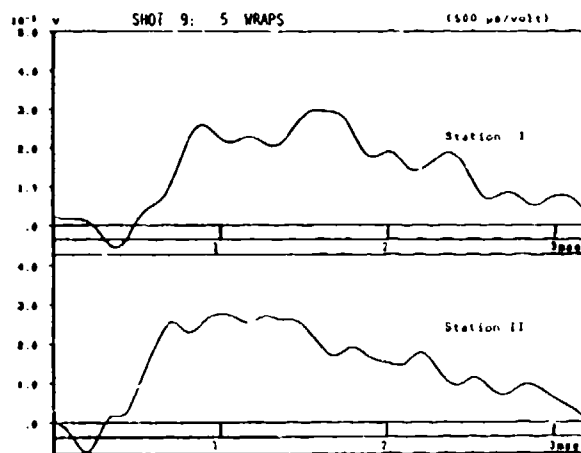


Figure 12 Measured Strain Data for Shot 9

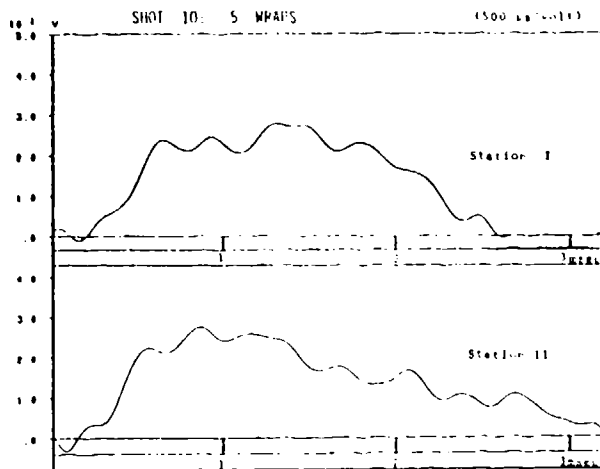


Figure 13 Measured Strain Data for Shot 10

Figure 14 illustrates the relationship between peak pressure and standoff distance for a given charge size. The recorded pressure were adjusted slightly to account for the gage response of the transducers [Ref. 8]. This data would provide the basis for later numerical prediction discussed later. The maximum strain for each shot is plotted as a function of charge size in Figure 15. Finally, peak accelerations at Station I increased linearly with charge size within the range of the experiment, as shown in Figure 16.

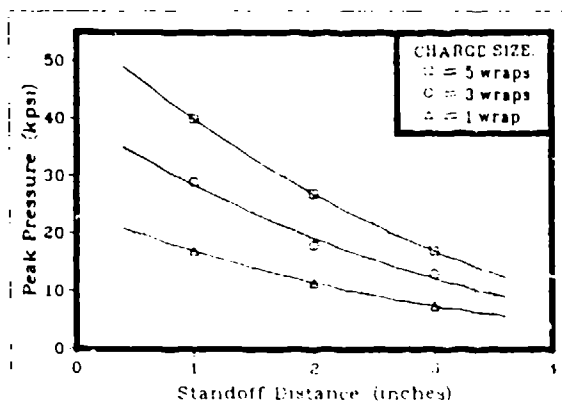


Figure 14 Peak Pressure vs. Standoff Distance

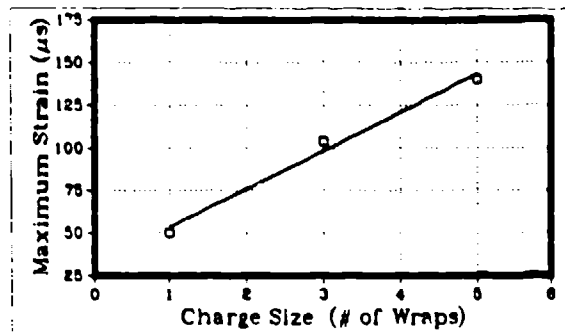


Figure 15 Maximum Strain vs. Charge Size

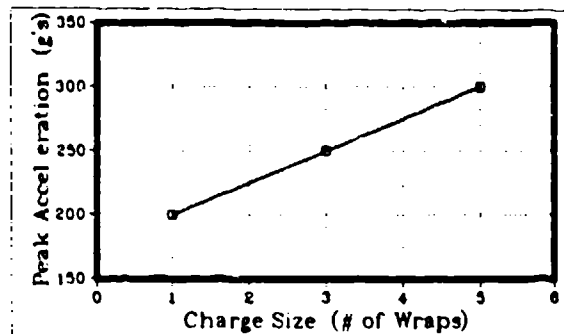


Figure 16 Maximum Acceleration vs. Charge Size

A. DEVELOPMENT OF A NUMERICAL MODEL

The experimental pressure data collected on the CAMPBELL tests was to be used as the basis for the impulsive loading input to a numerical scheme for predicting shaft response from an underwater detcord blast. A snapshot of this loading as a function of both time and standoff is illustrated in Figure 17 for a 3-wrap charge.

The axial shaft force was calculated using equation (3). Values for P_m were obtained from the relationship between peak pressure and standoff distance illustrated in Figure 14. The results are shown in Figure 18.

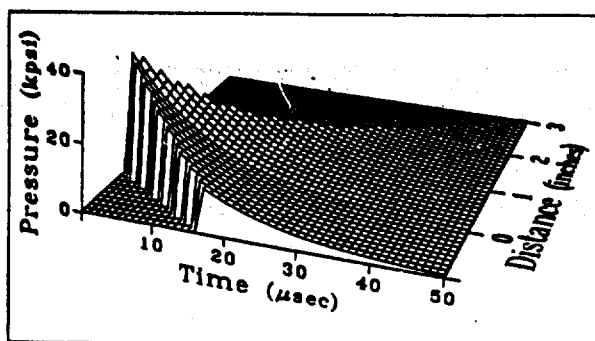


Figure 17 Unit Impulse Based on Experimental Results

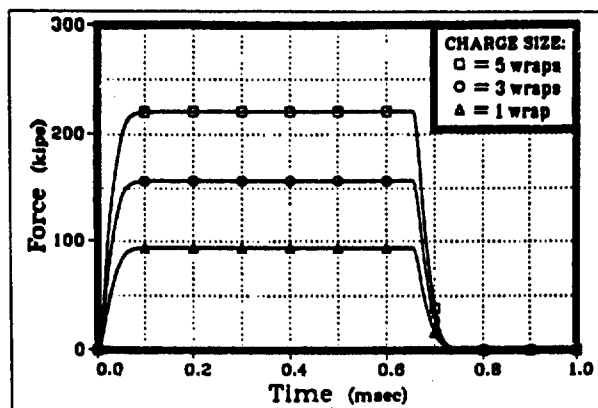


Figure 18 Force Applied to CAMPBELL's Shaft

B. COMPARISON OF NUMERICAL AND EXPERIMENTAL RESULTS

A good approximation of the forcing function illustrated in Figure 18 is a rectangular impulse. For this type of loading, the dynamic magnification factor, D is defined as, [Ref. 6]

$$D = 2 \sin[\pi(B)] \quad (12)$$

where B is the ratio of the load period to the period T at which the shaft responds. From Figure 18, the load period is 0.7 msec. The strain wave histories indicated that the half period of shaft response corresponding to the lowest excitation frequency is around 2 msec (i.e., T is in the vicinity of 4 msec). It can be shown [Ref. 8] that the natural frequencies of the shaft-propeller system can be expressed by,

$$\frac{2\pi fL}{a} \tan\left(\frac{2\pi fL}{a}\right) = \frac{M_s}{M_p} \quad (13)$$

where

f = natural frequency

L = shaft length

a = speed of sound in the shaft material

M_s = total mass of the shaft

M_p = mass of the propeller and boss nut

Solving equation (13) for the natural frequency in the region of interest for CAMPBELL yields a value of 270 Hz. This corresponds to a natural period of 3.71 msec. Inserting this result into equation (13) yields a dynamic magnification factor D of approximately 1.12.

Each of the strain profiles can be approximated analytically as a sine wave whose magnitude varies according to charge size. With this knowledge, equation (9) can be redefined accordingly for any fixed location on the shaft:

$$v(t) = (a) \max[\epsilon(x,t)] \sin(2\pi/T) \quad (14)$$

Similarly, for any given value of x (except right at the gear box), equation (10) can be expressed as,

$$u(t) = a \max[\epsilon(x,t)] \int_0^t \sin(2\pi/T) dt$$

$$\text{or} \quad (15)$$

$$u(t) = -(T/2\pi)(a) \max[\epsilon(x,t)] \cos(2\pi/T)$$

Finally, the expression for the maximum displacement of the shaft is simply,

$$u_{\max} = \max[u(x,t)] = (T/2\pi) (a) \max[\epsilon(x,t)] \quad (16)$$

As indicated in previous section, values of $\max[\epsilon(x,t)]$ used in equation (16) can be obtained experimentally by direct strain gage measurement, or numerically through the use of equation (11). Figure 19

summarizes the results obtained for maximum shaft displacement for both methods.

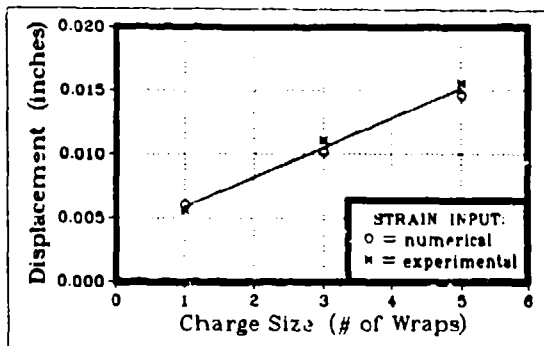


Figure 19 CAMPBELL Shaft Displacement vs. Charge Size

The numerically determined values display a linear relationship with increasing charge size that is adequately approximated by the experimental record within the range observed, supporting the assertion that the numerical model is an acceptable one for further prediction purposes.

C. NUMERICAL ANALYSIS OF DDG-2 SHAFT CONFIGURATION

Having established the validity of a method for predicting the response profile of the shaft in the case of CAMPBELL, a specific inservice shaft configuration will now be analyzed. The USS CHARLES F. ADAMS (DDG-2) class of guided-missile destroyers was chosen for this purpose. Experience among U.S. Navy diving supervisors indicates this large class of surface combatants is one of the most frequent candidates for waterborne propeller replacement.

Shaft blueprints for the ADAMS class were obtained from the planning yard. It was decided to analyze the port shaft, since it more closely resembles the configuration on CAMPBELL. Natural period of longitudinal vibration for the port shaft were computed using equation (13) and the shaft geometry defined by the blueprints. It was 3.8 msec which is close to that of CAMPBELL.

Given the larger shaft diameter of the ADAMS class over CAMPBELL, the length of each wrap of detord would be increased proportionally. Taking this into account, as well as the larger surface area of the propeller hub over which to carry the integration, the force which would be applied to the end of ADA4S' port shaft was predicted as was done for CAMPBELL, and the

results are shown in Figure 20. As expected, the shape of the loading is nearly identical to that experienced on CAMPBELL. The period of the load, however, would be 1.2 msec. Observing from Table 1 that the natural period of interest is $T = 3.8$ msec, equation (12) provides a dynamic magnification factor of 1.67. Utilizing equation (11) to obtain the maximum theoretical strains that would be experienced for a given charge size, the equivalent shaft displacements can be predicted using equation (16). These are plotted for the port shaft of USS CHARLES F. ADAMS (DDG-2) in Figure 21.

Table 1
Natural Shaft Periods for Both Ships.

Mode #	Natural Period (msec)	
	Campbell	Charles F. Adams
1	27.6	31.1
2	9.1	9.8
3	5.4	5.6
4	3.7	3.8
5	2.9	2.9
6	2.3	2.4
7	2.0	2.0

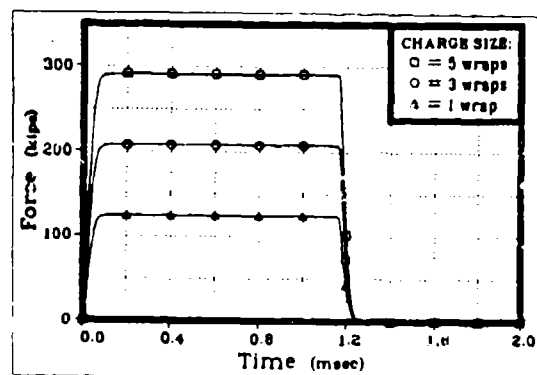


Figure 20 Predicted Force on ADAMS Shaft

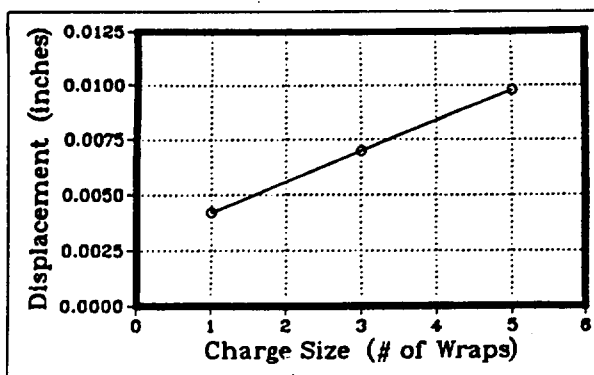


Figure 21 Predicted Shaft Displacement for ADAMS

CONCLUSIONS

According to [Ref. 2], the maximum static removal force to be used in unseating the propeller from an ADAMS-class destroyer is 400 tons (800 kips). From Figure 20, the maximum predicted force from a 5-wrap charge is 145 tons (290 kips). Multiplying this value by the dynamic magnification factor of 1.67 calculated for ADAMS, an equivalent force of 240 tons is obtained, leaving a considerable margin of safety under this criterion.

Although Figure 3 indicates a zero displacement condition for the shaft collar at the thrust bearing, this is only true for tensile loads. The initial tensile wave in the $-x$ direction will be reflected as another tensile wave in the $+x$ direction. Upon arrival at the propeller, the strain wave will be reflected again in the $-x$ direction, but this time as a wave of compression. By the time this compressive wave reaches the thrust bearing, it will be on its third trip along the shaft, and some dissipation of its magnitude is to be expected. However, as a conservative estimate, it is assumed that this wave arrives at the gear box undiminished.

The DDG-2 reduction gear technical manual [Ref. 9] defines a minimum allowable endplay on the shaft collar/thrust bearing interface of 0.019 inches. This is twice the displacement predicted for ADAMS from a 5-wrap detcord charge in Figure 21, a prediction that includes several conservative assumptions which realistically should provide for an even greater safety margin. This means that the shaft collar will not compress the forward bearing shoes sufficiently to transfer the shock loading indicated in Figure 16 to the reduction gears. It is therefore concluded that, at least within the range of charge sizes

tested, the use of detonating cord to remove a propeller from a ADAMS-class destroyer will result in no detrimental effects on the thrust bearings or the reduction gears. Given the extremely small magnitude of expected shaft displacement, it is also concluded that friction damage to strut, stern tube, or line shaft bearings, or to the stern tube seal itself, would be non-existent to any measurable degree.

In light of the obvious cost savings, the use of Navy divers to perform an increasing number of underwater maintenance and repair tasks in the future appears certain. Nevertheless, frequent objections have been raised against the conduct of underwater ship husbandry in general, and against the use of explosives to remove conventional propellers in particular. In both cases, the underlying problem has not been the methods themselves so much as the lack of quality control. The few specific instances where damage has resulted from using detcord in waterborne propeller replacement can each be attributed to a failure to follow established procedures and common sense. Where procedures are as followed, the use of detonating cord common sense. Where procedures are as followed, the use of detonating cord to remove a damaged propeller is considered a safe and viable alternative to other more costly and time consuming method.

LIST OF REFERENCES

1. Department of the Navy Specification NAVSEA S9086-HP-STM-000, Naval Ships Technical Manual, Chapter 245, Chang 1, November 1977.
2. Department of the Navy Specification NAVSEA 0994-LP-007-8020, Underwater Work Techniques Manual, Volume 2, November 1971.
3. E. I. du Pont de Nemours and Co., Blaster's Handbook, 16th Edition, 1980.
4. Department of Defense Military Specification MIL-C-17124C, Cord, Detonating, 23 June 1966.
5. Cole, Robert H., Underwater Explosions, Princeton University Press, 1948.
6. Clough, R., and Penzien, J., Dynamics of Structures, McGraw-Hill Book Company, 1975.
7. Rentz, T. R. and Shin, Y. S., On the Field Experiences of UNDEX Testing for a Stiffened Flat Plate Model, presented at the 55th Shock and Vibration Symposium, Dayton, Ohio, October 22-25, 1984. Also

appeared in Shock and Vibration Bulletin
55, June 1985.

8. Thomson, W. T., Theory of Vibration with Applications, 2nd Edition, Prentice Hall, 1981.
9. Department of the Navy Specification NAVSEA 341-1329/GEI-60419, DDG-2 Reduction Gear Technical Manual, August, 1965.

BLAST AND GROUND SHOCK

Dynamic Response of Armor Plate to Non-Penetrating Projectile Impact

W. Scott Walton
U.S. Army Combat Systems Test Activity
Aberdeen Proving Ground, Maryland

ABSTRACT

To investigate the instrumentation related problems of acceleration measurement on armor plates, a controlled experiment was conducted. A 38mm thick plate of rolled homogeneous armor (RHA) was subjected to impact by ball bearings and small caliber projectiles (.30 caliber to 20mm). Measurements of acceleration, velocity, displacement, and strain were made. Because of with continued difficulties acceleration and velocity instrumentation, a non-standard velocity measurement technique velocity measurement technique was used. Differentiation of the resulting velocity signals produced very short duration (1 microsecond) (1 microsecond) acceleration pulses of 1 to 3 million g's. The theoretical prediction was approximately 1 million g's.

INTRODUCTION

A number of instrumentation related difficulties have been encountered during measurements of acceleration on armor plate subject to projectile impact. A classic example is a test done by Devost and O'Brasky (reference 1) of the Naval Ordnance Laboratory using the 5"/54 gun in 1972. In that test, only the accelerometers that were mechanically decoupled from the plate survived impact. Similar results have been observed by the U.S. Army Combat Systems Test Activity using smaller caliber projectiles.

To investigate these problems, and to characterize the ballistic shock environment, a controlled experiment was conducted. Figure 1 shows an RHA test plate .038 by .914 by .914 meters bolted to a rigid support structure.

The test plates were attached using 18 bolts on a .864 meter square. Assuming these bolts to be simple support, the lowest theoretical resonant frequency of this configuration is

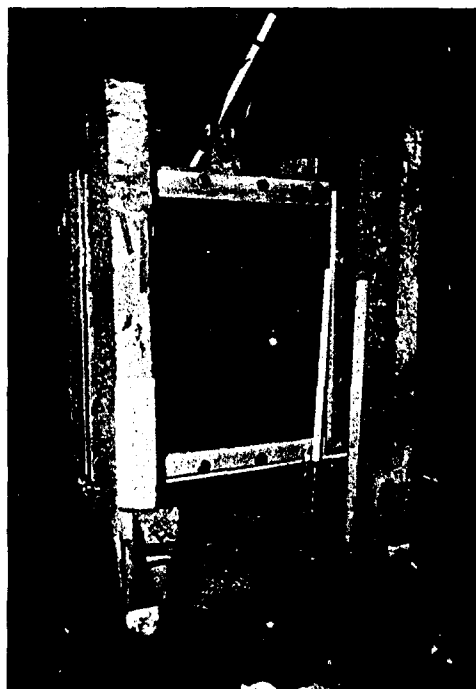


Figure 1. Photograph of RHA test plate .038 by .914 by .914 meters in rigid support structure. Note ball bearing, suspended from 2 wire pendulum, and hammers, used to check instrumentation prior to projectile impact.

TRANSDUCER LOCATIONS FOR BALLISTIC SHOCK TEST

All dimensions in Millimeters

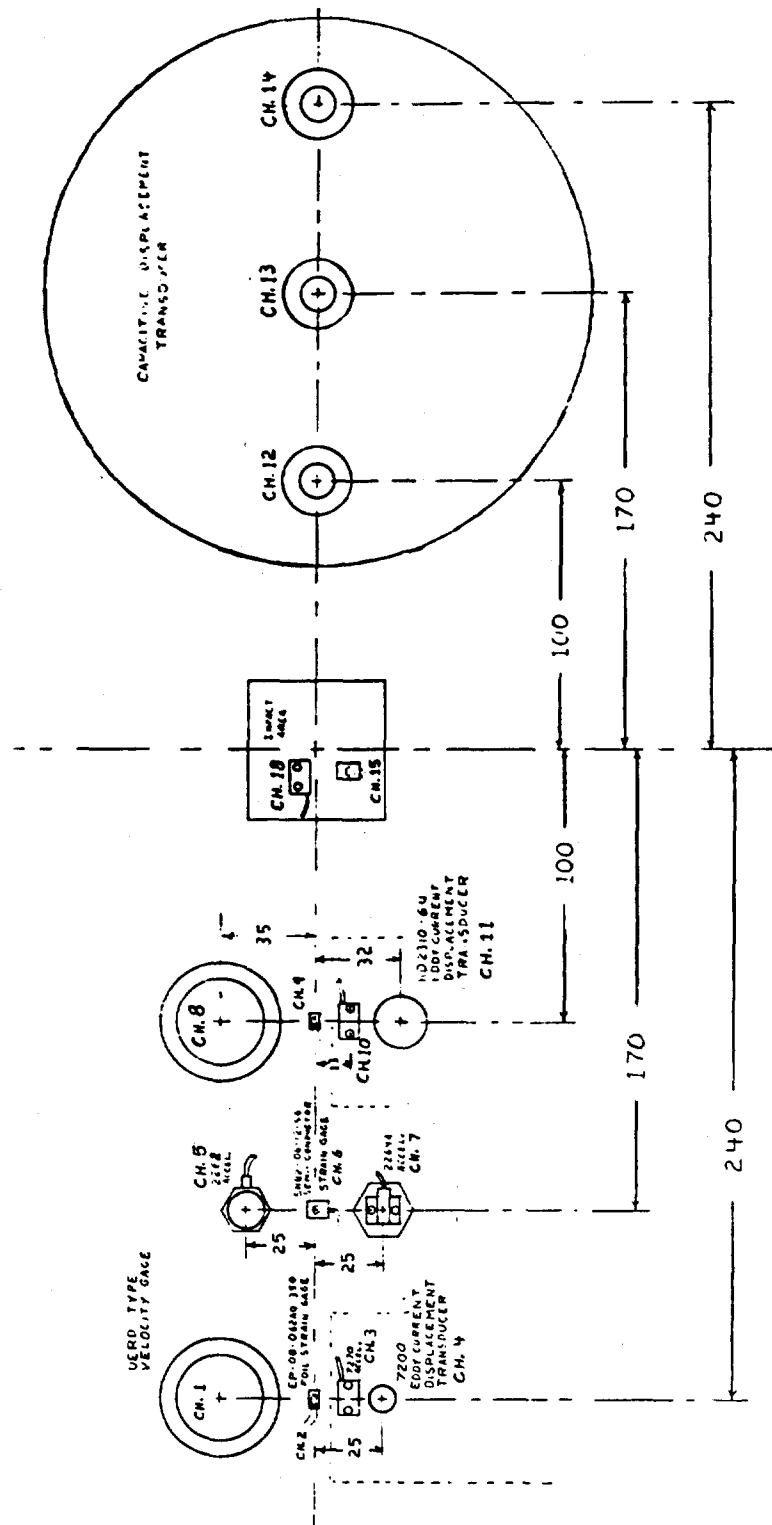


Figure 2. Instrumentation layout on back of plate.

249.6 Hz. The observed resonant frequencies of 4 different plates varied from 249 to 263 Hz., hence the assumption of simple support appears justified.

INSTRUMENTATION

Figure 2 shows the location of transducers used to measure the response of the back of the plate. Figure 3 is a photograph of the transducers. Three different models of piezoresistive accelerometers were used. Velocity transducers were supplied by the Underwater Explosion Research Division (UERD) of the Naval Ship Research and Development Center.

Displacement was measured using commercial non-contacting eddy-current probes and by a locally fabricated capacitive type displacement transducer fashioned after Erlich's design (Reference 2). Strain was measured using conventional foil type and semiconductor type strain gages.

Signal conditioning for all transducers was located in a box directly behind the support structure. This step was taken to obtain higher frequency response than is usually possible when transducers must drive long cables. A bridge conditioning electronics unit was fabricated for the accelerometers and strain gages to

provide 100 KHz frequency response through 150 meters of RG-58 cable.

BALL BEARING IMPACT

The impact of a 50mm diameter steel ball bearing was used to check the instrumentation prior to firing projectiles. This impact is of interest because the momentum change and the impact duration are similar to projectile impact, and because this type of impact has been analyzed mathematically by several authors.

As stated by Greszczuk (Reference 3), a half-sine function can be used as a reasonable estimate of the force vs. time profile for ball bearing impact. A half-sine pulse with a 124 micro-second duration and 40,000 Newton peak amplitude was shown to be a reasonable approximation of the ball bearing impact used in this experiment.

A computational technique used by Goldsmith (Reference 4) was used to analyze the lower modes of response of the armor plate to ball bearing impact. For a central transverse impact of a simply supported rectangular plate, the displacement in the Z direction of any point along the X axis of the plate can be calculated as a function of time using the equation shown in Figure 4.

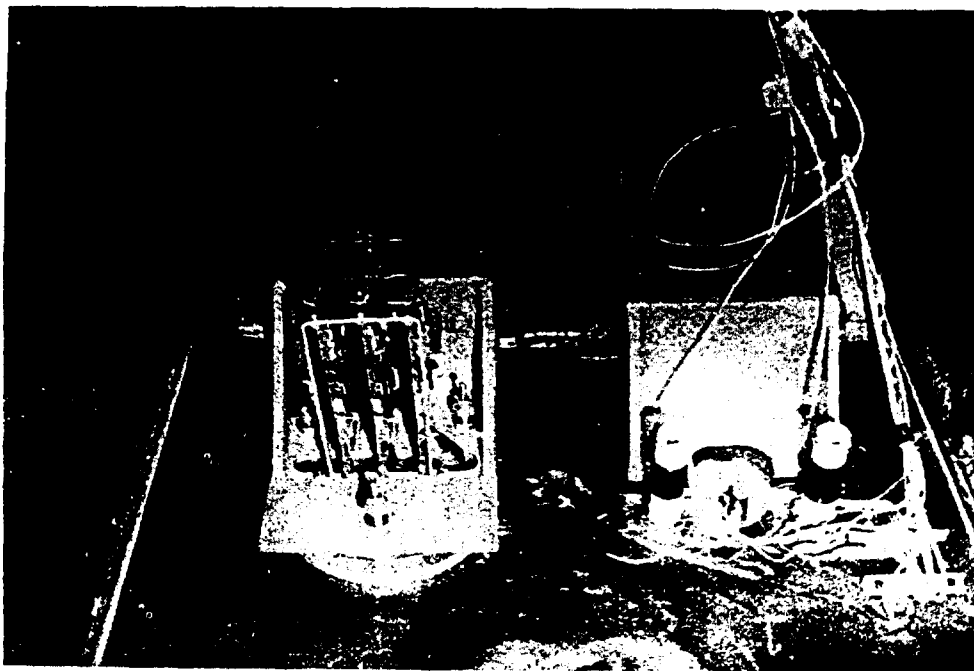


Figure 3. Photo of instrumentation on back of plate.

$$\begin{aligned} \text{Transverse Displacement} \\ z(x, \frac{n}{2}, t) = \frac{2\sqrt{3(1-\nu^2)}}{\pi^2 b^2 m n} \sum_{i=1,3,\dots}^{\infty} \sum_{k=1,3,\dots}^{\infty} \frac{\sin \frac{i\pi x}{m} \cdot (-1)^{\frac{i-1}{2}}}{\frac{i^2}{2} + \frac{k^2}{n^2}} \int_0^t \ddot{P}(\tau) \sin \pi^2 b \left[\sqrt{\frac{E}{3\rho(1-\nu^2)}} \right] \left[\frac{i^2}{m^2} + \frac{k^2}{n^2} \right] (t-\tau) d\tau \end{aligned}$$

$$\begin{aligned} \text{Radial Strain} \\ \epsilon = \frac{\partial^2 z}{\partial x^2} \cdot b = \frac{-2\sqrt{3(1-\nu^2)}}{b m^4} \sum_{i=1,3,\dots}^{\infty} \sum_{k=1,3,\dots}^{\infty} \frac{i^2 \cdot \sin \frac{i\pi x}{m} \cdot (-1)^{\frac{i-1}{2}}}{\frac{i^2}{2} + \frac{k^2}{n^2}} \int_0^t \ddot{P}(\tau) \sin \pi^2 b \left[\sqrt{\frac{E}{3\rho(1-\nu^2)}} \right] \left[\frac{i^2}{m^2} + \frac{k^2}{n^2} \right] (t-\tau) d\tau \end{aligned}$$

where: b = plate half-thickness (.01905 meters)
 m = n = length of side of plate (.8636 meters)
 ρ = density (7833 Kg/meter³)
 E = Modulus of elasticity (2.07×10^{11} newtons/meter²)
 ν = Poisson's ratio (0.3)

z = transverse displacement (in meters)
 x = distance from edge of plate (in meters)
 i = harmonic number
 k = harmonic number
 t = time (in seconds)
 τ = integration variable
 $P(t)$ = Force applied to plate
 (40,000 * sin 25335 t newtons)

Figure 4. Equations used to solve for displacement and strain on plate subjected to ball bearing impact.

Note that the displacement and strain can be calculated directly using the equations in Figure 4. Acceleration and velocity were obtained by numerically differentiating the calculated displacement values. The solutions were calculated using a time step of 5 microseconds and 11 harmonics.

Figure 5 compares the calculated and measured response of the plate to ball bearing impact. Although the plots show significant discrepancies, (40% on velocity) the measurements and the calculation demonstrate the same general trends.

Note how the half-sine shape of the forcing function dominates the measurements. The velocity and strain measurements at 0mm show a similar half-sine shape. As one would expect, the corresponding acceleration pulse is roughly a sine wave, passing through zero at the time when the velocity reaches its peak.

The strain signal is a tension pulse at the 0mm position and a compression pulse at the 170mm position. This transition from tension to compression was mentioned by Doyle (References 5 and 6) in his discussion of measuring the force vs. time of an impact by using strain signals. A resemblance to the half-sine shape of the forcing function clearly dominates both strain signals.

PROJECTILE IMPACT

Figure 6 shows the target plate and support structure on the firing range. Figure 7 shows some of the soft projectiles before and after impact. The projectile types and striking velocities are listed in Table 1.

In the previous section, it was mentioned that the characteristic signature of the forcing function could be seen as a compression pulse at the 170mm position. Figure 8 shows characteristic strain signatures of various projectile impacts. Note that the Ball Bearing and .30 Caliber Ball impacts produce a half-sine pulse of approximately 100 microsecond duration. The Fragment simulating projectiles produce a more triangular shaped pulse of 10 to 50 microseconds in duration.



Figure 6. Plate and support structure on firing range.

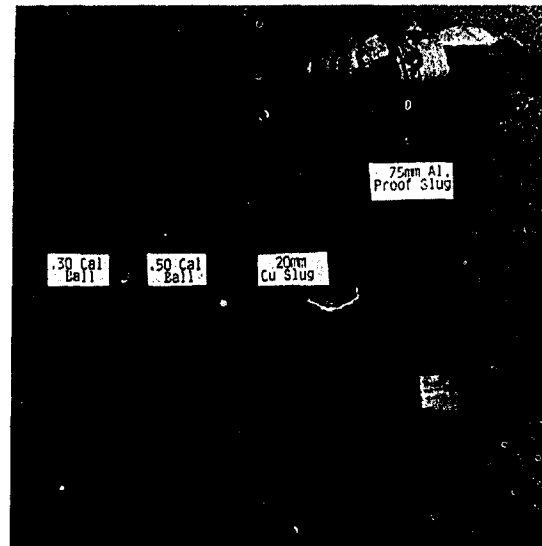


Figure 7. Soft projectiles before and after impact at 335 meters/second.

The long term (90 millisecond) response of the plate is shown in Figure 9. A hammer impact (H4) is compared to a projectile impact (Round #28). The hammer impact lasted approximately 2 milliseconds and this impact load primarily excites the 250 Hz resonance of the plate. Round 28 was a .30 caliber ball impact lasting approximately 120 microseconds, and it excites much higher frequencies.

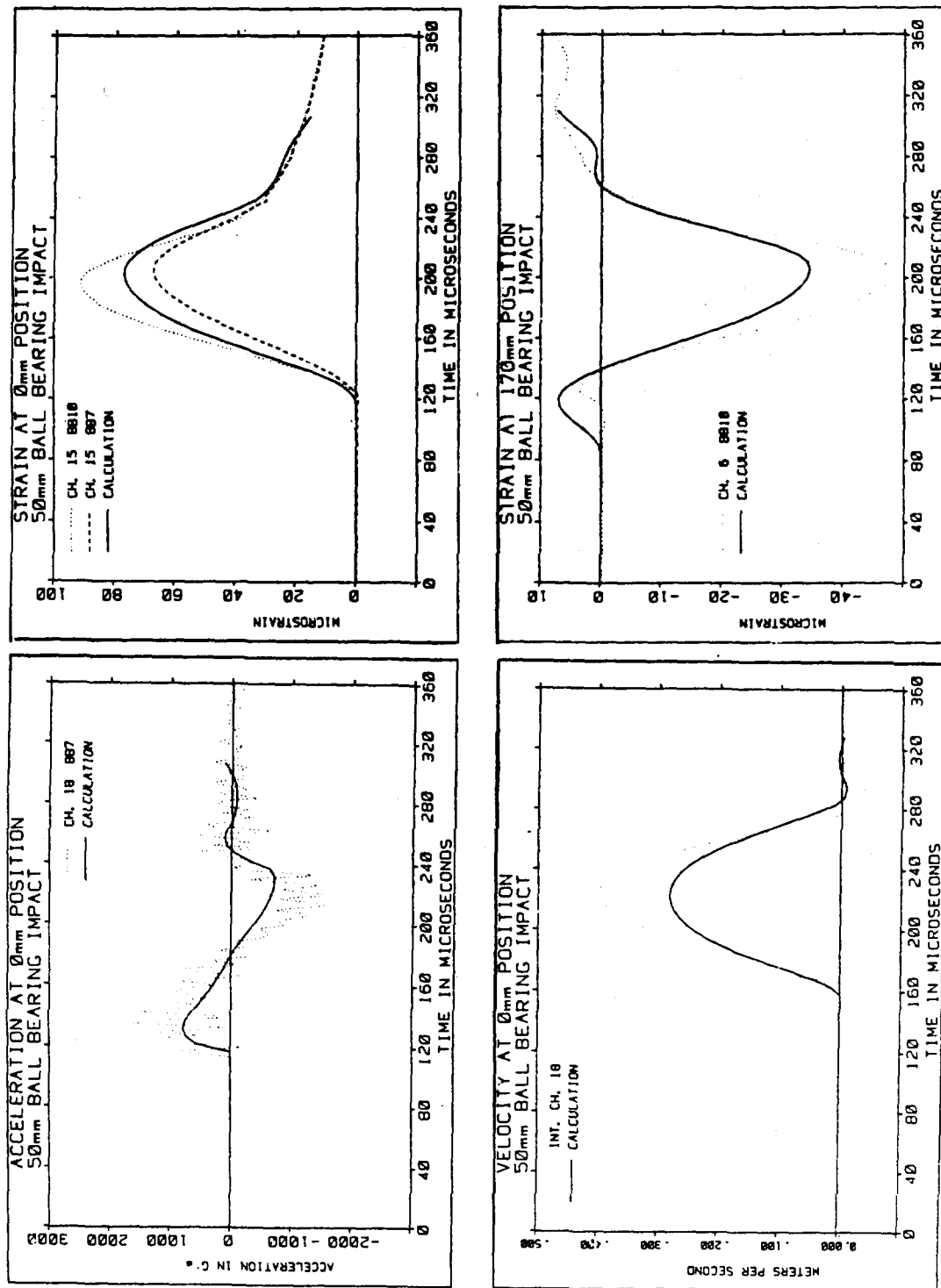


Figure 5. Response of plate to ball bearing impact. 0mm position is directly behind point of impact on surface opposite to side struck by ball bearing. 170mm position is 170mm to the left of the 0mm position.

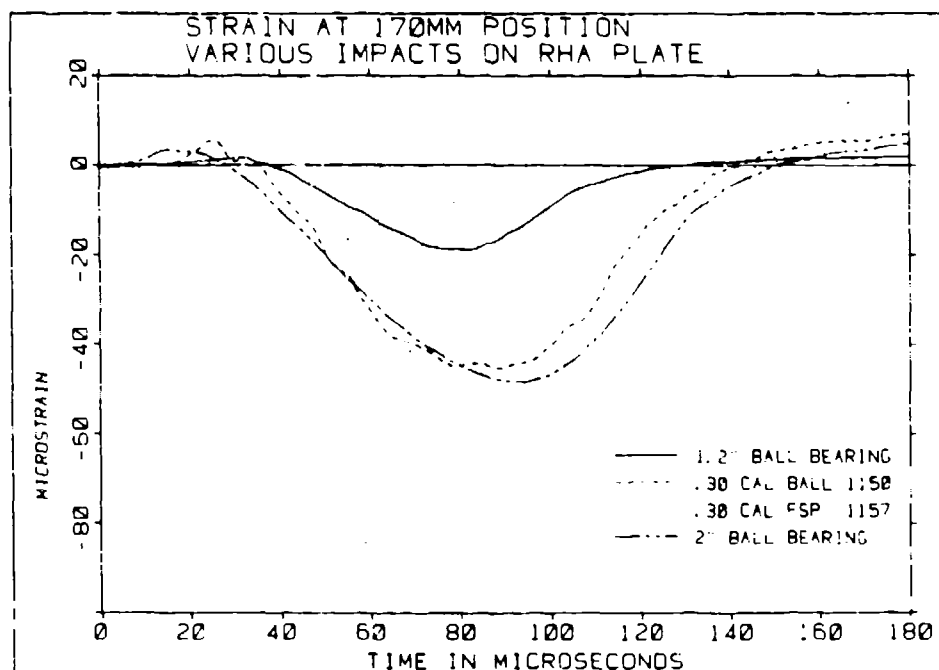
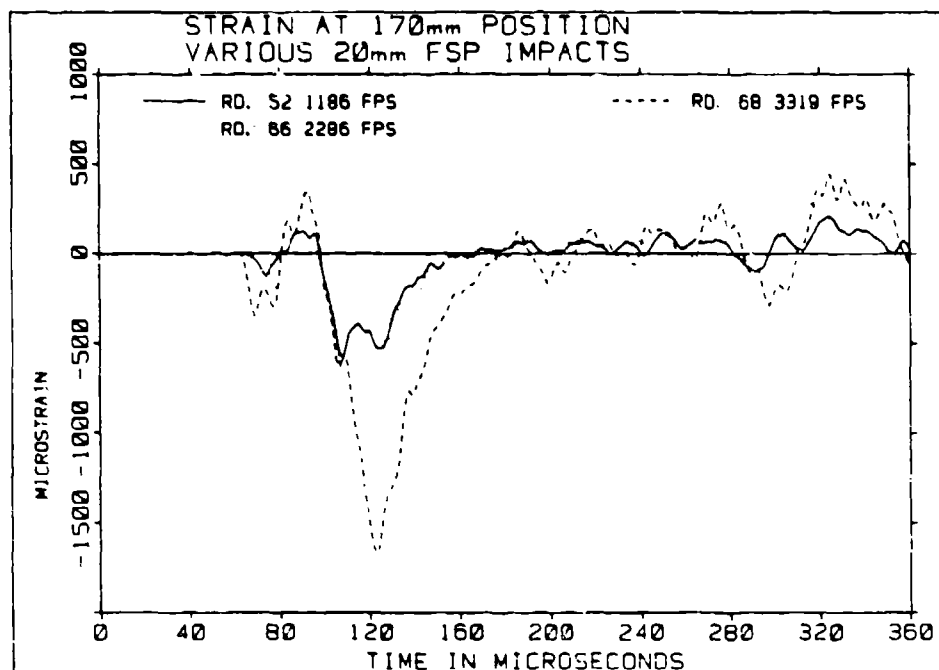


Figure 8. Strain signatures of various impacts. Upper figure shows 20mm FSP impacts at 361 MPS (1186 FPS), 697 MPS (2286 FPS), and 1012 MPS (3319 FPS). Note that strain magnitude increases, in proportion to striking velocity. Lower figure shows strain signatures of ball bearing and .30 caliber projectile impacts.

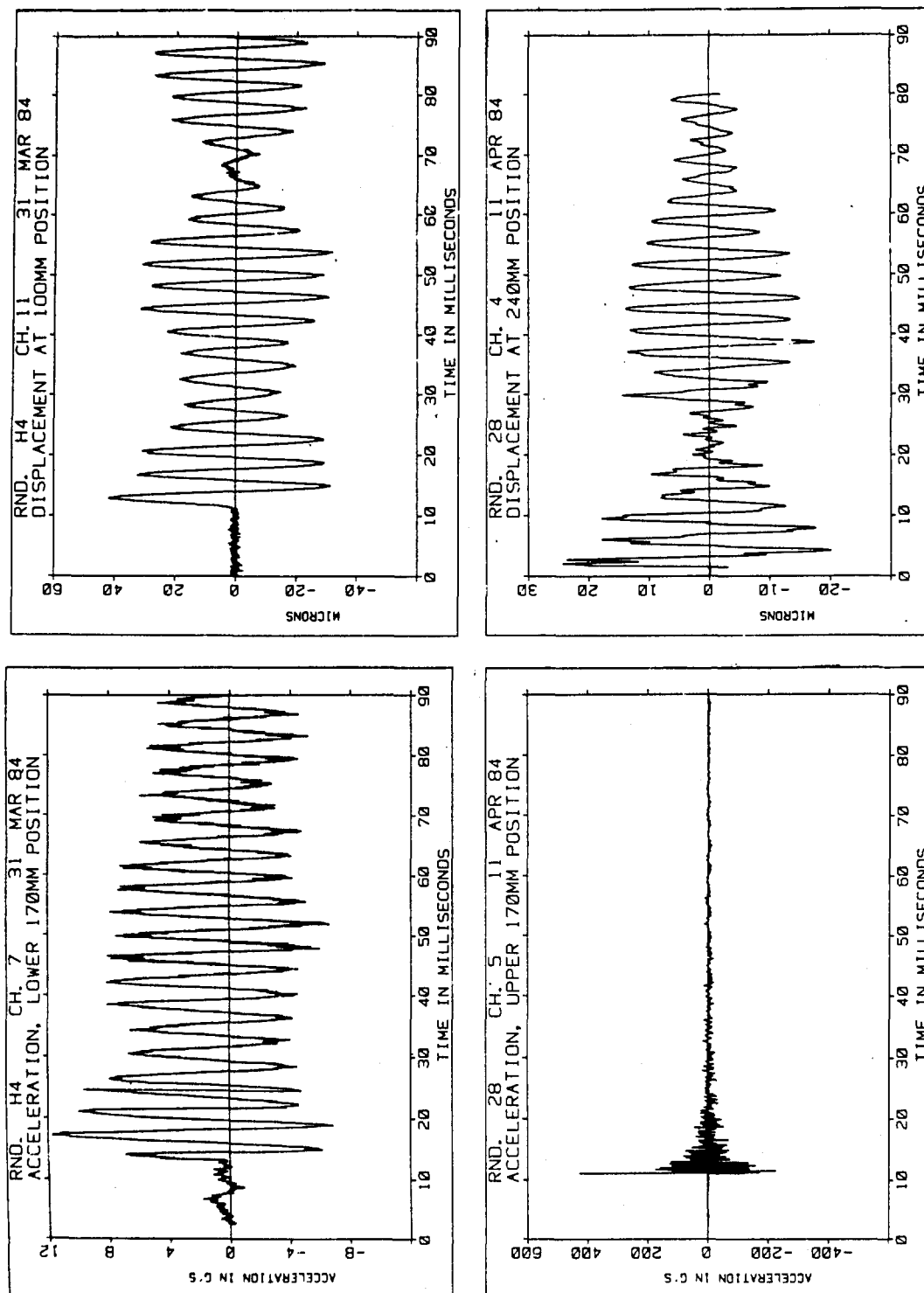


Figure 9. Long term response of plate to hammer impact (H4) and .30 caliber ball projectile impact. Projectile striking velocity was 335 meters/second.

Table 1. Types of Projectiles Fired

Bore	Type of Projectile	Projectile Mass In Grams	Nominal Striking Velocity in Meters/Sec (+30)
.30 Caliber	Fragment Simulator (Steel)	2.85	335, 671, & 1006
.30 Caliber	Ball (Lead Antimony)	9.85	335 & 671
.50 Caliber	Fragment Simulator (Steel)	13.42	335, 671, & 1006
.50 Caliber	Ball (Lead Antimony)	45.88	335 & 671
20mm	Fragment Simulator (Steel)	53.79	335, 671, & 1006
20mm	Copper Slug	58.98	335 & 671
75mm	Aluminum Proof Slug	2348.0	335

Note that the two displacement plots are similar in shape, and are dominated by the 250 Hz resonance of the plate. The two acceleration pulses are quite dissimilar. The acceleration from projectile impact is 2 orders of magnitude higher in amplitude and contains frequencies up to and above the 4 KHz limitation of the accelerometer used in channel 5.

During projectile impact, undamped accelerometers with high resonant frequencies indicated values as high as 200,000 g's and were destroyed. Yet damped accelerometers with low frequency response survived the same impact and indicated levels of only 200 g's, a discrepancy of 3 orders of magnitude!

PEAK DISPLACEMENT

Because displacement response was dominated by the 250Hz resonance, peak displacement measurements are not seriously affected by instrumentation frequency response limitations. Hence peak displacement is one of the most accurate measurements made in the ballistic shock environment.

An equation for calculating peak displacement was developed by Westine (Reference 7) for rectangular plates with clamped supports. Westine's equation, was modified by the author for central impact of a simply supported square plate by substituting

a spacial distribution that is described below. The peak displacement becomes:

$$Z_0 = \frac{M_0 V_0}{h^2 \sqrt{2.310E}}$$

Where Z_0 = Peak displacement at center of plate
 M_0 = Mass of striking projectile (.00985 Kg)
 V_0 = Velocity of striking projectile (335 meters/sec)
 h = Thickness of plate (.038 meters)
 ρ = Density of plate material (7833 Kg/meter³)
 E = Modulus of elasticity of plate material (2.07 x 10¹¹ Newtons/meter²)

Hence a .30 caliber ball projectile (9.85 grams) striking a 38mm thick plate at 335 meters/second results in a peak displacement of 37.3 microns at the center of the plate. The spatial distribution of the displacement (which satisfied the boundary conditions of simple support) is assumed to be:

$$Z = Z_0 \left[\frac{3}{2} \left(\frac{x}{X} \right) - \frac{1}{2} \left(\frac{x}{X} \right)^3 \right] \left[\frac{3}{2} \left(\frac{y}{Y} \right) - \frac{1}{2} \left(\frac{y}{Y} \right)^3 \right]$$

Where Z_0 = Peak displacement at center of plate
 Z = Peak displacement at any point X, Y
 X = Distance from side edge of plate to center (.432 meters)
 x = Distance from side edge of plate to point of interest (.332 meters)
 Y = Distance from top or bottom of plate to center (.432 meters)
 y = Distance from top or bottom of plate to point of interest (.432 meters)

Hence at a point on the central X axis of the plate, 100mm from the center of a .864 meter square, the peak displacement Z will be .926 of the peak displacement at the center of the plate. Thus, the predicted peak displacement at the 100mm position for a .30 caliber ball impact at 335 meters/second is 34.5 microns.

Figure 10 shows graphically the measured peak displacement values at the 100mm position for the various types of projectile impacts. Note that Westine's simple momentum prediction works well over a three order of magnitude variation in striking momentum.

PSEUDO VELOCITY GAGE

To rectify difficulties with surface velocity and acceleration measurements, a non-standard velocity measurement technique was used. A small pickup coil was epoxied directly to the armor plate and a magnet was suspended above the coil in a compliant casing as shown in Figure 11. Lacking any better name, and because the author did not think the idea would work, this arrangement was dubbed the "pseudo velocity gage".

A Hopkinson bar, instrumented as shown in Figure 12 was used to test the pseudo velocity gage. Figure 13 shows typical response of the strain gage, accelerometer, and pseudo velocity gage to an impact on the Hopkinson bar.

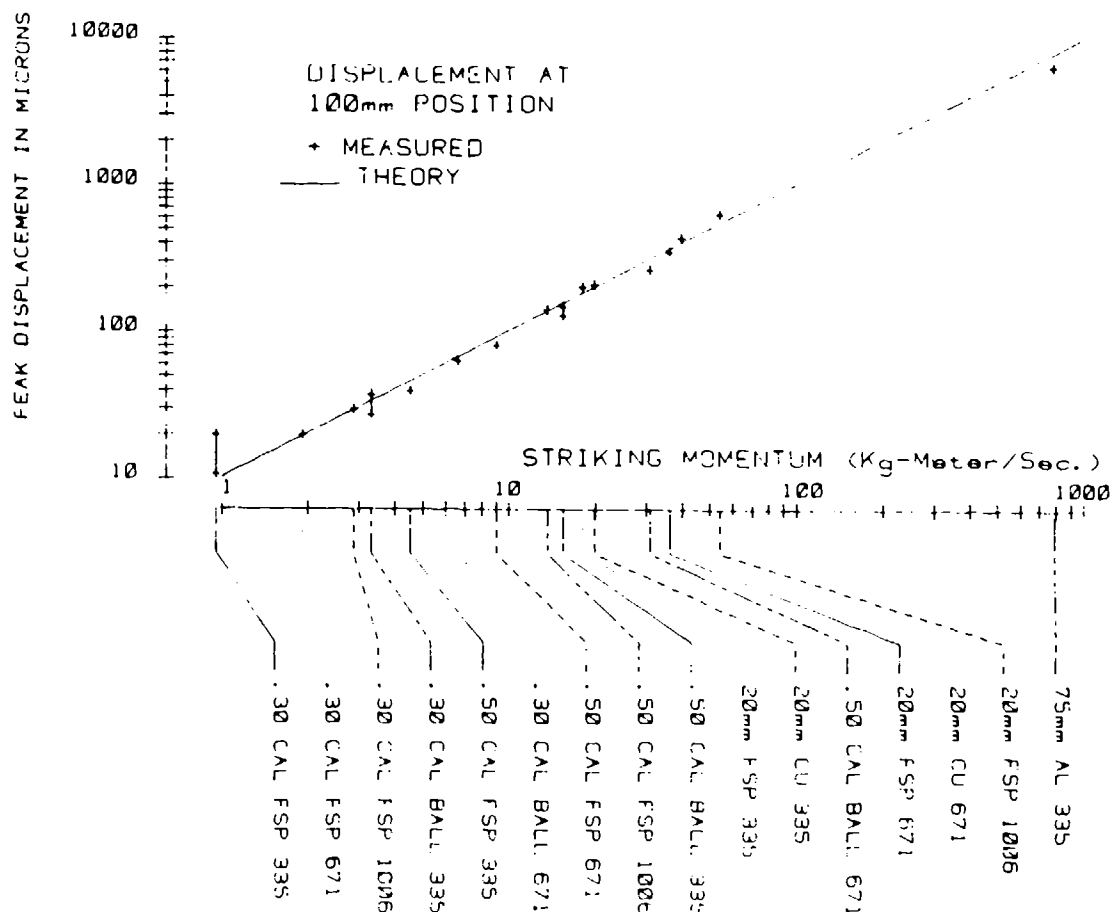


Figure 10. Correlation of measured peak displacement with momentum prediction for various types of projectiles and striking velocities.

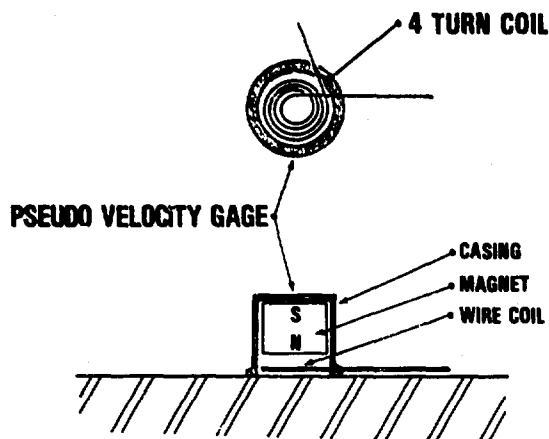


Figure 11. Schematic sketch of pseudo velocity gage. Casing is fabricated from compliant material, allowing magnet to remain stationary as coil on plate moves.

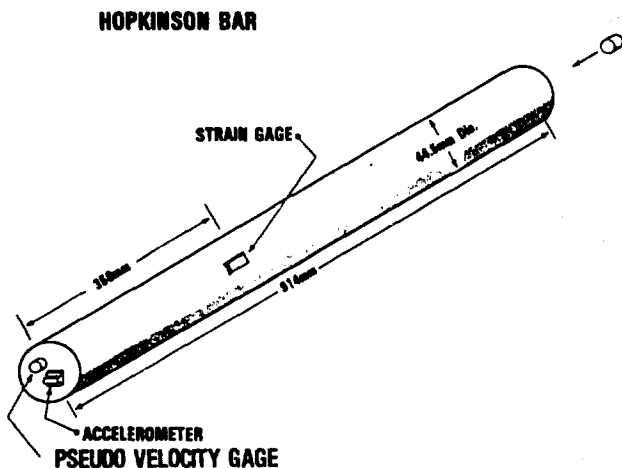


Figure 12. Sketch of Hopkinson bar used to test pseudo velocity gage.

As discussed by Brown (Reference 8) and others, the strain gage can be used to measure the velocity of the free end of a Hopkinson bar according to the relationship: $V = 2c\epsilon$

Where V = Velocity at the free end
 c = Wave velocity in the bar material
 ϵ = Strain measured on bar

Hence the Hopkinson bar provides two independent measurements of velocity: one obtained from the strain gage, and another obtained by integrating the accelerometer signal. As shown in Figure 14, the pseudo velocity gage signal agreed well with these other two measurements of velocity.

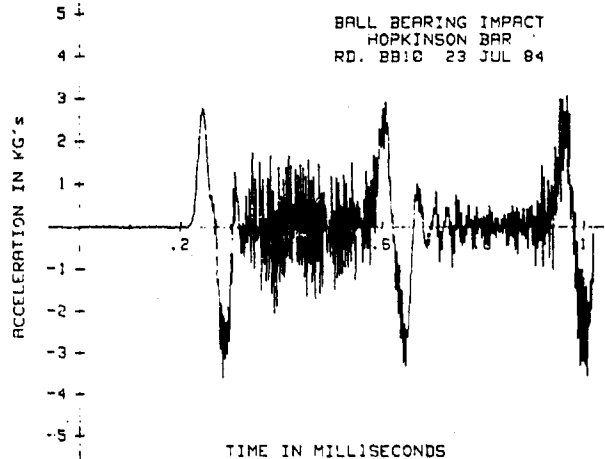
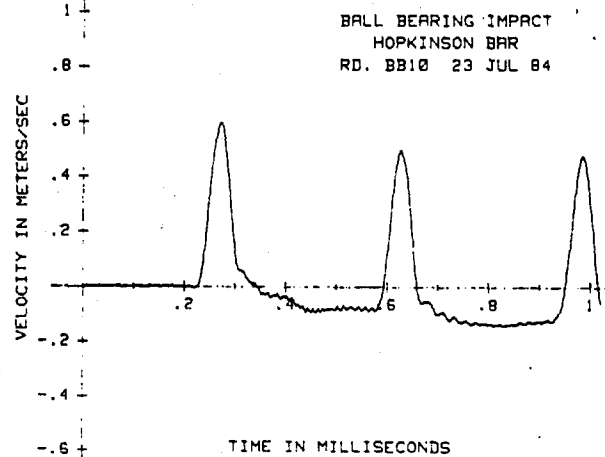
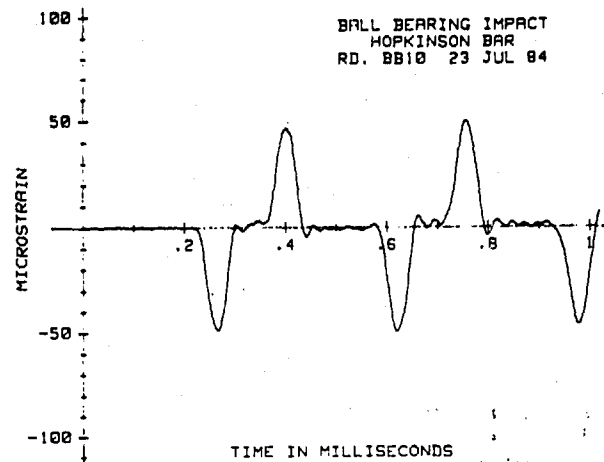


Figure 13. Response of Hopkinson bar to ball bearing impact, as measured by strain gage, pseudo velocity gage, and accelerometer.

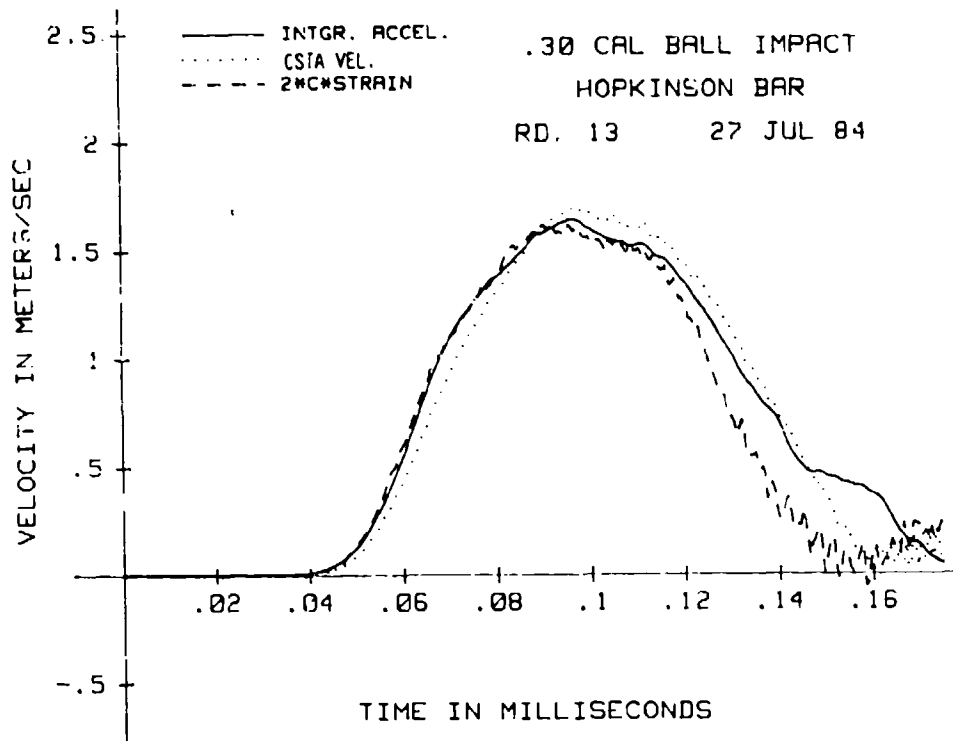


Figure 14. Comparison of pseudo velocity gage output with strain gage and integrated accelerometer measurements. Motion produced by impact of .30 caliber ball projectile (9.85 gram) striking Hopkinson bar at 335 meters/second.

FRAGMENT SIMULATING PROJECTILE IMPACT

Figure 15 shows the three types of Fragment Simulating Projectiles (FSP) used in this experiment. These steel projectiles were fabricated according to MIL-P-46593A and hardened to a value of 30 on the Rockwell C scale.

Acceleration measurements were most difficult during FSP impact. The previously mentioned three order of magnitude discrepancy in peak acceleration values occurred during a .30 caliber FSP impact. To avoid destroying more accelerometers, no acceleration measurements were made during 20mm FSP impact.

The 20mm FSP impact was chosen by Quigley (Reference 9) for analysis using a finite element code normally used to predict armor penetration. A pseudo velocity gage measurement from a 20mm FSP making a central impact on a .038 by .305 by .305 meter RHA plate was made directly behind the projectile impact point.

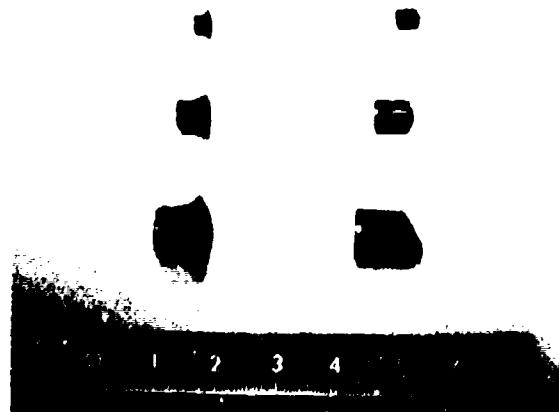


Figure 15. .30 caliber, .50 caliber, and 20mm FSP's before and after 335 meters/second impact.

A comparison of the pseudo velocity gage measurement with Quigley's prediction is shown in Figure 16. Note that the agreement is reasonably good.

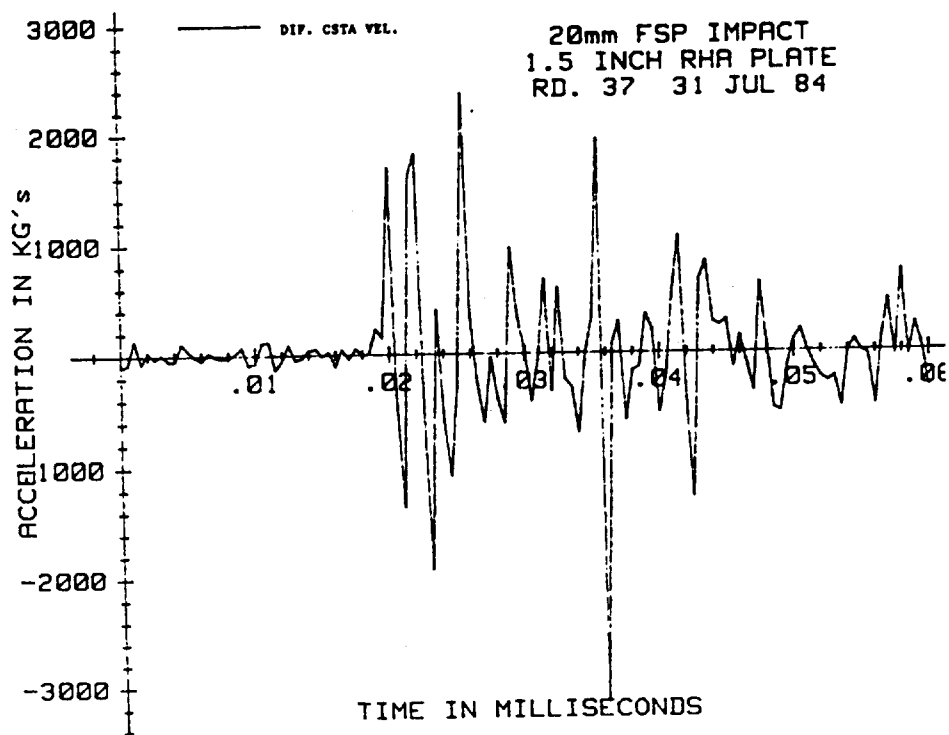
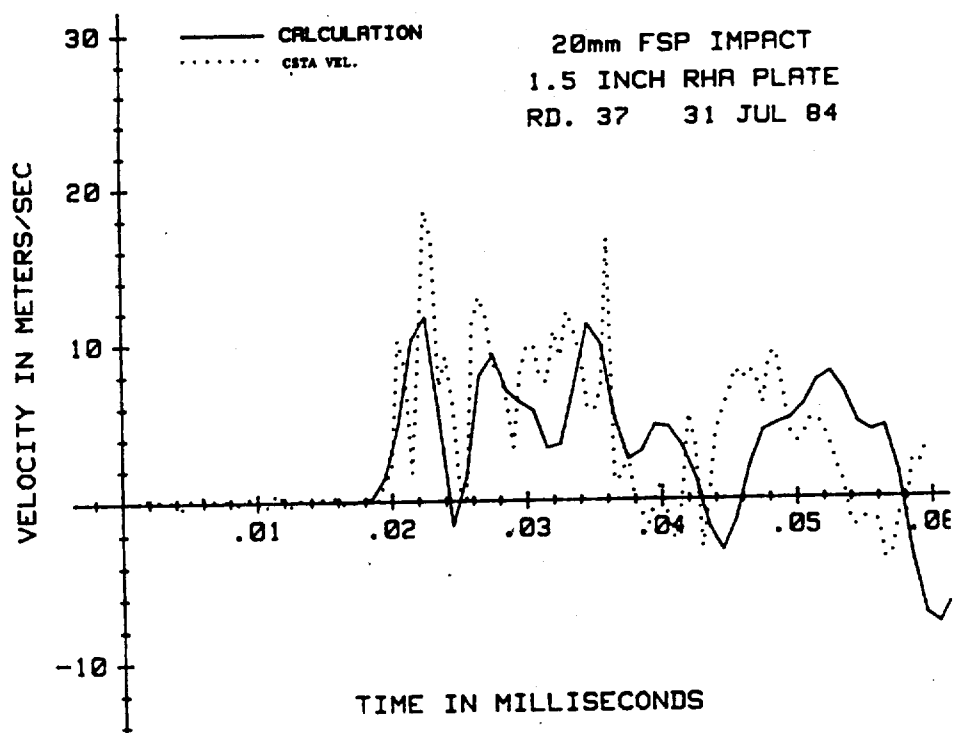


Figure 16. Velocity vs. time measured directly behind impact point on 1½-inch RHA plate. Projectile is 20mm Fragment Simulating Projectile (FSP) striking at 335 meters/second. Digitizing rate 2 million samples/second. Calculation performed by Quigley using finite element code. Acceleration vs. time signal obtained by differentiating pseudo velocity gage signal.

Figure 16 also shows the differentiated pseudo velocity gage signal. Note that the observed peak acceleration values (1 to 3 million g's) agree reasonably well with Quigley's prediction of approximately 1 million g's.

The large magnitude (1 million g's) of the observed acceleration pulse is well beyond the range of any commercial accelerometer, and explains the loss of accelerometers observed during earlier 20mm FSP impacts. The short duration of the pulses (1 microsecond) is assumed to be responsible for the wide discrepancies in peak acceleration observed between accelerometers with different frequency response during lower level (.30 caliber FSP) impacts.

CONCLUSIONS

1. The ballistic shock environment is characterized by very little displacement (measured in microns) and very large acceleration (measured in millions of g's).
2. Strain gages can be used to obtain characteristic signatures related to the loading function of non-penetrating projectile impacts.
3. In a controlled environment (i.e., when a stable reference point is available), displacement can be measured readily. Peak displacement values can be adequately estimated using the momentum of the striking projectile.
4. The "pseudo velocity gage" provides an adequate surface velocity measurement in a 1 dimensional environment.
5. Direct measurement of acceleration with accelerometers that are currently available commercially, is impossible in the ballistic shock environment due to the high level (millions of g's) and short duration (microsecond) of the pulses present.

REFERENCES

1. DeVost, Val, and O'Brasky, James, "5"/54 Gun Projectile Armor Penetration Shock Measurement 1972", Presentation at the SNR Working Group Meeting on Standardization of Ballistic Shock Measuring Procedures, Data Evaluation Procedures, and Assessment, Aberdeen Proving Ground, MD, June 1983 (unpublished).

2. Erlich, David C., "Ultra Sensitive Surface Motion Transducer", Ninth Transducer Workshop, Telemetry Group, Range Commanders Council, White Sands Missile Range, NM, April 1977, pp. 408-427.

3. Zukas, Nicholas, Swift, Greszczuk, and Curran, Impact Dynamics, John Wiley and Sons, New York, 1982.

4. Goldsmith, Werner, Impact, Edward Arnold Publishers Ltd., London, Great Britain, 1960.

5. Doyle, James F., "An Experimental Method for Determining the Dynamic Contact Law", Experimental Mechanics, Volume 24 - Society for Experimental Stress Analysis, Brookfield Center, Conn, March 1984, pp. 10-16.

6. Doyle, James F., "Further Developments in Determining the Dynamic Contact Law", Experimental Mechanics, Volume 24 - Number 4, Society for Experimental Mechanics, Brookfield Center, Conn, December 1984, pp. 265 - 270.

7. Westine, Peter S., et al, Ballistic Shock in Armored Vehicles Subjected to Impulsive Loads, R and D Center Laboratory Technical Report No. 12786, U.S. Army Tank - Automotive Command, Warren, Michigan, September 1983.

8. Brown, G. Wayne, "Accelerometer Calibration with the Hopkinson Pressure Bar", Instrument Society of America Preprint No. 49.3.63., 18th Annual ISA Conference and Exhibit, September 1963, Chicago, Illinois.

9. Private Communications from Ennis F. Quigley, U.S. Army Ballistic Research Laboratory, May 1984.

Discussion

Mr. Sill (ENDEVCO): As the designer of the accelerometer that he so well destroyed, I want to say two things in agreement. We take great pains to soften the blow on our Hopkinson bar. We have aluminum mitigators and specially shaped projectiles to give us very low frequency content pulses by which we can calibrate and test the accelerometer. Sometimes we forget to put in the piece of aluminum. We get a direct metal-to-metal impact, and destroy accelerometers ourselves, with indicated accelerations well in excess of 200,000 or 300,000 g's. So, I wholeheartedly believe in what you have done. I have a question about your calibration technique. We are careful to make sure the pulse length is long so the assumptions involved in the Hopkinson bar-type calibration hold. What were your pulse lengths, and did you worry about that frequency content?

Mr. Walton: We used a ball bearing impact to calibrate the pseudo-velocity gage, and it was anywhere from 80 to 100 microseconds in duration. That is an important thing to remember, because above 100 microseconds, the little casing for the pseudo-velocity gage is no longer stationary. It starts to move, and your results start to drift off. Below 80 microseconds you have trouble with the accelerometer. I call it the ICE CREAM calibration. It stands for In-Situ, that is the Ice part. Cream is Calibration Required Each Mounting. Every time I put a pseudo-velocity gage on, I have to drill two little 4-40 holes, get a 32 microinch finish, and hang the plate with something that is high enough to excite this pseudo-velocity gage, but low enough not to destroy the accelerometer. There are not a lot of things that fall into that narrow region.

Mr. Weiss (RCA): From what you are saying, your responses were right at the edge of your instrumentation. I suspect as you increase the capabilities of the instrumentation, you will get even higher accelerations, and higher accelerations of even shorter duration. That is all right, but what is the practical significance of all this? Where does it connect to your design?

Mr. Walton: That is the same question my boss asks. I guess the reason I did this investigation, and I have pushed this so far is we have to make measurements on plates to find out what is there. Before we can do that, maybe on something that is slightly removed where the high frequencies are damped out, or not transmitted as well, we have to have some general idea of what is there on the plate's surface; it is very high frequency. I don't think one megahertz is too bad for an impact of a 20 millimeter projectile at 1,100 feet per second. As we get higher impact velocities, and as we get smaller plates, the frequencies become higher. If we get away from the impact area, the frequencies become smaller. The nice thing about the pseudo-velocity gage is that it tells

me where I can put an accelerometer, so it will survive. At this point that is perhaps the most practical application; it survives when the accelerometer doesn't, so that is very important.

Mr. Chalmers (Naval Ocean Systems Center): I was wondering how your strain gages held up under those conditions.

Mr. Walton: No problem! The strain gages survived almost all of the time. The only problem we had with them was when we used the foil type which had the little solder tabs on the strain gage. The place where the solder was, blew apart. The gage stayed on, and the wires stayed on; but, the little solder tab had some mass to it, it flew off, and it was gone. However, the semi-conductor type with the built-in leads survived rather well.

Mr. DeLeon (ITT Gilfillan): With that kind of acceleration, I would think your material would spall.

Mr. Walton: No, not yet. It won't take much more before it starts to spall. We have noticed we are getting big bulges at velocities approaching 100 meters per second. Above that, the armor will start to spall.

EVALUATION OF SHOCK RESPONSE IN COMBAT VEHICLES:

SCALE MODEL RESULTS

James F. Unruh
Daniel J. Pomeroy
Dennis C. Scheidt

Southwest Research Institute
San Antonio, Texas

A program of shock measurements in a scaled simulated armored vehicle was instituted to support an effort of shock protection of secondary components in combat vehicles. The scale model was subjected to airblast, land mine blast, and kinetic energy projectile impact. Results from in-depth evaluation of the scale model airblast test data are presented with the specific objectives to: 1) assess the reliability of the recorded data, 2) conduct Fourier and shock spectrum analysis of the valid test data, 3) determine the approximate metric for data display relative to secondary equipment survivability, and 4) describe loads acting on the test fixture for future correlating analyses. Fourier and shock response spectra analysis of the valid data showed the scale model response was dominated by ringout of the various fundamental panel modes and a significant amount of response energy was contained within the first five to seven panel resonant modes of vibration. The acceleration shock response spectrum used for vibration specification of secondary equipment mounted to the test structure appeared to display the importance of the fundamental panel response much clearer than plots of Fourier amplitude spectral densities.

INTRODUCTION

A program of shock measurements in a scaled simulated armored vehicle was instituted by the U. S. Army Tank Automotive Command (TACOM) to support the Shock Protection of Secondary Components in Combat Vehicles program. The scale model concept, design specification, instrumentation configuration, etc., were developed by Southwest Research Institute personnel during a previous program [1]. The test fixture, weighing 1,600 pounds and representing a 1/4 scale model of a 102,000-pound tank, was subjected to nonpenetrating airblast, kinetic energy projectile impact, and land mine detonation ballistic threats. The Ballistic Measurements Branch of the Materials Test Directorate (MTD) provided the instrumentation for measurement of selected test fixture response parameters, including 22 channels of surface-mounted accelerometers and two interior pressure transducers. Preliminary time domain data reduction was carried out by the Analytical Branch of MTD. Many channels showed baseline offsets, which historically plague high-shock measurements, and many channels exhibited ringing which could not be totally explained by the transducer characteristics [2].

An initial investigation into analytically predicting the measured time history responses in the 1/4 scale test fixture is reported in Reference 1. Analysis procedures with varying degrees of sophistication or complexity were developed ranging from impulse-momentum balances to structural dynamic finite element model time history analyses. Results of the study indicated that a more in-depth analysis of the measured data would be necessary to insure valid comparison of predictions to test data. The objective of the present study was to conduct a more in-depth evaluation of the scale model test data to: 1) assess the reliability of the recorded data, 2) conduct Fourier and shock spectrum analysis of the valid test data, 3) determine the approximate metric for data display relative to secondary equipment survivability, and 4) describe loads acting on the test fixture, the test fixture material properties, etc., for future correlating analyses. The work was reported in three volumes: Volume I presented a data summary of all available information on the test model ballistic loading, scaling parameters, and expected responses [3]; Volume II presented detailed test data response

time histories, Fourier spectra and shock spectra data for the airblast ballistic loading [4]; and Volume III presented similar response data for the kinetic energy projectile and land mine ballistic loadings [5]. In the present paper, discussions will be limited to a brief description of airblast response data results to demonstrate the content of the information contained in References 3 through 5.

TEST PROGRAM

Test Fixture

The test fixture, schematically shown in Figure 1, is a 1/4 scale model of a conceptual tank. The boxlike structure was 68.5 inches front to rear, 35.75 inches side to side and 22.25 inches deep, supported off the ground on all four corners with 4.5 x 18.0 x 1.0 inch spacer blocks. The total height of the test fixture was 26.75 inches. The exterior side walls of the test fixture were 1/4-inch thick armor plate with 1/4-inch thick low carbon steel interior walls and roof panels. The floor panels were mainly 3/4-inch thick armor plate, except for the center panel which was 3/8-inch thick. The tank engine was simulated with a block mass as indicated in Figure 1. All seams of the test fixture were welded, except for the bolted roof panels which facilitated removal for instrumentation. Two side panels of the test fixture were fitted with isolated added masses to simulate mounted secondary equipment. The test fixture was supported on the ground under its own weight and thus was free to move subject to the ground plane constraint.

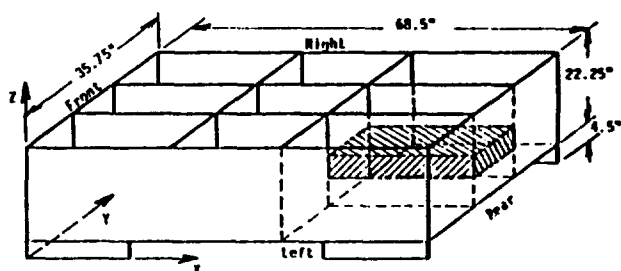


Fig. 1 1/4-Scale of a conceptual tank, three-dimensional view (shown with top removed)

Estimates of the test fixture panel resonances below 1,000 Hz were made in order to help interpret peaks in the spectral data. The resonant frequency estimates were based on panels with all edges clamped (see page 261 of Reference 6). The panel frequency estimates are

given in Table 1. For the side panels, which are attached to a roof panel, the frequency estimates given in Table 1 are considered to be somewhat high since the effectiveness of the roof to side panel attachment is not a fully-clamped support.

Instrumentation and Data Acquisition

The accelerometer locations are shown as positions 1 through 14 in the exploded view of the test fixture given in Figure 2. A total of 22 accelerometer positions/orientations were used to acquire the data. Several types of accelerometers were used according to availability and the expected input levels.

Test data was recorded on two IRIG Wide-Band Group I FM one-inch magnetic tape recorders at a speed of 60 in./sec. In addition to the 12 data channels, a voice track was available to key the run type and countdown for the start of the recorded events. Prior to the event, transducer calibration signals were recorded on each tape channel in the form of either a step function or sine wave.

Ballistic Loading

The test fixture was subjected to airblast, kinetic energy projectile impact, and land mine ballistic impulses. Three runs of each type of loading were recorded on both tape recorders. As previously stated, present discussion will be limited to the airblast loading runs. The airblast loading employed spherical charges of C-4 explosive ranging in weight from 3.1 to 3.625 pounds. The charges were placed on the ground to the right of the test fixture center at distances of six, eight and ten feet from the right side of the test fixture. The charge weight and coordinate locations for test runs are shown schematically in Figure 3.

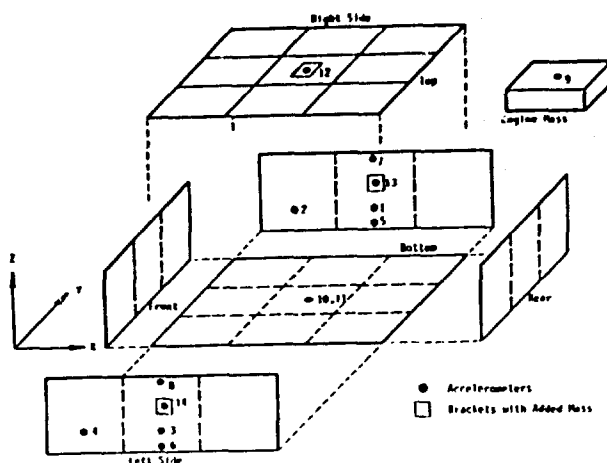


Fig. 2 Transducer positions

TABLE 1
Panel Frequency Estimates - Out of Plane Response

Panel	Transducer Position	Size** (inches)	Material	Weight* (lbs)	Estimated Frequencies Based on Clamped Edges (Hz)
Left Side Center	3, 6, 8 14*	$\frac{1}{4} \times 21 \times 21\frac{1}{2}$ $\frac{1}{4} \times 21 \times 21\frac{1}{2}$	Armor	31.94 +2	188, 384, 567, 690 Shear support > 1000 Hz
Left Side Front	4	$\frac{1}{4} \times 23\frac{1}{2} \times 21\frac{1}{2}$	Armor	35.37	177, 332, 374, 527, 589
Bottom Center	10, 11	$3/8 \times 13 \times 21$	Armor	28.97	618, 841, 1236, 1401, 1624
Top Center	12*	$\frac{1}{4} \times 13 \times 21$	Low Carbon	19.31 +1.0	286., 411, 560, 823, 933, 1081
Right Side Center	1, 5, 7 13*	$\frac{1}{4} \times 21 \times 21\frac{1}{2}$ $\frac{1}{4} \times 21 \times 21\frac{1}{2}$	Armor	31.94 +2	188, 384, 567, 690 Shear support > 1000 Hz
DO Right Side Front	2	$\frac{1}{4} \times 23\frac{1}{2} \times 21\frac{1}{2}$	Armor	35.37	177, 332, 374, 527, 589
Engine Mass	9	$4\frac{1}{2} \times 23\frac{1}{2} \times 13$	Low Carbon	363.5	

*Transducer mounted on compliant "shock" support with additional mass.

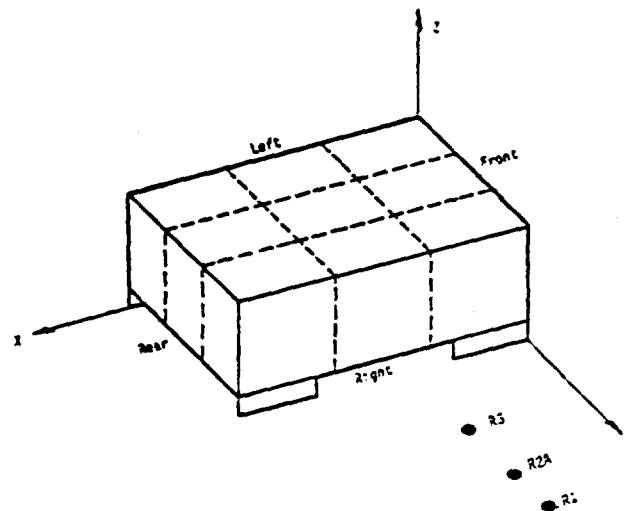
**Free edge size.

*Add 0.50 lbs for instrumentation and mounting block.

All data recorded was to measure responses to the shock input loads. There was no acquired data that would measure the input loads directly and, therefore, an analytical prediction of the loads on the test fixture was made. For the airblast condition, the loads are produced by the impingement of air shock on the structure. The parameters considered included: 1) the type, amount, and configuration of the explosive, 2) the location of the charge relative to the test fixture and other elements including the ground, and 3) the geometry of the test fixture (rectangular with one face perpendicular to the explosive charge). Based on these parameters, the pressure time histories at various locations on the test fixture were calculated in terms of the arrival time, peak pressure, and pulse duration.

Prediction of airblast loading on the exterior walls of the vehicle is based on the procedures given in Technical Manual TM 5-1300 [7]. Some of the methods and data presented in TM 5-1300 are outdated. In these cases, the most current information available was used in making estimates of the airblast loading, using data from References 8, 9, and 10. Under sea-level ambient atmospheric conditions, the detonation of an explosive charge propagates a shock wave into the atmosphere. An idealized shock wave resembles the time history shown in Figure 4. When the shock wave first arrives, t_a , a very steep jump in pressure occurs to a pressure above atmospheric pressure (an overpressure), P_s . This pressure then decays in a modified exponential form until it reaches zero at the time, t_d . Thereafter, the pressure continues to decay to below atmospheric pressure.

Eventually, the negative gauge pressure reaches a minimum and rises back to atmospheric. Often, the generalized history shown in Figure 4 is



Run No.	Charge Wt* (lb)	Location		
		X (in)	Y (in)	Z (in)
1	3.10	34.25	155.75	0.
2A	3.625	34.25	131.75	0.
3	3.625	34.25	107.75	0.

* C-4 Sphere

Fig. 3 Airblast loading configurations

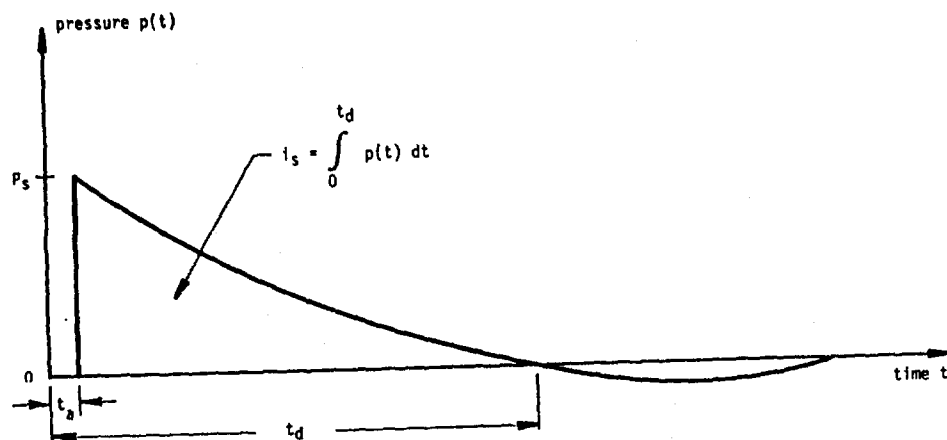


Fig. 4 Free-field shock wave

approximated by using a triangular pulse with an infinitely steep rise at the shock front and ignoring the negative phase of loading. The duration of the pulse, T , will be less than t_d so that the positive phase of loading will have the same area under the curve when a triangular loading is used. The area under a pressure time history is termed specific impulse. In Figure 4, impulse is the area under the over-pressure history up to the time t_d when the negative overshoot begins to occur.

Historically, the airblast parameters described above have been based on graphs developed from empirical formulations and experimental data [7-10]. The parameters are defined in terms of the standoff distance, R , and the equivalent weight of TNT, W , of the explosive. Detailed calculation procedures for peak pressures and pulse durations for the test configurations are beyond the scope of this paper; however, such details can be found in Reference 3. Typical peak loading estimates for the centers of the right-side panels of the test fixture are given in Table 2. As can be seen by these estimates, the reflected pressure pulse duration varied from one-half to two milliseconds, with peak pressures on the order of 50 to 300 pounds per square inch. The predicted peak pressures and pulse time durations were less for the roof panels, rear panels and side panels of the test fixture than the front panels, as expected, since these panels provide a grazing path for the blast wave.

The scale model relationships used to develop the test fixture are given in Table 3. The major nondimensional term used was the ratio of inertia to strength. When considering equal density and strength for the model and prototype with a geometric scale of 1 to 4, the result is the scale factors listed in Table 3. Here we

note that prototype accelerations will be one-fourth of the model measured accelerations and prototype loading, or response time durations will be four times as long. Likewise, model response frequencies will be one-fourth that of the model.

TABLE 2
Airblast Loading Right Side
Pressure Time Histories

Coordinates (in)			Run No.	Time of Arrival t_a (msec)	Peak Pressure P_p (psi)	Impulse I_p (lb-sec/ in ²)	Duration t_r (msec)
x	y	z					
11.40	35.75	15.66	1	3.15	57	4.99×10^{-2}	1.76
			2A	2.18	126	6.76×10^{-2}	1.07
			3	1.42	294	8.56×10^{-2}	0.58
34.20	35.75	15.66	1	3.06	64	5.35×10^{-2}	1.68
			2A	2.08	146	7.39×10^{-2}	1.01
			3	1.31	359	9.65×10^{-2}	0.54
57.12	35.75	15.66	1	3.15	57	4.98×10^{-2}	1.76
			2A	2.19	126	6.75×10^{-2}	1.07
			3	1.42	293	8.55×10^{-2}	0.58

Data Analysis

A preliminary review of all taped data channels, via visual inspection of oscillographs, eliminated a majority of the questionable data. The time histories were digitized at several different sampling rates with corresponding filtering to obtain a measure of the effect of possible transducer response and to obtain a feel for the importance of high-frequency response. The analog recorded signals

TABLE 3
Scale Model Relationships

Non-dimensional Ratios		
$\frac{\rho V^2}{\sigma}$	$\frac{\text{Inertia}}{\text{Strength}}$	(the major term)
$\frac{M}{\rho L^3}$	$\frac{\text{Lumped mass}}{\text{Distributed mass}}$	
$\frac{tV}{L}$	Kinematic similarity	
$\frac{W}{\rho L^3}$	$\frac{\text{Energy release}}{\text{Strength}}$	
Assumptions:		
1) Constant density	ρ ratio = 1.0	
2) Constant strength	σ ratio = 1.0	
3) Geometric Scale	L ratio = $\lambda = 1/4$	
Scaled Factors:		
Quantity	Symbol	Scale Factor (model/prototype)
Material density	ρ	1.0
Material strength	σ	1.0
All geometry, deflections	L	1/4
Velocity	V	1.0
Time	t	1/4
Acceleration	a	4.0
Lumped Mass	M	1/64
Energy Release Explosive	W	1/64
Structural Strain	ϵ	1.0
Energy per Unit Volume	E	1.0
Response Frequency	f	4.0

were played into a Zonic 6080 4-channel spectrum analyzer using a 10% pretrigger to insure capture of the initial response in the data window. An exponential weighting window was used to reduce signal leakage for data which was not "rung out" within the data block. The sampling frequency, cutoff frequency, and frequency resolution for the spectral data versus sampling period are shown in the following table:

Sampling Period (sec)	Sampling Frequency (Hz)	Cutoff Frequency (Hz)	Frequency Resolution (Hz)
0.01	102,400.	40,000.	100.
0.05	20,480.	8,000.	20.
0.40	2,560.	1,000.	2.5

The Fourier decomposition of the recorded signals was displayed in terms of an amplitude spectral density; that is, the effects of analysis resolution bandwidth (Bw) are emphasized in the data display. The amplitude spectral density is a plot of the Fourier amplitude for the given frequency band divided by the square of the resolution bandwidth, i.e., amplitude/(Bw)², and thus had units of amplitude per Hertz squared.

Shock spectrum analysis of the recorded test fixture acceleration responses was carried out to evaluate imposed shock criteria for secondary equipment attached to the walls of a combat vehicle. The shock spectrum is defined as the maximum response of a set of linear oscillators to the shock recorded as a function of the natural frequency of the oscillator [11]. There are a number of response parameters (deflection, velocity, acceleration, relative or absolute motions) that can be computed for the shock spectrum. The most widely-used shock spectra for secondary equipment evaluation is the maximum spectrum derived from a base-excited system with absolute acceleration input and absolute acceleration response.

Shock spectrum analysis was conducted using a Spectral Dynamics Model SD 321 analyzer on the maxi mode. Maxi mode measures the peak response, positive or negative polarity either during the application of the input or after the input subsides. The analyzer captured a 0.1-second time window with a sampling rate of 40,000 Hz. The 0.1-second time window was sufficient to capture even the longest duration event. The analysis resolution was 1/12 octave in the range from 10 through 10,000 Hz. Analyses were carried out at several oscillator damping levels.

TYPICAL RESPONSE DATA

Typical time history and spectral response data from airblast loading of the test fixture for a panel near the source (location #1) are given in Figures 5a through 5c and for a panel shielded from the source (location #3) in Figures 6a through 6c. These data are for lateral (Y) panel response. The time history data are given for signal durations of 0.40 and 0.05 seconds. The peak response on the time histories are best detected in the 0.05-second time window which is attributed to quantization error [12] associated with the data window sampling rate. The peak acceleration for the panel nearest to the source is read from Figure 5b at -642,000 in/sec² or 1,662 g's. The shielded panel response peaked at -162,500 in/sec² or 420 g's as read from Figure 6b. The 20-Hz bandwidth spectra of Figures 5c and 6c correspond directly to the 0.05-second time histories. From the spectral density plots, we can see that a majority of the response energy is contained in distinct resonances below 1,000 Hz for both the near source and shielded panels. The following peak analysis of the data in Figure 6c verifies this visual observation.

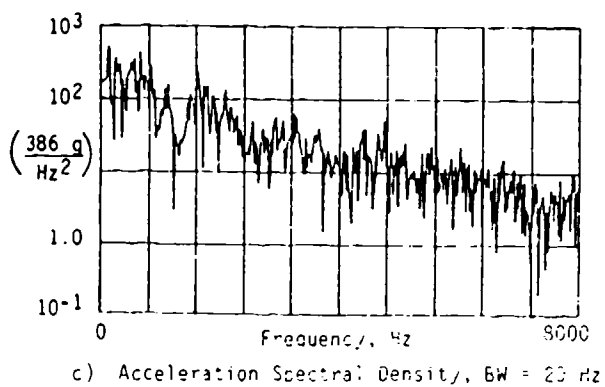
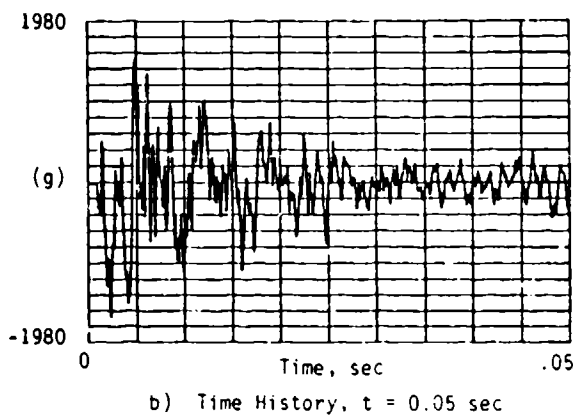
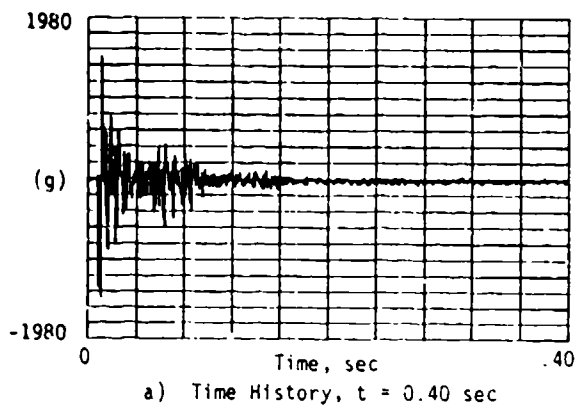


Fig. 5 Airblast response data panel
near source, 1-Y RZA

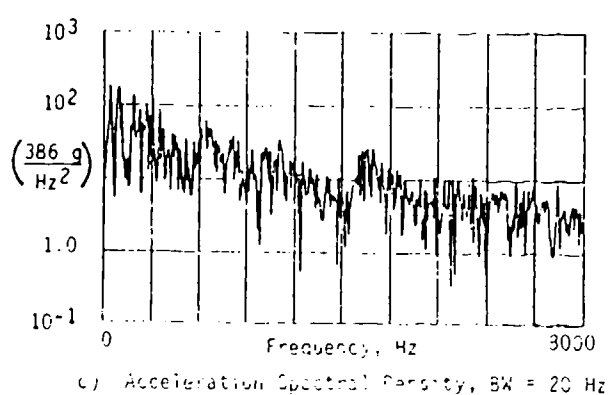
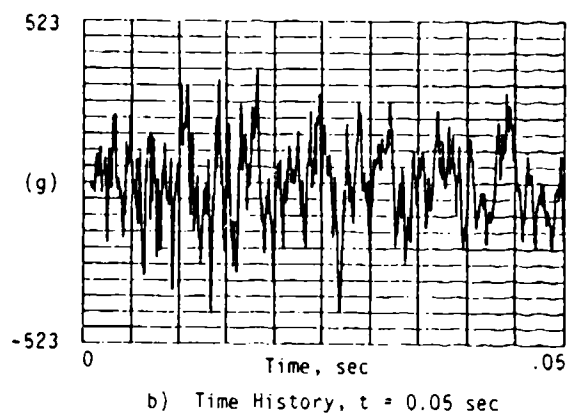
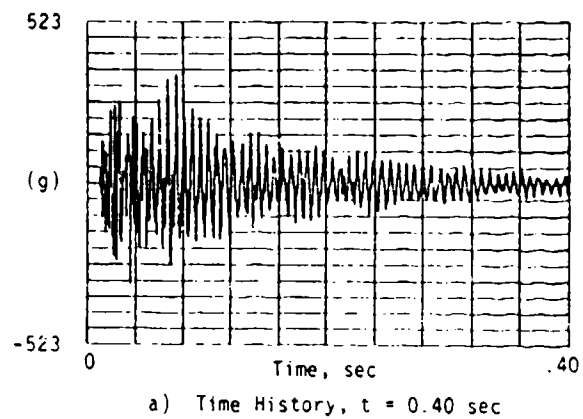


Fig. 6 Airblast response data panel
shielded from source, 3-Y R7A

Peaks from Figure 6c less than 1,000 Hz

Ref. Frequency (Hz)	Spectral Density (in/sec ² /Hz ²)	Amplitude	
		(in/sec ²)	(g's)
140	2.27x10 ²	9.08x10 ⁴	235.
300	2.14x10 ²	8.56x10 ⁴	222.
500	1.36x10 ²	5.44x10 ⁴	141.
710	1.04x10 ²	4.16x10 ⁴	108.
805	1.20x10 ²	4.80x10 ⁴	124.
Expected Peak	(SRSS)	1.50x10 ⁵	389.

As can be seen by this data, the five highest Fourier amplitudes contained in the spectrum out to 805 Hz result in an expected peak acceleration of 389 g's which compares well to the 420-g peak taken from the time history. Thus, if one can obtain accurate response out to, for example, 1,000 Hz, a good estimate of the peak expected response can be made. In the above peak acceleration estimate, the phase of each contributing spectral component was assumed to be randomly distributed and, thus, the square root of the sum of the squares (SRSS) method of addition was used.

Summary acceleration data for the airblast run 2A are given in Table 4. The time history and frequency response data for all valid data channels were evaluated for peak acceleration response, apparent resonance response and spectral regions where haystacks of high response were present. The 8-KHz analysis range spectrum were mainly used for the generation of this data since the 1-KHz analysis data are too narrow to capture the overall response and the 40-KHz data were potentially influenced by transducer resonance response. Comparison of the frequency at which spectral peaks occur in the data and the estimate of resonant panel frequencies given in Table 1 indicate that the test fixture response was dominated by panel resonances within the first five to ten modes.

Acceleration response spectra for response locations 1-Y and 3-Y are given in Figures 7 and 8, respectively. The response spectra are plotted for oscillator damping values of 0.5%, 1%, and 5%, where the upper response curve corresponds to 0.5% damping. The response amplification of equipment at the panel resonances are clearly visible in these shock spectra. The importance of higher-frequency response is also noted where amplification above the ZPA (zero period acceleration) extends well beyond 1,000 Hz.

TABLE 4
Summary of Acceleration Responses, Airblast Run 2A

Response Point	Peak Response in Time History (g)			Apparent Resonance Response (Hz)	Frequency Ranges of Apparent Haystacks of Energy Response
	Analysis Range				
	40 KHz T = 0.01 sec	8 KHz T = 0.05 sec	1 KHz T = 0.40 sec		
1-Y	1662.	1662.	1344. 1505.		120-160
3-Y	339.	301. 420.	152. 178. 355.	142	260-340, 500-850
4-Y	448.	387. 459.	194. 253.	142	250-340, 500-700
7-Y	2023.	2023.	2023.	128, 142	250-300
8-Y	459.	250. 378.	163. 301.	142	260-300, 500-550, 620-550, 720-820
10-Z	453.	453.	448.	516	
13-Y	2466.	2466.	1417. 1788.	129, 144	
14-Y	402.	301. 347.	162. 233.	142	250-300, 500-540

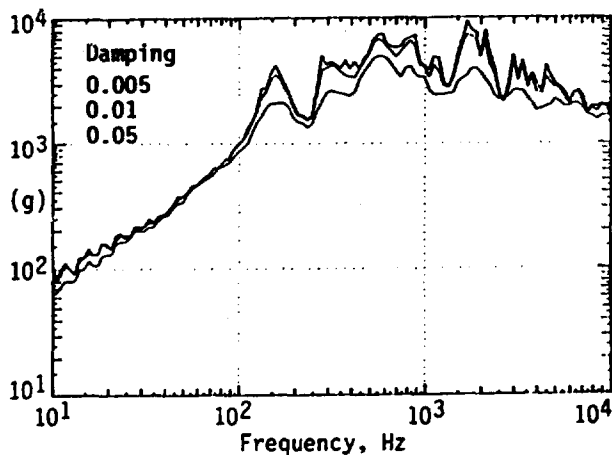


Fig. 7 Acceleration response spectrum, 1-Y RZA, 1/12 octave resolution

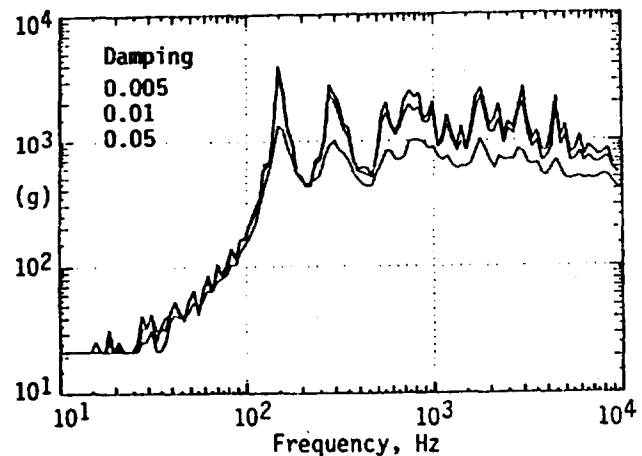


Fig. 8 Acceleration response spectrum, 3-Y RZA, 1/12 octave resolution

CONCLUSIONS

The vibration response data recorded during a test of a 1/4 scale model combat vehicle subjected to airblast ballistic excitations was analyzed for valid data recording, peak accelerations, spectral response, and shock response for secondary equipment mounted on the walls of the vehicle. Estimates of the loading conditions were made; however, there was no direct measurement of the loads for validation. Fourier and shock response spectra analysis of the valid data support the following observations:

- 1) Test fixture response was dominated by ring-out of the various fundamental panel modes, and a significant amount of response energy was contained within the first five to ten panel resonant modes of vibration.
- 2) The acceleration shock response spectrum, used for vibration specification of secondary equipment mounted to the test structure, appeared to display the importance of the fundamental panel response much clearer than plots of Fourier amplitude spectral densities.

ACKNOWLEDGMENT

This work was supported by the U.S. Army Tank-Automotive Command Research and Development Center, under Contract DAAE07-84-C-R-115, and is greatly appreciated.

LIST OF REFERENCES

1. Westine, P. S., Morris, B. L., Cardinal, J. W., and Steward, S. E., "Ballistic Shock in Armored Vehicles Subjected to Impulsive Loads," U. S. Army Tank-Automotive Command TR 12786, June 1983.
2. See Appendix A of Reference 3 for unpublished MTD preliminary data analysis summary.
3. Unruh, J. F., Scheidt, D. C., and Pomeroy, D. J., "Data Analysis of Scale Model Armored Vehicle Response to Ballistic Impulses: Volume I, Procedures and Data Summary," USATACOM Report 13112, August 1985.
4. Unruh, J. F., Scheidt, D. C., and Pomeroy, D. J., "Data Analysis of Scale Model Armored Vehicle Response to Ballistic Impulses: Volume II, Air Blast Response Data," USATACOM Report 13112, August 1985.
5. Unruh, J. F., Scheidt, D. C., and Pomeroy, D. J., "Data Analysis of Scale Model Armored Vehicle Response to Ballistic Impulses: Volume III, Kinetic Energy Projectile and Land Mine Response Data," USATACOM Report 13112, August 1985.
6. Blevins, R. D., Formulas for Natural Frequency and Mode Shape, Van Nostrand Reinhold Co., 1979.

7. Dept. of the Army Technical Manual TM 5-1300, "Structures to Resist the Effects of Accidental Explosions," June 1969.
8. Baker, W. E., et al., Explosion Hazards and Evaluation, Elsevier Scientific Publishing Company, New York, 1983.
9. DOE/TIC-11268, "A Manual for the Prediction of Blast and Fragment Loadings on Structures," Nov. 1980.
10. Westine, P. S., and Hokanson, J. C., "Procedure to Predict Plate Deformations from Land Mine Explosions," U. S. Army TACOM Contract No. DAAE07-74-C-0192, Warren, Michigan, August 1975 (confidential).
11. Harris, C. M., and Crede, C. E., eds., Shock and Vibration Handbook, 2nd ed., McGraw-Hill, 1961.
12. Bendat, J. S., and Piersol, A. G., Random Data: Analysis and Measurement Procedures, Wiley Interscience, 1971.

YIELD EFFECTS ON THE RESPONSE OF A BURIED BLAST SHELTER

T. R. Slawson, S. C. Woodson, and S. A. Kiger
U.S. Army Engineer Waterways Experiment Station
Vicksburg, Mississippi

Three dynamic tests were conducted on 1/4-scale structural models of a Civil Defense blast shelter. The dynamic loading was generated using a High-Explosive Simulation Technique (HEST) to simulate the peak overpressure and overpressure decay of a nuclear detonation. Simulated nuclear weapon yields and overpressures were varied from 2.1 TJ (0.5 kt) at 1.10 MPa (160 psi) to 40 TJ (9.5 kt) at 0.83 MPa (120 psi) to determine overpressures from various weapon yields that resulted in the same structural response. The results of these tests indicate that response of the blast shelter model was approximately equal for the simulated yield-overpressure combinations listed above. These data were used to verify pre-test response calculations for the MINOR SCALE Event, a high-explosive (HE) test of a full-scale blast shelter sponsored by the Defense Nuclear Agency (DNA).

INTRODUCTION

A Civil Defense blast shelter capable of surviving 0.34-MPa (50-psi) peak overpressure from a 4,200-TJ (1-Mt) nuclear detonation has been designed for the Federal Emergency Management Agency (FEMA). The structural design criteria and the levels of initial and residual radiation dictated an earth-covered or buried structure. Structural response calculations were made using a computer code (Reference 1) developed at the Waterways Experiment Station (WES) that includes soil-structure interaction effects. The first design of the shelter was experimentally verified in a series of static and dynamic tests (Reference 2) on 1/4-scale models. Two series of static slab element tests were performed to investigate the effects of shear stirrup details (Reference 3) and principal reinforcement details (Reference 4) on the load-deflection behavior of the roof slab. Three static box tests (Reference 5) were performed to investigate alternate roof-wall joint details to improve constructibility of the shelter. Data from these tests were used to improve the structural design. The shelter design consists of a shallow-buried, three-bay, box-type structure constructed of cast-in-place reinforced concrete. The roof clear span-to-thickness (L/t) ratio is 15 and the ratio of depth of burial to clear span (DOB/L) is 0.36. Tests indicate that the design will withstand a 4,200-TJ (1-Mt) surface burst at a peak overpressure of approximately 0.83 MPa (120 psi) with the reserve capacity to withstand repeated loadings. Dual-use considerations require the shelter design to meet conventional building codes. The U.S. Army Engineer Huntsville Division (HND)

compared the structural design to conventional designs (Reference 6) and concluded that the current design could not be significantly reduced if the American Concrete Institute (ACI) code requirements (Reference 7) for dead and construction loads were met.

A full-scale version of the blast shelter was tested in the MINOR SCALE HE Event, a 33.5-TJ (8-kt) nuclear simulation conducted at White Sands Missile Range, New Mexico, in June 1985. The primary objective of the preliminary study documented herein was to determine the range from ground zero required in MINOR SCALE to produce the results expected from a 4,200-TJ (1-Mt) detonation at 0.34 MPa (50 psi). The three 1/4-scale dynamic tests and the test results are discussed in this paper.

TEST DESCRIPTION AND RESULTS

The 1/4-scale models used in the tests had L/t ratios of 15, tensile steel ratios of 0.012, concrete compressive strengths of 21 MPa (3,000 psi), and steel yield strengths of 410 MPa (60 ksi). Each element was instrumented to measure rebar strains, soil-structure interface pressure, floor acceleration, roof acceleration, and roof deflection. Free-field measurements included airblast pressure, soil stress, and free-field acceleration. The test configuration for each test is shown in Figure 1. The test bed was constructed in a 6.1- by 6.1- by 2.1-m (20- by 20- by 7-ft) excavated pit. Sand backfill was placed and compacted in 15.2-cm (6-in.) lifts from the floor of the excavation to a depth of burial (DOB) of 0.3 m (1 ft) over the instrumented structure for each test. After backfilling, the HEST charge cavity was con-

structured on the ground surface above the model structure. The charge cavity consisted of a wooden framing system covered with plywood and contained the high-explosive detonation cord that generated the blast loading. The charge cavity was covered with uncompact sand and overburden to momentarily simulate the blast pressure and thus simulate the peak overpressure and pressure decay of a nuclear weapon detonation. Charge cavities for these tests measured 4.9 m by 4.9 m (16 ft by 16 ft) in plan for test YE1 and 3.7 m by 3.7 m (12 ft by 12 ft) in plan for tests YE2 and YE4. Charge cavity depths were 0.91 m (3 ft) for test YE1, 0.61 m (2 ft) for test YE2, and 0.30 m (1 ft) for test YE4. The number of strands of detonating cord was varied to change the charge density and thus increase or decrease the peak cavity pressure. Charge densities were 0.26 kg/m³ (0.016 pcf) for test YE1, 0.64 kg/m³ (0.040 pcf) for test YE2, and 0.58 kg/m³ (0.036 pcf) for test YE4. Pressure decay was controlled by charge density, cavity thickness (initial cavity volume), and overburden height. Overburden heights were 1.22 m (4 ft) for test YE1 and 0.61 m (2 ft) for tests YE2 and YE4. The charge cavity parameters were varied to simulate the desired nuclear overpressures. A more detailed description of HEST is given in Reference 8.

Table 1 is a test matrix showing nuclear weapon simulation data and maximum midspan roof response for the three tests. A typical posttest damage photograph is shown in Figure 2. A typical airblast pressure record is shown in Figure 3. The weapon simulations, listed in Table 1, were determined by a least squares fit of nuclear overpressure time histories (Reference 9) to airblast pressure data recovered in each test. The duration of the fit was 20 msec.

DATA ANALYSIS

The results of tests YE1 and YE4 were similar and can be used to infer yield effects. A 35-percent increase in peak overpressure resulted in approximately the same damage when weapon yield was reduced from 40 TJ (9.5 kt) to 2.1 TJ (0.5 kt). Figure 4 compares the data from tests YE1 and YE4 with a predicted isodamage curve for a 40-TJ (9.5-kt) weapon at a 0.83-MPa (120-psi) damage level. The VSRS code (Reference 1) predicts that an increase in peak overpressure of 30 percent is required to maintain the same level of damage from the reduced weapon yields of these tests.

To use the results of these 1/4-scale tests to predict the required pressure level in the MINOR SCALE HE Event, the test weapon yields must be scaled up to full scale. Using cube root scaling, the test weapon yields shown in Table 1 should be multiplied by 64 to convert to prototype yields. Therefore, the scaled weapon yields for tests YE1 and YE4 were 2,500 TJ (610 kt) and 130 TJ (32 kt), respectively. Based on these two data points, it is estimated that the peak overpressures

should be increased by approximately 50 percent if the prototype weapon yield is reduced from 4,200 TJ (1 Mt) to 34 TJ (8 kt) to result in the same damage level.

CONCLUSIONS AND RECOMMENDATIONS

The results of tests YE1 and YE4 verify the computational procedure used to make predictions for the MINOR SCALE HE Event. It is recommended that the prototype blast shelter be placed at 0.52 MPa (75 psi) in the MINOR SCALE Event.

ACKNOWLEDGMENT

This work was sponsored by the Federal Emergency Management Agency (FEMA), Washington, D.C. Mr. Tom Provenzano (FEMA) was the Program Manager. The field tests were supervised by Mr. Randy Holmes, Structures Laboratory, Waterways Experiment Station (WES), Vicksburg, MS, and were instrumented by Messrs. Phil Parks and Bill Strahan, Instrumentation Services Division, WES.

REFERENCES

1. Kiger, S. A., Slawson, T. R., and Hyde, D. W.; "Vulnerability of Shallow-Buried Flat-Roof Structures"; Technical Report SL-80-7, Report 6, September 1984; U.S. Army Engineer Waterways Experiment Station, Vicksburg, MS.
2. Slawson, T. R., et al; "Structural Element Tests in support of the Keyworker Blast Shelter Program"; Technical Report (in publication); U.S. Army Waterways Experiment Station, Vicksburg, MS.
3. Woodson, S. C.; "Effects of Shear Stirrup Details on Ultimate Capacity and Tensile Membrane Behavior of Reinforced Concrete Slabs"; Technical Report (in publication); U.S. Army Engineer Waterways Experiment Station, Vicksburg, MS.
4. Woodson, S. C., and Garner, S. B.; "Effects of Reinforcement Configuration on Reserve Capacity of Concrete Slabs"; Technical Report (in publication); U.S. Army Engineer Waterways Experiment Station, Vicksburg, MS.
5. Woodson, S. C., et al; "Evaluation of Roof-Wall Connection Details for the Keyworker Blast Shelter"; Technical Report (in progress); U.S. Army Engineer Waterways Experiment Station, Vicksburg, MS.
6. Department of the Army; "Structural Cost Optimization for Keyworker Blast Shelters"; March, 1984; U.S. Army Corps of Engineers, Huntsville Division, Huntsville, AL.
7. American Concrete Institute; 1983; "ACI 318-83: Building Code Requirements for Reinforced Concrete"; Detroit, MI.

8. Wampler, H. W., Leith, G. G., and Furbee, M. E.: 1978; "A Status and Capability Report on Nuclear Airblast Simulation Using HEST," Proceedings of the Nuclear Blast and Shock Simulation Symposium, 29-30 November 1978, Volume 1, General Electric-TEMPO, Santa Barbara, CA.

9. Spelcher, S. J. and Brode, H. L., "Airblast Overpressure Analytic Expression for Burst Height, Range, and Time Over an Ideal Surface," PSR Note 385, November 1981 (with updates through November 1982), Pacific-Sierra Research Corporation, Santa Monica, CA.

Table 1. Test Matrix

Test	Nuclear Yield		Weapon Simulations Peak Overpressure		Maximum Midspan Deflection	
	kt	kt	MPa	psi	cm	in.
YE1	39.7	0.5	0.83	120	1.8	0.70
YE2	8.4	2.0	1.27	184	11.4	4.50
YE4	2.1	0.5	1.12	162	1.6	0.60

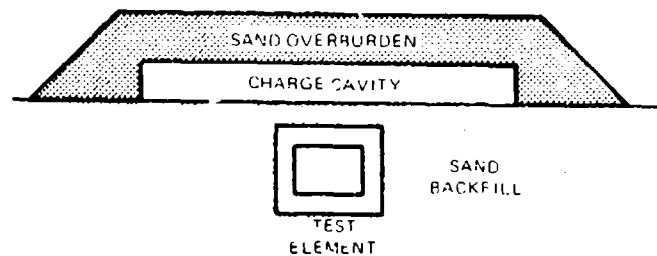


Figure 1. Test Configuration



Figure 2. Typical Posttest Damage

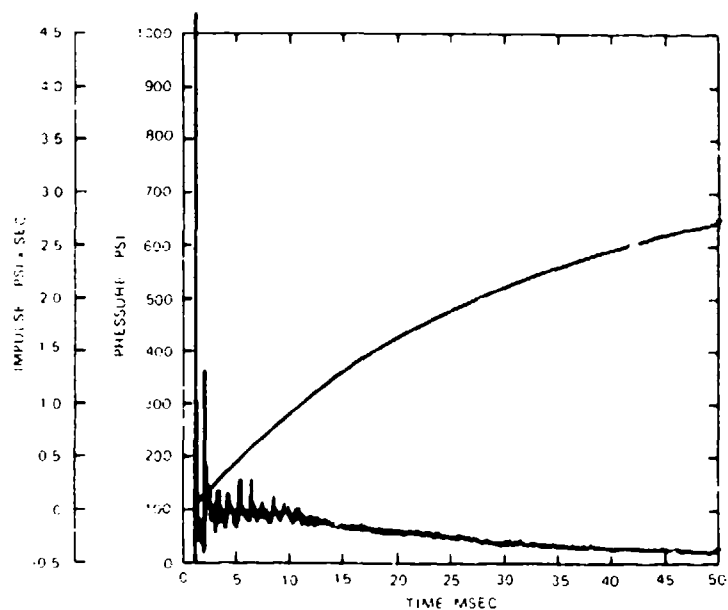


Figure 3. Typical Airblast Pressure Record

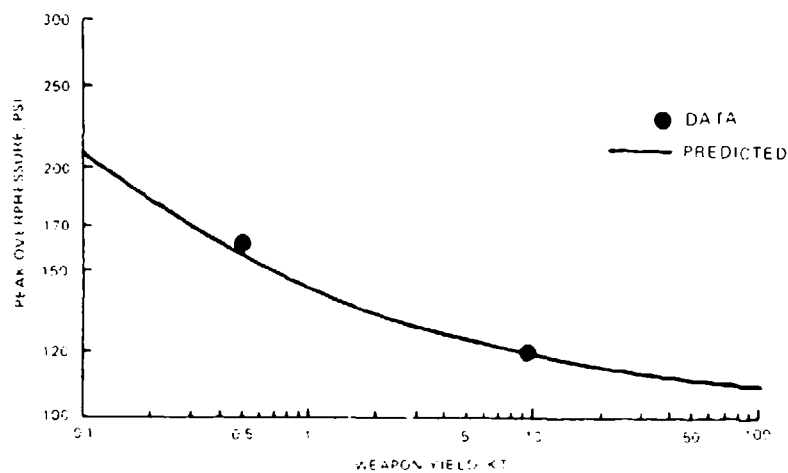


Figure 4. Comparison of Theoretical 1/4-Scale Isodamage Curve with Data

Discussion

Mr. Cooper (Defense Nuclear Agency): You said you used the quarter scale models. What kind of confidence do you have in scaling for testing purposes? Do you have a feel for what size scale models you can use to simulate prototype behavior?

Mr. Kiger: We have had a lot of luck and experience looking at quarter scale structural models and scaling them up to larger scale models. In this case we went from quarter scale to full scale successfully. If the model is smaller than that, you cannot use conventional construction techniques; you may have to use the larger rebars or wire that you would rather not use. I am not confident in anything much less than quarter scale. I have seen sixteenth or twentieth scale structural models, but the failure modes don't look right. Maybe it is my interpretation. It is important to get the right failure modes in these structures if you wish to simulate the full scale structures. So, to answer your question, I think quarter scale is as small as I am comfortable with without some strong justification.

Mr. Cooper: You were at the limit there?

Mr. DeLeon (ITT Gilfillan): How do you correlate your area under the impulse curve when you are testing? Did you have to correlate that in your data?

Mr. Kiger: You use cube root scaling to get the correct impulse.

Mr. DeLeon: Is it the same as the one megaton?

Mr. Kiger: No, the impulse will not be the same. In this case it will be an eighth smaller or a fourth smaller on the quarter scale. Psi scaled is one. The second scale is like your scale factor. So, you should put less impulse on your model to get an accurate simulation.

Mr. DeLeon: When you scale it to one quarter scale, your deflection curve is not a function of the loading pattern. It seems to correlate with the deflection curve when you take the deflection curve into your scaling factor. If you go from a quarter scale model to full scale, the loading pattern on the scaled structure should have changed immensely.

Mr. Kiger: We tested several different sizes, and you do get very similar loading patterns on the small scale structures as they deflect. Your total impulse will be to a different scale. The pressures are the same.

Mr. Flathau (JAYCOR): If you take the peak, and we are scaling or looking at the deflection, the peak deflections will scale with time. We scale the deflections as the lengths scale, and also time is the inverse. It is scaling properly. Time is in the deflection domain also.

Mr. Kiger: The only question is whether cube root scaling is valid, and is it widely accepted in the community? If you use cube root scaling, you will get one over lambda times the impulse on the model structure that you get on the prototype structure. So, you will reduce impulse.

SHELTER RESPONSE IN A SIMULATED 1-MT NUCLEAR EVENT

S. C. Woodson, S. A. Kiger, T. R. Slawson
U.S. Army Engineer Waterways Experiment Station
Vicksburg, Mississippi

A full-scale, 18-man capacity corrugated metal blast shelter was tested using a High Explosive Simulation Technique (HEST). The HEST simulated the airblast component of a 4,200-TJ (1-Mt) nuclear surface burst with a peak overpressure of approximately 0.37 MPa (55 psi). The main chamber of the shelter was 9 m (29 ft) long, 2.7 m (9 ft) in diameter, and constructed from 10-gage, galvanized corrugated steel. The shelter was buried to a depth of 1.2 m (4 ft) in compacted sand. In-structure shock acceleration data recorded during the test were used to generate shock spectra at damping equal to 5 percent of critical. These shock spectra can be used to evaluate equipment and occupant survivability. Results indicate that occupant survivability is highly probable with no injury, and that survivability of generators and communication equipment can be achieved by shock isolation.

INTRODUCTION

The Waterways Experiment Station (WES) conducted a verification test of an 18-man civil defense blast shelter in support of the Federal Emergency Management Agency (FEMA) Keyworker Blast Shelter Program. FEMA tasked the U.S. Army Engineer Division, Huntsville (HND) to investigate feasible expedient keyworker blast shelter designs, and WES supported the HND effort with a design verification test of an 18-man galvanized steel expedient shelter. An expedient shelter is one consisting of prefabricated components which can be installed in a time period of less than 2 weeks when an international crisis develops. Expedient shelters generally have a 20-man or less capacity.

Shelter design parameters required that the shelter survive a peak overpressure of 0.34 MPa (50 psi) from a 4,200-TJ (1-Mt) nuclear weapon detonation. The structural design criteria and the levels of initial and residual radiation associated with the threat weapon dictated an earth-covered or buried structure. A depth of burial of 1.2 m (4 ft) was required to meet these criteria.

The dynamic test was performed to investigate structural response and to evaluate survivability of the shelter's equipment and inhabitants. Three instrumented mannequins were placed inside the shelter to investigate occupant survivability. This paper describes the dynamic test and analyzes the shock environment within the shelter. A more detailed description of the test procedure and results is presented in Reference 1.

TEST DESCRIPTION AND RESULTS

The shelter consisted of a 2.7-m (9-ft) diameter galvanized corrugated steel culvert section approximately 9 m (29 ft) long with end plates, ventilation equipment, a generator, bunks, and an entryway with a blast closure. Two instrumented anthropomorphic mannequins (one sitting and one prone) were placed on two of the shelter's 18 wall-mounted bunks. Another mannequin was placed in the standing position. Triaxial accelerations measured the response of each mannequin during the test, and a high-speed camera monitored the motion of the mannequins. The structure and free field were instrumented to measure blast pressure, soil stress, steel strains, accelerations, and structural deflections. A total of 60 channels of data were recorded during the test.

The test configuration and locations of the two accelerometers discussed in this paper are shown in Figure 1. The test pit measured approximately 15 by 11 by 5 m (48 by 36 by 16 ft). A 0.6-m (2-ft) layer of flume sand was placed in the test bed prior to placement of the shelter. The sand backfill was placed and compacted in 15-cm (6-inch) lifts from the floor of the excavation to a depth of burial of 1.2 m (4 ft) over the instrumented structure. After backfilling, the charge cavity was constructed on the ground surface above the shelter. The 15- by 11- by 1-m (48- by 36- by 3-ft) charge cavity consisted of a wooden framing system covered with plywood and contained the high-explosive detonating cord. A 1.2-m (4-ft) layer of uncompacted sand overburden was placed over the charge cavity, confining the blast pressure to simulate the peak overpressure and overpressure decay of a nuclear weapon detonation.

The weapon simulation was determined by choosing the best fit, in a least squares sense, of 45 msec of the airblast data to an actual nuclear weapon pressure-time history as defined by Speicher and Brode in Reference 2. The procedure used to select the best fit is defined in some detail in Reference 3. The best fit weapon simulation was a 4,200-TJ (1-Mt) yield at a peak overpressure of 0.37 MPa (55 psi).

Posttest observations revealed only minor structural damage. Permanent diameter changes were less than 2.5 cm (1 in.), and rigid body displacements were limited to approximately 1.3 cm (0.5 in.). The entranceway, closure, and entranceway-shelter connections incurred no damage, and the end plates of the main chamber were undeformed. Also, the mechanical air-moving system and generator were functional posttest. Posttest mannequin positions were similar to pretest settings.

IN-STRUCTURE SHOCK

In-structure shock is typically represented in terms of shock spectra. Shock spectra are plots of the maximum responses, usually of relative displacement, pseudovelocity, and/or absolute acceleration of all possible linear oscillators with a specified amount of damping to a given input base acceleration-time history. Predictions of shock spectra for vertical effects from a 4,200-TJ (1-Mt) surface burst were made by Applied Research Associates, Inc. (Reference 4). The predicted shock spectra at the 0.34-MPa (50-psi) peak overpressure level are presented in Figure 2.

Vertical shock spectra were generated from acceleration data recovered in the dynamic test using a computer code developed at WES. The experimentally determined shock spectra were calculated using damping of 5 percent of critical and smoothed versions are shown in Figures 3 and 4 for accelerometers A6 and A9, respectively. As shown in Figure 1, accelerometer A6 was located on the steel structure and A9 was located on the plywood floor of the shelter. Comparison of Figures 2 and 3 shows that maximum values of velocity and displacement of the structure are less than predicted, but that the maximum value of acceleration (38 g's) is greater than the predicted 29 g's. Comparison of Figures 2 and 4 shows that maximum values of velocity (95 in./sec) and acceleration (80 g's) of the plywood floor are higher than the predicted (80 in./sec and 29 g's, respectively), and that the maximum value of displacement (0.8 inch) is lower than the predicted 4.2 in. Note that the simulated peak overpressure is slightly greater than the 0.34-MPa threat overpressure. At frequencies greater than about 100 Hz, the experimentally determined shock spectra may not be representative of shock spectra due to an actual nuclear detonation. This is the result of oscillations in the surface airblast loading that is characteristic of the HEST charge

cavity. The maximum acceleration value of 80 g's shown in Figure 4 reflects a shift from a calculated value of about 120 g's, resulting in a maximum plywood floor acceleration twice that of the structure. It is believed that the calculated value was affected by the oscillations in the HEST airblast loading that would not be present in overpressures generated by actual nuclear weapons.

SURVIVABILITY

The vertical shock spectra in Figures 3 and 4 can be used to determine whether shock isolation is needed for a given piece of equipment, provided fragility curves for the equipment are known. Alternatively, these shock spectra can be used to write shock resistance specifications that equipment must be able to withstand. Figure 5 compares the experimentally determined shock spectra with safe response spectra for typical floor-mounted equipment from Reference 5. Figure 5 shows that motor generators and communication equipment should be shock isolated to survive. The generator inside the tested shelter was supported on vibration mounts on a mounting skid and incurred no damage.

References 6 and 7 discuss human shock tolerance. The effects of shock on personnel inside the structure depend on the magnitude, duration, frequency, and direction of the motion. Also, the position of the man at the time of shock influences its effect. References 6 and 7 conclude that a standing man will receive compressive injuries in the body-supporting bones if the upward floor acceleration exceeds 20 g's during a long-duration loading. The injury threshold increases as the duration of the load decreases. Reference 7 recommends using a maximum design acceleration of 10 g's at frequencies at or below man's resonant frequency in the standing position (10 Hz). The experimentally determined shock spectra show that, at overpressures slightly higher than the design overpressure, no injury will occur. Since human shock tolerance is higher in the seated and prone positions than in the standing position, the probability of injury decreases.

Impact injuries occur at much lower accelerations than compressive bone fractures. Generally, impact injuries may occur at accelerations of 0.5 to 1 g for an unrestrained man in the standing position or seated positions. These injuries are the result of falling and hitting the floor or other objects. Impact injuries may be reduced by padding or restraining to prevent movement. High-speed photography monitored the response of the three unrestrained anthropomorphic mannequins during the test. The high-speed movie footage showed that impact injuries are not probable, although vertical accelerations of 3, 6, and 9 g's were measured on the prone, standing, and sitting mannequins, respectively.

CONCLUSIONS AND RECOMMENDATIONS

Based on results of the full-scale dynamic test, in-structure shock in the 18-man Keyworker Blast Shelter is within acceptable limits for occupants. It is recommended that typical blast-shelter equipment such as generators and communication equipment be shock isolated to ensure survivability.

ACKNOWLEDGEMENT

This work was sponsored by the Federal Emergency Management Agency (FEMA), Washington, D.C. Mr. Tom Provenzano, FEMA, was the Program Manager. The field test was supervised by Mr. Randy Holmes, Structures Laboratory, Waterways Experiment Station (WES), Vicksburg, MS, and instrumented by Mr. Phil Parks, Instrumentation Services Division, WES.

REFERENCES

1. Woodson, S. C., et al., "Dynamic Test of a Galvanized Steel Keyworker Blast Shelter," (in preparation), U.S. Army Engineer Waterways Experiment Station, Vicksburg, Mississippi.
2. Speicher, S. J., and Brode, H. L., "Airblast Overpressure Analytic Expression for Burst Height, Range, and Time Over an Ideal Surface," PSR Note 385, November 1981 (with updates through November 1982), Pacific-Sierra Research Corporation, Santa Monica, California.
3. Miakar, P. F., and Walker, R. E., "Statistical Estimation of Simulated Yield and Overpressure," "The Shock and Vibration Bulletin, Bulletin 50, Part 2, September 1980, The Shock and Vibration Information Center, Naval Research Laboratory, Washington, D.C.
4. "Multiple Burst Damage Patterns and Ground Shock Analysis of Effects on Buried Structures," Progress Report No. 2 (Draft April 1982), Applied Research Associates, Incorporated, Alexandria, Virginia.
5. U.S. Army Technical Manual TM 5-855-1, "Fundamentals of Protective Design for Conventional Weapons," 1984, U.S. Army, Washington, D.C.
6. "Personnel and C-E Equipment Shock Tolerance," Summary Report, 1977, Boeing Aerospace Company, Seattle, Washington.
7. Crawford, R. E., et al., "The Air Force Design Manual for Design and Analysis of Hardened Structures," 1974, Air Force Weapons Laboratory, Kirtland Air Force Base, New Mexico.

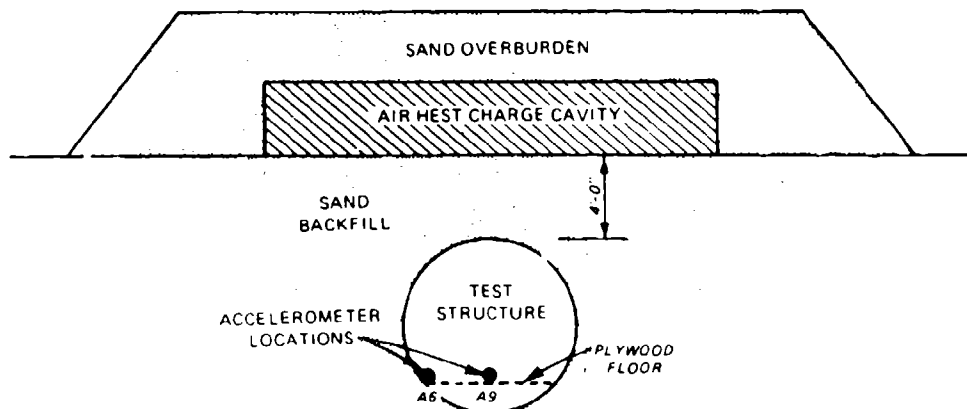


Figure 1. Test Configuration and Accelerometer Locations

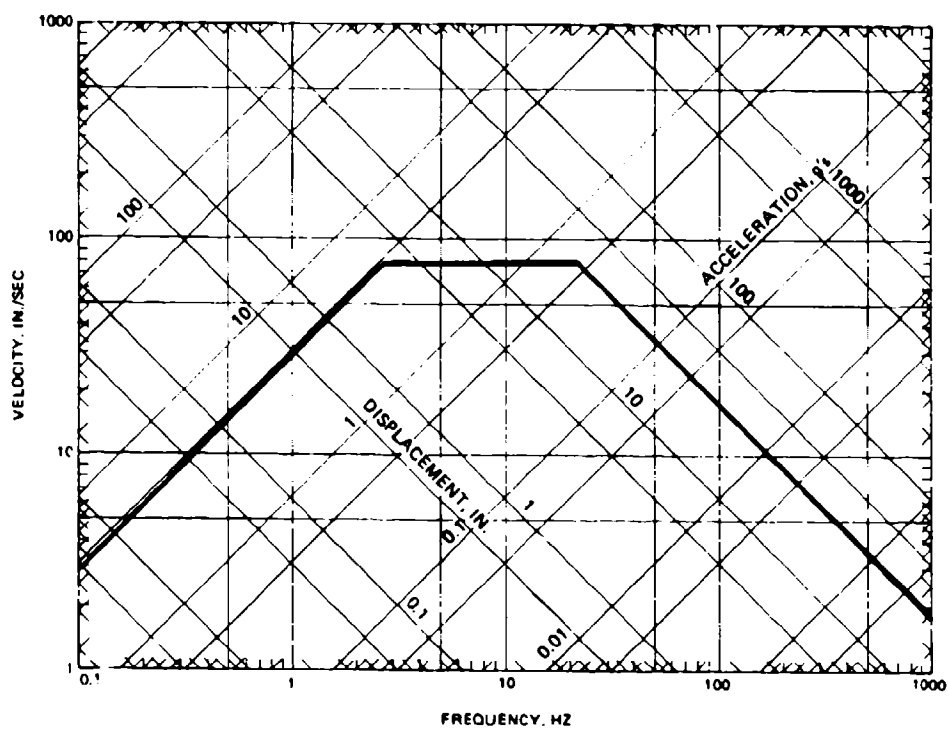


Figure 2. Predicted Shock Spectra

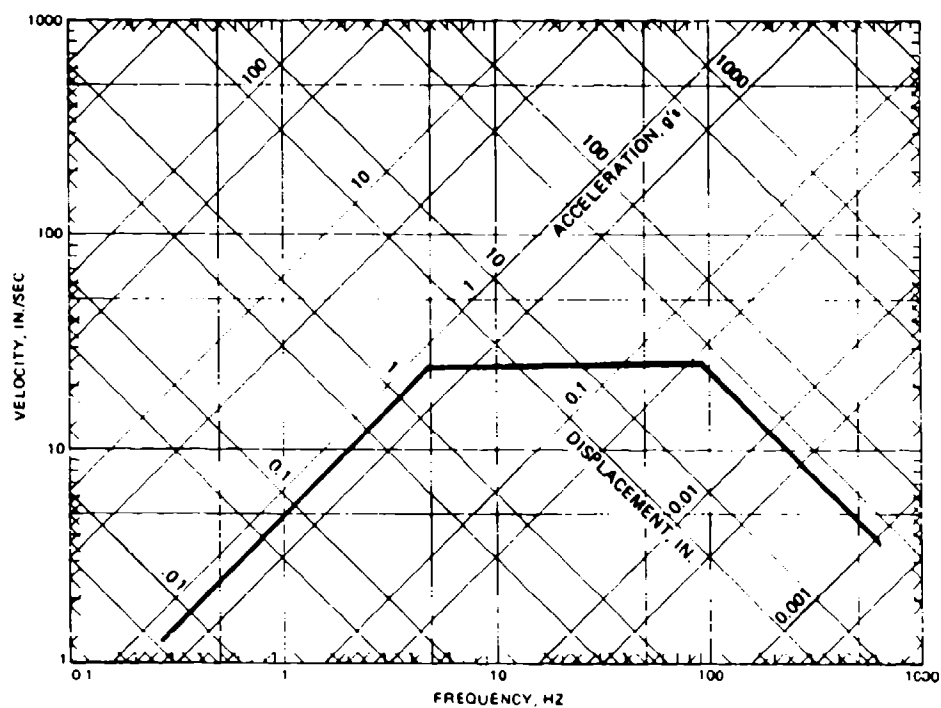


Figure 3. Vertical Shock Spectra from Accelerometer A6

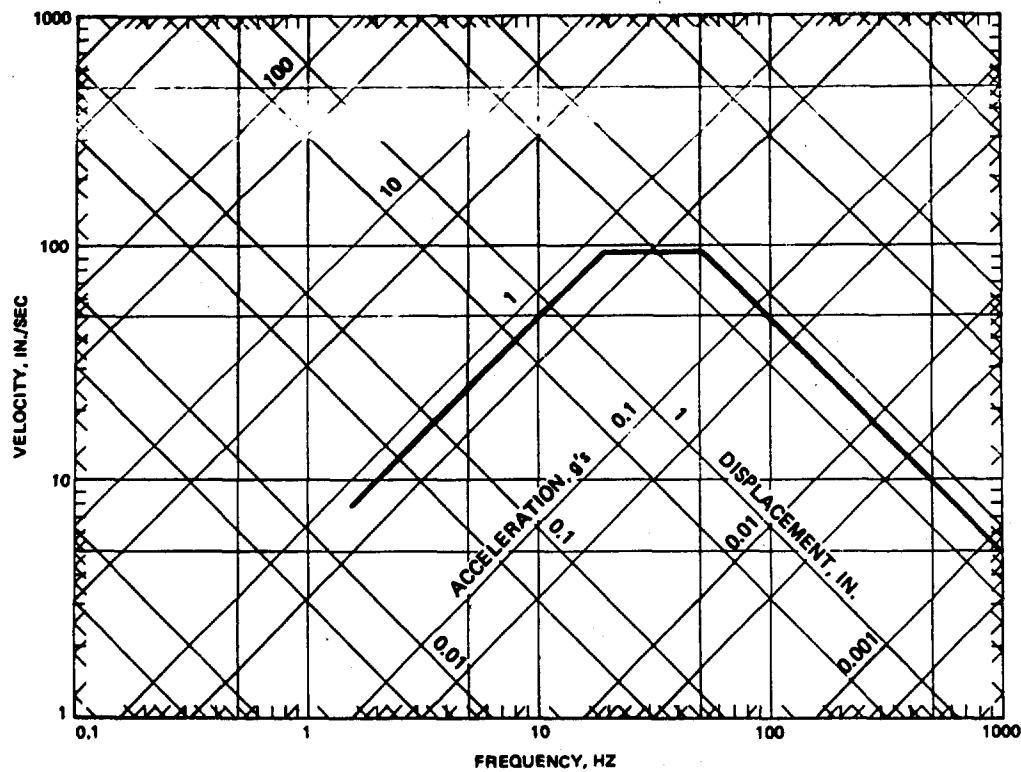


Figure 4. Vertical Shock Spectra from Accelerometer A9

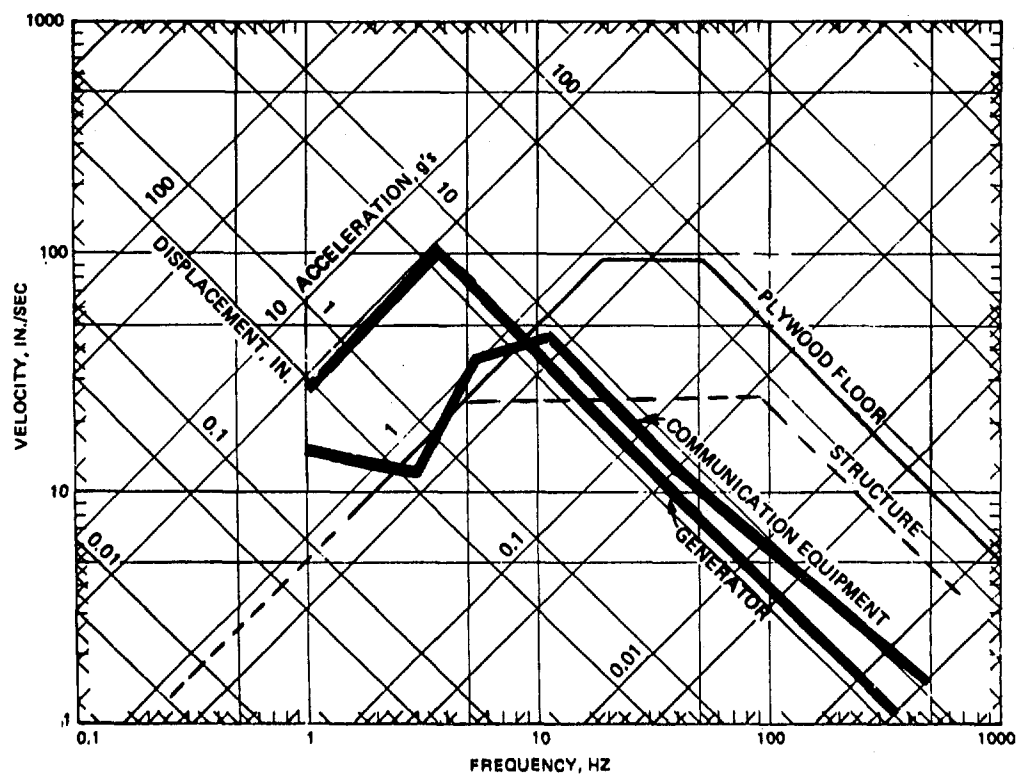


Figure 5. Comparison of Experimental Shock Spectra with Response Spectra for Typical Floor-Mounted Equipment

Discussion

Mr. Unruh (Southwest Research Institute): Did you have any pressure gages on the interior to measure noise like a booming noise inside the shelter?

Mr. Woodson: We did have an air-blast pressure gage mounted inside the structure. As I recall, it measured a very low overpressure, something like two psi.

Mr. Unruh: Was that dynamic overpressure or just a very low frequency?

Mr. Woodson: Basically, it was a static overpressure after filling that large a volume.

VIBRATION CHARACTERISTICS OF A LARGE-SCALE BURIED STRUCTURE

F. D. Dallriva and S. A. Kiger
Research Structural Engineers
U.S. Army Engineer Waterways Experiment Station
Vicksburg, Mississippi

A high-explosive dynamic test was conducted on a large-scale (approximately 1/2-scale) reinforced concrete box-type structure at a depth of burial (DOB) of 20 percent of the roof span. Prior to the high-explosive test, vibration tests were conducted on the structure both before and after placement of the sand backfill. The objectives of the vibration tests were to determine the effects of the soil cover on the structure's vibration characteristics (i.e., natural frequencies, mode shapes, and damping) and to evaluate possible scale effects by comparison with results from previous tests conducted on a similar structure at a smaller scale. Results obtained for the roof of the structure are presented in this paper. Addition of the sand backfill reduced natural frequencies and increased damping ratios for the roof of the large-scale structure. The frequencies of the smaller structure were not changed significantly after addition of the backfill, which was most likely due to the nonlinear nature of the soil-structure interaction effects caused by the backfill. The fundamental frequencies corresponded well before addition of the backfill, which indicated no significant scale effects, at least in the elastic range before backfill.

INTRODUCTION

A large-scale reinforced concrete box-type structure was tested dynamically by the U.S. Army Engineer Waterways Experiment Station in support of the Shallow-Buried Structures Program sponsored by the Defense Nuclear Agency. The dynamic loading was produced using a High-Explosive Simulation Technique (HEST) to simulate the overpressure and duration associated with a nuclear detonation. One of the test objectives was to determine the effects of scaling on the structural response by comparison with previous tests conducted on smaller scale models. Another objective was to evaluate current analysis procedures for predicting structural response to simulated nuclear overpressures. An important parameter in the analysis of buried structures involves the determination of soil-structure interaction effects. For example, when conducting a single-degree-of-freedom analysis to determine roof response, the natural period of the roof must be determined. Soil cover on the structure should influence vibration characteristics in two ways (Reference 1). First, because the soil has shear strength, deflections of one part of the soil relative to another will generate shear forces that tend to confine the structure, restricting its motion and increasing its natural frequency, while some of the soil is expected to move with the structure, producing an added mass effect and decreasing its natural frequency.

The procedure discussed in Reference 2 modifies the frequency calculated for the uncovered structure by a multiplication factor to account for the addition of the soil cover. However, it places a limit on this added mass effect stating that below some critical DOB, a further increase in depth of soil cover would provide no corresponding increase in the soil-mass effect on the period of vibration. It suggests that a conservative value (from a vulnerability analysis perspective) for this critical depth be taken equal to the span of the roof slab. The objectives of the vibration test on the large-scale buried structure were: (1) to evaluate scale effects by comparing these test results with previous results obtained from vibration tests conducted on an identical structure one-half the size of this test structure, and (2) to determine the effects of the soil cover on the vibration characteristics of the structure. This paper describes the test procedure and results obtained for vibration tests conducted on the roof of the structure before and after addition of the sand backfill.

MODEL STRUCTURE

The test structure was constructed of cast-in-place, steel-reinforced concrete. The inside dimensions were 2.44 metres (8 feet) high by 2.44 metres (8 feet) wide by 9.75 metres (32 feet) long, and overall thickness of the roof, floor, and walls was 0.285 metre

(11.2 inches). Concrete cover over the principal reinforcing steel was .0254 metre (1 inch) which produced an effective depth of 0.243 metre (9.6 inches). Principal reinforcing steel was 1 percent for both tension and compression. The model was constructed on 0.762 metre (2.5 feet) of sand, and sand backfill was placed around and over the structure to a depth of 0.488 metre (19.2 inches). This provided a DOB equal to 20 percent of the roof span. All sand was placed in 0.152-metre (6-inch) lifts and vibrated to a density of about 1,682 kg/m³ (105 lb/ft³). Structural details and backfill details are shown in Figure 1.

EXPERIMENTAL PROCEDURE

A grid was established on the roof inside the structure, and the intersections of the grid lines were used as force input locations. A piezoelectric accelerometer was mounted on the roof for output in the vertical direction. The force input points and accelerometer location are shown in Figure 2. A technique employing an instrumented impulse hammer was used to excite the structure. The hammer used was a PCB Model GK291B50 5.44-kilogram (12-pound) impulse hammer. A load cell in the hammer recorded the force-time input and the structural response was measured by the accelerometer. Peak input force levels varied between hammer hits, but were approximately 5.33 kilonewtons (1,200 pounds). Force and acceleration measurements were digitally recorded as transfer functions (acceleration divided by force) using a structural dynamics analyzer. To average down random noise, each point was hit five times. The analyzer used was a ZONIC Model 6080 Multichannel Signal Processor. The input and output were also recorded using analogue equipment as a backup. Access to the structure after placement of the backfill was provided by a corrugated metal culvert which was installed during the backfilling process.

EXPERIMENTAL RESULTS AND DISCUSSION

The frequency response functions obtained from the measured accelerations and input force signals using the FFT analyzer were used to estimate the modal parameters of the structure (i.e., natural frequencies, mode shapes, and damping ratios). Typical plots of frequency response functions, and corresponding coherence plots obtained before and after placement of the backfill are shown in Figure 3. As can be seen, the resonant peaks obtained for the uncovered structure are much more narrow than for the buried case, indicating a likely increase in the damping due to the soil cover. Comparison of the test results before and after backfill indicates that the resonant frequencies of the roof decreased after backfill. The fundamental mode of vibration is the most important mode when considering the response of the roof to

blast loads. The frequency of the fundamental mode before placement of the backfill was 78 Hz and after placement of the backfill was 53 Hz. These results provide evidence that at a 20-percent DOB in sand backfill, the added mass effect is greater than the corresponding stiffening effect provided by the backfill. A comparison of these results was made with those obtained for an identical structure one-half the size of this structure (Reference 3) which was buried at a DOB of 50 percent of the roof span in sand. Those results indicated no significant change in the resonant frequencies before and after placement of the backfill. At this DOB, the stiffening effect apparently offset the effect due to the added mass, thereby causing the resonant frequencies to remain unchanged. Another probable reason for differences in the frequency characteristics of the large- and small-scale structures after addition of the backfill is the nonlinear nature of the soil-structure interaction. The confining (stiffening) effects of the surrounding soil backfill are deflection dependent. Because the small-scale structure was excited with an electro-hydraulic vibrator at a peak force of about 2.22 kilonewtons (500 pounds), much larger relative deflections occurred; therefore, larger confining forces were generated. This resulted in an apparent stiffer (higher frequency) structure. The resonant frequency of the fundamental mode of vibration for the smaller structure before placement of the backfill was 152 Hz. This corresponds well with the value of 78 Hz obtained for the large-scale structure since the frequencies should differ theoretically by a factor of two. Mode shapes corresponding to the fundamental mode of vibration of the roof for the uncovered and covered structure are shown in Figure 4.

Damping of the roof was increased after backfill. This result was expected since the soil backfill should allow energy to be more efficiently radiated away from the structure during vibration. Damping ratios for the uncovered structure ranged from 1.8 to 7.0 percent of critical. After placement of backfill, the damping ratios ranged from 7.1 to 12.3 percent of critical.

Expressions given in Reference 2 for the period of vibration of a one-way reinforced concrete slab with fixed ends were used to calculate natural frequencies of the roof before and after placement of the backfill for comparison with experimental results. The roof slab fundamental period is given by:

SI Units	English Units
$T = L^2 / 21,580 d p^{1/2}$	$T = L^2 / 5,900 d p^{1/2}$

where

T = natural period, seconds
 L = slab span, metres (feet)
 d = effective depth of slab, metres (inches)

p = tension steel reinforcement ratio, which is assumed to be the same at the center and at the edges of the slab

For the large-scale structure:

$$T = .0113 \text{ seconds}$$

and the fundamental frequency is

$$f = 88.5 \text{ Hz (78 Hz measured)}$$

The fundamental period after addition of the soil backfill is given by:

SI Units	English Units
$T_r = T (0.8 h/d_c + 1)^{1/2}$	$T_r = T (9.6 h/d_c + 1)^{1/2}$

where

T = period of vibration of the roof slab uncovered

h = depth of soil cover over the roof (but not greater than the roof span), metres (feet)

d_c = total thickness of the roof slab, metres (feet)

For the large-scale structure covered

$$T_r = 0.0174$$

and the fundamental frequency is

$$f_r = 57.5 \text{ Hz (53 Hz measured)}$$

The experimental and calculated values of the fundamental frequency for the uncovered structure differ by about 13 percent and for the covered structure by about 7 percent. The expressions given above seem to be reasonable estimates of the natural period for this particular structure in both the buried and uncovered configurations.

CONCLUSIONS

The frequencies obtained before addition of the backfill for the fundamental mode of vibration of the large-scale structure correspond well with that obtained for the smaller scale structure in Reference 3. This seems to indicate an absence of any significant scaling effects in the elastic deflection range for the uncovered configuration. The addition of the soil

backfill to the large-scale structure effectively reduced the frequencies and increased damping ratios; however, the frequencies of the smaller scale structure did not change significantly after addition of the backfill. This can probably be attributed to the greater DOB of the smaller structure relative to its span and the nonlinear nature of the soil-structure interaction. Reference 3 indicates that the effect of soil on natural frequencies and damping appears to be dependent upon the structure/soil stiffness ratio and that parametric studies employing vibration testing should be conducted on concrete slabs having various span-to-thickness ratios with a variety of carefully controlled backfill conditions. Care should be used, therefore, when applying semiempirical design manual techniques such as those presented in Reference 2.

ACKNOWLEDGEMENTS

This work was sponsored by the Defense Nuclear Agency in support of the Shallow-Buried Structures Program. Mr. Jim Cooper was the work unit manager. The vibration tests described in this paper were conducted by Mr. V. P. Chiarito and Mr. R. S. Wright, Structural Mechanics Division, and Mr. S. W. Guy, Instrumentation Services Division, U.S. Army Engineer Waterways Experiment Station.

REFERENCES

1. Volz, R. D. and Kiger, S. A., "An Evaluation of the Separated Bay Concept for a Munition Assembly Complex; An Experimental Investigation of the Department of Energy Building 12-64 Complex"; Technical Report SL-83-6, September 1983, U.S. Army Engineer Waterways Experiment Station, Vicksburg, Mississippi.
2. Halmiwanger, J. D., Hall, W. J., and Newmark, N. M., "Approximate Methods for the Vulnerability Analysis of Structures Subjected to the Effects of Nuclear Blast"; Report No. U-275-76, June 1976, N. M. Newmark Consulting Engineering Services, Urbana, Illinois.
3. Crowson, R. D., Essex-Diamond Ore Research Program, Vibration Tests and Analyses of Essex-V Model Structures"; Technical Report TR N-78-2, August 1978, U.S. Army Engineer Waterways Experiment Station, Vicksburg, Mississippi.

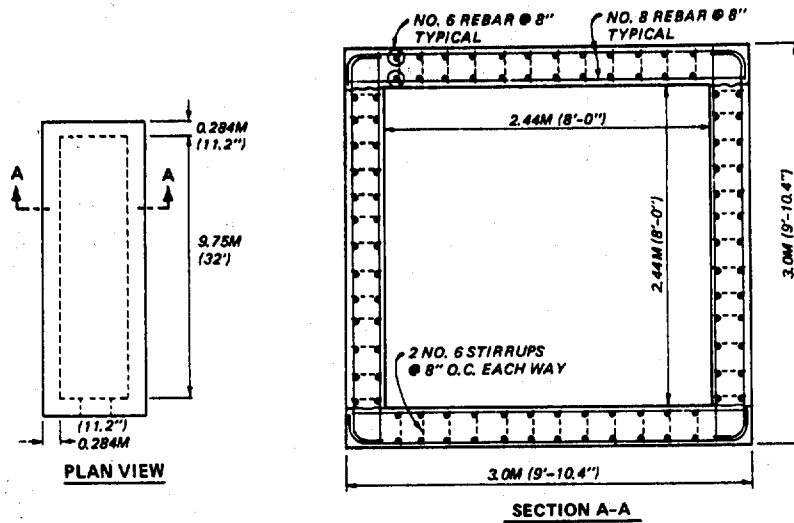


Figure 1. Structural Dimensions and Details

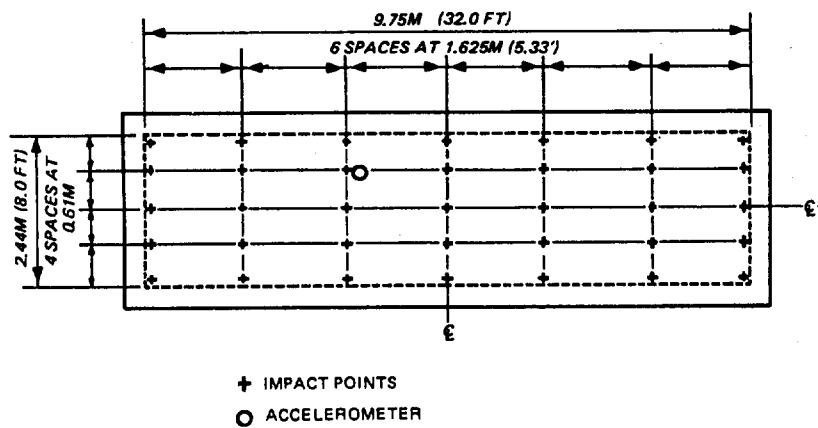


Figure 2. Roof Plan Showing Impact Point and Accelerometer Locations

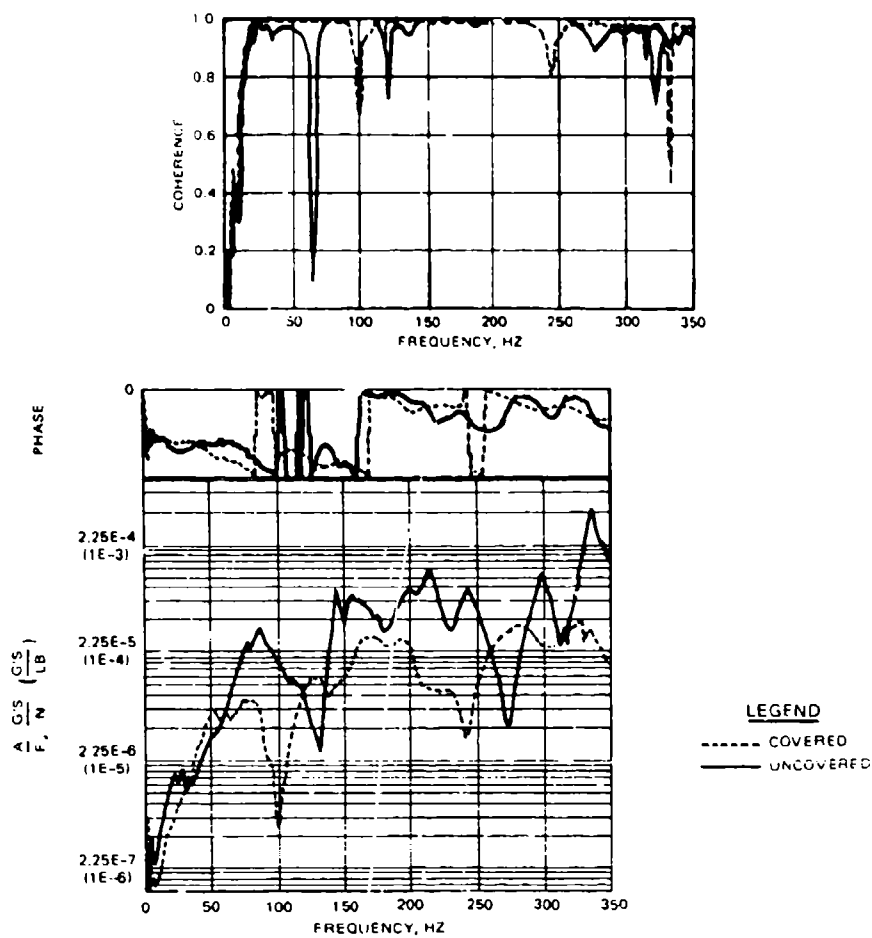


Figure 3. Typical Plot of Frequency Response Function

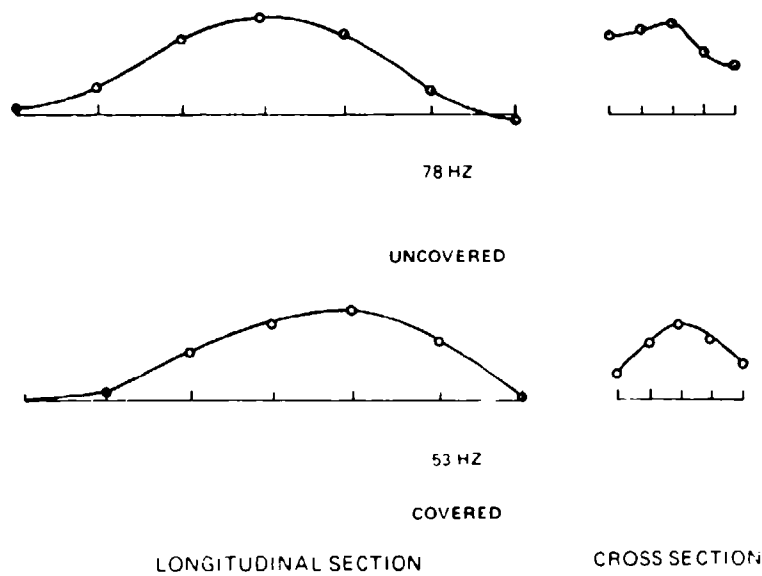


Figure 4. Fundamental Mode Shapes of Roof, Uncovered and Covered

A "NUMERICAL GAUGE" FOR STRUCTURAL ASSESSMENT

T. Krauthammer
Department of Civil and Mineral Engineering
University of Minnesota
Minneapolis, Minnesota 55455

A simplified numerical procedure for the behavioral assessment of reinforced concrete structural systems under the effects of blast and shock is presented, and demonstrated. This approach is based on the consideration of specific structural behavior mechanisms, and soil-structure interaction which are known to determine the systems performance. A computer code was developed which can be employed by the designer and analyst as a "numerical gauge" for obtaining pre- and post-event structural assessments based on design or site information. A total of sixteen actual cases were studied by the present approach, and the results are presented and discussed.

INTRODUCTION AND BACKGROUND

Structural response under the effects of blast and shock loading conditions is of concern to hardened facilities designers who usually employ advanced numerical techniques, such as finite element codes, for the assessment of protective systems. These procedures are expensive and require significant resources for obtaining adequate results, and the engineer would prefer to employ simple numerical tools for fast, yet accurate, structural analyses. Also, if such procedures were available they would be employed for pre test predictions and for post-test evaluation of model structures. This idea is not new, however, the present method may add to the flexibility of this general approach. Previous studies have demonstrated the effectiveness of employing single-degree-of-freedom (SDOF) systems for the assessment of structural response under various types of dynamic loads. That approach was further refined in order to explicitly consider the effects of specific structural mechanisms, soil-structure interaction, and loading conditions on the dynamic structural response. The analyst can represent design changes through their influence on these mechanisms, and observe the resulting variations in the structural behavior. This approach was employed at the University of Minnesota for the analyses of shallow-buried reinforced concrete box-type structures under simulated nuclear blast effects, and also for highlighting the differences between that type of behavior and the response of similar structures under the effects of localized conventional detonations.

As a result of these studies it was possible to demonstrate that complicated structural mechanisms can be accurately formulated into a SDOF approach, and that a simplified numerical method can provide accurate predictions and post-test assessments of the structural behavior. Furthermore, this analytical technique can be employed as a "gauge" for performing rapid and inexpensive numerical experiments providing accurate results for hardened systems assessment.

Structural behavior under blast and shock induced loads can be divided into two principal groups. The first group includes structures under simulated nuclear environments while the second is composed of structures subjected to localized effects such those associated with conventional explosives. The following discussion will emphasize the differences between these two cases.

Flat-roof structures under simulated nuclear loads have been studied both experimentally and through numerical evaluations in order to understand their behavior under severe blast loading conditions [9,10,12,14,16,20,21,22,25, and 26]. It was noticed experimentally [9] that the roofs exhibited two types of behavior as follows. One group of structures had a flexural response while another group was influenced primarily by shear. At that point it became extremely important to understand both the flexural and shear modes of behavior, and to be able to predict that performance based on rational models for structural mechanisms. The structures were analyzed by finite element techniques

[6,15,16,25] where it was possible to reproduce the observed behavior; nevertheless, such analyses were expensive and time consuming. Another analytical approach was proposed based on a SDOF computation combined with a Timoshenko Beam model, and a shear stress vs. shear slip model for the concrete [21]. A different simplified approach was proposed based on introducing structural resistance functions into a SDOF technique, and including modified failure criteria for separating flexural cases from those controlled by shear [12]. That approach seemed to produce behavior predictions that were on average within seven percent from the experimental data. The quality of the numerical results indicated that it would be possible to improve the results by using more accurate descriptions of structural mechanisms and soil-structure interaction effects, as described in [14]. Indeed, including explicit models for dynamic shear and thrust effects on reinforced concrete slabs improved the numerical results to be on average within five percent from the experimental values.

Structural behavior under the detonation of conventional explosives is a subject of renewed interest. Crawford *et al.* [3] compiled existing information based on practical experience and limited scientific studies, and provided recommendations on the computation of environments, structural response, and the design against such effects. Nevertheless, many effects may not be accurately computed from the recommendations in [3], and one needs to employ later information by Drake and Little [4], Henrych [5], Kiger and Albritton [8], Vretblad [23], and Westine and Friesenhahn [24] which provided further data on the subject. Based on those studies it seems to be rational to expect differences in behavior between structures under simulated nuclear effects, and those subjected to localized high explosive environments, as briefly outlined by Krauthammer and Parikh [13]. In order to study such differences, and to perform a meaningful comparison it was decided to choose two sets of experiments performed by the same investigators [8, and 9] on very similar structural systems. One set of experiments [8] was governed by localized effects while for the other [9] simulated nuclear effects were employed. The comparison will be performed by employing the SDOF approach that will serve as a "numerical gauge" to highlight the differences in the structural responses. Furthermore, the "gauge" will also be used to identify the nature of such differences, and their physical origin.

EXPERIMENTAL OBSERVATIONS AND BEHAVIOR

Structures Under Simulated Nuclear Environment

Data from tests on shallow-buried box-type structures, as presented in several publications [7,9,10,20, and 22], can be combined with results from previous studies on this topic [2,6,12,14,15,16,21 and 25] for providing a description of the systems behavior.

When the simulated airblast is applied to the soil free surface a corresponding shock wave is induced in the soil which travels vertically downward until meeting with the structure. Based on data from soil stress gauges and interface pressure gauges it seems that the shock front is quite planar, and any modulation in the interface pressures will appear as a result of wave reflections and soil-structure interaction that includes soil arching. Naturally, this later pressure-time history is not uniformly distributed over the roof slab. The structural response was controlled either by shear that may result in a direct shear failure at the supports at a very early time (based on the test data in references [9] and [22] this time seems to be slightly over one msec after the arrival of the shock front), or by flexure where the roof slab may exhibit membrane effects initially in compression and later possibly also in tension. From the observed behavior it becomes quite clear that in the event that direct shear is the mode of failure the structure will not be allowed sufficient time to develop any meaningful flexural response, and therefore one can justify the uncoupling of the direct shear response from a possible flexural response. Furthermore, one may wish to adopt a reliable model for direct shear in order to be able to represent the observed shear failures, and such a model may not have to include the possible effects of moments and rotations at the shear failure region.

Additional information on these structures was summarized in [14], and it contains a detailed discussion on the relationships between structural behavior and analytical capabilities.

Structures Under Localized Conventional Effects

The two structures tested under the effects of conventional detonations were geometrically identical to those tested under simulated nuclear effects. There were some differences in the material properties for steel and concrete, as adequately discussed in [8]. Overall, there were five shots for structure 3C, and eight shots for structure 3D. Each shot was performed by the detonation of a 21 lb. (9.5 kg) spherical TNT charge at distances between 2.7 ft (0.8 m) to 10 ft (3.0 m). The charges were buried to be positioned at the structure mid-height, and thus, it was expected that the peak pressures would be measured at the wall slab center while the load on the slab would be distributed symmetrically to that point. The main difference between the structures was that in structure 3C the slab thickness was 5.6 in. (142 mm) while it was 13 in. (330 mm) for structure 3D, and the free span wall slab dimensions were 4 x 16 feet (1.2 x 4.9 m). The structural behavior for the various events during these tests were described in [8], and are summarized as follows.

Structure 3C: Tests 1 through 3 were conducted with the charges located geometrically away from the midlength of the structure, and the structure sustained no structural damage due to Test 1 at a range of 8 ft. (2.44 m). Moderate cracking was observed at the center portion of the wall section after Test 2 at a range of 6 ft (1.83 m), and the cracks radiated longitudinally along the wall. Test 3 was conducted on the opposite side of the structure at a range of 4 ft. (1.22 m), and this test produced extensive damage to the wall, which was displaced inward approximately 10.5 in. (267 mm). Breaching of the wall was believed to be imminent due to the large displacement and the considerable amount of concrete spalling, but response of the wall section appeared to be in a flexural mode. The affected wall section was approximately 4 ft. (1.22 m) high by 8 ft. (2.44 m) long. Test 4 was conducted at a range of 2.7 ft. (0.82 m) from the end wall of the box and produced catastrophic damage to the end wall, which was completely blown away and into the interior of the structure. Test 5 was also at a range of 2.7 ft. (0.82 m) but was located between the midlength and the end wall of the structure. This explosion also produced catastrophic damage, and a large portion of the wall was destroyed, and the reinforcing mat was ruptured and drastically displaced. Tests 3 and 5 bracket the charge range to produce breaching of this structure wall and should lie between 2.7 and 4 ft. (0.82 and 1.22m).

Structure 3D: Structural damage to Structure 3D was not visible until the completion of Test 6, located at a 4 ft. (1.22 m) standoff distance. (Tests 3 through 5 were attenuation tests on the structure end wall). Test 6 produced minor longitudinal cracks on the structure wall. The explosion effects from Test 7 at a range of 2.7 ft. (0.82 m) were sufficient to produce moderate cracking of the wall, roof slab, and floor slab. Vertical cracks on the wall continued as transverse cracks across the roof and floor, and up and down the opposite wall, indicating that the entire structure responded as a large box-beam. When the charge was moved in to a 2 ft. (0.61 m) range, the structure was breached. A gaping hole was blown in the side of the wall, and the wall section was displaced inward to the opposite wall. Response of the structure wall during this explosive loading appeared to be in a shear mode. The block of wall blown in was nearly intact, indicating that very little flexural response occurred. The shearing mode of response appeared to be more typical of a direct shear rather than a diagonal shear.

The observed behavior of the test structures, and information provided in the literature indicate that one should anticipate important differences in structural response between the simulated nuclear and localized conventional loads. Localized effects will tend to cause localized damage while the simulated nuclear loads will tend to affect an entire slab or even the whole structure. The arising differences will have to be highlighted by the

numerical approach, and careful attention needs to be paid to the corresponding differences in the structural mechanisms which govern the response.

LOADING FUNCTIONS AND STRUCTURAL MECHANISMS

The analytical approach adopted for the present study is based on a SDOF approximation for the shallow-buried reinforced concrete box-type structures that were studied by several investigators, as discussed previously here. This basic approximation is well known, and has been discussed and used extensively for the analyses of linear problems, one such example is the book by Biggs [2]. There are well established procedures for deriving the various parameters that would be required for a SDOF formulation, and these will not be repeated here. However, when the system under consideration is known to behave in the nonlinear dynamic domain several modifications have to be introduced into the parameter definitions. The background for such models was provided in previous publications by Beck *et al.* [1], Kiger *et al.* [10], Kiger and Painter [11], Krauthammer [12, and 14], Krauthammer and Parikh [13], and Windham and Curtis [25]. Wolf [27] provided extensive discussions on the incorporation of soil-structure interaction into various analytical procedures including some nonlinear aspects of behavior, and that information can be used to guide the development of the proposed approach. The parameters that need to be considered for the analysis consist of the applied load function, the structural resistance in the flexural domain, the slab shear resistance, damping, soil-structure interaction effects, and the mass. These parameters will be defined and formulated to comply with the system behavior, as presented previously here.

The SDOF approach as applied for pretest predictions was described in [12], where the resistance function for reinforced concrete slabs, and a discussion of failure criteria were presented. As mentioned in [12], one can find an excellent discussion on the topic of load-deflection relationships for reinforced concrete slabs in the book by Park and Gamble [19], and the current approach is a combined and modified version of the methods in [12-14, 17, and 19].

Loading Functions

One of the most important parameters that affects the structural behavior is the loading function. Such functions are provided as force-, or pressure-time histories, and they are applied to the model structure. There is a distinct difference between load functions that could be associated with a nuclear environment and their counterparts corresponding to a conventional detonation. These differences can be well defined based on available information on the subject [2, 9, and 20]. In general, a simulated nuclear detonation will produce a pressure pulse characterized by a steep rise, a

peak pressure P_0 , and a long exponential decay. A conventional detonation will produce a pulse of a similar shape, but the duration is significantly shorter than that of the nuclear load [3,4,5,23, and 24]. Another significant difference between these loads is the issue of spatial distribution. While a nuclear load can be simulated by a uniformly distributed pressure-time history the conventional detonation produces a pressure pulse that is rather localized and therefore it has to be represented by a function of time and geometrical space. This fundamental difference between the two loading cases is known to affect the structural response, and the proposed "numerical gauge" should be sufficiently sensitive in order to highlight these differences.

Previous studies [1,2,9, and 12] have demonstrated that one can employ a uniformly distributed pressure-time history related to the simulated nuclear environment for the analysis of hardened facilities. In order to employ a similar technique for the conventional explosives domain one needs to introduce several changes in the loading function. First, one can employ any of the models proposed in the literature, as mentioned above, for the simulation of the load, however, the differences between those methods will not be discussed here. Regarding the load applications to the "numerical gauge", the spatial distribution must be incorporated into the time history since the approach is based on the SDOF procedure in which only one geometrical space coordinate is available. An averaging process must be performed in order to obtain from the localized pressure pulse an equivalent uniformly distributed pressure-time history. This process can be performed in several possible ways, and here only two of these possibilities will be presented.

The first approach is to consider a vertical strip of unit width and of length L , where L is the height of the loaded wall, as shown in Figure 1. the strip is divided into N equal segments each having an area A_i . The distance from the center of the detonation to the center of each segment is computed as R_i , and one can compute the time of arrival, t_i , of the pressure pulse and the corresponding normal peak pressure $P_{0,i}$ based on an acceptable model for pressure vs. range, and the angle between the radius vector and the normal to the surface. One can employ the existing models for describing the pressure-time histories at the center of each segment, and then for each time step to perform the following operation:

$$P(t) = \frac{\sum_{i=1}^N A_i P_i(t)}{\sum_{i=1}^N A_i} \quad (1)$$

The result is a pressure-time history that incorporates different times of arrival, and the spatial pressure distribution. The approach can be further modified by applying it to a general rectangular area rather than a strip, and the area could have dimensions from L by L , to L by $2L$, or according to the procedure proposed in [11]. In this case, the averaging will be performed in two dimensions, and Eq. (1) can be easily modified accordingly.

The other approach is based on the assumption that the spherical detonation front will create a circular pattern on the vertical wall when the wall plane is normal to the radius. For this case Eq. (1) can be modified further so that the A_i are the areas of N concentric rings, and R_i is the distance from the center of detonation to the centerline of each ring, as shown in Figure 1. In the present study both the strip and circular averaging methods were employed, and two of the pressure-time histories for circular averaging are shown in Figure 2.

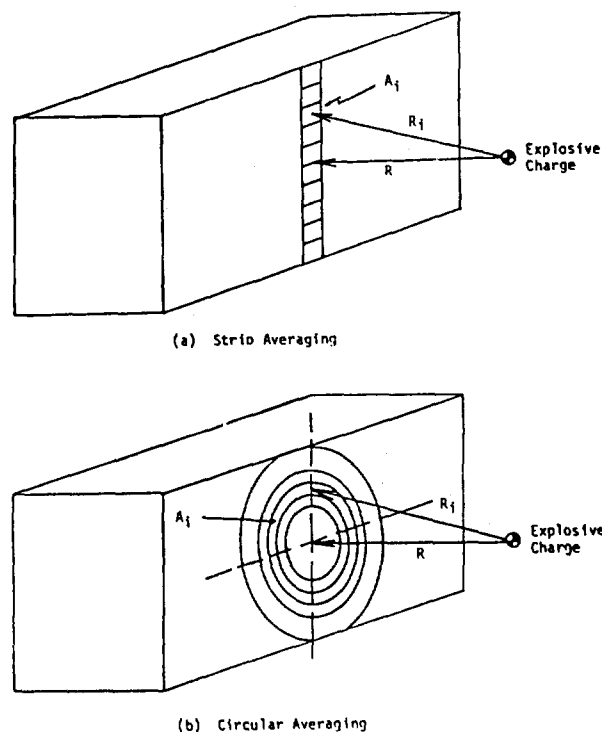


Fig. 1 - Pressure Averaging techniques

Flexural Resistance for Slabs

A typical resistance curve for a fixed reinforced concrete slab has four characteristic points, as shown in Figure 3. First, these points will be defined, and then various assumptions will be presented concerning the behavior between these points. Point A corresponds to the

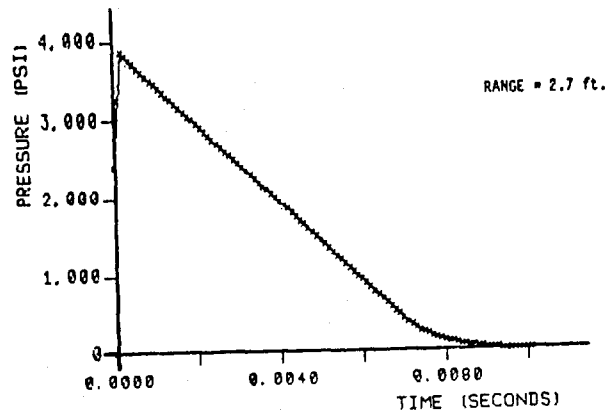
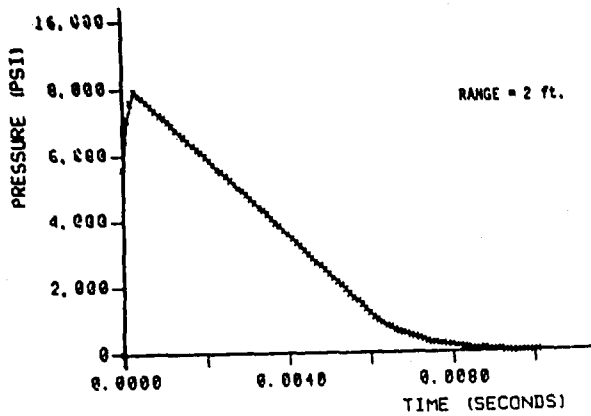


Fig. 2 - Pressure-time histories

initial unloaded condition and zero central deflection. Peak resistance is represented by point B and one may employ the formulations as proposed by Park [17], and Park and Gamble [19] to compute it. A simplified formulation that also accounts for externally applied in-plane compressive forces was proposed in the literature [12, and 14] and can be employed for computing the load carrying capacity at point B of the proposed model. Here, that approach was further modified, as follows. (The original formulation was presented in English units, and therefore, the results may be converted to SI units if required.)

$$wL_x^2 \frac{(3 \frac{L_y}{L_x} - 1)}{24} -$$

$$0.85\beta_1 f'_c h^2 \left[\frac{L_y}{L_x} (0.188 - 0.281\beta_1) \right.$$

$$+ (0.479 - 0.490\beta_1) \quad (2)$$

$$+ 2 \left[\frac{L_y}{L_x} F_x (d_{1x} - d_{2x}) \right.$$

$$+ F_y (d_{1y} - d_{2y}) \left. \right]$$

$$+ \left[\frac{L_y}{L_x} N_x (d_{1x} - \frac{h}{2}) + N_y (d_{1y} - \frac{h}{2}) \right]$$

in which w = uniformly distributed load on the slab; L_x , L_y = short and long dimensions of a rectangular slab, respectively; β_1 = parameter depends on the concrete compressive strength and varies linearly between 0.85 for $f'_c \leq 4000$ psi to 0.65 for $f'_c \geq 8000$ psi; f'_c = uniaxial compressive strength of concrete; h = slab total thickness; F_x , F_y = forces per unit length in steel bars along the x and y directions, respectively; d_{1x} , d_{1y} = slab effective depth

along the x and y directions, respectively; d_{2x} , d_{2y} = distance from slab compressive face to the compressive reinforcement along the x and y directions, respectively; and N_x and N_y = thrust per unit length in the x and y directions, respectively.

A significant modification to the present model is obtained by considering plasticity effects for the ultimate resistance of uniformly loaded rectangular slabs with all edges restrained, as discussed in References [17, and 19]. If it is assumed that the slab has equal top and bottom reinforcement ratios then it can be shown that:

$$\frac{wL_x^2}{24} (3 \frac{L_y}{L_x} - 1) -$$

$$0.85 f'_c \beta_1 h^2 \left(\frac{L_y}{L_x} (0.188 - 0.141 \beta_1) \right.$$

$$+ (0.479 - 0.245 \beta_1) + \frac{\epsilon'_y}{16} \left(\frac{L_x}{h} \right)^2 \frac{L_y}{L_x} (3.5 \beta_1 - 3)$$

$$+ \frac{\epsilon'_x}{16} \left(\frac{L_x}{h} \right)^2 \left[2 \frac{L_y}{L_x} (1.5 \beta_1 - 1) + (0.5 \beta_1 - 1) \right]$$

$$- \frac{\beta_1}{16} \frac{L_y}{L_x} \left(\frac{L_x}{h} \right)^4 \left[(\epsilon'_y)^2 \frac{L_y}{L_x} + (\epsilon'_x)^2 \right] \quad (3)$$

$$+ 2F_y (d_{1y} - d_{2y}) + 2F_x \left[\left(\frac{L_y}{L_x} \right) (d_{1x} - d_{2x}) \right] +$$

$$+ \left[\left(\frac{L_y}{L_x} \right) N_x (d_{1x} - \frac{h}{2}) + N_y (d_{1y} - \frac{h}{2}) \right]$$

Also,

$$\epsilon' = \epsilon + \frac{2t}{L} = \frac{\left(\frac{1}{hE_c} + \frac{2}{LS}\right) \left[0.85 f'_c \beta_1 \left(\frac{h}{2} - \frac{\Delta}{4}\right)\right]}{1 + 0.2125 \frac{f'_c \beta_1 \beta L^2}{\delta} \left(\frac{1}{hE_c} + \frac{2}{LS}\right)} \quad (4)$$

in which t is the outward displacement of the slab boundary, ϵ'_x and ϵ'_y represent the shortening of the slab in the x and y directions respectively including elastic, creep, and shrinkage effects, and can be computed from the expression, as provided in [19]. E_c is the elastic modulus for concrete, S is the amount of lateral restraint provided by the support and backfill (E_c and S are provided in units of stress), Δ is the amount of central deflection for the slab, and β is a fraction representing the location of a yield line with respect to the slab dimension L (i.e., a hinge at the center provides $\beta = 0.5$, etc.). Eq. (5) can be employed for the x and y directions by introducing the corresponding values for the various parameters. When the values of ϵ'_x and ϵ'_y are derived from Eq. (4) they can be introduced into Eq. (3) from which one obtains the peak resistance, w_{max} . The resistance function is then computed as discussed in [12, and 14], and briefly summarized later herein.

The difference in the structural response between the simulated nuclear and the localized loads has to be reflected in this mechanism. All the slabs under consideration had a length to width ratio of 4:1 which implies that the

behavior under uniformly distributed loads tends to approach that of one-way slabs [19]. However, when the loads are localized the behavior should be in the two-way slab range. The adjustment is performed through the ratio L_y/L_x which appears in Eqs. (2, and 3). For the nuclear domain that ratio should assume the actual length of width ratio for the particular slab (4 in the present case), while in the conventional domain it is quite smaller reflecting the localized effects. Information presented in [8] may suggest that the ratio L_y/L_x can vary between 1 to 2, or as suggested in [11] that ratio can be defined by the anticipated pressure distribution over the slab.

Point C in Figure 3 represents the transition into the tensile membrane region. One may compute the tensile membrane resistance by employing formulations that were proposed by Park and Gamble [19], or a more generalized formulation [12] that may describe the slab resistance just before, during, and after the transition into the tensile region, as follows.

$$w' = \frac{8(M_n + TA)}{L^2} \quad (5)$$

in which w' = uniformly distributed load on membrane (force per unit length); M_n = bending moment in the slab central region; T = reinforcement tensile force; Δ = central deflection; and L = membrane span length. The central deflection for points B and C can be assumed as follows: for point B, $0.5h$, and for point C, $2h$. The resistance curve segments between these characteristic points are defined next, as illustrated in Figure 3.

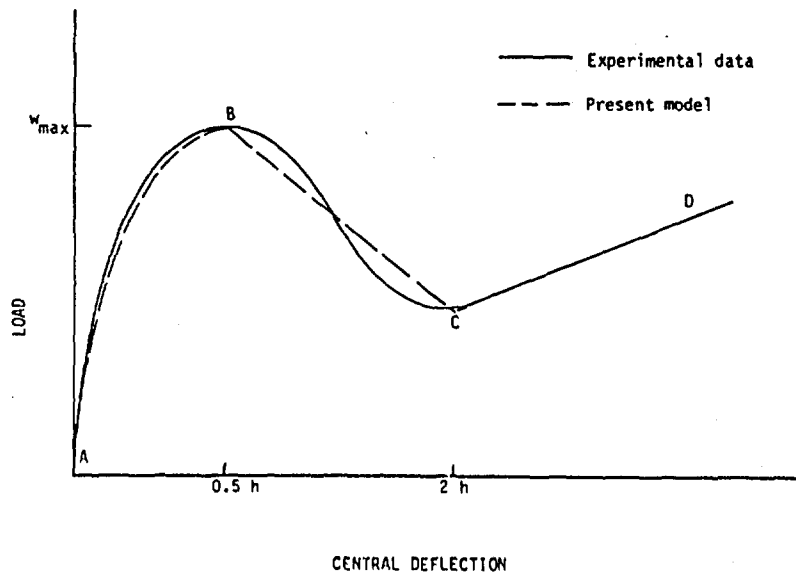


Fig. 3 - Load-deflection relationship

Segment AB: Four conditions are known for segment AB of the curve that include the slope (K_0) where K_0 is the initial stiffness of the slab and can be approximated as discussed in [2,11,12, and 14], and value (0) at A, and the slope (0) and value (w_{max}) at B. A second order polynomial which has the following form can be used to satisfy these conditions:

$$w = \left(-\frac{4w_{max}}{h^2} \right) \Delta^2 + \left(\frac{4w_{max}}{h} \right) \Delta \quad (6)$$

where w_{max} is the value of w obtained from Eqs. (2, or 3).

Another possibility is to employ a third order polynomial which satisfies the same conditions, as discussed in [12].

Segment BC: The decay in structural resistance beyond the peak at B was previously formulated in the literature [17, and 19] and such models may be employed for analysis. Here, however, it is assumed that the behavior between B and C is linear (which is reasonably close to experimental observations, and which simplifies the numerical procedures). Point C is defined by the straight line CD, and a central deflection at C which is assumed to be $2h$.

Segment CD: A straight line which is defined by Eq. (2).

Externally Applied Thrust

The peak structural resistance in the compression membrane mode can be enhanced if external in-plane compressive forces are applied to the slab, as discussed in [12]. For the box-type structures under consideration those forces vary with time since they are generated by the horizontal component of the pressure pulse that propagates vertically through the soil. In the procedure adopted here from [14], the vertical pressure pulse in the soil is traced at each time step, the load on the vertical wall is computed, and then one computes the reactions in the roof and floor slabs that correspond to the applied load. These reactions are the externally applied compressive forces that enhance the peak structural resistance, and are introduced into Eqs. (2, or 3) as N_x and N_y , respectively, in the slabs. In the nuclear domain, the horizontal stresses which are generated by the propagating pressure pulse in the backfill can be computed as a ratio of the vertical stress. That ratio was estimated to be about 1.0 for clay while about 0.5 for sand [9,25, and 26] and from the same references one can obtain values for the seismic wave velocity in the backfill materials that can be employed for the determination of the loading condition on the vertical walls. This procedure represents one aspect of soil-structure interaction and its effect on structural behavior.

Under localized effects the contribution of the in-place forces is not as direct as in the

nuclear domain since the pressure will reach the center of the loaded slab earlier than the perpendicular slabs. That time delay needs to be reflected in the structural formulation as a function of range and seismic velocity. Since the attenuation of pressures is quite significant that influence will be considerably smaller than in the nuclear domain, and the values of N_x and N_y will be affected considerably depending on the range from the detonation.

Dynamic Shear Resistance

Shear resistance in slabs was discussed by Park and Gamble [19], but the issues of direct shear under dynamic effects were not considered. The type of shear failures that was observed in the simulated nuclear tests [9, and 22] resembled interface shear transfer in flexural members with very small shear span to depth ratios. An excellent discussion of interface shear transfer was provided by Park and Paulay [18], and it can be supplemented with additional information on shear strength in reinforced concrete structures from more recent publications, as discussed in [14]. The present model is based on the developments reported in [14], and is briefly presented next.

The information that is available for interface shear transfer in members having well anchored main reinforcement without axial (in-plane) forces, and a shear span to depth ratio less than about 0.5 can be employed to form the relationship between shear stress to shear slip as illustrated in Figure 4. The various straight line segments in that model are defined as follows.

Segment OA: the response is elastic, and the slope, K_s , of the curve is defined by the shear resistance, τ_s , for a slip of 4×10^{-3} in. (0.1 mm). That resistance is given by the expression:

$$\tau_s = 165 + 0.157 f'_c \quad (7)$$

here both τ_s and f'_c are in psi. The initial response should be taken as elastic to not greater than $\tau_m/2$.

Segment AB: the slope of the curve decreases continuously with increasing displacements until a maximum strength, τ_m , is reached at a slip of 12×10^{-3} in. (0.3 mm). The maximum strength, τ_m , is given by the expression

$$\tau_m = 8 \sqrt{f'_c} + 0.8 \rho_{vt} f_y \leq 0.35 f'_c \quad (8)$$

where τ_m , f'_c , and f_y are in psi, ρ_{vt} is the ratio of total reinforcement area to area of plane which it crosses, and f_y is the yield strength of reinforcement crossing the plane.

Segment BC: the shear capacity remains constant with increasing slips. C corresponds to a slip of 24×10^{-3} in. (0.6 mm), as noted in the discussion for Segment AB.

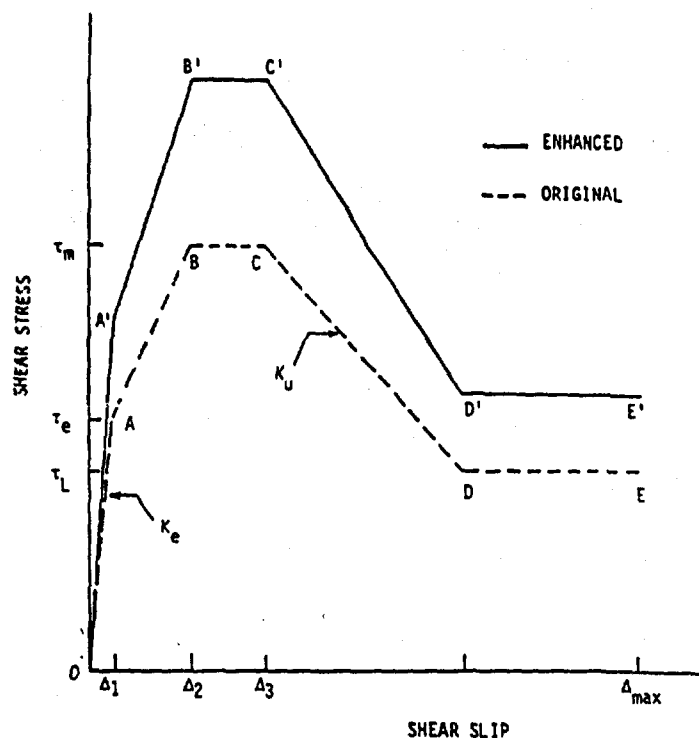


Fig. 4 - Dynamic shear resistance (after [14])

Segment CD: the slope of the curve is negative, constant, and independent of the amount of reinforcement crossing the shear plane. The slope (in units of psi/in.) is given by the expression:

$$K_u = 2,000 + 0.75 f'_c \quad (9)$$

Point D is located at a limiting shear strength τ_L , as defined later.

Segment DE: the capacity remains essentially constant until failure occurs at a slip of $\Delta_{s,max}$. For a well-anchored bar the slip for failure is given by the expression

$$\Delta_{s,max} = C \left(\frac{e^x - 1}{120} \right) \quad (\text{in inches}) \quad (10)$$

where

$$x = \frac{900}{2.86 \sqrt{f'_c} d_b} ; C = 2.0 ;$$

$$d_b = \text{bar diameter (in inches)} \quad (11)$$

and the limiting shear capacity, τ_L , is given by

$$\tau_L = \frac{0.85 A_{s,b} f'_s}{A_c} \quad (\text{psi}) \quad (12)$$

where: $A_{s,b}$ = area of bottom reinforcement; f'_s = tensile strength of bottom reinforcement; and A_c = cross-sectional area.

This model which represents a shear stress-shear slip relationship is based on data from static tests, and without the effects of compressive stresses on the concrete shear strength. As a result it was required to modify the model, and to include such effects, as discussed in [14]. Another change was introduced into the original model for shear in order to account for reversal loads, also presented in [14]. The shear stress-shear slip relationship was defined as an envelope for positive and negative displacements (since the slabs had the same amount of reinforcement for tension and compression, no modification of the relationship was required for rebound displacements), and the following simple numerical scheme was introduced to allow for displacement reversals. As the shear force loads the slab support the stress-displacement relationship follows the envelope in the corresponding direction, and upon unloading it changes to motion along the initial slope until a zero stress is obtained. At that point the relationship changes again to a straight line

which will lead it to a point on the envelop that is equivalent to the previous point on the envelop, but represents displacements in the opposite direction. If the slab continues to displace in that direction one follows the shear envelop until a reversal occurs which follows a similar pattern as before. This pattern can be followed until the system returns to rest, or the shear displacement reaches Δ_{max} that indicates a shear failure.

In this study it was assumed that the mechanisms for direct shear resistance are the same in both the nuclear and conventional domains of response, while the only difference will be introduced due to the definition of the "acting slab". In the nuclear domain the entire slab is effected, and the direct shear failure appears at the slab-wall connection. Under localized loads the affected zone will be smaller than the total slab, as previously discussed herein, and the failure will occur along those boundaries.

Effective Mass

In the description of the structural behavior and the corresponding discussion it was shown that the shear and flexural responses seemed to be rather independent. In order to validate this observation it was assumed that the present analysis would be conducted on two SDOF systems one for flexural- and the other for shear-type behavior. One of the important SDOF parameters is the system mass, and one can employ the well known procedures of approximate dynamic analysis for such purpose, as discussed in [14]. This information was employed in the present flexural analysis since the aspect ratio for the roof slabs (i.e. length to width ratio) was 4 in all the cases under simulated nuclear effects, and according to present knowledge of slab behavior these slabs should behave as one-way systems [19]. There were two slab thicknesses that were considered, the first type was 5.6 inches (142 mm), and the second was 13.5 inches (343 mm). In the flexural analysis it was assumed that the thinner slabs would exhibit a more ductile behavior, hence the mass factor 0.33 was chosen, while the thicker slabs should be more rigid and the mass factor 0.5 was employed. Furthermore, since the soil is pushed by the applied pressure to load the structure, and since there was sufficient evidence [9 and 10] to support the assumption that only part of the soil mass participated in the flexural motions of the systems it is required to assign a mass factor to the soil overburden. Also, it is known from previous studies on dynamic soil arching [10] that stiff structures attract higher loads than flexible structures, and therefore it was reasonable to assume that the same mass factors employed for the determination of slab effective mass can be used for the soil mass (i.e. thin slabs: 0.33, and thick slabs: 0.5). For the shear analyses it was known that failure occurred early and the entire roof slab was pushed into the box, followed by the soil overburden. This suggested to employ a mass

factor of 1.0 for the slab and soil in the SDOF for shear.

When the behavior of slabs under localized effects is of interest one needs to re-evaluate these mass factors based on an assumed deformation pattern, similarly to the approach proposed by Biggs [2], and Kiger and Painter [11]:

$$K_M = \left[\int_A m \phi^2(x,y) dA \right] / M_t \quad (13)$$

in which K_M = mass factor, m = mass per unit area of slab, $\phi(x,y)$ = deformed shape of slab, and M_t = total slab mass.

For fixed edged slabs having a square shape K_M varies between 0.31 in the elastic-plastic range and 0.33 in the plastic range. If the slab length to width ratio is 2 then K_M varied between 0.41 for the elastic-plastic range and 0.25 for the plastic range.

Regarding the mass factor for the soil under conventional detonation effects one can employ the mass of a cone having a base defined by the effective slab and the height equals the range from the center of slab to the charge, as shown in Figure 5. The resulting mass factor is 0.33 indicating that only on third of the total soil backfill, corresponding to the effective slab, will participate in the motion. This behavior is unlike the uniform assumptions for the slab under nuclear effects.

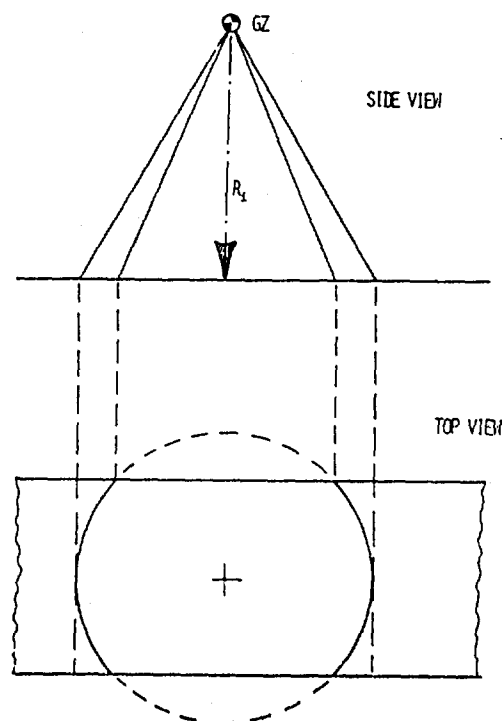


Fig. 5 - Effective mass simulation

Damping Ratio

Typical damping ratios, ζ , for reinforced concrete structures are between 5% to 10%, and such factors can be incorporated into SDOF analyses. However, one should account for radiation damping due to dynamic soil-structure interaction, as discussed in [14], and it was decided for the analysis of the structures under simulated nuclear effects to use ζ values between 20% to 40%. In the present study a value of 20% was used for the flexural analysis (30% for the thick slab where more soil-structure contact was anticipated), and 5% for the shear analysis since radiation damping was already included in the flexural analysis. This combination of damping ratios was chosen since it was compatible with existing information on the behavior of these, and other similar systems. Although one may expect somewhat higher SSI damping under localized effects it is not expected that such values would exceed 40%, and therefore it was decided to study the damping effects in future research.

NUMERICAL PROCEDURE

The behavior and parameters as described in the preceeding sections were combined to perform the evaluation of shallow-buried reinforced concrete structures similarly to the procedure in [14], and the present computational scheme is illustrated in Figure 6. The numerical integration of the SDOF equations of motion was performed by the Newmark β method, as discussed in [12, and 14], for two SDOF systems.

The present approach consists of two SDOF systems one for evaluating the flexural response, considering the response of a section located at the center of the slab while the second is employed for monitoring the shear response at the supports as shown in Figure 7. For each time step the motions of the slab center are computed, as discussed in [14], from which it is possible to derive a distribution of inertia forces on the slab, and then combine such forces with the applied load for obtaining a shear force at the supports. That shear force

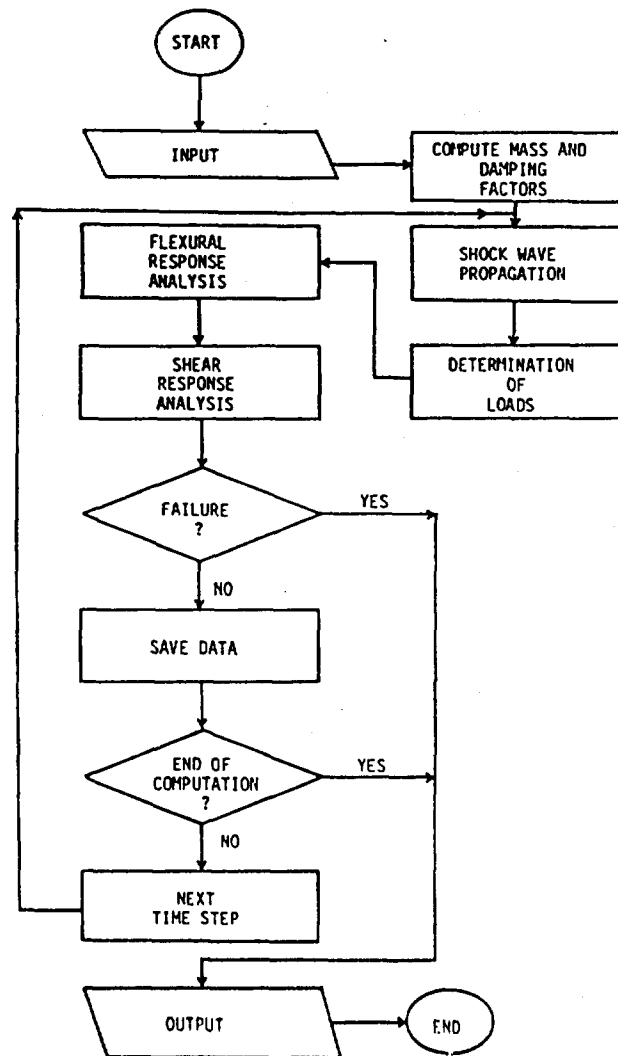
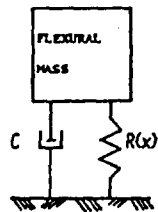


Fig. 6 - Numerical procedure

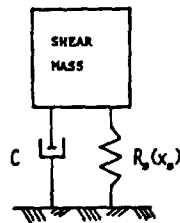
FIRST STAGE



INPUT
FORCE $F(t)$
MATERIALS
GEOMETRY

OUTPUT
 $A(t)$, $v(t)$, $x(t)$

SECOND STAGE



INPUT
SAME

OUTPUT
 $A_s(t)$, $v_s(t)$, $x_s(t)$

Fig. 7 - SDOF systems

is used to drive the second SDOF system which provides the shearing motions at the supports. The slab responses at the center and at the supports is compared to failure criteria which include an ultimate tensile strain of reinforcing bars, a critical shear slip $\Delta_{s,max}$ at the supports, and also a central deflection which may limit the serviceability of the structure. In all cases the structural dimensions and material properties were "as tested", and the applied loads were based on blast pressure measurements for the simulated nuclear cases [9, and 22], or the conventional detonations [8]. For the blast pressure it was found in [14] that the best results were obtained when the peak pressure was a simple average of all the peak pressures recorded by the blast pressure gauges in a test, and the time history was a segmental approximation of one of the records, as described in [12, and 14]. For the localized effects the load pulse was based on the averaging process which provided an equivalent uniformly distributed pressure function, as previously discussed herein, and the information provided in [8].

The present highly nonlinear problems were approximated by two uncoupled simpler problems, each represented by a separate SDOF system. Under such conditions it was possible to employ parameters that can be defined as equivalent mass, damping, and structural resistance to be driven by the corresponding load functions (i.e. an equivalent blast pressure pulse for the flexural analysis, and the resulting support shear force for the shear analysis).

RESULTS

Seven cases under a simulated nuclear load have been analyzed by the present approach [14], and the results are presented in Table 1. The first six cases have been analyzed previously based on nominal design dimensions and material properties, as discussed in [12], and the results were, on average, within seven percent from the experimental data. In [14], the "as tested" properties were used together with the contributions of variable in-plane forces in the slab, and shear stresses at the supports. The improvements of the results, as reported in [14] compared to those obtained earlier [12] is clear, as shown in Table 1, and it is even possible to specify accurately the time at which the shear failure occurred.

When the present approach for computing the structural response under simulated nuclear effects was employed for the analysis of the structures under conventional detonation effects the outcome was far from the observed behavior, as reported in [8]. The results indicated that most structures exhibited shear failures or large flexural deformations, unlike the actual structural behavior. When these results were inspected it became obvious that one needs to activate different behavioral parameters in the analysis. Also, the pressures were assumed to be uniformly distributed similarly to a nuclear environment, and that caused a significant overloading of the structures. These changes were implemented in stages for observing the effects of such variations on the results. Soon it became clear that indeed the proposed modifications gradually improve the results. For example, in Table 2 are the results for the structures under the conventional detonation loads when first the only change was in the applied load using the circular averaging procedure (noted by column ** in Table 2), as previously described here, and then are the results when a modified resistance function of Eq. (2), damping properties, and thrust effects were combined with the modified load (noted by column *** in Table 2). The new results were significantly closer to the observed behavior, as described in [8]. However, since not all permanent deflections were reported in [8], it was impossible to compute the actual difference between the present analytical results and the experimental data for all cases. An important observation relates to the time for shear failure which is usually less than 0.1ms for the conventional cases, as compared to slightly over 1ms for the nuclear cases. Another important observation was made based on the analysis of the shear failures (cases 3C5 and 3D8), and it is related to the nature of these failures. The analyses were performed several times with time steps between 1.0ms to 0.001ms, and it was noticed that for structure 3C5 the failure occurred in the time between 0.05ms to 0.1ms, while for structure 3D8 the failure always occurred within the first computational time step. Based on these results one can conclude that structure

3C5 exhibited a dynamic direct shear failure which is a form of structural response while structure 3D8 failed as a result of a wave propagation phenomenon. The difference in the observed shear failure response was caused by the closer detonation for case 3D8, as compared to case 3C5 (i.e. a scaled range of 0.725 for 3D8, and 0.98 for 3C5).

DISCUSSION AND CONCLUSIONS.

Similar structures tend to exhibit different behaviors depending on the nature of loading conditions to which they are subjected. These conditions can activate different soil-structure interaction and structural resistance mechanisms that will be responsible for the observed behavioral differences. When the analyst employs a multi-purpose numerical approach, such as a powerful finite element or finite difference code, the computations and interpretation of results require large resources before a meaningful conclusion is reached. This is primarily due to the fact that such codes are indeed multi-purpose, and as a result they cannot be easily "tuned" to specific behavioral ranges. The computation procedure will tend to "activate" a number of possible responses, and only after some time the dominant modes of behavior will govern. Furthermore, the difficult issue of direct shear usually will require special features in a multi-purpose code, otherwise the computation will not be able to exhibit such effects.

The present approach is an example of removing many possible behavioral modes from the analyses, and including only those that are known, or that are expected to dominate the structural response. Furthermore, the present approach is such that different types of input data will activate different components of the program, and as a result one achieves an efficient numerical treatment of various structural analyses. The components to be employed for each computation will be chosen in an objective manner by the computer code following the behavioral aspects of hardened systems under nuclear, or conventional detonation effects, as previously presented herein. Hence, this is a simplified "tuned" numerical procedure based on the analytical SDOF approach, and the similarity between the present approach and the operational principles for choosing an experimental gauge, such as a SDOF accelerometer, were the reasons behind the definition of the term "numerical gauge". The overall approach is rather simple, one creates a "gauge" that is tuned automatically by the code to a specific expected range of behavior, and then subjects the "gauge" to the anticipated (or known) loading conditions. The "gauge", as illustrated in Figure 8, provides data on the structural behavior indicating, quite accurately, the magnitude of significant behavioral modes. The analyst can employ such information for "tuning" a multi-purpose numerical code from which he can obtain detailed information for the entire structure on motions,

stresses, cracking, etc. that the present approach cannot provide. Also, the present approach can be used for fast and inexpensive assessments of structures during the design stage in order to verify various assumptions regarding the effects of design parameters on the anticipated response.

The information and examples presented here illustrate how such a numerical approach can be adopted and modified for similar cases. Naturally, the analyst may wish to add or remove parts of the "numerical gauge" for tuning the method to a specific behavioral range. Also, it would be possible to employ fundamental structural analysis capabilities in order to generate the required resistance functions from the moment-curvature relationships that can be computed for a given cross-section. Such efforts are currently underway at the University of Minnesota.

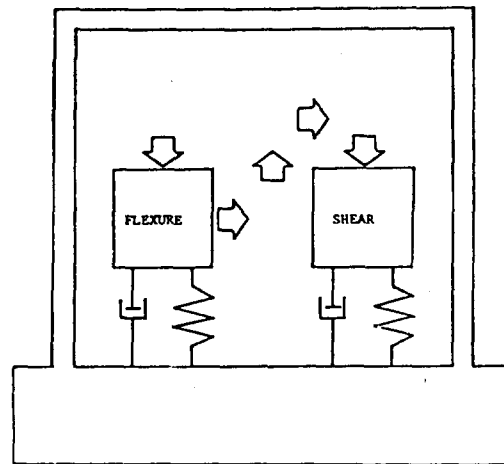


Fig. 8 - Numerical gauge concept

REFERENCES

1. Beck, J.E., et al. "Single-Degree-of-Freedom Evaluation", Final Report AFWL-TR-80-99, Air Force Weapons Laboratory, March 1981.
2. Biggs, J.M., "Introduction to Structural Dynamics", McGraw-Hill, 1964.
3. Crawford, R.E., et al., "Protection from Nonnuclear Weapons", Air Force Weapons Laboratory, Technical Report No. AFWL-TR-70-127, February 1971 (limited distribution).
4. Drake, J.L., and Little, C.D., "Ground Shock from Penetrating Conventional Weapons", Proc. Symposium on the Interaction of Non-Nuclear Munitions with Structures, USAFA Colorado Springs, May 1983.

TABLE 1

Summary of Results for Simulated Nuclear Environment

Test No.	Observed Behavior or Failure Mode	Measured Permanent Deflection Δ (mm)	Computed Permanent Deflection Δ_2 (mm) from [12]	Computed Permanent Deflection Δ_1 (mm) from [14]	Δ_1/Δ	Δ_2/Δ
1*	Flexure	12.7	19.5	16.2	1.28	1.53
2*	Shear Failure	Shear Failure	Shear Failure	Shear Failure at 1.02 ms	1.0	1.0
3*	Flexure	152.4	124.5	152.4	1.0	0.81
4*	Flexure	304.8	368.3	309.9	0.98	1.16
5*	Flexure	78.4	72.1	81.3	1.03	0.91
6*	Shear Failure	Shear Failure	Shear Failure	Shear Failure at 1.06 ms	1.0	1.0
LB**	Flexure	185.4	Not performed	182.9	0.99	NA
				Average:	1.04	1.07

* - Data from Ref. [9]

** - Data from Ref. [20]

5. Henrych, J., "The Dynamics of Explosions and Its Use", Elsevier, 1979.
6. Ghaboussi, J., Millavec, W.A., and Isenberg, J., "R/C Structures Under Impulsive Loading", ASCE Journal of Structural Engineering, Vol. 110, No. 3, March 1984, pp. 505-522.
7. Keenan, W.A., "Shear Stress in One-Way Slabs Subjected to Blast Load", Technical Memorandum, M-51-77-10, Naval Civil Engineering Laboratory, August 1977.
8. Kiger, S.A., and Albritton, G.E., "Response of Buried Hardened Box Structures to the Effects of Localized Explosions", U.S. Army Engineer Waterways Experiment Station, Technical Report SL-80-1, March 1980 (limited distribution).
9. Kiger, S.A., Getchell, J.V., Slawson, T.R., and Hyde, D.W., "Vulnerability of Shallow-Buried Flat Roof Structures", U.S. Army Engineer Waterways Experiment Station, Technical Report SL-80-7, six parts, September 1980 through September 1984, (Limited distribution).
10. Kiger, S.A., "The Effects of Earth Cover on the Response of Reinforced Concrete Slabs", International Symposium on Dynamic Soil-Structure Interaction, University of Minnesota, September 1984.
11. Kiger, S.A., and Painter, J.T., "A Computational Procedure for Response of Buried Structures to Conventional Weapons", Proc. 2nd Symposium on the Interaction of Non-Nuclear Munitions with Structures, Panama City Beach, Florida, April 15-18, 1985, pp. 41-44.
12. Krauthammer, T., "Shallow Buried RC Box-Type Structures", ASCE Journal of Structural Engineering, Vol. 110, No. 3, March 1984, pp. 637-651.
13. Krauthammer, T., and Parikh, M., "Structural Response Under Localized Dynamic Loads", Proc. 2nd Symposium on the Interaction of Non-Nuclear Munitions with Structures, Panama City Beach, Florida, April 15-18, 1985, pp. 52-55.
14. Krauthammer, T., Bazeos, N., and Holmquist, T.J., "Modified SDOF Analysis of RC Box-Type Structures", ASCE Journal of Structural Engineering, Vol. 112, No. 4, April 1986, pp. 726-744.
15. Murtha, R.N., and Crawford, J., "Dynamic Shear Failure Predictions of Shallow-Buried Reinforced Concrete Slabs", Technical Memorandum M-51-81-04, Naval Civil Engineering Laboratory, May 1981.

TABLE 2
Results for Conventional Detonation, Modified Approaches

Test No.	Range [m]	Scaled Range $R/W^{1/3}$	Observed Behavioral or Failure Mode	Measured Permanent Condition, Deflection [mm]	Computed Permanent Deflection [mm] **	Computed Permanent Deflection [mm] ***
3C1*	2.44	2.9	Flexure	No damage	22.6	19.8
3C2*	1.83	2.17	Flexure	Moderate Cracking	59.7	45.5
3C3*	1.22	1.45	Flexure	267.0	>280.0 at 11.6 ms	254.2
3C5*	0.82	0.98	Shear	Massive Failure	Shear Failure at $t < 0.7$ ms	Shear Failure at $t < 0.63$ ms
3D1*	2.44	2.9	Flexure	No visible damage	13.5	10.7
3D2*	1.83	2.17	Flexure	No visible damage	32.2	24.4
3D6*	1.22	1.45	Flexure	Minor Flexural Cracking	107.7	75.4
3D7*	0.82	0.98	Flexure	Moderate Flexural Cracking	462.0	141.3
3D8*	0.61	0.725	Shear	Catastrophic Shear Failure	Shear Failure at $t < 0.1$ ms	Shear Failure at $t < 0.001$ ms

* Data from Ref. [8].

** Modified Load only

*** Further Modification

16. Murtha, R.N., and Holland, T.J., "Analysis of WES FY82 Dynamic Shear Test Structures", Naval Civil Engineering Laboratory, Technical Memorandum No. 51-83-02, December 1982.
17. Park, R., "Ultimate Strength of Rectangular Concrete Slabs Under Short-Term Uniform Loading with Edges Restrained Against Lateral Movement", Proc. Inst. Civ. Eng., Vol. 28, June 1964, pp. 125-150.
18. Park, R., and Pauly, T., "Reinforced Concrete Structures", Wiley-Interscience, 1975.
19. Park, R., and Gamble, W.L., "Reinforced Concrete Slabs", Wiley-Interscience, 1980.
20. Parsons, R., and Rinehart, E., "Kachina Test Series: Butterfly Maiden", Air Force Weapons Laboratory, Final Report No. AFWL-TR-82-132, Vol. I-II, June 1983 (Limited distribution).
21. Ross, T.J., "Direct Shear Failure in Reinforced Concrete Beams Under Impulsive Loading", Air Force Weapons Laboratory, Final Report No. AFWL-TR-83-84, September 1983.
22. Slawson, T.R., "Dynamic Shear Failure of Shallow-Buried Flat-Roofed Reinforced Concrete Structures Subjected to Blast Loading", Final Report SL-84-7, U.S. Army Engineer Waterways Experiment Station, April 1984.
23. Vretblad, B., "Versuche Mit Ladungen im Boden - Ergebnisse", Proc. 6th International Symposium on Protective Structures, Monnheim, West Germany, 25-27 September 1984.
24. Westine, P.S., and Friesenhahn, G.J., "Free-Field Ground Shock Pressures From Buried Detonations in Saturated and Unsaturated Soils", Proc. Symposium on the Interaction of Non-Nuclear Munitions with Structures, USAFA Colorado Springs, May 1983.
25. Windham, J.E., and Curtis, J.O., "Effect of Backfill Property and Airblast Variations on the External Loads Delivered to Buried Box Structures", Final Report S-78-5, U.S. Army Engineer Waterways Experiment Station, March 1981.
26. Windham, J.E., "Soil Property Data for Foam Hest Tests of Shallow Buried Structures with Clay Backfill", U.S. Army Engineer Waterways Experiment Station, March 1981.
27. Wolf, J.P., "Dynamic Soil-Structure Interaction", Prentice-Hall, 1985.

Discussion

Mr. Cooper (Defense Nuclear Agency): Your system seems to shortcut and look at the deficiency of a single degree-of-freedom system in having to identify the failure mode for your analysis to work. If I understand you correctly, you are saying as long as you have modelled the either-or situation, your single degree-of-freedom can pick up either the flexure or shear type of failure.

Mr. Krauthammer: Essentially, the system consists of having the dominant failure mechanisms incorporated in it. Once the load is applied the system will lock into the dominant failure mechanism between the various modes that we provided. The results seem to indicate it indeed detects the one that causes failure. It provides information both on flexure, shear, and in-plane effects. It reasonably predicts soil-structure interaction and damping. So, I believe, from the information that can be provided from this analysis, one could have a very nice global picture of structural behavior without going into details.

ACTIVE ONE-DIMENSIONAL PROTECTIVE LAYERS

SHLOMO GINSBURG
KANSAS UNIVERSITY TRANSPORTATION CENTER
LAWRENCE, KANSAS

THIS PAPER DESCRIBES NUMERICAL ANALYSES OF ONE-DIMENSIONAL CONFIGURATIONS CONSISTING OF HIGH EXPLOSIVE CHARGES EMBEDDED IN INERT PROTECTIVE LAYERS. EMPHASIS IS PUT ON THE FEASIBILITY OF EMPLOYING ACTIVE LAYERS, AS MEANS FOR ACHIEVING PROTECTION AGAINST BLAST AND OTHER LOADS. THE BEHAVIOR OF ACTIVE PROTECTION SCHEMES IS DISCUSSED. SEVERAL PARAMETERS ARE STUDIED, IN ORDER TO DETERMINE FEASIBLE AND EFFECTIVE ARRANGEMENTS OF LAYERS. THE ADVANTAGES OF ACTIVE PROTECTION OVER A PASSIVE ONE IS POINTED OUT. FURTHER STUDIES ARE RECOMMENDED.

INTRODUCTION

MOST "CONVENTIONAL" PROTECTIVE SCHEMES ARE BASED ON PASSIVE LAYERS [1]; I.E., THEY CONSIST OF INERT LAYERS WHICH REDUCE THE EFFECTS OF DONOR SYSTEMS TO AN ACCEPTABLE LEVEL. THE MAIN DISADVANTAGES OF SUCH PROTECTION ARE: (1) USUALLY, THEY ARE EFFECTIVE FOR PROTECTION AGAINST A GIVEN TYPE OF DONOR, AND IT IS DIFFICULT OR IMPOSSIBLE TO ACCOUNT FOR OTHER DONORS, (2) THEY OFTEN FAIL UNDER MULTIPLE LOADS FROM SEVERAL DONORS, (3) IT IS RELATIVELY EASY TO DEVELOP NEW DONORS WHICH RENDER THE PASSIVE PROTECTION USELESS, AND (4) PASSIVE PROTECTION IS VERY COSTLY. THIS STUDY DEALS WITH A DIFFERENT CONCEPT, THAT OF ACTIVE PROTECTION. THE BASIC IDEA IS TO EMPLOY HIGH EXPLOSIVE (H.E.) CHARGES EMBEDDED IN CONVENTIONAL LAYERS, FIG. 1

(IT SHOULD BE NOTED THAT, THE SENSORY SYSTEM IS NOT DISCUSSED IN THIS PAPER). AS SHALL BE SHOWN LATER, ACTIVE PROTECTION CAN OVERCOME THE MAJOR SHORTCOMINGS OF PASSIVE ONES.

IN THIS STUDY, ONE-DIMENSIONAL LAYERS ARE TREATED. ALL THE CASES ARE BASED ON NUMERICAL ANALYSES [2]. THE OUTCOME OF THIS RESEARCH CAN BE CONSIDERED A (PRELIMINARY) FEASIBILITY STUDY OF THE CONCEPT. EACH CASE DESCRIBED HERE CONSISTS OF SINGLE OR MULTI-LAYERED CONFIGURATION, SUBJECTED TO A TRIANGULAR (P, t) PRESSURE PULSE WHICH REPRESENTS THE EFFECTS OF A DONOR (MAINLY BLAST). COMPARISONS BETWEEN THE BEHAVIOR OF PASSIVE AND ACTIVE LAYERS HAVING (VIRTUALLY) THE SAME DIMENSIONS SERVE FOR STUDYING THE CHARACTERISTICS OF BOTH PROTECTION SCHEMES.

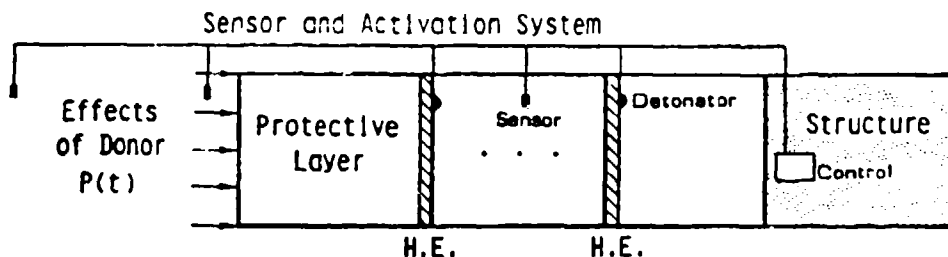


FIGURE 1: SCHEMATIC OF ACTIVE PROTECTION.

SINGLE CHARGE

THE FIRST CASE DISCUSSED HERE CONSISTS OF A CONFIGURATION WITH A SINGLE HE CHARGE PLACED IN THE MIDDLE OF A SOLID. THE STRUCTURE IS SUBJECTED TO A SHORT HIGH-PRESSURE PULSE (REPRESENTING A DETONATION OF SEVERAL THOUSAND POUNDS OF TNT). FIG. 2 SHOWS THE EARLY STAGES

OF THE PROCESS, WHERE THE APPLIED LOAD INDUCES A SHOCK WAVE PROPAGATING IN THE POSITIVE x -DIRECTION (TO THE RIGHT), AND THE ACTIVATED CHARGE RESULTS IN SHOCK FRONTS WHICH PROPAGATE IN TWO DIRECTIONS. FIG. 3 SHOWS THE STRESS PROFILE AT A LATER STAGE, WHEN INTERACTION BETWEEN THE SHOCK FRONTS TAKES PLACE.

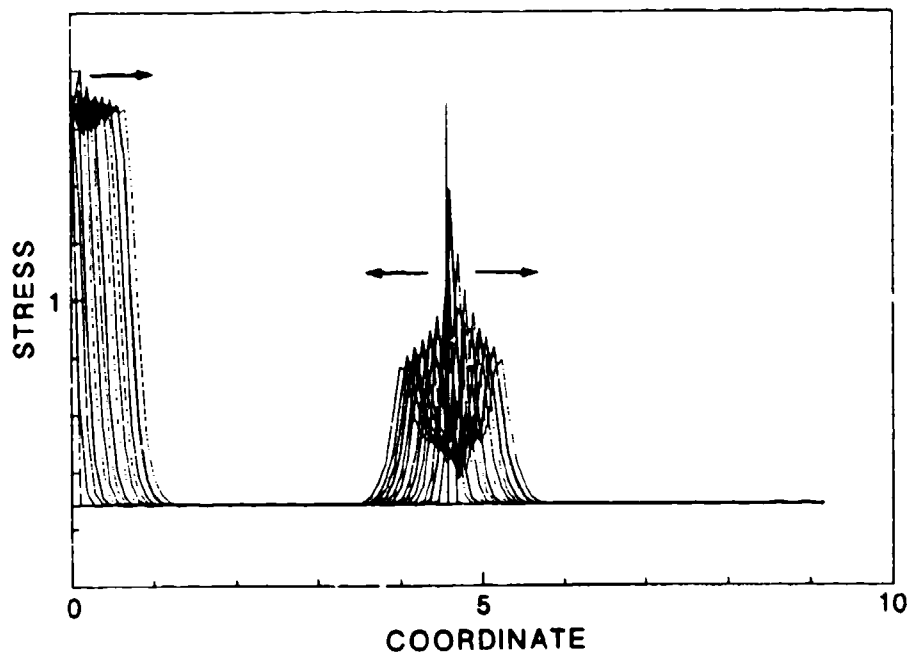


FIGURE 2: STRESS PROFILES AT EARLY STAGE.

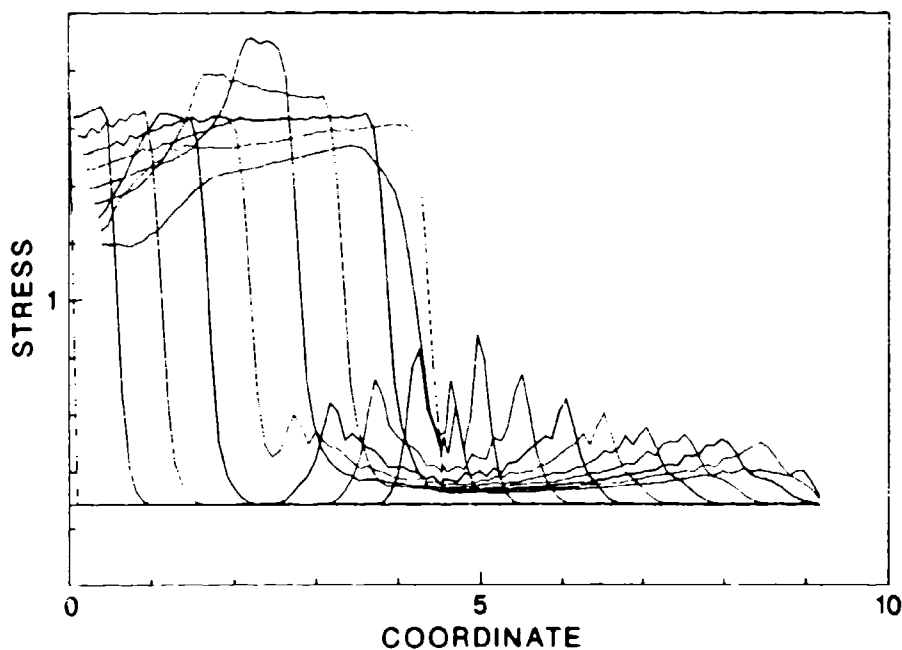


FIGURE 3: STRESS PROFILES AT TIME OF FIRST SHOCK INTERACTION.

THE STRESS HISTORY AT THE STRUCTURE'S RIGHT FACE IS SHOWN IN FIG. 4. HERE, COMPARISON BETWEEN ACTIVE AND PASSIVE CONFIGURATIONS IS DISPLAYED. IT IS OBVIOUS THAT THE ACTIVE PROTECTION REDUCES THE STRESS AT THE FACE UNDER CONSIDERATION BETTER THAN A PASSIVE ONE. ALTERNATIVELY, BY EMPLOYING ACTIVE LAYERS, LESS MATERIAL IS REQUIRED TO ACHIEVE THE SAME LEVEL OF PROTECTION.

WHEN THE PEAK PRESSURE OF THE APPLIED LOAD IS DOUBLED, THE ACTIVE PROTECTION STILL DEMONSTRATES THE ABILITY TO REDUCE THE STRESSES BETTER THAN A PASSIVE CONFIGURATION, FIG. 5. BUT, IN THIS CASE, THE EFFICIENCY OF THE SINGLE CHARGE IS REDUCED.

IN ORDER TO MAINTAIN THE EFFICIENCY OF THE ACTIVE PROTECTION FOR LARGER DONOR SYSTEMS, IT IS NECESSARY TO INCREASE THE AMOUNT OF HE. IT HAS BEEN FOUND THAT, BY EMPLOYING A LARGER SINGLE-CHARGE CONFIGURATION, THE PROTECTION CAN BE USED EFFECTIVELY FOR LARGER DONORS. OF COURSE, THERE IS AN OPTIMAL CHARGE FOR ANY GIVEN (DESIGN) DONOR, AND IT IS POSSIBLE TO ASSESS THE BEHAVIOR OF THE PROTECTIVE STRUCTURE FOR DONORS WHICH ARE EITHER LARGER OR SMALLER THAN THE DESIGN DONOR. A BETTER ALTERNATIVE YET IS A MULTIPLE-CHARGE CONFIGURATION, DISCUSSED IN THE NEXT SECTION.

MULTIPLE CHARGES

USING SEVERAL HE CHARGES, INSTEAD OF A SINGLE ONE IS MOST BENEFICIAL, FOR THE FOLLOWING REASONS: (1) IN ORDER TO PROTECT AGAINST A GIVEN DONOR, IT IS (SOMETIMES) POSSIBLE TO ACTIVATE ONE OR MORE, BUT NOT ALL CHARGES, SO THAT REPEATED APPLIED LOADS CAN BE ACCOUNTED FOR, (2) IN A MULTIPLE-CHARGE SYSTEM ONE HAS A SELECTION OF MODES WHICH CAN BE EMPLOYED, E.G., THE MOST ADEQUATE CHARGE(S) FOR THE ACTUAL DONOR (WHICH MIGHT DIFFER FROM THE DESIGN DONOR), AND (3) BY ACTIVATING THE CHARGES IN A CERTAIN ORDER (LOCATION AND TIMING CAN BE CONTROLLED, TO A CERTAIN DEGREE), A MORE FLEXIBLE PROTECTION IS ACHIEVED, COVERING DIFFERENT DONORS MORE EFFECTIVELY.

FIG. 6 SHOWS THE EARLY STAGES OF A TWO-CHARGE DETONATION. THE CASE ILLUSTRATED HERE CORRESPONDS TO THE SAME DONOR AND INERT MATERIAL AS THOSE OF THE FIRST CONFIGURATION (FIGS. 2,3,4, AND THE CORRESPONDING PLOTS OF FIG. 5). IT HAS BEEN DETERMINED THAT, THIS ARRANGEMENT IS MORE EFFICIENT THAN THE PASSIVE SCHEME, FOR BOTH THE FIRST DONOR TREATED, AS WELL AS THE ONE WITH A DOUBLE PEAK PRESSURE.

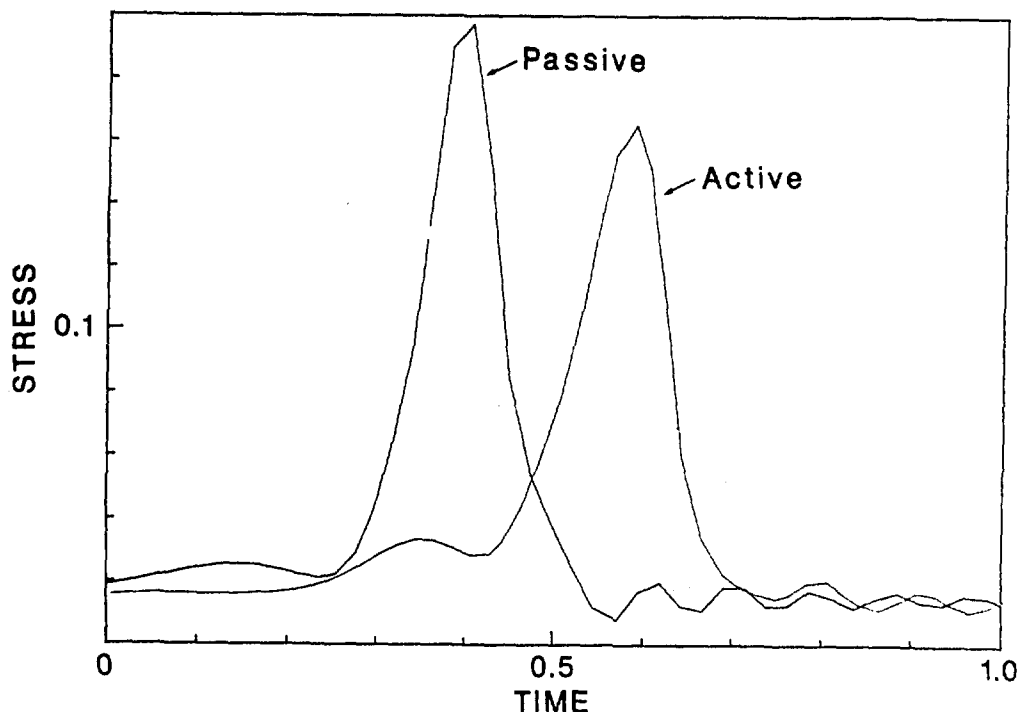


FIGURE 4: STRESS HISTORY AT RIGHT FACE.

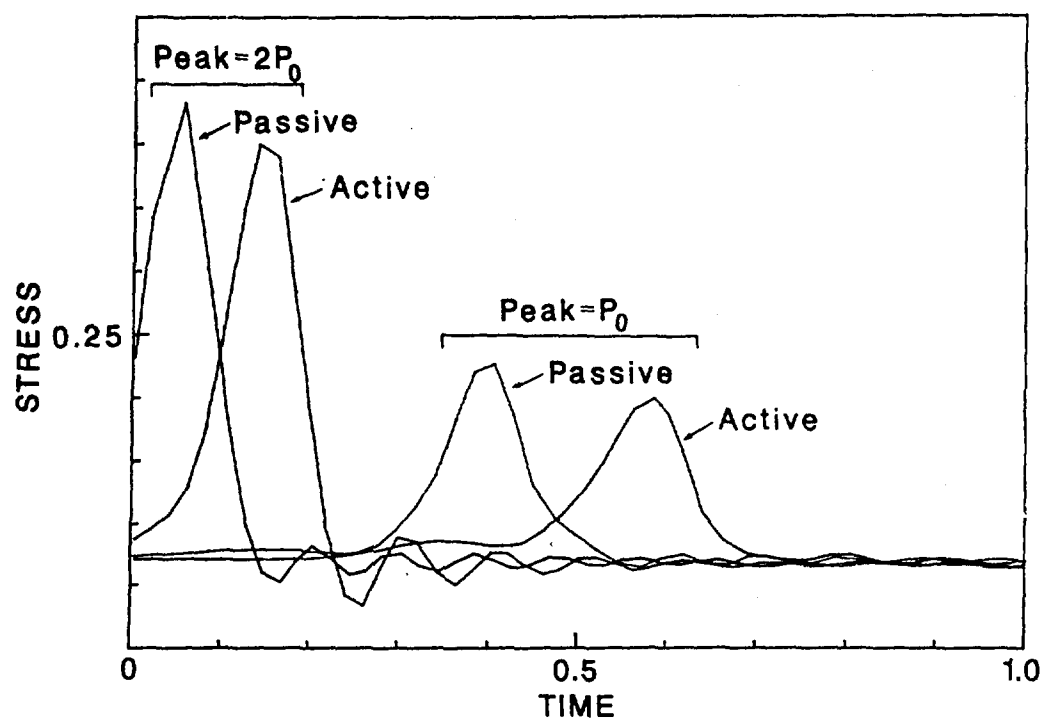


FIGURE 5: STRESS HISTORIES FOR TWO DONORS.

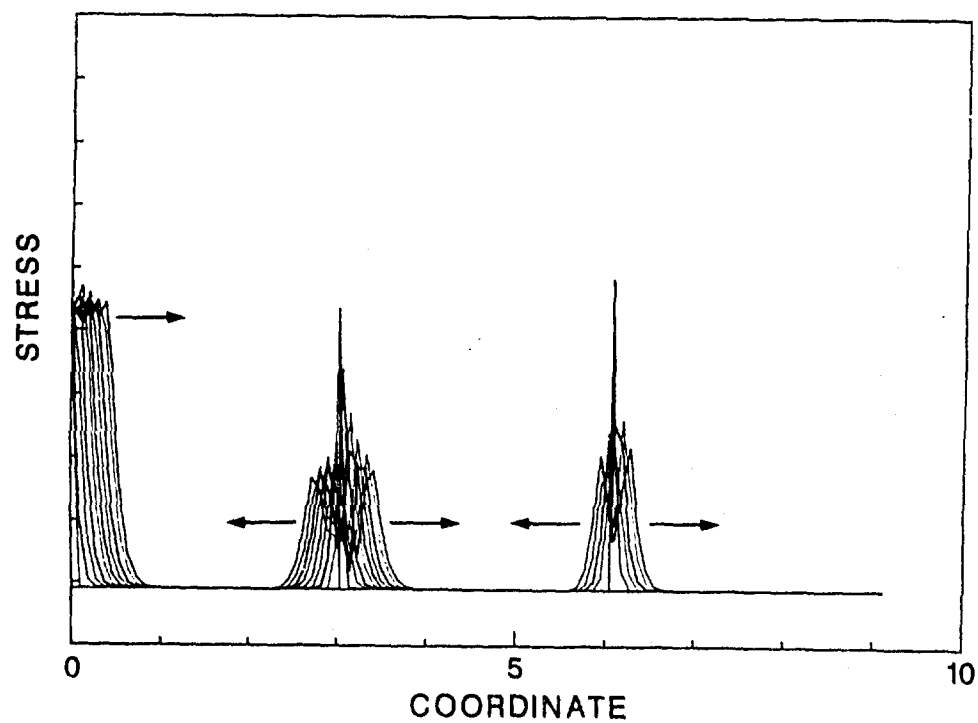


FIGURE 6: TWO-CHARGE DETONATION.

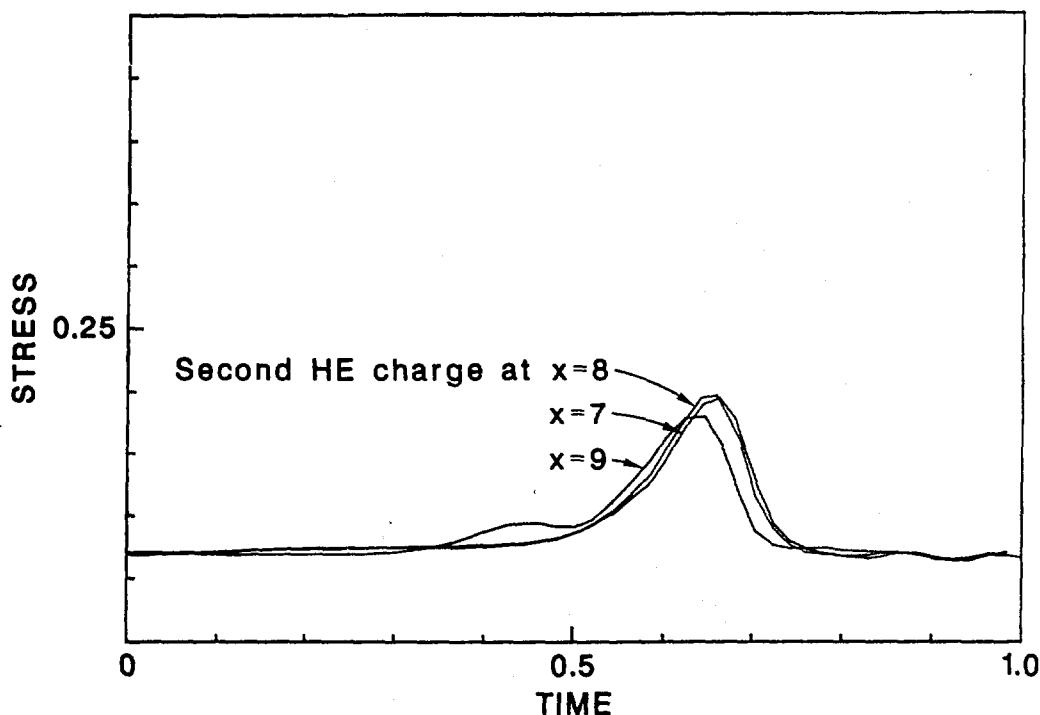


FIGURE 7: STRESS HISTORIES FOR TWO-CHARGE CONFIGURATIONS-LOCATION OF SECOND CHARGE VARIED.

FIG. 7 SHOWS THE RESULTS OF A PARAMETRIC STUDY, WHERE THE LOCATION OF THE SECOND CHARGE, PLACED FURTHER AWAY FROM THE DONOR IS VARIED. IT IS OBVIOUS THAT, THIS PARAMETER IS SIGNIFICANT, AND COULD BE CHOSEN SO THAT A WIDER RANGE OF DONORS CAN BE ANSWERED FOR. IT IS ALSO INTERESTING TO NOTE THAT, FOR THIS CASE, COMBINING THE TWO CHARGES INTO A SINGLE ONE, LOCATED AT THE CENTER OF THE INERT MATERIAL, RESULTS IN AN EFFICIENT ARRANGEMENT FOR THE GIVEN LOAD. BUT, FOR A WIDER SPECTRUM OF DONORS, THIS ALTERNATIVE IS LESS EFFICIENT THAN TWO-CHARGE SCHEMES.

CONCLUSION

THE FEASIBILITY STUDY PRESENTED HERE SHOWS THAT, THE CONCEPT OF ACTIVE PROTECTION OFFERS MANY ADVANTAGES OVER PASSIVE CONFIGURATIONS OF LAYERS. THE ACTIVE PROTECTION IS OFTEN MORE EFFECTIVE THAN THE PASSIVE ONE, THUS, ALLOWING SAVINGS IN SIZE, AND REDUCTION OF COST. THE ACTIVE PROTECTION IS CAPABLE OF REDUCING THE EFFECTS OF VARIOUS TYPES OF DONOR SYSTEMS, INCLUDING REPEATED LOADS.

IN ORDER TO IMPLEMENT THE CONCEPT OF ACTIVE PROTECTION FOR REALISTIC ENGINEERING PROBLEMS, IT IS NECESSARY TO EXTEND THE STUDIES DESCRIBED HERE TO TWO-DIMENSIONAL AND THREE-DIMENSIONAL GEOMETRIES. ALSO, IT IS IMPORTANT TO VERIFY THE LATTER BY EXPERIMENTS.

REFERENCES

1. GINSBURG, S., TENE, Y., AND KIRSCH, U., "OPTIMIZATION OF PROTECTIVE LAYERS," RESEARCH REPORT NO. 010-766, TECHNION RESEARCH AND DEVELOPMENT FOUNDATION, 1980.
2. LAWRENCE, R.J., AND MASON, D.S., "WONDY IV-A COMPUTER PROGRAM FOR ONE-DIMENSIONAL WAVE PROPAGATION WITH REZONING," SANDIA LABORATORIES REPORT NO. SC-RR-71-0284, 1975.

ACKNOWLEDGEMENT

THIS STUDY IS PART OF A MORE COMPREHENSIVE RESEARCH ON OPTIMIZATION OF PROTECTIVE STRUCTURES. THIS MATERIAL IS BASED UPON WORK SUPPORTED BY THE NATIONAL SCIENCE FOUNDATION UNDER GRANT NO. CEE-8306300.

Discussion

Mr. Haworth (Rockwell International): What criteria did you use to size the relative magnitude of pressure pulses? I noticed your protective high explosive pulse was less than the original pulse. What criteria did you use to select that ratio?

Mr. Ginsburg: Do you mean the amount of charge?

Mr. Haworth: Yes. How did you select your charge ratio?

Mr. Ginsburg: I have to admit at first I took one which I felt was right, and that was based on some previous experience. The question of the amount of charge and how to distribute the charges within a configuration is important and needs further study. I tested a configuration with varying amounts of high explosives to see if we can optimize, and there is certainly an optimum for a given dollar. There is an optimum charge within a given configuration; but, the size of the layers, the types of materials, the materials properties, if you have control over them, and then the distribution of charges, is a function of the weapon system, or a series of weapons, because it is not enough to design for one. You may want to include optional capabilities for repeated loads or different types. I have not covered that. There is a tremendous amount of work that still needs to be done.

Mr. Krauthammer (University of Minnesota): The procedure you proposed seems interesting, but there are some questions about the validity of the approach. First, to get a meaningful reduction in the peak pressures, a significant amount of protective explosion must be placed between the weapon system and the structure. Since you will use a more-or-less similar amount of explosive to get the meaningful reduction at a closer distance from the structure, you may create more damage from the protective explosion than from the weapon itself. Then, just using the concepts of conventional warfare, you are not talking about one or two detonations hitting the target, but you are talking sometimes about hundreds of detonations hitting the target. I do not see how you can control the number of protective explosions because they might trigger each other. Before you know it, you are left again with a passive system that needs to stand and provide protection.

Mr. Ginsburg: You raised a few important questions. I do not pretend to have answers to all of them because it needs further study. First, triggering sympathetic detonations is the least worry. You can protect the system from that if you design it correctly. The second is inducing damage to the structure by the protection. Of course, when you design, you have to make sure that your criteria for damage to the structure are not violated by your own system. This is apparent even in these preliminary studies where the original load with

a double peak caused, in my case, spalling. Whereas, the active protection did not. So again, that is something that you can control. Regarding multiple loadings - of course, if the structure is passive and the weapon can destroy it, then it destroys it. If with the active protection, you can protect it better than the passive, then you got something done. If you have 100 hits on your target, then both will not work unless you have some 100 or 200 charges. So, this might be impractical; I do not know. I am comparing the passive protection with the active one, and there is always a chance another weapon would destroy both. However, the question is, "Can I use active protection to protect against a weapon that destroys a passive one?" The answer is definitely, "Yes, and with much more flexibility." So, the comparison should be between these two, and not with a case where it will not work anyway. If it does not work with passive, it will not work with active in a case of 100 hits and so forth.

Mr. Flathau (JAYCOR): It seems to me, if I were to ring this whole structure with explosives, I am talking about many, many pounds of explosive, and I am also talking about an expense; so there has to be some trade-off, especially if you are talking about multiple layers. Would I be better off to put more mass into the structure itself, or to do something to the structure? I think this certainly would be true if we are talking about the case that Professor Krauthammer talked about, as you get one, two, three, four, five - many, many explosives. So, trying to look at what you are doing is one thing, and then looking at the total system approach.

Mr. Ginsburg: Theoretically, if you want to protect a structure by burying it a few miles underneath the surface, it might work, I do not know. You have to pay for it; you have to pay for any protection. You can make it more massive, and the easiest way is to bury it deep. There are two severe limitations. One is even while you are working on the design, someone is designing a weapon to defeat that. So, once you bury it, forget about it; that's it for better or for worse, you do not know. History always shows that if you come up with a good protection scheme, in no time somebody else comes up with a weapon, so, there is no reason to assume it will not happen again. The trade-off is money. Sometimes you do not have the space to provide massive protection. This might save space. Second, even if hundreds or thousands of pounds of high explosives are needed, that is cheap. In fact, it will be much cheaper than the sensory system which is needed to detect the kind of weapon, the size of the weapon, the beginning of its detonation, or the forces, during the time it has to decide how to activate the protection system. Take another example - surface ships. You cannot bury them. You cannot protect them with masses of steel, concrete, sand, and so forth. This might work. So, I won't say it will always work. It is a question of what type of structure you have

to protect. However, when you compare it one to one with the passive protection, there is no question that it has advantages.

Mr. Flathau: It also has many disadvantages. One disadvantage is it needs more maintenance than a passive protection system; this can be expensive over the years. The amount of real estate that is needed is another disadvantage.

Mr. Ginsburg: Let's look at the example. This is the size of the initial protection - inert or active. The amount of high explosive is small; it is less than one hundredth of this. So, it does not change in terms of real estate or anything else. Still, it is more effective than the inert configuration. So, the question of real estate is irrelevant in this case. The question about maintenance, certainly, that is a big question and a good one. I do not know. If we do not try a realistic implementation, we will never know. So, this offers less material and a more effective means for controlling a wider spectrum of weapons. How much it will cost, and how much maintenance it needs are questions I cannot answer.

Mr. Krauthammer (University of Minnesota): You assumed the protective layer will always be between the structure and the weapon. However, you have no control over where the weapon system will be delivered. You might have a problem if the weapon system is delivered between the protective layer and the structure. Then, you will have the additional detonation of the protective layer, and instead of having one pulse hitting the structure, you will have two. The other possibility is if the protective layer detonates, and the weapon is on the so-called "safe side", you will remove protective material from the passive system. Then, you will essentially reduce the passive resistance of the system. So, you have a huge array of parameters that have significant contributions to the resistance of the system over a very narrow range of variation. I do not believe this simplistic approach, or the one-dimensional example you showed, really demonstrates the effectiveness of the system.

Mr. Ginsburg: Certainly, this is a feasibility study that you must do first to figure out if you can do it at all. The weapon might be activated. If it is a missile that penetrates a certain amount and then explodes, this system is much superior to any other because you can destroy the missile when it hits. If you have a good sensory system that says, "Hey, I've been hit by this mess," and the computer says, "Oh, this mess, it might be this kind of missile. Let's explode layer 1." You can destroy or intercept a weapon before it penetrates that much to cause damage, and we cannot do this with any other system. So, that is an advantage. If we are talking about massive inert protection including high explosive charges, then, you really do not destroy your protection when you activate one layer. In fact, if it is a buried structure, you hardly do anything to the core of

the protection. So, I can see many realistic situations where you can activate one, or two, or ten layers, and still have a reserve of active layers without any damage to the entire protection.

DEPENDENCE OF FREE-FIELD IMPULSE ON THE DECAY TIME OF ENERGY EFFLUX FOR A JET FLOW

Kevin S. Fansler
Ballistic Research Laboratory
Aberdeen Proving Ground, Maryland

Until now, the peak energy efflux at the jet exit was considered the significant parameter in a scaling approach to estimate the peak overpressure, time-of-arrival, and positive phase duration from guns and shock tubes. The resulting predictions for the peak overpressure and time-of-arrival were satisfactory but the positive phase duration prediction was poor. This predicted value of the positive phase duration is used with the peak overpressure prediction to obtain an estimate of an important quantity: the impulse. Here we investigate the characteristic exhaust decay time for the energy efflux at the jet exit as a possible additional significant parameter that might be used to improve predictions for the impulse. Numerical simulation was used to establish that the impulse value depends upon this parameter. Comparison between simulation and experiment is satisfactory. This additional parameter was used to correlate the available impulse data. It was determined that the additional parameter significantly improves the prediction capability of the scaling method for predicting the impulse. An idealized wave form together with the predicted peak overpressure can be used to obtain an estimate of the positive phase duration. This approach yields less satisfactory agreement with the duration data but this fact is relatively unimportant since the impulse is the quantity of importance.

1. INTRODUCTION

Guns and shock tubes under operation generate large pressure waves that can be harmful to nearby personnel and equipment. Industry and the Army employ these devices extensively and need to be acquainted with the salient characteristics of these blast waves. For these devices, the magnitude of the energy efflux from the tube exit and its history determine the characteristics of the blast wave and the associated gas-plume structure. Two principal characteristics of blast waves are the peak overpressure and the impulse. The impulse is the time integral of the pressure at a field point of interest. The positive phase duration is another often-used characteristic; it is the time duration for the positive pulse of a blast wave to pass over the field point. If we know the peak pressure and the positive phase duration value, the impulse for the wave can be estimated easily by assuming a simple expression for the pressure as a function of time.

Scaling theory is used extensively to predict blast wave characteristics; this approach yields simple but powerful methods. The scaling theory for instantaneous-energy blast waves [1] is well known and accepted. Reynolds [2] used a point blast scaling theory developed by Hopkinson [3] to treat gun-generated blast waves. Later, Westine [4] developed a scaling law from point blast theory but, in addition, introduced the length of the barrel as an important parameter. This modification permits his method to be applied successfully over a variety of weapons.

More recently, Smith [5], Fansler and

Schmidt [6], and Schmidt and Duffy [7] have predicted the blast wave characteristics from these devices by applying scaling theory to blasts generated by constant energy efflux conditions. Smith [5] and Fansler and Schmidt [6] selected the peak energy deposition rate as the significant parameter. With a steady energy deposition rate assumed in the dimensional analysis, the nondimensionalized quantities of peak pressure, time-of-arrival and impulse depend only upon the distance divided by the scaling length. For a given polar angle as measured from the axis, this scaling length for the blast wave varies as the square root of the peak energy deposition rate. However, the blast waves are highly directional, with their strengths decreasing with increasing polar angle from the forward axis direction. The form for the variation of peak overpressure with angle from the axis is obtained from moving charge theory [5]; it possesses one free parameter that determines how rapidly the overpressure falls off with the increase of polar angle. The assumed formulation for the peak overpressure generates two other free parameters. One parameter is the value for the exponent power of the distance from the gun muzzle; it determines how fast the peak pressures fall off with distance. The other parameter is the value for the constant coefficient of the scaling expression. The available data are then used with the given scaling relation to perform a least squares fit that establishes values for the three free parameters. Smith [5] applied the scaling approach to a particular weapon, however, Fansler and Schmidt [6] assumed the resulting scaling expressions were universally applicable when using the initial energy-deposition rate as the characteristic value. The Fansler and Schmidt [6] model successfully

predicts the peak overpressure and times-of-arrival for a variety of gun weapon systems. On the other hand, the method predicts that the positive phase duration increases with distance in a completely different fashion than for the well-studied instantaneous energy deposition explosions. However, the original generating method for the blast wave should have less relevance to the behavior of the blast wave as it travels away from its origin. Thus, for the larger distances, the behavior of the positive phase duration for the two cases should be quite similar.

It is the objective of this work to provide an improved prediction scheme for the impulse by modifying the scaling approach of Fansler and Schmidt [6]. From the data already accumulated, it appears that the energy-deposition rate decay affects the impulse. However, the waveforms obtained by experiment have significant amounts of noise generated by possible gage vibrations and turbulence; perhaps, the amount of turbulence can affect the impulse magnitude. The turbulence magnitude may in turn depend upon some other significant parameter such as the velocity of the projectile, etc. Thus, it is difficult to determine from the data whether the positive phase duration depends predominantly upon the energy efflux decay rate. To study this relationship, we use the Euler finite difference code, DAWNA, that calculates the blast wave field along the boreline of a gun [8]. It uses shock fitting, takes into account the decay rate of the energy efflux quantity, and executes much faster than a numerical axisymmetric scheme.

BACKGROUND AND SCALING DEVELOPMENT

As mentioned before, Fansler and Schmidt [6] assumed that the blast wave depended on the energy efflux. The functional dependence of the peak overpressure is expressed as

$$P = P(r, \rho_a, a_a, dE/dt) \quad (1)$$

Here r is the distance from the center of the explosion, ρ_a is the ambient density, a_a is the ambient sound speed, and dE/dt is the characteristic value for the rate of energy deposition. For a spherical blast, we assume the ideal equation of state; dimensional analysis yields a scaling length:

$$L \sim (dE/dt) / (\rho_a a_a) \quad (2)$$

and a nondimensionalized peak overpressure:

$$\begin{aligned} \bar{P} &= P / P_a \\ &= \bar{P}(r/L). \end{aligned}$$

In this report the overbarred quantity is defined as the quantity non-dimensionalized by

the significant quantities for the scaling analysis. The momentum of the propellant gas results in the strength of the blast wave decreasing markedly with polar angle. Smith [5] noted the similarity between moving-charge blast waves and gun blast waves. From moving charge theory, he obtained a scaling length, L , for muzzle blast,

$$L'/L = \mu \cos \theta + (1 - \mu \sin^2 \theta)^{1/2} \quad (4)$$

Here, μ is the momentum index and is a measure of the directionality of the blast. It is a free parameter that is found by a least squares fit to experiment. With Equation (4), the resultant form of the overpressure relationship is assumed as,

$$\bar{P} = K (r/L')^n \quad (5)$$

with the values of $K=2.4$, $n=-1.1$, and $\mu=0.78$ giving the best fit to the peak overpressure data. These data were collected from a variety of guns [6]. The resulting expression, when cast in the interior ballistic formulation and when some simplifying assumptions are made, resembles the form obtained by Westine [4].

A further consequence of the dimensional analysis is that the positive phase duration should have the following functional dependence:

$$\begin{aligned} \bar{\tau} &= \tau a_a / L' \\ &= \bar{\tau}(r/L') \end{aligned} \quad (6)$$

Because of the general appearance of the 30mm data [6], we used a linear fit to obtain the predictive curve for $\bar{\tau}$ [6]. Figure 1 shows the fitted curve with the corresponding data. There is considerable scatter of the data around the fitted curve. The data also do not show any tendency to go toward the far-field asymptotic relation; i.e., the positive phase duration increases asymptotically as the square root of the log of the distance divided by some constant. Figure 2 shows 30mm data with the parameters being the angular position and firing conditions. The impulse could only be obtained directly from the set of experiments that was used to produce the results of Figure 2. Only data from these experiments were used to obtain the results of the present report. It is noted that some data subgroups are clustered so that there is not much overlap between the subgroups. These subgroups correspond to different polar angles or different values of L'/L . It is desirable to have substantial overlap of the subgroups to improve the reliability of the data and thus the derived results. This could have been accomplished by collecting data for larger distances. However, the facilities and instru-

mentation did not allow data acquisition at these larger distances.

The observations of linear behavior of the data at the larger distances and the only fair correspondence with the curve fit caused us to search for an additional significant parameter. A possible significant parameter is the characteristic emptying time of the propellant from the gun barrel. As noted before, the peak overpressure for a given distance and polar angle increases slowly, but insignificantly for most practical purposes, with increasing emptying time. However, the impulse may have a stronger dependence on the emptying time of the barrel.

A dimensional analysis performed with a characteristic emptying time, α , as a significant variable yields the π group,

$$\beta \sim (\alpha a_\infty)/L^* \quad (7)$$

This is not a good working parameter since it is difficult to establish how α is defined and how to find its value easily. Corner [9] discusses the barrel emptying time and its relationship with easily observed parameters. To a first approximation,

$$\alpha \sim L/V_p \quad (8)$$

With the proportionality substituted into Equation (7), the new working π group can be defined as,

$$\beta = (a_\infty L)/(L^* V_p) \quad (9)$$

This new parameter can be interpreted as the ratio of the emptying time of the tube to the characteristic time for the development of the blast wave. We shall call the new parameter the nondimensional emptying time. Figure 3 shows the normalized energy efflux versus the nondimensional time divided by the nondimensional emptying time constant for a 30mm cannon, or equivalently, the time nondimensionalized by L/V_p . If the first part of the emptying process is deemed more important than the latter parts, we can assume an exponential function to fit the first part of the data. This approximation to the curve shows that the efflux data values are high compared with the fitted function for the longer times. The approximation shows that the exponential emptying time constant is $\alpha = (L/V_p)/1.63$. Thus, the exponential emptying time constant divided by L/V_p is 0(1), which agrees with intuition. With the nondimensional emptying time now assumed as a significant grouping, the functional forms for the impulse

and positive phase duration are

$$\bar{I} = \bar{I}(r/L^*, \beta), \quad (10)$$

$$\bar{T} = \bar{T}(r/L^*, \beta). \quad (11)$$

In the present paper, we have treated the impulse as the primary parameter since it is used directly to assess vulnerability of actual or contemplated structures. Previously, an assumed form for the positive phase duration was correlated with available positive phase duration data and the impulse was then obtained using the most primitive form of the Friedlander waveform [1], which is,

$$(p-p_\infty)/p_\infty = \bar{P} [1-(t-t_a)/\tau] \exp[-((t-t_a)/\tau)]. \quad (12)$$

Here, t_a is the time of arrival of the blast wave front. However, the prior approach introduces a source of inaccuracy in the predictive method because the assumption of a specific waveform is an approximation.

As mentioned in the introduction, noise from turbulence and other sources were superimposed upon the waveforms. Such factors introduced difficulty in ascertaining that the emptying time was a major significant variable. Moreover, the limited range of distances over which the data were taken also makes it difficult to assert what the significant variables are with confidence. To isolate the effect of the emptying time from other possible significant parameters, we use numerical simulation. We chose the DAWNA code [8], which computes the flow properties of the blast wave along the gun boreline. Although the method calculates the flow properties along the centerline, by the assumptions of the scaling approach, the results are applicable to the gun blast for arbitrary polar angle. In the jet plume portion, the property distribution of a steady jet is assumed along the centerline and the shock layer between the Mach disc and the blast wave front is computed with a finite difference method. The discontinuities are obtained using a shock fitting technique. The method executes rapidly compared to an axisymmetric code and the position of the discontinuities are determined exactly whereas shock capturing schemes portray discontinuities as more or less steep rises or falls in the calculated gasdynamic quantities.

RESULTS AND DISCUSSION

The simulation performed was for the 30mm cannon firing the projectile at 572 m/s with a peak pressure of 3600 kPa. These conditions are for one of the firing conditions used in an

earlier study [10]. To investigate the relationship between the dimensionless emptying time and the impulse, the value of β was varied from 1.37 to infinity, or equivalently, the barrel length was varied from 10 calibers to infinity. For a 40 caliber length barrel, the energy efflux history is shown in Figure 3. As discussed before, the time is proportional to the barrel length. Figure 4 shows overpressure versus time at different distances from the muzzle for the above conditions. The value of β is 5.47 or equivalently, the barrel length is 40 calibers. The wave generally resembles waves generated by instantaneous energy explosions. Figure 5 shows calculated waveforms with various barrel emptying times for a dimensionless distance of 4.54 calibers from the muzzle. The waveforms for larger emptying times result in larger values for the positive phase durations. Furthermore, the shape of the wave does not maintain similarity as the emptying time is increased. Thus, the similarity between the waves generated by instantaneous energy explosions and waves for finite energy explosions should become weaker as the dimensionless emptying time increases. In fact, for this position, the positive phase duration for the barrel of infinite length is longer than for the times calculated. In effect, the jet appears to be sustaining a positive pressure at some field positions, as one might intuitively expect.

The positive phase duration versus the distance from the muzzle for different values of the dimensionless emptying time is shown in Figure 6. For finite values of the emptying time, the positive phase duration at first increases rapidly and then starts to level off. This behavior occurs since at early times the blast wave strength is large and the front of the wave then travels at speeds appreciably greater than the speed of sound while the part of the wave where the overpressure is zero is traveling near the speed of sound. As the wave travels from the muzzle, the peak overpressure decreases and the wave front speed approaches the ambient sound speed. In the asymptotic limit, the positive phase duration involves a logarithmic term. For constant energy efflux, the positive phase duration increases rapidly with distance to very large values as was noted from Figure 5.

Figure 7 gives the simulated impulse as a function of the distance from the muzzle for various values of the dimensionless emptying time. The impulse appears to decrease rapidly which we should expect since the overpressure is decreasing more rapidly than the inverse power of the distance and the positive phase duration is increasing relatively slowly. Figure 8 shows that the impulse increases slowly but significantly with the barrel exhaust time. Figure 9 shows a comparison between the simulated values of the impulse and some experimental values for comparable values of the dimensionless emptying time. These data were obtained from the primitive waveform data for an earlier study

[10]. The utilization of this additional parameter produces a marked improvement over the original predictive model of Fansler and Schmidt [6]. Although the comparable emptying times are smaller for the simulation, they predict higher values for the impulse. The simulated curves also show a steeper decline of the impulse with distance but this would be expected since simulations predict a steeper decline in peak overpressure than actually occurs. The reason for the steeper decline is not known. Considering that the simulation is based on a model that is a gross simplification of the muzzle blast flow, the agreement is quite good.

The complete data set [10] was used in seeking a correlating relationship with the nondimensional emptying time is shown in Figure 10. The data cover a range over the nondimensional time from 3.23 to 32.3 which does not completely encompass the ranges occupied by gun weapons. Nevertheless, a correlation was sought with extrapolation to these ranges that would hopefully not result in large predictive errors. Further available data can later be added to yield an improved prediction. It was decided to employ a simple form devoid of any logarithmic expressions that the impulse might be tending to asymptotically. We have no data for performing a least squares fit in the far field. The nondimensional impulse was assumed to have a form such that when the data were fitted and the free parameters determined,

$$\bar{I} = 0.5 (r/L)^{-0.6} \beta^{0.2} \quad (13)$$

This form can easily be understood and used and shows that the impulse varies as a weak power law function of the barrel exhaust time and is consistent with how the simulated values of the impulse vary with the efflux decay time. A least squares fit was also attempted with the addition of the polar angle as an explicit variable but very little improvement in the correlation was obtained.

To display all the results on a plot, the function \bar{I} must be transformed to a function depending on only one variable. Dividing \bar{I} by the last factor in Equation (13), one obtains the reduced value of the impulse, I_r , that is no longer dependent on the nondimensional emptying time. Figure 11 shows the reduced impulse data together with the prediction. The scatter of the reduced data is significantly diminished by utilizing the barrel exhaust time in the correlation. Of course, some of the scatter can be attributed to random variations. Nevertheless, we have need of a larger data set with measurements performed for longer distances from the muzzle.

Now that we have developed a predictive expression for the more important quantity, the impulse, we can return to the positive phase duration and investigate whether an adequate

predictive expression can be easily obtained. Of course, from Figure 5 we should expect that the impulse would not vary linearly with the positive phase duration. If we assume the Friedlander relationship as given in Equation (12), a very simple relationship exists between the nondimensional impulse and the nondimensional positive phase duration,

$$\bar{I} = \bar{P} \bar{\tau} / e. \quad (14)$$

Utilizing the expression for \bar{I} in Equation (13) and the expression for \bar{P} as given in Equation (5), we find

$$\bar{\tau} = 0.566 (r/r')^{0.5} \beta^{0.2} \quad (15)$$

As before with the impulse, the dimensionless positive phase duration is transformed to a function of the nondimensional distance. The positive phase duration data are likewise divided by $\beta^{0.2}$. The comparison between the predictive curve and the reduced data is shown in Figure 12. The data trend and the predictive curve have different slopes. It appears that a more complex wave shape would need to be assumed to adequately predict the positive phase duration. However, this would seem to be wasted effort since with data being digitized and processed with computers, the impulse can easily be determined for a wave.

Although the data used here were obtained from gun weapons, the results should be applicable to any device that produces a jet flow with decaying energy efflux. Schmidt and Duffy⁷ obtained pressure data in the field external to the exit of the shock tube. They did not obtain the impulse but they did measure the positive phase duration. They found that for r held constant:

$$\tau \sim \exp(0.25 \cos \theta) \quad (16)$$

Using Equation (16) and Equation (9),

$$\tau \sim (r'/r)^{0.3} \quad (17)$$

A comparison of the two expressions is shown in Figure 13. The agreement is satisfactory as it should be since the shock tube essentially generates its blast wave in the same manner as for a gun weapon.

SUMMARY AND CONCLUSIONS

An older predictive scheme for blast waves generated from gun weapons that is based on a scaling approach has not produced entirely satisfactory results. For example, this older model, which utilizes the peak energy deposition rate as the significant parameter, predicts that the positive phase duration increases linearly with the distance from the jet exit. However, for the well-studied explosions that are generated by instantaneous energy deposition, this sort of behavior does not exist. For these explosions, the positive phase duration at first increases steeply with the distance but the rate of increase with distance falls off rapidly as the wave travels away from its origin. It would seem that much the same behavior should exist for blast waves generated by jet flows that exit from gun tubes or shock tubes. The analysis of the data upon which the model was developed reveals that subgroups of the data occupy only a limited domain and do not overlap extensively. The data could also depend on another significant parameter that could produce the puzzling linear relationship between the positive phase duration and the scaled distance from the jet exit. A possible significant parameter could be barrel exhaust time for the energy efflux passing the exit plane. To test this possibility, we employed a numerical simulation scheme that calculates the fluid-dynamic quantities along the boreline. Although the simulation scheme is limited to only one direction, this is not a major impediment since the current scaling approach allows application of the results to all polar angles. The numerical scheme also executes very quickly and allows for isolation from turbulence and other phenomena occurring in the actual gun blast flow.

The simulation results show that the impulse increases with the decay time of the energy efflux. Moreover, comparisons of experiment data with simulation results show a similar dependence of the impulse upon the decay time of the energy efflux. Thus, it is felt that the barrel exhaust time is a significant parameter for improving the correlation of the impulse data. We correlated the data utilizing the new variable and obtained a power law dependence of the impulse upon the nondimensional energy efflux exhaust time. The predicted impulse increases at a slower rate for the larger distances, as it should. We can obtain corresponding positive phase duration values by using the most primitive Friedlander relation together with the predicted peak overpressures to construct idealized waveforms. This approach generates a simple expression for the positive phase duration. Comparison with the phase duration data yields different slopes and only fair agreement. It is concluded that the positive phase duration prediction should only be used when there are no impulse data to compare with. A case in point is the shock tube results obtained by Schmidt and Duffy [7], that had only

the positive phase duration data readily available. The results of the present prediction agree reasonably well with the shock tube results even though we have used the simple Friedlander relationship.

In conclusion, the impulse given to nearby structures by guns or shock tubes can now be more accurately predicted in a range of distances where possible injury can result to personnel and equipment. This relationship is not applicable to very large distances from the gun or shock tube. Data have not yet been collected for correlation to these distances and the present function does not contain a logarithmic expression that is essential for the asymptotic form.

REFERENCES

1. W. E. Baker, Explosions in Air, U. Texas Press, Austin, 1973.
2. G. T. Reynolds, "Muzzle Blast Pressure Measurements," Report. No. PMR-21, Princeton University, April 15, 1944.
3. B. Hopkinson, British Ordnance Minutes 13565, 1915.
4. P. Westine, "The Blast Field About the Muzzle of Guns," The Shock and Vibration Bulletin, Vol. 39, Pt. 6, pp. 139-149, March 1969.
5. F. Smith, "A Theoretical Model of the Blast from Stationary and Moving Guns," First International Symposium on Ballistics, Orlando, FL, 13-15 November 1974.
6. K. S. Fansler and E. M. Schmidt, "The Relationship Between Interior Ballistics, Gun Exhaust Parameters, and the Muzzle Blast Overpressure," AIAA/ASME 3rd Joint Thermophysics, Fluids, Plasma and Heat Transfer Conference, St. Louis, Missouri, 7-11 June 1982.
7. E. M. Schmidt and S. J. Duffy, "Noise from Shock Tube Facilities," AIAA Paper 85-0049, January 1985.
8. J. Erdos and F. del Guidice, "Calculation of Muzzle Blast Flowfields," AIAA Journal, Vol. 13, No. 8, August 1975, pp. 1048-1056.
9. J. Corner, Theory of the Interior Ballistics of Guns, John Wiley, NY, 1950.
10. K. S. Fansler, and G. E. Keller, "Variation of Free-Field Muzzle Blast with Propellant Type," ADPA 6th International Symposium on Ballistics, Orlando, FL, October 1981.

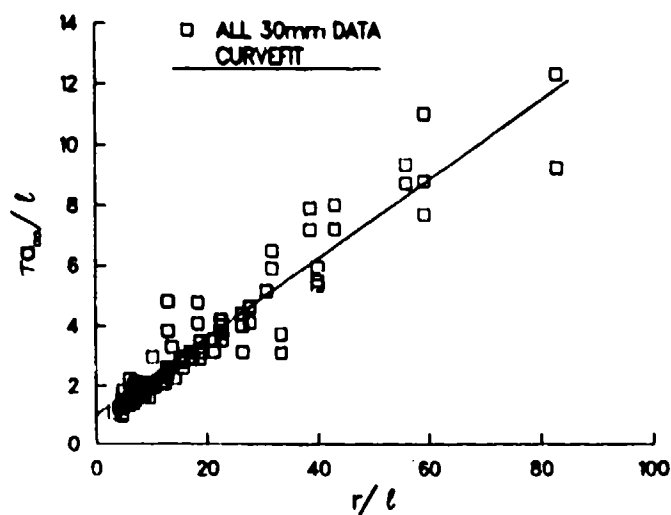


Fig. 1. Positive Phase Duration Data from 30mm Firings and Accompanying Curve Fit of Reference 6

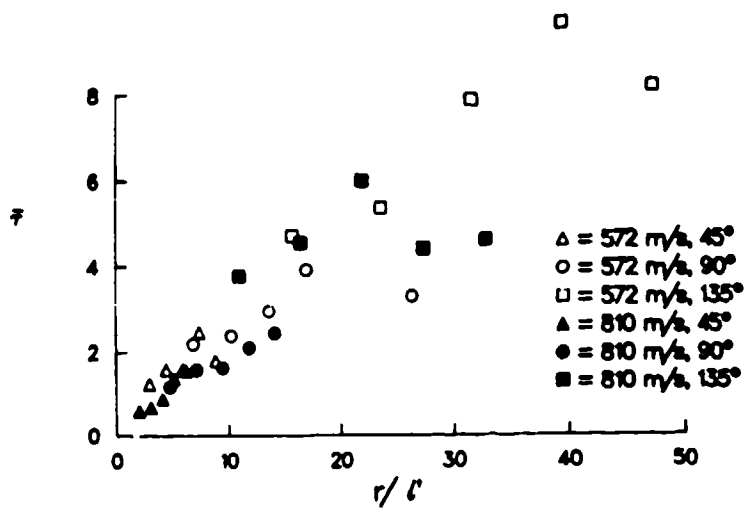


Fig. 2. Positive Phase Duration Data Delineated into Subgroupings

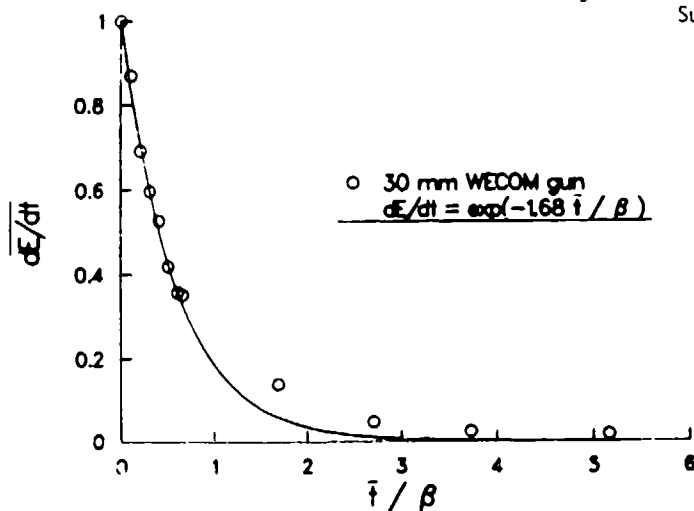


Fig. 3. Energy Efflux versus Nondimensionalized Time for 30mm WECOM Cannon with Exponential Approximation

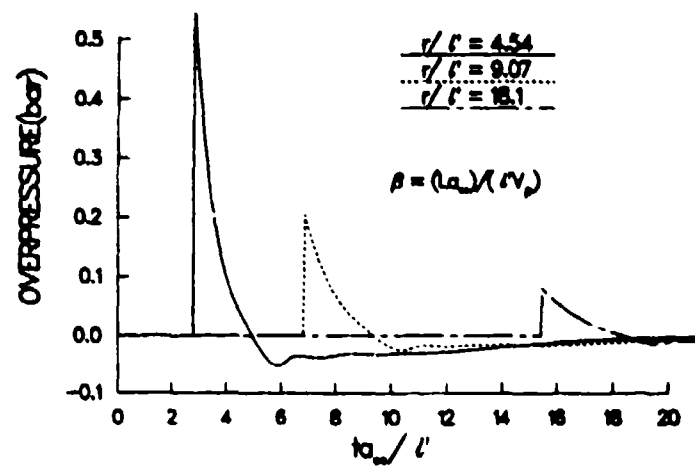


Fig. 4. Blast Wave Overpressure versus Time for Different Distances from the Muzzle. Simulation of 30mm Cannon with 40 Caliber Barrel Length

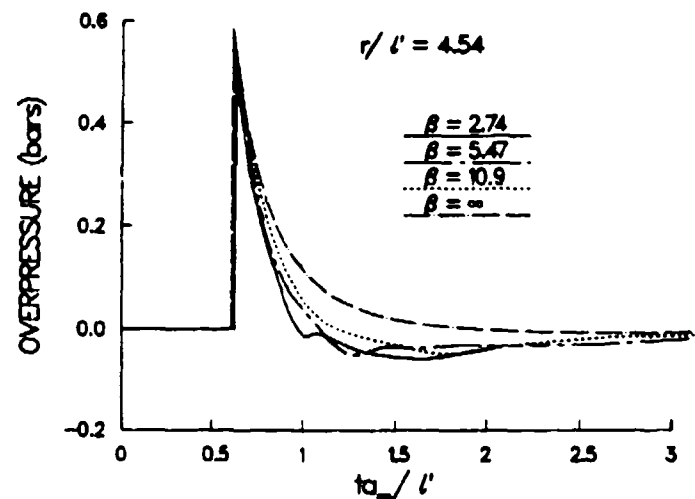


Fig. 5. Waveform Comparison for Different Energy Decay Times

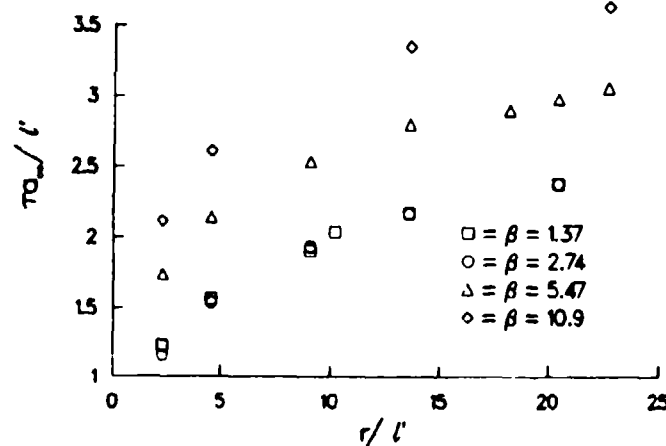


Fig. 6. Positive Phase Duration versus Distance from Muzzle for Different Energy Efflux Decay Times

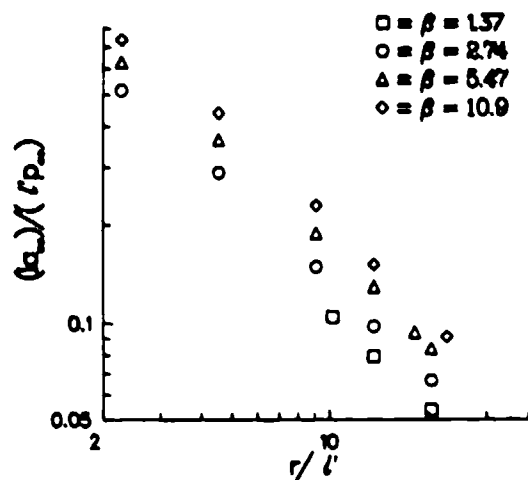


Fig. 7. Dimensionless Impulse versus Distance from Muzzle for Different Energy Efflux Decay Times

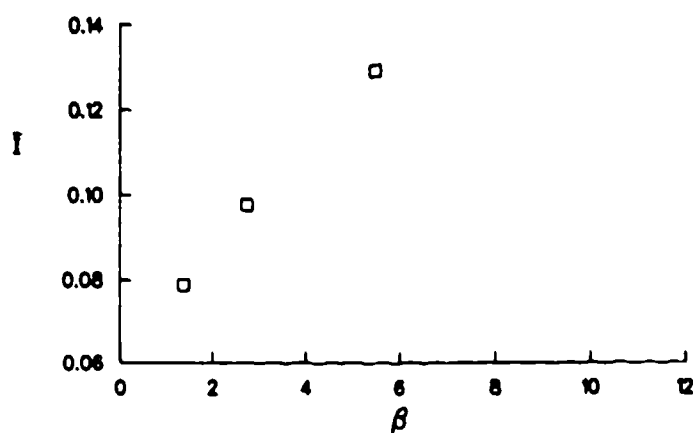


Fig. 8. Impulse versus the Energy Efflux Decay Time

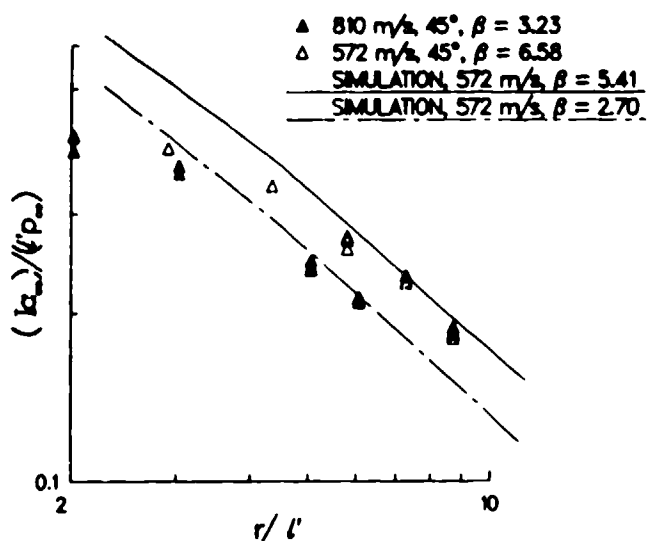


Fig. 9. Comparison of Simulated and Experimental Values for the Impulse

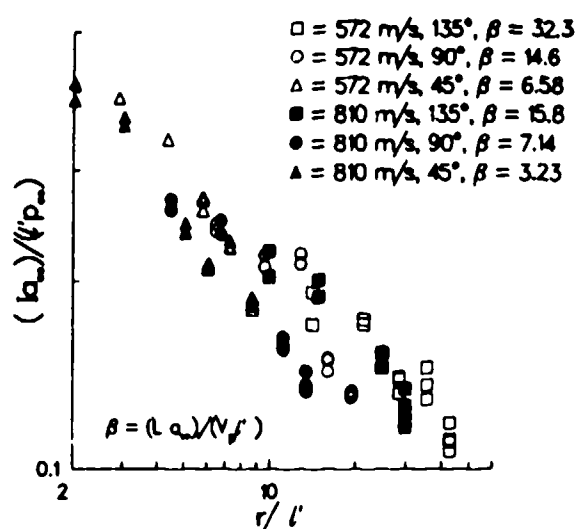


Fig. 10. Scaled Impulse Data versus Scaled Distance for 30mm Cannon

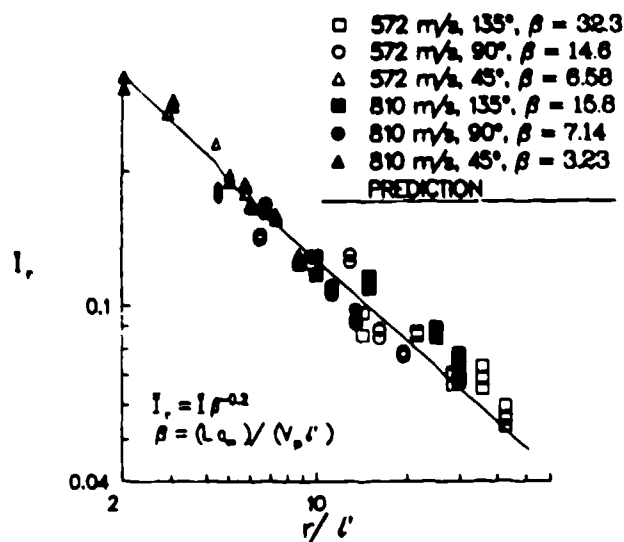


Fig. 11. Reduced 30mm Impulse Data Compared with Present Prediction

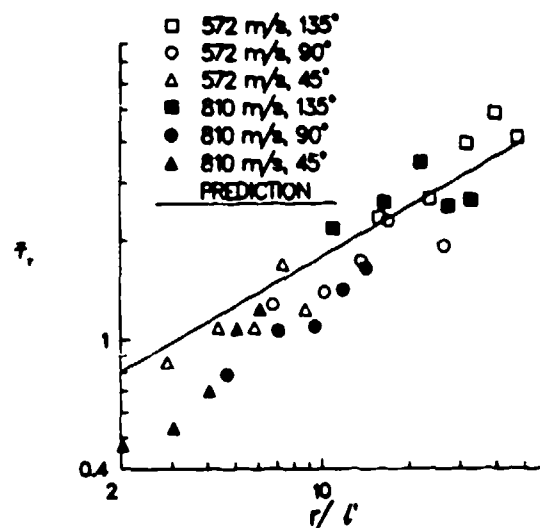


Fig. 12. Reduced Positive Phase Duration Data Compared with Corresponding Prediction. The Prediction Utilized Predicted Peak Overpressure and the Friedlander Waveform

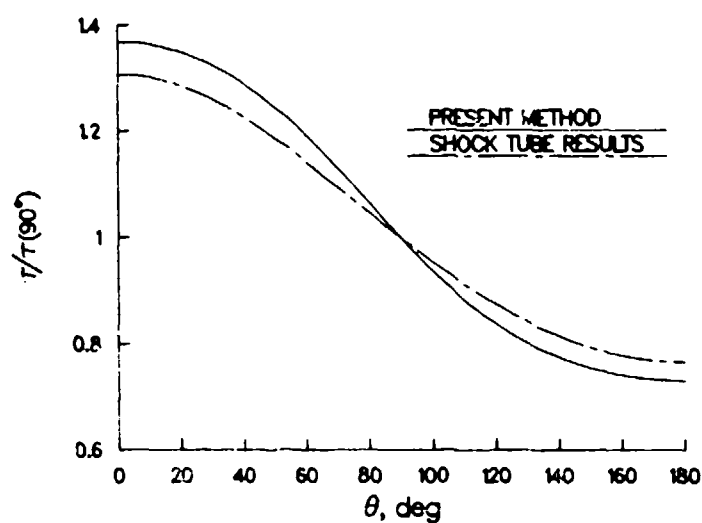


Fig. 13. Comparison of Two Predictions for the Positive Phase Duration versus the Polar Angle. Reference 7 Prediction was Derived from Shock Tube Data

COMPUTER IMPLEMENTATION OF A MUZZLE BLAST PREDICTION TECHNIQUE

C. W. Heaps, K. S. Fansler, E. M. Schmidt
Ballistic Research Laboratory
Aberdeen Proving Ground, Maryland

A computer code is developed that generates contour maps of peak incident overpressure, peak reflected overpressure, blast wave time of arrival, and blast wave positive phase duration. The code is based upon a free field muzzle blast scaling technique that is extended to treat blast wave reflection from surfaces. The predictions of the computer program are shown to compare reasonably well with experiment.

NOMENCLATURE			
A_e	area of bore	p_m	muzzle pressure for propellant immediately before projectile ejection
a_m	propellant sound speed at muzzle immediately before projectile ejection	p_∞	ambient pressure
a_∞	ambient sound speed	p_1	pressure behind incident shock
B	fraction of propellant burnt	p_R	pressure behind reflected shock
C	propellant mass	\bar{p}	incident overpressure (atm)
D	bore diameter of gun	\bar{p}_R	reflected overpressure (atm)
E	internal energy of propellant gas immediately prior to projectile ejection	\vec{r}	vector directed from muzzle to field point of interest
h	distance from the origin of the contour plane to the muzzle	r	magnitude of \vec{r}
i	scale length for explosion	R	gas constant
i'	effective scaling length that varies with angle from boreline	t_a	blast wave time of arrival
m_p	projectile mass	T_m	propellant temperature at muzzle immediately before uncorking
m_1	effective projectile mass accounting for bore friction ($= 1.05 m_p$)	T_a	adiabatic flame temperature of propellant
M	Mach number of incident shock	T_{mean}	mean temperature of propellant gas
M_1	streamline Mach number in front of incident shock	\vec{u}	unit vector parallel to boreline
M_2	streamline Mach number behind incident shock	U	combined volume of chamber and bore
\vec{n}	unit vector normal to contour plane	v_p	exit velocity of projectile
\vec{p}	vector directed from the boreline to the field point of interest that is normal to the shockwave surface	Z	$(r/i')^{-1.1}$
		α_1	wave angle of incident shock
		α_2	wave angle of reflected shock
		γ	specific heat ratio

NOMENCLATURE (continued)

δ_1	flow deflection angle through incident shock
δ_2	flow deflection angle through reflected shock
δ_{max}	maximum stream deflection consistent with regular shock reflection
η	angle between \vec{r} and \vec{P}
θ	polar angle from boreline to field point
μ	momentum index
$\vec{\ell}$	vector along boreline designating apparent origin of blast wave
w	cubic polynomial used in the approximation of the reflected pressure coefficient curves
τ	blast wave positive phase duration
ϕ	angle between boreline and contour plane
γ	ratio of heat losses to kinetic energy
α	roughness factor

INTRODUCTION

High levels of muzzle blast overpressure can have adverse effects on weapon crew members, nearby structures, and instrumentation. Control of these effects requires the ability to predict the details of the blast pulse as a function of weapon design and emplacement, propellant and projectile characteristics, and launch conditions. Additionally, techniques to reduce or control the blast through changes in these properties are of practical importance. Fansler and Schmidt [1] developed scaling relations that permit estimation of peak incident overpressure, blast wave time of arrival, and positive phase duration. Comparison of these estimates with experiment demonstrates that the scaling approach provides a reasonable initial estimate of muzzle blast characteristics. Since the relations are sensitive to weapon launch conditions and propellant charge design, they may be used to study the influence of these properties on muzzle blast.

The present work has two main objectives. The first is to extend the scaling approach to treat the problem of pressure loadings on surfaces adjacent to the weapon. The second is to use the scaling relations in the development of a computer code called BLAST that plots contour maps of the muzzle blast quantities. We believe that the results obtained from the scaling relations are most easily interpreted when presented

in this form.

The remainder of this report may be outlined as follows. First we present the scaling relations used to calculate the incident overpressure, blast wave time of arrival, and positive phase duration at points on a surface that can have any desired orientation with respect to the cannon boreline. From the calculations of incident overpressure and time of arrival, the reflected blast overpressure on the surface of interest is determined. For all of the blast properties, an algorithm is established to generate contour plots. Representative plots obtained from BLAST are selected for comparison with experimental results.

FREE FIELD MUZZLE BLAST CALCULATIONS

The free field blast computations are performed using scaling relations developed by Fansler and Schmidt. Their scaling approach has been described in detail [1]; hence, only the final results of the work are presented here. The quantities of interest in the free field blast problem are the peak incident overpressure in atmospheres, \bar{P} , the blast wave time of arrival, t_a , and the positive phase duration, τ . The expressions derived for these quantities are summarized by

$$\bar{P} = 2.4Z \quad (1a)$$

$$t_a = \frac{r}{a_\infty} f(Z) - \frac{\ell^*}{a_\infty} (0.94 \cos \phi + 9.24) \quad (1b)$$

$$\tau = (\ell^*/a_\infty) [1 + 0.13 (r/\ell^*)] \quad (1c)$$

where

$$\ell^* = \ell [\mu \cos \phi + (1 - \mu^2 \sin^2 \phi)^{1/2}] \quad (1d)$$

$$Z = (r/\ell^*)^{-1.1}, \text{ and} \quad (1e)$$

$$f(Z) = 1 + 10Z - (Z^2/1.2) + (Z^3/2.3) - (Z^4/3.4) + (Z^5/4.5) - (Z^6/5.6). \quad (1f)$$

For subsonic exit flow ($V_p < a_m$)

$$x = 0 \left\{ \frac{(8.62 \times 10^{-3}) p_m a_m}{(\gamma-1) p_m a_m} \left[1 + \frac{\gamma(\gamma-1)}{2} \right] \cdot \left[\frac{2}{\gamma+1} \left(1 + \frac{(\gamma-1)}{2} \frac{V_p^2}{a_m^2} \right) \right]^{\frac{\gamma-1}{\gamma-1}} \right\}^{1/2} \quad (2)$$

For supersonic exit flow ($V_p > a_m$),

$$x = (9.23 \times 10^{-2}) D \cdot$$

$$\left[\frac{p_m V_p}{(\gamma-1) p_m a_m} \left(1 + \frac{\gamma(\gamma-1)}{2} \frac{V_p^2}{a_m^2} \right) \right] \quad (3)$$

To use these relations, it is necessary to know the weapon characteristics and propellant gas properties at shot ejection. When the latter are not known from experiment, they may be determined using interior ballistics theory. The user of BLAST has the option of employing the following simplistic interior ballistics model to obtain the gas properties at shot ejection.

Lagrangian interior ballistics as given by Corner [2] is utilized. The internal energy of the propellant gases immediately prior to projectile ejection is given by

$$E = \frac{BCRT_{\text{mean}}}{\gamma-1} = \frac{BCRT_a}{\gamma-1} - 1/2 (m_1 + C/3) (1+x) V_p^2 \quad (4)$$

where B is the fraction of propellant burnt, C is the propellant mass, m_1 is the effective projectile mass accounting for bore friction, and x is the ratio of heat losses to kinetic energy. The following semi-empirical formulation for x is used

$$x = \frac{(10500) D^{3/2} (T_a - 300) u}{A_p V_p^2 (m_p + C/3) r} \quad (5)$$

where u is the roughness factor and $F = 1.7 + 671 D^{1/2} (D^2/L)^{-0.26}$. In this report the roughness factor is taken as 1.35, an average of large and small gun values. If we assume an ideal gas the muzzle pressure is given by

$$p_m = \frac{(\gamma-1) E}{U [1 + C/(3m_1)]} \quad (6)$$

where U is the combined volume of the bore and chamber. The following expression is obtained for the exit sound speed of the propellant gases

$$a_m = (\gamma R T_m)^{1/2} = \left(\gamma(\gamma-1) E / [C + C^2/(3m_1)] \right)^{1/2} \quad (7)$$

Results obtained from this simple theory were compared with those of a more exact computer model [3] and shown to produce similar results. Once the weapon characteristics and launch conditions are determined, the scaling relations given in Equation (1) are used to compute \bar{P} , t_a , and τ as functions of r and θ .

The contour plotting algorithm requires the evaluation of these functions at regularly spaced points (gridpoints) in the plotting domain. The values of r and θ must therefore be determined for each gridpoint. The geometry of the problem is shown in Figure 1. The origin of the polar coordinate system in which contours are plotted is the perpendicular projection of the muzzle of the gun into the plane of interest. The distance from the origin to the muzzle is h , and ϕ is the angle between the plane and the boreline of the gun. The contour algorithm requires a rectangular grid in the contour plane. For this reason, the gridpoints are located in a cartesian coordinate system originating at the muzzle of the gun. The x - y plane of this coordinate system is taken parallel to the contour plane; thus, any point in the contour plane is defined by $(x, y, -h)$. The distance from the muzzle to a point in the plane is given by the magnitude of r :

$$r = (x^2 + y^2 + h^2)^{1/2} \quad (8)$$

Let \hat{u} be a unit vector parallel to the boreline. The angle θ between \hat{u} and \hat{r} is given by

$$\theta = \cos^{-1} \frac{\hat{r} \cdot \hat{u}}{r} = \cos^{-1} \left[\frac{y \cos \phi + h \sin \phi}{(x^2 + y^2 + h^2)^{1/2}} \right]^{1/2} \quad (9)$$

The values of r and θ may be used to obtain \bar{P} , t_a , and τ from the scaling relations at each point in the contour plane.

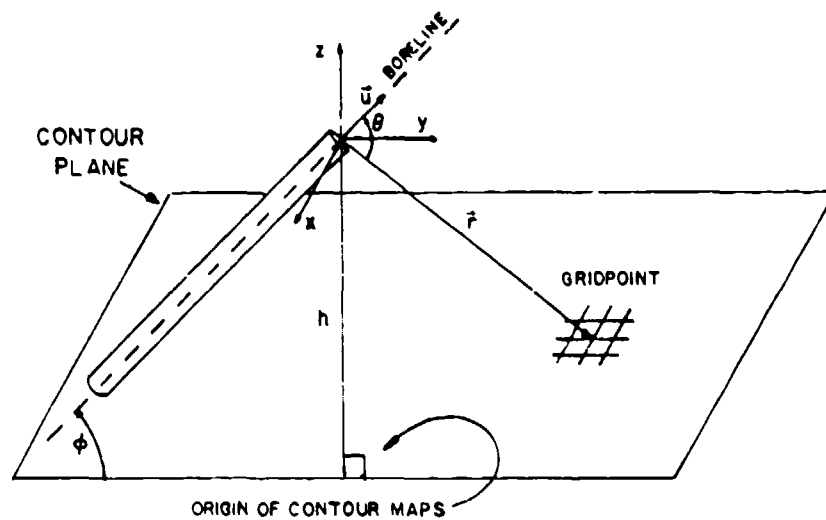


Fig. 1. Geometry of the Problem of Determining r and θ at a Point in a Plane with Arbitrary Orientation with Respect to the Boreline

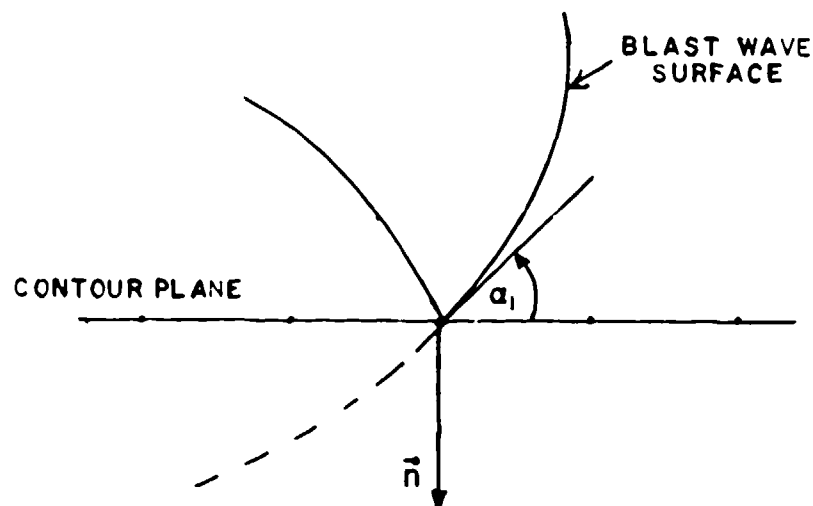


Fig. 2. Geometry Illustrating the Shock Wave Angle of Incidence at a Gridpoint

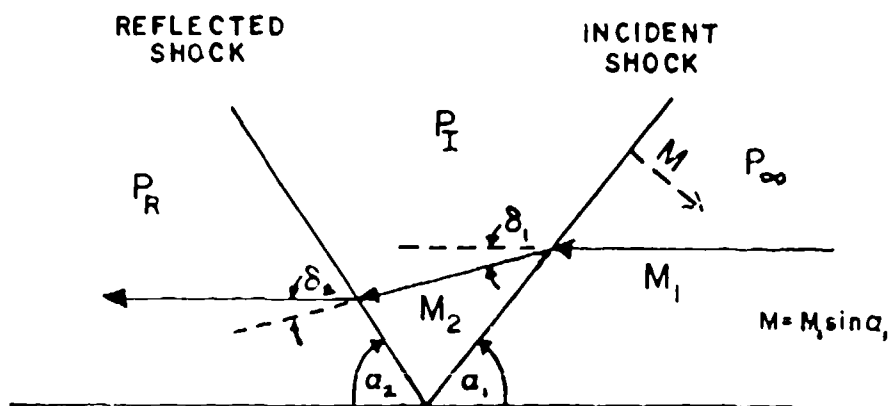


Fig. 3. The Oblique Shock Wave Solution for Reflected Shock

REFLECTED SHOCK WAVE CALCULATIONS

The reflection of shock waves from surfaces can be quite complex. Edney [4] has identified a number of possible flow structures depending upon the strength of the incident wave and the angle of reflection. In the present context, the process is considerably simplified. Only two types of reflection are considered: regular and single Mach stem [5].

For points very close to the reflecting surface (the contour plane), the blast may be considered planar. The shock wave angle of incidence, α_1 , is simply the angle between the direction of propagation of the blast and the surface normal, \vec{n} , to the contour plane (Figure 2). One method of obtaining the direction of propagation of the blast wave is to evaluate the gradient of t_a since the shape of the wave is equivalent to the surface defined by constant t_a . This gradient is normal to the blast wave surface; therefore, it points in the direction of propagation. The difficulty with this approach is that the computer time required to evaluate the gradient of t_a at each grid point is excessive. In the Appendix, we describe an alternate method for calculating the shock wave angle of incidence. This alternate method may be shown to be mathematically equivalent to the gradient approach, but it is more efficient computationally. In BLAST we use the approach described in the Appendix.

Once the shock wave angle of incidence, α_1 , is obtained, we determine whether regular reflection or Mach reflection of the shock wave occurs. The first step in this procedure is to shift from a fixed reference frame to one moving along the reflecting surface at the same velocity as the shock waves. In this reference frame the shock wave is stationary and has a streamline flowing through it parallel to the reflecting surface (Figure 3). The relations for compressible flow through an oblique shock wave [6] are applicable to this system.

The Mach number of the streamline in the region in front of the incident shock is given by

$$M_1 = \left[\frac{\gamma+1}{2\gamma} \left(\frac{p_1 - p_\infty}{p_\infty} \right) + 1 \right] / \sin^2 \alpha_1 \quad (10)$$

where p_1 and p_∞ are the pressures behind and in front of the incident shock, respectively. Across the incident shock, the flow is deflected through an angle, δ_1 , given by

$$\delta_1 = \tan^{-1} \left[2(\cot \alpha_1) \frac{M_1^2 \sin^2 \alpha_1 - 1}{M_1^2 (\gamma + \cos 2\alpha_1) + 2} \right] \quad (11)$$

and the Mach number behind the incident shock is obtained from

$$M_2 = \left[\frac{(\gamma-1) \frac{p_1}{p_\infty} + (\gamma-1)}{2\gamma \frac{p_1}{p_\infty}} \right]^{1/2} / \sin(\alpha_1 - \delta_1) \quad (12)$$

The question of whether regular reflection is possible may now be addressed. The maximum stream deflection for a specified upstream Mach number is given approximately by

$$\delta_{\max} = \frac{4}{3\sqrt{3}} \frac{(M_1^2 - 1)^{3/2}}{M_1^2 (\gamma + 1)} \quad (13)$$

If $\delta_1 \geq \delta_{\max}$, regular reflection is not possible and Mach reflection occurs. If $\delta_1 < \delta_{\max}$, regular reflection occurs and the analytic solution for the reflected overpressure may proceed.

If regular reflection is possible, the flow is deflected through the reflected shock. This deflection angle, δ_2 , must be equal to δ_1 because the boundary condition requires the flow to be parallel to the reflecting surface. Equation (11) applied to the flow across the reflected shock, with $\delta_1 = \delta_2$, yields

$$2(\cot \alpha_2) \frac{M_2^2 \sin^2 \alpha_2 - 1}{M_2^2 (\gamma + \cos 2\alpha_2)} - \tan \delta_2 = 0 \quad (14)$$

where α_2 is the wave angle of the reflected shock. Equation (14) is solved for α_2 by iteration. Once α_2 is known, the following equation is used to determine the pressure behind the reflected shock, p_R

$$\frac{p_R}{p_1} = \frac{2\gamma}{\gamma+1} (M_2^2 \sin^2 \alpha_2 - 1) + 1 \quad (15)$$

Finally, the reflected overpressure in atmosphere is given by

$$\overline{P}_R = \frac{P_R - P_\infty}{P_\infty} = \frac{P_R}{P_1} \frac{P_1}{P_\infty} - 1 \quad (16)$$

A computational problem arises in the preceding development as α_1 approaches zero. The expression for M_1 given in Equation (10) becomes arbitrarily large due to the $\sin \alpha_1$ term in the denominator. To avoid this difficulty we do not use the relations presented above for angles of incidence less than one degree. For angles of incidence less than this value, the solution for plane shock wave reflection normal to the surface is adequate. In this special case the ratio of reflected overpressure to incident overpressure is given by

$$\frac{P_R}{P_1} = \frac{(3\gamma-1) P_1 - (\gamma-1)}{(\gamma-1) P_1 + (\gamma+1)} \quad (17)$$

If regular reflection does not occur ($\alpha_1 \geq \alpha_{\max}$) it is impossible to obtain an analytic solution for the reflected overpressure using the theory of simple oblique waves. In this case the reflected overpressure is extracted from empirical results. A typical data plot of reflected overpressure versus shock wave angle of incidence for various incident overpressures [7] is presented in Figure 4. Similar data from a variety of sources were examined and two general features noted. First, beyond a certain angle of incidence whose value depends on the incident overpressure, the reflected overpressure curves may be approximated by straight lines. To determine the equations of these lines a point and slope are needed. At $\alpha_1 = 90^\circ$, the blast wave is at grazing incidence to the surface and the ratio of reflected to incident overpressure equals one, independent of the incident overpressure. Thus, the right end point of all the straight lines is defined. The slopes of the lines are taken to be a function of the incident overpressure and are obtained for 11 values of this parameter. Lagrangian interpolation is then used to obtain a slope for any intermediate value of incident overpressure. The interpolation procedure is also used to determine the angle of incidence beyond which the linear approximation is valid.

The second feature apparent in the empirical plots pertains to the region near the maxima of the reflected overpressure curves. For values of α_1 between the regular reflection and the linear interpolation regimes, the curves have a shape that can be approximated by cubic polynomials in α_1 . The four boundary values

needed to evaluate the polynomial are provided from the solutions at points A and B of Figure 5. The reflected overpressure at point A, $\pi(\alpha_A)$, is determined from the analytic solution for regular reflection. The slope at A, $\pi'(\alpha_A)$, can be approximated by taking a finite difference. At point B, $\pi(\alpha_B)$ and $\pi'(\alpha_B)$ are obtained from the Lagrangian interpolation procedure described above. The four-term polynomial at A is

$$\pi(\alpha_A) = \pi_0 + \pi_1 \alpha_A + \pi_2 \alpha_A^2 + \pi_3 \alpha_A^3 \quad (18)$$

The derivative of this polynomial is

$$\pi'(\alpha_A) = \pi_1 + 2\pi_2 \alpha_A + 3\pi_3 \alpha_A^2 \quad (19)$$

with two corresponding equations at point B. These four equations are solved for the four unknown coefficients π_0 , π_1 , π_2 , and π_3 .

The joining of the regular reflection solution, the cubic fit, and the linear fit produces a continuous variation of reflected overpressure coefficient versus angle of incidence for any specified incident overpressure. Results of this procedure are plotted in Figure 6. While this method of determining the reflected overpressure is relatively simple, it substantially reproduces the empirical plots as is demonstrated by comparison with experimental data (Figure 7).

THE CONTOUR PLOTTING METHOD

The results of the analysis have been formulated as a computer code, BLAST, which is programmed in FORTRAN 77 and is designed for interactive use on graphics terminals.

The method used to plot the contours is relatively standard and originated from an ALGOL computer code [8]. A grid is constructed covering the region of space that is of interest. This grid is composed of many small rectangular cells. At each corner of every cell (a gridpoint), the value of the function to be plotted must be known. Each contour value is processed individually, i.e., all contours at a particular level are plotted before moving to the next level. The search for contours at a particular level begins by locating all the contours that intersect the outside boundary of the grid (open contours). The search along the boundary progresses counterclockwise from the bottom left corner of the grid until two adjacent gridpoints are found that bound the contour level. To avoid repeatedly finding and plotting the same contours, an additional requirement is imposed: the larger functional values must be to the right of the intersection point of the

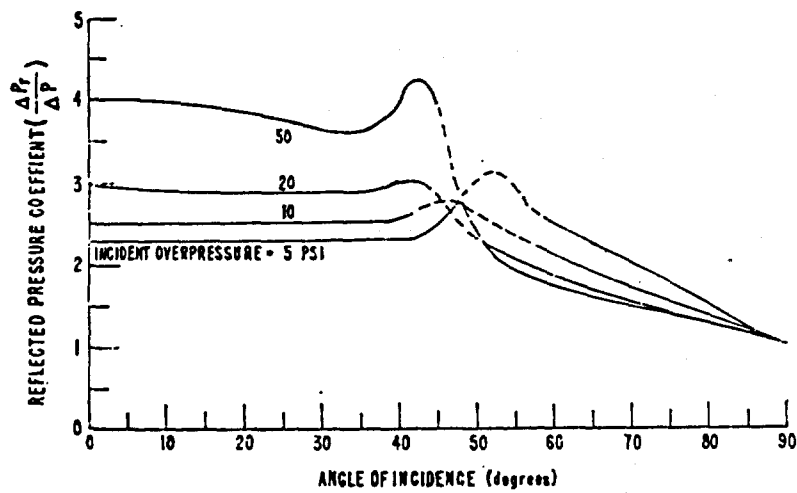


Fig. 4. Reflected Pressure Coefficient vs. Angle of Incidence for Various Incident Overpressures

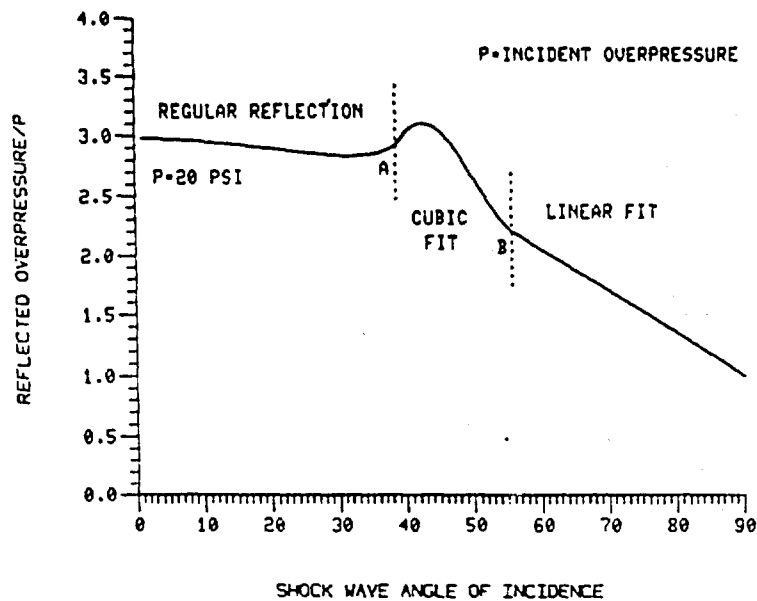


Fig. 5. The Three Regions of a Typical Reflected Overpressure vs. Angle of Incidence Curve (BLAST Generated)

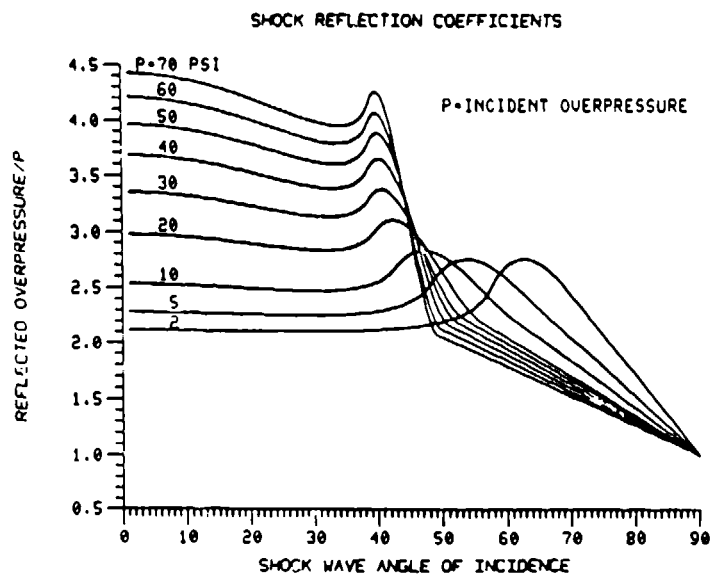


Fig. 6. Reflected Pressure Coefficient vs. Angle of Incidence for Various Incident Overpressures, Obtained by Method used in BLAST

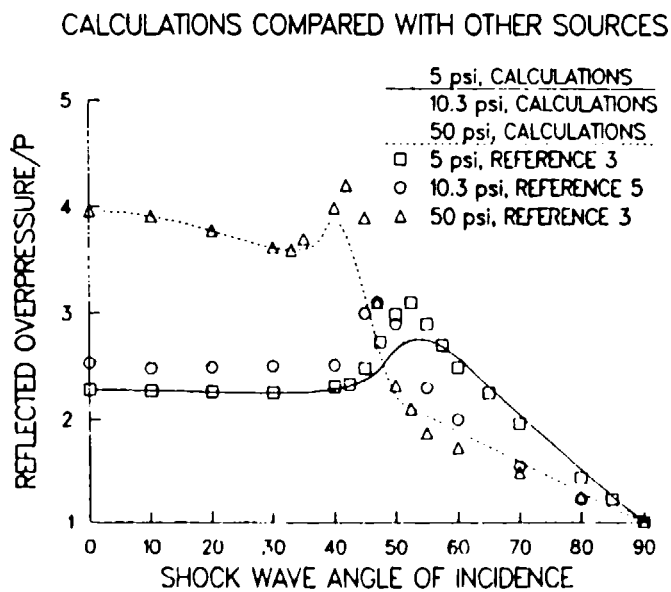


Fig. 7. Comparisons Between Reflection Pressure Results Obtained with BLAST and from Other Sources

contour and the grid boundary for the point to be recognized as the beginning of a contour. Once the beginning of a contour is found, it is followed cell by cell through the grid by comparison of adjacent grid points. The precise path of the contour across any cell boundary is determined by linear interpolation. The coordinates of this interpolated point are passed to a plotting subroutine which uses a commercial graphics package, DISSPLA, to draw each line segment on the plotting device. Because the grid squares are very small, there is no perception of the contour lines being composed of straight segments.

After all the open contours at a particular level are located and plotted, the grid is searched for closed contours at that level. The closed contours, once found, are followed through the grid and plotted in the same manner as the open contours. When plotting of the closed contours is complete, the process is repeated for the next contour level.

RESULTS

In Figure 8, we present contour maps, generated by BLAST, of peak incident overpressure, peak reflected overpressure, blast wave time of arrival, and positive phase duration. Maps of incident overpressure, time of arrival, and positive phase duration are generated within thirty seconds on a VAX 11/780. Plots of reflected overpressure require additional computations and are produced in approximately five minutes. The predictions shown are for the 30 mm, XM230 Chain Gun. The weapon is positioned parallel to the contour plane with the muzzle 0.26 meter distant from the origin of the contour grid. The strong directional dependence of the muzzle blast field is readily apparent in the plots of incident and reflected overpressure. The contours of time of arrival represent the blast wave surface as it propagates outward from the muzzle. This surface rapidly becomes spherical with a center displaced in the forward direction. The positive phase duration map shows the rate of increase of the blast wavelength to be larger in the forward direction than to the rear of the muzzle.

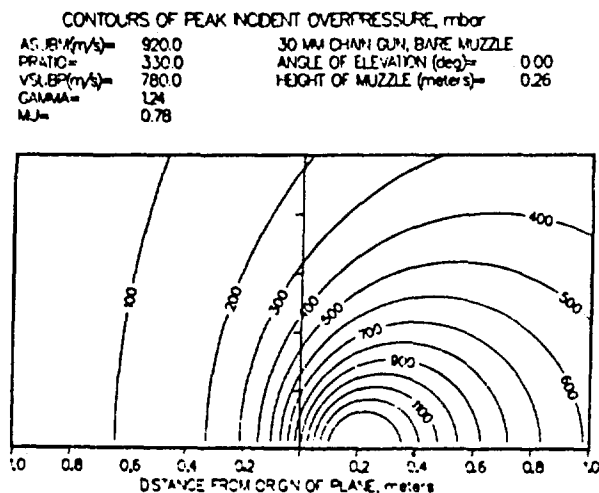
To check the validity of our model, we compare BLAST predictions with experimental blast measurements obtained in a previous test program [9] of the 30 mm Chain Gun. For these tests, pressure transducers were mounted in a linear array on an aluminum plate. The plate was then aligned at angles of zero and minus five degrees relative to the line of fire, with separations of 0.26 meter and 0.23 meter respectively. For the zero degree orientation, data were collected with the transducer array aligned both parallel and normal to the line of fire. For the minus five degree orientation, only the parallel array alignment was used. In Figures 9, 10, and 11 we compare the experimental measurements of reflected overpressure, time of

arrival, and positive phase duration for each of the three transducer orientations. In these plots the abscissa, S , denotes distance on the plate surface measured from the point on the plate nearest the muzzle. Negative values of S indicate positions behind the muzzle.

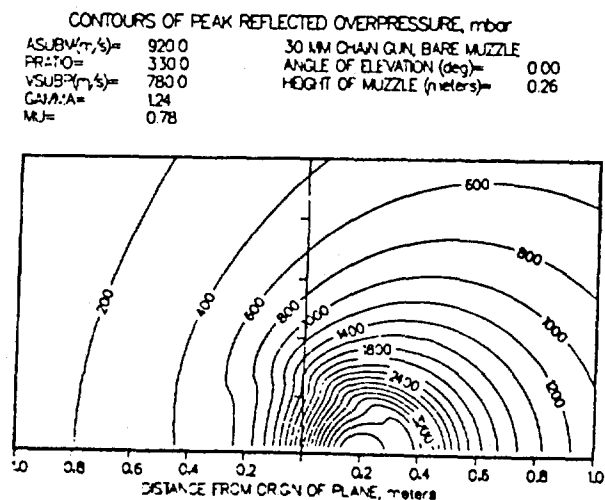
Figure 9 shows that the peak reflected overpressure measurements agree very favorably with BLAST predictions, particularly along the line of fire. The small plateau which is apparent in each of the predicted curves denotes the transition from regular reflection to Mach reflection of the incident wave. For this blast field, the effect appears too small to be defined experimentally. From the plots of time of arrival in Figure 10, we see that the location of minimum t_a predicted by BLAST is shifted forward from the location measured experimentally; however, the shape of the experimental t_a distribution is predicted quite well. It is obvious from Figure 11 that there is a definite deficiency in the positive phase duration scaling relation. We note that the expression for τ was determined by fitting scaled experimental data and that the scatter in this data justified only a simple linear curve fit. Clearly, a more complete analysis is desirable.

CONCLUSIONS

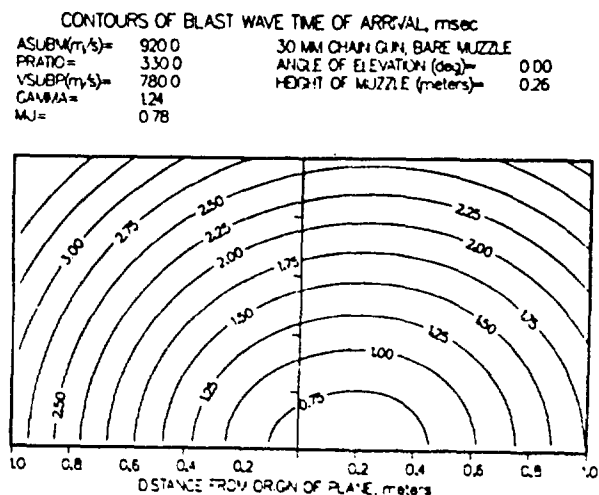
The muzzle blast pressure distribution on a surface located in the vicinity of a cannon has been calculated. The computational procedure accounts for shock reflection processes and is based upon previously developed scaling relations describing muzzle blast. The approach is formalized in a computer program, BLAST, that calculates and plots contour maps of peak incident overpressure, peak reflected overpressure, blast wave time of arrival, and positive phase duration. The contours are plotted in a plane having an arbitrary orientation with respect to the gun tube. The overpressure and time of arrival predictions compare favorably with experimental measurements. The positive phase duration is over-predicted by BLAST due to problems in the scaling expression used. BLAST is completely interactive and requires only minutes of computer (VAX 11/780) time to run.



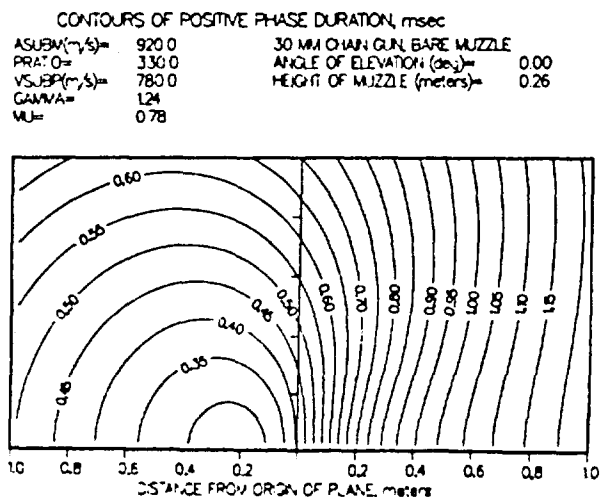
a



b



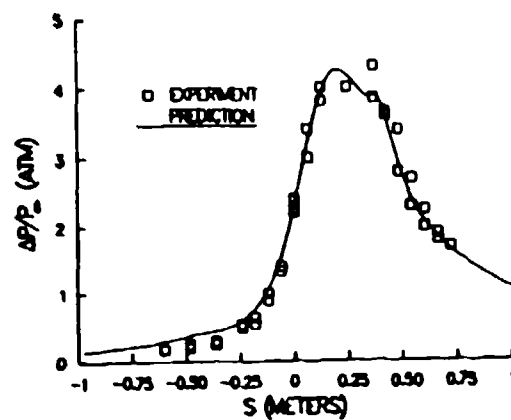
c



d

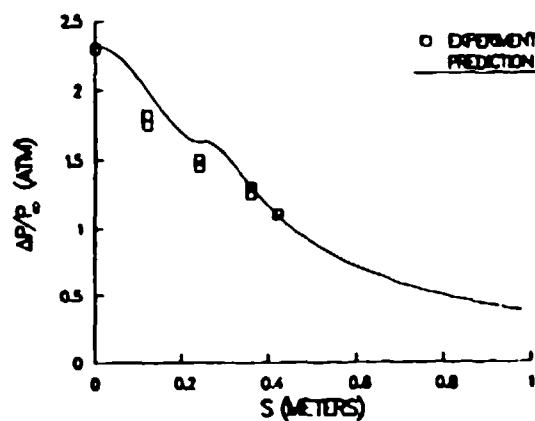
Fig. 8. Contour Maps of Peak Incident Overpressure (a), Peak Reflected Overpressure (b), Blast Wave Time of Arrival (c), and Positive Phase Duration (d)

0° Plate Orientation,
Parallel to Line of
Fire



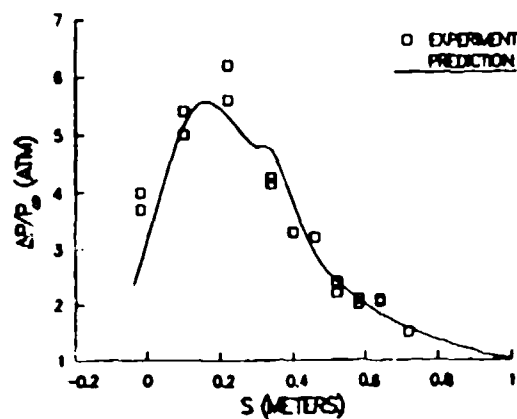
a

0° Plate Orientation
Perpendicular to Line
of Fire



b

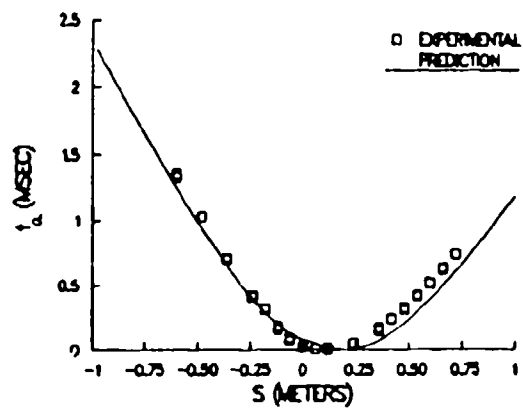
-5° Plate Orientation,
Parallel to Line of
Fire



c

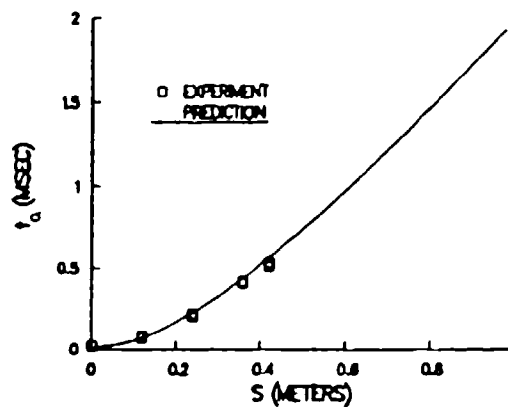
Fig. 9. Comparison of Predicted Peak Reflected Overpressure with Experiment

0° Plate Orientation,
Parallel to Line of
Fire



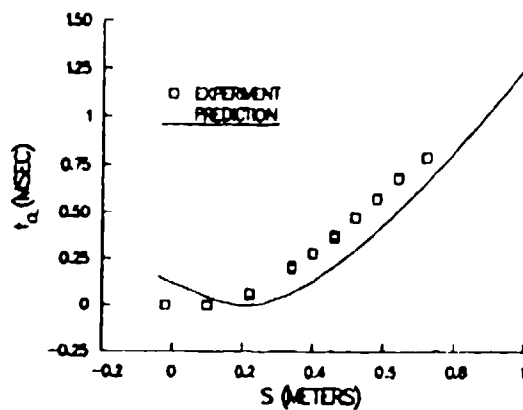
a

0° Plate Orientation,
Perpendicular to Line
of Fire



b

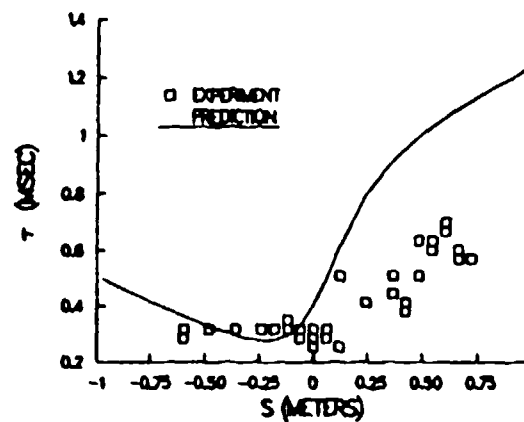
60° Plate Orientation,
Parallel to Line of
Fire



c

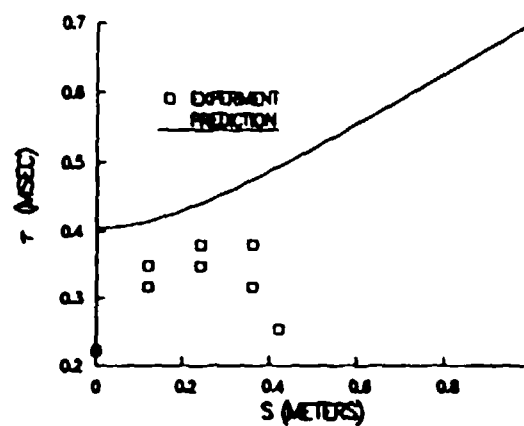
Fig. 10. Comparison of Predicted Blast Wave Time of Arrival with Experiment

0° Plate Orientation,
Parallel to Line of
Fire



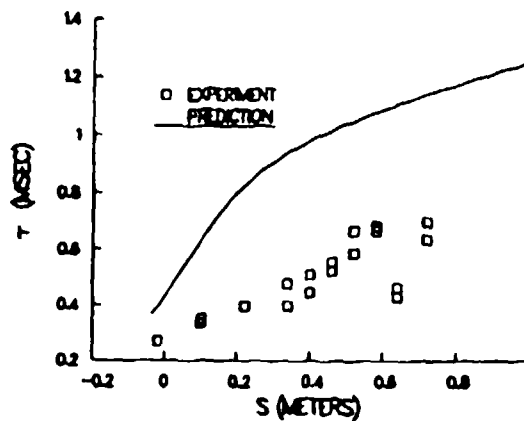
a

0° Plate Orientation,
Perpendicular to Line
of Fire



b

-5° Plate Orientation,
Parallel to Line of
Fire



c

Fig. 11. Comparison of Predicted Positive Phase Duration with Experiment

APPENDIX

Analysis for Obtaining the Shock Wave Angle of Incidence

We wish to obtain the angle between the incident shock and the contour plane. In Figure A-1, A is the point of interest in the contour plane, \vec{r} is the vector directed from the muzzle to A, θ is the angle between the boreline and \vec{r} , ϕ is the angle between the boreline and the contour plane, and h is the distance from the muzzle to the contour plane along a line normal to the plane.

We define \vec{p} as the vector which is directed from the boreline to A and is normal to the shockwave surface. We then have

$$\vec{p} = \vec{r} - \vec{z} \quad (\text{A-1})$$

where \vec{z} is a vector along the boreline as shown in Figure A-1. The angle between \vec{r} and \vec{p} is designated as α_1 . The components of \vec{p} are found to be

$$p_x = x_A \quad (\text{A-2})$$

$$p_y = y_A - z \cos \phi \quad (\text{A-3})$$

$$p_z = z_A - z \sin \phi \quad (\text{A-4})$$

The magnitude of \vec{p} , p , is found from the law of sines:

$$\frac{\sin(180^\circ - \alpha_1 - \phi)}{r} = \frac{\sin \phi}{p} \quad (\text{A-5})$$

Upon rearrangement, Equation (A-5) becomes

$$\xi = \frac{r \sin \phi}{\sin(\alpha_1 + \phi)} = \frac{r \sec \phi}{\tan \alpha_1 + 1} \quad (\text{A-6})$$

The cosine of the angle of incidence is given by

$$\cos \alpha_1 = \frac{\vec{p} \cdot \vec{r}}{p r} = \frac{x_A^2 + y_A^2 + z_A^2 - 2 z_A z \sin \phi}{(p_x^2 + p_y^2 + p_z^2)^{1/2} r} \quad (\text{A-7})$$

where \vec{n} is the unit normal to the contour plane. To use Equation (A-7) we must first obtain ξ . If n is known, Equation (A-6) may be employed to find ξ . The discussion below describes how n may be found.

Referring again to Figure A-1 we see that

$$\tan n = - \frac{1}{r} \left(\frac{dr}{d\theta} \right)_{t_a} \quad (\text{A-8})$$

where $(dr/d\theta)_{t_a}$ denotes the derivative of r with respect to θ along a contour of time of arrival, t_a . To obtain $(dr/d\theta)_{t_a}$ the following identity is used:

$$\left(\frac{dr}{d\theta} \right)_{t_a} = - \left(\frac{\partial t_a}{\partial \theta} \right)_r / \left(\frac{\partial t_a}{\partial r} \right)_\theta \quad (\text{A-9})$$

Recall that

$$t_a = \frac{x'}{a_\infty} [X f(Z) + C_1 + C_2 \cos \psi] \quad (\text{A-10})$$

where

$$X = r/x', \quad Z = x'^{-1.1}$$

and

$$x' = x'(\theta)$$

Hence, the chain rule may be applied to yield

$$\left(\frac{\partial t_a}{\partial \theta} \right)_r = \frac{dt_a}{dX} \left(\frac{\partial X}{\partial \theta} \right)_r + \left(\frac{\partial t_a}{\partial \psi} \right)_X \quad (\text{A-11})$$

$$\left(\frac{\partial t_a}{\partial r} \right)_\theta = \frac{dt_a}{dX} \left(\frac{\partial X}{\partial r} \right)_\theta + \left(\frac{\partial t_a}{\partial \psi} \right)_X \quad (\text{A-12})$$

Furthermore, by differentiation, we find

$$\left(\frac{\partial X}{\partial \theta} \right)_r = - \frac{r}{(x')^2} \frac{dx'}{d\theta} \quad (\text{A-13})$$

$$\left(\frac{\partial X}{\partial r} \right)_\theta = \frac{1}{x'} \quad (\text{A-14})$$

$$\left(\frac{\partial t_a}{\partial \theta}\right)_x = \frac{t_a}{x} \frac{dx'}{d\theta} - \frac{x'}{a_\infty} C_2 \sin \theta, \quad (A-15)$$

and

$$\left(\frac{\partial t_a}{\partial r}\right)_x = 0. \quad (A-16)$$

The following result is obtained from Reference 1:

$$\frac{dt_a}{dx} = \frac{x'}{a_\infty} \left(\frac{x^{1.1}}{1 + x^{1.1}} \right). \quad (A-17)$$

Equations (A-11) and (A-12) may now be rewritten as

$$\begin{aligned} \left(\frac{\partial t_a}{\partial \theta}\right)_r &= \frac{1}{a_\infty} \frac{dx'}{d\theta} \left[\frac{a_\infty t_a}{x'} - x \left(\frac{x^{1.1}}{1 + x^{1.1}} \right) \right] \\ &\quad - \frac{x'}{a_\infty} C_2 \sin \theta \end{aligned} \quad (A-18)$$

and

$$\left(\frac{\partial t_a}{\partial r}\right)_\theta = \frac{1}{a_\infty} \left(\frac{x^{1.1}}{1 + x^{1.1}} \right). \quad (A-19)$$

Substitution of Equations (A-18) and (A-19) into (A-9) yields

$$\begin{aligned} \left(\frac{dr}{d\theta}\right)_{t_a} &= \frac{dx'}{d\theta} [x - \bar{t}_a (1 + x^{-1.1})] \\ &\quad + C_2 x' (1 + x^{-1.1}) \sin \theta \end{aligned} \quad (A-20)$$

where

$$\bar{t}_a = \frac{a_\infty t_a}{x'}.$$

Finally we obtain

$$\begin{aligned} \tan \eta &= \frac{1}{r} \frac{dx'}{d\theta} [\bar{t}_a (1 + \frac{1}{x^{1.1}}) - x] \\ &\quad - \frac{C_2}{x} (1 + \frac{1}{x^{1.1}}) \sin \theta \end{aligned} \quad (A-21)$$

In summary, to determine α_1 , we first compute η from Equation (A-21). Equation (A-6) is then used to obtain ξ , which is substituted into Equations (A-2) through (A-4) to determine the components of \vec{p} . Finally, Equation (A-7) is used to calculate α_1 . This approach is less time-consuming than direct computation of the gradient of t_a because we make use of dt_a/dx which is available to us from previous analysis.

ACKNOWLEDGMENT

The authors would like to thank David H. Lyon for developing a number of original programming improvements used in this effort.

REFERENCES

1. K. S. Fansier and E. M. Schmidt, "The Prediction of Gun Muzzle Blast Properties Utilizing Scaling," U. S. Army Ballistic Research Laboratory, Aberdeen Proving Ground, Maryland, ARBRL-TR-02504, July 1983 (AD B075859L).
2. J. Corner, Theory of the Interior Ballistics of Guns, John Wiley, New York, 1950.
3. Private communication from Brian Bertrand.
4. B. E. Edney, Effects of Shock Impingement on the Heat Transfer Around Blunt Bodies, AIAA Journal, Vol. 16, No. 1, January 1968, pp. 15-21.
5. B. P. Bertrand, "Measurement of Pressure in Mach Reflection of Strong Shock Waves in a Shock Tube," U. S. Army Ballistic Research Laboratory, Aberdeen Proving Ground, Maryland, MR-2196, June 1972 (AD 746613).
6. H. W. Liepmann and A. Roshko, Elements of Gas Dynamics, J. Wiley, New York, 1957.
7. S. Glasstone, Editor, The Effects of Nuclear Weapons, Dept. of the Army Pamphlet No. 50-3, March 1977, p. 123.
8. B. R. Heap, et al, "Three Contouring Algorithms," NPL-81, National Physical Laboratory, Teddington, England, Dec 1969.
9. E. M. Schmidt, "Muzzle Blast Pressure Loadings on Aircraft Surfaces," U. S. Army Ballistic Research Laboratory, Aberdeen Proving Ground, Maryland, ARBRL-MR-73336, February 1984 (AD A 139132).

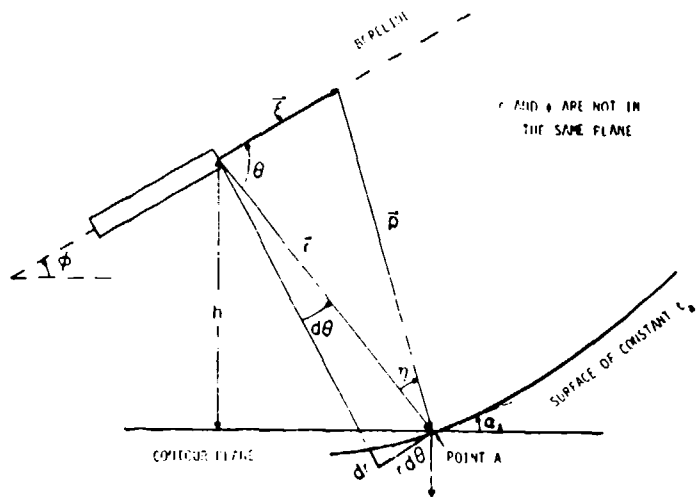


Fig. A-1. Geometry of the Shock Wave Angle of Incidence Calculation

Discussion

Mr. Bennett (Air Force Weapons Laboratory):

Could your technique be applied to shock tubes predicting the overpressure coming out the end, and how it is dissipated over distance?

Mr. Heaps: Yes, I believe it can. The analysis should apply equally well for shock tubes as well as guns.

Mr. Bennett: Our specific concern is a shock tube where the floor of the shock tube is at ground level, so you don't have a full, open area as you would at the end of a gun barrel.

Mr. Fansler: That problem has been addressed by Ed Schmidt. It is in an AIAA paper.

Mr. Fotleo (Martin Marietta Orlando): Would this technique be helpful in predicting the pressures acting on the back end of a projectile as it exits the gun? I know that is a near-field kind of pressure, but that has been one of the problems with the fall-off of the pressure acting on the base of the projectile. Consequently, you would find the set-forward loading you would get on the Copperhead and the Navy guided projectile.

Mr. Heaps: I think it could be used for that application.

Mr. Fansler: We looked at this problem some years ago. Again, I can give you the reference to that.

INTERIM DESIGN CRITERIA AND ACCEPTANCE TEST SPECIFICATIONS FOR BLAST-RESISTANT WINDOWS

Gerald E. Meyers
Naval Civil Engineering Laboratory
Port Hueneme, California

Preliminary design criteria for blast resistant windows exposed to blast overpressures are recommended. Design procedures and design curves for fully tempered glass are presented and parametrized according to glass thickness, glass dimensions, glass aspect ratio, peak blast overpressures, and effective blast duration. Design criteria for frames and a test certification procedure are also discussed. Additionally, various materials to enhance the safety of glass, when shattered, are discussed. Finally, design examples are presented.

INTRODUCTION

Historical records of explosion effects demonstrate that airborne glass fragments from failed windows are often the major cause of injuries from explosions. Also, failed window glazing often leads to additional injuries as blast pressure can enter interior building spaces and subject personnel to high pressure jetting, incident overpressure, secondary debris impact and thrown body impact. These risks are heightened in modern facilities, which often have large areas of glass for aesthetic reasons.

Guidelines are presented for the design, evaluation, and certification of windows to survive safely a prescribed blast environment described by a triangular-shaped pressure-time curve. Window designs using thermally tempered glass based on these guidelines can be expected to provide a probability of failure equivalent to that provided by current safety standards for safely resisting wind loads.

The guidelines are presented in the form of load criteria for the design of both the glass panes and framing system for the window. The criteria account for both bending and membrane stresses and their effect on maximum principal stresses and the nonlinear behavior of glass panes. The criteria cover a broad range of design parameters for rectangular-shaped glass panes: a pane aspect ratio $1.00 \leq a/b \leq 2.00$, pane area $1.0 \leq ab \leq 25 \text{ ft}^2$, and nominal glass thickness $1/4 \leq t \leq 1-1/2 \text{ inches}$. Presently, the design criteria are for blast resistant windows with thermally treated, tempered glass.

INTERIM DESIGN CRITERIA FOR GLAZING

Glazing Materials

The design criteria cover thermally tempered glass meeting the requirements of Federal

Specifications DD-G-1403B and DD-G-451d. Additionally, thermally tempered glass is required to meet the minimum fragment weight requirements of ANSI Z97.1-1984, Section 5.1.3(2).

Annealed glass is the most common form of glass available today. Depending upon manufacturing techniques, it is also known as plate, float or sheet glass. During manufacture, it is cooled slowly. The process results in very little, if any, residual compressive surface stress. Consequently, annealed glass is of relatively low strength when compared to tempered glass. Furthermore, it has large variations in strength and fractures into dagger-shaped, razor-sharp fragments. For these reasons, annealed glass is not recommended for use in blast resistant windows.

Thermally tempered glass is the most readily available tempered glass on the market. It is manufactured from annealed glass by heating to a high uniform temperature and then applying controlled rapid cooling. As the internal temperature profile relaxes towards uniformity, internal stresses are created. The outer layers, which cool and contract first, are set in compression, while internal layers are set in tension. As it is rare for flaws, which act as stress magnifiers, to exist in the interior of tempered glass sheets, the internal tensile stress is of relatively minimal consequence. As failure originates from tensile stresses exciting surface flaws in the glass, precompression permits a larger load to be carried before the net tensile strength of the tempered glass pane is exceeded. Thermally tempered glass is typically four to five times stronger than annealed glass.

The fracture characteristics of tempered glass are superior to those of annealed glass. Due to the high strain energy stored by the prestress, tempered glass will eventually fracture into small cube-shaped fragments instead of the razor-sharp and dagger-shaped fragments

associated with fracture of annealed glass. Breakage patterns of side and rear windows in American automobiles are a good example of the failure mode of thermally or heat-treated tempered glass.

Glass can also be tempered chemically by a bath process where ions are exchanged between the bath and the glass. Denser packing of the molecules close to the surface of glass plate results and produces a layer of compression. Precompression levels between 10,000 and 50,000 psi are reported by industry. As the molecular packing and precompression layer is usually not deeper than 0.012 inch from each surface (compared with 20 to 22% of overall thickness from each surface for thermally tempered glass), less strain energy is stored in the glass plate and consequently the fracture pattern resembles that of annealed glass.

A common problem with some commercially available chemically tempered glass is that the precompression depth or case depth is thin enough (0.001 inch) to be pierced by surface flaws (often 0.004 inch deep). If this occurs, the surface flaws will penetrate the inner tensile layer. The resulting stress concentration about the tip of the flaw in the tensile regime of the cross-section will often induce premature failure.

Only chemically tempered glass with a precompression depth greater than 0.010 inch offers reliable enough performance for use in blast-resistant design. Several types of chemically tempered glass are now under investigation by the Naval Civil Engineering Laboratory (NCEL) for future inclusion in blast-resistant window design criteria.

If chemically tempered glass with a precompression greater than thermally tempered glass and a deep enough precompression level can be reliably produced at a reasonable cost, it may be, as a laminated cross section with polycarbonate as the inner ply, the ideal material for blast- and ballistic-resistant glazing. Not only will the glass exhibit more strength than thermally tempered glass, but as it will fail in a manner similar to annealed glass with large glass fragments, it will offer a degree of fragment and ballistic resistance. This is because the large shards of glass, although fractured by the first ballistic projectile, are held in place by the interlaminar material and can flatten, slow down, and tumble subsequent ballistic projectiles for catch by the polycarbonate. The degree of fragment and ballistic resistance will be related to the cross-sectional thickness and make-up of the laminate. Also, as a failed cross section will resemble a cracked American automobile windshield, visibility will be maintained in a failed or cracked lite. This can be paramount if the glazing is used in a physical security or other critical setting.

Semi-tempered glass is often marketed as safety or heat-treated glass. However, it exhibits neither the dicing characteristic upon breakage nor the higher tensile strength associated with fully tempered glass. Semi-tempered glass is not recommended for blast resistant

windows unless it is laminated. If laminated with polycarbonate inboard lites, semi-tempered glass can provide a degree of ballistic resistance as well as moderate blast resistance. Again, the degree of fragment and ballistic resistance will be related to the cross-sectional thickness and make-up of the laminate.

Another common glazing material is wire glass, annealed glass with an embedded layer of wire mesh. Its only use is as a fire resistant barrier. Wire glass has the fracture and low strength characteristics of annealed glass and although the wire binds fragments, it presents metal fragments as an additional hazard. Wire glass is never recommended for blast resistant windows.

The design of blast resistant windows is currently restricted to heat-treated fully-tempered glass meeting both Federal Specification DD-G-1403B and ANSI Z97.1-1984. Tempered glass meeting only DD-G-1403B may possess a surface precompression of only 10,000 psi. At this level of precompression, the fracture pattern is similar to annealed and semi-tempered glass. Tempered glass meeting the minimum fragment specifications of ANSI Z97.1-1984 (Section 5.1.3(2)) has a higher surface precompression level and tensile strength which improves the capacity of blast resistant windows. Additionally, failure results in smaller cubical-shaped fragments.

Although thermally tempered glass exhibits the safest failure mode, failure under blast loading still presents a significant health hazard. Results from blast tests reveal that upon fracture, tempered glass fragments may be propelled in cohesive clumps that only fragment upon impact into smaller rock-salt shaped fragments. Even if the tempered glass breaks up initially into small fragments, sufficient blast pressure can propel the fragments at a high enough velocity to constitute a severe hazard. Computer simulations at NCEL indicate that a 6-psi blast pressure with an effective duration of 50 msec can eject glass fragments from a 54 x 36 x 3/8-inch thermally tempered lite at speeds up to 80 mph. Also, biomedical experts report that the 58-ft-lb criterion for acceptable fragments should not be applied to tempered glass because of the high likelihood of sharp edge and corner impact by the fragments. Laminating the glass with polyvinyl butyral, adding a polycarbonate inner ply or, in some cases, applying a fragment retention film (discussed in the Fragment Protection Film section) to the inside face of the glass can significantly improve safety.

Design Stresses

The design stress is the maximum principal tensile stress allowed for the glazing. The design stress was derived for a prescribed probability of failure, using a statistical failure prediction model similar to that under development by the ASTM (Committee E06.51). Thus, failure of the glazing is assumed to occur when the maximum principal tensile stress exceeds a design stress associated with a prescribed

probability of failure. For the full range of design parameters ($1.0 \leq ab \leq 25 \text{ ft}^2$, $1.00 \leq a/b \leq 2.00$ and $1/4 \leq t \leq 1\text{-}1/2$ inches), and a stress intensity duration of 1 second, the model predicted a design stress for tempered glass of 16,000 psi based on a probability of failure $P(F) \leq 0.001$.

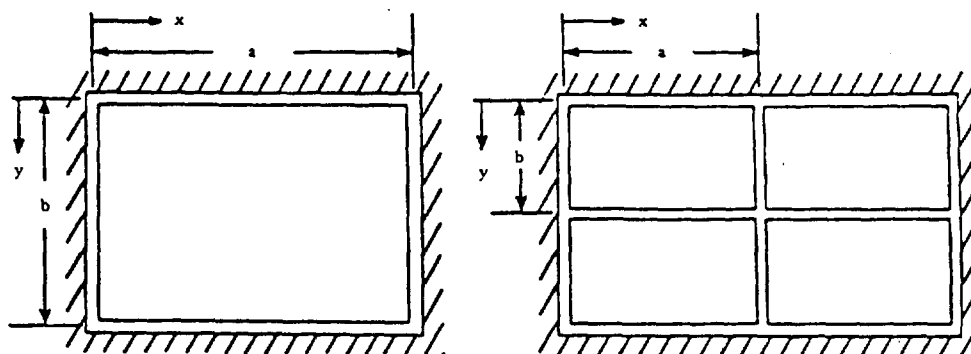
These design stresses for blast resistant glazing are slightly higher than those commonly used in the design for one-minute wind loads. However, these higher design stresses are justified on the basis of the relatively short stress intensity duration (always considerably less than one second) produced by blast loads.

Dynamic Response to Blast Load

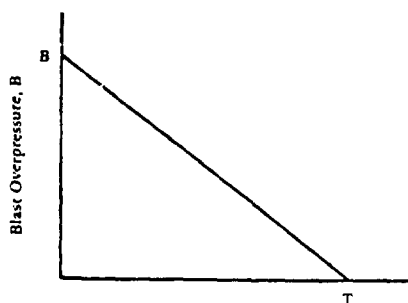
An analytical model was used to predict the blast load capacity of tempered glazing. Characteristic parameters of the model are illustrated in Figure 1.

The glazing is a rectangular glass plate having a long dimension, a , short dimension, b , thickness, t , poisson ratio, $\nu = 0.22$, and elastic modulus, $E = 10,000,000$ psi. The plate is simply supported along all four edges, with no in-plane and rotational restraints at the edges in accordance with observed window boundary conditions (Anians). The relative bending stiffness of the supporting frame members is assumed to be infinite relative to the pane. Recent static load tests indicate that the allowable frame member deflections in the design criteria of $1/264$ of span will not measurably reduce pane strength.

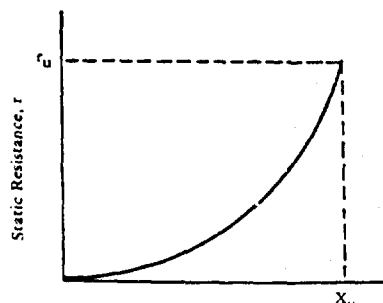
The blast pressure loading is described by a peak triangular-shaped pressure-time curve as shown in Figure 1b. The blast pressure rises instantaneously to a peak blast pressure, B , and then decays with a blast pressure duration, T . The pressure is uniformly distributed over the surface of the plate and applied normal to the plate.



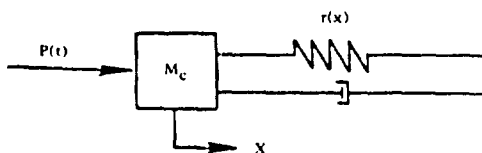
(a) Window pane geometry



(b) Blast loading



(c) Resistance of glass pane



(d) Dynamic response model

Figure 1. Characteristic parameters for glass pane, blast loading, resistance function and response model.

The resistance function (static uniform load, r , versus center deflection, X) for the plate accounts for both bending and membrane stresses. The effects of membrane stresses produce nonlinear stiffening of the resistance function as illustrated in Figure 1c. The failure deflection, X_u , is defined as the center deflection where the maximum principle tensile stress at any point in the glass first reaches the design stress, f_u , of 16,000 psi.

The model used a single degree of freedom system to simulate the dynamic response of the plate, as shown in Figure 1d. In order to be conservative, no damping of the window pane is assumed. Future charts for rebound will include damping with the coefficient of critical damping based on actual blast test results. The applied load, $P(t)$, is shown in Figure 1b. The resistance function, $r(x)$, is shown in Figure 1d. Given the design parameters for the glazing, the design or failure stress, f_u , and the blast load duration, T , the model calculated the peak blast pressure, B , required to fail the glazing by exceeding the prescribed probability of failure, $P(F)$, of 0.001. The model also assumed failure to occur if the center deflection exceeded ten times the glazing thickness. This restricts solutions to the valid range of the Von Karman plate equations used to develop the resistance function for the glazing while also preventing edge disengagement of the glass lite.

Design Charts

Charts are presented in Figures 2 to 21 for both the design and evaluation of glazing to survive safely a prescribed blast loading with a probability of failure no greater than 0.001. The charts relate the peak blast pressure capacity, B , of thermally tempered glazing to all combinations of the following design parameters: $a/b = 1.00, 1.25, 1.50, 1.75$ and 2.00 ; $1.00 \leq ab \leq 25 \text{ ft}^2$; $12 \leq b \leq 60$ inches; $2 \leq T \leq 1,000$ msec; and $t = 1/4, 5/16, 3/8, 1/2, 5/8, 3/4, 1$, and $1-1/2$ inches (nominal). Thermally tempered glass up to $3/4$ inch thick can be easily purchased in the United States. Only limited quantities of 1-inch-thick thermally tempered glass are available. The 1-1/2-inch-thick thermally tempered glass is only available in a laminated format with a polyvinyl butyral (PVB) inner layer.

As it is highly probable that the extremely high strain rates associated with the response of windows to blast loading will enable the polyvinyl butyral (PVB) inner layer to transmit transverse or horizontal shear and result in a monolithic behavior of the glass lite, the design curves for 1-1/2-inch-thick glass will most likely be proved valid for laminated glass. However, until planned blast load tests are completed by the Naval Civil Engineering Laboratory, the blast load capacity for laminated thermally tempered glass should be 75% of the posted value in Figures 5, 9, 13, 17, and 21. This downward load capacity adjustment is common in designing laminated glass for wind loadings.

It is expected that aircraft grade (AG) polyvinyl butyral, being stiffer than the more

common architectural grade (SR), will enhance monolithic glass plate behavior. Until blast load testing and evaluation are complete, the aircraft grade polyvinyl butyral is suggested as the choice interlaminar material.

Each chart has a series of curves. Each curve corresponds to the pane dimension shown to the right of the curve. Adjacent to the pane dimension is the value of B (peak blast pressure capacity) corresponding to $T = 1,000$ msec. The posted value of B is intended to reduce errors when interpolating between curves.

The charts are based on the minimum thickness of fabricated glass allowed by Federal Specification DD-G-451d. However, the nominal thickness should always be used in conjunction with the charts, i.e., $t = 1/4$ inch instead of the possible minimum thickness of 0.219 inch used in design.

FRAGMENT PROTECTION

In those cases where it is impossible or uneconomical to design for complete blast protection, the danger from glass fragments should be minimized. Commercial products have been developed which offer a relatively inexpensive method to improve the shatter resistance of window glass and significantly decrease the energy and destructive capability of glass fragments.

Laminated Glass

In terms of fragment retention, a laminated blast-resistant lite offers significant advantage over monolithic glass. If glass failure occurs, the polyvinyl butyral may retain most of the glass fragments. However, this is highly dependent upon the post failure pressure-time history of the blast loading. Generally, a greater margin of safety between glass failure and fragment ejection exists for short-duration blast loads characterized by small and close-in explosive charges. Under long-duration blast loads associated with large explosive charge weights, such as munition storage areas or nuclear explosions, or under blast loads much higher than design a considerably smaller factor of safety may be attributed to the lamination as the failed lite may be propelled as a single body into the interior of the structure. However, in this failure mode the pane will probably travel a smaller distance than the ejected glass fragments and a smaller percentage of the interior space will be impacted by glass fragments. Also, if a projectile passes through the glass, most spalled glass fragments will be retained. Depending upon the energy imparted to the failed lite by the pressure time history of an explosion, a decorative crossbar or grillwork may provide an additional increase in safety from a failed laminated glass lite.

Environmental durability of polyvinyl butyral is a known and proven quantity. Long-term use in automobile and aerospace windows indicates that few, if any, problems of environmental degradation will be encountered.

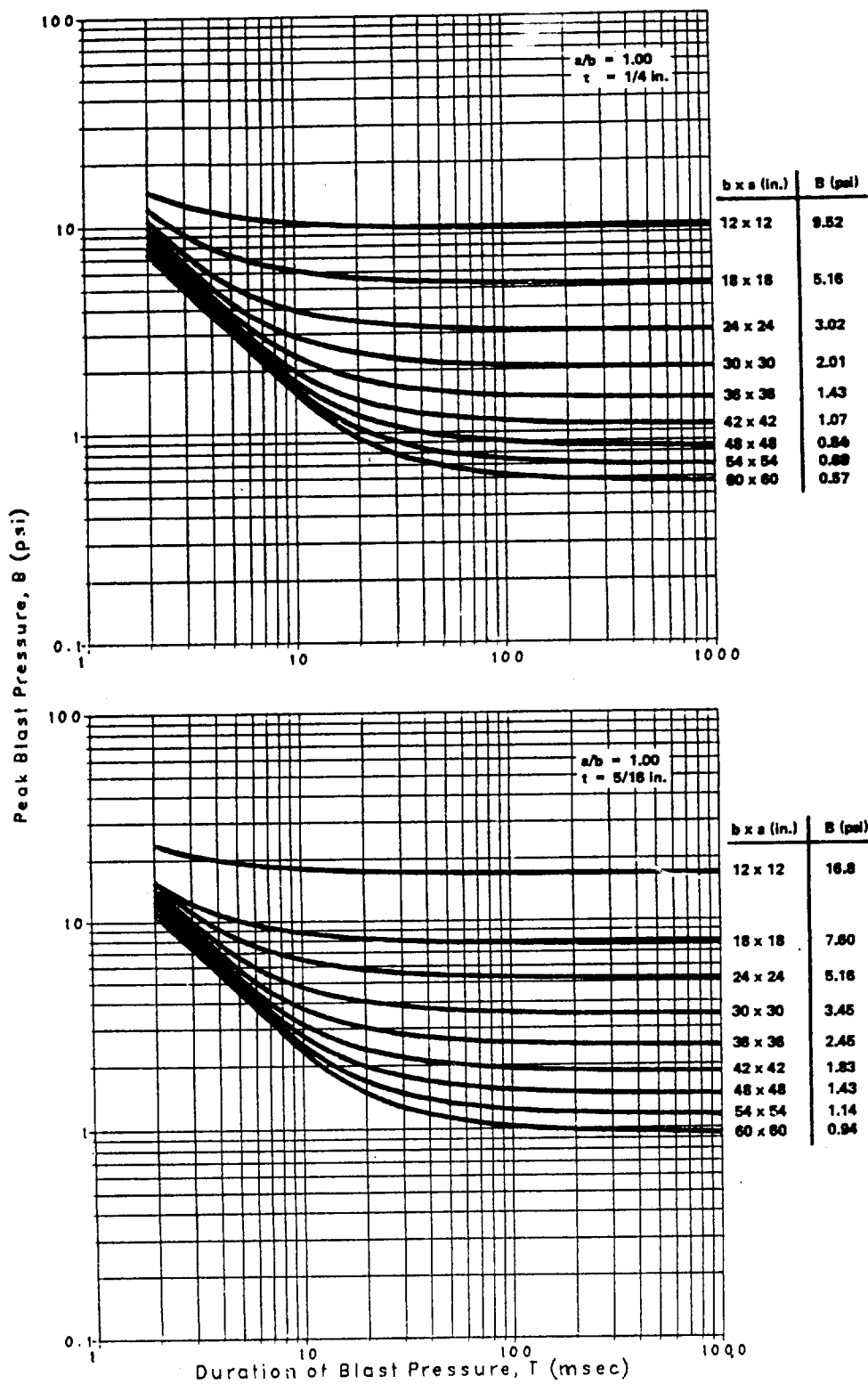


Figure 2. Peak blast pressure capacity for tempered glass panes: $a/b = 1.00$, $t = 1/4$ and $5/16$ in.

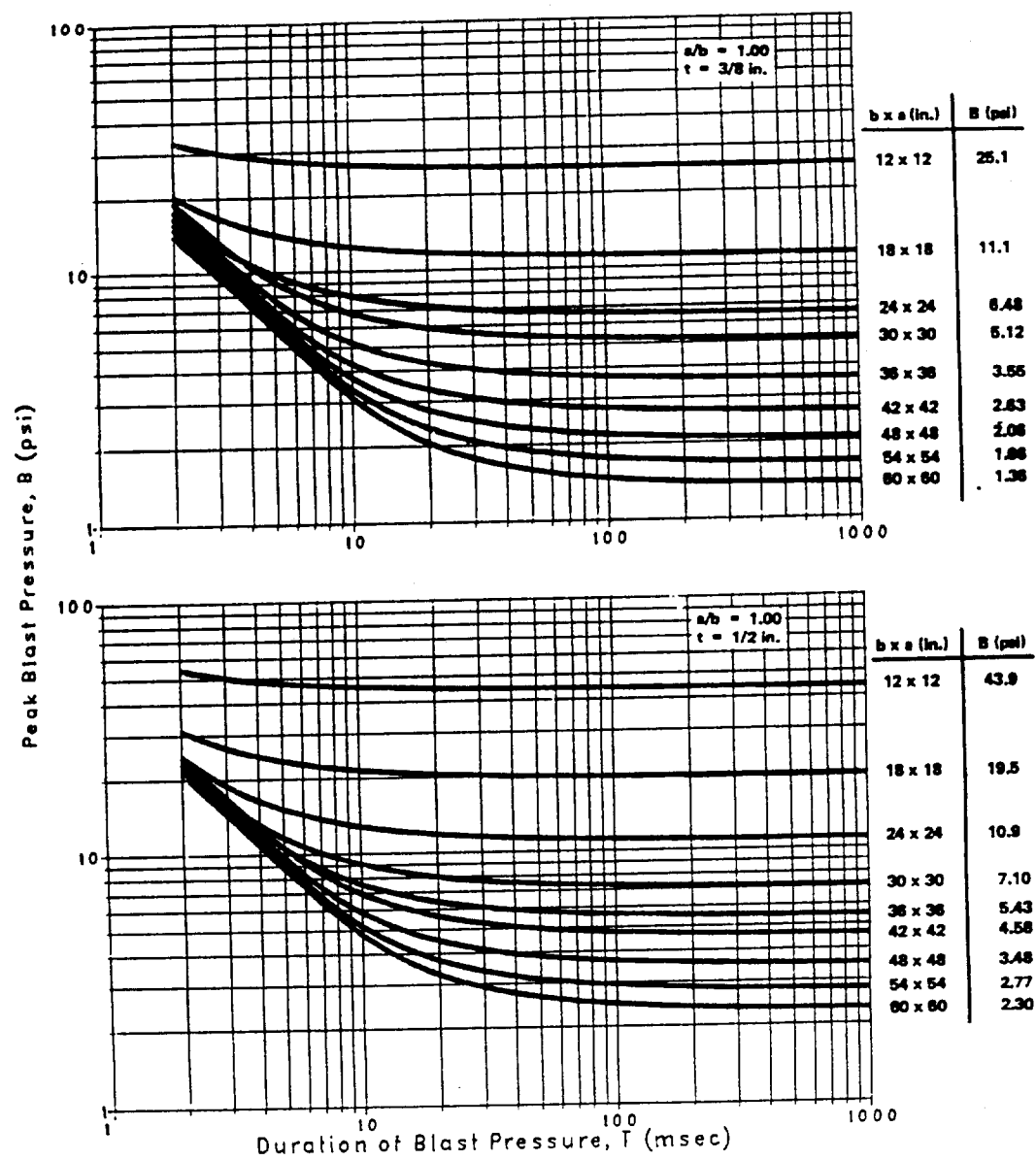


Figure 3. Peak blast pressure capacity for tempered glass panes: $a/b = 1.00$, $\tau = 3/8$ and $1/2$ in.

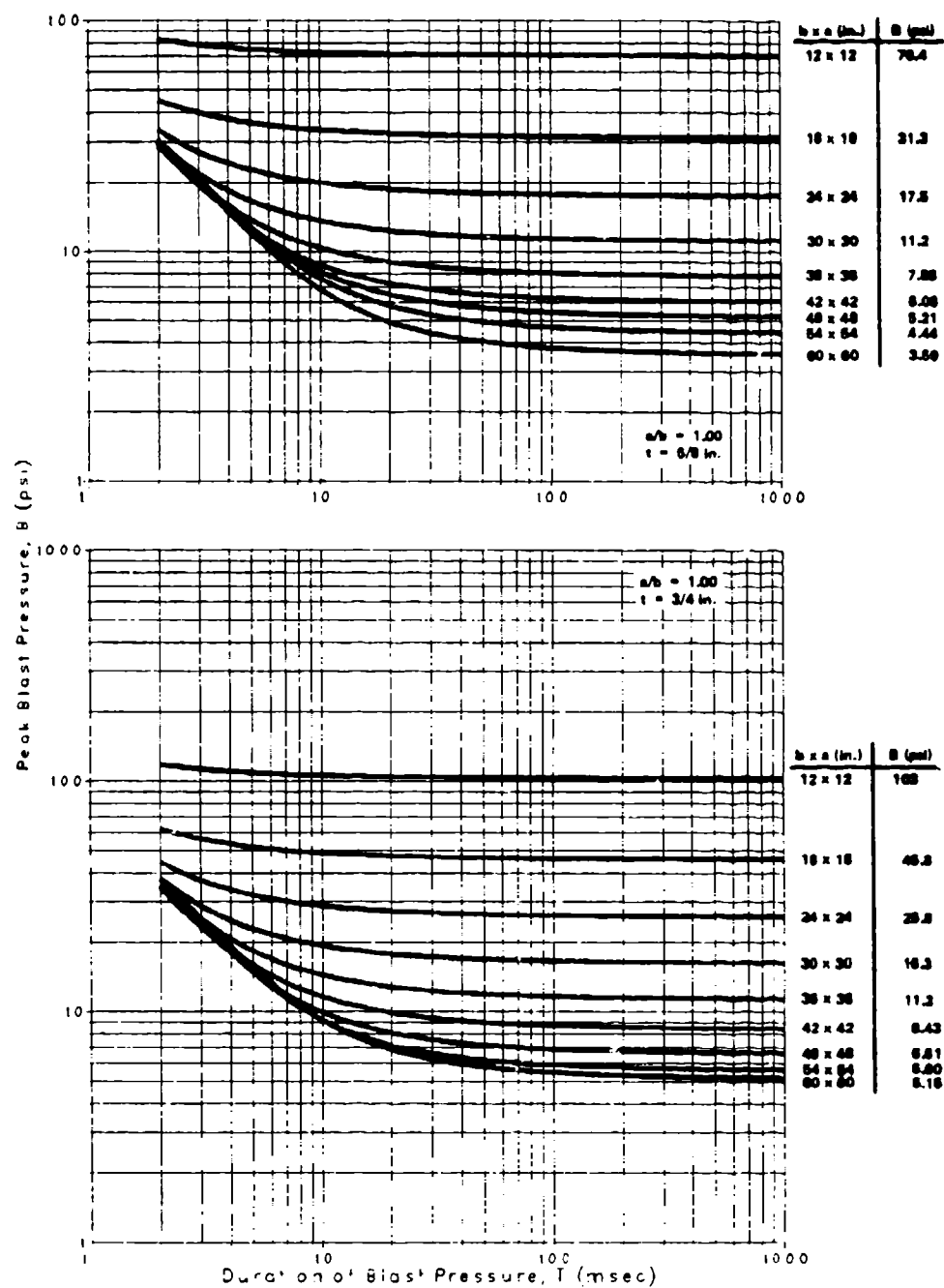


Figure 4. Peak blast pressure capacity for tempered glass panes. $a/b = 1.00$, $t = 5/8$ and $3/4$ in.

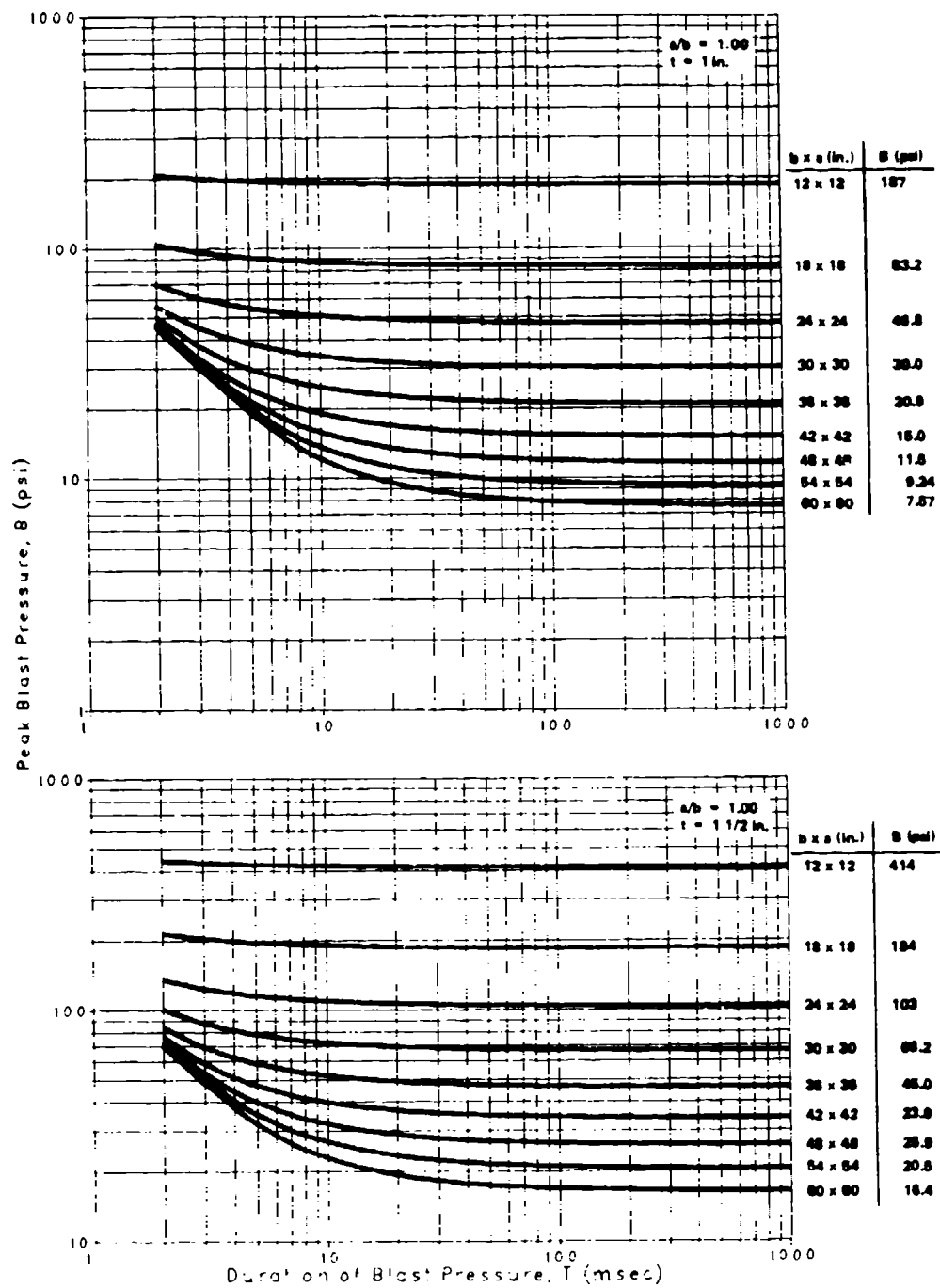


Figure 5 Peak blast pressure capacity for tempered glass panes $a/b = 1.00$, $t = 1$ and $1 \frac{1}{2}$ in.

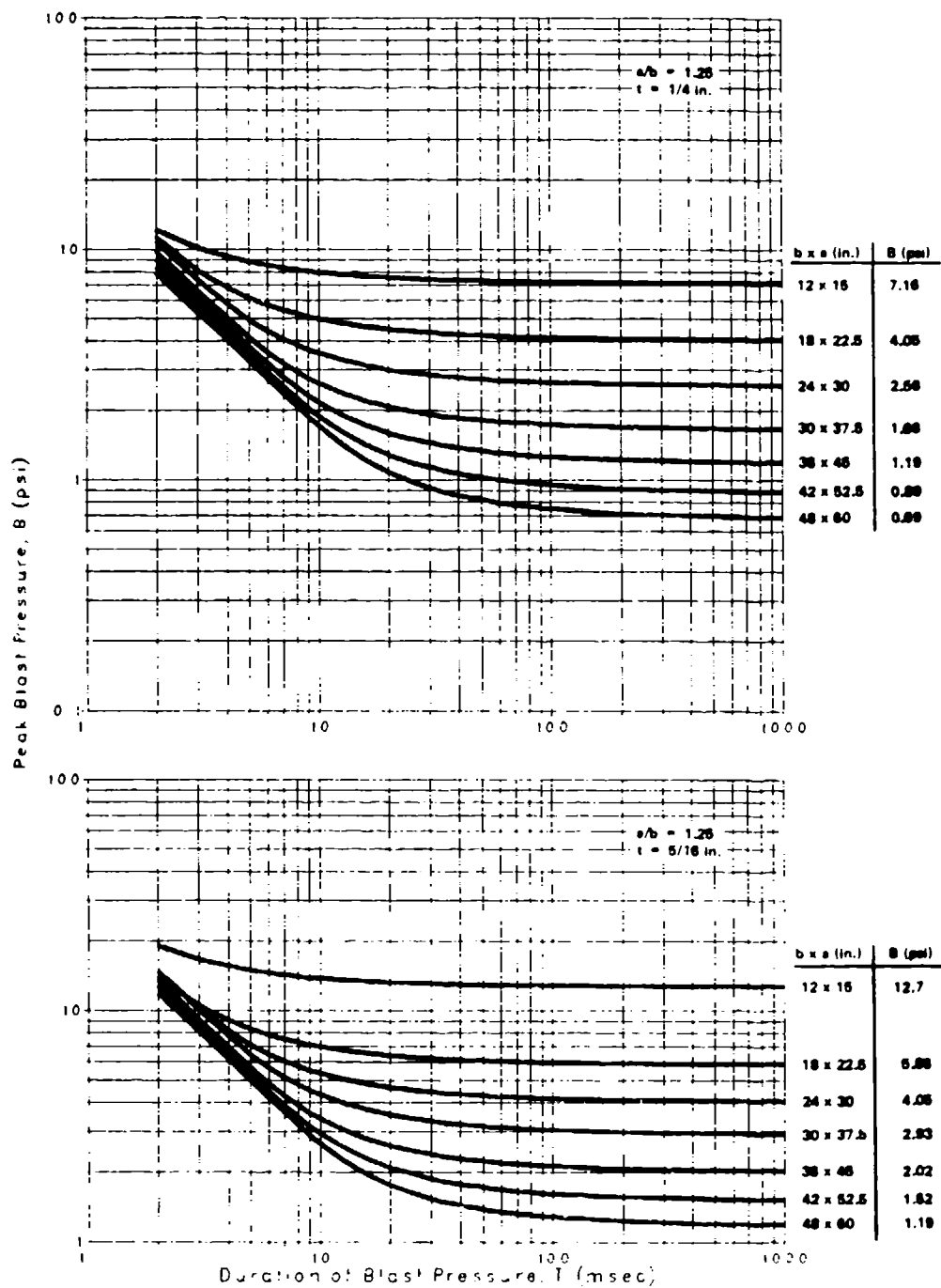


Figure 6 Peak blast pressure capacity for tempered glass panes $a/b = 1.25$ $t = 1/4$ and $5/16$ in.

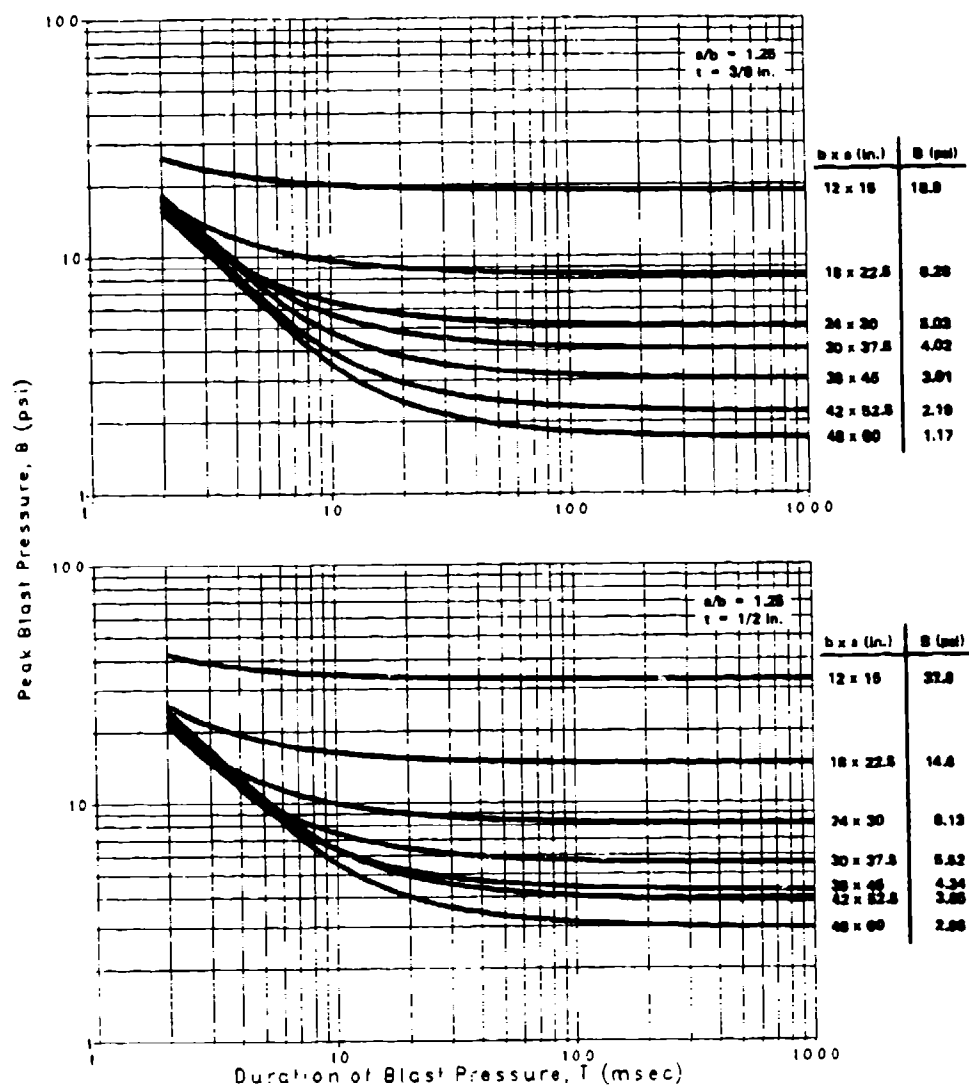


Figure 7 Peak blast pressure capacity for tempered glass panes $a/b = 1.25$, $t = 3/8$ and $1/2$ in.

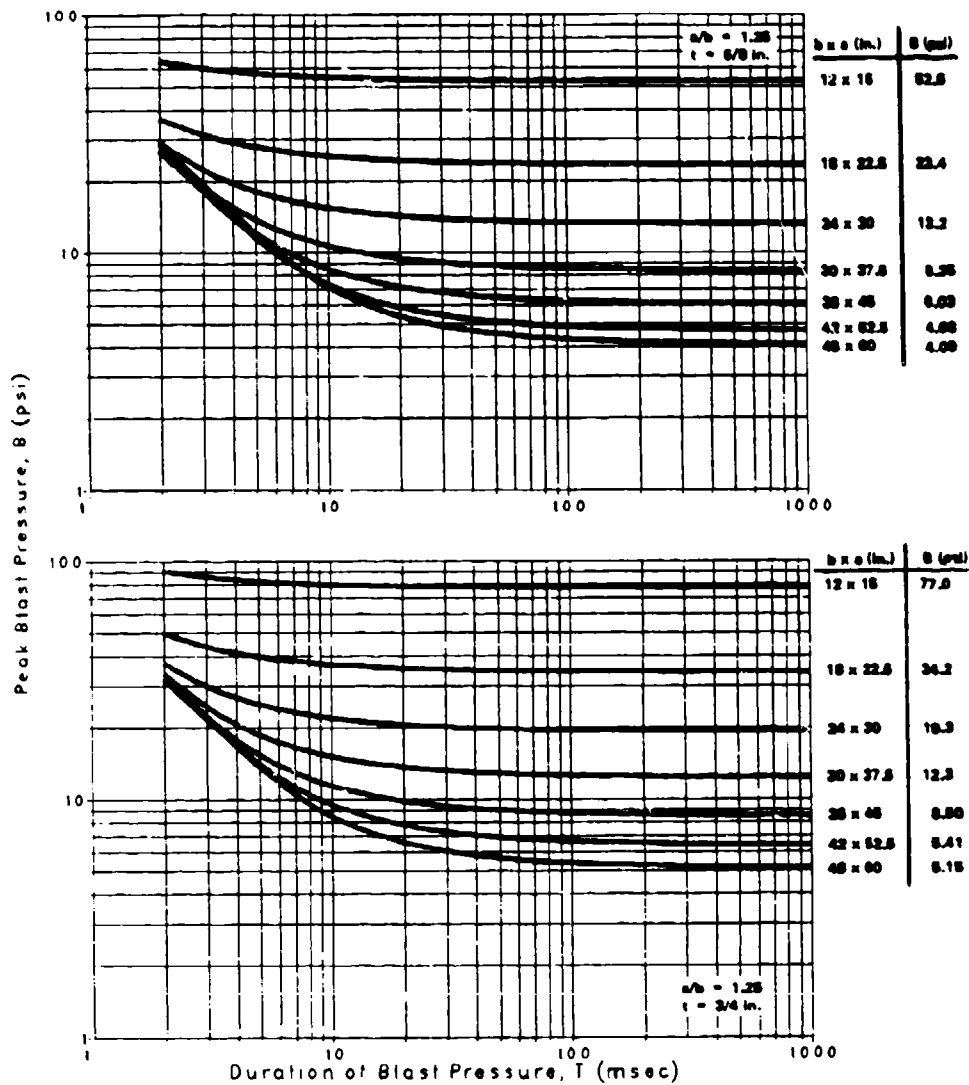


Figure 8 Peak blast pressure capacity for tempered glass panes. $a/b = 1.25$, $t = 5/8$ and $3/4$ in.

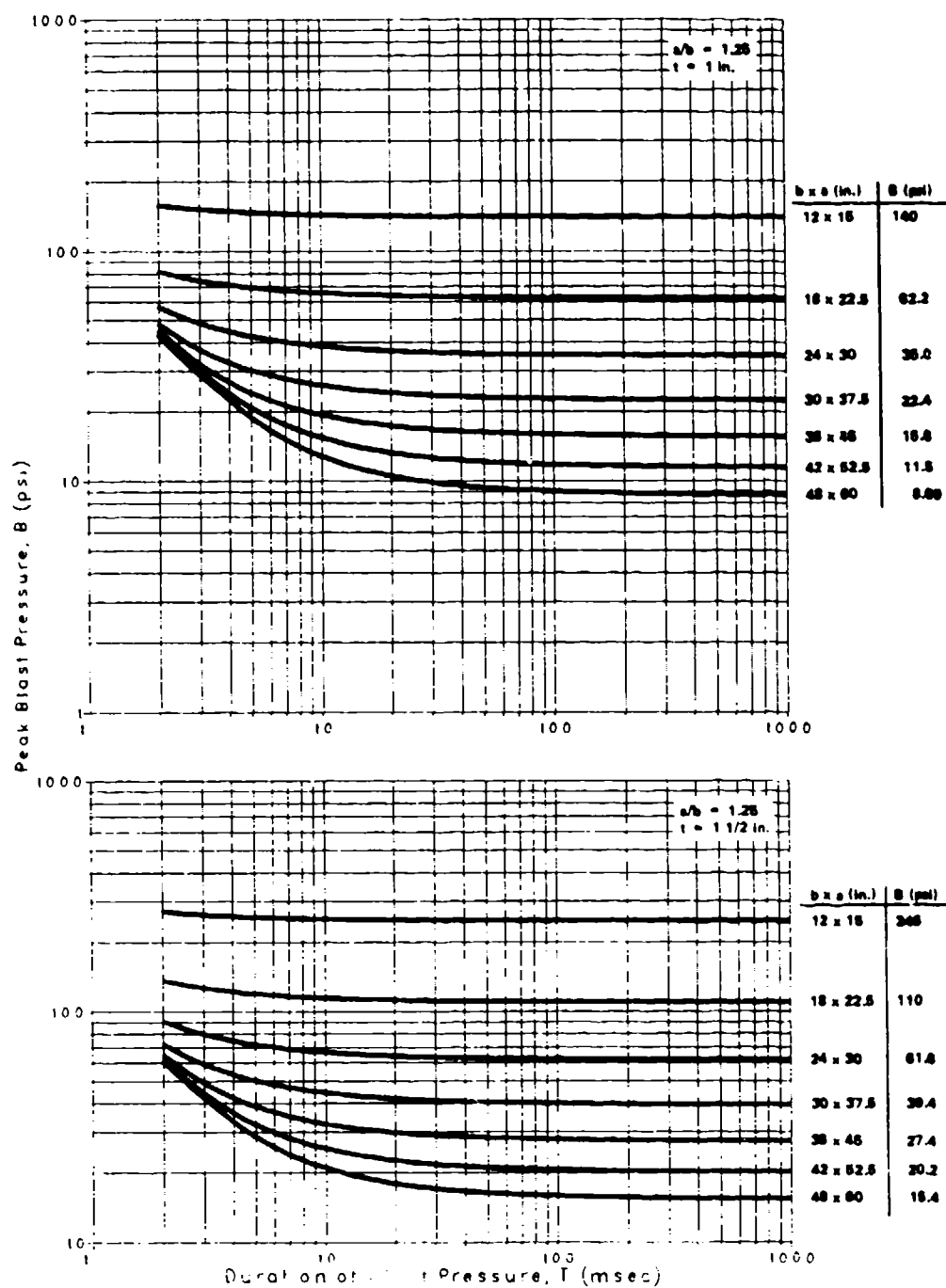


Figure 9 Peak blast pressure capacity for tempered glass panes $a/b = 1.25$, $t = 1$ and $1 \frac{1}{2}$ in.

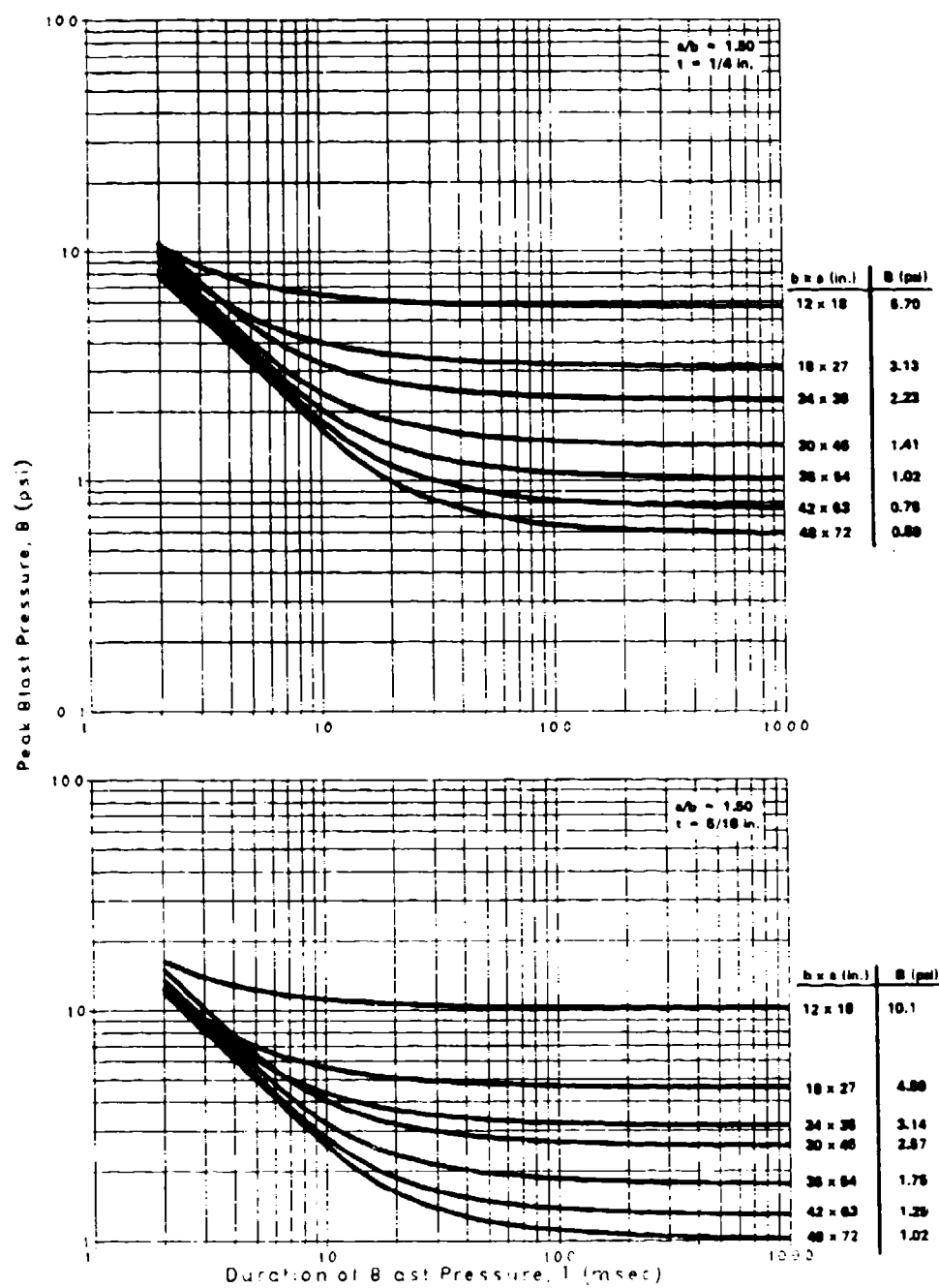


Figure 10 Peak blast pressure capacity for tempered glass panels with $a/b = 1.50$, $t = 1/4$ and $5/16$ in.

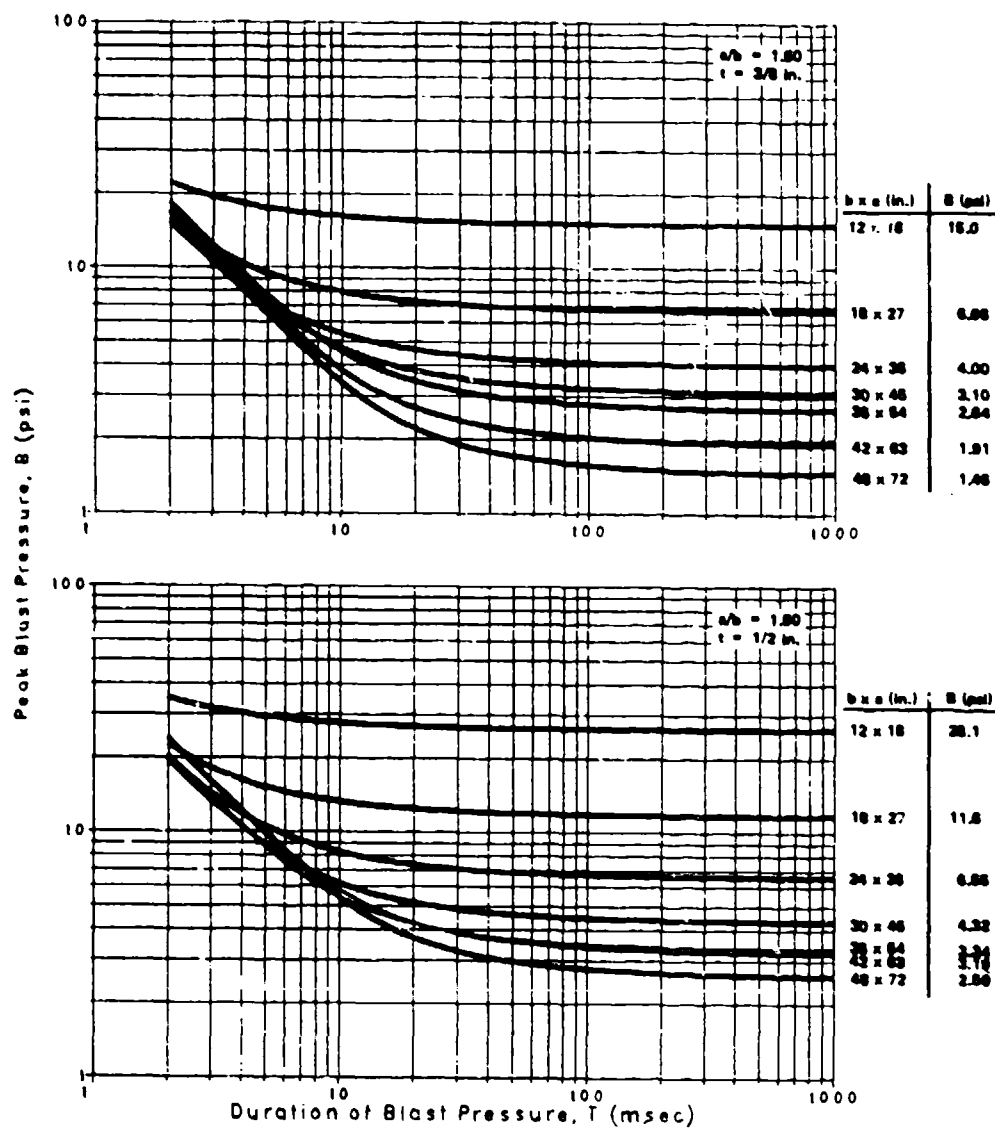


Figure 11. Peak blast pressure capacity for tempered glass panes $a/b = 1.50$, $t = 3/8$ and $1/2$ in

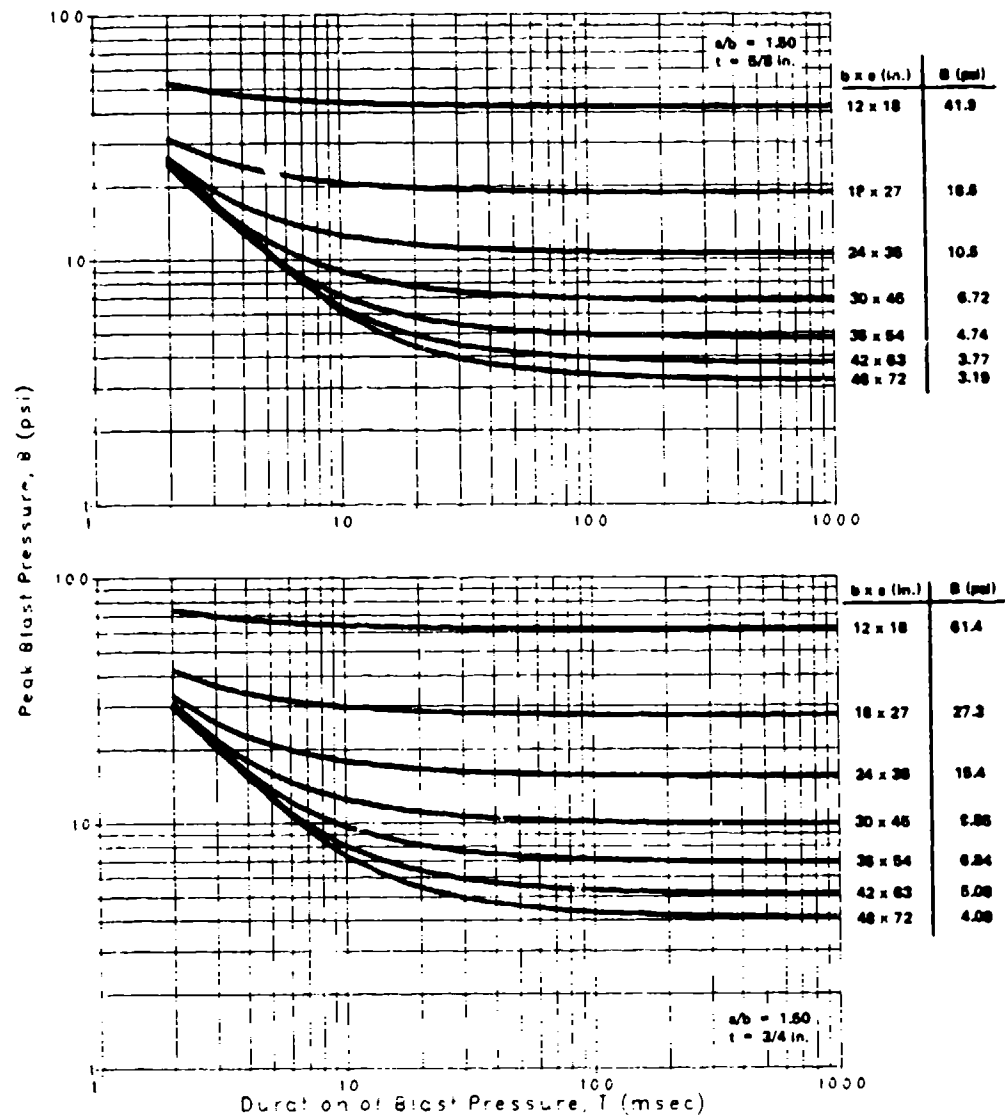


Figure 12 Peak blast pressure capacity for tempered glass panes: $a/b = 1.50$, $t = 5/8$ and $3/4$ in.

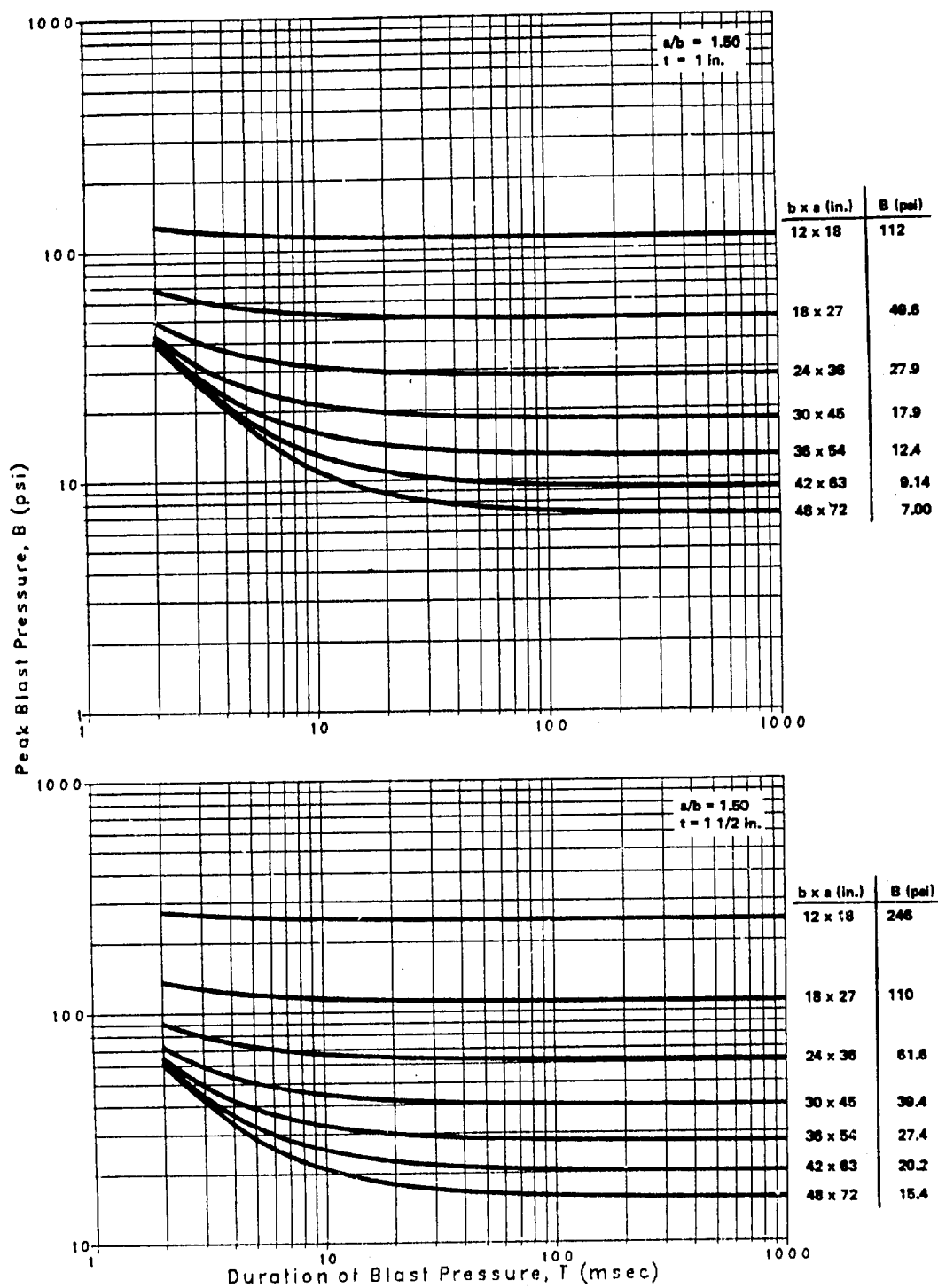


Figure 13. Peak blast pressure capacity for tempered glass panes: $a/b = 1.50$, $t = 1$ and $1 \frac{1}{2}$ in.

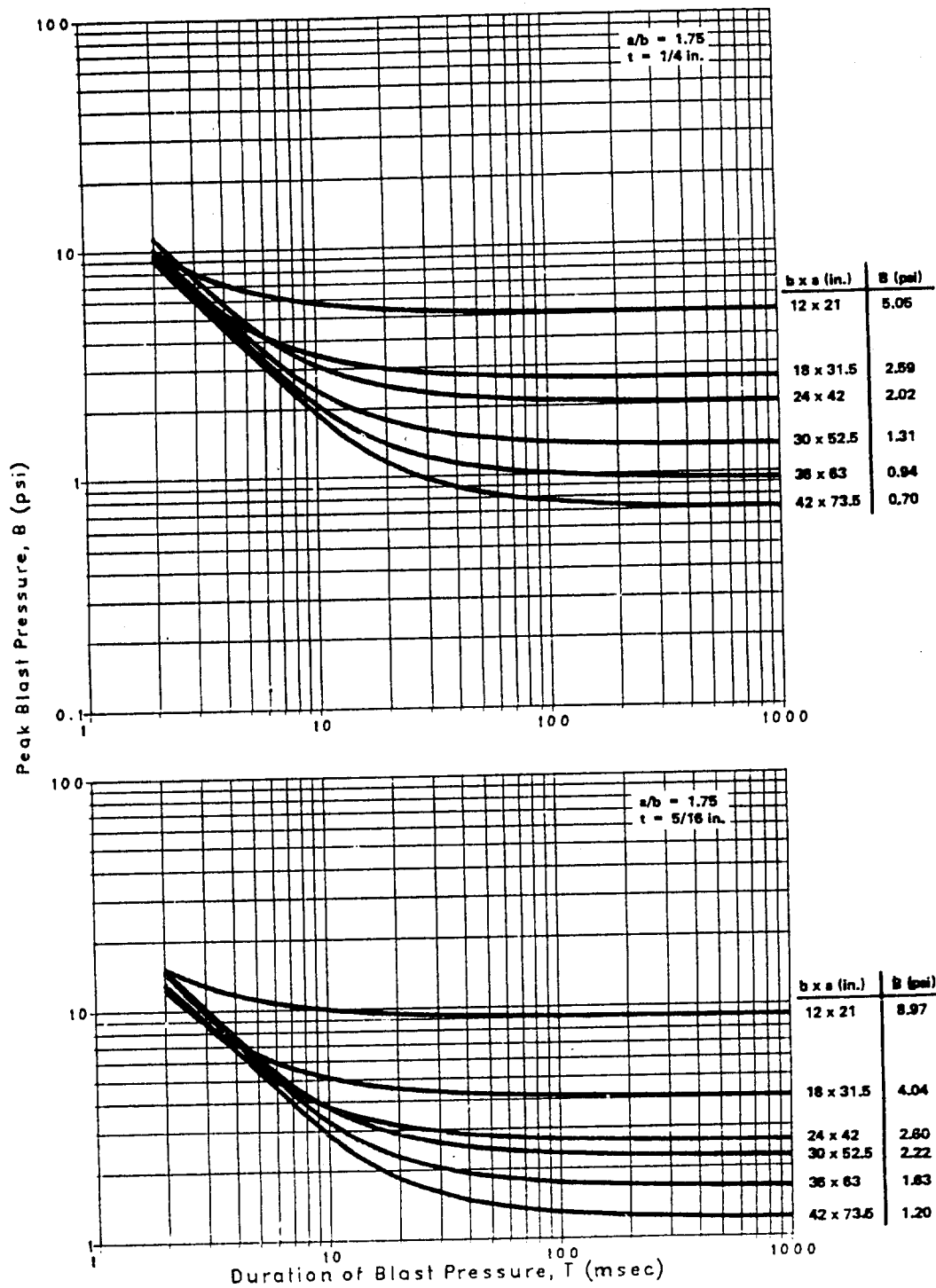


Figure 14. Peak blast pressure capacity for tempered glass panes: $a/b = 1.75$, $t = 1/4$ and $5/16$ in.

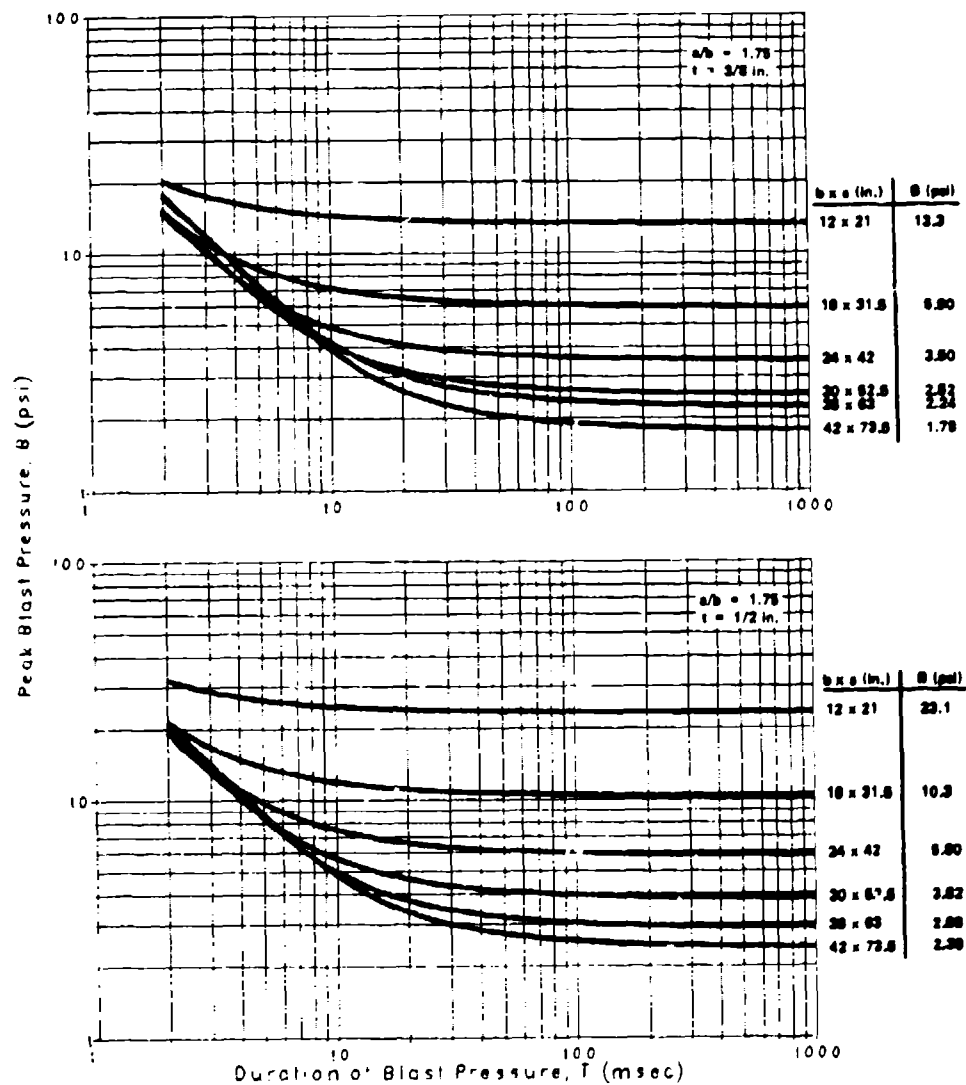


Figure 15 Peak blast pressure capacity for tempered glass panes $a/b = 1.75$; $t = 3/8$ and $1/2$ in.

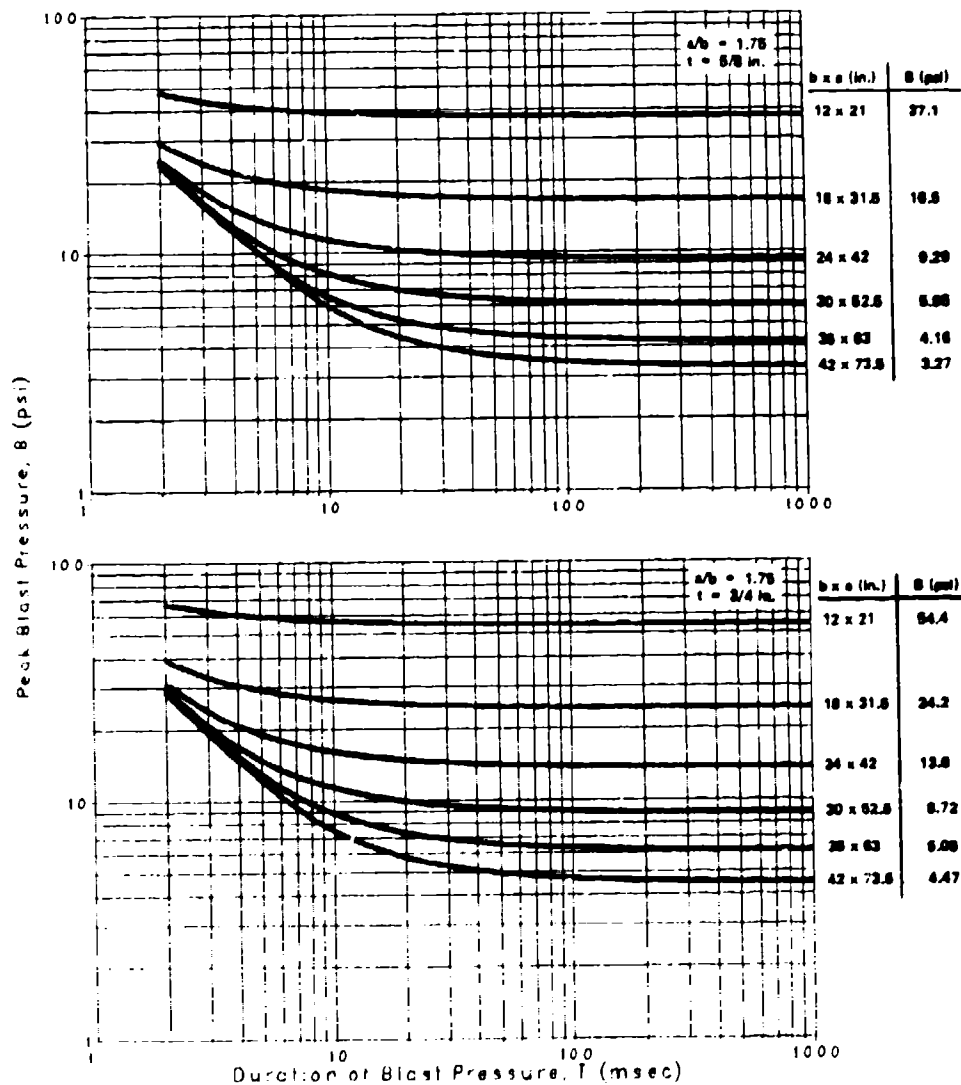


Figure 16. Peak blast pressure capacity for tempered glass panes - $a/b = 1.75$, $t = 5/8$ and $3/4$ in.

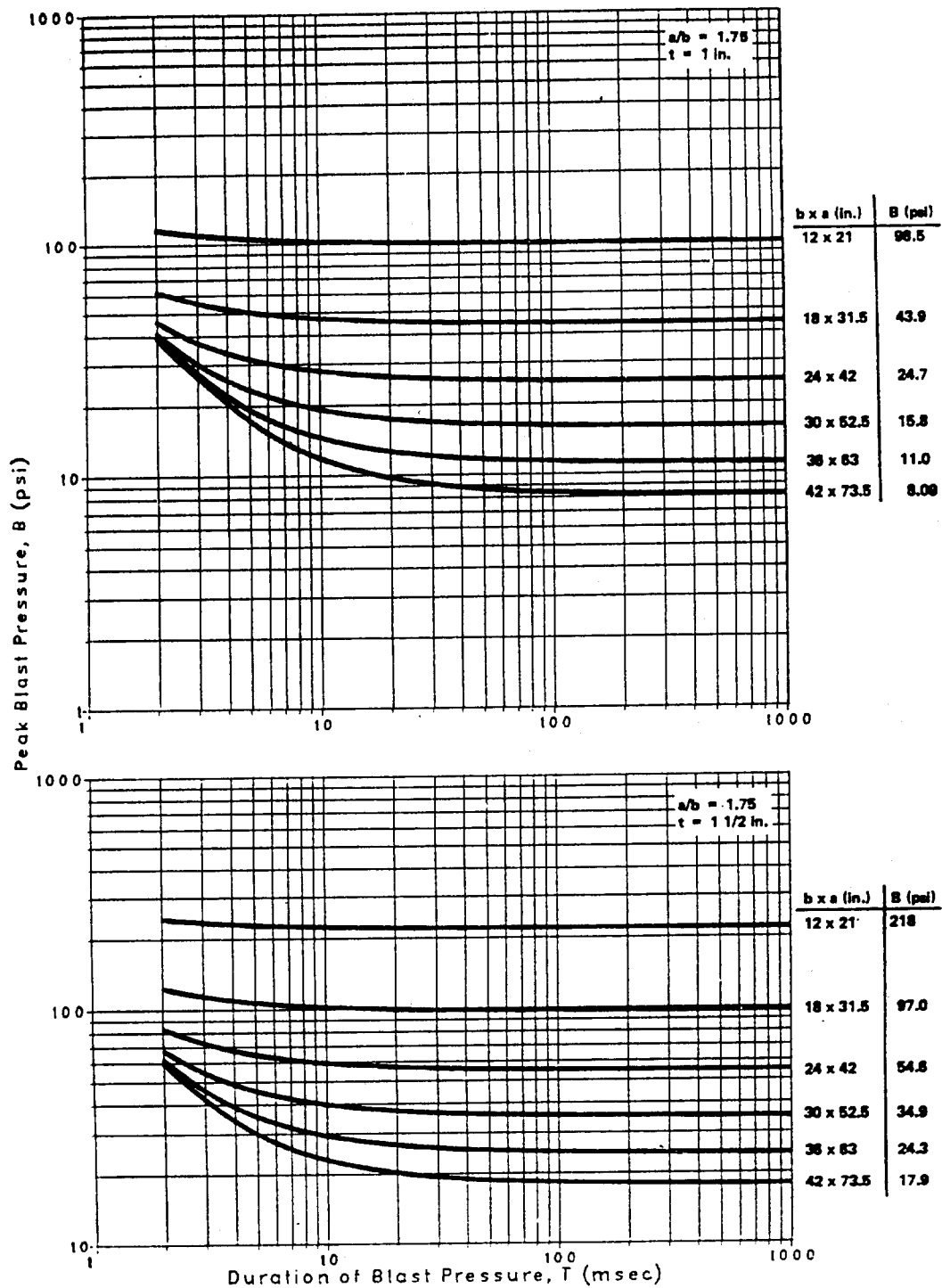


Figure 17. Peak blast pressure capacity for tempered glass panes: $a/b = 1.75$, $t = 1$ and $1 \frac{1}{2}$ in.

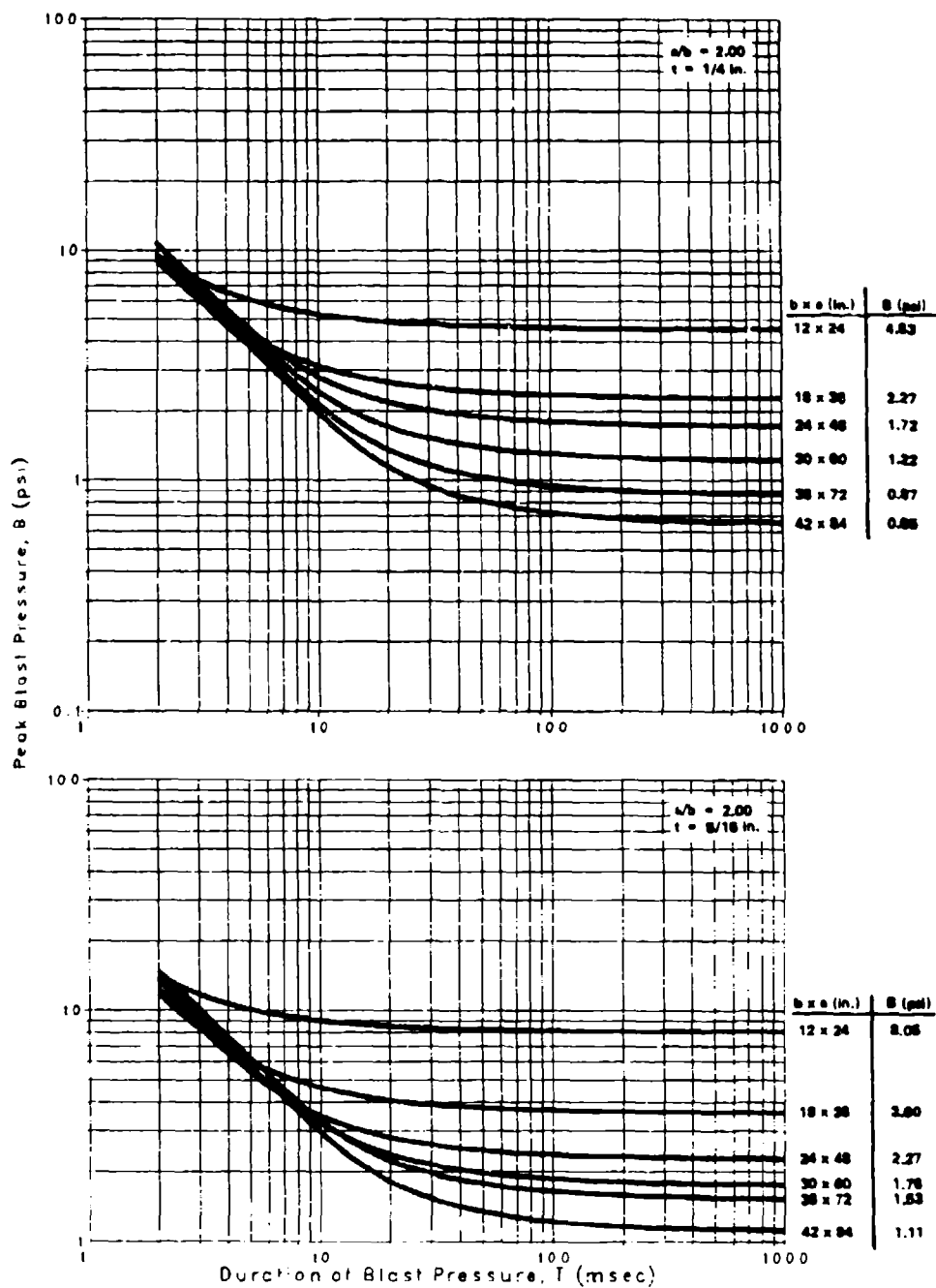


Figure 1d. Peak blast pressure capacity for tempered glass panes, $a/b = 2.00$, $t = 1/4$ and $5/16$ in.

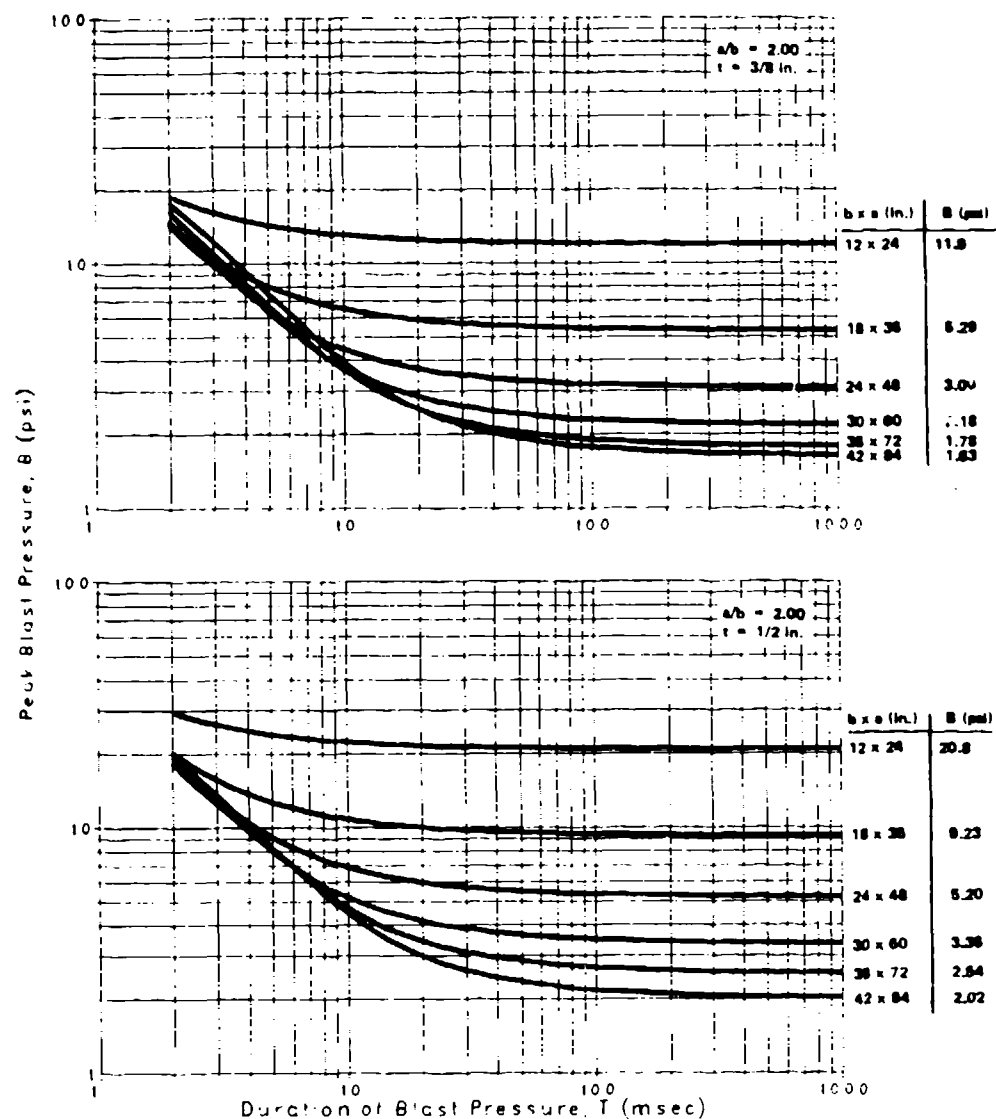


Figure 19. Peak blast pressure capacity for tempered glass panes. $a/b = 2.00$, $t = 3/8$ and $1/2 \text{ in.}$

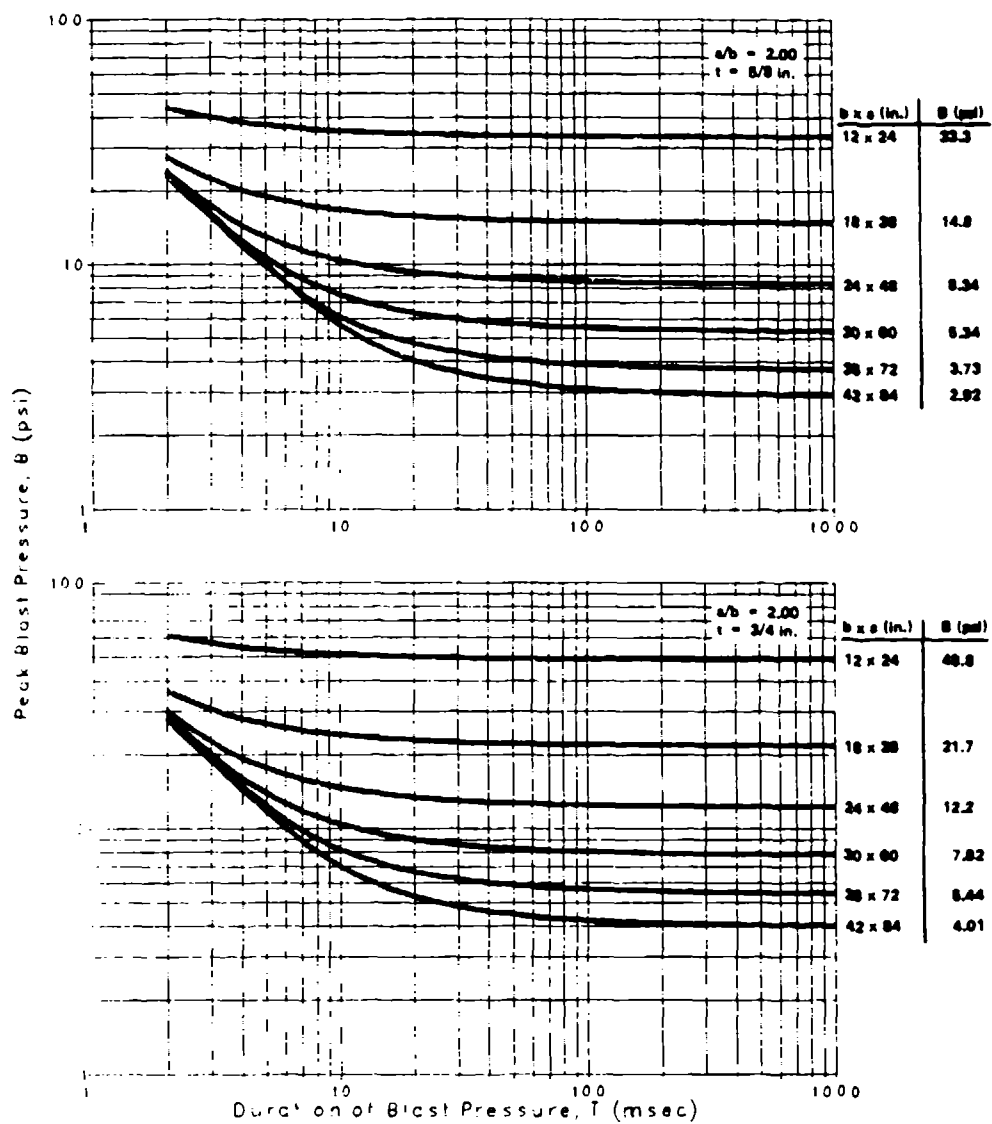


Figure 20. Peak blast pressure capacity for tempered glass panes $a/b = 2.00$, $t = 5/8$ and $3/4$ in.

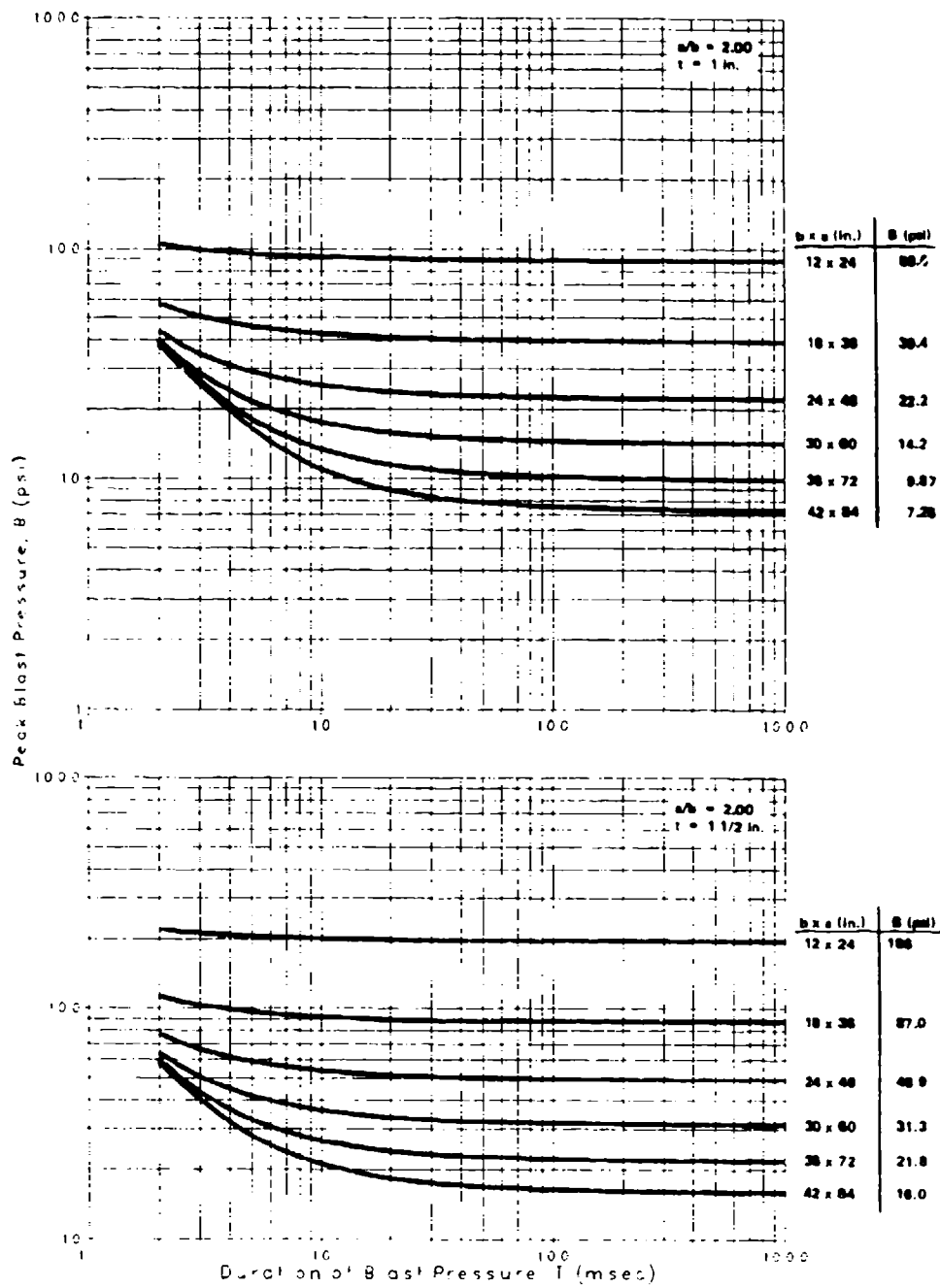


Figure 21. Peak blast pressure capacity for tempered glass panes, $a/b = 2.00$, $t = 1$ and $1 \frac{1}{2}$ in.

Fragment Retention Film

Another product, which will enhance protection from glass fragments, is a clear plastic (polyester) film which self-adheres to the inside surface of window panes. The film is particularly beneficial for retrofitting previously installed windows. Typical films are about 0.002 to 0.006 inch thick with a self-adhesive face. The film is often commercially referred to as shatter resistant film, safety film, or security film. Under short-duration blasts, characterized by small and close-in explosions, blast tests have indicated that the film will hold the glass in position even though the glass is shattered. Under long-duration blast loads relative to the natural period of vibration of the glass pane, or under much higher than design blast loads, it is unknown if the membrane strength of the film will be exceeded and the fractured pane may be propelled as a single body. Consequently, fragment retention films with the highest membrane strength should be chosen. Also, where new glass is fitted with film or where the cost-benefit ratios allow in retrofitting, the film should be installed over the entire glass area and into the frame bite.

If a complete pane of film reinforced glass is blown away from its frame by a higher than design or long-duration blast wave, it may travel as a single piece while adhering to the film. In this configuration, tests indicate that it will travel a shorter distance and the individual fragments from unfilmed glass and will be less hazardous because of the shielding effect of the film. If a structural crossbar or grillwork, which can be decorative, is secured across the opening with enough strength to absorb the energy of impact from the failed lite, the glass will be prevented from being propelled across a room. Additionally, if a projectile passes through the film-reinforced glass, the glass immediately around the hole will ordinarily adhere to the film. The result is that any fragments broken free by the impact will be fewer in number and lower in energy content, than without the film.

There are additional benefits from fragment retention film. The film can be tinted to improve the heat balance of the structure. Also, like laminated glass, the film affords benefits in terms of physical security. Additionally, the film also protects the inner tensile surface of the glazing from scratches and humidity, thus reducing strength degradation of the glazing with time. Finally, in the event of a multiple blast explosion where the glass will be progressively weakened by the effects of ceramic fatigue, fragment retention film can provide an additional factor of safety.

Polycarbonate

Another material that can significantly enhance the fragment resistance of glazing is a polycarbonate inner lite. The polycarbonate can either be laminated to the inboard side of the glass, installed as an inner pane in an insu-

lated dual pane unit, or bolted across the inside of the frame as a "quick-and-dirty" retrofit. Although analysis indicates that polycarbonate, because of its low elastic modulus relative to glass (1/30), will not measurably increase the strength of glass in a laminated or composite lite, it will act as a highly effective spall shield and very significantly increase resistance to fragment penetration, impact, and direct physical assault. If the polycarbonate is placed behind any of the glasses that failed in large shards, some bullet or ballistic resistance can be obtained. Unfortunately, because of the break pattern of thermally tempered glass, it is not possible to attain multiple shot ballistic resistance from thermally tempered glass backed by polycarbonate. Chemically tempered glass with a deep precompression layer over 0.010 inch and a thickness of at least 1/4 inch mounted outboard of the polycarbonate will provide a sound basis for ballistic as well as blast design. As with all ballistic-resistant windows, field tests will be required to find the optimum glass-polycarbonate cross section.

Currently polycarbonate is glazed into a frame in a manner similar to glass, although with a larger frame engagement or bite. In this edge configuration, the polycarbonate will probably fail under blast load by edge disengagement. However, if a technology can be developed to adequately grip the polycarbonate and develop its ductility and membrane strength, the blast capacity of polycarbonate increases dramatically. Preliminary analysis indicates that a tenfold increase in blast resistance is possible. Research by the author is currently underway at NCEL in this regard.

Polycarbonate's main disadvantage is that it is subject to greater environmental degradation than glass, especially from the effects of abrasion and ultraviolet radiation. Chemical coatings or a layer of glass over each exterior surface is commonly used to protect polycarbonates from both abrasion and ultraviolet radiation.

Polycarbonates are resistant to most chemicals. However, it is susceptible to aromatic hydrocarbons, esters, ketones, and acetone phenols.

Polycarbonate will burn when a flame is held to it. However, it will tend to extinguish itself when the flame is removed. Rated as a class CC-1 material, it is much less combustible than acrylic (plexiglass). However, local fire codes should be consulted.

Optical properties of polycarbonate are good; it will transmit 85% of entering light.

Because polycarbonate has a temperature expansion coefficient about 10 times greater than glass, it cannot be laminated to glass with polyvinyl butyral. Instead it must be laminated with proprietary urethane materials, which allow thermally induced sliding between glass and polycarbonate.

Currently, NCEL recommends that in situations where glass fragment control is the prime concern, polycarbonate not be laminated with the glass but rather be stacked behind the glass,

with or without an air gap. Not only is the initial high cost of a lamination precluded, but if the polycarbonate degrades over time, it can be replaced without replacing the glass. Also, if the outer glass develops a crack or fracture, it can also be replaced independently. In situations where ballistic threat is also a design concern, the laminated composite should be used, as it is advantageous to keep fractured glass in place to aid in flattening, tumbling, and slowing bullets.

INTERIM DESIGN CRITERIA FOR FRAME

Sealants and Gaskets

The sealant and gasket design should be consistent with industry standards and should be continuous around the perimeter of the glass pane.

Frame Loads

The window frame must develop the static design strength of the glass pane, r_u , given in Table 1. Otherwise, the design is inconsistent with frame assumptions and the peak blast pressure capacity of the window pane predicted from Figures 2 to 21 will produce a failure rate in excess of the prescribed failure rate. This results because frame deflections induce higher principal tensile stresses in the pane, thus reducing the strain energy capacity available to safely resist the blast loading.

In addition to the load transferred to the frame by the glass, frame members must also resist a uniform line load, r_u , applied to all exposed members.

1. Deflection: No frame member should have a relative displacement exceeding 1/264 of its span or 1/8 inch, whichever is less.
2. Stress: The maximum stress in any member should not exceed $f_y/1.65$, where f_y = yield stress of the members material.
3. Fasteners: The maximum stress in any fastener should not exceed $f_y/2.00$.

The design loads for the glazing are based on large deflection plate theory, but the resulting transferred design loads for the frame are based on an approximate solution of small deflection theory for laterally loaded plates. Analysis indicates this approach to be considerably simpler and more conservative than using the frame loading based exclusively on large deflection membrane behavior, characteristic of window panes. The effect of the load applied directly to the exposed frame members of width, w , should also be considered. According to the assumed plate theory, the design load, r_u , produces a line shear, V_x , applied by the long side, a , of the pane equal to:

$$V_x = C_x r_u b \sin (\pi x/a) + r_u w \quad (1)$$

The design load, r_u , produces a line shear, V_y , applied by the short side, b , of the pane equal to:

$$V_y = C_y r_u b \sin (\pi y/b) + r_u w \quad (2)$$

The design load, r_u , produces a corner concentrated load, R , tending to uplift the corners of the window pane equal to:

$$R = -C_R r_u b^2 \quad (3)$$

Distribution of these forces, as loads acting on the window frame, is shown in Figure 22. Table 2 presents the design coefficients, C_x , C_y , and C_R for practical aspect ratios of the window pane. Linear interpolation can be used for aspect ratios not presented. The loads given by Equations 1, 2, and 3 should be used to check the frame mullions and fasteners for compliance with the deflection and stress criteria stated above. It is important to note that the design load for mullions is twice the load given by Equations 1 to 3 in order to account for effects of two panes being supported by a common mullion.

Special design consideration should be taken so that the deflection of the building wall will not impose deflections on the frame. Where it is impossible to achieve enough building wall rigidity, it is recommended that the frames be pinned to the structure in a manner to permit a 2-degree wall rotation.

Rebound Stresses

Under a short duration blast load, the window will rebound with a negative (outward) deflection. The stresses produced by the negative deflection must be safely resisted by the window while positive pressures act on the window. Otherwise, the window which safely resists stresses induced by positive (inward) displacements will later fail in rebound while positive pressure still acts. This will propel glass fragments into the interior of the structure. However, if the window fails in rebound during the negative (suction) phase of the blast loading, glass fragments will be drawn away from the structure.

Rebound criteria are currently not available for predicting the equivalent static uniform negative load (resistance), r_u , that the window must safely resist for various blast load durations. However, analysis indicates that for $T \geq 100$ msec, significant rebound does not occur during the positive blast pressure phase for the range of design parameters given in Figures 2 to 21. Therefore, rebound can be neglected as a design consideration for $T \geq 100$ msec. For $T < 100$ msec, it is recommended that the rebound charts in NAVFAC P-397 be used to estimate r_u .

Table 1. Static Design Strength, r_u (psi), for Tempered Glass*

[a = long dimension of glass pane (in.); b = short dimension of glass pane (in.)]

ASPECT RATIO = 1.00

Glass Size, b x a (in.)	Static Design Strength (psi) for a Window thickness, t, of --							
	1.5 in.	1.0 in.	3/4 in.	5/8 in.	1/2 in.	3/8 in.	5/16 in.	1/4 in.
12x12	827	374	206	141	87.7	50.3	27.5	20.2
13x13	705	319	176	120	74.7	42.8	23.9	17.6
14x14	608	275	151	103	64.5	36.9	21.1	15.5
15x15	529	240	132	90.1	56.1	32.2	18.7	14.2
16x16	465	211	116	79.2	49.3	28.3	16.7	13.4
17x17	412	187	103	70.1	43.7	25.5	15.1	12.7
18x18	368	166	91.6	62.5	39.0	23.1	14.1	12.6
19x19	330	149	82.2	56.1	35.0	21.0	13.5	12.1
20x20	298	135	74.2	50.7	31.6	19.2	12.9	11.0
21x21	270	122	67.3	46.0	28.6	17.7	12.7	10.0
22x22	246	111	61.3	41.9	26.4	16.3	12.6	9.20
23x23	225	102	56.1	38.3	24.4	15.1	11.8	8.52
24x24	207	93.6	51.5	35.2	22.7	14.3	10.9	7.91
25x25	191	86.3	47.5	32.4	21.2	13.8	10.1	7.43
26x26	176	79.8	43.9	30.0	19.7	13.4	9.39	7.00
27x27	163	74.0	40.7	27.9	18.5	12.9	8.80	6.62
28x28	152	68.8	37.9	26.2	17.4	12.8	8.26	6.22
29x29	142	64.1	35.3	24.6	16.4	12.6	7.78	5.86
30x30	132	59.9	33.0	23.2	15.4	12.6	7.39	5.53
31x31	124	56.1	30.9	21.9	14.6	12.0	7.04	5.22
32x32	116	52.7	29.0	20.8	14.2	11.3	6.71	4.94
33x33	109	49.5	27.4	19.7	13.8	10.6	6.39	4.69
34x34	103	46.7	26.0	18.7	13.5	10.0	6.07	4.45
35x35	97.2	44.0	24.8	17.8	13.2	9.50	5.77	4.23
36x36	91.9	41.6	23.6	17.0	12.8	9.05	5.50	4.04
37x37	87.0	39.4	22.5	16.2	12.7	8.63	5.24	3.86
38x38	82.5	37.3	21.5	15.4	12.7	8.24	5.01	3.69
39x39	78.3	35.5	20.5	14.8	12.6	7.88	4.79	3.53
40x40	74.4	33.7	19.7	14.4	12.5	7.57	4.58	3.39
41x41	70.8	32.1	18.8	14.1	11.9	7.30	4.39	3.25
42x42	67.5	30.6	18.1	13.8	11.4	7.04	4.21	3.12
43x43	64.4	29.2	17.3	13.5	10.9	6.80	4.05	3.00
44x44	61.5	27.9	16.7	13.2	10.4	6.56	3.90	2.89
45x45	58.8	26.8	16.0	13.0	9.99	6.32	3.75	2.78
46x46	56.3	25.8	15.4	12.9	9.59	6.08	3.62	2.68
47x47	53.9	24.9	14.9	12.8	9.24	5.86	3.49	2.58
48x48	51.7	24.0	14.5	12.7	8.91	5.65	3.37	2.49
49x49	49.6	23.2	14.2	12.6	8.59	5.45	3.25	2.41
50x50	47.6	22.4	14.0	12.6	8.30	5.27	3.15	2.33
51x51	45.8	21.6	13.7	12.4	8.02	5.09	3.04	2.25
52x52	44.0	20.9	13.5	11.9	7.76	4.92	2.95	2.18
53x52	42.4	20.2	13.3	11.5	7.54	4.76	2.85	2.11
54x54	40.8	19.6	13.1	11.1	7.33	4.61	2.77	2.05
55x55	39.4	19.0	12.9	10.7	7.13	4.47	2.68	1.99
56x56	38.0	18.4	12.8	10.3	6.94	4.33	2.60	1.93
57x57	36.7	17.8	12.7	9.99	6.76	4.20	2.53	1.87
58x58	35.4	17.3	12.7	9.66	6.59	4.08	2.45	1.82
59x59	34.2	16.8	12.6	9.38	6.40	3.97	2.38	1.77
60x60	33.1	16.3	12.6	9.11	6.22	3.85	2.32	1.72

*Panels to the right and below stepped dividing line exhibit membrane behavior at design loads.

(continued)

Table 1. Continued*

[a = long dimension of glass pane (in.); b = short dimension of glass pane (in.)]

ASPECT RATIO = 1.25

Glass Size, b x a (in.)	Static Design Strength (psi) for a Window Thickness, t, of --							
	1.5 in.	1.0 in.	3/4 in.	5/8 in.	1/2 in.	3/8 in.	5/16 in.	1/4 in.
12x15	617	280	154	105	65.5	37.5	20.5	15.2
13x16.25	526	238	131	89.5	55.8	32.0	17.9	13.5
14x17.5	454	205	113	77.2	48.1	27.6	15.8	12.3
15x18.75	395	179	98.5	67.2	41.9	24.0	14.2	11.1
16x20	347	157	86.6	59.1	36.8	21.1	13.0	10.2
17x21.25	308	139	76.7	52.4	32.6	19.0	12.0	9.86
18x22.5	274	124	68.4	46.7	29.1	17.2	11.1	9.78
19x23.75	246	112	61.4	41.9	26.1	15.8	10.3	9.72
20x25	222	101	55.4	37.8	23.6	14.6	9.96	9.54
21x26.25	202	91.3	50.3	34.3	21.4	13.6	9.79	8.69
22x27.5	184	83.2	45.8	31.3	19.7	12.8	9.78	7.95
23x28.75	168	76.1	41.9	28.6	18.2	12.0	9.70	7.30
24x30	154	69.9	38.5	26.3	17.0	11.3	9.49	6.75
25x31.25	142	64.4	35.5	24.2	15.9	10.7	8.77	6.27
26x32.5	132	59.6	32.8	22.4	14.9	10.2	8.14	5.83
27x33.75	122	55.2	30.4	20.8	14.1	9.98	7.57	5.45
28x35	113	51.4	28.3	19.5	13.4	9.80	7.07	5.12
29x36.25	106	47.9	26.4	18.4	12.8	9.79	6.63	4.81
30x37.5	99.0	44.7	24.6	17.4	12.3	9.77	6.23	4.54
31x38.75	92.5	41.9	23.1	16.4	11.7	9.71	5.87	4.31
32x40	86.8	39.3	21.7	15.6	11.2	9.65	5.54	4.09
33x41.25	81.6	37.0	20.4	14.9	10.7	9.22	5.25	3.90
34x42.5	76.9	34.8	19.4	14.2	10.3	8.71	4.98	3.71
35x43.75	72.6	32.9	18.5	13.6	10.1	8.24	4.74	3.53
36x45	68.6	31.1	17.6	13.1	9.93	7.81	4.52	3.36
37x46.25	64.9	29.4	16.8	12.7	9.80	7.41	4.32	3.20
38x47.5	61.6	27.9	16.1	12.3	9.79	7.05	4.14	3.06
39x48.75	58.5	26.5	15.5	11.8	9.78	6.72	3.97	2.92
40x50	55.6	25.2	14.8	11.4	9.75	6.42	3.82	2.80
41x51.25	52.9	24.0	14.3	11.0	9.71	6.13	3.66	2.68
42x52.5	50.4	22.8	13.8	10.6	9.66	5.87	3.51	2.57
43x53.75	48.1	21.8	13.4	10.3	9.47	5.63	3.37	2.47
44x55	45.9	20.8	13.0	10.2	9.06	5.40	3.24	2.37
45x56.25	43.9	20.0	12.6	10.0	8.68	5.19	3.11	2.28
46x57.5	42.0	19.3	12.3	9.87	8.32	5.00	3.00	2.19
47x58.75	40.3	18.6	11.9	9.80	7.99	4.81	2.89	2.11
48x60	38.6	17.9	11.5	9.79	7.67	4.64	2.78	2.03
49x61.25	37.0	17.3	11.2	9.78	7.37	4.49	2.68	1.96
50x62.5	35.6	16.7	10.9	9.77	7.11	4.34	2.59	1.89
51x63.75	34.2	16.2	10.6	9.74	6.85	4.21	2.50	1.83
52x65	32.9	15.7	10.3	9.70	6.61	4.08	2.42	1.77
53x66.25	31.7	15.3	10.2	9.67	6.33	3.96	2.34	1.71

*Panels to the right and below stepped dividing line exhibit membrane behavior at design loads.

(continued)

Table 1. Continued*

[a = long dimension of glass pane (in.); b = short dimension of glass pane (in.)]

ASPECT RATIO = 1.50

Glass Size, b x a (in.)	Static Design Strength (psi) for a Window Thickness, t, of --							
	1.5 in.	1.0 in.	3/4 in.	5/8 in.	1/2 in.	3/8 in.	5/16 in.	1/4 in.
12x18	493	223	123	83.8	52.3	29.9	16.3	11.9
13x19.5	420	190	105	71.4	44.5	25.5	13.9	10.5
14x21	362	164	90.2	61.6	38.4	22.0	12.3	9.43
15x22.5	315	143	78.6	53.6	33.4	19.2	11.1	8.88
16x24	277	125	69.1	47.2	29.4	16.8	10.0	8.26
17x25.5	245	111	61.2	41.9	26.0	14.9	9.31	8.14
18x27	219	99.1	54.6	37.3	23.2	13.3	8.85	8.02
19x28.5	196	89.0	49.0	33.4	20.8	12.3	8.84	7.90
20x30	177	80.3	44.2	30.2	18.8	11.4	7.83	7.78
21x31.5	161	72.8	40.1	27.4	17.1	10.6	7.81	7.62
22x33	147	66.4	36.5	24.9	15.6	9.86	7.80	7.03
23x34.5	134	60.7	33.4	22.8	14.2	9.32	7.77	6.45
24x36	123	55.8	30.7	21.0	13.1	8.98	7.77	5.95
25x37.5	113	51.4	28.3	19.3	12.4	8.64	7.63	5.50
26x39	105	47.5	26.2	17.9	11.7	8.24	7.19	5.10
27x40.5	97.3	44.1	24.3	16.6	11.0	7.86	6.69	4.74
28x42	90.5	41.0	22.6	15.4	10.4	7.85	6.24	4.42
29x43.5	84.3	38.2	21.0	14.4	9.89	7.85	5.83	4.14
30x45	78.8	35.7	19.7	13.4	9.42	7.84	5.47	3.88
31x46.5	73.8	33.4	18.4	12.8	9.16	7.83	5.13	3.64
32x48	69.3	31.4	17.3	12.2	8.91	7.82	4.83	3.43
33x49.5	65.1	29.5	16.2	11.6	8.65	7.72	4.55	3.27
34x51	61.4	27.8	15.3	11.1	8.34	7.62	4.30	3.13
35x52.5	57.9	26.2	14.4	10.6	8.05	7.28	4.07	3.00
36x54	54.7	24.8	13.6	10.2	8.02	6.90	3.85	2.87
37x55.5	51.8	23.5	13.0	9.78	7.99	6.55	3.66	2.74
38x57	49.1	22.2	12.5	9.42	7.96	6.22	3.47	2.61
39x58.5	46.6	21.1	12.0	9.21	7.93	5.92	3.33	2.50
40x60	44.3	20.1	11.6	9.01	7.91	5.64	3.21	2.39
41x61.5	42.2	19.1	11.2	8.82	7.88	5.38	3.09	2.29
42x63	40.2	18.2	10.8	8.60	7.85	5.13	2.98	2.19
43x64.5	38.4	17.4	10.4	8.35	7.77	4.91	2.88	2.10
44x66	36.6	16.6	10.1	8.12	7.69	4.70	2.77	2.02
45x67.5	35.0	15.9	9.71	7.90	7.62	4.50	2.66	1.94
46x69	33.5	15.2	9.42	7.69	7.35	4.31	2.56	1.86
47x70.5	32.1	14.5	9.25	7.62	7.06	4.14	2.47	1.79
48x72	30.8	13.9	9.08	7.55	6.78	3.97	2.38	1.73

*Panels to the right and below stepped dividing line exhibit membrane behavior at design loads.

(continued)

Table 1. Continued*

[a = long dimension of glass pane (in.); b = short dimension of glass pane (in.)]

ASPECT RATIO = 1.75

Glass Size, b x a (in.)	Static Design Strength (psi) for a Window Thickness, t, of --							
	1.5 in.	1.0 in.	3/4 in.	5/8 in.	1/2 in.	3/8 in.	5/16 in.	1/4 in.
12x21	436	197	109	74.2	46.3	26.5	14.4	10.2
13x22.75	372	168	92.6	63.2	39.4	22.6	12.3	8.91
14x24.5	320	145	79.9	54.5	34.0	19.5	10.6	8.01
15x26.25	279	126	69.6	47.5	29.6	17.0	9.46	7.32
16x28	245	111	61.2	41.7	26.0	14.9	8.52	6.83
17x29.75	217	98.4	54.2	37.0	23.0	13.2	7.85	6.36
18x31.5	194	87.8	48.3	33.0	20.6	11.8	7.30	5.93
19x33.25	174	78.8	43.4	29.6	18.5	10.6	6.88	5.76
20x35	157	71.1	39.1	26.7	16.7	9.71	6.49	5.73
21x36.75	142	64.5	35.5	24.2	15.1	8.96	6.12	5.70
22x38.5	130	58.8	32.4	22.1	13.8	8.36	5.84	5.68
23x40.25	119	53.8	29.6	20.2	12.6	7.87	5.73	5.57
24x42	109	49.4	27.2	18.6	11.6	7.43	5.71	5.27
25x43.75	100	45.5	25.1	17.1	10.7	7.11	5.70	5.00
26x45.5	92.9	42.1	23.7	15.8	9.97	6.81	5.69	4.67
27x47.25	86.2	39.0	21.5	14.7	9.37	6.52	5.66	4.35
28x49	80.1	36.3	20.0	13.6	8.83	6.24	5.45	4.05
29x50.75	74.7	33.8	18.6	12.7	8.38	5.98	5.21	3.79
30x52.5	69.8	31.6	17.4	11.9	8.01	5.82	4.98	3.56
31x54.25	65.4	29.6	16.3	11.1	7.66	5.74	4.70	3.36
32x56	61.3	27.8	15.3	10.4	7.35	5.73	4.43	3.17
33x57.75	57.7	26.1	14.4	9.93	7.11	5.71	4.17	3.00
34x59.5	54.3	24.6	13.5	9.46	6.89	5.70	3.94	2.85
35x61.25	51.3	23.2	12.8	9.02	6.67	5.69	3.73	2.72
36x63	48.5	21.9	12.1	8.62	6.45	5.67	3.54	2.60
37x64.75	45.9	20.8	11.4	8.30	6.24	5.63	3.37	2.49
38x66.5	43.5	19.7	10.8	8.00	6.04	5.44	3.21	2.37
39x68.25	41.3	18.7	10.3	7.73	5.87	5.26	3.06	2.26
40x70	39.3	17.8	9.91	7.47	5.80	5.09	2.93	2.16
41x71.75	37.4	16.9	9.52	7.26	5.74	4.93	2.82	2.06
42x73.5	35.6	16.1	9.15	7.07	5.72	4.71	2.71	1.97
43x75.25	34.0	15.4	8.81	6.90	5.70	4.50	2.61	1.89
44x77	32.4	14.7	8.50	6.73	5.69	4.30	2.51	1.81
45x78.75	31.0	14.0	8.24	6.55	5.70	4.12	2.42	1.74

*Panels to the right and below stepped dividing line exhibit membrane behavior at design loads.

(continued)

Table 1. Continued*

[a = long dimension of glass pane (in.); b = short dimension of glass pane (in.)]

ASPECT RATIO = 2.00

Glass Size, b x a (in.)	Static Design Strength (psi) for a Window Thickness, t, of --							
	1.5 in.	1.0 in.	3/4 in.	5/8 in.	1/2 in.	3/8 in.	5/16 in.	1/4 in.
12x24	391	177	97.6	66.6	41.5	23.8	13.0	9.05
13x26	333	151	83.1	56.7	35.4	20.3	11.0	7.81
14x28	287	130	71.7	48.9	30.5	17.5	9.52	6.87
15x30	250	113	62.4	42.6	26.6	15.2	8.31	6.29
16x32	220	99.7	54.9	37.5	23.4	13.3	7.43	5.81
17x34	195	88.3	48.6	33.2	20.7	11.9	6.72	5.40
18x36	174	78.7	43.4	29.6	18.5	10.6	6.26	5.03
19x38	156	70.7	38.9	26.6	16.6	9.49	5.86	4.71
20x40	141	63.8	35.1	24.0	14.9	8.56	5.51	4.56
21x42	128	57.9	31.9	21.7	13.6	7.85	5.19	4.46
22x44	116	52.7	29.0	19.8	12.4	7.25	4.90	4.42
23x46	107	48.2	26.6	18.1	11.3	6.73	4.64	4.39
24x48	97.8	44.3	24.4	16.6	10.4	6.39	4.55	4.37
25x50	90.2	40.8	22.5	15.3	9.56	6.08	4.47	4.32
26x52	83.4	37.7	20.8	14.2	8.84	5.79	4.40	4.24
27x54	77.3	35.0	19.3	13.2	8.23	5.55	4.39	4.01
28x56	71.9	32.5	17.9	12.2	7.73	5.29	4.38	3.74
29x58	67.0	30.3	16.7	11.4	7.27	5.07	4.37	3.50
30x60	62.6	28.4	15.6	10.7	6.86	4.86	4.31	3.28
31x62	58.6	26.6	14.6	9.98	6.57	4.67	4.25	3.09
32x64	55.0	24.9	13.7	9.36	6.32	4.58	4.08	2.93
33x66	51.7	23.4	12.9	8.80	6.08	4.52	3.85	2.78
34x68	48.7	22.1	12.2	8.31	5.87	4.47	3.64	2.64
35x70	46.0	20.8	11.5	7.91	5.66	4.41	3.44	2.51
36x72	43.5	19.7	10.8	7.53	5.47	4.40	3.26	2.39
37x74	41.2	18.6	10.3	7.18	5.29	4.39	3.11	2.28
38x76	39.0	17.7	9.73	6.86	5.12	4.38	2.97	2.18
39x78	37.0	16.8	9.24	6.62	4.96	4.37	2.84	2.08
40x80	35.2	16.0	8.78	6.40	4.81	4.34	2.72	1.98
41x82	33.5	15.2	8.37	6.23	4.67	4.30	2.60	1.89
42x84	31.9	14.5	8.03	6.05	4.60	4.25	2.50	1.80

*Panels to the right and below stepped dividing line exhibit membrane behavior at design loads.

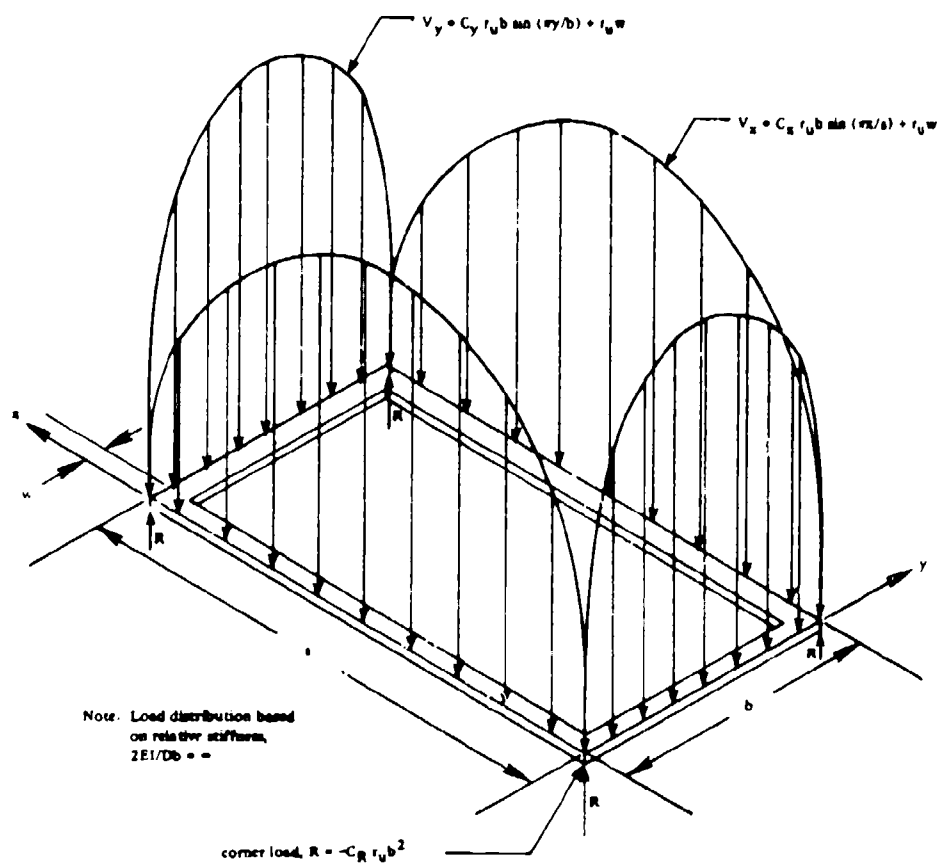


Figure 22. Distribution of lateral load transmitted by glass pane to the window frame.

Table 2. Coefficients for Frame Loading

a/b	C_R	C_x	C_y
1.00	0.065	0.495	0.495
1.10	0.070	0.516	0.516
1.20	0.074	0.535	0.533
1.30	0.079	0.554	0.551
1.40	0.083	0.570	0.562
1.50	0.085	0.581	0.574
1.60	0.086	0.590	0.583
1.70	0.088	0.600	0.591
1.80	0.090	0.609	0.600
1.90	0.091	0.616	0.607
2.00	0.092	0.623	0.614

CERTIFICATION TESTS

Certification tests of the entire window assembly are required unless analysis demonstrates that the window design is consistent with assumptions used to develop the design criteria presented in Figures 2 to 21. The certification tests consist of applying static uniform loads on at least two sample window assemblies until failure occurs in either the tempered glass or frame. Although at least two static uniform load tests until sample failure are required, the acceptance criteria presented below encourage a larger number of test samples. The number of samples, beyond two, is left up to the vendor. Results from all tests shall be recorded in the calculations. All testing shall be performed by an independent and certified testing laboratory.

A probability of failure under testing of less than 0.025 with a confidence level of 90% is considered sufficient proof for acceptance. This should substantiate a design probability of failure, $P(F)$, under the design blast load of 0.001.

Test Procedure - Window Assembly Test

The test windows (glass panes plus support frames) shall be identical in type, size, sealant, and construction to those furnished by the window manufacturer. The frame assembly in the test setup shall be secured by boundary conditions that simulate the adjoining walls. Using either a vacuum or a liquid-filled bladder, an increasing uniform load shall be applied to the entire window assembly (glass and frame) until failure occurs in either the glass or frame. Failure shall be defined as either breaking of glass or loss of frame resistance. The failure load, \hat{r} , shall be recorded to three significant figures. The load should be applied at a rate of 0.5 r_u per minute which corresponds to approximately one minute of significant tensile stress duration until failure. Table 1 presents the static design resistance, r_u , for old tempered glass correlated with a probability of failure, $P(F)$, = 0.001 and a stress intensity duration of 1 second. However, new glass will be tested under a loading where the duration of significant net tensile stress will be about 1 minute. The longer duration of loading will weaken the glass through ceramic fatigue, while the use of new glass will tend to induce failure at a higher load capacity. In order to account for these variations from design conditions, the static load capacity of a glass pane for certification testing, r_s , is calculated as:

$$r_s = 0.876 r_u \quad (4)$$

Acceptance Criteria

The window assembly (frame and glazing) are considered acceptable when the arithmetic mean of all the samples tested, \bar{r} , is such that:

$$\bar{r} \geq r_s + s \alpha \quad (5)$$

where: r_s = static load capacity of the glass pane for certification testing

s = sample standard deviation

α = acceptance coefficient

For n test samples, \bar{r} is defined as:

$$\bar{r} = \frac{\sum_{i=1}^n \hat{r}_i}{n} \quad (6)$$

where \hat{r}_i is the recorded failure load of the i th test sample. The standard sample deviation, s , is defined as:

$$s = \sqrt{\frac{\sum_{i=1}^n (\hat{r}_i - \bar{r})^2}{(n-1)}} \quad (7)$$

The minimum value of the sample standard deviation, s , permitted to be employed in Equation 5 is:

$$s_{\min} = 0.145 r_s \quad (8)$$

This assures a sample standard deviation no better than ideal tempered glass in ideal frames.

The acceptance coefficient, α , is tabulated in Table 3 for the number of samples, n , tested.

As an aid to the tester, the following informational equation is presented to aid in determining if additional test samples are justified. If:

$$\bar{r} \leq r_s + s \beta \quad (9)$$

then with 90% confidence, the design will not prove to be adequate with additional testing. The rejection coefficient, β , is obtained from Table 3.

Rebound Tests

The window that passes the window assembly test is an acceptable design if the window assembly design is symmetrical about the plane of the glass or if the design blast load duration, T , exceeds 100 msec. Otherwise, the window design must pass a rebound load test to prove that the window assembly can develop the necessary strength to resist failure during the rebound phase of response. The rebound tests shall be conducted using a procedure similar to the window assembly tests, except r_u shall be substituted for r_s in Equations 4, 8 and 9 and

Table 3. Statistical Acceptance and Rejection Coefficients

Number of Window Assemblies	Acceptance Coefficient	Rejection Coefficient
<u>n</u>	<u>α</u>	<u>β</u>
2	4.14	.546
3	3.05	.871
4	2.78	1.14
5	2.65	1.27
6	2.56	1.36
7	2.50	1.42
8	2.46	1.48
9	2.42	1.49
10	2.39	1.52
11	2.37	1.54
12	2.35	1.57
13	2.33	1.58
14	2.32	1.60
15	2.31	1.61
16	2.30	1.62
17	2.28	1.64
18	2.27	1.65
19	2.27	1.65
20	2.26	1.66
21	2.25	1.67
22	2.24	1.68
23	2.24	1.68
24	2.23	1.69
25	2.22	1.70
30	2.19	1.72
40	2.17	1.75
50	2.14	1.77

the uniform load shall be applied on the inside surface of the window assembly. The loading rate shall be 0.5 r_u per minute.

Installation Inspection

A survey of past glazing failures indicates that improper installation of setting blocks, gaskets or lateral shims, or poor edge bite is a significant cause of failure because of the resultant unconservative support conditions. In order to prevent premature glass failure, a strenuous quality control program is required.

Preliminary Validation

Presently, an adequate data base for the evaluation and validation of blast resistant window design criteria has yet to be developed. In FY86, NCEL plans blast load validation tests on blast resistant windows. However, the proposed blast resistant window design criteria appear to be conservative when compared to the existing blast load test data on tempered glass (Weissman, et al.).

The design criteria are compared to test data from explosive load tests of tempered glass

in Table 4. As a statistically significant data base does not exist, the data should only be used for orientation. With this perspective in mind, no evidence of invalidation of the design criteria is apparent. Significantly, some glass failures in the tests are clearly induced by premature frame failure.

The blast load capacity design criteria assume that the glass has not been exposed to more than one explosive load. Because each large stress experience resulting from an explosive load will expand the microscopic flaw network or flaw web in the glass, the glass, in a probabilistic sense, will be weaker after each explosive episode. As most of the explosive glass tests in Table 4 are repeated until failure, an unspecified reduction in the survivable blast load is most likely exhibited by the test results in Series II.

A partial analytical check is also made on the presented design curves (Figures 2 to 21). A comparison with an energy method solution for extremely long-duration (but instantly applied) blast loads is presented in Table 5. The NCEL design load criteria presented in Table 5 are based upon an effective blast load duration, T , of 1,000 msec. At durations of this magnitude, the ratio of blast duration, T , to the natural period of vibration of the glass pane, T_n , is large enough to be considered infinite.

Table 5 also presents the static design strength, r_u , of each of the panes. It is

extremely significant to note that in glass lites where membrane action is developed, the blast load capacity of the lite is considerably less than one-half the static load capacity of the lite. In other words, in a glass lite with a small thickness-to-short-side ratio, t/b , an assumption of a usually conservative dynamic increase factor of two can be very unconservative. This is the case with all glass panes to the right or below the stepped dividing line in Table 1.

As orientation, the design center deflection, X_u , the effective linear stiffness, k_{eff} , and the natural period, T_n , of each plate are also reported. A technical discussion of Table 5 is presented in the appendix.

SAMPLE PROBLEMS

The following examples demonstrate the application of the design criteria in the design and evaluation of windows to safely survive blast overpressures from explosions.

Problem 1--Evaluation of Tempered Glass Panes

Given: A control room at a bomb practice range has tempered glass windows meeting both Federal Specification DD-G-1403B and the minimum fragment requirement of ANSI Z97.1-1984. The dimensions of the pane are: $a = 48$ inches,

Table 4. Measured and Predicted Dynamic Strength of Windows Subjected to Dynamic Blast Loads

Window					Blast Parameters		NCEL Design Prediction		Comments
a (in.)	c (in.)	a/b	t (in.)	Glass Type	B (psi)	T (msec)	B (psi)	T (msec)	
43.25	28.375	1.52	1/4	tempered	4.4	45	1.75	45	ARRADCOM dynamic test no. 5, Series I. Glass survived (Ref 2).
62.75	47.00	1.34	1/4	tempered	4.4	45	0.91	45	ARRADCOM dynamic test no. 5, Series I. Glass survived.
62.75	47.00	1.34	1/4	tempered	4.4	45	0.91	45	ARRADCOM dynamic test no. 5, Series I. Glass failed.
43.25	28.375	1.52	1/4	tempered	4.4	45	1.75	45	ARRADCOM dynamic test no. 5, Series I. Glass survived.
43.25	28.375	1.52	3/8	tempered	4.4	45	3.45	45	ARRADCOM dynamic test no. 5, Series I. Glass survived.
62.75	47.00	1.34	1/4	tempered	4.4	45	0.91	45	ARRADCOM dynamic test no. 5, Series I. Glass survived.
62.75	47.00	1.34	3/8	tempered	4.4	45	1.96	45	ARRADCOM dynamic test no. 5, Series I. Glass survived.
43.25	28.375	1.52	1/4	tempered	1.0	48	1.75	48	ARRADCOM test no. 1, Series II. Tempered glass in aluminum frame survived.
43.25	28.375	1.52	1/4	tempered	1.2	50	1.75	50	ARRADCOM test no. 2, Series II. Glass failure occurred due to frame distortion.
43.25	28.375	1.52	1/4	tempered	2.3	50	1.75	50	ARRADCOM test no. 3, Series II. Glass survived in strengthened frame.
43.25	28.375	1.52	1/4	tempered	3.1	50	1.75	50	ARRADCOM test no. 4, Series II. Glass fails due to frame distortion.

Table 5. Comparison of Blast Load Capacity of Tempered Glass Panes by NCEL Design Criteria Loads and Independent Energy Methods

Pane Size (in.)			NCEL Design Criteria Load, B (psi)	Predicted Design Load (Energy Method), B (psi)	Static Design Strength, r_u (psi)	Design Center Deflection, x_u (in.)	Effective Stiffness, k_{eff} (psi/in.)	Effective Natural Period, T_{eff} (msec)
a	b	t						
54	36	1/4	1.02	0.987	2.87	1.15	1.71	28.9
54	36	3/8	2.64	2.60	6.00	1.09	4.74	22.1
54	36	1/2	3.34	3.31	7.70	0.80	8.26	19.3
54	36	3/4	6.84	6.82	13.6	0.53	25.5	13.6
54	36	1	12.4	12.4	24.8	0.40	62.5	10.1
54	36	1-1/2	27.4	27.4	54.7	0.27	20.5	6.77
36	36	1/4	1.43	1.39	4.04	0.91	3.06	20.3
36	36	1/2	5.43	5.42	12.8	0.70	15.6	13.2
36	36	1	20.9	20.8	41.6	0.37	114	7.02
27	18	3/8	6.66	6.65	13.4	0.27	49.2	6.86
27	18	3/4	27.3	27.3	54.6	0.13	408	3.39
18	12	1/4	5.70	5.70	11.9	0.19	58.9	4.92
18	12	1	112	112	223	0.04	5,065	1.11
60	30	1/2	3.36	3.34	6.86	0.57	11.8	17.00
60	30	1	14.2	14.2	28.4	0.28	103	8.28

b = 48 inches, and t = 1/2 inch. No blast load will exceed 50 msec.

Find: Maximum blast load capacity of the windows.

Solution: Step 1: Tabulate the design parameters needed to enter Figures 2 to 21.

$$a/b = 48/48 = 1.00$$

$$b = 48 \text{ in.}$$

$$t = 1/2 \text{ in. (nominal)}$$

$$T = 50 \text{ msec}$$

Step 2: Enter the bottom design graph on Figure 3 and find that the design blast pressure is:

$$B = 3.85 \text{ psi}$$

Problem 2--Design of Tempered Glass Panes

Given: A nonoperable window having a single pane of glass. Glazing: heat-treated tempered glass meeting Federal Specification DD-G-1403B and the minimum fragment requirements ANSI Z97.1-1984. Dimensions of pane: a = 54 in., b = 36 in. Blast loading: B = 4.5 psi, T = 500 msec.

Find: Minimum thickness of glazing required for a probability of failure less than 0.001.

Solution: Step 1: Tabulate the design parameters needed to enter Figures 2 to 21.

$$a/b = 54/36 = 1.50$$

$$b = 36 \text{ in.}$$

$$B = 4.5 \text{ psi}$$

$$T = 500 \text{ msec}$$

Step 2: Enter Figures 2 to 21 with the design parameters from Step 1 and find the minimum glazing thickness.

The top graph of Figure 12 applies for the given design parameters. Enter Figure 12 and find the minimum glazing thickness required for $B = 4.5$ psi and $T = 500$ msec is:

$$t = 5/8 \text{ in.}$$

ANS

Problem 3--Design Loads for Window Frame

Given: A nonoperable window has a single pane of glass. Glazing: heat-treated tempered glass meeting Federal Specification DD-G-1403B and ANSI Z97.1-1984. Dimensions of the pane: $a = 37.5$ in., $b = 30$ in. Frame width: $w = 2$ in. Blast loading: $B = 12$ psi, $T = 1,000$ msec.

Find: Thickness of glazing required for a probability of failure equal to or less than 0.001 and design loading for window frame.

Solution: Step 1: Tabulate the design parameters needed to enter Figures 2 to 21.

$$a/b = 37.5/30 = 1.25$$

$$b = 30 \text{ in.}$$

$$B = 12 \text{ psi}$$

$$T = 1,000 \text{ msec}$$

Step 2: Select the minimum glazing thickness.

Enter the lower graph of Figure 8, which applies for the given design parameters. The minimum glazing thickness required is:

$$t = 3/4 \text{ in. nominal}$$

ANS

Step 3: Calculate the static ultimate uniform load that produces the same maximum frame load as the blast load.

Enter Table 1 for tempered glass with a pane size of 37.5 by 30 in., $a/b = 1.25$ and $t = 3/4$ in., and find the static uniform design load capacity of the glazing is:

$$r_u = 24.6 \text{ psi}$$

Thus, the window frame must be designed to safely support, without undue deflection, a static uniform load equal to 24.6 psi applied normal to both the glazing and exposed frame members.

Step 4: Calculate the design loading for the window frame.

Enter Table 2 with $a/b = 1.25$, and find by interpolation the design coefficients for the frame loading are:

$$C_R = 0.077$$

$$C_x = 0.545$$

$$C_y = 0.543$$

From Equation 3, the concentrated load in each corner of the pane is:

$$\begin{aligned} R (\text{corners}) &= -0.077 (24.6)(37.5)^2 \\ &= 2,660 \text{ lb} \end{aligned}$$

ANS

From Equation 1, the design loading for the frame in the long direction (a) is:

$$\begin{aligned} V_x &= 0.545 (24.6)(30) \sin (\pi x/37.5) \\ &\quad + 24.6(2) \end{aligned}$$

$$V_x = 402 \sin (\pi x/37.5) + 49.2 \text{ lb/in.}$$

ANS

From Equation 2, the design loading for the frame in the short direction (b) is:

$$\begin{aligned} V_y &= 0.543 (24.6)(30) \sin (\pi y/37.5) \\ &\quad + 24.6(2) \end{aligned}$$

$$V_y = 400 \sin (\pi y/40) + 49.2 \text{ lb/in.}$$

ANS

Distribution of the design load of the pane on the frame is shown in Figure 22.

Problem 4--Design Loads for Multi-pane Frame

Given: A nonoperable window consists of four equal size panes of glass. Glazing: heat-treated tempered glass meeting Federal Specification DD-G-1403B and the minimum size fragment requirements of ANSI Z97.1-1984. Dimensions of the panes: $a = 22.5$ in., $b = 18$ in. The exposed frame width is 3 in. Blast loading: $B = 14$ psi, $T = 50$ msec.

Find: Minimum thickness of glazing required for a probability of failures equal to or less than 0.001 and the design loads for the framing system.

Solution: Step 1: Tabulate the design parameters needed to enter Figures 2 to 21.

$$a/b = 22.5/18 = 1.25$$

$$b = 18 \text{ in.}$$

$$B = 14 \text{ psi}$$

$$T = 50 \text{ msec}$$

Step 2: Select the minimum glazing thickness.

Enter the bottom graph on Figure 7, which applies for the given design parameters. The minimum glazing thickness required is:

$$t = 1/2 \text{ in. nominal} \quad \text{ANS}$$

Step 3: Calculate the static ultimate uniform load that produces the same maximum reactions on the window frame as the blast load.

Enter Table 1 with $b = 18 \text{ in.}$, $a/b = 1.25$ and $t = 3/16 \text{ in.}$, and find the static design uniform load capacity of the glazing is:

$$r_u = 29.1 \text{ psi}$$

The window frame must be designed to safely support, without undue deflections, a static uniform load equal to 29.1 psi applied perpendicular to the glazing and to the exposed surface of the frame members.

Step 4: Calculate the design loading for the window frame.

Enter Table 2 with $a/b = 1.25$. With interpolation, the design coefficients for the frame loading are:

$$C_R = 0.077$$

$$C_x = 0.545$$

$$C_y = 0.543$$

From Equation 3, the concentrated loads in the corners of each pane are:

$$\begin{aligned} R (\text{corners}) &= -0.077 (29.1)(18)^2 \\ &= -726 \text{ lb} \quad \text{ANS} \end{aligned}$$

From Equation 1, the design loading for the long spans of the frame and mullions are:

$$\begin{aligned} V_x &= 0.545 (29.1)(18) \sin (\pi x / 22.5) \\ &\quad + 29.1(3) \\ &= 285 \sin (\pi x / 22.5) + 87.3 \text{ lb/in.} \quad \text{ANS} \end{aligned}$$

From Equation 2, the design loading for the short spans of the frame and mullions are:

$$\begin{aligned} V_y &= 0.543 (29.1)(18) \sin (\pi y / 18) \\ &= 284 \sin (\pi y / 18) + 87.3 \text{ lb/in.} \quad \text{ANS} \end{aligned}$$

The design loads for the window frame are shown in the following figure and table and are illustrated below.

Problem 5--Design Acceptance Based upon Certification Test Results

Given: A window $54 \times 36 \times 3/8$ -inch with a single pane of tempered glass is designed to safely resist a blast load, B , of 2.7 psi with an effective blast duration, T , of 200 msec. Certification testing involved testing three window assemblies ($n = 3$) to failure. Failure loads, \hat{r}_i , were recorded at 14.0, 17.0, and 13.7 psi.

Find: Determine if the window design is acceptable based on results from the certification tests.

Solution: Step 1: Tabulate the design parameters needed to enter Table 1:

$$b = 36 \text{ in.}$$

$$a/b = 54/36 = 1.50$$

$$t = 3/8 \text{ in. nominal}$$

Step 2: Employing Table 1, select the static design load, r_u , corresponding to the glass pane geometry.

$$r_u = 6.90 \text{ psi}$$

Calculate the static load capacity of the tempered glass for certification from Equation 4:

$$r_s = 0.876 r_u = 6.04 \text{ psi}$$

Step 3: Calculate the arithmetic mean, \bar{r} , of all the samples tested.

Using Equation 6:

$$\begin{aligned} \bar{r} &= \frac{\sum_{i=1}^n \hat{r}_i}{n} \\ &= \frac{(14.0 + 17.0 + 13.7)}{3} \\ &= 14.9 \text{ psi} \end{aligned}$$

Step 4: Using Equation 7, calculate the sample standard deviation, s .

The sample standard deviation, s , is calculated using Equation 6 as,

$$\begin{aligned} s &= \sqrt{\frac{\sum_{i=1}^n (\hat{r}_i - \bar{r})^2}{(n - 1)}} \\ &= \sqrt{\frac{(14.0 - 14.9)^2 + (17.0 - 14.9)^2 + (13.7 - 14.9)^2}{(3 - 1)}} \\ &= 1.82 \text{ psi} \end{aligned}$$

Step 5: Verify that the sample standard deviation, s , is larger than the minimum value, s_{\min} , prescribed in Equation 8.

$$\begin{aligned} s &= 1.82 \text{ psi} > s_{\min} \\ &= 0.145 r_s \\ &= 0.145 (6.04) \\ &= 0.876 \text{ psi} \end{aligned}$$

Thus, $s = 1.82 \text{ psi}$ is the appropriate value to use in subsequent calculations.

Step 6: Using Table 3, select the acceptance coefficient, α , that correlates with the three samples tested.

Entering Table 3, with $n = 3$, find:

$$\alpha = 3.05$$

Step 7: Verify that the window and frame passed the certification tests by meeting the conditions of Equation 5:

$$\begin{aligned} \bar{r} &= 14.9 \text{ psi} \geq r_s + s \alpha \\ &= 6.04 + 1.82 (3.05) \\ &= 11.6 \text{ psi} \end{aligned}$$

Therefore, the window assembly design is considered safe for the prescribed blast loading.

Problem 6--Design Rejection Based upon Certification Test Results

Given: A window 30 x 30 x 1/4 inch with a single pane of tempered glass is designed to safely resist a blast load, B , of 4.0 psi with an effective blast duration, T , of 200 msec. Certification testing involved testing three window assemblies ($n = 3$) to failure. Failure loads, \hat{r}_i , were 6.39, 7.49, and 8.47 psi.

Find: Determine if the window design is acceptable based upon results from the certification tests.

Solution: Step 1: Tabulate the design parameters needed to enter Table 1.

$$\begin{aligned} b &= 30 \text{ in.} \\ a/b &= 30/30 = 1.00 \\ t &= 1/4 \text{ in.} \end{aligned}$$

Step 2: Employing Table 1 select the static design load, r_u , corresponding to the pane geometry.

$$r_u = 5.53 \text{ psi}$$

The static load capacity of tempered glass for certification testing, r_s , is calculated according to Equation 4 as:

$$r_s = 0.876 r_u = 4.84 \text{ psi}$$

Step 3: Calculate the arithmetic mean, \bar{r} , of all the samples tested:

$$\begin{aligned} \bar{r} &= \frac{\sum_{i=1}^n \hat{r}_i}{n} \\ &= \frac{(6.39 + 7.49 + 8.47)}{3} \\ &= 7.45 \text{ psi} \end{aligned}$$

Step 4: Employing Equation 7, calculate the sample standard deviation, s .

The sample standard deviation, s , is calculated as:

$$\begin{aligned} s &= \sqrt{\sum_{i=1}^n \frac{(\hat{r}_i - \bar{r})^2}{(n-1)}} \\ &= \sqrt{\frac{(6.39-7.45)^2 + (7.49-7.45)^2 + (8.47-7.45)^2}{(3-1)}} \\ &= 1.04 \text{ psi} \end{aligned}$$

Step 5: Verify that the sample deviation, s , is larger than the minimum value, s_{\min} , prescribed in Equation 8.

$$\begin{aligned} s &= 1.04 \text{ psi} > s_{\min} \\ &= 0.145 r_s \\ &= 0.145 (4.84) \\ &= 0.702 \text{ psi} \end{aligned}$$

Thus, $s = 1.04 \text{ psi}$ is the appropriate value to use in subsequent calculations.

Step 6: Using Table 3, select the acceptance coefficient, α , and the rejection coefficient, β , for $n = 3$. Entering Table 3 with $n = 3$, find,

$$\begin{aligned} \alpha &= 3.05 \\ \beta &= 0.871 \end{aligned}$$

Step 7: Verify if the window and frame passed the certification tests by meeting the conditions of Equation 5:

$$\begin{aligned}\bar{r} &= 7.45 \text{ psi} < r_s + s \sigma \\ &= 4.84 + 1.04 (3.05) \\ &= 8.01 \text{ psi}\end{aligned}$$

Therefore, the window assembly design does not satisfy Equation 4 and is considered unsafe for the prescribed design blast loading.

ACKNOWLEDGMENTS

The author wishes to express his appreciation and gratitude to all the following dedicated scientists, engineers and other professionals who made this study possible. Particular thanks go to Dr. Lynn Beason and Dr. James Morgan of Texas A&M University for their pioneering and high quality work on maximum allowable stress levels in glass and to Mr. Donald Moore of the Jet Propulsion Laboratory for his work on the load, stress, and deflection relationships of glass panes. Additionally, the author thanks Dr. J. Minor and Dr. C.V.G. Vallabhan of Texas Technical University for their unselfish and excellent advice. Finally, the author expresses a special thanks to Mr. William Keenan for his many valuable suggestions and insights, without which this paper would have been impossible.

BIBLIOGRAPHY

- American National Standards Institute (1984). Safety performance specifications and methods of test for safety glazing material used in buildings, ANSI Z97.1-1975. New York, N.Y., 1975.
- American Society for Testing and Materials (1982). Structural performance of glass in exterior windows, curtain walls, and doors under the influence of uniform static loads by destructive method, ASTM Standard (draft), Draft of proposed standard by ASTM Committee E06.51. Philadelphia, Pa., Oct 1982.
- Anians, D. (1980). Experimental study of edge displacements of laterally loaded window glass plates, Institute for Disaster Research, Texas Technical University. Lubbock, Tex., Jun 1980.
- Beason, W.L. (1980). A failure prediction model for window glass, Texas Technical University, NSF/RA 800231. Lubbock, Tex., May 1980.
- Beason, W.L. (1982). TAMU glass failure prediction model, preliminary report, Texas A&M University. College Station, Tex., Mar 1982.
- Beason, W.L., and Morgan, J.R. (undated). "A glass failure prediction model," submitted for publication in the Journal of the Structural Division, American Society of Civil Engineers.
- General Services Administration (1972). Glass, plate (float), sheet, figured, and spandrel (heat strengthened and fully tempered), Federal Specification DD-G-1403B. Washington, D.C., 1972.
- General Services Administration (1977). Federal specification glass, plate, sheet, figured (float, flat, for glazing, corrugated, mirrors and other uses), Federal Specification DD-G-451d. Washington, D.C., 1977.
- Levy, S. (1942). Bending of rectangular plates with large deflections, NACA TechNote 845, 1942.
- Meyers, G.E. (1984). "Preliminary design procedure for blast-hardened window panes," paper presented at the Defense Department Explosive Safety Seminar, Houston, Tex., Aug 1984.
- Moore, D.M. (1980). Proposed method for determining the thickness of glass in solar collector panels, Jet Propulsion Laboratory, Publication 80-34. Pasadena, Calif., Mar 1980.
- Moore, D.M. (1982). Thickness sizing of glass plates subjected to pressure loads, Jet Propulsion Laboratory, FSA Task Report No. 5101-291. Pasadena, Calif., Aug 1982.
- PPG Industries (1981). PPG glass thickness recommendations to meet architect's specified 1-minute wind load. Pittsburg, Pa., Mar 1981.
- Timoshenko, S., and Woinowsky-Krieger, S. (1959). Theory of plates and shells. New York, N.Y., McGraw-Hill Book Company, 1959.
- U.S. Army Picatinny Arsenal, National Bomb Data Center (1973). A method for improving the shatter resistance of window glass, General Information Bulletin 73-9. Dover, N.J., Nov 1973.
- Vallabhan, C.V.G., and Wang, B.Y. (1981). Nonlinear analysis of rectangular glass plates by finite difference method, Texas Technical University, Institute for Disaster Research. Lubbock, Tex., Jun 1981.
- Weissman, S., Dobbs, N., Stea, W., and Price, P. (1978). Blast capacity evaluation of glass windows and aluminum window frames, U.S. Army Armament Research and Development Command, ARLCO-CR-78016. Dover, N.J., Jun 1978.

LIST OF SYMBOLS

- | | |
|----------------|--|
| a | Long dimension of glass pane, in. |
| B | Peak blast overpressure, psi |
| b | Short dimension of glass pane, in. |
| B _e | Peak blast overpressure predicted by an energy method, psi |

C	Shear coefficient for load passed from glass pane to its support frame
D	Modulus of rigidity of glass pane, in.-lb
E	Modulus of elasticity, psi
f_u	Design stress and allowable principal tensile stress in glass pane for prescribed P(F), psi
f_y	Yield stress of frame members and fasteners, psi
I	Moment of inertia of window frame, in. ⁴
k_{eff}	Effective linear stiffness, psi/in.
n	Number of window assemblies tested
m_e	Effective mass (lb-msec ² /in.)
P	Blast overpressure at any time, psi
P(F)	Probability of failure of glass pane
R	Uplifting nodal force applied by glass pane to corners of frame, lb
r	Resistance, psi
\bar{r}	Test load at failure of frame or glass during certification tests, psi
\bar{r}	Mean failure load of n samples, psi
r_{eff}	Effective resistance, psi
r_s	Static load capacity of tempered glass for certification testing, psi
r_u	Design static load capacity of the glass pane, psi
r_u^-	Uniform static negative load capacity of the window assembly, psi
s	Sample standard deviation, psi
T	Effective duration of blast load, msec
t	Nominal thickness of glass pane, in.; elapsed time, msec
T_n	Natural period of vibration of the glass pane, msec
U	Strain energy in pane, psi-in.
U_r	Strain energy under resistance function, psi-in.
V_x	Static load applied by glass pane to long edge of frame, lb/in.
V_y	Static load applied by glass pane to short edge of frame, lb/in.

w	Width of exposed surface of window frame, in.
x	Distance from corner measured along long edge of glass pane, in.
X	Center deflection of pane, in.
X_u	Center deflection of pane at r_u , in.
α	Acceptance coefficient
β	Rejection coefficient
ν	Poisson's ratio

Appendix

ENERGY METHOD CALCULATIONS

The strain energy capacity of the plate, U, will be equal to the capacity blast load, B_e , times its center design displacement, X_u , times the deflection shape function g(x,y):

$$U = B_e \cdot X_u \int_0^a \int_0^b g(x,y) dA \quad (A-1)$$

The strain energy in the pane will equal the area under the resistance function (based on center deflection) times the deflected shape function, g(X,y) of the pane:

$$U = \int_0^{X_u} r dx \cdot \int_0^a \int_0^b g(x,y) dA \quad (A-2)$$

It is conservative to neglect the small contribution of the inertial energy of the plate's motion. Fortunately, the integral of the shape functions in Equation A-2 cancels out. Simplifying Equations A-1 and A-2 yields Equation A-3:

$$B_e = \frac{\int_0^{X_u} r dx}{X_u} \quad (A-3)$$

The integral is calculated by numerically integrating the resistance function (uniform load-center deflection) of each of the glass panes by the trapezoidal method (15 segments). The validity of the assumed resistance functions have been confirmed by static load tests on tempered glass by NCEL.

The effective stiffness, k_{eff} , can be visualized as the slope of an equivalent resistance function, which contains the strain energy

storage capacity as the actual resistance function. For high thickness-to-short-side glass pane ratios, where no membrane action is present, the effective stiffness will be the actual stiffness.

The effective stiffness, k_{eff} , can be defined as:

$$k_{eff} = \frac{r_{eff}}{X_u} \quad (A-4)$$

where r_{eff} is the load that k_{eff} would manifest at displacement X_u .

However, the strain energy, U_r , under the linear resistance function for s_r statically applied load is:

$$U_r = 1/2 r_{eff} \cdot X_u \quad (A-5)$$

This is already calculated as the integral in Equation A-3.

Manipulating A-3 and substituting into Equations A-5 and A-4 yields:

$$k_{eff} = 2 B_e / X_u \quad (A-6)$$

The natural period of the pane can then be defined as:

$$T_n = 2 \pi \sqrt{m/k_{eff}} \quad (A-7)$$

The effective mass of the plate, m , is defined as the glass lites mass multiplied by a load mass factor, k_{LM} . For a simply supported plate, the load mass factor is calculated as:

$$k_{LM} = 0.63 + 0.16 (\text{aspect ratio} - 1) \quad (A-8)$$

SHOCK TESTING AND ANALYSIS

SHOCK RECONSTRUCTION FROM THE SHOCK SPECTRUM

Charles T. Morrow
Consultant
Encinitas, California

Earlier papers by the author have disclosed an algorithm for rapid computation of the undamped residual shock spectrum, with phase as well as magnitude information, and have showed that the phase information can, by differentiation with respect to angular frequency, be converted to a simple function of frequency, designated the Apparent Starting Time. Since such a spectrum is simply related to the Fourier transform (Fourier spectrum), reconstructing the shock time history from it should be possible, at least in principle.

Indeed, the derivation for this reconstruction would be trivial, except that, to provide the same fractional resolution in each frequency decade, a logarithmic frequency scale, with frequency increments proportional to frequency, was chosen for the computation of the residual spectrum. Many of these increments are much larger than those of a Fourier series approximation or Discrete Fourier Transform (DFT) covering the same frequency range. Therefore a new approximating summation must be obtained from the integral Fourier transform as a summation of integrals over the successive frequency increments. The integrands must be expressed in terms of something that changes less rapidly with frequency than the phase angle -- expressed for example in terms of the Apparent Starting Time of the undamped residual shock spectrum.

Shocks that exhibit nulls in the magnitude of their undamped residual spectrum at certain frequencies, and consequent phase reversals at these frequencies, can not be reconstructed by this algorithm as it now stands. For example, the wave reconstructed from the spectrum of a square wave shows no resemblance to the original. On the other hand, reconstruction of a terminal-peak sawtooth is as accurate as one can expect with a 2000 Hz upper frequency limit on the spectrum. Shocks to which equipment in use is subject, and desirable test shocks, can be reconstructed.

Whereas the usual reconstruction from the DFT, carried out for an extended time, yields a shock that repeats at a period equal to the duration of the original time history, a shock reconstructed from the undamped residual shock spectrum with a logarithmic frequency scale shows no such periodicity. This in principle simplifies the inverse transform method of construction of responses of a mechanical system, which may persist long after shock termination.

INTRODUCTION

SHOCK SPECTRUM papers [1-3] by the author have disclosed an algorithm for digital computation of mechanical responses to shock and digital computation of undamped residual shock spectra. The Indirect Fourier Transform (IFT) algorithm is based on the observation that any shock time history can be approximated by a series of straight lines connecting sufficiently closely spaced points on the curve, as shown in Figure 1. This is equivalent to expressing the shock raw data as a series of discontinuities of acceleration slope, or acceleration, or both. Consequently, if the response of any linear mechanical system to a ramp of unit slope change and to a unit step function are

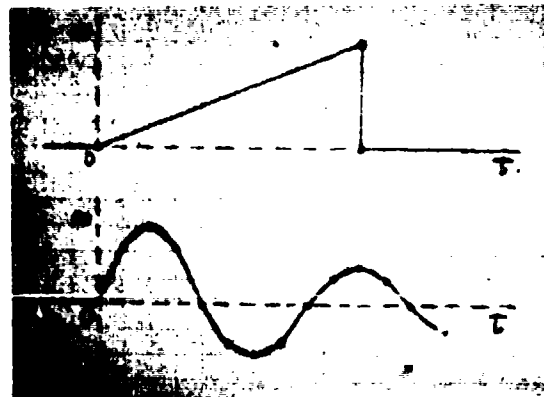


Figure 1. Straight-Line Approximations

known, the response of that system to any shock can be computed.

The response of an undamped simple mechanical resonator, for any instant between t_k and t_{k+1} can be approximated by

$$a_r(t) = C_0 + C_1 t + C_2 \cos 2\pi f t + C_3 \sin 2\pi f t, \quad (1)$$

if t_k and t_{k+1} are so close that the curve between them is nearly straight, or by

$$a_r(t) = C_0 + C_1(t-t_k) + C_2 \cos 2\pi f(t-t_k) + C_3 \sin 2\pi f(t-t_k), \quad (2)$$

where t is the time in seconds, f is the frequency in Hz, and both equations contain four arbitrary constants.

Equation (2), especially when used with constant time increments, leads to the simpler response computation. For time t_k , the previous solution is given a time shift to express it in terms of $t-t_k$ instead of $t-t_{k-1}$ and the response resulting from any discontinuity of slope or acceleration at t_k is added in, to yield a new approximating solution in the form of Equation (1), with new values for the arbitrary constants C_0 , C_1 , C_2 and C_3 . The response is then evaluated for $t=t_k$.

$$a_r(t_k) = C_0 + C_1, \quad (3)$$

and the algorithm moves on to $t=t_{k+1}$. The primary operations are multiplications and additions similar to those of the FFT algorithm -- no brute force evaluation of trigonometric functions is necessary except at the beginning before response computation is under way. Computation is performed only for the frequencies of the resonances of the mechanical system -- in this case only one.

Equation (1), however, leads more directly to a unique spectrum. The frequencies are not constrained to be in a harmonic relationship as in the FFT algorithm. Therefore, a logarithmic distribution of frequencies has been chosen, to provide constant fractional resolution in each frequency decade -- 301 frequencies in total for the three decades from 2 to 2000 Hz. Of the four arbitrary constants, it is necessary only to compute successive values for C_2 and C_3 . No instantaneous response evaluations are necessary. The final values of C_2 and C_3 , after all shock data inputs, yield an undamped residual shock spectrum with a magnitude $R(f)$, given by the square root of the sum of the squares, since

$$C_2 = R(f) \cos \theta, \quad \text{and} \quad (4)$$

$$C_3 = R(f) \sin \theta, \quad (5)$$

and an inherent phase angle given by

$$\theta = \tan^{-1} C_3 / C_2. \quad (6)$$

Like the phase angle of the Fourier transform, θ is a rapidly changing function of frequency. However, the

Apparent Starting Time of the residual response, obtained by the derivative

$$AST = T_s = d\theta/d\omega, \quad (7)$$

where

$$\omega = 2\pi f \quad (8)$$

is the angular frequency in radians per second, is a plottable, well behaved function. This is a weighted starting time. If energy is imparted to the simple system by the shock primarily at one specific time, the AST will be approximately equal to that time. If the energy is imparted primarily at two different instants, the AST will be in the middle.

While θ and the AST are best understood in terms of Equation (1), it is possible to use Equation (2), again without response computations, and make corrections to the final constants. Applying Equation (4) to C_2 and C_3 of Equation (2) would yield an AST measured from shock termination rather than from the beginning of the shock. For proper results, the shock duration must be added to this, or else a time shift must be imparted to Equation (2) to convert its coefficients to C_0 and C_1 of Equation (1), before any phase angles or relationships to the Fourier transform are explored.

Total computation time for this form of the algorithm or its inverse, with sufficiently refined software, would be crudely comparable to that of the FFT algorithm or its inverse. The IFT algorithm uses fewer frequencies and does not require any computations for zeros after shock termination. The FFT algorithm utilizes redundancy in its computation matrix and to eliminate many of the matrix elements from separate computation. For construction of responses from shock data in the time domain, both types of algorithm are slow compared to the extended IFT algorithm.

RELATION TO THE FOURIER TRANSFORM

A relationship between the undamped residual shock spectrum and the Fourier transform was first published in 1951 (4). The derivation to follow expresses it in suitable form for present use.

The complex exponential Fourier transform of a time function $a(t)$ is given by

$$\begin{aligned} F(f) &= \int_{-\infty}^{\infty} a(s) e^{-j2\pi f s} ds \\ &= \int_{-\infty}^{\infty} a(s) [\cos 2\pi f s - j \sin 2\pi f s] ds \\ &= F_{\text{real}}(f) + j F_{\text{imag}}(f) \\ &= F_C(f) - j F_S(f), \end{aligned} \quad (9)$$

where the real part is equal to the cosine transform

$$\begin{aligned} F_{\text{real}} &= F_C(f) \\ &= \int_{-\infty}^{\infty} a(s) \cos 2\pi f s ds, \end{aligned} \quad (10)$$

and the imaginary part is the negative of the sine transform

$$F_{imag} = -F_s(f) \\ = -\int_{-\infty}^{\infty} a(s) \sin 2\pi f s ds. \quad (11)$$

The first [1] of the three previous papers overlooked the minus sign in Equation (11), which requires a reversal of the sign in the numerical printout of the the second [2] paper, but nothing else is affected. In particular, the relationship between the final values of the last coefficients of Equation (1) and the real and imaginary parts of the exponential transform [1] is still given by

$$F_{real} = C_s/2\pi f \quad (12)$$

and

$$F_{imag} = C_c/2\pi f. \quad (13)$$

Accordingly, since $a(t)$ can be reconstructed from the Fourier transform, it can also be reconstructed in principle from the various values of the two coefficients, versus frequency, that yield the undamped residual shock spectrum.

INVERSE TRANSFORMATION

If the frequencies for the new algorithm for undamped residual shock spectrum computation had been chosen in a harmonic rather than a logarithmic relationship, reconstructing $a(t)$ from the shock spectrum would be quite straightforward and trivial. It would be necessary only to construct a discrete Fourier transform (DFT) by means of application of Equations (12) and (13) to successive frequencies and then compute the inverse of the DFT. The DFT is, after all, merely a succession of Fourier series coefficients multiplied through by a constant factor proportional to the fundamental frequency. Its inverse could be taken confidently whether or not the Fourier transform had been devised. However, the undamped residual spectrum computed for frequencies in a logarithmic relationship, with finite spacing, does not lead directly to an invertible logarithmic version of the DFT -- the phase angle changes too rapidly at the higher frequencies. It is necessary to examine carefully the theoretical inversion of the Fourier transform and to devise new terms that are integrals over frequency increments. From the Fourier integral theorem,

$$a(t) = \int_{-\infty}^{\infty} F(f) e^{j2\pi f t} df \\ = \int_{-\infty}^{\infty} [F_{real}(f) + jF_{imag}(f)] e^{j2\pi f t} df \\ = \int_{-\infty}^{\infty} [F_{real}(f) \cos 2\pi f t \\ - F_{imag}(f) \sin 2\pi f t] df \\ + j \int_{-\infty}^{\infty} [F_{real}(f) \sin 2\pi f t \\ + F_{imag}(f) \cos 2\pi f t] df \\ = \int_{-\infty}^{\infty} [F_{real}(f) \cos 2\pi f t \\ - F_{imag}(f) \sin 2\pi f t] df \\ + 2j \int_0^{\infty} [F_{real}(f) \sin 2\pi f t \\ - F_{imag}(f) \cos 2\pi f t] df. \quad (14)$$

The logic of this progression of expressions is as follows. The first expression contains the simplest possible statement of the inversion of the complex exponential Fourier transform. In the second expression, the transform is split into real and imaginary parts. In the third expression, the exponential is split into real and imaginary parts and the resulting real and imaginary terms are separated. From Equations (2) and (3), the imaginary terms both contain a product of an odd function of f and an even function of f , which must integrate to zero. This leads to the fifth and final expression, which is valid provided that integration through zero does not encounter an infinite value. In that event, exclusion of a short frequency interval about zero frequency may still permit an inversion that is useful in practice.

In the present paper, integration is restricted to the range from 2 to 2000 Hz, the range most commonly used in shock and vibration testing, with the logarithmic frequencies of the IFT algorithm [2], since a spectrum must be obtained by that algorithm before reconstruction can be accomplished. By making some assumptions about the behaviour of the magnitude of the undamped residual and the behaviour of the AST, it should be possible to extend the integration to lower frequencies. However, the only effect of this would be to introduce some response components at periods longer than 1/2 second, with a very minor practical effect except with shocks or responses lasting of the order of 0.1 second or more.

1/2

The next step is to derive an approximate expression for an integral of the form of Equation (14) over a single frequency increment

$$\Delta f_1 = f_1 - f_{1-1}, \quad (15)$$

by expressing the integrand in terms of variables that vary only very slowly over the frequency increment. The obvious problem variable, θ , is approximated over the frequency increment by a linear equation

$$\theta = 2\pi(f - f_{1-1})t_s + \theta_{1-1}, \quad (16)$$

derived from Equation (7) and equivalent to a reversal of the method of computing the AST. Accordingly, the contribution to the integral by the frequency increment Δf_1 is given, through use of Equations (4), (5), (12) and (13), by

$$\Delta_1(t) = 2 \int_{f_{1-1}}^{f_1} [F_{real}(f) \cos 2\pi f t \\ - F_{imag}(f) \sin 2\pi f t] df \\ = [R(f_1)/\pi f_1] \int_{f_{1-1}}^{f_1} [\cos \theta \sin 2\pi f t - \sin \theta \cos 2\pi f t] d\theta \\ = [R(f_1)/\pi f_1] \int_{\theta_{1-1}}^{\theta_1} \sin 2\pi f t - \theta d\theta \quad (17)$$

By application of Equation (15), this becomes an expression with f as a variable only in the first part of the argument of the sine function.

$$\begin{aligned} \Delta_i t &= -[R(f_i)/\pi f_i] \\ &\times \int_{f_{i-1}}^{f_i} \sin[2\pi f(t-t_s) + 2\pi f_{i-1}t_s - \theta_{i-1}] df \\ &= [R(f_i)/2\pi^2 f_i(t-t_s)] \\ &\times \left\{ \cos[2\pi f_i(t-t_s) - \theta_{i-1} + 2\pi f_{i-1}t_s] \right. \\ &\quad \left. - \cos[2\pi f_{i-1}(t-t_s) - \theta_{i-1} + 2\pi f_i t_s] \right\}. \end{aligned} \quad (18)$$

The final expression of Equation (18) is the difference of two very similar formulas -- by itself without numerical testing in a computer program, it offers no obvious hint of how well it can perform. Notice, however, that it yields no absolute reconstructed value -- only, when properly summed over frequency, the difference between the reconstructed value for one instant and that for the next instant. In numerical implementation of the algorithm, the reconstructed value is set to zero, or to the constant acceleration prior to shock initiation, for the last instant prior to the first instant to be computed. Then Equation (18) is evaluated, brute force, for the next instant and for all frequencies, summed, and added to the existing reconstructed value to obtain the next value. Computations for later instants, instead of complete re-evaluation of the expressions for all frequencies, merely involve shifting the angles in the arguments of the cosine functions by $2\pi f_i \Delta t$ and $2\pi f_{i-1} \Delta t$, where Δt is a constant time increment between instants for response computation. This is done by the formula for the cosine of the sum of two angles and involves for each successive instant only a simple multiply-add-on operation per frequency, similar to those of the IFT and FFT algorithms, once the initial cosines and sines of all $2\pi f_i(t-t_s)$ and the cosines and sines of all $2\pi f_i \Delta t$ have been computed.

The last expression of Equation (18) would not be valid as written and would result in a "division by zero" error message for $t=t_s$ exactly, if for any frequency this should happen during the sequence of time values, since the denominator would be zero. However, since

$$\lim_{x \rightarrow 0} \sin x / x = 1, \quad (19)$$

and

$$\cos x - \cos y = 2 \sin[(x+y)/2] \sin[(x-y)/2] \quad (20)$$

Equation (18) can be converted to a product

$$\begin{aligned} \Delta_i t &= -[R(f_i)/\pi^2 f_i(t-t_s)] \sin[2\pi f_i(t-t_s)] \\ &\times \sin[\pi f_{i-1}(t-t_s) - \theta_{i-1} + 2\pi f_i t_s] \end{aligned} \quad (21)$$

that approaches a limit

$$\lim_{t \rightarrow t_s} \Delta_i t = -[R(f_i)/\pi f_i] \sin(2\pi f_{i-1}t_s - \theta_{i-1}), \quad (22)$$

which is applied at most once per frequency instead of Equation (17), since $t=t_s$ is very unlikely and occurs at most once per frequency.

Accordingly, the final result is not a Fourier series summation but a summation over frequency, from 2 to 2000 Hz, of terms given by Equation (18), with Equation (22) as a one-time backup for any frequency for which it ever happens that $t=t_s$. Otherwise, in proceeding from one response instant to the next, each term receives multiply-add-on operations and a new summation of terms is obtained and added to the previous response value.

The value of θ for the lowest frequency is obtained directly from the cosine and sine components of the undamped residual spectrum, using Equation (4). The remaining values are obtained from successive values of the AST, using Equation (15).

Equation (21), with Equation (22) as a backup, could be used instead of Equation (18). In fact, this was the first way the algorithm was tested. However, it is slower than Equation (18), especially on the first brute force evaluation, and it requires more memory.

NUMERICAL RESULTS

An IFT program in BASIC was stripped of routines unnecessary for the experiment, and the above reconstruction algorithm was implemented in the memory made available. This made it possible to obtain the undamped residual spectrum, with both cosine and sine factors in a memory matrix, from constant time increment shock input data, and then reconstruct the shock numerically by the present algorithm.

A constant time increment of 1/2 millisecond was chosen for data inputs for a 10 millisecond 100g terminal-peak sawtooth. To verify the spectral characteristics and store them in memory, the residual magnitude and the apparent starting time were plotted in succession on the video screen. Then the reconstruction routine was applied. The reconstructed value was set to zero for $t=1/2$ millisecond. The results, in accordance with Equation (20), are plotted in Figure 2.

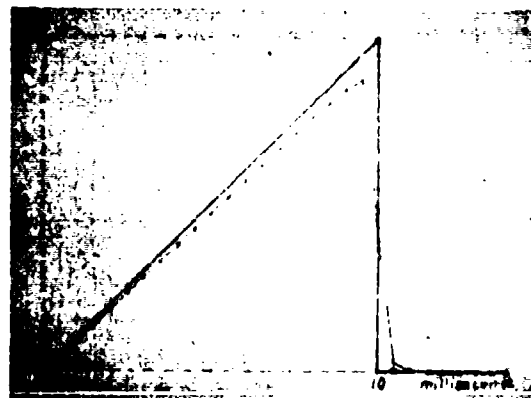


Figure 2. Terminal-Peak Sawtooth Reconstructed

The reconstruction is as close to the original as one can expect with only a frequency range from 2 to

2000 Hz. Higher frequencies would permit a sharper initial bend and a sharper terminal peak. However, the reconstructed value for 10 milliseconds is close to the midpoint of the acceleration discontinuity, as it should be. Another run, in accordance with Equation (18), was about 2g higher, with slightly better accuracy -- this difference was negligible, but Equation (18) is preferable for memory utilization and computation time.

A DFT or Fourier series with lowest frequency 2 Hz would be expected to produce a pulse, shaped with comparable accuracy, but recurring every half second. Another run with the algorithm, utilizing Equation (18), with 1 millisecond time increments, was made out past one second. The reconstructed numbers waved about very slowly of the order of 1 or 2g, but there was not a hint of a repetition of the sawtooth pulse.

On the other hand, an attempt to reconstruct a 10 millisecond 100g square wave yielded an irregular wave bearing no resemblance to the original. The reason for this is that Equation (14) is not valid throughout a frequency increment that contains a null in $R(f)$, which is always accompanied by a 180° reversal of θ . The computation of the AST by the IFT algorithm requires a 180° correction when this occurs -- the one thing thus left out of the computation of R and T is the listing of any frequencies at which a null occurs. Of course, the reconstruct algorithm could be made more elaborate, to include a means for estimating the null frequencies and reinserting the phase discontinuities. This would hardly be worthwhile, since the nulls ordinarily occur only for symmetrical pulses such as the square wave and half sine wave. These pulses do not occur in the actual environment to be simulated in test, and, because of the nulls, are undesirable test shocks.

CONCLUSION

A shock time history can be reconstructed from the undamped residual shock spectrum, with logarithmic frequencies, as obtained through the Indirect Fourier Transform algorithm, provided that the Apparent Time has been computed and that the spectral magnitude $R(f)$ contains no absolute null at any frequency. Under the same circumstances, the undamped residual shock spectrum, like the Fourier transform or DFT, can be accepted as a complete description of the shock, containing in the frequency domain all the information that existed in the time domain.

In an effort begun before the work reported here and still continuing, the programs of the first three papers [1-3] have successfully been combined into a single program, simplified, compressed into smaller memory, made easier to use, and executed without need for deletion of any parts not in immediate use. Several ways have been identified to make the repeated operations of the spectral analysis run faster, so as to make the program compare more favorably with those of dedicated computers. In time, more hardware simulations will be provided, and some novel ways of inputting shock data will be added. One intent is to sell a version of the composite program as a supplement to a complete rewrite of the author's book on shock and vibration engineering, together with any additional programs that may be developed to provide

illustrations for the text. The program improvised for the present paper was adequate to demonstrate some important principles. If it also shows promise of being sufficiently useful in practice, a decision may be made to refine it and make it available with the other programs.

The anonymous reviewers of the present paper were both patient with the initial draft and conscientious in the preparation of comments. All comments have had an effect on the final manuscript and have resulted in improvement.

REFERENCES

1. C. T. Morrow, "Indirect Fourier Transform and Shock Response", SHOCK AND VIBRATION BULLETIN 52, Part 4, pp. 37-45, 1982.
2. C. T. Morrow, "Shock Spectral Analysis by Personal Computer", using the IFT Algorithm", SHOCK AND VIBRATION BULLETIN 53, Part 1, pp. 97-102, 1983.
3. C. T. Morrow, "Shock Response Analysis by Personal Computer, using the Extended IFT Algorithm", SHOCK AND VIBRATION BULLETIN 54, Part 2, pp. 131-141, 1984.
4. H. Southworth, Jr., "Derivation of a Relationship between the 'Residual' Shock Spectrum and the Fourier Integral Spectra", SHOCK AND VIBRATION BULLETIN 29, Part 4, p. 408, The Shock and Vibration Information Center, 1951.

Discussion

Mr. Hanna (Synergistic Technology): How long did the reconstruction take on your processor?

Mr. Morrow: I programmed this in BASIC. It is interpretive BASIC. I made no attempt to speed it up by compiling it or by using a machine language subroutine. It took several minutes, but it could be speeded up.

THE SHOCK RESPONSE SPECTRUM AT LOW FREQUENCIES

David O. Smallwood
Sandia National Laboratories
Albuquerque, NM

This paper shows that for small damping the correct acceleration shock response spectrum will roll off with a slope of 6 dB/octave on a log-log plot. An undamped acceleration shock spectrum and the shock spectrum based on a relative displacement model will roll off with a slope of 12 dB/octave.

Introduction

The slope of the shock spectrum at low frequencies is typically evaluated by using a well known relationship between the undamped residual shock response spectrum and the magnitude of the Fourier spectrum [1]. This has led to the common belief that the shock response of shocks with a low velocity change, like a pyrotechnic shock, will have a low frequency slope of 12 dB/octave. But anyone who has examined these shocks has seen data which violates this assumption. Several suggestions have been offered to explain the slopes which are different from 12 dB/octave including:

- o The spectrum doesn't really roll off at 12 dB/octave
- o Zero offsets cause the spectrum to roll off at a slope different from 12 dB/octave
- o Truncation errors cause the problem
- o Incorrect algorithms are being used to calculate the spectrum

Each of these suggestions are examined in this paper.

Models

Before I can discuss the shock response spectrum we must examine the single-degree-of-freedom (SDOF) models which are used to evaluate the shock response spectrum. A large number of models are used, but they can be reduced to variations of just two models, which I will discuss.

Acceleration Model- The input to this model is the absolute acceleration of the base of the SDOF system. The response of the SDOF system is the absolute acceleration of the mass. The transfer function of this system in the complex Laplace domain is given by

$$H_a(s) = \frac{2\zeta\omega_n s + \omega_n^2}{s^2 + 2\zeta\omega_n s + \omega_n^2} \quad (1)$$

The impulse response of this model is given by

$$h_a(t) = \omega_n(1 - \zeta^2)^{-1/2} \exp(-\zeta\omega_n t) \sin(\omega_d t + \phi) \quad (2)$$

where

$$\phi = \tan^{-1}[2\zeta(1 - \zeta^2)^{1/2} / (1 - 2\zeta^2)]$$

ζ = the fraction of critical damping

ω_n = the natural frequency, $(K/M)^{1/2}$

ω_d = the damped natural frequency, $\omega_n(1 - \zeta^2)^{1/2}$

This is the most commonly used model in the aerospace industry.

Relative Displacement Model- The input to this model is the absolute acceleration of the base of the SDOF system. The response of the system is the relative displacement between the base and the mass. If the relative displacement is expressed in terms of an equivalent static acceleration,

$$\ddot{y}_{eq} = (y-x)\omega_n^2 \quad (3)$$

the transfer function becomes

$$H_d(s) = \frac{\omega_n^2}{s^2 + 2\zeta\omega_n s + \omega_n^2} \quad (4)$$

The impulse response of this system is given by

$$h_d(t) = \omega_n (1 - \zeta^2)^{-1/2} \exp(-\zeta\omega_n t) \sin(\omega_d t) \quad (5)$$

This model is commonly used in the Navy and the seismic industry.

The Relationship Between the Fourier Spectrum and Shock Response Spectrum

A well known relationship exist between the undamped residual shock response spectrum and the magnitude of the Fourier spectrum[2].

$$S_r(\omega_n) = \omega_n |A(\omega_n)| \quad (6)$$

where

S_r = undamped residual-shock-response spectrum
 ω_n = natural frequency (rad/s)
 $A(\omega_n)$ = magnitude of the Fourier Spectrum of the acceleration input evaluated at ω_n

We will also use the relationship

$$\frac{d^n f(t)}{dt^n} \leftrightarrow (j\omega)^n F(\omega) \quad (7)$$

where \leftrightarrow means a Fourier transform pair,

and

$$f(t) \leftrightarrow F(\omega).$$

We can now derive the slope of the undamped residual shock response spectrum. Note that both models reduce to the same form for the undamped case. The velocity change, Δv , of an input acceleration is given by its Fourier spectrum evaluated at zero frequency. The Fourier spectrum is continuous and smooth near the origin. Therefore, for frequencies near zero this gives

$$S_r(\omega_n) = \Delta v \omega_n \quad (8)$$

which is a slope of 1 on a log-log plot or 6 dB/octave.

If the velocity change is zero, but the displacement change, Δd , is nonzero, the Fourier spectrum of the velocity for small frequencies is given by Δd . The use of Eq (7) and then Eq (6) yields

$$S_r(\omega_n) = \omega_n^2 \Delta d \quad (9)$$

for frequencies near zero. This gives the spectrum a slope of 2 on a log-log plot or 12 dB/octave near zero frequency.

If the displacement change is also zero, but its integral is a nonzero value, Δc , the undamped residual shock spectrum near zero frequency is given by

$$S_r(\omega_n) = \omega_n^3 \Delta c \quad (10)$$

This results in a slope of 3 or 18 dB/octave at low frequencies.

Slope of the Damped Shock Spectrum at Low Frequencies

In this section I will investigate the correct slope for the damped shock response spectrum at low frequencies. If the velocity change of the transient is nonzero and the velocity monotonically increases to its final value, the transient can be represented by an impulse when the product of natural frequency of the SDOF system and the sampling interval is much less than one. I can then represent the waveform by the impulse

$$x(t) = \Delta v \delta(t) \quad (11)$$

Looking first at the acceleration model the residual response is given by

$$\ddot{y}(t) = \Delta v h_a(t) \quad (12)$$

The primary response for an impulsive input is zero. If I make the assumption that the damping is small the maximum of the impulse response is approximately

$$h_{\max}(t) = \omega_n \quad (13)$$

This gives

$$S(\omega_n) = \Delta v \omega_n \quad (14)$$

which is the same result as Eq. 8. The same result is achieved for the relative displacement model. Thus the common assumption, that the residual response dominates the low frequency response and that the relationship between the Fourier spectrum and the undamped residual shock spectrum can be used to estimate that response, is valid for this case. We get a slope of 1 or 6 dB/octave at the low frequencies.

If the velocity does not increase monotonically to its final value (i.e. zero crossings of the acceleration waveform exist) this analysis is not valid. We must now represent the input waveform as a series of impulses. To examine this problem I will first consider the response of a damped SDOF system to an impulse when the time is small. The impulse response of the acceleration model can be approximated for small values of time and damping by

$$h_a(t) = \omega_n (\omega_n t + 2\zeta) \quad (15)$$

* A slope of 1 is not precisely 6 dB/oct, but this value will be used in this paper.

For the relative displacement model

$$h_d(t) = \omega_n^2 t, \quad (16)$$

which is the same as for the acceleration model except the second term is zero. The acceleration response for early times and small damping is then given by

$$\ddot{y}(t) = \Delta v \omega_n (\omega_n t + 2\zeta). \quad (17)$$

The response can be approximated by a straight line for early times. Equation (17) can be derived in a different way. If we assume that the mass of the oscillator remains essentially stationary with respect to the base, the force on the mass is given by

$$F = Kx + C\dot{x} \quad (18)$$

where

$$2\zeta\omega_n = C/M$$

and where x is the base input displacement. The acceleration of the mass is then approximately

$$\ddot{y}(t) = (K/M)x(t) + (C/M)\dot{x}(t)$$

or

$$\ddot{y}(t) = \omega_n^2 x(t) + 2\zeta\omega_n \dot{x}(t) \quad (19)$$

If

$$\ddot{x}(t) = \Delta v \delta(t)$$

then

$$\begin{aligned} \dot{x}(t) &= \Delta v \text{ and} \\ x(t) &= \Delta v t. \end{aligned}$$

These results give

$$\ddot{y}(t) = \Delta v \omega_n^2 t + \Delta v 2\zeta\omega_n$$

which is the same as Eq (17). Equations (17)-(19) show that the mass accelerations for early times is dominated by two terms: a stiffness force proportional to the base displacement and a damping force proportional to the base velocity.

These equations will now be used to write a more general expression for the response to a sequence of impulses. These expressions will then be used to estimate the primary response of waveforms where the velocity does not increase monotonically. Let the input be given by

$$\ddot{x}(t) = \sum_{i=1}^L A_i \delta(t - i\tau) \quad (20)$$

where δ is the unit impulse function, and A_i is the velocity change of each impulsive input. If the total pulse duration is short compared to the period of the SDOF system (i.e. $\tau\omega_n L \ll 1$)

and the damping is small, the response of the system can be approximated by a sum of responses like Eq (17)

$$y(t) = \sum_{i=1}^L A_i \omega_n [\omega_n(t - i\tau) + 2\zeta] U(t - i\tau) \quad \text{for } t \leq L \quad (21)$$

where

$U(t)$ = the unit step function.

This response is just a sequence of straight lines whose slope changes at each impulsive input. The maximum response will occur at one of these changes in slope. The response at the impulsive input at time $m\tau$ can be evaluated as

$$\ddot{y}(m\tau) = \sum_{i=1}^L A_i \omega_n [\tau_n(m-i) + 2\zeta] U(m-i). \quad (22)$$

The primary response can be approximated by the largest of this set of values, $y_{\max}(m\tau)$, for some value of m between 1 and L . Thus for the damped case the maximum response will be of the form

$$\ddot{y}_{\max}(m\tau) = C_1 \omega_n^2 + C_2 \omega_n. \quad (23)$$

The undamped case will always be of the form

$$\ddot{y}_{\max}(m\tau) = C_3 \omega_n^2. \quad (24)$$

The relative displacement model will give a maximum primary response of the form

$$\ddot{y}_{eq \max}(m\tau) = C_4 \omega_n^2 \quad (25)$$

We can now see that the primary response for the relative displacement model, and for the undamped acceleration model will always have a slope of 2 or 12 dB/octave at low frequencies. If the slope of the residual response is greater than 12 dB/octave the residual response must be less than the primary response for a very low frequency. The final slope of the shock response spectrum will be 12 dB/octave.

The damped acceleration model will have two regions of interest. For the intermediate frequencies where the first term of Eq (23) dominates, the primary spectrum will have a slope of 12 dB/octave. At the very low frequencies where the second term of Eq (23) dominates the slope will be 6 dB/octave. Thus the primary response must be greater than or equal to the residual response which rolls off with a slope of at least 6 dB/octave. The conclusion is that for small damping, the maximax shock spectrum for the acceleration model will always have a low frequency slope of 6 dB/octave.

The usual assumption is that the residual spectrum is larger than the primary spectrum at low natural frequencies. We see that this is the case for single sided waveforms, but is not true for double sided acceleration pulses.

Two examples will illustrate this important result. For the first example, consider an acceleration input as given by Figure 1. The velocity and displacement waveforms for this acceleration are shown in Figures 2 and 3. The input can be approximated by three impulses

$$\ddot{x}(t) = \delta(t-0.001) - 2\delta(t-0.023) + \delta(t-0.045) \quad (26)$$

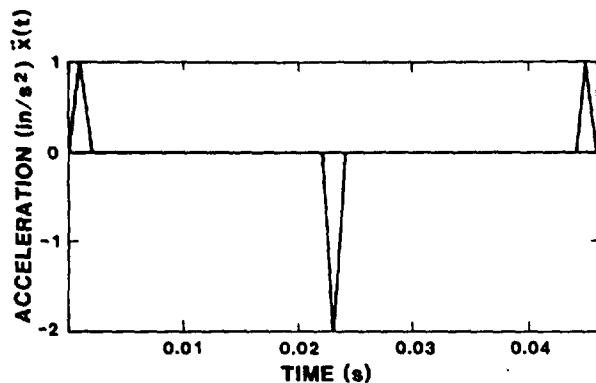


Figure 1 Base Input Acceleration, Basically Three Impulses

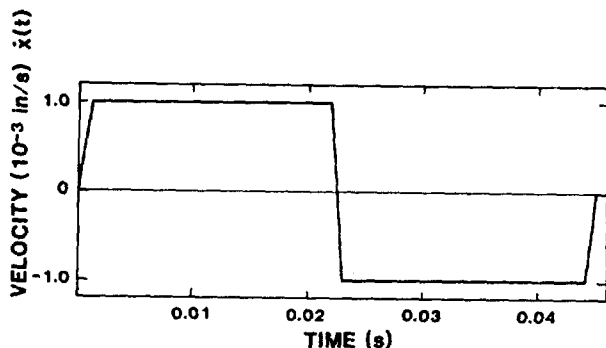


Figure 2 Base Input Velocity

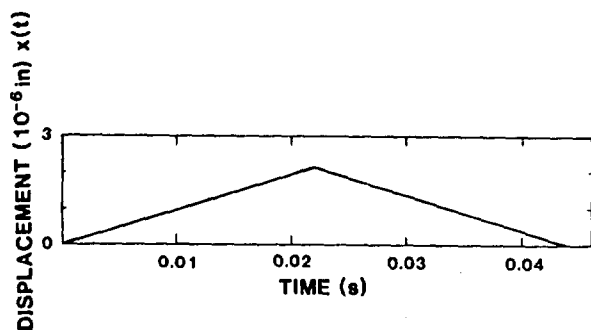


Figure 3 Base Input Displacement

The approximate response given for a time step of 1 ms is given by Eq (21) as

$$\begin{aligned} \ddot{y}(10^{-3}m) = & (10^{-3}) \omega_n \{ [10^{-3} \omega_n(m-1) + 2\zeta] U(m-1) \\ & - 2 [10^{-3} \omega_n(m-23) + 2\zeta] U(m-23) \\ & + [10^{-3} \omega_n(m-45) + 2\zeta] U(m-45) \} \end{aligned} \quad (27)$$

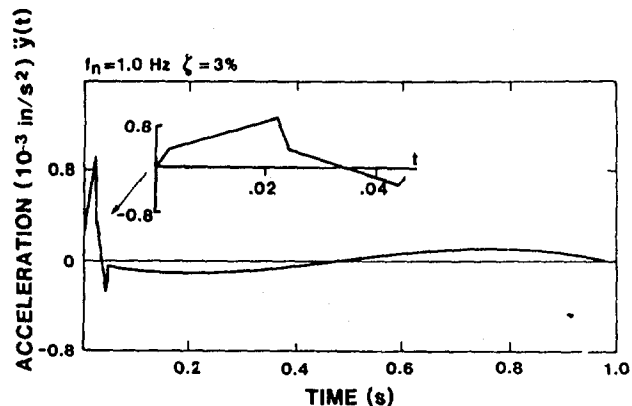


Figure 4 Acceleration Response of 1-Hz, 3% Damped System to the Input of Figure 1.

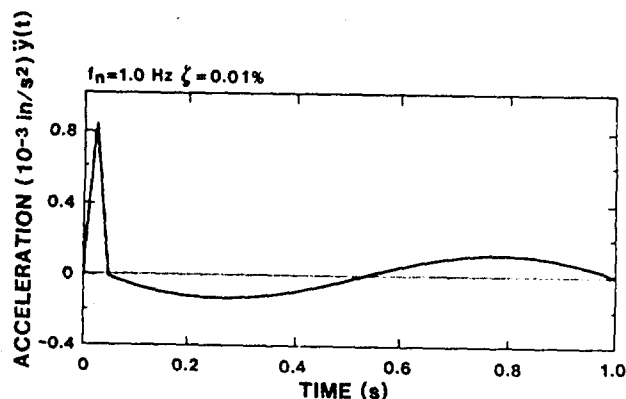


Figure 5 Acceleration Response of 1-Hz, 0.01% Damped System to the Input of Figure 1.

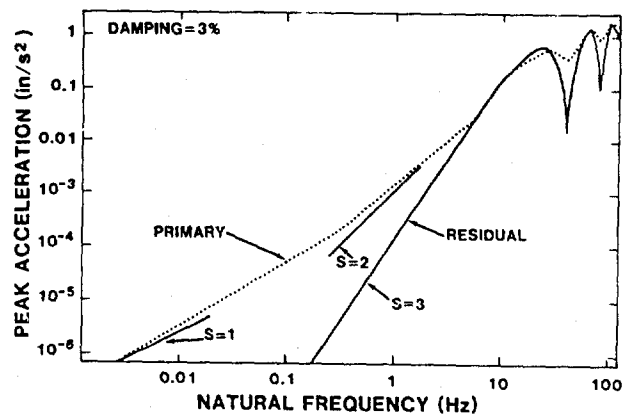


Figure 6 Acceleration Shock Response Spectrum of the Input of Figure 1.

The acceleration response for a natural frequency of 1 Hz and 3% damping is shown as Figure 4. The inset in Figure 4 is the acceleration expanded for the early portion of the period. The primary response is close to the straight line approximation predicted by Eq (21). Equation (19) predicts that the primary response at low frequencies will be proportional to the base displacement if the system is

undamped. Figure 5 shows the response for a damping of 0.01. A comparison of Figures 3 and 5 confirms the above prediction. In both Figures 4 and 5, the primary response is larger than the residual response.

The shock spectrum for this input is given in Figure 6. The shock spectrum at the low frequencies can be predicted using Eq (27). For example, the spectrum at 0.1 Hz can be estimated by noting that the maximum response will occur near $t = 22$ ms

$$\ddot{y}_{\max} = 2\pi(.1)(10^{-3})\{10^{-3}(2\pi)(.1)(21) + 2(.03)\} \quad (28)$$

$$\ddot{y}_{\max} = 4 \times 10^{-5} \text{ in/s}^2,$$

which agrees with Figure 6.

A second example is given by the WAVSYN in Figure 7. The WAVSYN pulse is defined by

$$x(t) = A \sin(2bt) \sin(2ft) \quad \text{for } 0 < t < T \quad (29) \\ = 0 \quad \text{elsewhere}$$

where

- A = the amplitude
- f = the frequency of the pulse
- b = the frequency of a half sine window, f/N
- T = the pulse duration, $N/(2f)$
- N = an odd integer greater than 1.

In Figure 7, $A = 1$ g, $N = 39$, and $f = 1$ Hz. The velocity and displacement changes for this waveform are zero. The above discussion shows the residual spectrum should have a slope of 12 dB/octave, and the primary spectrum should have a final slope of 6 dB/octave. Figure 8 is the acceleration shock spectrum of this waveform. We can see the region just below 1 Hz where the residual response is larger, the area at about 0.5 Hz where the response is dominated by the primary response damping forces, and at the very low frequencies the characteristic final slope of 6 dB/octave.

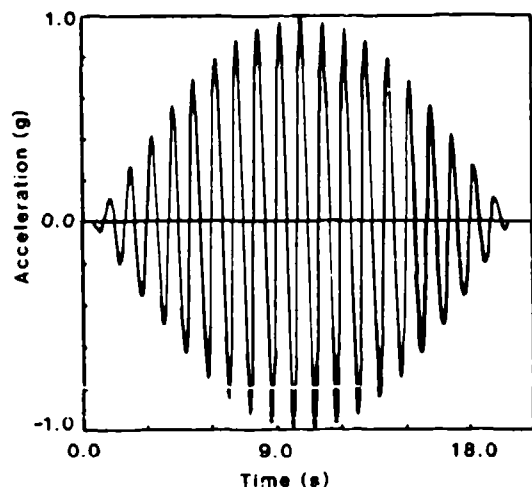


Figure 7 A 1-Hz, 1-g, 39-Half Cycle, WAVSYN Pulse

Errors Caused by Zero Offsets

A small error in the zero line of an acceleration waveform can cause large errors in the low frequency end of the shock response spectrum. The error occurs because the zero offset will cause an error in the final velocity of the waveform. A small error integrated over the entire length of the time history can result in a substantial velocity error. The offset will appear to the shock spectrum calculations as a square wave of a duration equal to the pulse duration. An example is shown in Figure 9, and Figure 10 (curves a and c). Figure 9 is an acceleration input composed of the sum of two exponentially decaying sinusoids. One component is at 100 Hz with an amplitude of 1 g. The second is a highly damped component at a much lower frequency whose amplitude and delay were chosen to force the velocity and displacement changes to be zero. Figure 10, curve a, is the shock spectrum of this waveform. A 0.05 g zero offset was added to the waveform and the shock spectrum was recomputed (curve c on Figure 10). The offset looks like an added square wave with an amplitude of 0.05 g. The shock spectrum of this square wave has a peak amplitude of 0.1 g. Since the duration of this square wave is 0.2048 s the first peak in the shock spectrum of this component will be at about 2.4 Hz. Curve c of Figure 10 confirms these predictions.

One of the dangers of these errors is that the errors can propagate into specifications derived from the measured shock spectrum, which in turn leads to tests with unreasonable velocity and displacement requirements.

Errors Caused by Waveform Truncation

Truncation of an acceleration waveform can also cause errors in the low frequency end of the shock response spectrum. As for the offset errors, these errors are caused by an incorrect final velocity. The error in the final velocity divided by the pulse duration and converted to acceleration units will give an approximation of

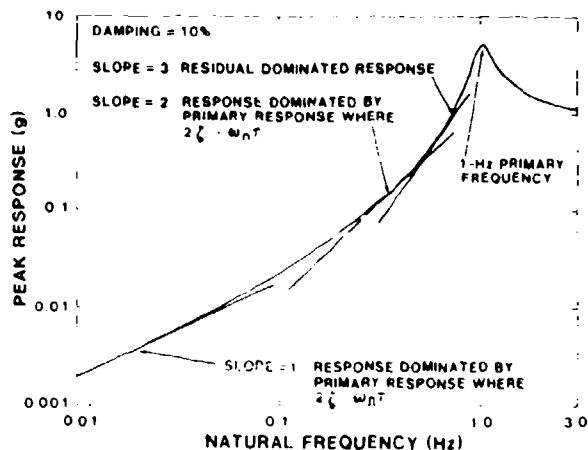


Figure 8 Shock Response Spectrum of a 1-Hz, 1-g, 39-Half Cycle, WAVSYN Pulse

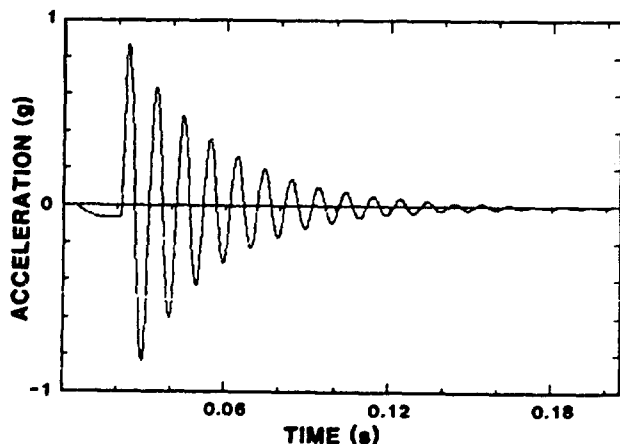


Figure 9 Acceleration of the Sum of Two Exponentially Decaying Sinusoids

the error. To illustrate, the waveform in Figure 9 was truncated at 0.0564 s. The resulting velocity error was about 0.18 in/s. This translates into an acceleration error of about 0.008 g. We would then expect an error in the shock spectrum of about twice this value (0.016 g) with the lowest frequency peak at about 8.9 Hz. Curve b, Figure 10 confirms this error.

As in the case of offset errors, the biggest danger of this error is the propagation of the error into specifications.

Incorrect Algorithms

This source of error cannot be discussed in detail without a thorough knowledge of the algorithm in question. Recursive digital filters are a popular method to calculate the shock response spectrum, and it is known that the filter weights are subject to serious roundoff problems at low natural frequencies. Careful attention must be paid to the calculation of these weights and to the details of the implementation at low natural frequencies. In some methods the data are filtered with a low pass digital filter and the data are then decimated before the spectrum is calculated at the low frequencies. This could lead to errors in calculating the primary spectrum, which has been demonstrated to be important at the low frequencies. More investigation is required in this area. A good test for any algorithm is to reproduce Figure 8.

Application to Pyrotechnic Shock Data

We can now use the above results to establish guidelines when viewing pyrotechnic and similar shock data when presented in the form of shock response data. First one must establish whether the acceleration model or the relative displacement model was used to calculate the shock response. This determines the final slope of the data. If the velocity change is zero, the shock response should have a final slope of 12 dB/octave or change from a slope of 12 dB/octave to 6 dB/octave (depending

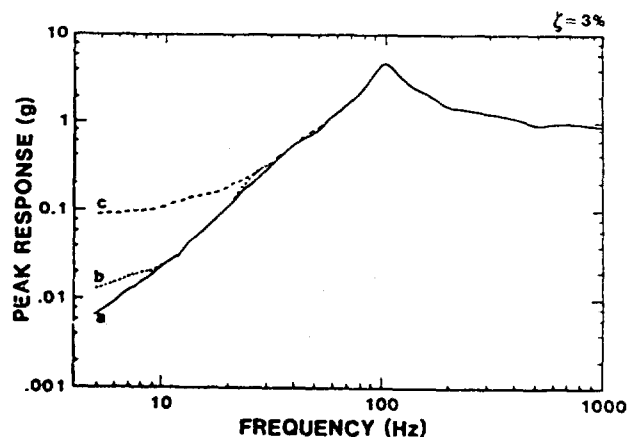


Figure 10 Shock Response Spectrum of the Acceleration Waveform Shown in Figure 9

on the model used) in a smooth manner as the frequency decreases. The curve will be concave. If a convex "bump" is observed at the low frequencies, the bump likely represents a velocity change which appears to the computations as a acceleration square wave added to the waveform.

Remember the shock spectrum of a square wave has an initial slope of 6 dB/octave, reaches a peak of twice its amplitude at a frequency equal to the inverse of twice its duration, has some ripples with each peak of the ripples reaching a magnitude of twice the amplitude, and continues along a line with a slope of zero at an amplitude of twice its amplitude as the frequency increases. Because of this characteristic shape of the shock spectrum of a square wave, the shock spectrum with an added square wave can appear to have a slope of zero at low frequencies. The amplitude of this area of zero slope will be a function of both the observed velocity change and the duration of the digitized waveform. If the velocity change is a constant and not an error caused by a zero offset or truncation, the amplitude of this area will decrease as the duration of the digitized waveform is increased. The magnitude of the velocity change can be estimated by dividing the shock spectrum amplitude in the region of the zero slope by two, multiplying by the pulse duration and converting to velocity units. If this velocity change is representative of the environment the data are probably valid. But if the velocity change is unreasonably large, the low end of the shock spectrum is in error. The source of the error can then be investigated.

The natural frequency where the shock spectrum should again start to decline is given by the inverse of twice the duration. The final slope at frequencies much less than the inverse of twice the duration will be 6 dB/octave.

Shock Spectrum at High Natural Frequencies

This is not the main topic of this paper, but I would like to make some comments on the subject. A common rule of thumb in transient data reduction is that you should sample the data with a minimum of 10 times the highest frequency of interest. Some have interpreted this rule to mean the shock response spectrum should not be calculated above a natural frequency which is greater than 1/10 th of the sampling frequency. Often this is overly conservative. The frequency content of the data is of primary concern, not the natural frequency of the SDOF system used in the shock spectrum calculations. The data must be sampled frequently enough to avoid large errors in the detection of the peak of the transient. Some authors [3] have suggested 6 to 10 samples/cycle for a 5% error bound. This is often conservative because it was assumed that the input was a sine wave at the highest frequency. Three or four samples of the highest frequency may be adequate for peak detection if the high frequency content is a small part of the total energy in the waveform. The important point is that the sample rate should be picked with only the characteristics of the input waveform in mind.

The next question is, will the algorithm used to calculate the shock response spectrum calculate the correct values for the range of natural frequencies desired. It is known that the oldest and simplest form of the recursive filter algorithm has serious errors as the natural frequency approaches half the sampling frequency [4]. Direct integration methods have similar problems. Using these algorithms the rule of 1/10 should be followed. But an improved algorithm [4] avoids this problem. If the improved algorithm is used the natural frequency can even be above the sampling frequency if the input transient peak has been adequately detected. The new algorithm assumes the input waveform can be adequately described by a series of straight lines connecting the sample points. The discontinuities in slope caused by the straight line segment approximation will generally introduce high frequency energy into the waveform and the shock spectrum will be slightly higher than the true value at the high frequencies. The errors of peak detection will always bias the results in the negative direction. The peak detection errors are usually the largest. The value approached for the shock spectrum as the natural frequency increases is the value of the largest sample in the set of data samples, and is as accurate as the detected peak value.

References

1. Y. Matsuzaki, and S. Kibe, "Shock and Seismic Response Spectra in Design Problems", Shock and Vibration Digest, 15(10)(Washington, DC: Shock and Vibration Information Center, Naval Research Laboratory, 83).

2. C.M. Harris and C.E. Crede, Shock and Vibration Handbook (New York: McGraw Hill, 1961), vol2, p23.
3. Kelly and Richman, Principles and Techniques of Shock Data Analysis, pp 152-153, SVM-5 (Washington, DC: Shock and Vibration Center, Naval Research Laboratory, 1969).
4. Smallwood, D.O., "An Improved Recursive Formula for Calculating Shock Response Spectra", The Shock and Vibration Bulletin 51(2), pp 211-217 (Washington, DC: Shock and Vibration Information Center, Naval Research Laboratory, May 1981).

Appendix A

Listing of Subroutine for a Ramp Invariant Simulation of a Single-Degree-of-Freedom System for the Calculation of the Shock Response Spectrum

REFERENCE: Smallwood D. O., "An Improved Recursive Formula for Calculating the Shock Response Spectra," Shock and Vibration Bulletin, No. 51, part 2, pp 211-217, May 1981.

SUBROUTINE FILMAX(Y,XX,FN,SR,Z,XM1,XM2,
& YM1,YM2,IFLAG)

C
C D. SMALLWOOD 4-14-80
C MODIFIED 8-15-80
C MODIFIED 12-17-84 MADE CALCULATION OF
C FILTER WEIGHTS A
C A SEPARATE SUBROUTINE
C
C APPROXIMATES A ONE-ZERO-TWO-POLE SINGLE
C DEGREE OF FREEDOM RESONATOR USING A RAMP
C INVARIANT SIMULATION AND RETURNS THE
C RESPONSE.
C
C Y-FILTER OUTPUT
C XX-FILTER INPUT
C Z-FRACTION OF CRITICAL DAMPING
C SR-SAMPLE RATE (SAMPLES/SEC)
C FN-NATURAL FREQUENCY OF RESONATOR (HZ)
C IFLAG.NE.0 FOR FIRST CALL TO ROUTINE
C SETUP FILTER COEFF.
C -0 USES FILTER COEFF. DETERMINED
C FROM A PREVIOUS CALL.
C
C NOTE: IFLAG CHANGED TO 0 AFTER 1ST
C CALL, MUST BE RESET BY
C USER FOR NEW FILTER.
C IFLAG=1 SETS UP AN BASE ACCEL. INPUT,
C ACCELERATION RESPONSE
C SHOCK SPECTRUM
C IFLAG=-1 SETS UP A BASE ACCELERATION,
C RELATIVE DISPLACEMENT
C (EXPRESSED IN EQUIVALENT STATIC
C ACCEL UNITS) SHOCK SPECTRUM.
C XM1=1ST PAST VALUE OF INTIAL INPUT
C XM2=2ND PAST VALUE OF INTIAL INPUT
C YM1=1ST PAST VALUE OF INTIAL RESPONSE
C YM2=2ND PAST VALUE OF INTIAL RESPONSE
C

```

      IF(FN) 4,4,5
4     Y=0.
      RETURN
C
C     1ST CALL SET UP FILTER COEFFICIENTS
C
5     IF(IFLAG) 3,10,3
3     CALL WGHT(FN,SR,Z,IFLAG,B0,B1,B2,A1P2,
      &          A2M1)
      IFLAG=0
10    Y=B0*XX +B1*XM1 +B2*XM2 +YM1+(YM1-YM2)
      & -A1P2*YM1-A2M1*YM2
      YM2=YM1
      YM1=Y
      XM2=XM1
      XM1=XX
      RETURN
      END

      SUBROUTINE FILTR(X,FN,SR,Z,ITYPE,ISIZE,Y)
C
C     SUBROUTINE TO FILTER A TIME HISTORY WITH A
C     SDOF FILTER USING A
C     RAMP INVARIANT FILTER SIMULATION
C
C     INPUT: X= INPUT DATA ARRAY
C             FN= NATURAL FREQUENCY (HZ)
C             SR= SAMPLE RATE OF INPUT DATA ARRAY
C                 (SAMPLES/SEC)
C             Z= FRACTION OF CRITICAL DAMPING
C             ITYPE=1--ABSOLUTE ACCELERATION MODEL
C                  -1--RELATIVE DISPLACEMENT MODEL
C             ISIZE= THE NUMBER OF POINTS IN THE
C                   X AND Y ARRAYS
C
C     OUTPUT: Y= OUTPUT DATA ARRAY
C
C     DO SMALLWOOD SANDIA NATIONAL LABS
C     ALBUQUERQUE NM 12-17-84
C
      DIMENSION X(1),Y(1)
C
C     FIND FILTER WEIGHTS
C
      CALL WGHT(FN,SR,Z,ITYPE,B0,B1,B2,A1P2,
      &          A2M1)
C
C     FILTER
C
      YM2=0.
      YM1=0.
      XM1=0.
      XM2=0.

      DO 10 I=1,ISIZE
      Y(I)=B0*X(I) +B1*XM1 +B2*XM2 +YM1
      & +(YM1-YM2)-A1P2*YM1-A2M1*YM2
      YM2=YM1
      YM1=Y(I)
      XM2=XM1
10    XM1=X(I)

      RETURN
      END

```

```

      SUBROUTINE WGHT(FN,SR,Z,IFLAG,B0,B1,B2,
      &          A1P2,A2M1)
C
C     D. SMALLWOOD 12-17-84
C
C     FINDS THE WEIGHTS FOR A ONE-ZERO-TWO-POLE
C     SINGLE DEGREE OF FREEDOM RESONATOR
C     WITH A RAMP INVARIANT SIMULATION.
C
C     INPUTS:
C             FN= NATURAL FREQUENCY (HZ)
C             SR= SAMPLE RATE (SAMPLES/SEC)
C             Z= FRACTION OF CRITICAL DAMPING
C             IFLAG=1 SETS UP AN BASE ACCEL INPUT
C                   ACCEL RESPONSE
C                   SHOCK SPECTRUM
C             IFLAG=-1 SETS UP A BASE ACCEL.
C                   RELATIVE DISPLACEMENT
C                   (EXPRESSED IN EQUIVALENT
C                   STATIC ACCEL UNITS) SHOCK
C                   SPECTRUM.
C
C     OUTPUT:
C             B0,B1,B2,A1P2,A2M1 THE FILTER WEIGHTS
C
C             DOUBLE PRECISION PI,W,WD,E,SP,DV,SQ,FACT,
C             & C,DZ
C             DATA PI/3.1415926535D0/
C
3     W=2.0D0*PI*DBLE(FN)/DBLE(SR)
      IF(W-1.0D-3) 1,2,2
1     X=SNGL(W)
C
C     USE THESE COEFFICIENTS WHEN W IS SMALL,
C     FOR BOTH MODELS
C
      A1P2= 2.0*Z*X +X*X*(1.0-2.0*Z*Z)
      A2M1=-2.0*Z*X +2.0*Z*Z*X*X
      IF(IFLAG) 35,10,20
2     DZ=DBLE(Z)
C
C     THESE ARE EXACT EXPRESSIONS,
C     USED WHEN W IS LARGE
C
C     USE THESE EXACT EXPRESSIONS WHEN W IS LARGE
C
      SQ=DSQRT(1.0D0-DZ*DZ)
      E=DEXP(-DZ*W)
      WD=W*SQ
      SP=E*DSIN(WD)
      FACT=(2.0D0*DZ*DZ -1.0D0)*SP/SQ
      C=E*DCOS(WD)
C
C     A1P2 AND A2M1 ARE THE SAME FOR BOTH MODELS
C     A1P2=A1+2 A2M1=A2-1
C
      A1P2=SNGL(2.0D0-2.0D0*C)
      A2M1=SNGL(-1.0D0+E*E)
      IF(IFLAG) 6,10,30
C
C     EXACT EXPRESSIONS, W LARGE,
C     RELATIVE DISPLACEMENT MODEL
C
6     B0=SNGL((2.0D0*DZ*(C-1.0D0) +FACT +W)/W)
      B1=SNGL((-2.0D0*C*W +2.0D0*DZ*(1.0D0-F*E)
      & -2.0D0*FACT)/W)
      B2=SNGL((E*E*(W+2.0D0*DZ) -2.0D0*DZ*C
      & +FACT)/W)

```

```

      GO TO 10
C
C   USE THESE COEFF. FOR SMALL W.
C   RELATIVE DISPLACEMENT MODEL
C
35  B0=X*X/6.
    B1=2.0*X*X/3.
    B2=X*X/6.

      GO TO 10
C
C   USE THE COEFF FOR ACCEL INPUT,
C   ACCEL OUTPUT MODEL
C
C   EXACT EXPRESSIONS FOR W LARGE.
C   ACCEL OUTPUT MODEL
C
30  SP=SP/WD
    B0=SNGL(1.0D0-SP)
    B1=SNGL(2.0D0*(SP-E*DCOS(WD)))
    B2=SNGL(E+E-SP)

      GO TO 10
C
C   USE THESE COEFF FOR SMALL W.
C   ACCEL OUTPUT MODEL
C
20  B0=Z*X+(X*X)*((1.0/6.0)-2.0*Z*Z/3.0)
    B1=2.0*X*X*(1.0-Z*Z)/3.0
    B2=-Z*X+ X*X*((1.0/6.0)-4.0*Z*Z/3.0)
10  RETURN
    END

```

Discussion

Mr. Galef (TRW): I have been investigating some of these things in considerable detail over recent years, and I have come to a different conclusion than you have. My conclusion has been that damping is a second order effect, or a considerably higher order effect, at low frequencies and high frequencies; damping is also a considerably higher order effect for many pulses, for the rest of the frequencies as well. The only time damping is really important is in an oscillatory function, such as the damped sine wave that you were using, and then damping is only important at frequencies near where the Fourier transform peaks. I believe your different conclusion may have resulted from using physically invalid pulses. That particular sine wave where you put a compensating acceleration at a low value for a long time prior to the thing, that does not happen in the real world. In the real world we have a very large, very short duration, compensating pulse to give us a net velocity of zero and a net displacement of zero. For that case, my results very clearly show the 12 dB per octave. Until I can perhaps clarify this with you, I think I will continue to reject data that shows 6 dB per octave with the same enthusiasm that I reject data that shows zero shift.

Mr. Smallwood: I encourage you to read the written version of the paper, because I think you will see my mathematics is fairly straight forward and indicates a problem. I agree with your conclusions on single-sided wave forms. They roll off at 6 dB per octave anyway. But I think you will see damping is important for the double-sided wave forms at the very low natural frequencies. The net result is you cannot represent these complicated wave forms as simple impulses, because you have to represent them by multiple impulses. When you do that, the primary response becomes dominant.

Mr. Rehard (National Technical Systems): If we are looking at frequencies of one Hz, when we calculate the response spectra from that low frequency, what kind of error would come in between one Hz and DC? How do you know that there isn't a zero shift only by looking at the time history? You would have to look at the time history, because it will try to look flat the closer you get to zero.

Mr. Smallwood: When the natural period of the single degree-of-freedom system gets long, compared to the complete data window through which you look at the data, then I think you will ultimately see the shock spectrum start to roll off. It is flat only to those natural frequencies whose period is comparable to the period of the data window that you use to look at the data. If the period of the window you use to look at the data is one second long, I would expect frequencies a decade below one Hz will start to show a slope again of 6 dB per octave. That flatness does not go on forever down to DC. Eventually, it will turn around and

roll off. Often, it is so far down, 40 dB or 60 dB down, that people really do not worry about it; they are not concerned about it. So, you never even plot the shock spectrum, but you use very low frequencies.

Mr. Rehard: It is a tough question for me because I do not know where the two would end. I do not know if I could ever prove it, or not, that it really turns around and does 6 dB.

Mr. Smallwood: The only thing that you can do is to extend the natural frequency down lower and lower. That gets to be computationally expensive. That is the reason people do not normally do it.

RELATIVE CONSERVATISM OF DROP TABLE
AND SHAKER SHOCK TESTS*

Thomas J. Baca and Teddy D. Blacker
Sandia National Laboratories
Albuquerque, New Mexico

Judging the conservatism of a mechanical shock test is a crucial concern of the engineer responsible for interpreting the outcome of the test. Either an overtest or an undertest can have devastating implications if the former results in a costly redesign of the structure being tested, or if the latter fails to properly qualify the structure for use in its design environment. The objective of this paper is to quantitatively compare the relative conservatism of haversine and decaying sinusoid shock test input pulses which are generated on drop tables and electro-dynamic shakers. A complete evaluation of test conservatism between the laboratory and field shock environment requires characterization of shock severity and consideration of this characterization's statistical variation. A shock intensity spectrum (SIS) is introduced as a new shock characterization which provides information on the severity of the shock as a function of frequency. Test conservatism is quantified in terms of an Index of Conservatism (IOC) and a novel criterion called an Overtest Factor (OTF). Accelerometer measurements were made on the fixed end of a cantilever beam structure. Data were gathered from a field shock environment and three laboratory test environments. The laboratory tests included two drop table test series and one decaying sinusoid test series. An analysis of test conservatism was carried out on the data using these new techniques. Results are presented for the case where multiple tests provide a complete statistical basis for IOC and OTF calculations and the case where only a single measurement is made from the field and laboratory environments. This research provides specific recommendations regarding the relative conservatism of two widely used shock test techniques. It also describes a general methodology which can be applied in the comparison of any two shock environments.

INTRODUCTION

Laboratory shock testing of aerospace components is a critical step in the development of shock resistant hardware. The laboratory test provides high confidence that the structure will survive its operational shock environment. The validity of the shock test is initially based on a judgement of the adequacy of the shock test as it is defined in the test specification. The final evaluation of the adequacy of the test requires analysis of the actual test inputs. This paper introduces a methodology which can be applied to both of these crucial evaluations of test conservatism. An evaluation of the relative conservatism between both drop table and decaying sinusoid

shock data and a field shock environment is demonstrated on a cantilever beam structure. Both the data analysis techniques and the specific findings about the relative conservatism of these two test techniques will enhance the understanding of the engineer responsible for both shock test specification and post-test data analysis. The analytical methods described in this paper seek to instill a quantitative bent to the evaluation of shock test conservatism which all too often depends on "warm feelings" and "rules-of-thumb." The value of implementing meaningful shock test conservatism criteria is clear to any engineer who has had to justify the validity of his test specification after the test item which has failed the shock test is considered for a costly redesign.

*This work was performed at Sandia National Laboratories and supported by the U.S. Department of Energy under contract DE-AC04-76DP00789.

JUDGING SHOCK TEST CONSERVATISM

The engineer's dilemma of judging test conservatism begins with the definition of the field shock environment. Figure 1 shows an acceleration time history which was measured on the fixed end of an aluminum 12.7 x 2.54 x 0.64 cm (5 x 1 x 0.25 inch) cantilever beam mounted in a box-like fixture which was impacted by a pendulum hammer. This data will represent the "field" environment in this paper. The engineer now seeks to specify a shock test which will adequately test the structure. Two of the most common mechanical shock testing and electrodynamic shakers. (References 1 and 2 provide details of these test techniques.) The principal advantages of the drop table technique are that: 1) the simple pulse shapes (e.g., haversines) are readily created; and 2) high acceleration levels (exceeding 1000 g) can be attained. The shaker shock most often is composed of a summation of decaying sinusoid pulses. The synthesized pulse has a two-sided characteristic which is more realistic looking than the haversine pulse, but its peak accelerations are limited to the force rating of the shaker machine. The standard method for comparing the shocks created by these machines and the field shock environment is through the absolute acceleration shock response spectrum (denoted SAA in this paper). (See Reference 3 for further background information on SAA spectra.)

Figure 2 shows SAA spectra for the field data and three idealized test specifications. The standard approach to shock test specification would lead the engineer to specify the 1400 g x 0.33 ms haversine pulse. Both the 700 g x 0.33 ms haversine and the 350 g x 1500 Hz decaying sinusoid only partially cover the specified frequency range. It is interesting to note the

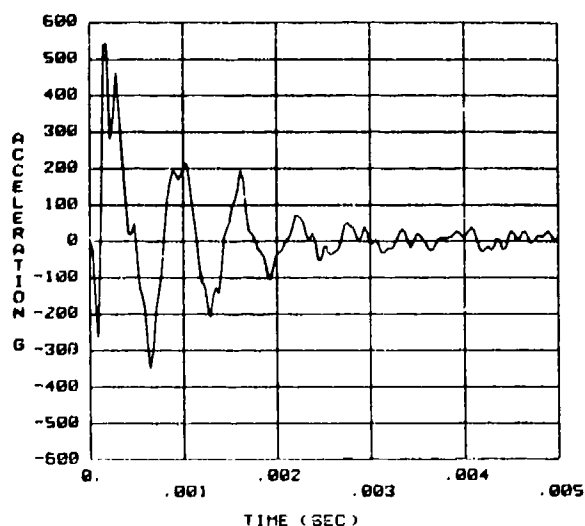


Figure 1 Representative Time History of Field Shock

results of a MSC/NASTRAN finite element analysis of this beam which the authors implemented by exciting a model of the cantilever beam by these idealized test inputs and the field data shown in Figure 1. Table 1 shows peak bending stresses at the base of the beam:

Table 1. Peak Bending Stress at the Base of the Cantilever Beam

ENVIRONMENT	STRESS (MPa) [psi]
FIELD DATA	34.5 [5,000]
1400 G HAVERSINE	112 [16,200]
700 G HAVERSINE	56 [8,100]
350 G DESIN	30.3 [4,400]

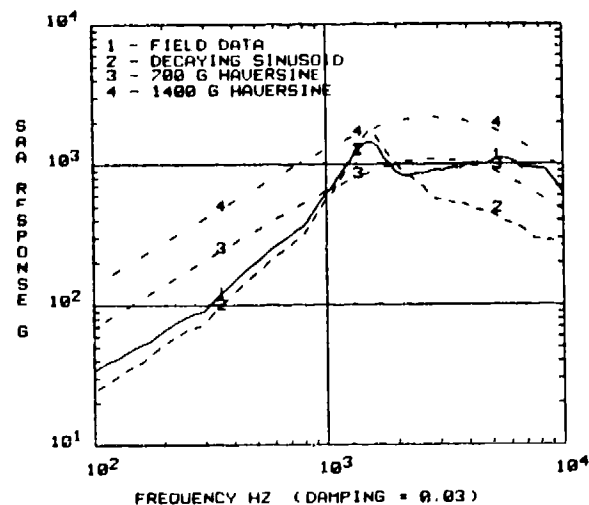


Figure 2 SAA Spectra for Field Data and Three Different Ideal Shock Test Inputs

The fact that the bending stresses from the haversine tests exceed the stress experienced during the field shock might be anticipated since Figure 2 shows that the SAA spectra for the haversines exceed the SAA spectrum for the field data and the decaying sinusoid (DESIN) at the fundamental modal frequency (318 Hz) of the beam. In this case, the engineer's knowledge of the structure being tested leads to an examination of the need for enveloping the entire frequency range of the spectrum. The real question then becomes one of determining the true frequency content of the field time history so that a determination of test conservatism can be made over the entire frequency spectrum.

One option is to look at other characterizations of the shock which are direct measures of the shock time history instead of a SAA response spectrum which plots peak response of single-degree-of-freedom oscillators excited by the shock time history versus their natural frequency. References 4-6 have employed shock characterizations such as ranked peak accelerations, and root-mean-square acceleration as a function of time and frequency to analyze shock data. In comparison to the SAA spectrum characterization in Figure 2, Figure 3 shows RMS acceleration as a function of frequency (FRMS) for all four shocks. The FRMS for an acceleration time history $\ddot{x}(t)$ having duration TD is defined below:

$$\text{FRMS}(F) \approx \left[\frac{2}{TD} \int_0^F |\ddot{X}(f)|^2 df \right]^{1/2} \quad (1)$$

where $\ddot{X}(f)$ is the Fourier transform of $\ddot{x}(t)$:

$$\ddot{X}(f) = \int_{-\infty}^{\infty} \ddot{x}(t) e^{-j2\pi ft} dt \quad (2)$$

and $j = \sqrt{-1}$. The FRMS plot gives the contribution to the overall RMS acceleration by all frequencies below the frequency at which the FRMS ordinate is plotted. The true frequency content of the time history is represented in the Fourier Amplitude Spectrum, $|\ddot{X}(f)|$, but FRMS has the advantage of providing an amplitude value which has some physical significance. The value of the FRMS plot is demonstrated by observing in Figure 3, for example, that the haversine shocks do not have frequency content which contributes to the overall RMS above ~6000 Hz where the FRMS becomes flat. An improvement to the manner by which we look at frequency domain RMS will be made in the following section. It is sufficient to say at this point that the engineer has an alternative to SAA spectra if a representation of the intensity and frequency content of a shock time history is desired.

Once a measure of shock severity is chosen, the engineer must evaluate the effect of the variability of the shock characterization on test conservatism. This entire area is often

ignored in the test specification process. It is a fact that little data may be available early in a component test program, but as field data is collected and more component laboratory tests are conducted, the engineer can gather statistical information on any shock characterization of interest. It is also possible to assume a certain amount of variability (e.g., a coefficient of variation) based on past experience. Using this statistical information to quantify shock conservatism is a topic dealt with in Reference 4 where an Index of Conservatism (IOC) is defined as follows:

$$\text{IOC} = \frac{\bar{C}_T - \bar{C}_F}{\sqrt{\sigma_T^2 + \sigma_F^2}} = \frac{M}{\sigma_M} \quad (3)$$

where M is the mean margin of conservatism, \bar{C}_T and \bar{C}_F are the mean shock characterization values for the test (T) and field (F) environments, and σ_M , σ_T , and σ_F are the corresponding standard deviations. Figures 4a and 4b graphically represent the IOC. Note that the main advantage of the IOC is that it is not dependent on an assumption of a probability distribution, while it still incorporates the statistical properties of the field and laboratory test data. The IOC provides a practical means of quantifying shock conservatism to the engineer. The matter of determining how the degree of overtest associated with a laboratory test specification relates to a specific IOC value will be dealt with later in this paper.

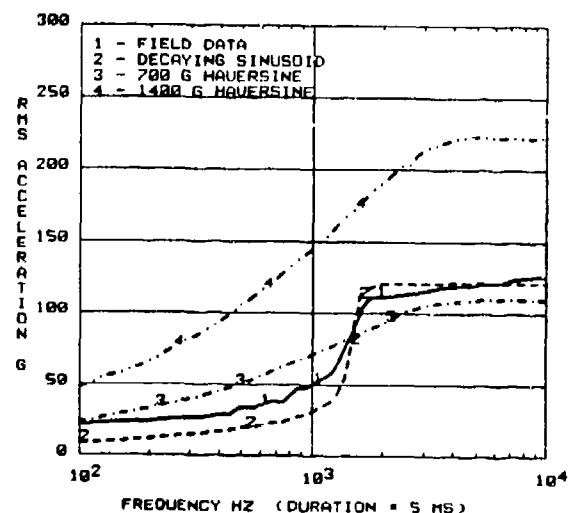


Figure 3 FRMS Plot for Field Data and Three Ideal Test Inputs

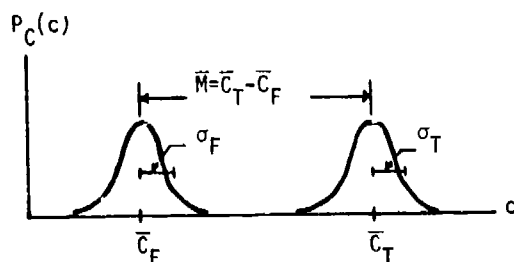


Figure 4a Probability Density Functions of Field and Laboratory Test Shock Environments

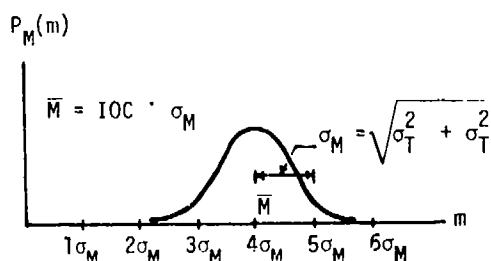


Figure 4b Probability Density Function of the Margin of Conservatism M

THE SHOCK INTENSITY SPECTRUM

A new spectral quantity can be defined which incorporates frequency, amplitude, and duration information about the shock time history. The Shock Intensity Spectrum (SIS) at a frequency F_i given by the following equation:

$$SIS(F_i) = [FRMS(F_i * \sqrt{r}) - FRMS(F_i / \sqrt{r})] \quad (4)$$

where $F_{i+1} = F_i * r$.

(Note that $r = 1.2$ is used in this paper.)

The $SIS(F_i)$ ordinate value represents the contribution to the overall RMS of the shock time history by frequencies in the i th logarithmic frequency interval. The duration information comes from the fact that FRMS is calculated for a specified analysis time interval. Comparisons of SIS between different shock time histories must be made using the same analysis duration since FRMS is dependent on the duration, TD, in Equation (1). This duration information associated with an SIS plot is a characteristic of the SIS plot which must be clearly stated on the plot just as a critical damping ratio must be specified on an SAA spectrum plot. Figures 5 and 6 show normalized SIS plots for ideal haversine and decaying sinusoid pulses. These curves were generated using the exact solution for the

Fourier Amplitude Spectrum of normalized haversine and decaying sinusoid shock pulses which is given in Reference 6. Plots of SIS for the field shock and test pulses discussed previously

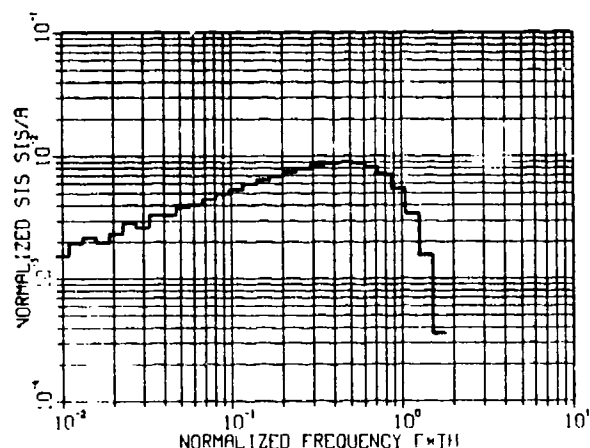


Figure 5 Normalized SIS (SIS/A) vs. Normalized Frequency ($F*TH$) for a Haversine Pulse with Amplitude A. Baseline Duration TH, and $TD/TH = 15$ (TD = Analysis Duration)

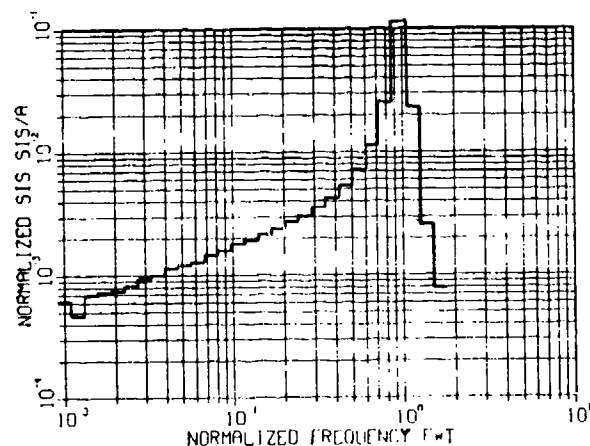


Figure 6 Normalized SIS (SIS/A) vs. Normalized Frequency ($F*T$) for a Decaying Sinusoid Pulse with Amplitude A, Sinusoidal Period T, Decay Rate $Z = 0.05$, and $TD/T = 15$ (TD = Analysis Duration)

are presented in Figure 7. Note that the SIS plot clearly shows the drop-off of high frequency content in idealized test inputs. The SIS analysis also shows the relative significance of predominant frequencies more accurately than the SAA spectrum. This is shown

in the comparison of the SIS (Figure 7) and SAA (Figure 2) for the field data where the ~3000 Hz and ~6000 Hz peaks in the SAA spectrum are of the same order of magnitude as the predominant peak at ~1500 Hz, while the SIS peaks at these same frequencies are an order of magnitude less than the SIS peak at ~1500 Hz. These advantages of the shock intensity spectrum motivated its use as the shock characterization for studying the relative conservatism of drop table and decaying sinusoid shaker shock data.

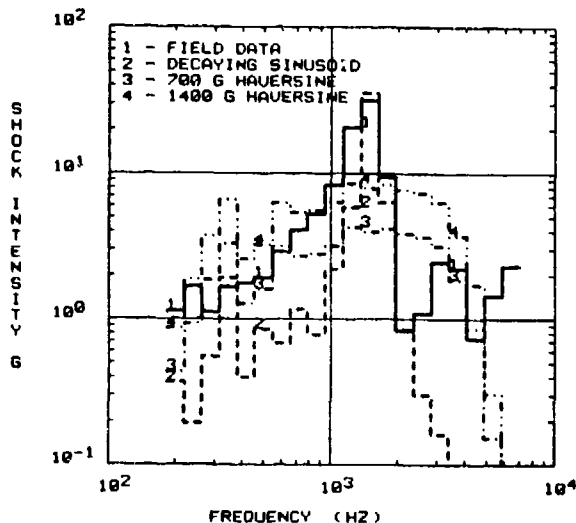


Figure 7 SIS Plot for Field Data and Three Ideal Test Inputs

CALCULATION OF OVERTEST FACTORS

The final analysis tool which must be introduced is the Overtest Factor (OTF). The OTF is defined as follows:

$$OTF = \frac{\bar{C}_T}{\bar{C}_{T,I}} \quad (5)$$

where $\bar{C}_{T,I}$ is the mean characterization of the test data which give the desired IOC value of I. Thus, the OTF defines how many times greater the actual mean test characterization, \bar{C}_T , is than the mean test characterization, $\bar{C}_{T,I}$, having an Index of Conservatism of I. Information about the variability of the test and field environments is included in the calculation of the OTF in the following manner. Let

$$R = \frac{\bar{C}_T}{\bar{C}_F} \quad (6)$$

and

$$R_I = \frac{\bar{C}_{T,I}}{\bar{C}_F} \quad (7)$$

and express I from Equation (3) as:

$$I = \frac{R_I \bar{C}_F - \bar{C}_F}{\sqrt{\sigma_F^2 + \sigma_I^2}} = \frac{(R_I - 1)}{\sqrt{k_F^2 + R_I^2 k_T^2}} \quad (8)$$

where k_F and k_T are the coefficients of variation for the field and test environments, respectively. Equation (8) can then be solved to give R_I , and the OTF is found using Equations (7) and (5). The OTF is useful because it allows the engineer to see directly how a test characterization from the completed test compares with the test input which would be needed to create a desired Index of Conservatism. Overtest Factors for the drop table and decaying sinusoid test are given in the next section.

ANALYSIS OF TEST CONSERVATISM

Analysis of the relative conservatism between the drop table, the decaying sinusoid, and field test data was carried out using a computer program developed to implement the analytical procedures described previously. The data base consisted of twenty-two field shocks, twenty-three ~1400g x 0.33 ms haversine shocks (denoted DROP1), twenty-five ~700 g x 0.33 ms haversine shocks (denoted DROP2), and twenty-five decaying sinusoid pulses (denoted DESIN). The SIS and SAA spectra are the shock characterizations which were chosen for the test conservatism analysis.

Figures 8a and 8b are plots of coefficient of variation, k , versus frequency for the SIS and SAA spectra, respectively. Average values of k over the entire frequency range shown in the plots are also noted. This data indicates the SIS spectrum has a larger amount of variability than the SAA plots. The curves in Figures 8a and 8b were used to justify the decision to use an overall coefficient of variation of 0.15 in subsequent calculations of IOC and OTF used for comparisons of individual field and test time histories.

The plots of SIS and SAA means, plus and minus one standard deviation, are presented in Figures 9-11. Figure 9a underscores the usefulness of the SIS spectrum in revealing that frequency content of the field data exceeds the DROP1 data at ~1500 Hz, even though the SAA spectrum indicates a higher DROP1 level over all frequencies. The predominance of the 1500 Hz frequency component in the field data is emphasized in the SIS plots, while the SAA spectra show comparable levels at frequencies above 1500 Hz.

Once the mean and coefficient of variation have been determined by a statistical analysis of all of the data, IOC (Figure 12) and OTF (Figure 13) plots can be created by implementing Equations (3) and (5) on the computer. Negative values on the IOC plots indicate an undertest.

and positive values indicate an overtest. It is important to observe that while the decaying sinusoid test is unconservative over most of the frequency range, it alone provides a conservative test at the predominant frequency (~1500 Hz) of the field data.

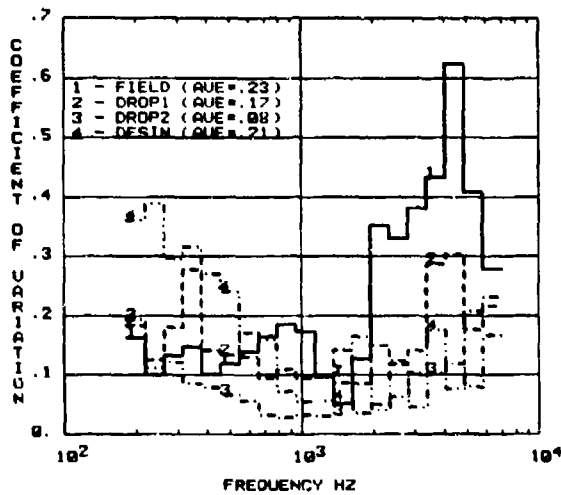


Figure 8a Coefficient of Variation of Field and Test Data SIS Plots (Time Duration = .005 Seconds)

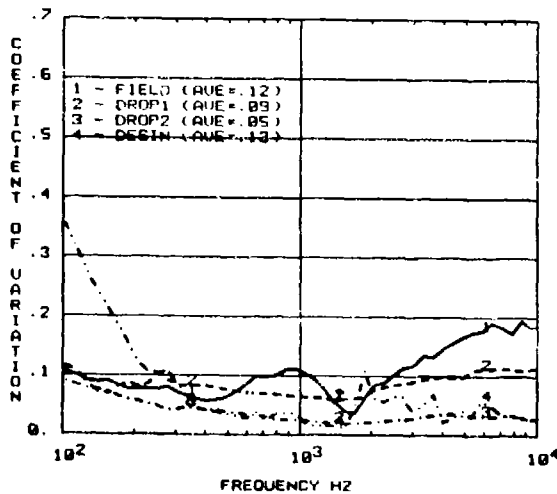


Figure 8b Coefficients of Variation of Field and Test Data SAA Plots (Damping = 0.03)

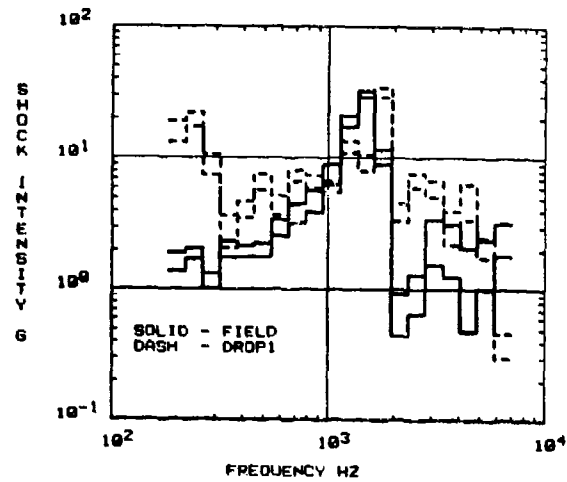


Figure 9a Comparison of Mean \pm One Standard Deviation SIS Between Field Data and DROP1 Test Data (Time Duration = 0.005 Seconds)

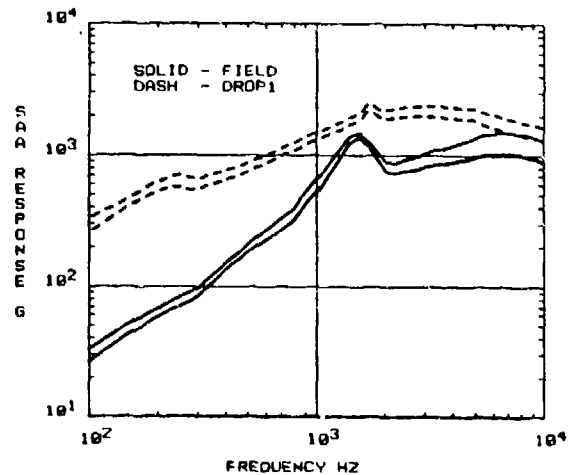


Figure 9b Comparison of Mean \pm One Standard Deviation SAA Data Between Field Data and DROP1 Test Data (Damping = 0.03)

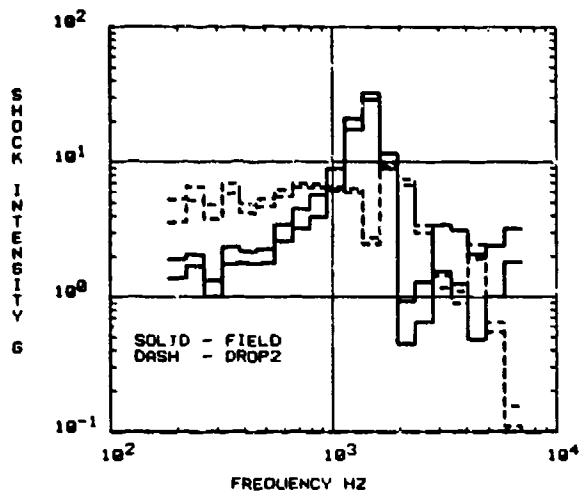


Figure 10a Comparison of Mean \pm One Standard Deviation SIS Data Between Field Data and DROP2 Test Data (Time Duration = 0.005 Seconds)

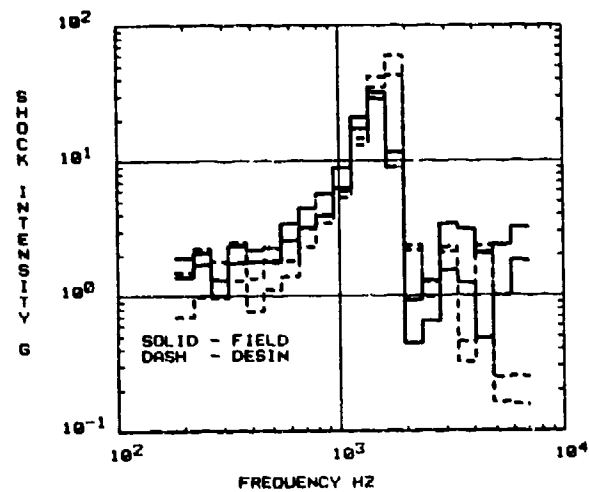


Figure 11a Comparison of Mean \pm One Standard Deviation SIS Data Between Field Data and DESIN Test Data (Time Duration = 0.005 Seconds)

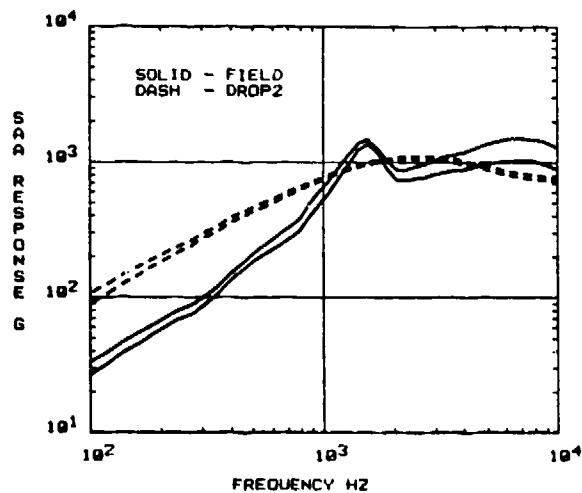


Figure 10b Comparison of Mean \pm One Standard Deviation SAA Data Between Field Data and DROP2 Test Data (Damping = 0.03)

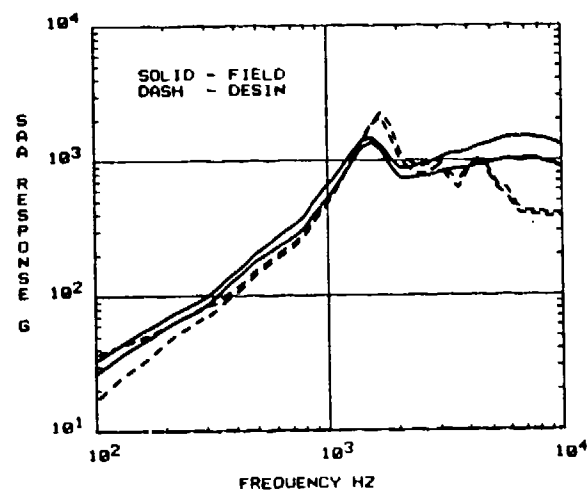


Figure 11b Comparison of Mean \pm One Standard Deviation SAA Data Between Field Data and DESIN Test Data (Damping = 0.03)

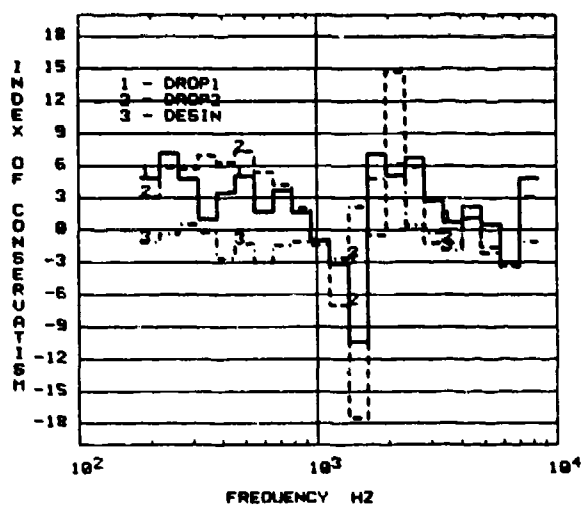


Figure 12a IOC Comparison for Shock Intensity Spectrum Between Field Data and the Three Test Data Series

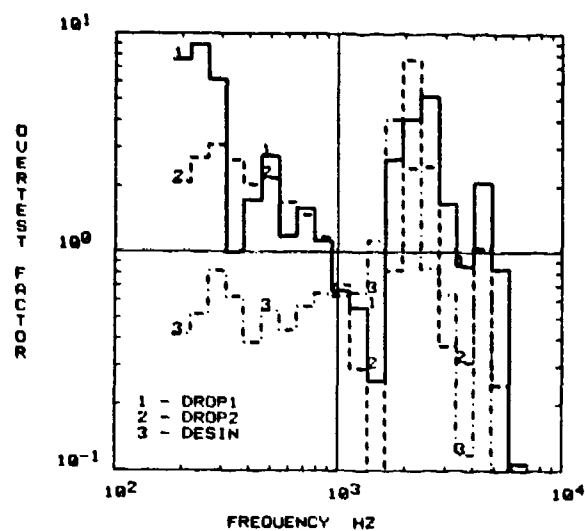


Figure 13a Overtest Factor for SIS with IOC=1

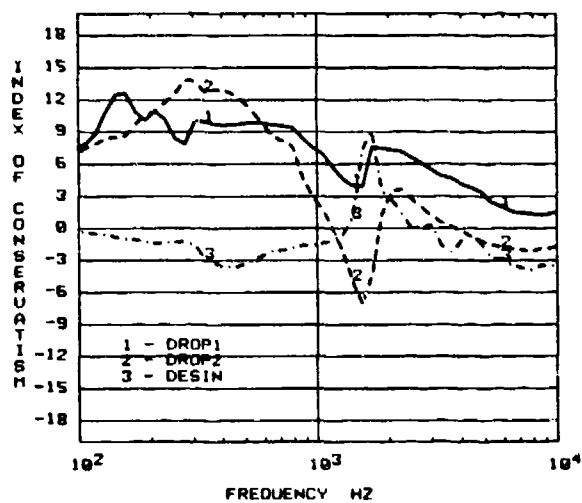


Figure 12b IOC Comparison for SAA Between Field Data and the 3 Test Data Series

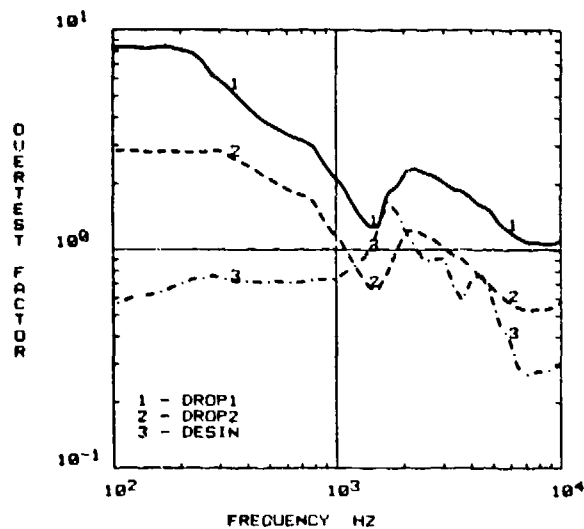


Figure 13b Overtest Factor Plot for SAA with IOC=1

The Overtest Factor plots in Figure 13 were calculated for a desired IOC value of one. This value was chosen as a reasonable degree of conservatism that would be sought in a component shock test. The OTF plot clearly shows the frequency range of overttest. The undertest experienced at 1500 Hz during the drop table tests is also clearly shown in Figure 13a. Should the analyst decide to use an average OTF value instead of the values at specific frequencies in Figures 13a and 13b, a graphical comparison of the average OTF values can be produced as shown in Figure 14. This simple plot of average OTF supports a conclusion that on the average, the drop table shocks are conservative, while the decaying sinusoid is not conservative.

One final analysis of the data involved using a single record from each of the test series and a coefficient of variation value of 0.15 to observe the changes in the conservatism analysis. The IOC and OTF were not significantly altered as is evidenced by the average OTF plot shown in Figure 15. Thus, for the data studied, a good indication of test conservatism can be estimated with only one field time history and one laboratory test record.

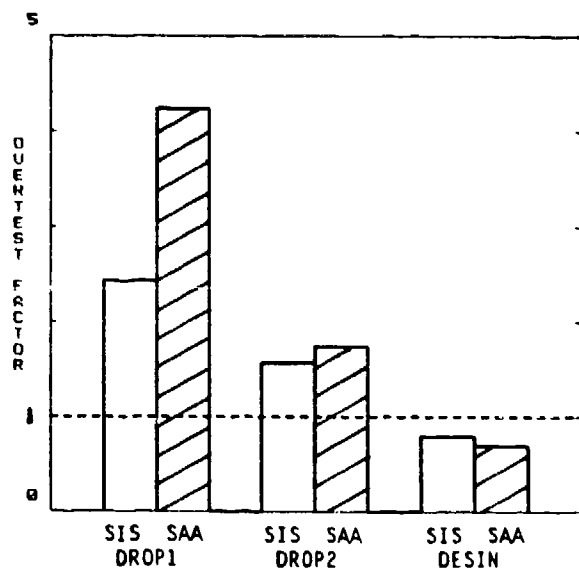


Figure 14 Average Overtest Factors for Full Ensemble of Test Inputs with IOC=1

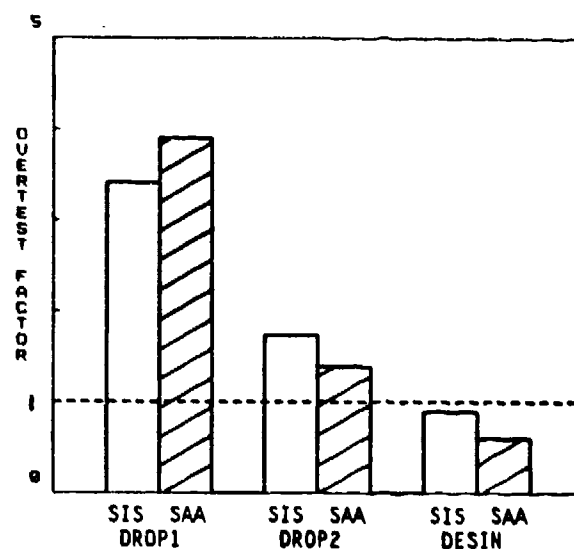


Figure 15 Average Overtest Factors for Single Test Inputs with IOC=1. (Assumed Coefficient of Variation: $k_T=k_F=0.15$)

CONCLUSIONS

Relative conservatism between the drop table shock tests and the decaying sinusoid shaker test has been analyzed using both shock intensity spectra (SIS) and absolute acceleration shock response spectra (SAA) as characterizations. Both an Index of Conservatism (IOC) and an Overtest Factor (OTF) plot was created for each shock characterization as a quantitative measure of shock conservatism. The SIS spectrum was shown to be a meaningful shock characterization because it reflects the amplitude, frequency content and duration of a shock time history. Overall, both the DROP1 and DROP2 table shock were conservative tests even though the SAA spectrum of the DROP2 test did not completely envelop the field data SAA spectrum. The comparable decaying sinusoid test data showed the test was on the average slightly underconservative. Utilizing the SIS spectrum revealed a narrow frequency range where the drop table test did not provide a conservative test in spite of the fact that SAA analysis implied a conservative test. In all cases, statistical variability of the shock characterizations was incorporated in the analyses.

The analysis technique presented in this paper represents a powerful tool which an analyst responsible for interpreting the results of the shock test can use to quantitatively judge test conservatism. Use of this technique will result in a better understanding of what the outcome of a shock test really means, and should foster the creation of shock test specifications which more consistently relate the field and test laboratory shock environments.

REFERENCES

1. Vigness, I., and Sullivan, J.R., "Shock Testing Machines," Shock and Vibration Handbook, Second Edition, Harris, C. M., and Crede, C. E., eds., New York: McGraw-Hill, 1976, pp.26-1, 19.
2. Smallwood, D.O., "Time History Synthesis for Shock Testing on Shakers," Seminar on Understanding Digital Control and Analysis in Vibration Test Systems, Greenbelt, Maryland, June 1976, pp. 23-41.
3. Kelly, R.D., and Richman, G., Principles and Techniques of Shock Data Analysis, The Shock and Vibration Information Center, USDOD, SVM-5, 1969.
4. Baca, T.J., "Characterization of Conservatism in Mechanical Shock Testing of Structures," SAND82-2186, Sandia National Laboratories, May 1983.
5. Baca, T.J., "Evaluation and Control of Conservatism in Drop Table Shock Tests," Shock and Vibration Bulletin, Vol. 53, Part 1, 1983, pp. 163-176.
6. Baca, T.J., "Alternative Shock Characterizations for Consistent Shock Test Specifications," Shock and Vibration Bulletin, Vol. 54, Part 2, 1984, pp. 109-130.